

NOTE TO USER

Page not included in the original manuscript are unavailable from the author or university. The manuscript was microfilmed as received.

XLVI

This is reproduction is the best copy available

UMI[®]

**Structures, thermochemistry, and dynamics of negative gas phase
cluster ions studied by pulsed-ionization high pressure mass
spectrometry and computational quantum chemistry techniques**

by

Bogdan Bogdanov

A thesis
presented to the University of Waterloo
in fulfilment of the
thesis requirement for the degree of
Doctor of Philosophy
in
Chemistry

Waterloo, Ontario, Canada, 2001

© Bogdan Bogdanov 2001



National Library
of Canada

Acquisitions and
Bibliographic Services

395 Wellington Street
Ottawa ON K1A 0N4
Canada

Bibliothèque nationale
du Canada

Acquisitions et
services bibliographiques

395, rue Wellington
Ottawa ON K1A 0N4
Canada

Your file *Votre référence*

Our file *Notre référence*

The author has granted a non-exclusive licence allowing the National Library of Canada to reproduce, loan, distribute or sell copies of this thesis in microform, paper or electronic formats.

The author retains ownership of the copyright in this thesis. Neither the thesis nor substantial extracts from it may be printed or otherwise reproduced without the author's permission.

L'auteur a accordé une licence non exclusive permettant à la Bibliothèque nationale du Canada de reproduire, prêter, distribuer ou vendre des copies de cette thèse sous la forme de microfiche/film, de reproduction sur papier ou sur format électronique.

L'auteur conserve la propriété du droit d'auteur qui protège cette thèse. Ni la thèse ni des extraits substantiels de celle-ci ne doivent être imprimés ou autrement reproduits sans son autorisation.

0-612-65224-6

Canada

The University of Waterloo requires the signatures of all persons using or photocopying this thesis. Please sign below, and give address and date.

Abstract

The interactions between halide ions and a variety of organic molecules have been investigated using pulsed-ionization high pressure mass spectrometry (PHPMS), and a variety of *ab initio*, density functional theory (DFT), and composite quantum chemistry methods. The organic substrates include alcohols, alkyl halides, trifluoromethyl halides, and fluorinated ether and acetones. The computations were performed to get more insight into the structures of the ion-molecule complexes and transition states, to model the experimental thermochemistry and IR characteristics of neutrals and ion-molecule complexes, and to obtain information on the potential energy surfaces for some reactions.

The standard enthalpy (ΔH°) and entropy (ΔS°) changes associated with the formation of the halide ion-alcohol complexes, $X^-(ROH)_n$ ($X = F, Cl, Br, I$; $R = CH_3, CH_3CH_2, (CH_3)_2CH, (CH_3)_3C$; $n = 1, 2, 3$), show that observed trends are mainly due to the radius of the halide ion, the alcohol polarizability, and the dipole-dipole repulsion and steric interactions when X , R , and n are the different variables, respectively. The ΔH° and ΔS° values obtained from the PHPMS experiments could be modeled accurately by computations at the MP2(full)/6-311++G(d,p)//B3LYP/6-311+G(d,p) level of theory. In addition, scaled MP2(full)/6-311++G(d,p) and B3LYP/6-311+G(d,p) normal mode vibrational frequencies were in good agreement with the limited amount of results obtained by others from vibrational predissociation spectroscopy (VPDS) experiments. Experimental kinetic data and computations show that the formation of the $Cl^-(HOCH_3)$ complex proceeds through a more complex mechanism than initially expected.

For a series of solvated S_N2 complexes, $(S)X^-(RY)$ ($X, Y = Cl, Br$; $R = (CH_3)_2CH$; $S = CH_3OH, CH_3CN, (CH_3)_2CO, CH_3CF_2H$), the ΔH° and ΔS° values associated with their formation were determined using PHPMS and solvent effects were observed. In addition, *ab initio* computations on a series of solvated S_N2 reactions confirm solvent effects on the energetics of these micro-solvated systems, as well as different binding characteristics in the solvated S_N2 complexes and transition states, indicating solvent reorganization.

Nucleophilic displacement reactions between halide ions and trifluoromethyl halides proceed through a back-side attack S_N2 mechanism, while complex formation proceeds through a front-side attack mechanism. For the $Cl^-(BrCF_3)$, $Cl^-(ICF_3)$, and $Br^-(BrCF_3)$ complexes the ΔH° and ΔS° values associated with their formation were determined by PHPMS. Good to excellent agreement was obtained with results from calculations at the B3LYP/6-311+G(3df)//B3LYP/6-311+G(d) level of theory. The S_N2 reaction proceeds through a direct mechanism and is initiated by electron transfer. Results from potential energy surface computations indicate that at ion kinetic energies above the threshold the reaction can take place without going through the $[XCF_3Y]^\ddagger$ transition state. Simulated cross sections show qualitative agreement with results obtained from FT-ICR experiments.

The thermochemistry measured by PHPMS for the formation of a series of chloride ion-fluorinated ether and acetone clusters shows the distinct influence of the number of fluorine atoms and the substitution pattern. Insights into the structures and thermochemistry was obtained from computations at the MP2/[6-311++G(3df,3dp)/6-311+G(2df,p)]//MP2/[6-31+G(d)/6-31G(d)] level of theory. In general, excellent agreement was obtained. Formation of the $Cl^-(CF_2HO CF_2H)$, $Cl^-(CF_3C(O)CF_2H)$, and the $Cl^-(CF_3C(O)CF_3)$ complexes gave rise to large negative ΔS° values, indicating hindrance of the methyl group rotations. The G3(MP2) was successfully applied to reproduce experimental deprotonation enthalpy changes, $\Delta_{acid}H^\circ_{298}$, accurately for a large series of (in)organic acids. Finally, new Fourier-transform infrared (FT-IR) spectra of fluoroacetone and pentafluoroacetone were recorded, while computations at the HF/6-31G(d) and B3LYP/6-311++G(3d,3p) levels of theory were used to model the IR spectra of a series of fluorinated acetones.

Acknowledgements

After a little bit more than five years of graduate school I have almost come to the end of a period in my life where I have spend most of my time in schools. Looking back it almost seems like yesterday when my parents took me for my first school day. Overall those years have been useful, interesting, and fun, but long. Fortunately, learning and teaching will not stop once I will leave the school world to enter the “real” world.

I would like to thank Professor T. B. McMahon for giving me the opportunity to come to Canada to continue my scientific training by doing research in an interesting field of chemistry. Also thank you Terry for your trust in my capabilities, for the encouragements when I was uncertain if things were OK, for nominating me for awards, for the many small hints, for corrections made to this thesis and the manuscripts that made them better, and the many great dinner parties and interesting non-scientific talks.

Also thanks to my Ph.D. Advisory Committee members Professors M. Barra, W. P. Power, and A. L. Schwan for listening to me once a year and for reading my (morbidly obese) thesis.

Without financial assistance from the University of Waterloo and the Department of Chemistry I could not have started and continued my graduate studies, especially when I was still an international student, neither have attended various conferences that have been a very useful part of my scientific training.

I would like to thank my family for their constant love, support and trust, and for providing me with a solid base in life from which it is easy to explore and develop. We have always been so close, but by being far away for a while we have even become closer. I hope we will spend many more years together.

Also thanks to my relatives, friends, and ex-colleagues for their support and interest during my stay here.

I have been extremely fortunate to have met many very nice people in and outside of the University of Waterloo over the years that I have been here. All of them have contributed in their own unique way to my whole experience. First and most of all I

would like to thank Ms. Dorothy Sherk and Ms. Mavis Skelton for having given me a home away from home. Your love, kindness, friendship, support, wisdom, and so much more have been just wonderful, not just to me or my family, but to so many people. Also many thanks to Harvey and Gladys Stickley, and Kathleen Sherk for the time when they were in Vermont Street. May God bless you now and forever. I would to thank my initial “shadow student” Helen for giving me a smooth start when I came here, and for her advice and friendship. Without you my stay would have been so much different. Also many thanks to Cor and Tine Ambachtsheer for the nice visits and lunches, and for helping me being a little bit less poor. To all of you I did not mention, thank you and I know and will not forget you and your contributions.

I would also like to thank my (ex-) colleagues in the lab for their contributions to the friendly atmosphere, and for help and advice: Eugene, Feng, Graham, Guillaume, Kion, Jackie, Jan, Jeff, Jon, Mahmoud, Michael, Pauline, Sasha, Scott, Steven, Tanya, Tiffany, Tim, and Travis.

Special thanks to Kion, who was my office mate for over one year in total, and during those periods I had the most fun of my whole stay here in the lab. Also thank you for introducing me to the wonderful world of Gaussian. In addition, the numerous afternoon patio visits, and visits to the Grad House, movies, The Huether, The Fox, Failte, and so on were always fun and interesting. You are one of the few people I have met with a true passion for quality and science, and I hope you can enjoy the latter one until you retire. Skaal and have a beer and G&T on me!

Dave Bowen and Dave Rieder from the Science Shop, and Sander Mommers have been very helpful during the hardest period of my stay here, when the 8-80 provided me with lots of frustration and no signals and data, but also with an opportunity to learn new things that have given me a new look on chemistry and gas phase ion chemistry.

Colin Campbell of IST has been on numerous occasions a tremendous help when I had Mathcad problems.

Without the help of Professor R. J. LeRoy, Greg Clark, Doug Weir, and Michael Miao no Gaussian computations could have been performed on Watsci, Scienide, and Isenguard.

Dustin Dickens is thanked for his helped with recording the FT-IR spectra of the fluorinated acetones in Chapter 7.

I would like to thank Dozia, Steve, and Carey, and the many students for their contributions to making being a chemistry TA a pleasant and valuable experience. I never could have imagined that I would ever be a Dutch TA or Zwarte Piet. Thank you Dr. Zweers (Sander) and Geertje for giving me the unique opportunity to help many students with learning my native language. In addition, I would like to thank Dr. Zweers for given me the opportunity to become more cultured by the visits to the Concertgebouw Orkest and Stratford Festival performances, and for keeping my Dutch taste by visiting the Toko.

Toni thanks a lot for all our talks about soccer, politics, Europe, and so on. I will miss looking for news and making prints for you.

I would like to thank Professors J. D. Goddard and F. Tureček, and Drs. Y. Okuno and T. Sølling (Theis) for giving me valuable advice to run certain types of computations.

Without the help, advice, and support of Professor N. M. M. Nibbering (Nico) and Drs. J. C. Kleingeld (Jan) and H. E. K. Matimba (Henri) I never would have come here.

I would like to thank Professor S. Hammerum and Dr. S. Ingemann (Steen) for having me participate in their fluorophenol and anisol project.

It is also time to acknowledge all the good and inspiring teachers I had and fortunately I have already known for a long time how fortunate I have been in that respect. Thank you. I have tried hard to be a good teacher myself as I have tried to be a good student.

Thanks to all my (ex-) roommates who have made my stay when I was not in the office or lab nice, interesting, and memorable.

Thank you Martina for giving me the initial inspiration and courage to do what I have done, and I hope I have given you the same to follow your dreams. Hab ein schönes Leben.

Also thanks to the inventors of the telephone, e-mail, Internet, and Gaussian. Without them my stay would have been lonelier and less interesting, and my thesis a lot thinner and more blah blah blah.

Last, but not least, I would like to thank my dearest Jen for all her help and support. Your love and friendship have given me new energy, courage, creativity, motivation, and hope to finish this project in time and with pride and joy.

After acknowledging a lot of other people, it is also time to acknowledge myself. To date I have not seen any thesis where this was done. It is time to say that I am proud of what I have accomplished, not only scientifically, but most of all as a person. Very few decisions in a life may be made with 100% certainty. This has not been one of them. But I think it has been a good one, despite that I had to sacrifice other things that are and/or were very dear to me. Since I have been here I have worked in a very dedicated and consistent manner, always trying to look for something more interesting and pushing myself. At least I know that I want to be a chemist, and being a physical chemist for a while has made me a better chemist. It is a pity that some of the ideas that I got at the end of my thesis could not be explored by me, but I am already happy that I got the ideas. I am also glad that I have made time and spent money to do all kinds of other things like sports, travelling, movies, getting my driver's license, and enjoying all kinds of bigger and smaller things. I do not want to deny that there have also been many moments of doubt about my capability, about being here, about what I really want, about where I want to be, about what else I could have been, about how I could have used this time learning other things instead of focussing more and more on less and less. At least this whole experience has not made me bitter and I know that years from now a smile will appear when I think of the time I have spent here.

I had some realistic expectations that could not be fulfilled due to circumstances beyond my control, but the true joy came from the unexpected things and people that came into my life. In addition, it brought me back in touch with the younger me, and closer to both my cultural backgrounds. Finally, it got many times confirmed that the unconditional love my parents gave/give me is one of the most important and most beautiful things in a person's life. Thank you!

To my parents

Aan mijn ouders

Мојим Родитељима

Table of Contents

Abstract		iv
Acknowledgements		vi
Table of Contents		xi
List of Tables		xvii
List of Illustrations		xxvii
List of Abbreviations		xlvii
Chapter 1	Introduction	1
	1.1 Gas Phase Cluster Ions	1
	1.1.1 Generation	1
	1.1.2 Structures	2
	1.1.3 Reactivity	2
	1.2 Ion Solvation	4
	1.2.1 Condensed Phase	4
	1.2.2 Gas Phase	6
	1.3 Ion Thermochemistry	6
	1.3.1 Definitions	6
	1.3.2 Methods	7
	1.3.2.1 Equilibrium Reactions	7
	1.3.2.2 Threshold CID	8
	1.3.2.3 Light Induced Reactions	9
	1.3.2.4 Kinetic Method	11
	1.4 Uni- and Bimolecular Gas Phase Ion-Molecule Reactions	13
	1.4.1 RRKM Theory	13
	1.4.2 ADO Theory	14
	1.5 Ion Spectroscopy	15
	1.6 Scope of Thesis	16
	1.7 References	17

Chapter 2	Experimental	21
2.1	Pulsed-ionization High Pressure Mass Spectrometry	21
2.2	Pulsed-ionization High Pressure Mass Spectrometer	25
2.3	Ion and Cluster Ion Formation	28
2.4	References	29
Chapter 3	Computational methods	31
3.1	Introduction	31
3.2	Hartree-Fock	31
3.3	MP2	33
3.4	B3LYP	33
3.5	Composite Methods	35
3.6	Basis Sets	35
3.7	Geometry Optimizations	37
3.8	Normal Mode Vibrational Frequencies and IR Intensities	37
3.9	Thermochemistry	40
3.10	NPA Charge	43
3.11	Software and Hardware	43
3.12	References	44
Chapter 4	Structures, thermochemistry, dynamics, and spectroscopy of halide ion and bihalide ion-alcohol clusters in the gas phase	46
4.1	Introduction	46
4.2	Experimental	49
4.3	Computational	53
4.4	Results and Discussion	54
4.4.1	Experimental Thermochemistry	54
4.4.2	Computational Thermochemistry	77
4.4.3	Computations versus Experiments	78
4.4.4	Other Computational Work	81

4.4.5	Structures	82
4.4.6	Natural Population Analysis Charges versus Thermochemistry	90
4.4.7	Kinetics of Complex Formation	95
4.4.8	Vibrational Frequencies	96
4.4.9	Vibrational Frequencies versus Thermochemistry	104
4.4.10	Potential Energy Surfaces	104
4.5	Conclusions	121
4.6	References and Notes	123
Chapter 5	Thermochemistry and structures of solvated S_N2 complexes and transition states in the gas phase	132
5.1	Introduction	132
5.2	Experimental	139
5.3	Computational	141
5.4	Results and Discussion	142
5.4.1	Structures	142
5.4.2	Experimental Thermochemistry	157
5.4.3	Computational Thermochemistry	167
5.4.4	Potential Energy Surfaces	180
5.5	Conclusions	183
5.6	References and Notes	184
Chapter 6	Gas phase S_N2 reactions of halide ions and trifluoromethyl halides: front- and backside attack versus complex formation	189
6.1	Introduction	189
6.2	Experimental	196
6.3	Computational	197
6.4	Results and Discussion	198
6.4.1	Structures	198
6.4.2	Experimental and Computational Thermochemistry	210

6.4.3	Normal Mode Vibrational Frequencies	231
6.4.4	Natural Population Analysis Charges	233
6.4.5	Potential Energy Surfaces	234
6.5	Conclusions	246
6.6	References	247
Chapter 7	Thermochemistry, structures, dynamics, and infrared spectroscopy of chloride ion-fluorinated ether and acetone complexes and neutrals in the gas phase	255
7.1	Introduction	255
7.2	Experimental	257
7.3	Computational	259
7.4	Results and Discussion	261
7.4.1	Structures	261
7.4.2	Experimental Thermochemistry	284
7.4.3	Computational Thermochemistry	298
7.4.4	Experiment versus Computations	302
7.4.5	Gas Phase Acidities of Fluorinated Acetones	303
7.4.6	Vibrational Frequencies of Fluorinated Acetones	307
7.4.7	Rotational Barriers	326
7.4.8	Natural Population Analysis Charges	327
7.4.9	Potential Energy Surfaces	328
7.5	Conclusions	330
7.6	References	332
Chapter 8	Conclusions	337
Appendix A	Electronic Energies	343
	Table A1	344
	Table A2	345
	Table A3	346

Table A4	347
Table A5	348
Table A6	349
Table A7	350
Table A8	351
Table A9	352
Table A10	353
Table A11	354
Table A12	355
Table A13	356
Table A14	357
Table A15	358
Table A16	359
Table A17	361
Table A18	363
Table A19	365
Appendix B Gaussian Input Files	366
B1 Frequency Calculation	367
B2 Transition State Calculation	368
B3 ECP Calculation	369
B4 Scan Calculation	371
Appendix C Simulated IR spectra	372
C1 CH ₃ OH	373
C2 F ⁻ (CH ₃ OH)	374
C3 Cl ⁻ (CH ₃ OH)	375
C4 Br ⁻ (CH ₃ OH)	376
C5 I ⁻ (CH ₃ OH)	377
C6 (CH ₃ OH)F ⁻ (CH ₃ OH)	378
C7 F ⁻ (CH ₃ OH)(CH ₃ OH)	379

C8	CF_3OH	380
C9	$\text{Cl}^-(\text{CF}_3\text{OH})$	381
C10	$(\text{ClH})\text{CF}_3\text{O}^-$	382
C11	$(\text{FH})\text{Cl}^-(\text{CF}_2\text{O})$	383
C12	HF	384
C13	HF_2^-	385
C14	$\text{HF}_2^-(\text{CH}_3\text{OH})$	386
C15	$(\text{CH}_3\text{OH})\text{HF}_2^-(\text{CH}_3\text{OH})$	387

List of Tables

Table 4.1	<p>Overview of the computational and experimental thermochemistry for the $F^- + ROH = F^-(ROH)$ clustering equilibria ($R = CH_3, CH_3CH_2, (CH_3)_2CH, (CH_3)_3C$; a = 6-311++G(d,p), b = 6-311+G(d,p), c = 6-311++G(3df,3pd)).</p>	59
Table 4.2	<p>Overview of the computational and experimental thermochemistry for the $Cl^- + ROH = Cl^-(ROH)$ clustering equilibria ($R = CH_3, CH_3CH_2, (CH_3)_2CH, (CH_3)_3C$; a = 6-311++G(d,p), b = 6-311+G(d,p), c = 6-311++G(3df,3pd)).</p>	60
Table 4.3	<p>Overview of the computational and experimental thermochemistry for the $X^- + ROH = X^-(ROH)$ clustering equilibria ($X = Br, I$; $R = CH_3, CH_3CH_2$; a = 6-311++G(d,p), b = 6-311+G(d,p), c = 6-311++G(3df,3pd), d = LanL2DZ, e = Stuttgart RLC ECP, f = CRENBL ECP).</p>	62
Table 4.4	<p>Overview of the computational and experimental thermochemistry for the $X^-(ROH) + ROH = X^-(ROH)_2$ clustering equilibria ($X = F, Cl$; $R = CH_3, (CH_3)_2CH$; a = 6-311++G(d,p), b = 6-311+G(d,p), c = 6-311++G(3df,3pd)).</p>	63
Table 4.5	<p>Overview of the experimental thermochemistry for the $F^-(ROH)_n + ROH = F^-(ROH)_{n+1}$ clustering equilibria ($R = CD_3, CH_3CH_2, (CH_3)_2CH, (CH_3)_3C$; $n = 1, 2$).</p>	64
Table 4.6	<p>Overview of the experimental thermochemistry for the $Cl^-(ROH)_n + ROH = Cl^-(ROH)_{n+1}$ clustering equilibria ($R = CH_3, CH_3CH_2, (CH_3)_2CH, (CH_3)_3C$; $n = 1, 2$).</p>	65

Table 4.7	Overview of the experimental thermochemistry for the $\text{Br}^-(\text{ROH})_n + \text{ROH} \rightleftharpoons \text{Br}^-(\text{ROH})_{n+1}$ clustering equilibria ($\text{R} = \text{CH}_3, \text{CH}_3\text{CH}_2, (\text{CH}_3)_2\text{CH}, (\text{CH}_3)_3\text{C}$; $n = 0, 1, 2$).	66
Table 4.8	Overview of the experimental thermochemistry for the $\Gamma(\text{ROH})_n + \text{ROH} \rightleftharpoons \Gamma(\text{ROH})_{n+1}$ clustering equilibria ($\text{R} = \text{CH}_3, \text{CH}_3\text{CH}_2, (\text{CH}_3)_2\text{CH}, (\text{CH}_3)_3\text{C}$; $n = 0, 1, 2$).	67
Table 4.9	Overview of the experimental thermochemistry for the $\text{F}^-(\text{CH}_3\text{OH}) + \text{ROH} \rightleftharpoons \text{F}^-(\text{ROH}) + \text{CH}_3\text{OH}$ clustering equilibria ($\text{R} = \text{CH}_3\text{CH}_2, (\text{CH}_3)_2\text{CH}, (\text{CH}_3)_3\text{C}$).	69
Table 4.10	Overview of the relative contributions of the $(\text{CH}_3\text{OH})\text{X}^-(\text{CH}_3\text{OH})$ and $\text{X}^-(\text{CH}_3\text{OH})(\text{CH}_3\text{OH})$ isomeric cluster ions at different temperatures ($\text{X} = \text{F}, \text{Cl}$).	80
Table 4.11	Overview of ΔH_{298}° for the $\text{X}^- + \text{ROH} \rightleftharpoons \text{X}^-(\text{ROH})$ clustering equilibria, and $\nu(\text{X}^-\cdots\text{HOR})$ and $\nu(\text{RO}-\text{H})$ harmonic normal mode vibrational frequencies of the $\text{X}^-(\text{ROH})$ complexes ($\text{X} = \text{F}, \text{Cl}, \text{Br}, \text{I}$; $\text{R} = \text{CH}_3, \text{CH}_3\text{CH}_2, (\text{CH}_3)_2\text{CH}, (\text{CH}_3)_3\text{C}$; a = 6-311++G(d,p), b = 6-311+G(d,p), e = Stuttgart RLC ECP).	105
Table 5.1	Overview of published work on solvated $\text{S}_{\text{N}}2$ reactions in the gas phase.	136
Table 5.2	Overview of the computational HF/a, MP2/a and experimental structural data of the solvent and methyl halide molecules studied.	143

Table 5.3	Overview of the computational MP2/a structural data of the halide ion-solvent molecule complexes.	144
Table 5.4	Overview of the computational MP2/a structural data of the (un)solvated S _N 2 complexes.	148
Table 5.5	Overview of the computational MP2/a structural data of the (un)solvated S _N 2 transition states.	152
Table 5.6	Overview of the experimental PHPMS thermochemistry for the X ⁻ + S = X ⁻ (S) (X = Cl, Br; S = CH ₃ OH, CH ₃ CN, (CH ₃) ₂ CO, CH ₃ CF ₂ H) and X ⁻ + RY = X ⁻ (RY) (X, Y = Cl, Br; R = (CH ₃) ₂ CH) clustering equilibria.	158
Table 5.7	Overview of the experimental PHPMS thermochemistry for the Cl ⁻ (S) + RCl = (S)Cl ⁻ (RCl) and Cl ⁻ (RCl) + S = (S)Cl ⁻ (RCl) (S = CH ₃ OH, CH ₃ CN, (CH ₃) ₂ CO, CH ₃ CF ₂ H; R = (CH ₃) ₂ CH) clustering equilibria.	159
Table 5.8	Overview of the experimental PHPMS thermochemistry for the Cl ⁻ (S) + RBr = (S)Cl ⁻ (RBr) and Cl ⁻ (RBr) + S = (S)Cl ⁻ (RBr) (S = CH ₃ OH, CH ₃ CN, (CH ₃) ₂ CO, CH ₃ CF ₂ H; R = (CH ₃) ₂ CH) clustering equilibria.	160
Table 5.9	Overview of the experimental PHPMS thermochemistry for the Br ⁻ (S) + RCl = (S)Br ⁻ (RCl) and Br ⁻ (RCl) + S = (S)Br ⁻ (RCl) (S = CH ₃ OH, CH ₃ CN, (CH ₃) ₂ CO, CH ₃ CF ₂ H; R = (CH ₃) ₂ CH) clustering equilibria.	161

Table 5.10	Overview of the computational and experimental literature thermochemical data for the $X^- + S \rightleftharpoons X^-(S)$ and $X^- + CH_3Y \rightleftharpoons X^-(CH_3Y)$ ($X = Cl, Br, S = H_2O, H_2S, NH_3, PH_3, SO_2, CH_3OCH_3$; $Y = Cl, Br, I$) clustering equilibria.	169
Table 5.11	Overview of the computational MP2//MP2 ΔH_{298}^0 values for the $X^-(S) + CH_3Y \rightleftharpoons (S)X^-(CH_3Y)$ and $X^-(CH_3Y) + S \rightleftharpoons (S)X^-(CH_3Y)$ ($X = Cl, Br, S = H_2O, H_2S, NH_3, PH_3, SO_2, CH_3OCH_3$; $Y = Cl, Br, I$) clustering equilibria.	171
Table 5.12	Overview of the computational MP2//MP2 ΔH_{298}^\ddagger and experimental ΔH^\ddagger values for the $X^- + CH_2YZ \rightarrow [XCH_2ZY]^-$ and $X^-(S) + CH_2YZ$ $\rightarrow [(S)XCH_2ZY]^-$ ($X = Cl, Br, Y = Cl, Br, I; Z = H, CN; S = H_2O, H_2S,$ $NH_3, PH_3, SO_2, CH_3OCH_3$) reactions.	172
Table 6.1	Overview of the computational B3LYP/a ([a/b] for $X = I$) and experimental structural data of CF_3X and CF_3X^{\bullet} ($X = Cl, Br, I$).	200
Table 6.2	Overview of the computational B3LYP/a structural data of the $X^-(YCF_3)$ and $X^-(CF_3X)$ complexes ($X = F, Cl, Br; Y = Cl, Br, I$).	204
Table 6.3	Overview of the computational B3LYP/a structural data of the $[XCF_3Y]^-$ transition states ($X, Y = F, Cl, Br$).	207
Table 6.4	Overview of the computational B3LYP/a structural data of the $[CF_3XY]^-$ transition states ($X, Y = Cl, Br$).	208
Table 6.5	Overview of the computational B3LYP/c//B3LYP/a and MP2(full)/a and experimental structural data of XY and XY^{\bullet} ($X, Y = Cl, Br, I$).	212

Table 6.6	Overview of the experimental PHPMS and computational B3LYP/c //B3LYP/a thermochemistry for the formation of $X^-(YCF_3)$ and $X^-(CF_3Y)$ complexes ($X = F, Cl, Br; Y = Cl, Br, I$).	214
Table 6.7	Overview of the computational B3LYP/c//B3LYP/a and experimental thermochemistry of the $X^- + CF_3Y \rightarrow Y^- + CF_3X$, $XY^{\bullet} + CF_3^{\bullet}$, $CF_3Y^{\bullet} + X^{\bullet}$, and $CF_3^- + XY$ reactions ($X = F, Cl, Br; Y = Cl, Br$).	216
Table 6.8	Overview of the experimental standard heats of formations ($\Delta_f H^\circ$) of various neutrals and (radical) anions.	217
Table 6.9	Overview of the computational B3LYP/c//B3LYP/a, MP2(full)/a, G3, and G3(MP2), and experimental electron affinities (EA) and bond dissociation energies (BDE) of various (radical) neutrals and radical anion.	219
Table 6.10	Overview of the computational B3LYP/c//B3LYP/a thermochemistry of the $X^- + CF_3Y \rightarrow [XCF_3Y]^-$ and $[CF_3XY]^-$ reactions ($X = F, Cl, Br; Y = Cl, Br$).	221
Table 6.11	Overview of the E_{cm} and E_{lab} values from computational B3LYP/c //B3LYP/a ΔH_{298}^\ddagger values for the various $X^- + CF_3Y \rightarrow [XCF_3Y]^-$ and $[CF_3XY]^-$ reactions ($X, Y = Cl, Br$).	223
Table 6.12	Overview of the computational B3LYP/a ([a/b] for $X = I$) and experimental normal mode vibrational frequencies for CF_3X ($X = Cl, Br, I$).	232

Table 7.1	Overview of the experimental and computational thermochemical data for the chloride ion-ether clustering equilibria $\text{Cl}^-(\text{ether-F}_n)_m + \text{ether-F}_n \rightleftharpoons \text{Cl}^-(\text{ether-F}_n)_{m+1}$ (ether = $(\text{CH}_3)_2\text{O}$, $(\text{CH}_3\text{CH}_2)_2\text{O}$, CH_3OCF_3 , $(\text{CF}_2\text{H})_2\text{O}$, $\text{CF}_3\text{OCF}_2\text{H}$, $(\text{CF}_3)_2\text{O}$; $m = 0, 1$).	286
Table 7.2	Overview of the experimental and computational thermochemical data for the chloride ion-acetone clustering equilibria $\text{Cl}^- + \text{acetone-F}_n \rightleftharpoons \text{Cl}^-(\text{acetone-F}_n)$ (acetone- F_n = $\text{CH}_3\text{C}(\text{O})\text{CH}_3$, $\text{CH}_3\text{C}(\text{O})\text{CH}_2\text{F}$, $\text{CH}_3\text{C}(\text{O})\text{CF}_3$, $\text{CF}_3\text{C}(\text{O})\text{CF}_2\text{H}$, $\text{CF}_3\text{C}(\text{O})\text{CF}_3$).	288
Table 7.3	Overview of the standard ambient G3(MP2) enthalpies, H_{298}° (G3(MP2)), and standard ambient G3(MP2), G3, and experimental heats of formation, $\Delta_f H_{298}^\circ$ (G3(MP2)), $\Delta_f H_{298}^\circ$ (G3), and $\Delta_f H_{298}^\circ$ (exp) of a series of molecules used to determine the standard ambient heat of formation of CH_3OCF_3 .	300
Table 7.4	Overview of the standard ambient G3(MP2) and G3 enthalpies, H_{298}° (G3(MP2)) and H_{298}° (G3), of a series of small to medium sized (in)organic acids and their conjugated bases.	305
Table 7.5	Overview of the standard ambient G3(MP2), G3, and experimental deprotonation enthalpies, $\Delta_{\text{acid}} H_{298}^\circ$ (G3(MP2)), $\Delta_{\text{acid}} H_{298}^\circ$ (G3), and $\Delta_{\text{acid}} H_{298}^\circ$ (exp), of a series of small to medium sized (in)organic acids.	306
Table 7.6	Overview of the scaled HF/6-31G(d), B3LYP/6-311++G(3d,3p), and experimental normal mode vibrational frequencies and IR intensities of $\text{CH}_3\text{C}(\text{O})\text{CH}_3$.	310

Table 7.7	Overview of the scaled HF/6-31G(d), B3LYP/6-311++G(3d,3p), and experimental normal mode vibrational frequencies and IR intensities of CH ₃ C(O)CH ₂ F.	314
Table 7.8	Overview of the scaled HF/6-31G(d), B3LYP/6-311++G(3d,3p), and experimental normal mode vibrational frequencies and IR intensities of CH ₃ C(O)CF ₃ .	317
Table 7.9	Overview of the scaled HF/6-31G(d), B3LYP/6-311++G(3d,3p), and experimental normal mode vibrational frequencies and IR intensities of CF ₃ C(O)CF ₂ H.	320
Table 7.10	Overview of the scaled HF/6-31G(d), B3LYP/6-311++G(3d,3p), and experimental normal mode vibrational frequencies and IR intensities of CF ₃ C(O)CF ₃ .	323
Table A1	Overview of the results from B3LYP/6-311+G(d,p), MP2(full)/6-311++G(d,p)//B3LYP/6-311+G(d,p), and B3LYP/6-311++G(3df,3pd)//B3LYP/6-311+G(d,p) computations for the halide ions and alcohols (d = LanL2DZ, e = CRENBL ECP, f = Stuttgart RLC ECP).	340
Table A2	Overview of the results from B3LYP/6-311+G(d,p), MP2(full)/6-311++G(d,p)//B3LYP/6-311+G(d,p), and B3LYP/6-311++G(3df,3pd)//B3LYP/6-311+G(d,p) computations for the halide ion-alcohol complexes (d = LanL2DZ, e = CRENBL ECP, f = Stuttgart RLC ECP).	341
Table A3	Overview of the results from B3LYP/6-311+G(d,p) and MP2(full)/6-311++G(d,p)//B3LYP/6-311+G(d,p) computations for the alcohol dimers and halide ion-alcohol dimers.	342

Table A4	Overview of the results from MP2(full)/6-311++G(d,p) computations for the halide ions, alcohols, and halide ion-alcohol complexes (d = LanL2DZ, f = Stuttgart RLC ECP).	343
Table A5	Overview of the results from G3(MP2) computations for the $F^-(HF)_n(CH_3OH)_m$ systems (n = 0, 1; m = 0, 1, 2).	344
Table A6	Overview of the results from HF/6-31+G(d,p), MP2(fc)/6-31+G(d,p), MP2(fc)/6-311+G(3df,2p)//MP2(fc)/6-31+G(d,p), and G2(MP2) computations for the chloride ion-solvent complexes.	345
Table A7	Overview of the results from HF/6-31+G(d,p), MP2(fc)/6-31+G(d,p), MP2(fc)/6-311+G(3df,2p)//MP2(fc)/6-31+G(d,p), and G2(MP2) computations for the solvated S_N2 complexes and transition states.	346
Table A8	Overview of the results from HF/6-31+G(d), HF/[6-31+G(d)/LanL2DZ(spdx)], MP2(fc)/6-31+G(d), MP2(fc)/[6-31+G(d)/LanL2DZ(spdx)], MP2(fc)/6-311+G(3df,2p)//MP2(fc)/6-31+G(d), and MP2(fc)/[6-311+G(3df,2p)/LanL2DZ(spdx)]//MP2(fc)/[6-31+G(d)/LanL2DZ(spdx)] computations for bromine and iodine containing S_N2 substrates and solvent molecules.	347
Table A9	Overview of the results from HF/6-31+G(d), HF/[6-31+G(d)/LanL2DZ(spdx)], MP2(fc)/6-31+G(d), MP2(fc)/[6-31+G(d)/LanL2DZ(spdx)], MP2(fc)/6-311+G(3df,2p)//MP2(fc)/6-31+G(d), and MP2(fc)/[6-311+G(3df,2p)/LanL2DZ(spdx)]//MP2(fc)/[6-31+G(d)/LanL2DZ(spdx)] computations for bromine and iodine containing (un)solvated S_N2 complexes and transition states.	348

Table A10	Overview of the results from B3LYP/[6-31+G(d)/LanL2DZ(sp)] and B3LYP/[6-311+G(3df,2p)/LanL2DZ(sp)]//B3LYP/[6-31+G(d)/LanL2DZ(sp)] computations for the CH ₃ Y and [ClCH ₃ Y] ⁻ systems (Y = Br, I).	349
Table A11	Overview of the results from B3LYP/6-311+G(d) and B3LYP/6-311+G(3df)//B3LYP/6-311+G(d) computations for halide ions and radicals, and some fluorinated hydrocarbons.	350
Table A12	Overview of the results from B3LYP/6-311+G(d) and B3LYP/6-311+G(3df)//B3LYP/6-311+G(d) computations for dihalides, trifluoromethyl halides, and their corresponding radical anions (d = LanL2DZ(sp) and LanL2DZ(sp)]//LanL2DZ(sp), f = LanL2DZ).	351
Table A13	Overview of the results from B3LYP/6-311+G(d) and B3LYP/6-311+G(3df)// B3LYP/6-311+G(d) computations for halide ion-trifluoromethyl halide complexes.	352
Table A14	Overview of the results from B3LYP/6-311+G(d) and B3LYP/6-311+G(3df)// B3LYP/6-311+G(d) computations for halide ion-trifluoromethyl halide transition states.	353
Table A15	Overview of the results from MP2(full)/6-311+G(d), G3, and G3(MP2) computations for halide ions and radicals, bihalide neutrals and radical anions, and trifluoromethyl halides and radical anions.	354
Table A16	Overview of the results from HF/6-31G(d), MP2(fc)/6-31G(d), and MP2(fc)/6-311+G(2df,p)//MP2(fc)/6-31G(d) computations of (fluorinated) ethers.	355

Table A17	Overview of the results from HF/[6-31+G(d)/6-31G(d)], MP2(fc)/[6-31+G(d)/6-31G(d)], and MP2(fc)/[6-311++G(3df,3pd)/6-311+G(2df,p)]//MP2(fc)/[6-31+G(d)/6-31G(d)] computations of chloride ion-(fluorinated) ether complexes.	357
Table A18	Overview of the results from HF/6-31G(d), MP2(fc)/6-31G(d), and MP2(fc)/6-311+G(2df,p)//MP2(fc)/6-31G(d) computations of (fluorinated) acetones, and HF/[6-31+G(d)/6-31G(d)], MP2(fc)/[6-31+G(d)/6-31G(d)], and MP2(fc)/[6-311++G(3df,3pd)//6-311+G(2df,p)]//MP2(fc)/[6-31+G(d)/6-31G(d)] computations of chloride ion-(fluorinated) acetone complexes.	359
Table A19	Overview of the results from HF and MP2(fc) computations for chloride ion and radical using various basis sets.	361

List of Illustrations

Figure 2.1	Qualitative display of the regions for various modes of diffusion in a typical PHPMS experiment with initially high ionization density.	23
Figure 2.2	Schematic of the PHPMS instrument used.	26
Figure 3.1	Flowchart for quasi-Newton algorithms for geometry optimizations.	38
Figure 4.1	Experimental Van't Hoff plots for the halide ion-alcohol clustering equilibria $X^-(ROH)_n + ROH \rightleftharpoons X^-(ROH)_{n+1}$ ($X = F, Br; R = CH_3; n = 0, 1, 2$).	55
Figure 4.2	Experimental Van't Hoff plots for the halide ion-alcohol clustering equilibria $X^-(ROH)_n + ROH \rightleftharpoons X^-(ROH)_{n+1}$ ($X = C, I; R = CH_3; n = 0, 1, 2$).	55
Figure 4.3	Experimental Van't Hoff plots for the halide ion-alcohol clustering equilibria $X^-(ROH)_n + ROH \rightleftharpoons X^-(ROH)_{n+1}$ ($X = F, Br; R = CH_3CH_2; n = 0, 1, 2$) (F,0 is a calculated Van't Hoff plot).	56
Figure 4.4	Experimental Van't Hoff plots for the halide ion-alcohol clustering equilibria $X^-(ROH)_n + ROH \rightleftharpoons X^-(ROH)_{n+1}$ ($X = C, I; R = CH_3CH_2; n = 0, 1, 2$).	56
Figure 4.5	Experimental Van't Hoff plots for the halide ion-alcohol clustering equilibria $X^-(ROH)_n + ROH \rightleftharpoons X^-(ROH)_{n+1}$ ($X = F, Br; R = (CH_3)_2CH; n = 0, 1, 2$) (F,0 is a calculated Van't Hoff plot).	57

Figure 4.6	Experimental Van't Hoff plots for the halide ion-alcohol clustering equilibria $X^-(ROH)_n + ROH = X^-(ROH)_{n+1}$ ($X = C, I; R = (CH_3)_2CH;$ $n = 0, 1, 2$).	57
Figure 4.7	Experimental Van't Hoff plots for the halide ion-alcohol clustering equilibria $X^-(ROH)_n + ROH = X^-(ROH)_{n+1}$ ($X = F, Br; R = (CH_3)_3C;$ $n = 0, 1, 2$) (F,0 is a calculated Van't Hoff plot).	58
Figure 4.8	Experimental Van't Hoff plots for the halide ion-alcohol clustering equilibria $X^-(ROH)_n + ROH = X^-(ROH)_{n+1}$ ($X = C, I; R = (CH_3)_3C;$ $n = 0, 1, 2$).	58
Figure 4.9	Experimental Van't Hoff plots for the fluoride ion-methanol/alcohol complex exchange equilibria $F^-(CH_3OH) + ROH = F^-(ROH) + CH_3OH$ ($R = CH_3CH_2, (CH_3)_2CH, (CH_3)_3C$).	70
Figure 4.10	Plot of the the negative standard enthalpy change for the $X^- + ROH = X^-(ROH)$ clustering equilibria, $-\Delta H^\circ(X^-(ROH))$, versus the alcohol polarizability, α_{ROH} .	72
Figure 4.11	Plot of the deprotonation enthalpy difference between ROH and HX, $\Delta_{acid}H(ROH) - \Delta_{acid}H(HX)$ versus the negative standard enthalpy change for the $X^- + ROH = X^-(ROH)$ clustering equilibria, $-\Delta H^\circ(X^-(ROH))$.	72
Figure 4.12	Single well potential energy surface for the halide ion-alcohol adducts.	73
Figure 4.13	Optimized MP2(full)/a structure of $F^-(CH_3OH)$.	83

Figure 4.14	Optimized MP2(full)/a structure of $\text{Cl}^-(\text{CH}_3\text{OH})$.	83
Figure 4.15	Optimized MP2(full)/a structure of $\text{Br}^-(\text{CH}_3\text{OH})$.	83
Figure 4.16	Optimized MP2(full)/[a/e] structure of $\text{I}^-(\text{CH}_3\text{OH})$.	84
Figure 4.17	Plot of the MP2(full)/a ([a/e] for $X = \text{I}$) calculated $X^- \cdots \text{H}-\text{OCH}_3$ angle, $A(X^- \cdots \text{H}-\text{OCH}_3)$, versus the $X^- \cdots \text{HOCH}_3$ distance, $R(X^- \cdots \text{HOCH}_3)$, ($X = \text{F}, \text{Cl}, \text{Br}, \text{I}$).	84
Figure 4.18	Optimized B3LYP/b structure of $\text{F}^-((\text{CH}_3)_3\text{COH})$.	86
Figure 4.19	Optimized B3LYP/b structure of $\text{Cl}^-((\text{CH}_3)_3\text{COH})$.	86
Figure 4.20	Optimized B3LYP/b structure of $(\text{CH}_3\text{OH})(\text{CH}_3\text{OH})$.	87
Figure 4.21	Optimized B3LYP/b structure of $(\text{CH}_3\text{OH})\text{F}^-(\text{CH}_3\text{OH})$.	88
Figure 4.22	Optimized B3LYP/b structure of $\text{F}^-(\text{CH}_3\text{OH})(\text{CH}_3\text{OH})$.	88
Figure 4.23	Optimized B3LYP/b structure of $(\text{CH}_3\text{OH})\text{Cl}^-(\text{CH}_3\text{OH})$.	91
Figure 4.24	Optimized B3LYP/b structure of $\text{Cl}^-(\text{CH}_3\text{OH})(\text{CH}_3\text{OH})$.	91
Figure 4.25	Optimized MP2(full)/6-31G(d) structure of $\text{HF}_2^-(\text{CH}_3\text{OH})$.	92
Figure 4.26	Optimized MP2(full)/6-31G(d) structure of $(\text{CH}_3\text{OH})\text{HF}_2^-(\text{CH}_3\text{OH})$.	92

- Figure 4.27** Plot of the MP2/a ([a/e] for X = I) negative standard ambient enthalpy for the $X^- + \text{CH}_3\text{OH} = X^-(\text{CH}_3\text{OH})$ clustering equilibrium, $-\Delta H^\circ_{298}(X^-(\text{CH}_3\text{OH}))$, versus the NPA charges on the halide ion, $-q(\text{NPA})(X^-)$, (X = F, Cl, Br, I). 94
- Figure 4.28** High pressure ion source mass spectrum at the following experimental conditions: $P_{\text{ion source}} = 4.0$ Torr, $T_{\text{ion source}} = 298$ K, $P(\text{CH}_4) = 765$ Torr, $P(\text{CH}_3\text{OH}) = 0.25$ Torr, $P(\text{CCl}_4) < 0.05$ Torr. 97
- Figure 4.29** Time-intensity profiles for the $^{35}\text{Cl}^-$, $^{35}\text{Cl}^-(\text{CH}_3\text{OH})$, and $^{35}\text{Cl}^-(\text{CH}_3\text{OH})_2$ ions at the ions source condition of Figure 4.28. 98
- Figure 4.30** Normalized time-intensity profiles of Figure 4.29. 98
- Figure 4.31** Plot of $1/k_{\text{app}}$ versus $1/[\text{CH}_4]$. 99
- Figure 4.32** Plot of $\ln(k_f/T^2)$ versus $1/T$ (S&C = Su and Chesnavich). 99
- Figure 4.33** Simulated IR spectrum of $(\text{CH}_3\text{OH})\text{Cl}^-(\text{CH}_3\text{OH})$ calculated at the B3LYP/b level of theory and scaled by 0.9640. 102
- Figure 4.34** Simulated IR spectrum of $\text{Cl}^-(\text{CH}_3\text{OH})(\text{CH}_3\text{OH})$ calculated at the B3LYP/b level of theory and scaled by 0.9640. 102
- Figure 4.35** Simulated IR spectrum of $(\text{CH}_3\text{OH})(\text{CH}_3\text{OH})$ calculated at the B3LYP/b level of theory and scaled by 0.9640. 103

- Figure 4.36** Plot of the MP2/a ([a/e] for X = I) calculated, $X^- \cdots HOCH_3$ and CH_3O-H normal mode vibrational frequencies, $\nu(X^- \cdots HOCH_3)$ and $\nu(CH_3O-H)$, respectively, versus the negative standard ambient enthalpy of association to form $X^-(CH_3OH)$, $-\Delta H_{298}^\circ(X^-(CH_3OH))$, (X = F, Cl, Br, I). 106
- Figure 4.37** Plot of the calculated B3LYP/b $X^- \cdots HOR$ and $RO-H$ normal mode vibrational frequencies, $\nu(X^- \cdots HOR)$ and $\nu(RO-H)$, respectively, versus the MP2(full)/a//B3LYP/b negative standard ambient enthalpy change to form $X^-(ROH)$, $-\Delta H_{298}^\circ(X^-(ROH))$ (X = F, Cl, Br, R = CH_3 , CH_3CH_2 , $(CH_3)_2CH$, $(CH_3)_3C$). 108
- Figure 4.38** Definition of the $X^- \cdots HOCH_3$ distance, $R(X^- \cdots HOCH_3)$, and the $X^- \cdots H-OCH_3$ angle, $A(X^- \cdots H-OCH_3)$, parameters used for the normal two-dimensional potential energy surface scans at the MP2/a ([a/e] for X = I) level of theory (X = F, Cl, Br, I). 110
- Figure 4.39** Plot of the MP2/a $F^-(CH_3OH)$ two-dimensional potential energy surface (contour lines in $kcal\ mol^{-1}$). 112
- Figure 4.40** Plot of the MP2/a $Cl^-(CH_3OH)$ two-dimensional potential energy surface (contour lines in $kcal\ mol^{-1}$). 113
- Figure 4.41** Plot of the MP2/a $Br^-(CH_3OH)$ two-dimensional potential energy surface (contour lines in $kcal\ mol^{-1}$). 114
- Figure 4.42** Plot of the MP2/[a/e] $I^-(CH_3OH)$ two-dimensional potential energy surface (contour lines in $kcal\ mol^{-1}$). 115

Figure 4.43	Plot of the MP2(fc)/g energy, $E_{\text{MP2}(\text{fc})/6-31-\text{G}(\text{d,p})}$, versus the $\text{F}^- \cdots \text{HOCH}_3$ distance, $R(\text{F}^- \cdots \text{HOCH}_3)$, from a relaxed scan computation.	116
Figure 4.44	Plot of the MP2(fc)/g energy, $E_{\text{MP2}(\text{fc})/6-31-\text{G}(\text{d,p})}$, versus the $\text{Cl}^- \cdots \text{HOCH}_3$ distance, $R(\text{Cl}^- \cdots \text{HOCH}_3)$, from a relaxed scan computation.	116
Figure 4.45	Plot of the MP2(fc)/[g/h] energy, $E_{\text{MP2}(\text{fc})/[6-31-\text{G}(\text{d,p})/\text{LanL2DZ}(\text{spd})]}$, versus the $\text{Br}^- \cdots \text{HOCH}_3$ distance, $R(\text{Br}^- \cdots \text{HOCH}_3)$, from a relaxed scan computation.	117
Figure 4.46	Plot of the MP2(fc)/[g/h] energy, $E_{\text{MP2}(\text{fc})/[6-31-\text{G}(\text{d,p})/\text{LanL2DZ}(\text{spd})]}$, versus the $\Gamma \cdots \text{HOCH}_3$ distance, $R(\Gamma \cdots \text{HOCH}_3)$, from a relaxed scan computation.	118
Figure 4.47	MP2(fc)/g energy profile for the $\text{Cl}^- + \text{CF}_3\text{OH} \rightarrow \text{CF}_3\text{O}^- + \text{HCl}$ gas phase proton transfer reaction.	120
Figure 5.1	Condensed phase unimodal reaction energy profile (R = reactants, TS = transition state, P = products).	133
Figure 5.2	Condensed phase double-well reaction energy profile for weak solvation (RC = reactants complex, PC = products complex).	133
Figure 5.3	Condensed phase double-well reaction energy profile for strong and asynchronous desolvation and ion-molecule complexation (desolv = desolvation).	134
Figure 5.4	Gas phase double-well reaction energy profile.	134

Figure 5.5	Optimized MP2(fc)/a structure of CH ₃ Cl.	145
Figure 5.6	Optimized MP2(fc)/a structure of Cl ⁻ (H ₂ O).	145
Figure 5.7	Optimized MP2(fc)/a structure of Cl ⁻ (H ₂ S).	145
Figure 5.8	Optimized MP2(fc)/a structure of Cl ⁻ (NH ₃).	146
Figure 5.9	Optimized MP2(fc)/a structure of Cl ⁻ (PH ₃).	146
Figure 5.10	Optimized MP2(fc)/a structure of Cl ⁻ (SO ₂).	146
Figure 5.11	Optimized MP2(fc)/a structure of (H ₂ O)Cl ⁻ (CH ₃ Cl).	149
Figure 5.12	Optimized MP2(fc)/a structure of (H ₂ S)Cl ⁻ (CH ₃ Cl).	149
Figure 5.13	Optimized MP2(fc)/a structure of (NH ₃)Cl ⁻ (CH ₃ Cl).	149
Figure 5.14	Optimized MP2(fc)/a structure of (PH ₃)Cl ⁻ (CH ₃ Cl).	150
Figure 5.15	Optimized MP2(fc)/a structure of (SO ₂)Cl ⁻ (CH ₃ Cl).	150
Figure 5.16	Optimized MP2(fc)/[c/d] structure of (H ₂ O)Cl ⁻ (CH ₃ Br).	151
Figure 5.17	Optimized MP2(fc)/[c/d] structure of (H ₂ O)Br ⁻ (CH ₃ Cl).	151
Figure 5.18	Optimized MP2(fc)/a structure of [(H ₂ O)ClCH ₃ Cl] ⁻ .	153
Figure 5.19	Optimized MP2(fc)/a structure of [(H ₂ S)ClCH ₃ Cl] ⁻ .	153

Figure 5.20	Optimized MP2(fc)/a structure of $[(\text{NH}_3)\text{ClCH}_3\text{Cl}]^-$.	153
Figure 5.21	Optimized MP2(fc)/a structure of $[(\text{PH}_3)\text{ClCH}_3\text{Cl}]^-$.	154
Figure 5.22	Optimized MP2(fc)/a structure of $[(\text{SO}_2)\text{ClCH}_3\text{Cl}]^-$.	154
Figure 5.23	Optimized MP2(fc)/[c/d] structure of $[(\text{H}_2\text{O})\text{ClCH}_3\text{Br}]^-$.	156
Figure 5.24	Optimized MP2(fc)/[c/d] structure of $[(\text{H}_2\text{O})\text{BrCH}_3\text{Cl}]^-$.	156
Figure 5.25	Optimized MP2(fc)/[c/d] structure of $[(\text{H}_2\text{O})\text{ClCH}_2\text{CNBr}]^-$.	156
Figure 5.26	Van't Hoff plots for the $\text{Cl}^- + \text{S} \rightleftharpoons \text{Cl}^-(\text{S})$ ($\text{S} = (\text{CH}_3)_2\text{CO}$, $\text{CH}_3\text{CF}_2\text{H}$) clustering equilibria.	162
Figure 5.27	Van't Hoff plots for the $\text{Br}^- + \text{S} \rightleftharpoons \text{Br}^-(\text{S})$ ($\text{S} = (\text{CH}_3)_2\text{CO}$, $\text{CH}_3\text{CF}_2\text{H}$) clustering equilibria.	162
Figure 5.28	Van't Hoff plots for the $\text{Cl}^-(\text{S}) + \text{RCl} \rightleftharpoons (\text{S})\text{Cl}^-(\text{RCl})$ and $\text{Cl}^-(\text{RCl}) + \text{S} \rightleftharpoons (\text{S})\text{Cl}^-(\text{RCl})$ ($\text{S} = \text{CH}_3\text{OH}$; $\text{R} = (\text{CH}_3)_2\text{CH}$) clustering equilibria.	163
Figure 5.29	Van't Hoff plots for the $\text{Cl}^-(\text{S}) + \text{RCl} \rightleftharpoons (\text{S})\text{Cl}^-(\text{RCl})$ and $\text{Cl}^-(\text{RCl}) + \text{S} \rightleftharpoons (\text{S})\text{Cl}^-(\text{RCl})$ ($\text{S} = \text{CH}_3\text{CN}$; $\text{R} = (\text{CH}_3)_2\text{CH}$) clustering equilibria.	163
Figure 5.30	Van't Hoff plots for the $\text{Cl}^-(\text{S}) + \text{RCl} \rightleftharpoons (\text{S})\text{Cl}^-(\text{RCl})$ and $\text{Cl}^-(\text{RCl}) + \text{S} \rightleftharpoons (\text{S})\text{Cl}^-(\text{RCl})$ ($\text{S} = (\text{CH}_3)_2\text{CO}$; $\text{R} = (\text{CH}_3)_2\text{CH}$) clustering equilibria.	164

- Figure 5.31** Van't Hoff plots for the $\text{Cl}^-(\text{S}) + \text{RCl} \rightleftharpoons (\text{S})\text{Cl}^-(\text{RCl})$ and $\text{Cl}^-(\text{RCl}) + \text{S} \rightleftharpoons (\text{S})\text{Cl}^-(\text{RCl})$ ($\text{S} = \text{CH}_3\text{CF}_2\text{H}$; $\text{R} = (\text{CH}_3)_2\text{CH}$) clustering equilibria. 164
- Figure 5.32** Van't Hoff plots for the $\text{Cl}^-(\text{S}) + \text{RBr} \rightleftharpoons (\text{S})\text{Cl}^-(\text{RBr})$ and $\text{Cl}^-(\text{RBr}) + \text{S} \rightleftharpoons (\text{S})\text{Cl}^-(\text{RBr})$ ($\text{S} = \text{CH}_3\text{OH}$; $\text{R} = (\text{CH}_3)_2\text{CH}$) clustering equilibria. 165
- Figure 5.33** Van't Hoff plots for the $\text{Cl}^-(\text{S}) + \text{RBr} \rightleftharpoons (\text{S})\text{Cl}^-(\text{RBr})$ and $\text{Cl}^-(\text{RBr}) + \text{S} \rightleftharpoons (\text{S})\text{Cl}^-(\text{RBr})$ ($\text{S} = \text{CH}_3\text{CN}$; $\text{R} = (\text{CH}_3)_2\text{CH}$) clustering equilibria. 165
- Figure 5.34** Van't Hoff plots for the $\text{Cl}^-(\text{S}) + \text{RBr} \rightleftharpoons (\text{S})\text{Cl}^-(\text{RBr})$ and $\text{Cl}^-(\text{RBr}) + \text{S} \rightleftharpoons (\text{S})\text{Cl}^-(\text{RBr})$ ($\text{S} = (\text{CH}_3)_2\text{CO}$; $\text{R} = (\text{CH}_3)_2\text{CH}$) clustering equilibria. 166
- Figure 5.35** Van't Hoff plots for the $\text{Cl}^-(\text{S}) + \text{RBr} \rightleftharpoons (\text{S})\text{Cl}^-(\text{RBr})$ and $\text{Cl}^-(\text{RBr}) + \text{S} \rightleftharpoons (\text{S})\text{Cl}^-(\text{RBr})$ ($\text{S} = \text{CH}_3\text{CF}_2\text{H}$; $\text{R} = (\text{CH}_3)_2\text{CH}$) clustering equilibria. 166
- Figure 5.36** Thermochemical cycle for the formation of solvated $\text{S}_{\text{N}}2$ complexes. 167
- Figure 5.37** Plot of $-\Delta H_{298}^{\circ}$ for the formation of $\text{Cl}^-(\text{S})$ versus $-\Delta H_{298}^{\circ}$ for the formation of $(\text{S})\text{Cl}^-(\text{CH}_3\text{Cl})$ and $[(\text{S})\text{ClCH}_3\text{Cl}]^-$ ($\text{S} = \text{H}_2\text{O}, \text{H}_2\text{S}, \text{NH}_3, \text{PH}_3, \text{SO}_2$). (the open circle and dotted line represent the expected value and trend line for $\text{S} = \text{SO}_2$ based on the other four solvent molecules). 175
- Figure 5.38** Schematic MP2/b//MP2/a potential energy profiles for the $\text{Cl}^- + \text{CH}_3\text{Cl}$ and $\text{Cl}^-(\text{S}) + \text{CH}_3\text{Cl}$ reactions ($\text{S} = \text{H}_2\text{O}, \text{H}_2\text{S}, \text{NH}_3, \text{PH}_3, \text{SO}_2$). 176

Figure 5.39	MP2[c/d] potential energy profiles for the $\text{Cl}^- + \text{CH}_3\text{Br} \rightarrow \text{Br}^- + \text{CH}_3\text{Cl}$ and $\text{Cl}^-(\text{H}_2\text{O}) + \text{CH}_3\text{Br} \rightarrow \text{Br}^- + (\text{CH}_3\text{Cl})(\text{H}_2\text{O})$ and $\text{Br}^-(\text{H}_2\text{O}) + \text{CH}_3\text{Cl}$ reactions.	182
Figure 6.1	Hypothetical potential energy profile for a condensed phase $\text{S}_{\text{N}}2$ reaction.	190
Figure 6.2	Hypothetical potential energy profile for a gas phase $\text{S}_{\text{N}}2$ reaction.	190
Figure 6.3	Optimized B3LYP/6-311+G(d) structure of CF_3Cl .	199
Figure 6.4	Optimized B3LYP/6-311+G(d) structure of CF_3Br .	199
Figure 6.5	Optimized B3LYP/[6-311+G(d)/LanL2DZ] structure of CF_3I .	199
Figure 6.6	Optimized B3LYP/6-311+G(d) structure of CF_3Cl^* .	202
Figure 6.7	Optimized B3LYP/6-311+G(d) structure of $\text{F}^-(\text{BrCF}_3)$.	202
Figure 6.8	Optimized B3LYP/6-311+G(d) structure of $\text{F}^-(\text{CF}_3\text{Br})$.	202
Figure 6.9	Optimized B3LYP/6-311+G(d) structure of $\text{Cl}^-(\text{ClCF}_3)$.	203
Figure 6.10	Optimized B3LYP/6-311+G(d) structure of $\text{Cl}^-(\text{CF}_3\text{Cl})$.	203
Figure 6.11	Optimized B3LYP/6-311+G(d) structure of $[\text{FCF}_3\text{Br}]^-$.	206
Figure 6.12	Optimized B3LYP/6-311+G(d) structure of $[\text{ClCF}_3\text{Cl}]^-$.	206
Figure 6.13	Optimized B3LYP/6-311+G(d) structure of $[\text{CF}_3\text{Cl}_2]^-$.	206

Figure 6.14	Atom labeling in the $[\text{CF}_3\text{XY}]^-$ transition states.	209
Figure 6.15	Optimized B3LYP/6-311+G(d) structure of $[\text{BrCF}_2\text{Cl}_2]^-$.	209
Figure 6.16	Optimized B3LYP/6-311+G(d) structure of $[\text{CF}_2\text{Cl}_2\text{Br}]^-$.	209
Figure 6.17	Van't Hoff plots for the halide ion-trifluoro methyl halide clustering equilibria $\text{X}^- + \text{CF}_3\text{Y} = \text{X}^-(\text{CF}_3\text{Y})$ ($\text{X} = \text{Cl}, \text{Br}; \text{Y} = \text{Br}$).	213
Figure 6.18	Schematic B3LYP/c//B3LYP/a potential energy profile for the various $\text{Cl}^- + \text{CF}_3\text{Cl}$ reactions.	225
Figure 6.19	Schematic B3LYP/c//B3LYP/a potential energy profile for the various $\text{Cl}^- + \text{CF}_3\text{Br}$ reactions.	226
Figure 6.20	Schematic B3LYP/c//B3LYP/a potential energy profile for the various $\text{Br}^- + \text{CF}_3\text{Br}$ reactions.	227
Figure 6.21	Gas phase double well potential energy diagram with the definitions of ΔE^\ddagger and ΔE for the Marcus expression applied to $\text{S}_{\text{N}}2$ reactions.	228
Figure 6.22	State correlation diagram for the non-identity $\text{S}_{\text{N}}2$ reaction $\text{Y}^- + \text{RX} \rightarrow \text{X}^- + \text{RY}$.	230
Figure 6.23	B3LYP/a potential energy surfaces for the $\text{F}^- + \text{CF}_3\text{Br} \rightarrow \text{Br}^- + \text{CF}_4$ and $\text{F}^- + \text{CF}_3\text{Br} = \text{F}^-(\text{BrCF}_3)$ reactions.	236
Figure 6.24	B3LYP/a potential energy scans for the $\text{Cl}^- + \text{CF}_3\text{Br} = \text{Cl}^-(\text{BrCF}_3)$ and $\text{Cl}^- + \text{CF}_3\text{Br} = \text{Cl}^-(\text{BrCF}_3)$ clustering equilibria.	237

Figure 6.25	HF/6-31G(d) potential energy surface for the $\text{Cl}^- + \text{CF}_3\text{Cl}$ back-side attack $\text{S}_{\text{N}}2$ reaction ($0 \leq E_{\text{HF/6-31G(d)}} \leq 80 \text{ kcal mol}^{-1}$, contour lines in 5 kcal mol^{-1} increments).	238
Figure 6.26	HF/6-31G(d) potential energy surface for the $\text{Cl}^- + \text{CF}_3\text{Cl}$ back-side attack $\text{S}_{\text{N}}2$ reaction ($-5 \leq E_{\text{HF/6-31G(d)}} \leq 0 \text{ kcal mol}^{-1}$, contour lines in $0.25 \text{ kcal mol}^{-1}$ increments).	239
Figure 6.27	B3LYP/a threshold energy pathway for the $\text{Cl}^- + \text{CF}_3\text{Cl} \rightarrow [\text{ClCF}_3\text{Cl}]^- \rightarrow \text{ClCF}_3 + \text{Cl}^-$ back-side attack $\text{S}_{\text{N}}2$ reaction.	240
Figure 6.28	HF/6-31G(d) threshold energy pathway hard-sphere line-of-centre cross section for the $\text{Cl}^- + \text{CF}_3\text{Cl} \rightarrow [\text{ClCF}_3\text{Cl}]^- \rightarrow \text{ClCF}_3 + \text{Cl}^-$ back-side attack $\text{S}_{\text{N}}2$ reaction as a function of Cl^- centre-of-mass kinetic energy.	242
Figure 6.29	Experimental relative Cl^- intensity as a function of the Br^- centre-of-mass kinetic energy of the $\text{Br}^- + \text{CF}_2\text{Cl}_2 \rightarrow \text{Cl}^- + \text{CF}_2\text{ClBr}$ $\text{S}_{\text{N}}2$ reaction (from Reference 88).	243
Figure 6.30	HF/6-31G(d) barrier height as a function of the $\text{Cl}-\text{C}-\text{Cl}$ angle from the $\text{Cl}^- + \text{CF}_3\text{Cl}$ potential energy surface in Figure 6.24.	244
Figure 6.31	HF/6-31G(d) angle-corrected hard-sphere line-of-centre cross section for the $\text{Cl}^- + \text{CF}_3\text{Cl} \rightarrow [\text{ClCF}_3\text{Cl}]^- \rightarrow \text{ClCF}_3 + \text{Cl}^-$ back-side attack $\text{S}_{\text{N}}2$ reaction as a function of Cl^- centre-of-mass kinetic energy.	245

Figure 7.1	Time-intensity profile for the $\text{Cl}^-((\text{CF}_2\text{H})_2\text{O}) + (\text{CF}_2\text{H})_2\text{O} = \text{Cl}^-((\text{CF}_2\text{H})_2\text{O})_2$ clustering equilibrium at the following experimental conditions: $P_{\text{ion source}} = 4.00$ Torr, $T_{\text{ion source}} = 352$ K, $P(\text{CH}_4) = 3.97$ Torr, $P((\text{CF}_2\text{H})_2\text{O}) = 0.03$ Torr, $P(\text{CCl}_4) \ll 0.01$ Torr.	258
Figure 7.2	Normalized time-intensity profile of Figure 7.1.	258
Figure 7.3	Optimized MP2/6-31G(d) structure of $(\text{CH}_3)_2\text{O}$.	262
Figure 7.4	Optimized MP2/6-31G(d) structure of $(\text{CH}_3\text{CH}_2)_2\text{O}$ (rotamer 1).	262
Figure 7.5	Optimized MP2/6-31G(d) structure of $(\text{CH}_3\text{CH}_2)_2\text{O}$ (rotamer 2).	262
Figure 7.6	Optimized MP2/6-31G(d) structure of CH_3OCF_3 .	263
Figure 7.7	Optimized MP2/6-31G(d) structure of $(\text{CF}_2\text{H})_2\text{O}$ (rotamer 1).	263
Figure 7.8	Optimized MP2/6-31G(d) structure of $(\text{CF}_2\text{H})_2\text{O}$ (rotamer 2).	263
Figure 7.9	Optimized MP2/6-31G(d) structure of $(\text{CF}_2\text{H})_2\text{O}$ (rotamer 3).	264
Figure 7.10	Optimized MP2/6-31G(d) structure of $\text{CF}_3\text{OCF}_2\text{H}$ (rotamer 1).	264
Figure 7.11	Optimized MP2/6-31G(d) structure of $\text{CF}_3\text{OCF}_2\text{H}$ (rotamer 2).	264
Figure 7.12	Optimized MP2/6-31G(d) structure of $(\text{CF}_3)_2\text{O}$.	265
Figure 7.13	Optimized MP2/6-31G(d) structure of $\text{CH}_3\text{C}(\text{O})\text{CH}_3$.	265
Figure 7.14	Optimized MP2/6-31G(d) structure of $\text{CH}_3\text{C}(\text{O})\text{CH}_2\text{F}$ (rotamer 1).	265

Figure 7.15	Optimized MP2/6-31G(d) structure of CH ₃ C(O)CH ₂ F (rotamer 2).	266
Figure 7.16	Optimized MP2/6-31G(d) structure of CH ₂ C(OH)CH ₂ F.	266
Figure 7.17	Optimized MP2/6-31G(d) structure of CH ₃ C(O)CF ₃ .	266
Figure 7.18	Optimized MP2/6-31G(d) structure of CH ₂ FC(O)CH ₂ F.	267
Figure 7.19	Optimized MP2/6-31G(d) structure of CF ₃ C(O)CF ₂ H.	267
Figure 7.20	Optimized MP2/6-31G(d) structure of CF ₃ C(O)CF ₃ .	267
Figure 7.21	Optimized MP2/[6-31+G(d)/6-31G(d)] structure of Cl ⁻ ((CH ₃) ₂ O).	270
Figure 7.22	Optimized MP2/[6-31+G(d)/6-31G(d)] structure of Cl ⁻ ((CH ₃ CH ₂) ₂ O) (rotamer 1).	270
Figure 7.23	Optimized MP2/[6-31+G(d)/6-31G(d)] structure of Cl ⁻ ((CH ₃ CH ₂) ₂ O) (rotamer 2).	270
Figure 7.24	Optimized MP2/[6-31+G(d)/6-31G(d)] structure of Cl ⁻ (CH ₃ OCF ₃).	271
Figure 7.25	Optimized MP2/[6-31+G(d)/6-31G(d)] structure of Cl ⁻ ((CF ₂ H) ₂ O) (rotamer 1).	271
Figure 7.26	Optimized MP2/[6-31+G(d)/6-31G(d)] structure of Cl ⁻ ((CF ₂ H) ₂ O) (rotamer 2, isomer 1).	271
Figure 7.27	Optimized MP2/[6-31+G(d)/6-31G(d)] structure of Cl ⁻ ((CF ₂ H) ₂ O) (rotamer 2, isomer 2).	272

Figure 7.28	Optimized MP2/[6-31+G(d)/6-31G(d)] structure of $\text{Cl}^-((\text{CF}_2\text{H})_2\text{O})$ (rotamer 4).	272
Figure 7.29	Optimized MP2/[6-31+G(d)/6-31G(d)] structure of $\text{Cl}^-(\text{CF}_3\text{OCF}_2\text{H})$ (rotamer 1).	272
Figure 7.30	Optimized MP2/[6-31+G(d)/6-31G(d)] structure of $\text{Cl}^-(\text{CF}_3\text{OCF}_2\text{H})$ (rotamer 2).	273
Figure 7.31	Optimized MP2/[6-31+G(d)/6-31G(d)] structure of $\text{Cl}^-((\text{CF}_3)_2\text{O})$.	273
Figure 7.32	Optimized MP2/[6-31+G(d)/6-31G(d)] structure of $\text{Cl}^-(\text{CH}_3\text{OCF}_3)_2$.	275
Figure 7.33	Optimized MP2/[6-31+G(d)/6-31G(d)] structure of $\text{Cl}^-((\text{CF}_2\text{H})_2\text{O})_2$.	275
Figure 7.34	Optimized MP2/[6-31+G(d)/6-31G(d)] structure of $\text{Cl}^-(\text{CH}_3\text{C}(\text{O})\text{CH}_3)$.	275
Figure 7.35	Optimized MP2/[6-31+G(d)/6-31G(d)] structure of $\text{Cl}^-(\text{CH}_3\text{C}(\text{O})\text{CH}_2\text{F})$ (rotamer 1).	276
Figure 7.36	Optimized MP2/[6-31+G(d)/6-31G(d)] structure of $\text{Cl}^-(\text{CH}_3\text{C}(\text{O})\text{CH}_2\text{F})$ (rotamer 2).	276
Figure 7.37	Optimized MP2/[6-31+G(d)/6-31G(d)] structure of $\text{Cl}^-(\text{CH}_2\text{C}(\text{OH})\text{CH}_2\text{F})$.	276
Figure 7.38	Optimized MP2/[6-31+G(d)/6-31G(d)] structure of $\text{Cl}^-(\text{CH}_3\text{C}(\text{O})\text{CF}_3)$.	278

Figure 7.39	Optimized MP2/[6-31+G(d)/6-31G(d)] structure of $\text{Cl}^-(\text{CF}_2\text{HC}(\text{O})\text{CF}_2\text{H})$.	278
Figure 7.40	Optimized MP2/[6-31+G(d)/6-31G(d)] structure of $\text{Cl}^-(\text{CF}_3\text{C}(\text{O})\text{CF}_2\text{H})$.	278
Figure 7.41	Optimized MP2/[6-31+G(d)/6-31G(d)] structure of $\text{Cl}^-(\text{CF}_3\text{C}(\text{O})\text{CF}_3)$.	280
Figure 7.42	Proposed covalent and electrostatic chloride ion-hexafluoroacetone complexes.	280
Figure 7.43	Optimized MP2(full)/6-31G(d) structure of $\text{CH}_3\text{C}(\text{O})\text{CH}_2^-$.	281
Figure 7.44	Optimized MP2(full)/6-31G(d) structure of $\text{CH}_3\text{C}(\text{O})\text{CHF}^-$.	281
Figure 7.45	Optimized MP2(full)/6-31G(d) structure of $\text{CH}_2\text{C}(\text{O})\text{CH}_2\text{F}^-$.	281
Figure 7.46	Optimized MP2(full)/6-31G(d) structure of $\text{CF}_3\text{C}(\text{O})\text{CH}_2^-$.	282
Figure 7.47	Optimized MP2(full)/6-31G(d) structure of $\text{CF}_3\text{C}(\text{O})\text{CF}_2^-$.	282
Figure 7.48	Optimized MP2(full)/6-31G(d) structure of CF_3O^- .	283
Figure 7.49	Optimized MP2(full)/6-31G(d) structure of $\text{CF}_3\text{O}^-(\text{CH}_3\text{Cl})$.	283
Figure 7.50	Optimized MP2(full)/6-31G(d) structure of $[\text{ClCH}_3\text{OCF}_3]^-$.	283

Figure 7.51	Van't Hoff plots for the chloride ion-ether clustering equilibria $\text{Cl}^- + \text{ether-F}_n = \text{Cl}^-(\text{ether-F}_n)$ (ether-F _n = (CH ₃) ₂ O, (CH ₃ CH ₂) ₂ O, CH ₃ OCF ₃ , (CF ₂ H) ₂ O, CF ₃ OCF ₂ H).	289
Figure 7.52	Van't Hoff plots for the chloride ion-ether clustering equilibria $\text{Cl}^-(\text{ether-F}_n) + \text{ether-F}_n = \text{Cl}^-(\text{ether-F}_n)_2$ (ether-F _n = CH ₃ OCF ₃ , (CF ₂ H) ₂ O).	289
Figure 7.53	Van't Hoff plots for the chloride ion-acetone clustering equilibria $\text{Cl}^- + \text{acetone-F}_n = \text{Cl}^-(\text{acetone-F}_n)$ (acetone-F _n = CH ₃ C(O)CH ₃ , CH ₃ C(O)CH ₂ F, CH ₃ C(O)CF ₃ , CF ₃ C(O)CF ₂ H, CF ₃ C(O)CF ₃).	290
Figure 7.54	Schematic G3(MP2) energy profile for the $\text{Cl}^- + \text{CH}_3\text{OCF}_3 \rightarrow$ $\text{CF}_3\text{O}^- + \text{CH}_3\text{Cl}$ gas phase S _N 2 reaction.	291
Figure 7.55	Simulated IR spectrum of CH ₃ C(O)CH ₃ from HF/6-31G(d) computations.	309
Figure 7.56	Simulated IR spectrum of CH ₃ C(O)CH ₃ from B3LYP/ 6-311++G(3d,3p) computations.	309
Figure 7.57	Experimental FT-IR spectrum of CH ₃ C(O)CH ₂ F.	311
Figure 7.58	Simulated IR spectrum of CH ₃ C(O)CH ₂ F (rotamer 1) of HF/ 6-31G(d) computations.	311
Figure 7.59	Simulated IR spectrum of CH ₃ C(O)CH ₂ F (rotamer 1) of B3LYP/ 6-311++G(3d,3p) computations.	312

Figure 7.60	Simulated IR spectrum of CH ₃ C(O)CH ₂ F (rotamer 2) of HF/6-31G(d) computations.	312
Figure 7.61	Simulated IR spectrum of CH ₃ C(O)CH ₂ F (rotamer 2) of B3LYP/6-311++G(3d,3p) computations.	313
Figure 7.62	Simulated IR spectrum of CH ₂ C(OH)CH ₂ F (enol) of HF/6-31G(d) computations.	313
Figure 7.63	Experimental FT-IR spectrum of CH ₃ C(O)CF ₃ .	315
Figure 7.64	Simulated IR spectrum of CH ₃ C(O)CF ₃ from HF/6-31G(d) computations.	315
Figure 7.65	Simulated IR spectrum of CH ₃ C(O)CF ₃ from B3LYP/6-311++G(3d,3p) computations.	316
Figure 7.66	Experimental FT-IR spectrum of CF ₃ C(O)CF ₂ H.	318
Figure 7.67	Simulated IR spectrum of CF ₃ C(O)CF ₂ H from HF/6-31G(d) computations.	318
Figure 7.68	Simulated IR spectrum of CF ₃ C(O)CF ₂ H from B3LYP/6-311++G(3d,3p) computations.	319
Figure 7.69	Experimental FT-IR spectrum of CF ₃ C(O)CF ₃ .	321
Figure 7.70	Simulated IR spectrum of CF ₃ C(O)CF ₃ from HF/6-31G(d) computations.	321

- Figure 7.71** Simulated IR spectrum of $\text{CF}_3\text{C}(\text{O})\text{CF}_3$ from B3LYP/6-311++G(3d,3p) computations. 322
- Figure 7.72** Simulated IR spectrum of $\text{CF}_3\text{C}(\text{O})\text{CF}_3$ (solid line) and $\text{Cl}^-(\text{CF}_3\text{C}(\text{O})\text{CF}_3)$ (dotted line) from B3LYP/[6-311++G(3df,3pd)/6-311++G(3d,3p)] computations. 325
- Figure 7.73** Plot of the MP2/[a/b] energy, $E_{\text{MP2}(\text{fc})/6-31+\text{G}(\text{d})/6-31\text{G}(\text{d})}$, versus the $\text{Cl}^-\cdots\text{CO}$ distance in $\text{Cl}^-(\text{CH}_3\text{C}(\text{O})\text{CH}_3)$, $\text{R}(\text{Cl}^-\cdots\text{CO})$, from a relaxed potential energy surface scan. 329
- Figure 7.74** Plot of the MP2/[a/b] energy, $E_{\text{MP2}(\text{fc})/6-31+\text{G}(\text{d})/6-31\text{G}(\text{d})}$, versus the $\text{Cl}^-\cdots\text{CO}$ distance in $\text{Cl}^-(\text{CF}_3\text{C}(\text{O})\text{CF}_3)$, $\text{R}(\text{Cl}^-\cdots\text{CO})$, from a relaxed potential energy surface scan. 329

NOTE TO USER

Page not included in the original manuscript are unavailable from the author or university. The manuscript was microfilmed as received.

XLVI

This is reproduction is the best copy available

UMI[®]

List of Abbreviations

$\Delta_{\text{acid}}\text{H}^{\circ}$	standard deprotonation enthalpy change or gas phase acidity
$\Delta_{\text{f}}\text{H}^{\circ}$	standard heat of formation
ΔG°	standard Gibbs' free energy change
ΔH°	standard enthalpy change
$\Delta_{\text{r}}\text{H}^{\circ}$	standard reaction enthalpy
ΔS°	standard entropy change
ADO	average dipole orientation
B	magnetic sector
B3LYP	Becke three-parameter Lee, Yang, and Parr non-local exchange functional
BDE	bond dissociation energy
BSSE	basis set superposition error
CID	collision induced dissociation
DEC	dissociative electron capture
DFT	density functional theory
E	electric sector
E1	unimolecular elimination reaction
E2	bimolecular elimination reaction
EA	electron affinity
E_{cm}	center-of-mass ion kinetic energy
ECP	effective core potential
EI	electron ionization
E_{lab}	laboratory-frame ion kinetic energy
EPDS	electron photodetachment spectroscopy
ESI	electrospray ionization
FA	flowing afterglow
FT-ICR	Fourier transform ion cyclotron resonance
FT-IR	Fourier transform infrared
G2	<i>Gaussian 2</i> theory

G2(MP2)	<i>Gaussian 2</i> MP2 theory
G3	<i>Gaussian 3</i> theory
G3(MP2)	<i>Gaussian 3</i> MP2 theory
GC/MS	gas chromatography-mass spectrometry
GIB	guided ion beam
HF	Hartree-Fock
HPMS	high pressure mass spectrometry
ICR	ion cyclotron resonance
IR	infrared
IRMPD	infrared multiphoton dissociation
ITMS	ion trap mass spectrometry
KIMMS	kinetic ion mobility mass spectrometry
LUMO	lowest unoccupied molecular orbital
MCA	methyl cation affinity
MCS	multi channel scalar
MD	molecular dynamics
MIKE	mass-analyzed ion kinetic energy spectrometry
MO	molecular orbital
MP2	second-order Møller-Plesset perturbation
MS	mass spectrometry
MS/MS	tandem mass spectrometry
NA	not available
NIPES	negative ion photoelectron spectroscopy
NIST	National Institute of Science and Technology
NMR	nuclear magnetic resonance
NPA	natural population analysis
PA	proton affinity
PD	photodissociation
PES	potential energy surface
PHPMS	pulsed-ionization high pressure mass spectrometry
QCISD(T)	quadratic configuration interaction singles doubles (triples)

QQQ	triple quadrupole
RRKM	Rice-Ramsperger-Kassel-Marcus
SIFT	selected ion flow tube
S _N 1	unimolecular nucleophilic substitution
S _N 2	bimolecular nucleophilic substitution
TCID	threshold collision induced dissociation
TIPPS	threshold ion pair production spectroscopy
TOF	time-of-flight
TST	transition state theory
UV/VIS	ultraviolet/visible
VPDS	vibrational predissociation spectroscopy
VT	variable-temperature
ZPE	zero point energy
ZTRID	zero-pressure thermal radiation induced dissociation

Chapter 1

Introduction

1.1 Gas Phase Cluster Ions

Clusters can be considered intermediate states of matter, and they have important relevance in many fields of science. The field of cluster research is too large to give a complete overview in this section,¹ and the emphasis here will be placed on gas phase ionic clusters. This is still a very large subject, and thus no emphasis will be put on aerosols, and metal cluster ions. Biological cluster ions will not be considered either, even though these are very important and interesting. Most work on gas phase ionic clusters has focussed on water cluster ions, both positively and negatively charged, mixed water clusters, or clusters containing other organic molecules.

1.1.1 Generation

Cluster ion sources can be divided into two main categories, neutral/ion hybrid sources and cluster ion sources.¹ In the first group, neutral clusters are primarily generated by supersonic expansion nozzle sources, both pulsed and continuous, and subsequent ionization can be achieved by discharges, electrons, or photons. Flow tubes,² high pressure mass spectrometry (HPMS) ion sources,³ and, recently, electrospray ionization (ESI) ion sources are examples of the second group.⁴ Details on the exact mechanisms for cluster ion formation in these various examples will not be discussed further here, since some of them involve subsequent reaction schemes.

In addition, monosolvated negative cluster ions have been generated by ion-molecule reactions at low pressures in ion cyclotron resonance (ICR) and Fourier-transform ion cyclotron resonance (FT-ICR) instruments.⁵

1.1.2 Structures

Insights into structures of cluster ions has been obtained from computations, both electronic structure⁶ and molecular dynamics (MD),⁷ thermochemical measurements,⁸ reactivity studies (see section 1.1.3), and ion mobility experiments.⁹

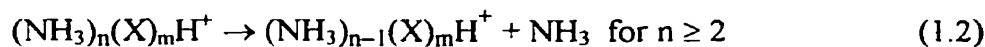
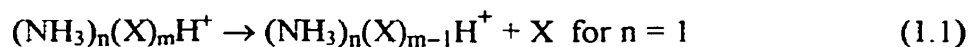
A term closely related to clusters is the so-called “magic numbers”. In general, cluster ions are produced in a wide distribution, $A^{\pm}(B)_n$. Magic numbers are associated with certain clusters that have higher than expected intensities in the observed distribution.¹ These increased intensities are closely related to energetically favorable structures. A prime example is $H^+(H_2O)_{21}$, in which a H_3O^+ core is surrounded by a cage of 20 water molecules, three of them interacting with the three H_3O^+ hydrogen atoms and all of them forming hydrogen bonds among themselves.¹⁰

For mixed cluster ions, systems with series of magic numbers have been found in which the identity of the core ion may change. Changes in thermochemical parameters like the standard enthalpy change (ΔH°) and the standard entropy change (ΔS°),¹¹ or the electron affinity (EA)¹² have been associated with changes in the structure or formation of new solvation shells.

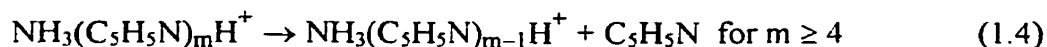
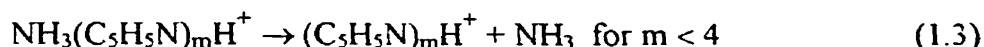
1.1.3 Reactivity

In many areas of chemistry the relationship between structure and reactivity plays a central role. For cluster ions, reactivity studies may include metastable unimolecular dissociations, ion-molecule reactions, and interaction with photons. Differences in the various observations as a function of the cluster size may be indicative of different structures. For these three types of reactivity various illustrative examples will be given.

Castleman and co-workers found that mixed protonated ammonia clusters, $(NH_3)_n(X)_mH^+$ with $X = CH_3C(O)CH_3$, CH_3CN , and $CH_3C(O)H$, have different metastable dissociation pathways depending on n (Reactions 1.1 and 1.2) as measured by reflectron time-of-flight (TOF) techniques.¹³

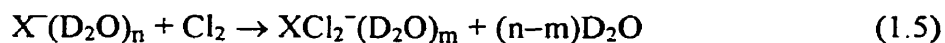


From the same group, for a series of $\text{NH}_3(\text{C}_5\text{H}_5\text{N})_m\text{H}^+$ cluster ions ($m = 1-5$) the following metastable dissociation pathways were observed (Reactions 1.3 and 1.4).¹³



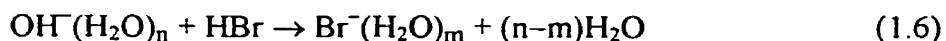
These results were explained by the fact that for $m < 4$ the proton will be bonded to the pyridine nitrogen atom due to its higher proton affinity (PA) than ammonia, while for $m \geq 4$ NH_4^+ will be the core ion, providing four sites for hydrogen bonding.¹³

Viggiano and co-workers reacted halide ion-water clusters, $\text{X}^-(\text{D}_2\text{O})_n$ ($\text{X} = \text{F}, \text{Cl}, \text{Br}, \text{I}; n = 1-16$) with Cl_2 at 140 K in a variable-temperature selected ion flow tube (VT-SIFT) instrument (Reaction 1.5).¹⁴

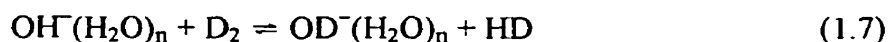


From *ab initio*¹⁵⁻¹⁹ and MD²⁰⁻²⁵ computations it has been shown that the halide ion can be located on the surface or within the interior of a water cluster. Size-dependent kinetics might be indicative of a transition in the structure, and it was assumed beforehand that the surface solvated state would be more reactive than the interior solvated state. For $\text{X} = \text{F}$ a substantial decrease in the rate constants was observed for $n \geq 4$ and for $\text{X} = \text{Cl}$ at $n = 6$. For $\text{X} = \text{Br}$ and I no substantial changes were observed up to $n = 16$ and 13, respectively. These results do not always agree with *ab initio* and/or MD computations, which sometimes predict transitions at

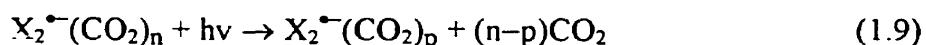
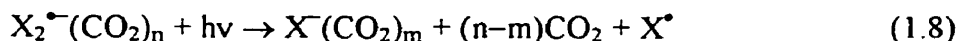
different cluster sizes. A similar kind of study was performed for $\text{OH}^-(\text{H}_2\text{O})_n$ with HBr at 100 K (Reaction 1.6), and for $n \leq 7$ the reaction proceeded at the collision rate constant, dropping to one third of the collision rate constant for $n = 11$.²⁶



In addition, H/D exchange reactions have also revealed cluster size dependent kinetics (Reaction 1.7).²⁷



Finally, Lineberger and co-workers showed the cluster size dependence of the photodissociation (PD) products for $\text{X}_2^-(\text{CO}_2)_n$ clusters ($X = \text{Br}, \text{I}; n = 1-20$).^{28,29} Reaction 1.8 was observed for uncaged clusters, while Reaction 1.9 took place for caged clusters. For $X = \text{Br}$, the transformation took place at $n = 12$, and at $n = 16$ for $X = \text{I}$.



1.2 Ion Solvation

1.2.1 Condensed phase

The degree of solvation of ionic compounds in various organic solvents is strongly dependent on the dielectric constant, ϵ , of a particular solvent. Based on the dielectric constant, solvents can be divided into two broad categories: polar and non-polar.³⁰ In non-polar solvents, with $\epsilon < 15$, ionic compounds will be highly associated. Quaternary ammonium salts, NR_4^+X^- , are an example of some exceptions,

since the R groups are very soluble in non-polar solvents.³⁰ The two most important solvent properties are the dipole moment, μ , and the molecular polarizability, α .

Solvent molecules will orient themselves around positive and negative ions differently. This orientation will be most pronounced in the innermost shell of solvent molecules, and will become increasingly random as the distance from the ion increases. Depending upon the structure of the solvent molecule, positive and negative ions may interact more or less strongly, thus giving rise to different degrees of solvation. The polarizability of a solvent will become more important for high molecular weight polar solvents and for large ions like Γ^- . Polar solvents can be further divided into two categories: protic and aprotic. The first group has the ability to form hydrogen bonds, and so negative ions will be strongly solvated by protic solvents. Dipolar aprotic polar solvents tend to interact more strongly with positive ions than with negative ions, since the positive ends of the dipole moment are more or less located in the middle of the molecule.

The reactivity of ions in the condensed phase can be strongly affected by the nearby presence of its counter ion. These so-called ion-pairs may exist in two distinct types: the contact ion-pair, M^+X^- , and the solvent separated ion-pair, $M^+|S|X^-$. From nuclear magnetic resonance (NMR)³¹ and ultraviolet/visible (UV/VIS)³² experiments it has been shown that these two species may be in equilibrium (Reaction 1.10).



Closely associated with the interactions in solvent separated ion-pairs are cation complexing agents like crown ethers and cryptands.³³ Cations bind very strongly with these molecules by multiple contacts, also known as chelation, mainly by ion-dipole interactions. Recently, research on anion selective receptor molecules and ions has gained popularity, and the main interactions in these systems are by hydrogen bonding and ion-dipole interactions.^{34,35} One of the most useful and well-known synthetic organic applications of ion solvation and ion-pair formation is phase transfer catalysis.³⁶

1.2.2 Gas phase

Gas phase ion solvation studied by mass spectrometric techniques has confirmed that many condensed phase phenomena are also operational in the gas phase. Examples are the different thermochemistry of cation and anion solvation by different solvents, the existence of solvation shells, intrinsic binding affinities for various cations onto crown ethers and cryptands, the existence of ion-zwitter ion complexes, and qualitative information on chelation. Unfortunately, no information on solvent separated ion-pairs has been obtained.

1.3 Ion Thermochemistry

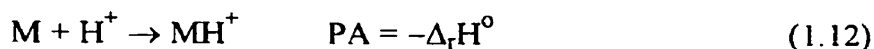
1.3.1 Definitions

The thermochemistry of ions and neutrals in the gas phase is closely associated with their structures and reactivities, and consequently it has been one of the most important fields of study in gas phase ion chemistry over the last three decades. It is beyond the scope of this section to give a complete overview of gas phase ion thermochemistry, and so only the four most important quantities associated with negative ions will be briefly discussed.

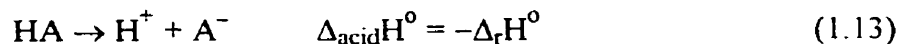
The EA of a neutral molecule is the negative reaction enthalpy for the following reaction (Reaction 1.11).³⁷



The PA of a neutral molecule is the negative reaction enthalpy for the following reaction (Reaction 1.12).³⁷



The gas phase acidity or deprotonation enthalpy, $\Delta_{\text{acid}}H^{\circ}$, for a neutral molecule is the negative reaction enthalpy for the following reaction (Reaction 1.13).³⁷



Finally, the heat of formation for a negative ion $M^{\bullet-}$, $\Delta_fH^{\circ}(M^{\bullet-})$, is given by Equation 1.14.³⁷ According to the Electron Convention, $\Delta_fH^{\circ}(e^-)$ is defined as 0.751 kcal mol⁻¹ (0.033 eV) at 298 K, derived from Fermi-Dirac statistics.³⁷

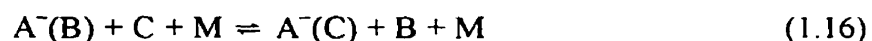
$$\Delta_fH^{\circ}(M^{\bullet-}) = \Delta_fH^{\circ}(M) - EA(M) + \Delta_fH^{\circ}(e^-) \quad (1.14)$$

Since most thermochemical data in this thesis are associated with binding enthalpies of anions onto neutral molecules studied by pulsed-ionization high pressure mass spectrometry (PHPMS), in the following sections a brief overview will be given of the various experimental methods used to obtain similar data. Emphasis will be placed on the various advantages and disadvantages of the methods, and the consequences for the reliability of the obtained thermochemical data, as well as the relative overall performance of the various methods.

1.3.2 Methods

1.3.2.1 Equilibrium Reactions

The two most common gas phase equilibrium reactions are clustering (Reaction 1.15) and exchange (Reaction 1.16) reactions.

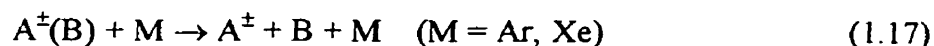


The first one is normally only observed at elevated pressures like in PHPMS,³ high pressure drift cells,³⁸ or selected ion flow tube (SIFT) instruments.³⁹ By measuring the equilibrium constants for Reactions 1.15 and 1.16 at different temperatures one can directly obtain ΔH° and ΔS° values. In general, PHPMS is restricted to volatile compounds, but Kebarle and co-workers coupled an ESI source to an HPMS source to measure equilibria involving ions of biological molecules and multiply charged (in)organic ions.⁴⁰ The advantage of measuring ΔS° is that it may provide insights into the structure of the cluster ion.

Exchange equilibria have been performed on ICR,⁴¹ both the drift cell and trapped ion types, and FT-ICR instruments.⁴² From the equilibrium constants of these experiments standard Gibbs' free energy changes (ΔG°) values at one temperature, in most cases at 298 K, can be obtained. By using an estimated or calculated ΔS° value, the ΔH° value can be determined, and this is referred to as the "third law" method.⁴³ In Section 2.1 various possible errors in PHPMS experiments are discussed that may give rise to errors in the thermochemical data obtained. In general, the agreement between ΔG° values from PHPMS and ICR or FT-ICR experiments is good. It has been argued that the "third law" method can give uncertainties in ΔH° values that are considerably better than those obtained from Van't Hoff plots.⁴³

1.3.2.2 Threshold CID

Binding enthalpies may also be obtained from low kinetic energy resolved threshold collision induced dissociation (TCID) experiments (Reaction 1.17).⁴⁴⁻⁴⁸



For these types of experiments guided ion beam (GIB),⁴⁵⁻⁴⁸ FT-ICR,⁴⁹ and flowing afterglow-triple quadrupole (FA-QQQ)⁴⁴ instruments have been used. By measuring the cross sections of Reaction 1.17, extrapolated to zero target gas

pressures, as a function of the centre-of-mass collision energy (E_{cm}), the binding or threshold energy at 0 K can be obtained by fitting the threshold region of the curve to Equation 1.18.⁴⁷

$$\sigma(E) = \sigma_0 \sum_i g_i P_D(E, E_i) \frac{(E + E_i - E_T)^n}{E} \quad (1.18)$$

In Equation 1.18, $\sigma(E)$ is the cross section for formation of the product ion at centre-of-mass energy E , E_T is the desired threshold energy, σ_0 is a scaling factor, n is an adjustable parameter related to the shape of the cross section, P_D is the probability of an ion with a given amount of energy dissociating within the experimental time window, and i denotes the ro-vibrational states having energy E_i and population g_i . In general, the results of these types of experiments agree well with data from equilibrium experiments, if available. Unfortunately, input from *ab initio* or density functional theory (DFT) computations is required, making this method not purely experimental. In addition, the presence of a centrifugal barrier for the reverse reaction may overestimate the binding enthalpy obtained.

1.3.2.3 Light Induced Reactions

Binding enthalpies of various cluster ions have been determined using photon induced processes, like electron photodetachment spectroscopy (EPDS), negative ion photo-electron spectroscopy (NIPES), and zero-pressure thermal radiation induced dissociation (ZTRID).

In EPDS experiments the complex ion population ($A^-(B)$) is being monitored as a function of the energy (wavelength) of the irradiated laser light (Reaction 1.19).



These kinds of experiments have been performed on ICR ⁵⁰ and FT-ICR ⁵¹ instruments. Yang *et al.* derived that at threshold the cross section for optical detachment of an electron, $\sigma(E)$, is directly proportional to the square root of the energy in excess of the threshold (Equation 1.20).⁵¹

$$\sigma(E) \propto (E - E_T)^{1/2} \quad (1.20)$$

For a series of halide alcohol complexes, $X^-(ROH)$, the binding energies determined were in general more negative than from other methods.⁵¹

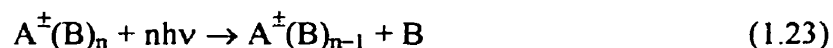
In NIPES the kinetic energy of the photo-electron is measured, and Bowen and co-workers showed that the binding energy, $D(A^-(B)_{n-1} \dots B)$, of a anion complex $A^-(B)_n$ can be approximated by Equation 1.21,⁵² where EA_a is the adiabatic electron affinity (Equation 1.22)

$$D(A^-(B)_{n-1} \dots B) \cong EA_a(A^*(B)_n) - EA_a(A^*(B)_{n-1}) \quad (1.21)$$

$$EA_a = h\nu_{laser} - KE(e^-) (0,0) \quad (1.22)$$

The (0,0) term corresponds to the transition from $v = 0$ in the negative ion ground state to $v = 0$ in the neutral ground state. In general, there is close agreement between data from NIPES experiments with other experimental data, if available.

Large cluster ions, *i.e.* with many vibrational modes, trapped in a FT-ICR cell can absorb blackbody radiation irradiated from the ion source wall until the internal energy is above the threshold for dissociation (Reaction 1.23).⁵³



At zero background pressure, the unimolecular dissociation constant, k_u , will be equal to $k_{abs}[hv]$, where k_{abs} is the rate at which the cluster absorbs photons, and $[hv]$ is the photon concentration. By performing these kinds of experiments at different FT-ICR cell temperatures, T , and plotting $\ln(k_u)$ versus $1/T$, the activation energy, E_a , can be obtained from the slope (Equation 1.24), where A is the frequency factor, and R is the universal gas constant.

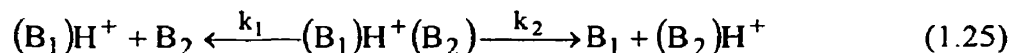
$$\ln(k_u) = \ln(A) - \frac{E_a}{RT} \quad (1.24)$$

In general, there is excellent agreement with data from PHPMS experiments, since the activation energy corresponds to the well depth of the cluster formation reaction. Furthermore, it has been shown by this method that dissociation energetics of large biological ions can be obtained.

1.3.2.4 Kinetic Method

The kinetic method was introduced by Cooks and co-worker over two decades ago to obtain thermochemical parameters for ions derived from large and non-volatile molecules.⁵⁴ In this section a brief overview of the kinetic method will be given. For a more detailed discussion of the kinetic method and its applications, the reader is referred to a review by Cooks.⁵⁵

A metastable proton-bound dimer, $(B_1)H^+(B_2)$, can dissociate in the field free region of a mass spectrometer into $(B_1)H^+$ and $(B_2)H^+$ (Reaction 1.25).



The unimolecular rate constant for each reaction path is given by Equation 1.26,⁵⁵ where R is the universal gas constant, T_{eff} is the effective temperature, h is

Planck's constant, Q^* and Q are the partition functions of the activated complex and the proton bound dimer, respectively, and ϵ_0 is the activation energy.

$$k = \frac{RT_{\text{eff}}}{h} \cdot \frac{Q^*}{Q} e^{-\epsilon_0/RT_{\text{eff}}} \quad (1.26)$$

For the two competing dissociations in Reaction 1.25, Equation 1.26 can be written as Equation 1.27.⁵⁵

$$\ln\left(\frac{k_1}{k_2}\right) = \ln\left(\frac{Q_1^*}{Q_2^*} \cdot \frac{Q_2}{Q_1}\right) + \frac{\Delta\epsilon_0}{RT_{\text{eff}}} \quad (1.27)$$

Since both reaction channels originate from the same ion, $Q_1 = Q_2$. In addition, if it is assumed that the two frequencies along the reaction coordinate in the activated complex are equal, that the difference in the entropy change for both reaction channels is negligible, and that the relative abundance of the $(B_1)H^+$ and $(B_2)H^+$ ions in the metastable ion kinetic energy (MIKE) spectrum is determined by the relative rates of dissociation, k_1 and k_2 , then Equation 1.27 can be written as follows (Equation 1.28),⁵⁵ where ΔPA is the difference in proton affinity between B_1 and B_2 .

$$\ln\left(\frac{(B_1)H^+}{(B_2)H^+}\right) = \frac{\Delta PA}{RT_{\text{eff}}} \quad (1.28)$$

Despite its usefulness for many systems investigated, the kinetic method has received significant criticism, concerning the concept of the effective temperature⁵⁶ and the neglect of the entropy term.⁵⁷ Various groups have developed procedures to deconvolute the enthalpy and entropy changes by comparing results from MIKE and MIKE/CID experiments, which correspond to different effective temperatures.^{58,59} For further details the reader is referred to the cited articles.

1.4 Uni- and Bimolecular Gas Phase Ion-Molecule Reactions

The understanding of the rates for chemical transformation of gas phase ions into products, whether by unimolecular dissociation or ion-molecule reactions, has been one of the central themes in gas phase ion chemistry from the early days. Understanding the appearance of mass spectra of simple organic ions in terms of ion structures and mechanisms for the formation of the various products, both ionic and neutral, has been a major driving force in developing theories to understand unimolecular dissociations.

In the following two sections the basic formulas and assumptions for the two most well known theories to explain unimolecular and bimolecular rate constants, the RRKM and ADO theories, respectively, will be presented.

1.4.1 RRKM Theory

The Rice-Ramsperger-Kassel-Marcus (RRKM) theory is the most widely used method to calculate unimolecular rate constants, $k(E)$, of systems with an internal energy distribution above the threshold for dissociation (Equation 1.29),⁶⁰ where σ is a symmetry factor that indicates the number of identical pathways that can be taken, $N^\ddagger(E - E_0)$ is the sum of vibrational and rotational quantum states for the transition state up to internal energy $E - E_0$, h is Planck's constant, $\rho(E)$ is the density of vibrational and rotational quantum states in the dissociation ion, and E_0 is the threshold energy for dissociation.

$$k(E) = \frac{\sigma \cdot N^\ddagger(E - E_0)}{h \cdot \rho(E)} \quad (1.29)$$

The RRKM theory is a statistical theory and it assumes that all states can contribute their non-fixed energy to the reaction. The redistribution of the vibrational energy is a fast and statistical process. Rotational energy may also contribute to a

reaction, although limitations due to conservation of angular momentum may prevent this from happening.

1.4.2 ADO Theory

In low pressure environments, like in a FT-ICR, the initial internally excited reactants complex $[A^\pm(B)]^*$ cannot be stabilized by third-body collisions or radiative stabilization, although the latter process has been observed for certain special systems.⁶¹ Consequently it will have a short lifetime, and it will either dissociate back to the reactants A^\pm and B through a “loose” transition state, or pass through a “tight” transition state to the products complex $[C^\pm(D)]^*$. The “tight” transition state can only be passed if its energy is lower than of the reactants. The dissociation rate constant of the $[A^\pm(B)]^*$ complex can be calculated using the RRKM expression. In order to calculate the rate constant for formation of the $[A^\pm(B)]^*$ complex the average dipole orientation (ADO) theory expression (Equation 1.30) can be used.⁶²

$$k_{\text{ADO}} = 2\pi q \sqrt{\frac{\alpha}{\mu}} + \mu_D q C \sqrt{\frac{8\pi\alpha}{\mu k_B T}} \quad (1.30)$$

In Equation 1.30, k_{ADO} is the collision rate constant (in $\text{cm}^3 \text{ molecule}^{-1} \text{ s}^{-1}$), q is the charge of the ion (in $\text{erg}^{1/2} \text{ cm}^{1/2}$), α is the molecular polarizability (in cm^3), μ is the reduced mass of the system (in g), C is an experimental constant (function of $\mu_D/\alpha^{1/2}$), μ_D is the permanent dipole moment of the neutral (in $\text{erg}^{1/2} \text{ cm}^{3/2}$), k_B is Boltzmann’s constant (in erg K^{-1}), and T is the absolute temperature (in K).

The efficiency of a reaction can be determined by dividing the experimental rate constant over the collision rate constant.

Finally, it has to be mentioned that other theories have been developed that, in many cases, provide results closer to experimental data, but they will not be discussed here.

1.5 Ion Spectroscopy

Isomeric distinction based on differences in thermochemistry and reactivity, both uni- and bimolecular, has been one of central themes in chemistry. Even before the introduction of modern spectroscopic techniques, various chemical methods were available to help chemists to distinguish isomers. Spectroscopic techniques like infrared (IR), NMR, UV/VIS, and mass spectrometry (MS) have been and continue to be indispensable tools for many fields of chemistry and other sciences. Until the widespread introduction of quantum chemistry software the field of gas phase ion chemistry had to do without many of the tools condensed phase chemists benefited from. On the other hand, using the available techniques most of the problems could be solved, and condensed phase chemists were experiencing problems gas phase ion chemists did not worry about.

Ion spectroscopy is still a relatively new and small field of study, and it has the potential to become more important and help solve problems present day gas phase ion chemistry techniques cannot deal with.^{63,64} It has already become a useful tool to test quantum theoretical models by comparing available experimental and calculated normal mode vibrational frequencies of gas phase ions, and to confirm the existence of one dominant isomer or various isomers simultaneously.

In this section a few techniques will be briefly discussed that have been used to date to study systems related to research presented in this thesis.

Halide ion-water complexes, with or without argon atoms, $X^-(H_2O)_n$ and $X^-(H_2O)_n(Ar)_m$, respectively, ($X = F, Cl, Br, I$; $n = 1-6$; $m = 1-4$), have been among the most extensively studied systems by vibrational predissociation spectroscopy (VPDS).⁶⁵⁻⁷⁴ In most cases the IR region from 2900-3700 cm^{-1} is covered, corresponding to the O-H stretch vibrations. By comparing experimental data of the cluster ions with results for “free” water and from *ab initio* computations, the influence of the halide ion on the shifts of O-H stretch vibrations, the exact identification of the O-H stretch vibrations, and consequently structural assignment of the cluster ions have been accomplished.

Similar experiments have also been performed on the $\text{Cl}^-(\text{HOCH}_3)_n$ ($n = 1-8, 10, 12$),⁷⁵ $\Gamma(\text{HOR})(\text{Ar})_m$ ($\text{R} = \text{CH}_3, \text{CH}_3\text{CH}_2, (\text{CH}_3)_2\text{CH}$; $m = 4-6$),⁷⁶ and $\text{Cl}^-(\text{NH}_3)$ ⁷⁷ systems.

Riveros and Eyler measured indirectly the IR absorption spectra of some halide ion-alcohol complexes by infrared multiphoton dissociation (IRMPD) experiments in the 920-1060 cm^{-1} region.⁷⁸ Some spectral shifts relative to “free” methanol could be observed. Eventually, high resolution Fourier-transform infrared (FT-IR) spectra of ions trapped in a FT-ICR cell will give gas phase ion chemists and theoretical chemists a new tool to investigate present day challenges in ion structures and to test computational results.

Finally, it has to be mentioned that IR spectra of ions have been recorded using matrix-isolation spectroscopy⁷⁹⁻⁸¹ and NIPES.⁸²

1.6 Scope of Thesis

The main scope of this thesis is to determine the thermochemistry of formation for a variety of negative gas phase cluster ions by PHPMS and computational quantum chemistry methods, as well as getting more insights into their structures and spectroscopic properties.

Most systems investigated have relevance in various fields of chemistry. A large portion of the work presented will provide new data, and has both confirmed some previously known theories, but has also given new and different insights into accepted observations and explanations of previously published work.

In Chapter 1 a general overview of the various aspects in this thesis has been given, trying to put the research performed in a larger context. In Chapters 2 and 3 descriptions of the experimental and theoretical methods used will be given. In Chapter 4 halide ion-alcohol clusters will be the main subject, while in Chapters 5, 6, and 7, the focus will be on solvated $\text{S}_{\text{N}}2$ complexes and transition states, halide ion-trifluoromethyl halide $\text{S}_{\text{N}}2$ reactions, and chloride ion-fluorinated ethers and acetones complexes, respectively. Finally in Chapter 8 the main conclusions of this thesis will be summarized, as well as suggestions for future research will be mentioned.

1.7 References

- 1 Castleman, Jr., A. W.; Bowen, Jr., K. H. *J. Phys. Chem.* **1996**, *100*, 12911 and references cited therein.
- 2 Böhme, D. K. *Int. J. Mass Spectrom.* **2000**, *200*, 97 and references cited therein.
- 3 Kebarle, P. "Pulsed High Pressure Mass Spectrometry". In "Techniques for the Study of Ion-Molecule Reactions"; Farrer, J. M.; Saunders, Jr., W. H., Eds.; Wiley-Interscience, New York, NY, **1988**, 221 and references cited therein.
- 4 Lee, S.-W.; Cox, H.; Goddard, III, W. A.; Beauchamp, J. L. *J. Am. Chem. Soc.* **2000**, *122*, 9201.
- 5 Takashima, K.; Riveros, J. M. *Mass Spectrom. Rev.* **1998**, *17*, 409 and references cited therein.
- 6 Pliego, Jr., J. R.; Riveros, J. M. *J. Chem. Phys.* **2000**, *112*, 4095.
- 7 Tuckerman, M.; Laasonen, K.; Sprik, M.; Parrinello, M. *J. Chem. Phys.* **1995**, *103*, 150.
- 8 Meot-Ner (Mautner), M.; Speller, C. V. *J. Phys. Chem.* **1986**, *90*, 6616.
- 9 Gotts, N. G.; von Helden, G.; Bowers, M. T. *Int. J. Mass Spectrom. Ion Processes* **1995**, *149/150*, 217.
- 10 Yang, X.; Castleman, Jr., A. W. *J. Am. Chem. Soc.* **1989**, *111*, 6845.
- 11 Yamdagni, R.; Kebarle, P. *J. Am. Chem. Soc.* **1972**, *94*, 2940.
- 12 Markovich, G.; Giniger, R.; Levin, M.; Chesnovsky, O. *Z. Phys. D* **1991**, *95*, 9416.
- 13 Tzeng, W. B.; Wei, S.; Castleman, Jr., A. W. *J. Phys. Chem.* **1991**, *95*, 585.
- 14 Seeley, J. V.; Morris, R. A.; Viggiano, A. A. *J. Phys. Chem.* **1996**, *100*, 15821.
- 15 Xantheas, S. S.; Dunning, Jr., T. H. *J. Phys. Chem.* **1994**, *98*, 13489.
- 16 Combariza, J. E.; Kestner, N. R.; Jortner, J. *Chem. Phys. Lett.* **1993**, *203*, 423.
- 17 Combariza, J. E.; Kestner, N. R. *J. Phys. Chem.* **1994**, *98*, 3513.
- 18 Combariza, J. E.; Kestner, N. R.; Jortner, J. *J. Chem. Phys.* **1994**, *100*, 2851.
- 19 Combariza, J. E.; Kestner, N. R.; Jortner, J. *Chem. Phys. Lett.* **1994**, *221*, 156.
- 20 Perera, L.; Berkowitz, M. L. *J. Chem. Phys.* **1993**, *99*, 4222.
- 21 Perera, L.; Berkowitz, M. L. *J. Chem. Phys.* **1994**, *100*, 3085.
- 22 Asada, T.; Nishimoto, K.; Kitaura, K. *J. Phys. Chem.* **1993**, *97*, 7724.

- 23 Dang, L. X.; Garret, B. C. *J. Chem. Phys.* **1993**, *99*, 2972.
- 24 Jorgensen, W. L.; Severance, D. L. *J. Chem. Phys.* **1993**, *99*, 4233.
- 25 Sremaniak, L. S.; Perera, L.; Berkowitz, M. L. *J. Phys. Chem.* **1996**, *100*, 1350.
- 26 Arnold, S. T.; Viggiano, A. A. *J. Phys. Chem.* **1997**, *101*, 2859.
- 27 Paulson, J. F.; Henschman, M. J. *Bull. Am. Phys. Soc.* **1982**, *27*, 108.
- 28 Alexander, M. L.; Levinger, N. E.; Johnson, M. A.; Ray, D. R.; Lineberger, W. C. *J. Chem. Phys.* **1988**, *88*, 6200.
- 29 Papanikolas, J. M.; Gord, J. R.; Levinger, N. E.; Ray, D. R.; Vorsa, V.; Lineberger, W. C. *J. Phys. Chem.* **1991**, *95*, 8028.
- 30 Lowry, T. H.; Schueller Richardson, K. "*Mechanisms and Theory in Organic Chemistry*"; Harper & Row, Publishers, New York, NY, **1987**, Chapter 2.
- 31 O'Brien, D. H.; Russell, C. R.; Hart, A. J. *J. Am. Chem. Soc.* **1979**, *101*, 633.
- 32 Simon, J. D.; Peters, K. S. *Acc. Chem. Res.* **1984**, *17*, 277.
- 33 Pedersen, C. J.; Frensdorff, H. K. *Angew. Chem. Int. Ed. Engl.* **1972**, *11*, 16.
- 34 Scheerder, J.; Engbersen, F. J.; Reinhoudt, D. N. *Recl. Trav. Chim. Pays-Bas* **1996**, *115*, 307 and references cited therein.
- 35 Schmidtchen, F. P.; Berger, M. *Chem. Rev.* **1997**, *97*, 1609 and references cited therein.
- 36 Jones, R. A. *Aldrichimica Acta* **1976**, *9(3)*, 35.
- 37 <http://webbook.nist.gov/chemistry/ion>
- 38 Kemper, P. R.; Bowers, M. T. *J. Am. Soc. Mass Spectrom.* **1990**, *1*, 197.
- 39 Seeley, J. V.; Morris, R. A.; Viggiano, A. A. *J. Phys. Chem.* **1997**, *101*, 4598.
- 40 Blades, A. T.; Klassen, J. S.; Kebarle, P. *J. Am. Chem. Soc.* **1996**, *118*, 12437.
- 41 Larson, J. W.; McMahon, T. B. *J. Am. Chem. Soc.* **1983**, *105*, 2944.
- 42 Tanabe, F. K. J.; Morgon, N. H.; Riveros, J. M. *J. Phys. Chem.* **1996**, *100*, 2862.
- 43 Mason, R. S.; Anderson, P. D. *J. Int. J. Mass Spectrom. Ion Processes* **1997**, *161*, L1.
- 44 Chyall, L. J.; Squires, R. R. *J. Phys. Chem.* **1996**, *100*, 16435.
- 45 DeTuri, V. F.; Hintz, P. A.; Ervin, K. M. *J. Phys. Chem. A* **1997**, *101*, 5969.
- 46 DeTuri, V. F.; Ervin, K. M. *J. Phys. Chem. A* **1999**, *103*, 6911.

- 47 Gailbreath, B. C. D.; Pommerening, C. A.; Bachrach, S. M.; Sunderlin, L. S. *J. Phys. Chem. A* **2000**, *104*, 2958.
- 48 Artau, A.; Nizzi, K. E.; Hill, B. T.; Sunderlin, L. S.; Wenthold, P. G. *J. Am. Chem. Soc.* **2000**, *122*, 10667.
- 49 van den Berg, K. J. *Ph.D. Thesis, University of Amsterdam, 1994*.
- 50 Mihalick, J. E.; Gatev, G. G.; Brauman, J. I. *J. Am. Chem. Soc.* **1996**, *118*, 12424.
- 51 Yang, Y.; Linnert, H. V.; Riveros, J. M.; Williams, K. R.; Eyler, J. R. *J. Phys. Chem. A* **1997**, *101*, 2371.
- 52 Coe, J. V.; Snodgrass, J. T.; Freidhoff, C. B.; McHugh, K. M.; Bowen, K. J. *J. Chem. Phys.* **1985**, *83*, 3169.
- 53 Dunbar, R. C.; McMahon, T. B. *Science* **1998**, *279*, 194 and references cited therein.
- 54 Cooks, R. G.; Kruger, T. L. *J. Am. Chem. Soc.* **1977**, *99*, 74.
- 55 Cooks, R. G.; Patrick, J. S.; Kothiaho, T.; McLuckey, S. A. *Mass Spectrom. Rev.* **1994**, *13*, 287.
- 56 Ervin, K. M. *Int. J. Mass Spectrom.* **2000**, *195/196*, 271 and references cited therein.
- 57 Armentrout, P. *J. Am. Soc. Mass Spectrom.* **2000**, *11*, 371 and references cited therein.
- 58 Cheng, X.; Wu, Z.; Fenselau, C. *J. Am. Chem. Soc.* **1993**, *115*, 4844.
- 59 Cerda, B. A.; Wesdemiotis, C. *J. Am. Chem. Soc.* **1996**, *118*, 11884.
- 60 Marcus, R. A.; Rice, O. K. *J. Phys. Colloid Chem.* **1951**, *55*, 894.
- 61 Fisher, J. J. *Ph.D. Thesis, University of Waterloo, 1990*.
- 62 Su, T.; Bowers, M. T. *J. Chem. Phys.* **1973**, *58*, 3027.
- 63 Baer, T. (Ed.) *Int. J. Mass Spectrom. Ion Processes* **1996**, *159*, 1-261 and references cited therein.
- 64 Duncan, M. A. *Int. J. Mass Spectrom.* **2000**, *200*, 571 and references cited therein.
- 65 Ayotte, P.; Nielsen, S. B.; Weddle, G. H.; Johnson, M. A.; Xantheas, S. S. *J. Phys. Chem. A* **1999**, *103*, 10665.
- 66 Ayotte, P.; Weddle, G. H.; Kim, J.; Kelley, J.; Johnson, M. A. *J. Phys. Chem. A* **1999**, *103*, 443.
- 67 Ayotte, P.; Weddle, G. H.; Johnson, M. A. *J. Chem. Phys.* **1999**, *110*, 7129.

- 68 Cabarcos, O. M.; Weinheimer, C. J.; Lisy, J. M.; Xantheas, S. S. *J. Chem. Phys.* **1999**, *110*, 5.
- 69 Ayotte, P.; Bailey, C. G.; Weddle, G. H.; Johnson, M. A. *J. Phys. Chem. A* **1998**, *102*, 3067.
- 70 Ayotte, P.; Weddle, G. H.; Kim, J.; Johnson, M. A. *Chem. Phys.* **1998**, *239*, 485.
- 71 Ayotte, P.; Weddle, G. H.; Kim, J.; Johnson, M. A. *J. Am. Chem. Soc.* **1998**, *120*, 12361.
- 72 Choi, J.-H.; Kuwata, K. T.; Cao, Y.-B.; Okumura, M. *J. Phys. Chem. A* **1998**, *102*, 503.
- 73 Bailey, C. G.; Kim, J.; Dessent, C. E. H.; Johnson, M. A. *Chem. Phys. Lett.* **1997**, *269*, 122.
- 74 Johnson, M. S.; Kuwata, K. T.; Wong, C.-K.; Okumura, M. *Chem. Phys. Lett.* **1996**, *260*, 551.
- 75 Cabarcos, O. M.; Weinheimer, C. J.; Martinez, T. J.; Lisy, J. M. *J. Chem. Phys.* **1999**, *110*, 9516.
- 76 Nielsen, S. B.; Ayotte, P.; Kelley, J. A.; Johnson, M. A. *J. Chem. Phys.* **1999**, *111*, 9593.
- 77 Weiser, P. S.; Wild, D. A.; Wolyneec, P. P.; Bieske, E. J. *J. Phys. Chem. A* **2000**, *104*, 2562.
- 78 Peiris, D. M.; Riveros, J. M.; Eyler, J. R. *Int. J. Mass Spectrom. Ion Processes* **1996**, *159*, 169.
- 79 Zhou, M.; Citra, A.; Liang, B.; Andrews, L. *J. Phys. Chem. A* **2000**, *104*, 3457.
- 80 Fridgen, T. D.; Zhang, X. K.; Parnis, J. M.; March, R. E. *J. Phys. Chem. A* **2000**, *104*, 3487.
- 81 Hudgins, D. M.; Bauschlicher, Jr., C. W.; Allamandola, L. J.; Fetzer, J. C. *J. Phys. Chem. A* **2000**, *104*, 3655.
- 82 Zanni, M. T.; Taylor, T. R.; Greenblatt, B. J.; Soep, B.; Neumark, D. M. *J. Chem. Phys.* **1997**, *107*, 7613.

Chapter 2

Experimental

2.1 Pulsed-ionization High Pressure Mass Spectrometry

Pulsed-ionization high pressure mass spectrometry (PHPMS) is the most successful technique to date to study gas phase ion-molecule equilibria and rates of approach to equilibrium.¹ In addition, ion-molecule reaction kinetics and temperature dependence of ion-molecule rates can be studied. This technique, among some others, has been used to construct thermochemical ladders for proton affinities (PA), gas phase acidities ($\Delta_{\text{acid}}H^\circ$), electron affinities (EA), methyl cation affinities (MCA), and stepwise solvation of positive and negative gas phase ions by neutral ligands.² The ions, generated in the field-free ion source by a variety of processes (see Section 2.3), diffuse through the gas to reach the ion source wall, where neutralization takes place. The trapping of the ions by the bath gas increases their lifetime to the ms regime, allowing full thermalization of the ion populations to take place. The thermal conductivity of the gas helps to equalize the temperature throughout the entire ion source. Ion sampling takes place by allowing considerable amounts of gas and ions to escape the ion source by molecular flow through the exit aperture or slit. One of the assumptions made with PHPMS to calculate equilibrium and rate constants is that the intensity of a given ion A^\pm at time t , $(A^\pm)_t$, is proportional to the concentration of A^\pm in the ion source, $[A^\pm]$. This applies to all ions present, and both time-independence and equality of the proportionality constants is assumed.

The diffusion current density, Γ , for the ions and electrons present in the ion source is composed of a free diffusion term, $D\nabla N$, due to a number density gradient, and a field induced particle drift, $N\mu E$ (Equations 2.1-2.3).^{1,3}

$$\Gamma_+ = -D_+ \nabla N_+ + N_+ \mu_+ E \quad (2.1)$$

$$\Gamma_- = -D_- \nabla N_- - N_- \mu_- E \quad (2.2)$$

$$\Gamma_e = -D_e \nabla N_e - N_e \mu_e E \quad (2.3)$$

In Equations 2.1-2.3, D is the diffusion coefficient for free diffusion, μ is the low-field mobility, and E is the electric field produced by the non-charge neutrality of the plasma. This “self-field” develops due to the initial rapid diffusion of the secondary electron generated by the electron beam pulse. Charge separation between the electrons and positive ions decreases, and the diffusion of both species increases until it becomes equal (Equation 2.4).

$$\Gamma_e = \Gamma_+ = \Gamma \quad (2.4)$$

It has been shown that the positive ion-electron pairs will diffuse twice as fast as free ions during the so-called positive ion-electron ambipolar diffusion (Equations 2.5 and 2.6).

$$\Gamma_+ = -2D_+ \nabla N_+ \quad (2.5)$$

$$\Gamma_e = -2D_+ \nabla N_e \quad (2.6)$$

Electrons can also be captured by neutral molecules in the ion source to form negative ions, and these will initially diffuse very slowly because $\Gamma_- \cong 0$. Eventually E will become 0, and the electrons are quickly lost by fast diffusion to the ion source wall. Γ_+ will become $-D_+ \nabla N_+$ again, and Γ_- will become equal to Γ_+ , and consequently $D_{\pm} \cong D_+ \cong D_-$. This stage is called the positive ion-negative ion ambipolar diffusion. Eventually the number densities of the positive and negative ions become so small, that a stage of free diffusion will be reached. These three stages of ion-electron diffusion are schematically shown in Figure 2.1.

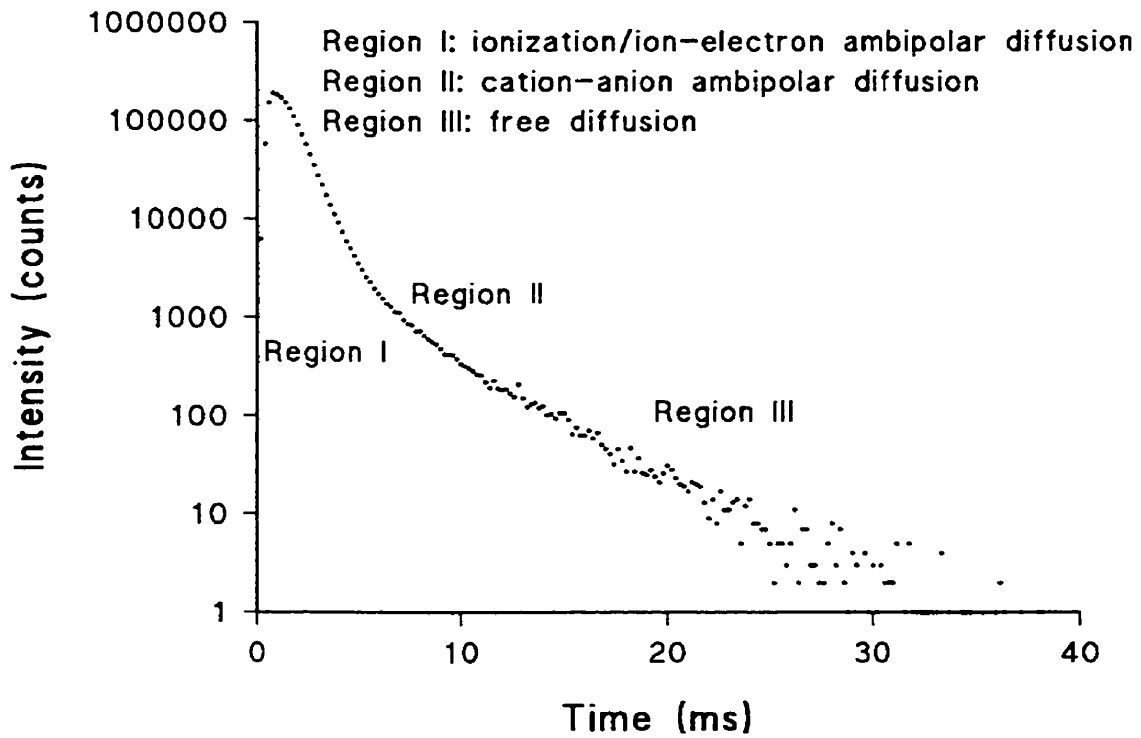


Figure 2.1 Qualitative display of the regions for the various modes of diffusion in a typical PHPMS experiment with initially high ionization density.

In general, ions are lost by diffusion to the wall or by ion-molecule reactions. The rate can be given by Equation 2.7.

$$v = v_D + v_{im} \quad (2.7)$$

It is assumed that all ions diffuse through the ion source with the same diffusion coefficient D . In reality there is a slight mass dependence (Equation 2.8), but it has no practical consequences for results from PHPMS experiments.

$$D \propto \frac{kT}{e(\alpha m_r)^{1/2}} \quad (2.8)$$

In Equation 2.8, k is the Boltzmann constant, T is the absolute temperature, e is the charge of the ion, α is the polarizability of the bath gas, and m_r is the reduced mass. Neutral molecules present in the ion source may also show mass dependent diffusion, and, as a consequence, concentration enrichment can take place, leading to incorrect equilibrium constants and rate constants. Grimsrud and co-workers showed that no enrichment was obtained with near-viscous flow, and that accurate rate constants for ion-molecule reactions could be obtained.⁴⁻⁶

There are a few aspects of PHPMS that may give rise to errors in thermochemical and kinetic data.⁷ These include the occurrence of non-equilibrium steady states, isomerization, isomerization following chemical ionization, pyrolysis of ions and neutrals, non-reactive systems and slow reactions, impurities and extraneous reactions, reactions outside the ion source, inaccurate vapor pressures, and mass coincidences. For most problems simple and practical solutions are available, and these have been summarized by Meot-Ner and Sieck.⁷ In addition, PHPMS is not able to selectively generate ions, no selective ejection of ions can take place, and in general no information on ion structures is directly available. These shortcomings have been solved by injecting mass-selected ions into a low field, variation of the temperature, high pressure drift cell and by using a reversed geometry, double focussing mass spectrometer or a triple quadrupole mass spectrometer to perform MIKE or CID experiments, respectively.

Finally, the errors associated with ΔG° measurements mainly come from errors in the absolute temperature, concentrations, and discrimination of ion transmission and detection, while errors in ΔH° values come from differential errors in the temperature, and changes in the concentrations during variable temperature studies. ΔH° can be measured accurately even in the presence of significant errors in ΔG° , because the sources of errors are independent. The standard deviations of the slope and intercept in Van't Hoff plots represent errors associated with random scatter.

More specific details on obtaining thermochemistry and kinetics are described in the relevant chapters.

2.2 Pulsed-ionization High Pressure Mass Spectrometer

All PHPMS experiments described in this thesis have been performed on an instrument constructed at the University of Waterloo.⁸ A schematic is shown in Figure 2.2.

Gas mixtures were prepared in a 5 L heated, stainless steel reservoir. For specific conditions and mixture compositions, see the relevant chapters for more detail. The sample reservoir pressure was measured with a Valydine Instruments AP-10 capacitance manometer. Methane bath gas and other gases were introduced from gas cylinders, while volatile liquids were introduced by injecting a known volume into the reservoir through a septum. The pressures of the liquids were determined from the ideal gas law. After mixing for 30 minutes, the gas mixture was allowed to flow through a heated stainless steel inlet line via a fine metering valve into the ion source. The ion source block was made of non-magnetic stainless steel and the ion source volume is approximately 1 cm³. The ion source pressure was measured with a Valydine Instruments AP-10 capacitance manometer attached to the gas inlet line. The ion source temperature was variable from ambient to 350°C using cartridge heaters embedded in a stainless steel sheath surrounding the ion source block. The ion source temperature was measured by an iron-constantan thermocouple embedded in the stainless steel block close to the ion source volume.

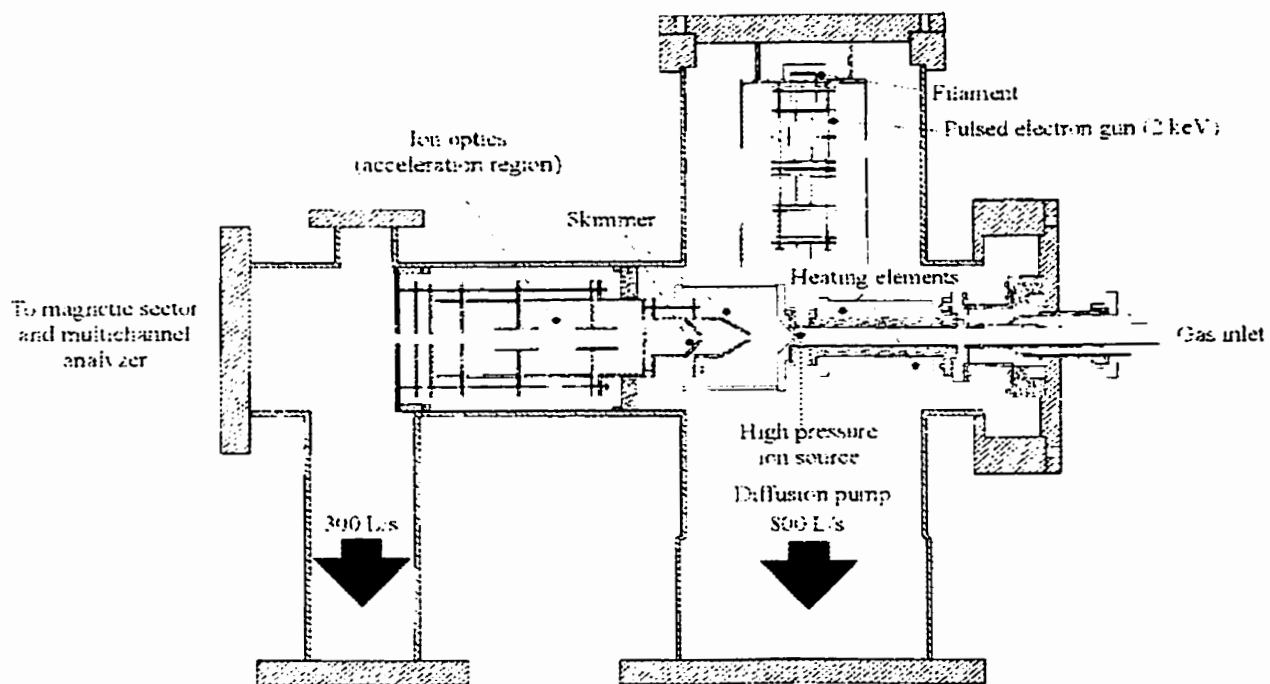


Figure 2.2 Schematic of the PHPMS instrument used.

Electrons with 2 kV kinetic energy from an externally mounted electron gun assembly initiated ionization of the gas mixture. Einzel lenses and deflection electrodes allowed focussing of the electron beam onto a small spot centred on a 150 μm Pt/Ir electron entrance aperture. The electron gun assembly was surrounded by a MU metal shield. Perpendicular to the electron entrance aperture, a similar ion exit aperture was located. Approximately 10^{-4} of the total number of ions exited the ion source through this aperture into the main housing, and they were accelerated finally by an ion lens assembly to -1500 V. The main housing was pumped by an Edwards 160M, 800 L s^{-1} Diffstak diffusion pump.

The ion acceleration region was mated to the main housing via a Teflon ring seal around one lens element containing a 2 mm aperture for ion transmission. The ion acceleration region was differentially pumped by an Edwards 63M, 200 L s^{-1} Diffstak diffusion pump. Mass analysis or selection was done by a VG Instrument MM 8-80 magnetic sector mass spectrometer, with a mass resolution of around 200. A magnetic sector actually selected ions according to their impulse (Equation 2.9).

$$r = \frac{mv}{Bze} \quad (2.9)$$

In Equation 2.9, r is the radius of the magnetic sector, m is the mass of the ion, v is the speed of the ion, B is the magnetic field strength, z is the nominal charge of the ion, and e is the elementary charge.

Ions were collected and counted by an off-axis Galileo channeltron electron multiplier assembly with deflection dynode. The electron beam pulse gated an Ortec 7150 multichannel analyzer configured in the multichannel scaling (MCS) mode to obtain time-resolved ion signals. The output of the channeltron electron multiplier was sent to a charge-sensitive preamplifier with a fixed voltage output pulse, which was sent to an Ortec amplifier-discriminator, and finally to an Ortec rate meter and multichannel analyzer. Ion-intensity profiles after collection were sent via an RS-232 interface to a PC, where data were normalised, stored, and plotted.

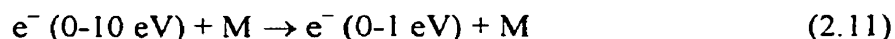
Finally, determination of equilibrium constants, rate constants, and thermochemical data were done by in-house software.

2.3 Ion and Cluster Ion Formation

The formation of anions and cluster ions in the ion source takes place through a series of reactions.⁹ The 2 kV electron beam will mainly ionize methane bath gas molecules (M) in a small volume just below the electron entrance aperture by cascade electron ionization (EI) (Reaction 2.10).



The secondary electrons formed will undergo numerous collisions ($\approx 10^6$) with methane molecules, and thermalisation takes place (Reaction 2.11).



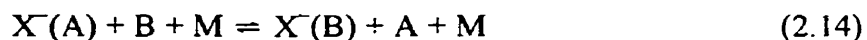
The rate of thermalisation will be fast relative to the rate of electron loss by ambipolar diffusion to the walls and prior to electron capture.⁴

Halide ions are formed by dissociative electron capture (DEC) of the thermalised secondary electron by appropriate halogen containing molecules that are present in the gas mixture in trace amounts (Reaction 2.12).



Finally, equilibrium cluster ion formation or exchange reactions in the presence of a third body molecule, usually methane bath gas, takes place in the ion source (Reactions 2.13 and 2.14).





In addition, ion/ion and radical/radical, and ion/radical recombination, neutralization, electron detachment, and electron radiolysis reaction can take place (Reaction 2.15-2.20), but these processes cannot be observed directly by the mass spectrometer. The presence of cluster ions containing neutrals generated by these processes may indicate their occurrence. However, the probability of these processes taking place is very small, due to the low concentrations of the ionic species involved in the ion source.



2.4 References

- 1 Kebarle, P. "Pulsed High Pressure Mass Spectrometry". In "Techniques for the Study of Ion-Molecule Reactions"; Farrer, J. M.; Saunders, Jr., W. H., Eds.; Wiley-Interscience, New York, NY, 1988, 221 and references cited therein.
- 2 McMahon, T. B. *Int. J. Mass Spectrom.* **2000**, *200*, 187 and references cited therein.
- 3 Hiraoka, K.; Morise, K.; Shoda, T. *Int. J. Mass Spectrom. Ion Processes* **1985**, *67*, 11 and references cited therein.
- 4 Knighton, W. B.; Grimsrud, E. P. *Int. J. Mass Spectrom. Ion Processes* **1991**, *109*, 83.

- 5 McGrew, D. S.; Knighton, W. B.; Bognar, J. A.; Grimsrud, E. P. *Int. J. Mass Spectrom. Ion Processes* **1994**, *139*, 47.
- 6 Williamson, D. H.; Knighton, W. B.; Grimsrud, E. P. *Int. J. Mass Spectrom. Ion Processes* **1996**, *154*, 15.
- 7 Meot-Ner (Mautner), M.; Sieck, L. W. *Int. J. Mass Spectrom. Ion Processes* **1991**, *109*, 187 and references cited therein.
- 8 Szulejko, J. E.; Fisher, J. J.; McMahon, T. B.; Wronka, J. *Int. J. Mass Spectrom. Ion Processes* **1988**, *83*, 147 and references cited therein.
- 9 Oster, T.; Kühn, A.; Illenberger, E. *Int. J. Mass Spectrom. Ion Processes* **1989**, *89*, 1 and references cited therein.

Chapter 3

Computational methods

3.1 Introduction

Over the past decade the application of quantum chemical computational methods has become an integral part of experimental gas phase ion chemistry of small to medium sized systems.¹ Results from these computations have provided significant insights into the structures, energetics, and kinetics of gas phase ions. Several methods are available and have been applied with varying degrees of success. Still, the only real test for the quality of a certain method for a variety of related systems is the extent of agreement with available and reliable experimental data.

In this chapter a brief overview of the various methods and basis sets used, and properties calculated in this thesis, including some important basic formulae, will be given.

3.2 Hartree-Fock

Ab initio electronic structure calculations use methods, solely based on quantum mechanics, to solve approximations to the Schrödinger equation (Equation 3.1).²

$$H\Psi = E\Psi \quad (3.1)$$

In Equation 3.1, H is the Hamiltonian operator, Ψ is the wavefunction, and E is the energy of the system. For a molecular system, Ψ is a function of the positions of the electrons (\vec{r}) and nuclei (\vec{R}) within the molecule. The Hamiltonian is made up of kinetic (T) and potential energy (V) terms (Equation 3.2).³

$$H = T + V \quad (3.2)$$

By applying the Born-Oppenheimer approximation, which states that the electron distribution within a molecular system depends on the position of the nuclei, the wavefunction can be simplified (Equation 3.3).³

$$\Psi(\vec{r}, \vec{R}) = \Psi_{electrons}(\vec{r}, \vec{R})\Psi_{nuclei}(\vec{R}) \quad (3.3)$$

The electronic Hamiltonian can be written as follows (Equation 3.4).³

$$\begin{aligned} H^{elec} = & -\frac{1}{2} \sum_i^{electrons} \left(\frac{\partial^2}{\partial x_i^2} + \frac{\partial^2}{\partial y_i^2} + \frac{\partial^2}{\partial z_i^2} \right) - \sum_i^{electrons} \sum_I^{nuclei} \left(\frac{Z_I}{|\vec{R}_I - \vec{r}_i|} \right) + \sum_i^{electrons} \sum_{j < i} \left(\frac{1}{|\vec{r}_i - \vec{r}_j|} \right) \\ & + \sum_I^{nuclei} \sum_{J < I} \left(\frac{Z_I Z_J}{|\vec{R}_I - \vec{R}_J|} \right) \end{aligned} \quad (3.4)$$

Two requirements for Ψ are that it should be normalized and anti-symmetric. According to molecular orbital (MO) theory, Ψ will be a linear combination of molecular orbitals. The Hartree product (Equation 3.5) is a method to form Ψ , but it is not anti-symmetric.³

$$\Psi(\vec{r}) = \prod_{i=1}^n \phi_i(\vec{r}_i) \quad (3.5)$$

A determinant is an anti-symmetric function that qualifies as a suitable linear combination of molecular orbitals. In addition, the electron spin must be taken into account. By substituting Equation 3.5 into Equation 3.4, and solving for Equation 3.1, an approximate wavefunction is obtained with an energy higher than the energy corresponding to the exact wavefunction. This is also known as the variational principle. By solving the Roothan-Hall equation iteratively (Equation 3.6),^{4,5} at convergence the energy will be minimized.

$$\sum_{\nu=1}^N (F_{\mu\nu} - \epsilon_i S_{\mu\nu}) c_{\nu i} = 0 \quad (3.6)$$

F is called the Fock matrix and S is the overlap integral. In the Hartree-Fock (HF) approximation there is a correction for electron-electron repulsion, in a way that every electron interacts with all other electrons in an average field.

3.3 MP2

Møller-Plesset (MP) perturbation theory is an approach to electron correlation by adding higher order excitations to Hartree-Fock theory as a non-iterative correction.⁶ This can be done by dividing the Hamiltonian into two parts (Equation 3.7).

$$H = H_0 + \lambda V \quad (3.7)$$

The λV term adds a small perturbation to the H_0 , which will give the HF solution, and thus gives the electron correlation. The second-order correction to the energy is given by Equation 3.8,⁷ with $V_{0s} = \langle \Phi_0^{(0)} | V | \Phi_s^{(0)} \rangle$, $\Phi_0^{(0)}$ is the ground state wavefunction of the unperturbed problem, and $\Phi_s^{(0)}$ the s^{th} excited state wavefunction.⁷

$$E_0^{(2)} = \sum_{s>0} \frac{V_{0s} V_{s0}}{E_0 - E_s} \quad (3.8)$$

Higher order corrections are possible that subsequently alter the sign of the energy correction term, but they also increase dramatically the computational costs.

3.4 B3LYP

Density functional theory (DFT) computations have become increasingly popular in recent years as alternative methods to conventional post-HF *ab initio* computations.⁸ The

main advantages are in the reduced computational costs, the larger size of systems accessible, and the chemical accuracy obtainable. DFT computations treat the electron correlation using functionals of the electron density (ρ) in a system. According to Kohn and Sham, the electronic energy is partitioned in several terms (Equation 3.9),⁹ where E^T is the kinetic energy term, E^V includes terms describing the potential energy of the nuclear-electron attraction and of the repulsion between pairs of nuclei, E^J is the electron-electron repulsion term, and $E^X + E^C$ (or E^{XC}) is the exchange-correlation term.

$$E = E^T + E^V + E^J + E^X + E^C \quad (3.9)$$

The latter term arises from the exchange energy from the anti-symmetry of the quantum mechanical wavefunction and the dynamic correlation in the motion of the individual electrons.³ Various types of functionals for E^T , E^X , and E^C have been developed over the years, including the so-called hybrid functionals. The popular Becke three-parameter Lee, Yang and Parr non-local exchange functional (B3LYP) method^{10,11} comprises functionals that are a mixture of HF and DFT exchange along with DFT correlation (Equation 3.10 and 3.11).³

$$E_{\text{hybrid}}^{XC} = c_{\text{HF}} E_{\text{HF}}^X + c_{\text{DFT}} E_{\text{DFT}}^{XC} \quad (3.10)$$

$$E_{\text{B3LYP}}^{XC} = E_{\text{LDA}}^X + c_0 (E_{\text{HF}}^X - E_{\text{LDA}}^X) + c_X \Delta E_{\text{B88}}^X + E_{\text{VWN3}}^C + c_C (E_{\text{LYP}}^C - E_{\text{VWN3}}^C) \quad (3.11)$$

This method provides accurate geometries and normal mode vibrational frequencies for large size systems, as well as reasonable thermochemistry.¹² Unfortunately, it has been noticed that transition state energies are systematically underestimated.¹³

3.5 Composite Methods

The development of composite quantum chemical procedures to calculate molecular energies like bond energies, enthalpies of formation, ionization potentials, electron and proton affinities, and gas phase acidities to chemical accuracy ($\pm 1-2$ kcal mol⁻¹) had an important impact on the thermochemistry of small to medium sized molecules and ions.

The *Gaussian-n* (Gn) theories are the most well-known ones,^{14,15} and they consist of a sequence of well defined calculations to arrive at a total energy of a given system. In general these methods are relatively expensive. In this thesis the G2(MP2),¹⁶ G3,¹⁷ and G3(MP2)¹⁷ methods have been used to test their suitability for the systems investigated, and to compare with the results of lower level computations. The G2 and G3 energies effectively correspond to the quadratic configuration interaction single double (triple) (QCISD(T)) or QCISD(T)/6-311+G(2df,2p)¹⁵ and QCISD(T,full)/G3Large¹⁷ levels of theory, respectively. For the G2(MP2) and G3(MP2) methods, a series of MP4 single point energy calculations have been replaced by one single MP2 calculations, hereby providing significant savings in computational costs, plus larger systems can be handled.

3.6 Basis Sets

A basis set is a pre-defined mathematical description of the orbitals within a system, used to perform the computation. By linear combinations of these one-electron functions the molecular orbitals can be approximated. The basis functions are centered on the atomic nuclei, and bear some resemblance to atomic orbitals. The *Gaussian* suite of programs uses Gaussian-type atomic functions as basis functions (Equation 3.12).³

$$g(\alpha, \vec{r}) = cx^n y^m z^l e^{-\alpha r^2} \quad (3.12)$$

In Equation 3.12, \vec{r} is composed of x, y, and z, and α is a constant determining the radial extent of the function. All Gaussian functions are normalized (Equation 3.13).³

$$\int_0^{\infty} g^2 = 1 \quad (3.13)$$

Linear combinations of these primitive Gaussians are used to form the actual basis functions, also called contracted Gaussians (Equation 3.14),³ where $d_{\mu p}$'s are fixed constants within a given basis set. For molecular orbitals the expression is as follows (Equation 3.15).³

$$\chi_{\mu} = \sum_p d_{\mu p} g_p \quad (3.14)$$

$$\phi_i = \sum_{\mu} c_{\mu i} \chi_{\mu} = \sum_{\mu} c_{\mu i} \left(\sum_p d_{\mu p} g_p \right) \quad (3.15)$$

Split valence basis sets (3-21G or 6-31G) have two or more sizes of basis functions for each valence orbital.³ A triple split valence basis set, indicated here as A-BCD, A orbitals are used to describe the core shell, and three basis sets, B-D, to describe the valence electrons. B, C, and D are the number of Gaussian functions to describe the orbitals. For instance, the 6-311G basis set uses 6 orbitals to describe the core electrons of the heavy atoms and 3 for hydrogen, while three basis sets are used to describe the valence electrons, each consisting of 3, 1, and 1 Gaussian function(s), respectively. The split valence basis sets allow the orbitals to change size, but not shape. Polarized functions are constructed by adding orbitals with higher angular momenta beyond that required for the ground state description of the atom. Diffuse functions are large size versions of s- and p-type functions. They allow orbitals to occupy a larger region of space, and they are important for systems where the electrons are relatively far from the nucleus, *e.g.* (radical) anions and excited states, and to describe absolute acidities accurately.

In addition, multiple polarized functions are also used frequently to describe the interactions between electrons in electron correlation methods. Finally, basis sets for atoms beyond the third row of the periodic table using a so-called effective core potential (ECP) are very important and popular.^{18,19} For these large atoms, the electrons near the

nucleus are treated in an approximate way, which include some relativistic effects. For instance, the 6-311++G(d,p) basis set adds diffuse function of both the hydrogen (+) and heavy atoms (+), while p and d polarized functions are added to the hydrogen and heavy atoms, respectively. In addition, polarized and diffuse functions can also be added to ECP's.

3.7 Geometry Optimizations

A potential energy surface is a mathematical relationship between the molecular structure (bond lengths, valence angle, torsions, and other internal coordinates) and the corresponding energy.^{3,20,21} It arises in a natural way from the Born-Oppenheimer approximation. Since there can be many degrees of freedom, it is impossible to visualize a complete potential energy. On such a surface there can be minima (local and global), maxima (local and global), and saddle points. Geometry optimizations are performed to locate minima or equilibrium structures on the potential energy surface(s). In Figure 3.1, a flowchart for quasi-Newton algorithms for geometry optimizations is shown.²² In order to locate a minimum, the gradient or the forces must be zero, and all eigenvalues of the Hessian, or second derivative matrix or force constant matrix, must be positive. The optimization is completed if four convergence criteria have been satisfied. For very weakly bound systems the potential energy surface near the global minimum is very flat, and for these “floppy systems” it can be hard to meet the convergence criteria. Locating a transition state structure follows the same route as for a minimum structure, except that one of the eigenvalues of the Hessian must be negative.

3.8 Normal Mode Vibrational Frequencies and IR Intensities

Calculation of the normal mode vibrational frequencies and IR intensities of the optimized geometries of molecules, cluster ions, and transition states is a useful tool to identify the nature of the systems of interest on the potential energy surface. Minimum structures are characterized by the presence of zero imaginary frequencies, while saddle

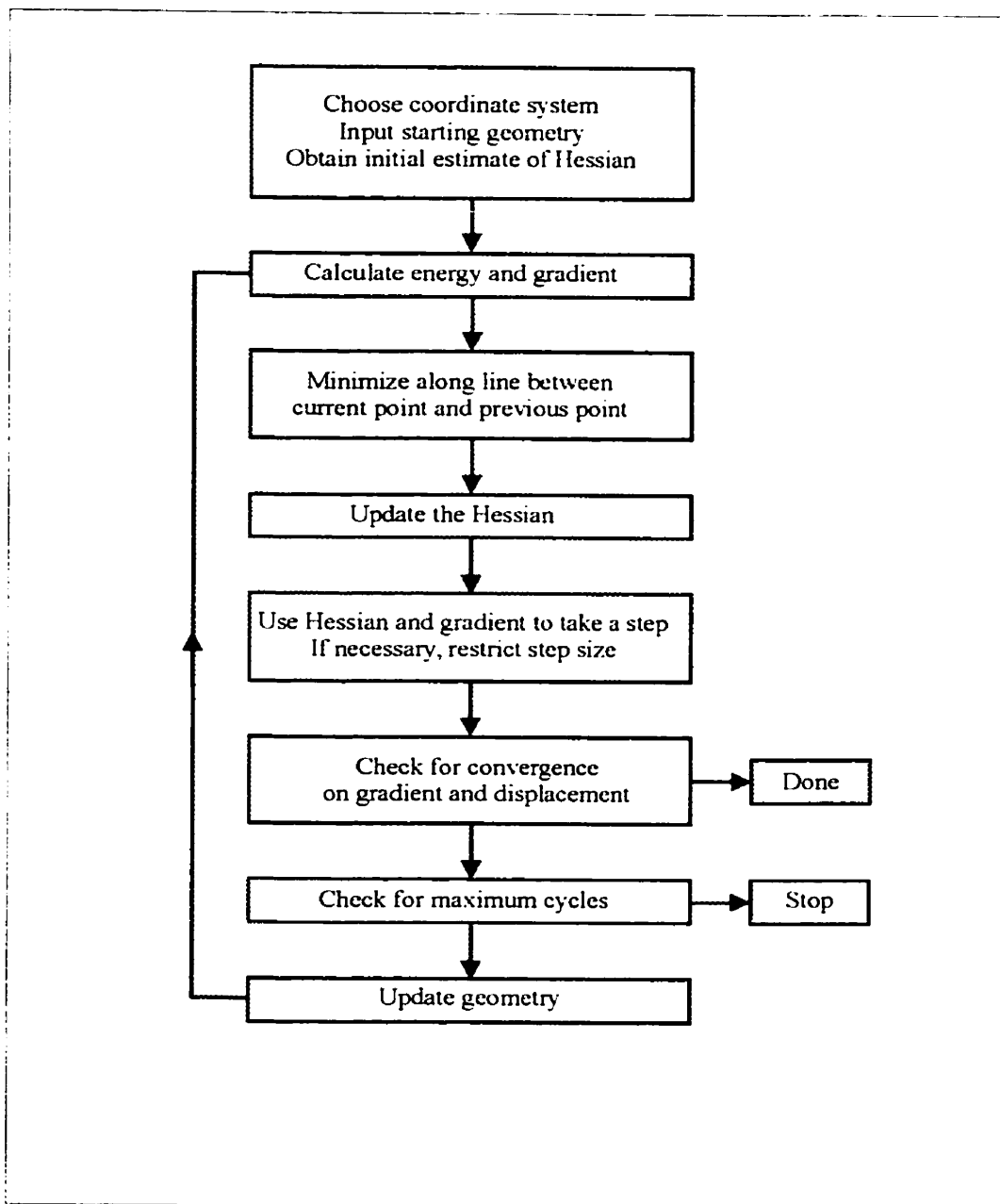


Figure 3.1 Flowchart for quasi-Newton algorithms for geometry optimizations.

points have one imaginary frequency.³ By comparison of experimental and calculated IR spectra, if available, one can assess the quality of the theoretical method chosen.

In general, the vibrational motions are treated as harmonic oscillators. In non-linear polyatomic molecules of N atoms, there are three degrees of freedom for both the translations and rotations, which leaves $3N-6$ non-zero normal mode vibrational frequencies due to molecular vibrations. A quadratic expression for the potential energy can be given by Equation 3.16.²³ Starting from this equation, the normal mode frequencies, ω_k , and the directional motion vectors, A_{jk} , can be determined from Equations 3.17-3.19.²³

$$V \approx \frac{1}{2} \sum_{i,j=1}^{3N} \left(\frac{\partial^2 V}{\partial q_i \partial q_j} \right) \Delta q_i \Delta q_j \quad (3.16)$$

$$\left(\sum_j^N H_{ij} A_{jk} \right) \omega_k^2 = \sum_j^N k_{ij} A_{jk} \quad (3.17)$$

$$k_{ij} = \left(\frac{\partial^2 V}{\partial q_i \partial q_j} \right) \quad (3.18)$$

$$H_{ij} = \sum_{a=1}^N m_a \left(\frac{\partial r_a}{\partial q_i} \right)_0 \left(\frac{\partial r_a}{\partial q_j} \right)_0 \quad (3.19)$$

For the HF, MP2, and B3LYP methods, analytical second derivatives of the energy with respect to the nuclear positions are available. In general, calculated normal mode vibrational frequencies need to be scaled in order to correct for the non-exact treatment of the electron correlation.²⁴ The absolute IR intensity, A_k (in km mol^{-1}), of the k^{th} normal mode can be calculated using Equation 3.20,¹² where 974.86 is a constant to give A the unit of km mol^{-1} , μ is the electric dipole moment, Q_k is the normal mode coordinate, and g_k is the degeneracy.

$$A_k = 974.86g_k \left| \frac{\partial \mu}{\partial Q_k} \right|^2 \quad (3.20)$$

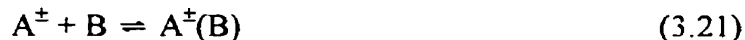
Weakly bound, non-covalent ion-molecule complexes have low, intermolecular frequencies that behave like anharmonic oscillators. No corrections are made for these.

The normal mode vibrational frequencies are used to calculate various thermochemical properties, such as the zero-point energies (ZPE) and vibrational entropies (see Section 3.9).

3.9 Thermochemistry

The *Gaussian* suite of programs will provide thermochemical data after performing a frequency calculation, and these data can be compared to experimental thermochemical parameters. In this section a brief overview will be given of the most important formulas used.

For a typical gas phase ion-molecule clustering equilibrium (Reaction 3.21), the ambient standard enthalpy changes and entropy changes can be calculated using the following formulas (Equations 3.22 and 3.23).²⁵



$$\Delta H_{298}^\circ = H_{298}^\circ(A^\pm(B)) - H_{298}^\circ(A^\pm) - H_{298}^\circ(B) \quad (3.22)$$

$$\Delta S_{298}^\circ = S_{298}^\circ(A^\pm(B)) - S_{298}^\circ(A^\pm) - S_{298}^\circ(B) \quad (3.23)$$

The various standard ambient enthalpy, H_{298}° , and entropy, S_{298}° , terms can be calculated from standard statistical mechanics (Equations 3.24-3.26).

$$H^{\circ}_{298} = E^{\circ}_{e,0} + \text{ZPE} + \int_0^{298} C_P(T) dT + RT \quad (3.24)$$

$$S^{\circ}_{298} = S^{\circ}_0 + \int_0^{298} \frac{C_P(T) dT}{T} \quad (3.25)$$

$$C_P(T) = \frac{R}{T^2} \left(\frac{\partial^2 \ln Q}{\partial (1/T)^2} \right) + R \quad (3.26)$$

$E^{\circ}_{e,0}$ is the standard electronic energy at 0 K, ZPE is the zero-point energy, $C_P(T)$ is the heat capacity at constant pressure, R is the universal gas constant, and Q is the total molecular partition function. The ZPE can be calculated from Equation 3.27.²⁶

$$\text{ZPE} = \frac{1}{2h} \sum_i \nu_i \quad (3.27)$$

The total entropy consists of electronic, translational, vibrational, and rotational terms. Since all systems investigated are in their ground state, electronic contributions will be omitted.

The translational partition function and entropy are given by Equations 3.28 and 3.29,²⁷ where m is the mass of the system, k_B is the Boltzmann constant, h is the Planck constant, V is the volume, and R is the universal gas constant.

$$q_T = \left(\frac{2\pi m k_B T}{h^2} \right)^{3/2} V \quad (3.28)$$

$$S_T = R \left(\ln q_T + \frac{5}{2} \right) \quad (3.29)$$

For a non-linear polyatomic molecule the rotational partition function and entropy are given by Equations 3.30-3.32,²⁷ where σ_R is the symmetry number for rotation, Θ is the rotational temperature, and I the moment of inertia.

$$q_R = \frac{\pi^{1/2}}{\sigma_R} \left(\frac{T^{3/2}}{\left(\prod_i \Theta_i \right)^{1/2}} \right) \quad (3.30)$$

$$\Theta = \frac{h^2}{8\pi^2 I k_B} \quad (3.31)$$

$$S_R = R \left(\ln q_R + \frac{3}{2} \right) \quad (3.32)$$

The rotational partition function for a specific normal mode vibration, k , is given by Equation 3.33,²⁷ where $\Theta_{v,k}$ is the vibrational temperature (Equation 3.34).²⁷

$$q_{v,k} = \frac{e^{-\Theta_{v,k}/2T}}{1 - e^{-\Theta_{v,k}/T}} \quad (3.33)$$

$$\Theta_{v,k} = \frac{h\nu_k}{k_B} \quad (3.34)$$

The overall vibrational partition function and entropy are given by Equations 3.35 and 3.36.²⁷

$$q_v = \prod_k \frac{e^{-\Theta_{v,k}/2T}}{1 - e^{-\Theta_{v,k}/T}} \quad (3.35)$$

$$S_v = R \sum_k \left(\frac{\Theta_{v,k}/T}{e^{\Theta_{v,k}/T} - 1} - \ln \left(1 - e^{-\Theta_{v,k}/T} \right) \right) \quad (3.36)$$

Treating low frequency vibrational modes or hindered rotations as harmonic oscillators can give large errors in the partition function, and consequently in the entropy.²⁸ In *Gaussian 98* there is the opportunity to have the program identify hindered rotations during a frequency calculation, and correct the thermochemistry based on a scheme including various methods.

3.10 NPA Charge

Natural bond orbital methods, including natural population analysis (NPA), describe the N-electron wave function $\Psi(1,2,\dots,N)$ in terms of localized orbitals or configurations that are closely related to chemical bonding concepts.²⁹ Each such localized basis set is complete and orthogonal, and can describe the electron density and other properties in a rapidly convergent way. In general, the NPA charges seem to give a more chemically intuitive consistent picture than, for instance, Mulliken population analysis.

3.11 Software and Hardware

All computations were performed using the *Gaussian 94*,³⁰ *Gaussian 98*,³¹ and *Gaussian 98W*³¹ suites of programs.

Gaussian 94 was run on a DEC Alphaserber 2100 5/250, with 4 64-bit DEC Alpha processors and 1 GB of memory. *Gaussian 98* was run on a Silicon Graphics Origin 200 with 4 64-bit MIPS R12000 processors and 4 GB RAM, and an IBM RS6000 SP.³² *Gaussian 98W* was run on a PIII Pentium 500 PC with 256 MB RAM.

3.12 References

- 1 Koch, W.; Hase, W. L. (Eds.) *Int. J. Mass Spectrom.* **2000**, *201*, 1-336 and references cited therein.
- 2 Schrödinger, E. *Ann. Physik* **1926**, *79*, 361.
- 3 Foresman, J. B.; Frisch, A. *Exploring Chemistry with Electronic Structure Methods*, 2nd ed.; Gaussian Inc.; Pittsburgh, PA, **1996**.
- 4 Roothaan, C. C. *Rev. Mod. Phys.* **1951**, *23*, 69.
- 5 Hall, G. G. *Proc. Roy. Soc. (London)* **1951**, *A205*, 541.
- 6 Møller, C.; Plesset, M. S. *Phys. Rev.* **1934**, *71*, 159.
- 7 Cremer, D. *Encyclopedia of Computational Chemistry*; von R. Schleyer, P.; Allinger, N. C.; Clark, T.; Gasteiger, J.; Kollman, P. A.; Schaefer III, H. F.; Schreiner, P. R. (Eds.); John Wiley & Sons; Chichester, UK. **1998**, *1706* and references cited therein.
- 8 Gill, P. M. W. in reference 7, 678 and references cited therein.
- 9 Kohn, W.; Sham, L. J. *Phys. Rev.* **1965**, *140*, A1133.
- 10 Lee, C.; Yang, W.; Parr, R. G. *Phys. Rev. B* **1988**, *37*, 785.
- 11 Becke, A. D. *J. Chem. Phys.* **1993**, *98*, 1372, 5648.
- 12 Hu, C.-H.; Chong, D. P. from reference 7, 664 and references cited therein.
- 13 Glukhovtsev, M. N.; Bach, R. D.; Pross, A.; Radom, L. *Chem. Phys. Lett.* **1996**, *260*, 558.
- 14 Pople, J. A.; Head-Gordon, M.; Fox, D. J.; Raghavachari, K.; Curtiss, L. A. *J. Chem. Phys.* **1989**, *90*, 5622.
- 15 Curtiss, L. A.; Raghavachari, K.; Trucks, G. W.; Pople, J. A. *J. Chem. Phys.* **1991**, *94*, 7221.
- 16 Curtiss, L. A.; Raghavachari, K.; Pople, J. A. *J. Chem. Phys.* **1993**, *98*, 1293.
- 17 Curtiss, L. A.; Raghavachari, K.; Redfern, P. C.; Rassolov, V.; Pople, J. A. *J. Chem. Phys.* **1998**, *109*, 7764.
- 18 Wadt, W. R.; Hay, P. J. *J. Chem. Phys.* **1985**, *82*, 284 and references cited therein.
- 19 Stevens, W. J.; Kraus, M.; Basch, H.; Jasien, P. G. *Can. J. Chem.* **1992**, *70*, 612.
- 20 Schlegel, H. B. in reference 7, 1136.

- 21 Shlick, T. in reference 7, 1142.
- 22 Reproduced from reference 20.
- 23 Cornell, W.; Louise-May, S. in reference 7, 1904.
- 24 Scott, A. P.; Radom, L. *J. Phys. Chem.* **1996**, *100*, 16502.
- 25 Bogdanov, B.; McMahon, T. B. *J. Phys. Chem. A* **2000**, *104*, 7871.
- 26 From reference 7, 3265.
- 27 <http://www.gaussian.com/thermo.htm> and references cited therein.
- 28 Ayala, P. Y.; Schlegel, H. B. *J. Chem. Phys.* **1998**, *108*, 2314 and references cited therein.
- 29 Reed, A. E.; Curtiss, L. A.; Weinhold, F. *Chem. Rev.* **1988**, *88*, 899.
- 30 Frisch, M. J.; Trucks, G. W.; Schlegel, H. B.; Gill, P. M. W.; Johnson, B. G.; Robb, M. A.; Cheeseman, J. R.; Keith, T.; Petersson, G. A.; Montgomery, J. A.; Raghavachari, K.; Al-Laham, M. A.; Zakrzewski, V. G.; Ortiz, J. V.; Foresman, J. B.; Peng, C. Y.; Ayala, P. Y.; Chen, W.; Wong, M. W.; Andres, J. L.; Replogle, E. S.; Gomperts, R.; Martin, R. L.; Fox, D. J.; Binkley, J. S.; Defrees, D. J.; Baker, J.; Stewart, J. P.; Head-Gordon, M.; Gonzales, C.; Pople, J. A. *Gaussian 94*, Revision B3, Gaussian Inc., Pittsburgh PA, **1995**.
- 31 Frisch, M. J.; Trucks, G. W.; Schlegel, H. B.; Scuseria, G. E.; Robb, M. A.; Cheeseman, J. R.; Zakrzewski, V. G.; Montgomery, Jr., J. A.; Stratmann, R. E.; Burant, J. C.; Dapprich, S.; Millam, J. M.; Daniels, A. D.; Kudin, K. N.; Strain, M. C.; Farkas, O.; Tomasi, J.; Barone, V.; Cossi, M.; Cammi, R.; Mennucci, B.; Pomelli, C.; Adamo, C.; Clifford, S.; Ochterski, J.; Petersson, G. A.; Ayala, P. Y.; Cui, Q.; Morokuma, K.; Malick, D. K.; Rabuck, A. D.; Raghavachari, K.; Foresman, J. B.; Cioslowski, J.; Ortiz, J. V.; Baboul, A. G.; Stefanov, B. B.; Liu, G.; Liashenko, A.; Piskorz, P.; Komaromi, I.; Gomperts, R.; Martin, R. L.; Fox, D. J.; Keith, T.; Al-Laham, M. A.; Peng, C. Y.; Nanayakkara, A.; Gonzalez, C.; Challacombe, M.; Gill, M. W.; Johnson, B.; Chen, W.; Wong, M. W.; Andres, J. L.; Gonzalez, C.; Head-Gordon, M.; Replogle, E. S.; Pople, J. A. *Gaussian 98*, Revision A.7 Gaussian, Inc., Pittsburgh PA, **1998**.
- 32 <http://www.ibmisp.uwaterloo.ca/hardware.html>

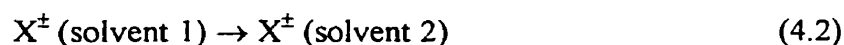
Chapter 4

Structures, thermochemistry, dynamics, and spectroscopy of halide ion and bihalide ion-alcohol clusters in the gas phase

4.1 Introduction

In the condensed phase, solvent effects are among the most important factors that determine structure-activity relationships. Examples include the lifetimes of biradicals,¹ the (non-) occurrence of exciplexes,² the energies of excited states,³ the reactivity of nucleophiles and leaving groups,⁴ ion-pair separation,⁵ acidities and basicities,⁶ photosensitization,⁷ and finally the effects on S_N1, S_N2, E1, and E2 types of reactions.⁹⁻²² In electrochemistry the degree of ion solvation determines the ion activity and mobility, and consequently the conductivity of the electrolyte solutions. In biochemistry one of the most important solvation phenomena is the solvation of zwitterionic amino acids which renders these species significantly more stabilized than their uncharged isomers.^{23,24}

Insights into condensed phase phenomena have been gained from thermodynamic measurements for the transfer of ions from the gas phase (Reaction 4.1) or from one solution into another (Reaction 4.2).



The most common quantity experimentally investigated is the free energy change of transfer, $\Delta_{\text{tr}}G$, and a large amount of data concerning many different ions and solvents has been obtained.^{25,26} These free energies of transfer frequently reveal the importance of hydrogen bonding to ion solvation. Water is the most common solvent and many of its unique chemical and physical properties are determined by the hydrogen-bonded network. Halide ions, especially chloride ion, are among the most common and important

anions in organic chemistry, biochemistry and mass spectrometry, and consequently halide ion-water interactions are among the most extensively studied.²⁷⁻⁴⁵ Gas phase ion chemistry has, for many decades, played an important role in studying ionic clusters and powerful techniques to generate and study micro-solvated ionic species have been developed.⁴⁶⁻⁵² Much insight into bulk behavior has been obtained by deducing solvent effects at a micro-solvated level. This has been done by investigating the thermochemistry, reactivity, and structures of solvated ions, and comparing these data with results from bare or non-solvated ions.^{27,53}

One of the most extensively studied phenomena with halide ion-water clusters is the occurrence and possible competition between interior and surface solvation. Most information to date has been obtained from *ab initio*^{36,41,54-58} and MD computations,^{37,39,59-61} but recently, ion spectroscopy has also been used to prove existence of features that had been either speculative or based upon computations.^{28-34,38,40,62-64} For the last three decades an impressive amount of data on ion solvation in the gas phase has been obtained that has proven to be useful in many fields of science such as atmospheric chemistry, surface science, and catalysis.⁶⁵⁻⁶⁷ Most of these data deal with relatively small systems, but the fundamental knowledge obtained from these small systems, by analogy, can be used readily for larger, more complex systems. One example is in the field of supramolecular chemistry, where the development of anion specific, host-guest systems is gaining more interest and importance.⁶⁸⁻⁷⁸ Understanding these systems in the condensed phase would be difficult without the full understanding of smaller systems in the gas phase and in micro-solvated environments. There are still many features that have not received sufficient attention.

Alcohols represent a class of protic solvents for which the halide ion complexes have recently received a renewed interest, both experimentally and theoretically.^{63,64,79-81} The polar, monoprotic alcohol molecules do not form extensive, hydrogen-bonded networks such as occurs with water molecules. One of the main questions for these systems is whether interior solvation will take place in the larger halide alcohol clusters. Carbacos *et al.* recently showed by vibrational predissociation spectroscopy (VPDS) on $\text{Cl}^-(\text{CH}_3\text{OH})_n$ clusters that for $n = 4$ one of the methanol molecules is bonded to one of the three other methanol molecules that make up the so-called first solvation shell around the chloride

ion.⁶³ It then would seem to be a logical step for future VPDS experiments to find out whether this asymmetric solvation is dependent on both the shape of the alcohol molecule and the type of halide ion. Among the experimental techniques used to study halide ion-protic solvent molecule clusters are HPMS,⁸²⁻⁸⁵ PHPMS,^{79,86-93} ICR,^{25,94,95} FT-ICR,^{91,96-99} EPDS,¹⁰⁰⁻¹⁰³ NIPES,¹⁰⁴⁻¹⁰⁶ IRMPD,^{107,108} VPDS,^{28-34,38,40,62-64} and TCID.^{80,81} In general, reasonable agreement is observed when comparing data obtained from these different techniques.

Surprisingly, thermochemical data for the equilibrium clustering of many halide ion-alcohol systems has never been determined. This is especially true for the higher order clusters (more than two solvent molecules) of the fluoride ion and the heavier halide ions (Br^- and I^-) with larger alcohol molecules ($\text{CH}_3\text{CH}_2\text{OH}$, $(\text{CH}_3)_2\text{CHOH}$, $(\text{CH}_3)_3\text{COH}$).

In the present work, a systematic study has been performed to obtain new experimental data as well as to evaluate existing thermochemical data, and to obtain computational data on mono- and some disolvated halide ion-alcohol complexes. For most of these species little or no computational data were previously available. In some cases the available computational data were obtained at higher levels of theory than the work presented here.^{79,97,104,109,110} One of the objectives was to find a single level of theory that is relatively fast, and that can reproduce experimental data for the halide ion-alcohol complexes well. Mono- and disolvated halide ion-alcohol complexes of course cannot be considered good model systems for halide ion solvation, but if it will be possible to model mono- and di-solvation accurately by obtaining, for instance, reliable thermochemical data, extension to larger halide ion-alcohol complexes can be made with more confidence. Those results may provide an accurate input for modeling the kinetics of the thermal unimolecular dissociation of halide ion-alcohol complexes, and to help in interpreting VPDS experiments on halide ion-alcohol complexes.

In addition, more insights into the details and trends of the structures, the thermochemistry, the IR spectroscopic characteristics, and the electronic nature of the hydrogen bond(s) formed would be desirable. It may, *a priori*, be expected that changing the halide ion, the alcohol ligand, and the number of ligands will have a pronounced effect on the thermochemistry. Identifying the intrinsic molecular and ionic properties responsible for the observed trends will provide insight into the different interactions

within the cluster ions. For these kinds of systems it seemed most logical, *a priori*, to use theoretical methods that included electron correlation, and consequently the Møller-Plesset second-order perturbation theory including all electrons (MP2(full)),¹¹¹ and the Becke three-parameter Lee, Yang, and Parr non-local, exchange correlation functional¹¹²⁻¹¹⁴ (B3LYP) methods seemed good choices in this respect. As well, these methods had been successfully applied to similar systems in the past.^{34,64,74,80,81,97,104,109,110} The MP2 method is a very time and memory intensive method compared to B3LYP, and its use is limited to systems containing a relatively small number of heavy atoms. The B3LYP method, on the other hand, can handle large systems well, while using a relatively small amount of CPU time. Extended basis sets including polarization and diffuse functions were used since these have been shown to model the relatively weak non-covalent interactions within the halide ion-alcohol complexes relatively well.

Finally, one- and two-dimensional potential energy surface (PES) scans were performed on the halide ion-methanol complexes to try to obtain some insights into the possible dynamics of halide ion-methanol complex formation, and the dynamics within the halide ion-methanol complexes.

4.2 Experimental

All experiments were carried out on two PHPMS instruments configured around either a VG 8-80 or a reversed VG 70-70 (magnetic sector (B)-electrical sector (E) geometry) mass spectrometer. The instruments, both constructed at the University of Waterloo, have been described in detail previously^{115,116} and in Chapter 2.

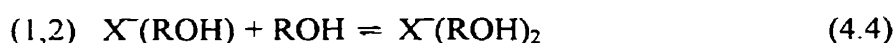
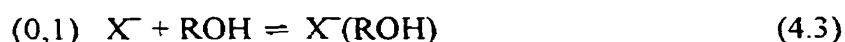
Gas mixtures were prepared in a 5 L heated stainless steel reservoir (60-85°C) using methane as the bath gas at pressures between 135-835 Torr. The halide ions, F⁻, Cl⁻, Br⁻, and I⁻ were generated from NF₃ (0.05-0.20% partial pressure), CCl₄ (< 0.01%), CH₃Br (0.25-1.50%), and CH₃I (< 0.01%), respectively, by DEC of thermalized electrons from 300 μs pulses of a 2 keV electron gun beam.

The four alcohols, CH₃OH, CH₃CH₂OH, (CH₃)₂CHOH, and (CH₃)₃COH were added to give relative amounts between 0.01% and 20%, depending on the temperature and the

nature of the experiments involved. The ion source pressure and temperature ranged between 3.5-10.0 Torr and 300-710 K, respectively.

Time intensity profiles of mass selected ions were monitored using a PC based multichannel scaler (MCS) data acquisition system, typically configured between 50-400 μ s dwell time per channel over 250 channels. Additive accumulations of ion signals resulting from 250-2000 electron gun beam pulses were typically used.

Equilibrium constants (K_{eq}) for the three consecutive stepwise halide ion solvation reactions (Reactions 4.3-4.5) are determined from Equations 4.6-4.8, respectively.



$$K_{eq.4.3} = \frac{\text{Int}(X^-(ROH))}{\text{Int}(X^-)} \cdot \frac{P^\circ}{P_{ROH,source}} \quad (4.6)$$

$$K_{eq.4.4} = \frac{\text{Int}(X^-(ROH)_2)}{\text{Int}(X^-(ROH))} \cdot \frac{P^\circ}{P_{ROH,source}} \quad (4.7)$$

$$K_{eq.4.5} = \frac{\text{Int}(X^-(ROH)_3)}{\text{Int}(X^-(ROH)_2)} \cdot \frac{P^\circ}{P_{ROH,source}} \quad (4.8)$$

In Equations 4.6-4.8 $\text{Int}(X^-)$, $\text{Int}(X^-(ROH))$, $\text{Int}(X^-(ROH)_2)$, and $\text{Int}(X^-(ROH)_3)$ the ion intensities of the X^- , $X^-(ROH)$, $X^-(ROH)_2$, and $X^-(ROH)_3$ ions at equilibrium for Reactions 4.3-4.5, P° is the standard pressure (1 atm), and $P_{ROH,source}$ is the partial pressure (in atm) of the alcohol in the ion source.

From the equilibrium constants, the standard Gibbs' free energy change (ΔG°) at different absolute temperatures (T) can be calculated from Equation 4.9.

$$\Delta G^\circ = -RT \cdot \ln(K_{eq}) \quad (4.9)$$

By combining Equations 4.9 and 4.10, the Van't Hoff equation (Equation 4.11) can be obtained. By plotting $\ln(K_{eq})$ versus $1/T$, ΔH° and ΔS° can be obtained from the slope and intercept, respectively.

$$\Delta G^\circ = \Delta H^\circ - T\Delta S^\circ \quad (4.10)$$

$$\ln(K_{eq}) = \frac{\Delta S^\circ}{R} - \frac{\Delta H^\circ}{R} \cdot \frac{1}{T} \quad (4.11)$$

It is possible to record mass spectra by switching the electron gun from the pulsed to the continuous mode. After leaving the ion source through the exit aperture, the ions are accelerated by an accelerating potential of 1500 V and by scanning the magnetic field from low to high field the different ions are detected consecutively.

For all $\text{NF}_3/\text{ROH}/\text{CH}_4$ mixtures, an ion with m/z 115 was always present. The relative intensities of m/z 115, 116, and 117 in the mass spectrum suggested that it contained one sulfur atom. This ion had the same m/z value as $\text{F}^-(\text{CH}_3\text{OH})_3$, and so CD_3OH was used instead of CH_3OH . For the CD_3OH synthesis 4 grams of CD_3OD (110.9 mmol, 4.50 mL) was put into a 25 mL round bottom flask. Magnesium (1.50 equivalents, 2.00 grams) was added, stirred, heated in a graphite bath, and refluxed. To the $\text{Mg}(\text{CD}_3\text{O})_2$ solution, 1.50 equivalents (3.00 mL) of H_2O were added. The CD_3OH formed was distilled off at 65°C and stored under an argon atmosphere. The $\%D_3$ versus $\%D_4$ was checked by gas chromatography/mass spectrometry (GC/MS) (HP 5890 Series II Gas Chromatograph, HP 5970A Series Mass Selective Detector) by determining the ratio of m/z 35 (CD_3OH^+) and m/z 36 (CD_3OD^+). It was found that $>95\%$ of the CD_3OD had been converted to

CD₃OH. By knowing the amount of CD₃OH/CD₃OD injected, and the densities and molecular weights of both compounds, the partial pressure of CD₃OH in the ion source could be calculated.

The NF₃ used contained approximately 50 ppm SF₆ which interfered with the formation of F⁻ from NF₃ by DEC (Reaction 4.12).



At 300 K, a rate constant for electron attachment to NF₃, k_T, of (7 ± 4) × 10⁻¹² cm² s⁻¹ was determined from FA Langmuir probe experiments.¹¹⁷ By using Equation 4.13, an average cross-section, ⟨σ⟩, for electron capture can be calculated.¹¹⁸

$$k_T = \int_0^{\infty} f_T(v) v \sigma(v) dv = \langle \sigma \rangle \langle v \rangle \quad (4.13)$$

In Equation 4.13, f_T(v) is the normalized velocity distribution of electrons at temperature T, v is the electron velocity, σ(v) is the electron velocity dependent cross section, and ⟨v⟩ is the average electron velocity at temperature T. At 300 K, ⟨v⟩ is 1.2 × 10⁷ cm s⁻¹, thus giving rise to ⟨σ⟩ = (5.8 ± 3.3) × 10⁻¹⁹ cm². This is much smaller than ⟨σ⟩ = (2.1 ± 0.4) × 10⁻¹⁴ cm² of SF₆, thus giving rise to electron capture reactions by SF₆ (Reactions 4.14 and 4.15).¹¹⁹⁻¹²¹



Ions with m/z 127 (SF₅⁻) and m/z 146 (SF₆⁻*) were indeed present in large abundances relative to F⁻ or the fluoride ion-alcohol complexes, F⁻(ROH)_n. In addition, ions at m/z 26 (CN⁻), m/z 39 (HF₂⁻), m/z 45 (CN⁻(HF)), and m/z 59 (H₂F₃⁻) were present, formed from neutrals generated by electron radiolysis reactions in the high

pressure ion source. In order to reduce the competing SF₆ reactions, it was removed from NF₃ by passing the NF₃ gas through a spiral shaped stainless steel cold trap. The cold medium was a liquid nitrogen/acetone slurry, which should have a temperature near the melting point of acetone of -94°C. At this temperature the vapor pressures of NF₃ and SF₆ are 726 kPa and 11.3 kPa, respectively.¹²⁰ This method reduced the amount of SF₆ to below 1 ppm, and indeed strongly reduced m/z 127 and 146 signals were observed relative to the F⁻(ROH)_n signals.

NF₃ was purchased from Air Products and Chemicals Inc. CCl₄ and (CH₃)₃COH were purchased from J. T. Baker Chemical Co. CH₃Br was purchased from Matheson. CH₃I, CH₃CH₂OH, and Mg were purchased from BDH Chemicals. CH₃OH and (CH₃)₂CHOH were purchased from Fisher Scientific Company. CD₃OD was purchased from Cambridge Isotope Labs. CH₄ was purchased from Praxair. All chemicals were used as received.

4.3 Computational

All computations were performed using the *Gaussian 94*¹²³ and *Gaussian 98*¹²⁴ suites of programs.

The following computational procedures were used. For the four halide ion-methanol complexes and fluoride ion-ethanol complex, computations were performed at the MP2(full)/6-311++G(d,p) **(a)**¹²⁵⁻¹²⁷ level of theory. At this level of theory, harmonic normal mode vibrational frequencies were scaled by 0.9489^{128,129} to obtain thermochemical data. For all systems studied B3LYP geometry optimizations and frequency computations were performed using the 6-311+G(d,p) **(b)**^{130,131} basis set. Single point energy computations on these B3LYP optimized structures were performed using MP2 in combination with the 6-311++G(d,p) basis set, or using B3LYP in combination with the 6-311++G(3df,3pd) **(c)**^{132,133} basis set. For the B3LYP computations, scaling factors of 1.000 and 0.9640 (X = F, Cl; R = CH₃, CH₃CH₂) were used.¹³⁴ For Γ, LanL2DZ **(d)**,¹³⁵ Stuttgart RLC ECP **(e)**,¹³⁶ and CRENBL ECP **(f)**^{137,138} were used in combination with the various basis sets for hydrogen, carbon, and oxygen. NPA charges^{139,140} were calculated for the F⁻(ROH) complexes (R = CH₃, CH₃CH₂,

(CH₃)₂CH, (CH₃)₃CH) at the B3LYP/**b** and MP2/**a**//B3LYP/**b** levels of theory, and for X⁻(CH₃OH) complexes (X = F, Cl, Br, I) at the MP2/**a** ([**a/e**] for X = I) levels of theory.

For the HF₂⁻(CH₃OH)_n (n = 0, 1, 2) ions, computations were performed at the G3(MP2) level of theory¹⁴¹.

Normal potential energy surface scans for the X⁻(CH₃OH) complexes were performed as follows. The structures of the X⁻(CH₃OH) complexes were optimized at the MP2/**a** ([**a/e**] for X = I) level of theory. Following this, z-matrices were constructed with two variables: (1) the X⁻...HOCH₃ distance (R), and (2) the X⁻...H-OCH₃ angle, as indicated in Figure 4.38. A total of 352 (X = F) or 432 (X = Cl, Br, I) single point energy calculations were performed at the same level of theory used to optimize the structures of the X⁻(CH₃OH) complexes by varying R and A between certain values (see Figures 4.39 to 4.42). No new geometry optimizations were performed for each step during the scan.

Relaxed potential energy surface scans were performed as well for the X⁻(CH₃OH) complexes at the MP2(fc)/6-31+G(d,p) (**g**)^{142,143} (X = F, Cl) and MP2(fc)/[6-31+G(d,p)/LanL2DZ(sp,d)] (**h**)^{135,144} (X = Br, I) level of theory, and for Cl⁻(CF₃OH) at the MP2(fc)/6-31+G(d,p) level of theory, where fc stands for frozen core approximation. The X⁻...HOCY₃ (Y = H, F) distance, R, was varied between certain values, depending on the halide ion, and the other degrees of freedom were optimized.

4.4 Results and Discussion

4.4.1 Experimental Thermochemistry

The results for the experimentally determined equilibrium constants, K_{eq}, for the three consecutive stepwise solvation reactions (Reactions 4.3 to 4.5) (X = F, Cl, Br, I; R = CH₃, CH₃CH₂, (CH₃)₂CH, (CH₃)₃C) are displayed in the Van't Hoff plots in Figures 4.1 to 4.8 and summarized in Tables 4.1 to 4.8. Included in these tables are results from computations and experimental literature values. The labels in Figures 4.1 to 4.8 indicate the various X_n systems investigated in this study.

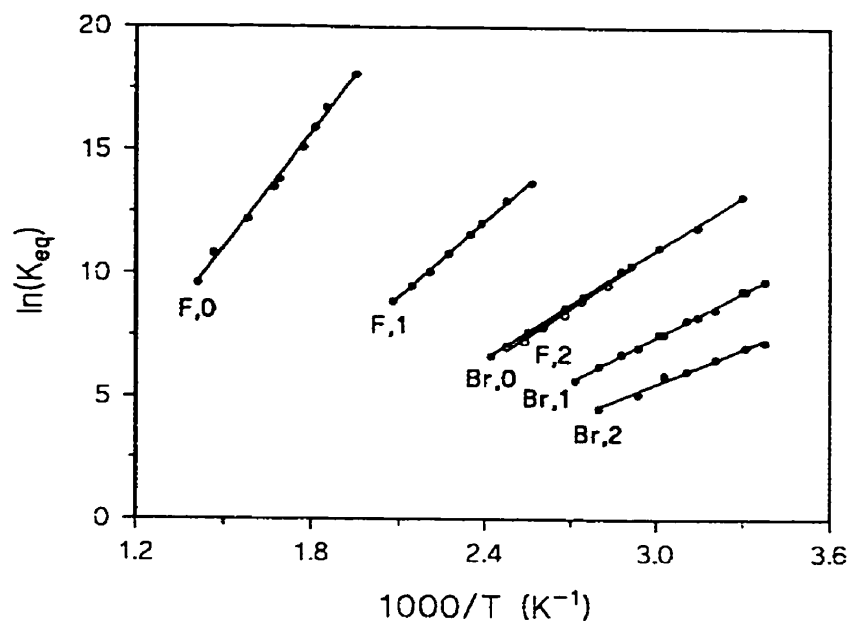


Figure 4.1 Experimental Van't Hoff plots for the halide ion-alcohol clustering equilibria $X^-(CH_3OH)_n + CH_3OH = X^-(CH_3OH)_{n+1}$ ($X = F, Br; n = 0, 1, 2$).

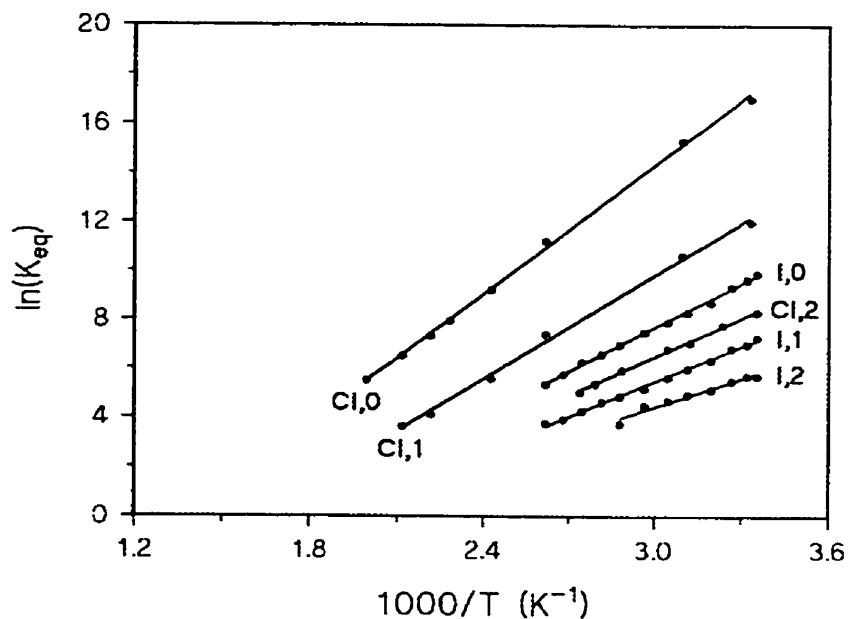


Figure 4.2 Experimental Van't Hoff plots for the halide ion-alcohol clustering equilibria $X^-(CH_3OH)_n + CH_3OH = X^-(CH_3OH)_{n+1}$ ($X = Cl, I; n = 0, 1, 2$).

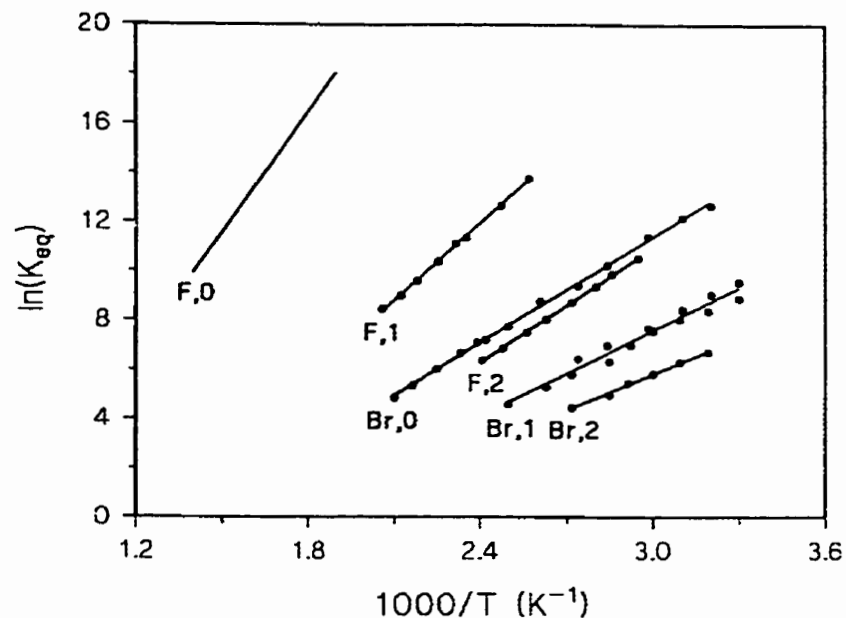


Figure 4.3 Experimental Van't Hoff plots for the halide ion-alcohol clustering equilibria $X^-(CH_3CH_2OH)_n + CH_3CH_2OH = X^-(CH_3CH_2OH)_{n+1}$ ($X = F, Br; n = 0, 1, 2$) (F,0 is a calculated Van't Hoff plot).

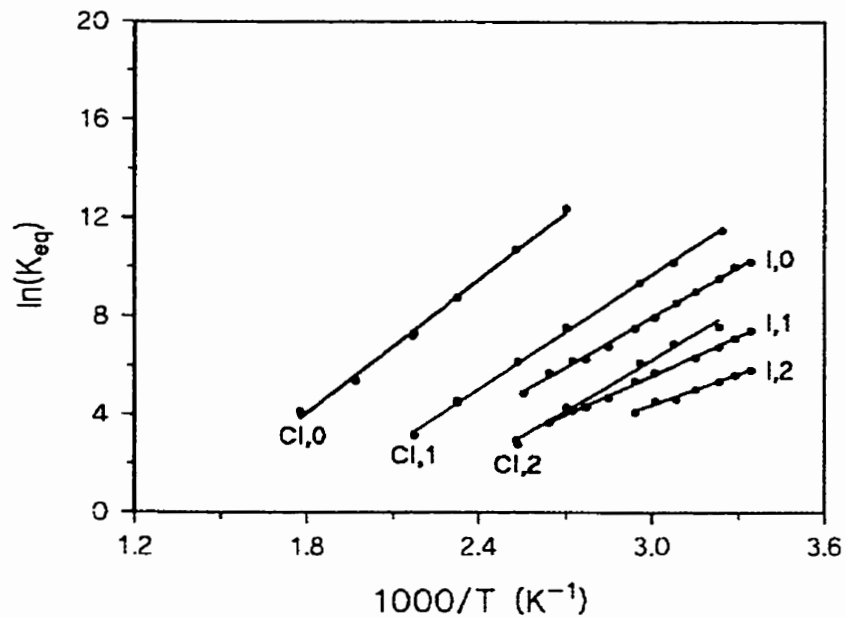


Figure 4.4 Experimental Van't Hoff plots for the halide ion-alcohol clustering equilibria $X^-(CH_3CH_2OH)_n + CH_3CH_2OH = X^-(CH_3CH_2OH)_{n+1}$ ($X = Cl, I; n = 0, 1, 2$).

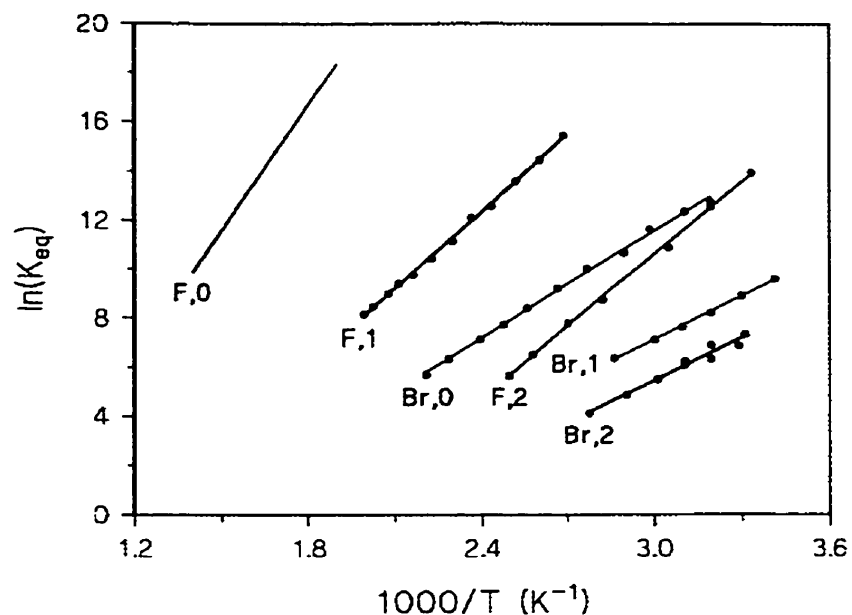


Figure 4.5 Experimental Van't Hoff plots for the halide ion-alcohol clustering equilibria $X^-((CH_3)_2CHOH)_n + (CH_3)_2CHOH = X^-((CH_3)_2CHOH)_{n+1}$ ($X = F, Br; n = 0, 1, 2$) (F,0 is a calculated Van't Hoff plot).

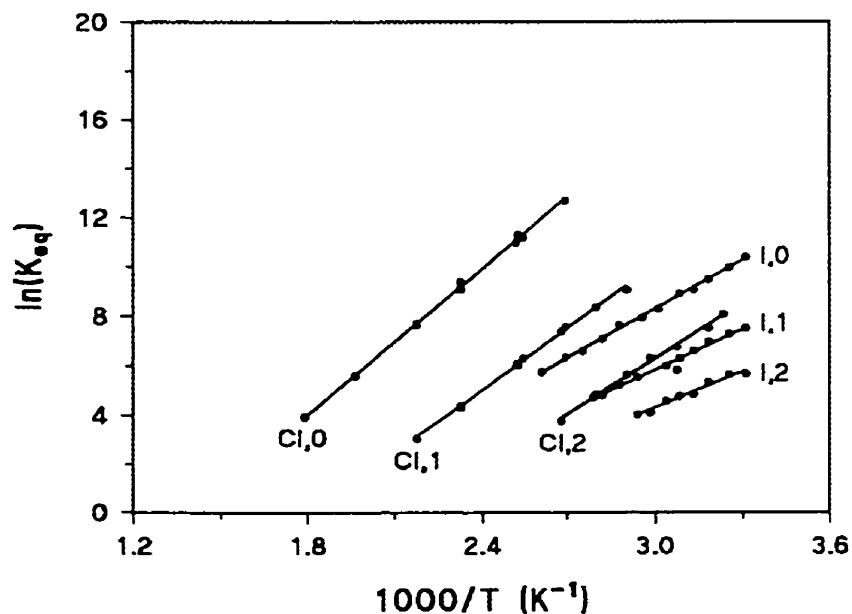


Figure 4.6 Experimental Van't Hoff plots for the halide ion-alcohol clustering equilibria $X^-((CH_3)_2CHOH)_n + (CH_3)_2CHOH = X^-((CH_3)_2CHOH)_{n+1}$ ($X = Cl, I; n = 0, 1, 2$).

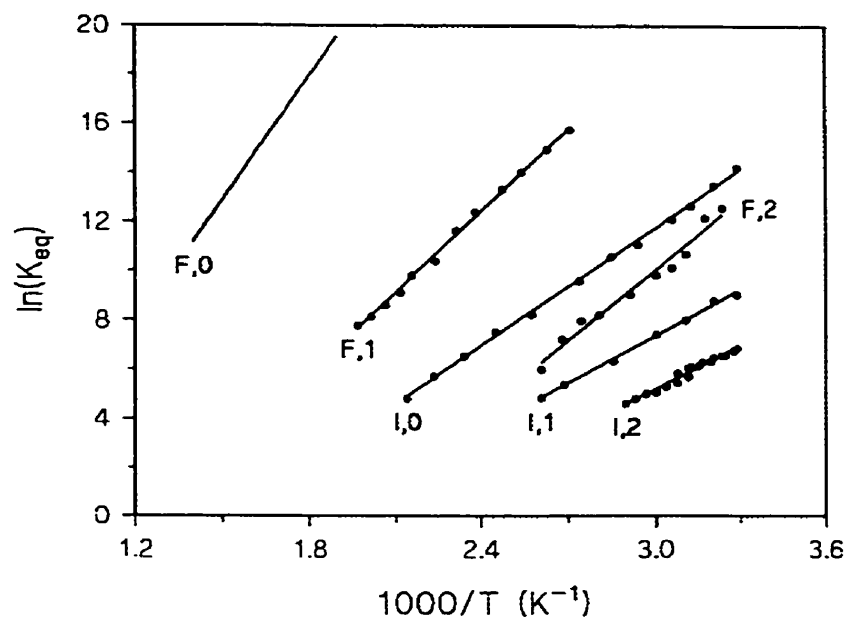


Figure 4.7 Experimental Van't Hoff plots for the halide ion-alcohol clustering equilibria $X^-((CH_3)_3COH)_n + (CH_3)_3COH \rightleftharpoons X^-((CH_3)_3COH)_{n+1}$ ($X = F, Br; n = 0, 1, 2$) (F,0 is a calculated Van't Hoff plot).

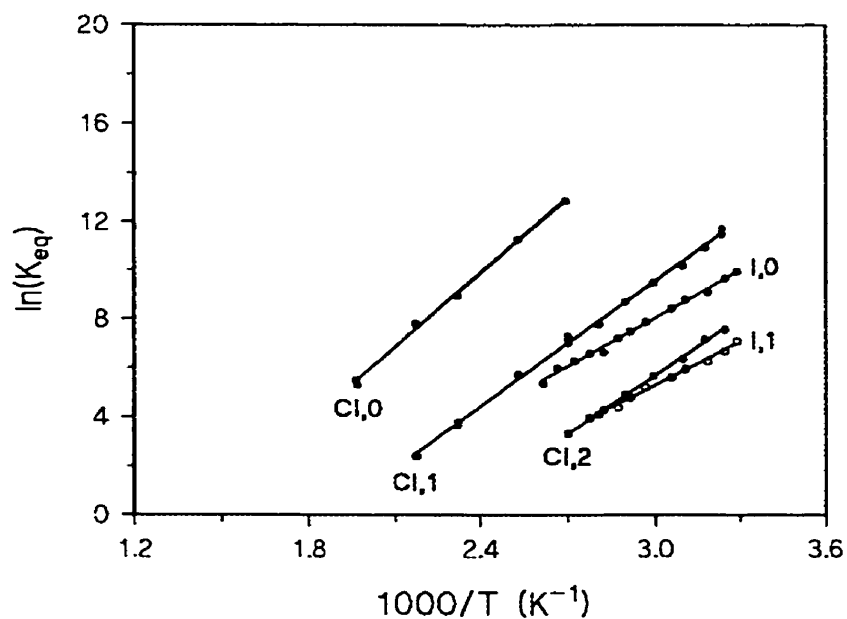


Figure 4.8 Experimental Van't Hoff plots for the halide ion-alcohol clustering equilibria $X^-((CH_3)_3COH)_n + (CH_3)_3COH \rightleftharpoons X^-((CH_3)_3COH)_{n+1}$ ($X = Cl, I; n = 0, 1, 2$).

Table 4.1 Overview of the computational and experimental thermochemistry for the $F^- + ROH \rightleftharpoons F^-(ROH)$ clustering equilibria (R = CH₃, CH₃CH₂, (CH₃)₂CH, (CH₃)₃C; **a** = 6-311++G(d,p), **b** = 6-311+G(d,p), **c** = 6-311++G(3df,3pd)).

X	ROH	(n,n+1)	method	ΔH°_{298} ^a	ΔS°_{298} ^b	method	ΔH° ^a	ΔS° ^b	reference
F	CH ₃ OH	(0,1)	MP2/a	-30.9	-22.9	ICR	-29.6	-22.6	48
			MP2/a//B3LYP/b	-31.0		PHPMS	-30.5 ± 0.7	-23.4 ± 1.2	91
			B3LYP/b	-31.6	-22.6	PHPMS	-23.3	-25.0	92
			B3LYP/c//B3LYP/b	-32.6		EPDS	-29.6 ± 0.5		103
						TCID	-29.4 ± 2.1		81
F	CH ₃ CH ₂ OH	(0,1)	MP2/a	-32.1	-24.6	ICR	-31.5	-24.9	48
			MP2/a//B3LYP/b	-32.0		PHPMS	-32.4 ± 0.5	-25.7 ± 1.3	this work
			B3LYP/b	-32.4	-22.2	TCID	-32.5 ± 0.7		81
			B3LYP/c//B3LYP/b	-33.6					
F	(CH ₃) ₂ CHOH	(0,1)	MP2/a//B3LYP/b	-33.2		ICR	-32.2	-26.5	48
			B3LYP/b	-32.5	-24.6	PHPMS	-33.5 ± 0.7	-26.2 ± 1.3	this work
			B3LYP/c//B3LYP/b	-35.2		TCID	-33.2 ± 0.7		81
F	(CH ₃) ₃ COH	(0,1)	MP2/a//B3LYP/b	-34.1		ICR	-33.3	-26.1	48
			B3LYP/b	-33.4	-25.5	PHPMS	-33.4 ± 0.7	-24.8 ± 1.2	this work
			B3LYP/c//B3LYP/b	-34.5		TCID	-32.7 ± 0.7		81

^a kcal mol⁻¹ ^b cal mol⁻¹ K⁻¹

Table 4.2 Overview of the computational and experimental thermochemistry for the $\text{Cl}^- + \text{ROH} \rightleftharpoons \text{Cl}^-(\text{ROH})$ clustering equilibria ($\text{R} = \text{CH}_3, \text{CH}_3\text{CH}_2, (\text{CH}_3)_2\text{CH}, (\text{CH}_3)_3\text{C}$; **a** = 6-311++G(d,p), **b** = 6-311+G(d,p), **c** = 6-311++G(3df,3pd)).

X	ROH	(n,n+1)	method	ΔH_{298}° ^a	ΔS_{298}° ^b	method	ΔH° ^a	ΔS° ^b	reference
Cl	CH ₃ OH	(0,1)	MP2/a	-16.6	-20.1	HPMS	-14.1	-14.8	83
			MP2/a//B3LYP/b	-16.6		HPMS	-14.2	-14.8	84
			B3LYP/b	-14.9	-19.2	ICR	-16.8	-22.9	95
			B3LYP/c//B3LYP/b	-14.9		PHPMS	-17.5 ± 0.1	-22.0 ± 0.2	85
					PHPMS	-17.4	-24.1	89	
					PHPMS	-17.1 ± 0.1	-22.6 ± 0.1	93	
					EPDS	-18.7 ± 0.5		103	
					PHPMS	-17.5 ± 0.3	-24.0 ± 0.7	this work	
Cl	CH ₃ CH ₂ OH	(0,1)	MP2/a//B3LYP/b	-17.2		ICR	-17.3	-23.1	95
			B3LYP/b	-14.9	-19.5	PHPMS	-17.6	-23.7	89
			B3LYP/c//B3LYP/b	-15.5		PHPMS	-17.9 ± 0.4	-24.3 ± 0.9	79
Cl	(CH ₃) ₂ CHOH	(0,1)	MP2/a//B3LYP/b	-18.7		ICR	-17.6	-23.3	95
			B3LYP/b	-14.8	-23.2	PHPMS	-18.3	-24.7	89
			B3LYP/c//B3LYP/b	-15.3		PHPMS	-19.4 ± 0.2	-27.1 ± 0.7	79

^a kcal mol⁻¹ ^b cal mol⁻¹ K⁻¹

Table 4.2 (continued)

X	ROH	(n,n+1)	method	ΔH°_{298} ^a	ΔS°_{298} ^b	method	ΔH° ^a	ΔS° ^b	reference
Cl	(CH ₃) ₃ COH	(0,1)	MP2/a//B3LYP/b	-19.5		HPMS	-14.2	-10.3	83
			B3LYP/b	-15.3	-23.7	PHPMS	-19.2	-27.0	86
			B3LYP/c//B3LYP/b	-15.7		ICR	-18.1	-23.4	95
						PHPMS	-19.8	-27.4	89
						PHPMS	-20.2 ± 0.4	-28.9 ± 1.0	79

^a kcal mol⁻¹ ^b cal mol⁻¹ K⁻¹

Table 4.3 Overview of the computational and experimental thermochemistry for the $X^- + ROH \rightleftharpoons X^-(ROH)$ clustering equilibria

($X = \text{Br, I}$; $R = \text{CH}_3, \text{CH}_3\text{CH}_2$; **a** = 6-311++G(d,p), **b** = 6-311+G(d,p), **c** = 6-311++G(3df,3pd), **d** = LanL2DZ,
e = Stuttgart RLC ECP, **f** = CRENL ECP).

X	ROH	(n,n+1)	method	ΔH_{298}^0 ^a	ΔS_{298}^0 ^b	method	ΔH^0 ^a	ΔS^0 ^b	reference
Br	CH ₃ OH	(0,1)	MP2/a	-14.6	-19.5	PHPMS	-13.9	-17.6	92
			MP2/a//B3LYP/b	-14.5		EPDS	-15.1 ± 0.4		103
			B3LYP/b	-12.2	-19.5	PHPMS	-14.5 ± 0.1	-21.9 ± 0.4	this work
			B3LYP/c//B3LYP/b	-12.4					
Br	CH ₃ CH ₂ OH	(0,1)	MP2/a//B3LYP/b	-14.7		FT-ICR	-14.4		97
			B3LYP/b	-12.5	-19.9	EPDS	-15.2 ± 0.6		103
			B3LYP/c//B3LYP/b	-12.6		PHPMS	-14.1 ± 0.2	-19.8 ± 0.4	this work
			MP2/[a/d]	-17.7	-20.0	PHPMS	-11.3	-17.8	87
I	CH ₃ OH	(0,1)	MP2[a/e]	-12.7	-19.6	PHPMS	-11.2	-17.1	92
			B3LYP/[b/d]	-14.4	-17.6	EPDS	-14.4 ± 0.4		103
			B3LYP/[c/d]//B3LYP/[b/d]	-15.2		PHPMS	-11.9 ± 0.2	-20.6 ± 0.5	this work
			B3LYP/[b/e]	-10.1	-18.3				
			B3LYP/[c/e]//B3LYP/[b/e]	-10.0					
			B3LYP/[b/f]	-16.5	-23.3				
			B3LYP/[c/f]//B3LYP/[b/f]	-18.2					

^a kcal mol⁻¹ ^b cal mol⁻¹ K⁻¹

Table 4.4 Overview of the computational and experimental thermochemistry for the $X^-(ROH) + ROH \rightleftharpoons X^-(ROH)_2$ clustering equilibria ($X = F, Cl$; $R = CH_3, (CH_3)_2CH$; **a** = 6-311++G(d,p), **b** = 6-311+G(d,p), **c** = 6-311++G(3df,3pd)).

X	ROH	(n,n+1)	method	ΔH_{298}^0 ^a	ΔS_{298}^0 ^b	method	ΔH^0 ^a	ΔS^0 ^b	reference
F	CH ₃ OH	(1,2-1)	MP2/a//B3LYP/b	-18.2		PHPMS	-19.8 ± 0.3	-22.5 ± 0.8	91
			B3LYP/b	-16.6	-29.3	PHPMS	-19.3	-23.2	92
		(1,2-2)	MP2/a//B3LYP/b	-19.7		PHPMS	-20.3 ± 0.3	-24.6 ± 0.8	this work
			B3LYP/b	-19.5	-23.1				
F	(CH ₃) ₂ CHOH	(1,2-1)	MP2/a//B3LYP/b	-24.3		PHPMS	-20.8 ± 0.2	-25.3 ± 0.6	this work
			B3LYP/b	-20.8	-29.7				
		(1,2-2)	MP2/a//B3LYP/b	-25.3					
			B3LYP/b	-24.3	-23.5				
Cl	CH ₃ OH	(1,2-1)	MP2/a//B3LYP/b	-13.6		HPMS	-13.0	-19.4	84
			B3LYP/b	-11.3	-29.2	PHPMS	-14.1	-22.0	89
		(1,2-2)	MP2/a//B3LYP/b	-14.2		PHPMS	-13.7 ± 0.2	-22.0 ± 0.5	93
			B3LYP/b	-11.8	-21.6	PHPMS	-14.1 ± 0.4	-22.8 ± 1.1	79

^a kcal mol⁻¹ ^b cal mol⁻¹ K⁻¹

Table 4.5 Overview of the experimental thermochemistry for the $F^-(ROH)_n + ROH \rightleftharpoons F^-(ROH)_{n+1}$ clustering equilibria
(R = CD₃, CH₃CH₂, (CH₃)₂CH, (CH₃)₃C; n = 1, 2).

X	ROH	(n,n+1)	this work		literature		method	reference
			$\Delta H^{\circ a}$	$\Delta S^{\circ b}$	$\Delta H^{\circ a}$	$\Delta S^{\circ b}$		
F	CD ₃ OH	(2,3)	-15.1 ± 0.6	-23.6 ± 1.6	-18.1 ± 0.1	-32.6 ± 0.6	PHPMS	91
					-14.5	-21.2	PHPMS	92
F	CH ₃ CH ₂ OH	(1,2)	-20.6 ± 0.3	-25.8 ± 0.6	-20.6 ± 0.5	-27.1 ± 1.2	PHPMS	91
F	CH ₃ CH ₂ OH	(2,3)	-15.6 ± 0.1	-25.1 ± 0.4				
F	(CH ₃) ₂ CHOH	(1,2)	-20.8 ± 0.2	-25.3 ± 0.6				
F	(CH ₃) ₂ CHOH	(2,3)	-17.6 ± 0.2	-31.0 ± 0.7				
F	(CH ₃) ₃ COH	(1,2)	-22.0 ± 0.4	-28.2 ± 0.8				
F	(CH ₃) ₃ COH	(2,3)	-18.3 ± 1.0	-35.2 ± 2.8				

^a kcal mol⁻¹ ^b cal mol⁻¹ K⁻¹

Table 4.6 Overview of the experimental thermochemistry for the $\text{Cl}^-(\text{ROH})_n + \text{ROH} = \text{Cl}^-(\text{ROH})_{n+1}$ clustering equilibria ($\text{R} = \text{CH}_3, \text{CH}_3\text{CH}_2, (\text{CH}_3)_2\text{CH}, (\text{CH}_3)_3\text{C}; n = 1, 2$).

X	ROH	(n,n+1)	literature		method	reference
			ΔH° ^a	ΔS° ^b		
Cl	CH ₃ OH	(2,3)	-12.3	-23.6	HPMS	84
			-11.8	-22.9	PHPMS	89
			-13.7 ± 0.2	-22.0 ± 0.5	PHPMS	85
			-11.5 ± 0.2	-21.6 ± 0.6	PHPMS	79
Cl	CH ₃ CH ₂ OH	(1,2)	-16.1	-25.9	PHPMS	89
			-15.3 ± 0.2	-26.7 ± 0.5	PHPMS	79
Cl	CH ₃ CH ₂ OH	(2,3)	-12.8	-25.8	PHPMS	89
			-13.9 ± 0.7	-29.3 ± 2.1	PHPMS	79
Cl	(CH ₃) ₂ CHOH	(1,2)	-15.6	-25.0	PHPMS	89
			-16.7 ± 0.3	-30.3 ± 0.7	PHPMS	79
Cl	(CH ₃) ₂ CHOH	(2,3)	-12.5	-26.1	PHPMS	89
			-14.9 ± 0.5	-32.2 ± 1.4	PHPMS	79
Cl	(CH ₃) ₃ COH	(1,2)	-14.9	-25.8	PHPMS	89
			-16.9 ± 0.2	-32.0 ± 0.5	PHPMS	79
Cl	(CH ₃) ₃ COH	(2,3)	-13.7	-31.0	PHPMS	89
			-15.8 ± 0.3	-36.0 ± 0.9	PHPMS	79

^a kcal mol⁻¹ ^b cal mol⁻¹ K⁻¹

Table 4.7 Overview OF THE experimental thermochemistry for the $\text{Br}^-(\text{ROH})_n + \text{ROH} \rightleftharpoons \text{Br}^-(\text{ROH})_{n+1}$ clustering equilibria
 (R = CH_3 , CH_3CH_2 , $(\text{CH}_3)_2\text{CH}$, $(\text{CH}_3)_3\text{C}$; n = 0, 1, 2).

X	ROH	(n,n+1)	this work			literature			reference
			$\Delta\text{H}^{\circ a}$	$\Delta\text{S}^{\circ b}$	$\Delta\text{H}^{\circ a}$	$\Delta\text{S}^{\circ b}$	method		
Br	CH_3OH	(1,2)	-12.0 ± 0.2	-21.4 ± 0.5	-12.5	-20.7	PHPMS	92	
Br	CH_3OH	(2,3)	-9.5 ± 0.5	-17.6 ± 1.6	-10.6	-21.6	PHPMS	92	
Br	$\text{CH}_3\text{CH}_2\text{OH}$	(1,2)	-11.5 ± 0.6	-19.4 ± 1.8					
Br	$\text{CH}_3\text{CH}_2\text{OH}$	(2,3)	-9.5 ± 0.3	-17.2 ± 0.9					
Br	$(\text{CH}_3)_2\text{CHOH}$	(0,1)	-14.4 ± 0.2	-20.3 ± 0.6	-14.6		FT-ICR	97	
					-16.5 ± 1.2		EPDS	103	
Br	$(\text{CH}_3)_2\text{CHOH}$	(1,2)	-12.3 ± 0.3	-23.0 ± 0.8					
Br	$(\text{CH}_3)_2\text{CHOH}$	(2,3)	-11.5 ± 0.8	-23.6 ± 2.4					
Br	$(\text{CH}_3)_3\text{COH}$	(0,1)	-15.8 ± 0.2	-24.2 ± 0.5					
Br	$(\text{CH}_3)_3\text{COH}$	(1,2)	-12.9 ± 0.4	-24.3 ± 1.2					
Br	$(\text{CH}_3)_3\text{COH}$	(2,3)	-11.6 ± 0.5	-24.4 ± 1.6					

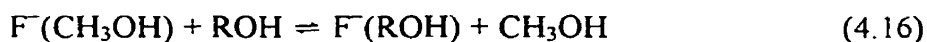
^a kcal mol⁻¹ ^b cal mol⁻¹ K⁻¹

Table 4.8 Overview of the experimental thermochemistry for the $\Gamma(\text{ROH})_n + \text{ROH} \rightleftharpoons \Gamma(\text{ROH})_{n+1}$ clustering equilibria
 (R = CH₃, CH₃CH₂, (CH₃)₂CH, (CH₃)₃C; n = 0, 1, 2).

X	ROH	(n,n+1)	this work		literature		method	reference
			$\Delta H^{\circ a}$	$\Delta S^{\circ b}$	$\Delta H^{\circ a}$	$\Delta S^{\circ b}$		
I	CH ₃ OH	(1,2)	-9.5 ± 0.2	-17.6 ± 0.5	-11.1	-22.6	PHPMS	92
I	CH ₃ OH	(2,3)	-7.7 ± 0.6	-14.4 ± 1.9	-9.8	-22.4	PHPMS	92
I	CH ₃ CH ₂ OH	(0,1)	-13.0 ± 0.2	-23.1 ± 0.7	-12.1	-18.9	PHPMS	87
					-11.7		FT-ICR	97
I	CH ₃ CH ₂ OH	(1,2)	-10.5 ± 0.2	-20.4 ± 0.6				
I	CH ₃ CH ₂ OH	(2,3)	-8.4 ± 0.5	-16.4 ± 0.7				
I	(CH ₃) ₂ CHOH	(0,1)	-13.1 ± 0.2	-22.7 ± 0.6	-12.2	-19.1	PHPMS	87
I	(CH ₃) ₂ CHOH	(1,2)	-11.0 ± 0.3	-21.3 ± 0.8				
I	(CH ₃) ₂ CHOH	(2,3)	-9.5 ± 0.7	-20.0 ± 2.2				
I	(CH ₃) ₃ COH	(0,1)	-13.1 ± 0.3	-23.3 ± 0.9	-12.1	-18.7	PHPMS	87
I	(CH ₃) ₃ COH	(1,2)	-11.3 ± 0.4	-23.4 ± 1.1				
I	(CH ₃) ₃ COH	(2,3)	NA	NA				

^a kcal mol⁻¹ ^b cal mol⁻¹ K⁻¹

The direct clustering of F^- onto CH_3CH_2OH , $(CH_3)_2CHOH$, and $(CH_3)_3COH$ could not be measured because of the very high binding enthalpies involved. In order to obtain ΔH° and ΔS° , F^- exchange reactions involving methanol and the other three alcohols were performed (Reaction 4.16).



By measuring the ΔH° and ΔS° values for these exchange equilibria and by using earlier experimental ΔH° and ΔS° values for fluoride ion clustering onto methanol from PHPMS experiments ($\Delta H^\circ = -30.5 \pm 0.7 \text{ kcal mol}^{-1}$ and $\Delta S^\circ = -23.4 \pm 1.2 \text{ cal mol}^{-1} \text{ K}^{-1}$), the corresponding thermochemical data for fluoride ion clustering onto CH_3CH_2OH , $(CH_3)_2CHOH$, and $(CH_3)_3COH$ could be determined experimentally. These values are summarized in Table 4.9 and the experimental Van't Hoff plots are shown in Figure 4.9. In Figures 4.3, 4.5, and 4.7 the Van't Hoff plots for the clustering of fluoride ion onto CH_3CH_2OH , $(CH_3)_2CHOH$, and $(CH_3)_3COH$, respectively, have been calculated and drawn based on the above discussion and consequently do not contain any experimental data points.

For the $F^- + ROH = F^-(ROH)$ clustering equilibria, $-\Delta H^\circ$ increase going from $R = CH_3$ to $(CH_3)_3C$. A similar trend has been observed by Larson and McMahon, but in general their ICR values are slightly lower than the values obtained from this work.⁴⁸ As a reference system for that work, a ΔH° value for the $F^- + H_2O = F^-(H_2O)$ clustering equilibrium by Kebarle and co-workers from HPMS experiments had been used ($\Delta H^\circ = -23.3 \text{ kcal mol}^{-1}$).⁸² Recently, Bowers and co-workers re-evaluated this system using a variable temperature (VT) high pressure drift cell, and found a value of $-26.2 \pm 0.8 \text{ kcal mol}^{-1}$, which was in excellent agreement with high level computations, including basis set superposition error (BSSE).³⁵ Results for $-\Delta H^\circ$ values for the $F^-(H_2O))_n + H_2O = F^-(H_2O)_{n+1}$ clustering equilibria ($n = 0, 1$) by Hiraoka and co-workers also confirmed that Kebarle's data may be too low.⁹⁰ The

Table 4.9 Overview of the experimental thermochemistry for the $F^-(CH_3OH) + ROH \rightleftharpoons F^-(ROH) + CH_3OH$ exchange equilibria (R = CH_3CH_2 , $(CH_3)_2CH$, $(CH_3)_3C$).

X	ROH	this work		literature		method	reference
		$\Delta H^{0 a}$	$\Delta S^{0 b}$	$\Delta H^{0 a}$	$\Delta S^{0 b}$		
F	CH_3CH_2OH	-1.9 ± 0.2	-2.3 ± 0.5	-1.9	-2.3	ICR	48
F	$(CH_3)_2CHOH$	-3.0 ± 0.2	-2.8 ± 0.2	-2.7	-3.0	ICR	48
F	$(CH_3)_3COH$	-2.9 ± 0.1	-1.4 ± 1.9	-3.7	-3.5	ICR	48

^a kcal mol⁻¹ ^b cal mol⁻¹ K⁻¹

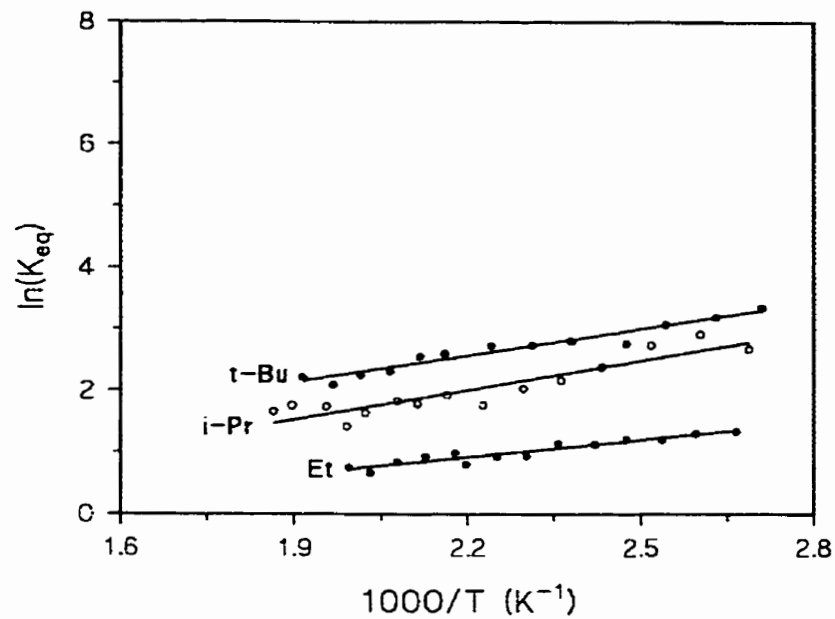


Figure 4.9 Experimental Van't Hoff plots for the fluoride ion-methanol/alcohol complex exchange equilibria $F^-(CH_3OH) + ROH = F^-(ROH) + CH_3OH$ ($R = CH_3CH_2, (CH_3)_2CH, (CH_3)_3C$).

previous determined ΔH° value for the $F^- + CH_3OH \rightleftharpoons F^-(CH_3OH)$ clustering equilibrium is in reasonable agreement with the ICR value by Larson and McMahon, while the results from Hiraoka and co-workers for the same reaction definitely seem anomalous.⁹²

The electrostatic interaction between a halide ion and an alcohol molecule, $V(r)$, can be described by an ion-dipole and ion-induced dipole model (Equation 4.17).^{145,146}

$$V(r) = \frac{-\mu \cdot q \cdot \cos\theta(r)}{r^2} + \frac{-\alpha \cdot q^2}{2r^4} \quad (4.17)$$

Going from ROH = CH₃OH to (CH₃)₃COH, the permanent electric dipole moment, μ , changes only slightly, whereas the polarizability of the alcohol molecules, α , increases from 3.32 to 8.82 Å³.¹⁴⁷ A plot of α versus $-\Delta H^\circ (X^-(ROH))$ confirms the expected relationship for all halide ion and alcohol combinations measured (Figure 4.10).

The $\Delta_{acid}H^\circ$ values of CH₃OH to (CH₃)₃COH⁸⁰ are larger than $\Delta_{acid}H^\circ$ for HF,¹⁴⁸ so that $F^-(ROH)$ is an accurate description for the fluoride ion alcohol complexes as shown by Mihalick *et al.* from EPDS experiments.¹⁰² In addition, IRMPD experiments of $F^-(CH_3OH)$ in a FT-ICR instrument confirmed that $F^-(CH_3OH) + nh\nu \rightarrow F^- + CH_3OH$ is indeed the lowest energy dissociation channel.¹⁰⁷ Low ion kinetic energy CID experiments by Wilkinson *et al.* in a FT-ICR instrument showed that for $F^-(ROH)$ adducts, for which the $\Delta_{acid}H^\circ$ value of the alcohol is very close to the $\Delta_{acid}H^\circ$ value of HF, both F^- and RO^- product ions were observed.⁹⁶ This was explained by assuming a double well potential energy surface with a very low barrier for proton transfer when $\Delta\Delta_{acid}H^\circ \approx 0 \text{ kcal mol}^{-1}$, whereas for larger $\Delta\Delta_{acid}H^\circ$ values, the potential energy surface converts into a single well. This hypothesis has been confirmed by high level *ab initio* computations. A linear relationship between $\Delta_{acid}H^\circ (ROH) - \Delta_{acid}H^\circ (HF)$ and ΔH° for $F^-(ROH)$ formation was established by Larson and McMahon.⁴⁸ In Figure 4.11 it can be seen that this relationship also applies to the

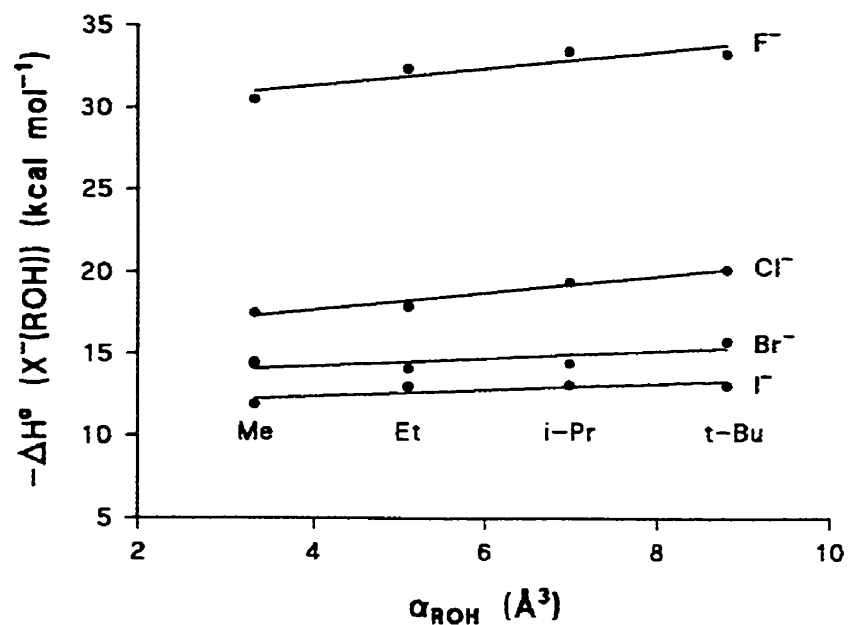


Figure 4.10 Plot of the negative standard enthalpy change for the $X^{-} + ROH = X^{-}(ROH)$ clustering equilibria, $-\Delta H^{\circ}(X^{-}(ROH))$, versus alcohol polarizability, α_{ROH} .

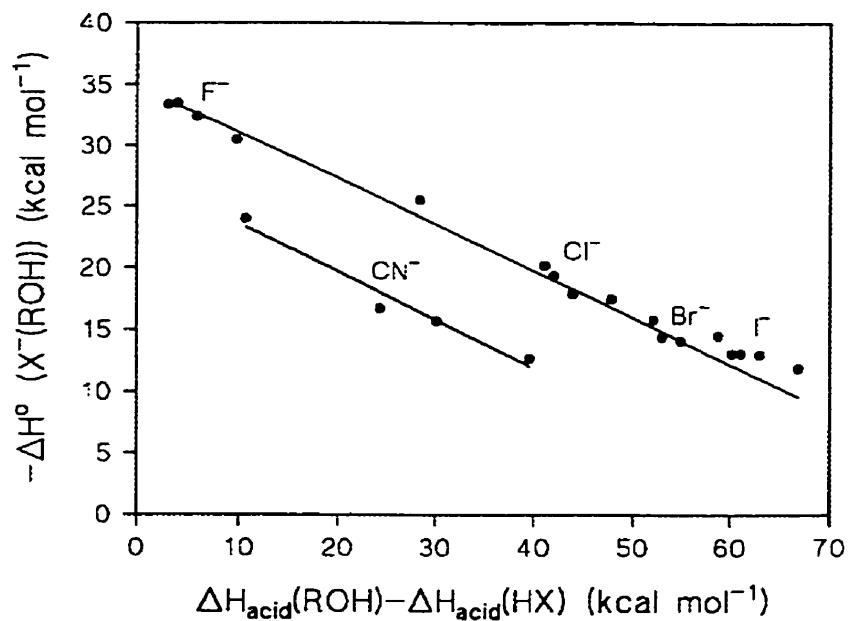


Figure 4.11 Plot of the negative standard enthalpy change for the $X^{-} + ROH = X^{-}(ROH)$ clustering equilibria, $-\Delta H^{\circ}(X^{-}(ROH))$, versus the deprotonation enthalpy difference between ROH and HX, $\Delta_{acid}H(ROH) - \Delta_{acid}H(HX)$.

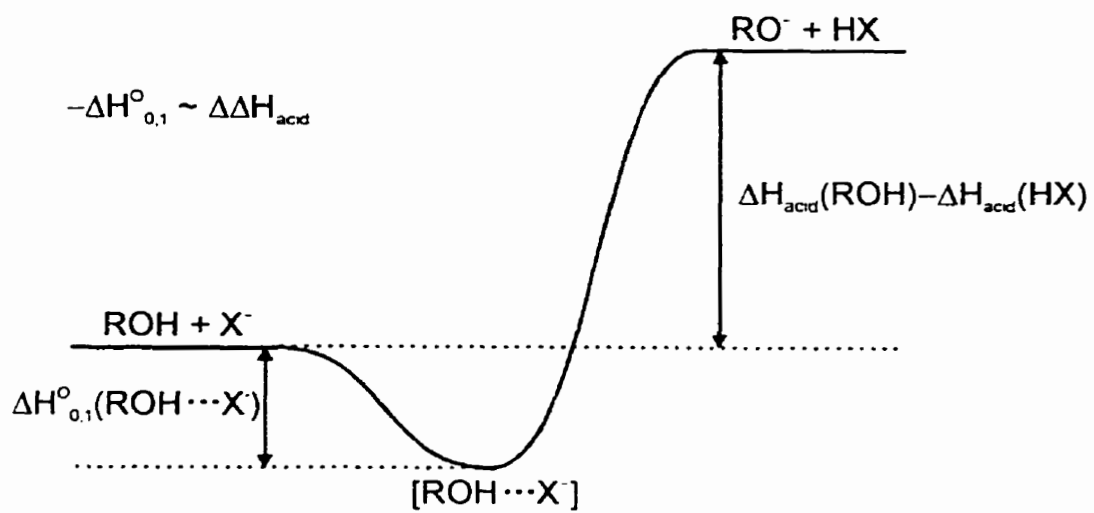
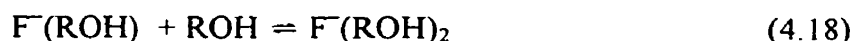


Figure 4.12 Single-well potential energy diagram for the halide ion-alcohol complexes.

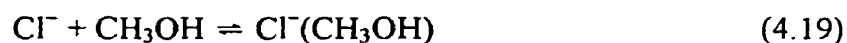
other three halide ions. This relationship might indicate the existence of a single well potential energy surface as shown in Figure 4.12. A similar kind of potential energy surface was suggested by Yang *et al.*,¹⁰³ although they did not propose any linearity or extension to larger molecules.

For the fluoride ion-alcohol molecule dimer clustering equilibria (Reaction 4.18), it can be seen in Tables 4.4 and 4.5 that $-\Delta H^\circ$ is considerably smaller than for the fluoride ion mono-solvated, and that ΔH° becomes slightly more negative going from CH_3OH to $(\text{CH}_3)_3\text{COH}$.



The $\Delta H^\circ = -20.3 \pm 0.3 \text{ kcal mol}^{-1}$ for $(\text{CH}_3\text{OH})\text{F}^-(\text{CH}_3\text{OH})$ is in reasonable agreement with data from Hiraoka and co-workers ($-19.3 \text{ kcal mol}^{-1}$)⁹² and earlier data from our laboratory ($-19.8 \pm 0.3 \text{ kcal mol}^{-1}$).⁹¹ For the other three alcohol molecules, no data are available in the literature, but the consistency in the observed trends is a good indication that the ΔH° values are of the correct magnitude. The main reason for the smaller ΔH° values of the (1,2) type of equilibria compared to the (0,1) type of equilibria can be found mainly in the increased dipole-dipole interaction¹⁴⁹ and steric effects between the alkyl groups. The dipole-dipole interaction is expected to be the main factor, and repulsion will be largest for the $\text{F}^-(\text{ROH})_2$ clusters and smallest for the $\text{F}^-(\text{ROH})$ clusters. This observation can be understood by the fact that the alcohol molecules will be closer together when bonded to F^- instead of H_2O . For the (2,3) type of equilibria, similar trends are observed as for the corresponding (1,2) type equilibria. $-\Delta H^\circ$ increases going from CH_3OH to $(\text{CH}_3)_3\text{COH}$ and all values are smaller than for Reaction (4.18).

The clustering of chloride ion onto methanol (Reaction 4.19) has been studied extensively.^{83,84,85,89,93,95,103}

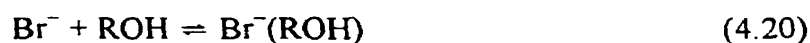


The result for ΔH° from the present work of $-17.5 \pm 0.3 \text{ kcal mol}^{-1}$ is in excellent agreement with most other PHPMS determinations. Kebarle's HPMS value of $-14.1 \text{ kcal mol}^{-1}$ is definitely too low,^{83,84} whereas the estimated ICR value of Larson and McMahon ($-16.8 \text{ kcal mol}^{-1}$) is in reasonable agreement.⁹⁵ The EPDS value by Yang *et al.* ($-18.7 \pm 0.5 \text{ kcal mol}^{-1}$) seems too high compared to all other values.¹⁰³ The observed trend in the ΔH° values going from CH_3OH to $(\text{CH}_3)_3\text{COH}$ can be explained by the increase in the polarizability of the alcohol molecule, as shown for $X = \text{F}$ in Figure 4.10. For the other three alcohol molecules most values, except those from HPMS, in general agree fairly well. For the chloride ion-alcohol (1,2) and (2,3) clustering equilibria, similar trends as for the corresponding fluoride ion systems can be observed, and the same arguments can be used to explain these trends qualitatively.

To this point, discussion of the trends of ΔS° has been deliberately delayed. In general, experimentally determined entropy changes can give some additional information on structural features of gas phase cluster ions. Good illustrative examples are the occurrence of bidentate clustering of chloride ion onto α,ω -diols¹⁵⁰ and the existence of electrostatic and covalent bound isomers of $(\text{CH}_3)_3\text{C}^+$ with small organic molecules at different temperatures.¹⁵¹ In general, the variations for the observed entropy changes can be attributed to internal rotational and vibrational contributions. Unfortunately no clear and consistent general trends in the ΔS° values as a function of X , R , and $(n,n+1)$ are observable. In addition, without computational structures and normal mode vibrational frequencies, discussion of changes in ΔS° is speculative. In the case of possible isomers with very different calculated ΔS°_{298} values, one may be more likely to choose one based on close resemblance with the experimental ΔS° value. It seems likely that upon complex formation, methyl group rotations will be hindered and that, especially for the higher order clusters with bulky alkyl groups, this effect will be even stronger. Based on computations on halide ion-water clusters, it has been shown that low ($< 200 \text{ cm}^{-1}$) intramolecular normal mode vibrational frequencies are introduced, and that their number increases and their value decreases by increasing the number of water molecules.^{56,58,62,152} It may be expected that this will have a large

impact on the vibrational entropy change. Finally it is obvious that in general there is a larger spread in the experimental ΔS° values from PHPMS than in the ΔH° values.

As already mentioned, there is surprisingly little thermochemical data in the literature on bromide and iodide ion-alcohol clusters.^{97,92,97,103} For both the bromide and iodide ion (0,1) clustering equilibria (Reactions 4.20 and 4.21), the $-\Delta H^\circ$ values increase slightly going from CH_3OH to $(\text{CH}_3)_3\text{COH}$.



In Figure 4.10 it can be seen that for Br^- and I^- ΔH° is almost independent of the polarizability, unlike for F^- and Cl^- . Due to the larger ionic radii, the $\text{X}^- \cdots \text{HOR}$ interactions will be weaker. In general there is good agreement with PHPMS^{87,92} and FT-ICR⁹⁷ results in the literature, while EPDS results show larger discrepancies.¹⁰³ For the FT-ICR results it was mentioned by the authors that the Br^- and I^- alcohol complexes undergo rapid dissociation by ZTRID,¹⁵³⁻¹⁵⁵ and that this may introduce some uncertainty in the results. For the (1,2) and (2,3) clustering equilibria, only results for the methanol clusters are available from PHPMS.⁹² These are slightly more exothermic, but the same overall trends are observable. As mentioned before, no clear and consistent trends in the ΔS° values are observable, including literature values. It may be expected that due to the relatively weak bonding the alcohol molecules are fairly mobile, making the structures more dynamical and realistic.

For the $\text{Br}^-(\text{H}_2\text{O})_n$ and $\text{I}^-(\text{H}_2\text{O})_n$ clusters the halide ions are bonded to the surface of a hydrogen-bonded water cluster.^{27-45,54-64} It may not be excluded, that in the PHPMS ion source, halide ion-alcohol clusters are also generated with surface solvated features. VPDS, in combination with *ab initio* computations, would be an excellent tool to investigate this.

4.4.2 Computational Thermochemistry

In Tables 4.1 to 4.4 overviews are given of the computational results for the association thermochemistry, together with the available experimental literature data. The ΔH°_{298} data for the MP2/a and MP2/a//B3LYP/b computations for the formation of $X^{-}(\text{CH}_3\text{OH})$ ($X = \text{F}, \text{Cl}, \text{Br}$) and $\text{F}^{-}(\text{CH}_3\text{CH}_2\text{OH})$ are identical. In general it took less CPU time to run the MP2/a//B3LYP/b computations than to run the MP2/a computations. Comparing the ΔH°_{298} data of MP2/a ([a/d] and [a/e] for $X = \text{I}$) to the B3LYP/b results ([b/d], [b/e], and [b/f] for $X = \text{I}$) for computations for the formation of $X^{-}(\text{CH}_3\text{OH})$ ($X = \text{F}, \text{Cl}, \text{Br}, \text{I}$), in general the MP2/a values are more negative than the B3LYP/b values (except for $X = \text{F}$). The MP2/a and B3LYP/b ΔS°_{298} values for the formation of $\text{F}^{-}(\text{CH}_3\text{OH})$ and $\text{Br}^{-}(\text{CH}_3\text{OH})$ are in excellent agreement, while for $\text{F}^{-}(\text{CH}_3\text{CH}_2\text{OH})$ and $\text{Cl}^{-}(\text{CH}_3\text{OH})$ there are small differences. The MP2/[a/d] and [a/e] ΔH°_{298} values for $\text{I}^{-}(\text{CH}_3\text{OH})$ show a large basis set effect, while for the ΔS°_{298} results there is no real difference. The large iodide ion basis set effects on the ΔH°_{298} results for the B3LYP computations remain, with [a/e] performing the best compared to experimental results. For ΔS°_{298} , the results of [b/d] and [b/e] are nearly identical, while for [b/f] they are quite different, as was the case for the ΔH°_{298} values. Use of a modified LanL2DZ basis set,¹⁵⁶ the Stuttgart Dresden ECP (SSD)^{157,158} basis set, or Truhlar's SVP+ basis set¹⁵⁹ might improve the results because of satisfying results when applied to anion systems. Comparing ΔH°_{298} results for B3LYP/b and B3LYP/c//B3LYP/b computations shows that there are no real improvements. Only for the fluoride ion complexes with $(\text{CH}_3)_2\text{CHOH}$ and $(\text{CH}_3)_3\text{COH}$ do the ΔH°_{298} values become 2.7 and 1.1 kcal mol⁻¹ more exothermic, respectively.

Finally, the effect of clustering on the barrier for CH_3 group rotation must be addressed. The non-linear $X^{-}\cdots\text{H}-\text{OCH}_3$ bond angle for all halide ions, but especially for $X = \text{Cl}, \text{Br},$ and I has been viewed as if the halide ion is interacting with the methyl group hydrogen atoms. At the MP2/a ([a/e] for $X = \text{I}$) level of theory the barriers for methyl group rotation for CH_3OH , $\text{F}^{-}(\text{HOCH}_3)$, $\text{Cl}^{-}(\text{HOCH}_3)$, $\text{Br}^{-}(\text{HOCH}_3)$, and

$\Gamma(\text{HOCH}_3)$ have been calculated to be 1.18, 0.44, 0.51, 0.55, and 0.81 kcal mol⁻¹, respectively. These data do not include ZPE or thermal corrections. Obviously, the barrier for methyl group rotation is increasing, and this is in qualitative agreement with the fact that it is believed that the $\text{X}^- \cdots \text{H}-\text{CH}_2\text{OH}$ interaction is increasing going from $\text{X} = \text{F}$ to I . On the other hand this may actually not be true, because on going from $\text{X} = \text{F}$ to I the $\text{X}^- \cdots \text{H}-\text{CH}_2\text{OH}$ distance actually increases from 3.105 Å to 3.919 Å. These values themselves are in good agreement with experimental data on CH_3OH (1.1 kcal mol⁻¹)¹⁶⁰ and computations by Wladkowski *et al.* on $\text{F}^-(\text{HOCH}_3)$ (0.5 kcal mol⁻¹).¹⁰⁹ DeTuri and Ervin calculated the barriers for methyl group rotation in CH_3OH , $\text{CH}_3\text{CH}_2\text{OH}$, $(\text{CH}_3)_2\text{CHOH}$, and $(\text{CH}_3)_3\text{COH}$ and the corresponding fluoride ion complexes at the MP2/6-311+G(2df,2p)/MP2/6-31G(d) level of theory,⁸¹ a method described by East and Radom.¹⁶¹ For the neutrals, barrier heights of 1.05, 1.36, 1.31, and 1.24 kcal mol⁻¹ were found, while for the fluoride ion complexes values of 0.29, 2.27, 2.12, and 2.11 kcal mol⁻¹ were obtained. For CH_3OH and $\text{F}^-(\text{CH}_3\text{OH})$ the barrier heights are close to the computational results from this work and the experimental data, but relatively different from the work by Wladkowski *et al.*¹⁰⁹ It is interesting that for the other three alcohol molecules the barrier for methyl group rotation actually increases upon complex formation with the fluoride ion. This may be caused by a stronger interaction between F^- and the methyl group hydrogen atoms due to closer interatomic distances. Unfortunately no other work on the other $\text{X}^-(\text{ROH})$ complexes has been performed to observe such trends and the intrinsic parameters that determine them.

4.4.3 Computations versus Experiments

It is of interest to compare the computational results from this thesis with the PHPMS data from this laboratory, since the latter comprise the most extensive study of halide ion-alcohol clusters to date. From Tables 4.1 to 4.4 it can be readily observed that, in general, there is good to excellent agreement between the PHPMS data and the results from MP2/a and MP2/a//B3LYP/b computations, but that in some cases B3LYP/b also performs very well. Some inconsistencies exist between the agreement

of ΔH° and ΔH°_{298} , and ΔS° and ΔS°_{298} , especially for $\Gamma(\text{CH}_3\text{OH})$ where iodide ion basis set effect is clearly observable.

Comparing these computations with other experimental results from various methods also aids in the understanding of the general performance of the different methods used for this study. If $\pm 1.0 \text{ kcal mol}^{-1}$ is taken as indicating good agreement between computational and experimental values, it can be concluded that MP2/a//B3LYP/b performs best overall. There is good agreement with most PHPMS (88%), EPDS (50%), TCID, (50%), ICR (38%), and FT-ICR (100%) data. B3LYP/b performs much more poorly with good agreement only in 75% of the TCID and ICR data, while B3LYP/c//B3LYP/b in general agrees poorly with all experimental data.

To compare the calculated ΔS°_{298} values with ΔS° values from other experiments, it can be seen from Tables 4.1 to 4.4 that only HPMS and PHPMS experiments provide ΔS° data. Most HPMS data are in poor agreement with all computations, and consequently they will not be considered here. The ΔS° values from ICR experiments are actually values calculated from simple statistical mechanics, and these were only used as estimates. In general there is good agreement between the MP2/a and B3LYP/b ΔS°_{298} values and the corresponding ICR values for most $X^-(\text{ROH})$ ($X = \text{F}, \text{Cl}$) clustering reactions. The spread in ΔS° values from PHPMS for $\text{Cl}^-(\text{ROH})$ is fairly small, and consequently the same argument applies as in comparing ΔS°_{298} and the ΔS° values from this work. For $\text{Br}^-(\text{CH}_3\text{OH})$ and $\Gamma(\text{CH}_3\text{OH})$ there are too few PHPMS ΔS° values available to have a useful comparison. A general conclusion for these systems could be that it depends on the method used and the data set in order to get a good or reasonable agreement.

For the two calculated (1,2) equilibria in Table 4.4 it can be seen that for the formation of $(\text{CH}_3\text{OH})X^-(\text{CH}_3\text{OH})$ ($X = \text{F}, \text{Cl}$) the ΔS°_{298} and ΔS° values show much better agreement than for the formation of $X^-(\text{CH}_3\text{OH})(\text{CH}_3\text{OH})$. In Table 4.10 it can be seen that the relative population of the $X^-(\text{CH}_3\text{OH})(\text{CH}_3\text{OH})$ clusters is small compared to the relative population of the $(\text{CH}_3\text{OH})X^-(\text{CH}_3\text{OH})$ clusters, and consequently it may be expected that the observed thermochemistry for the (1,2)

Table 4.10 Overview of the relative contributions of the $(\text{CH}_3\text{OH})\text{X}^-(\text{CH}_3\text{OH})$ and $\text{X}^-(\text{CH}_3\text{OH})(\text{CH}_3\text{OH})$ isomeric cluster ions at different temperatures ($\text{X} = \text{F}, \text{Cl}$).

T^a	$(\text{CH}_3\text{OH})\text{F}^-(\text{CH}_3\text{OH})$		$\text{F}^-(\text{CH}_3\text{OH})(\text{CH}_3\text{OH})$		$(\text{CH}_3\text{OH})\text{Cl}^-(\text{CH}_3\text{OH})$		$\text{Cl}^-(\text{CH}_3\text{OH})(\text{CH}_3\text{OH})$	
	$\Delta G_T^0{}^b$	%	$\Delta G_T^0{}^b$	%	$\Delta G_T^0{}^b$	%	$\Delta G_T^0{}^b$	%
10	-19.47	100.00	-17.91	0.00	-13.98	100.00	-13.31	0.00
20	-19.24	100.00	-17.61	0.00	-13.77	100.00	-13.02	0.00
50	-18.55	100.00	-16.74	0.00	-13.12	99.99	-12.14	0.01
100	-17.39	100.00	-15.27	0.00	-12.04	99.89	-10.68	0.11
150	-16.24	99.97	-13.81	0.03	-10.96	99.71	-9.22	0.29
200	-15.08	99.90	-12.34	0.10	-9.88	99.52	-7.76	0.48
250	-13.93	99.78	-10.88	0.22	-8.80	99.35	-6.30	0.65
300	-12.77	99.64	-9.41	0.36	-7.72	99.20	-4.84	0.80
350	-11.62	99.49	-7.95	0.51	-6.64	99.08	-3.38	0.92
400	-10.46	99.33	-6.48	0.67	-5.56	98.97	-1.92	1.03
450	-9.31	99.18	-5.02	0.82	-4.48	98.88	-0.46	1.12
500	-8.15	99.02	-3.55	0.98				
550	-7.00	99.88	-2.09	1.12				
600	-5.84	99.75	-0.62	1.25				

^a K ^b kcal mol⁻¹

cluster equilibria is mainly composed of the $(\text{CH}_3\text{OH})\text{X}^-(\text{CH}_3\text{OH})$ clusters thermochemistry.

All B3LYP/**b** $\Delta\text{H}^\circ_{298}$ and $\Delta\text{S}^\circ_{298}$ values were calculated using a scaling factor of 1.0000 as described earlier. For some $\text{X}^-(\text{ROH})$ systems ($\text{X} = \text{F}, \text{Cl}, \text{Br}; \text{R} = \text{CH}_3, \text{CH}_3\text{CH}_2$) $\Delta\text{H}^\circ_{298}$ and $\Delta\text{S}^\circ_{298}$ were also calculated using a scaling factor of 0.9640. For $\Delta\text{H}^\circ_{298}$ in general this resulted in a change of $\pm 0.1 \text{ kcal mol}^{-1}$, while for $\Delta\text{S}^\circ_{298}$ there was a change of smaller than $0.2 \text{ cal mol}^{-1} \text{ K}^{-1}$.

4.4.4 Other Computational Work

Various studies have been reported in the literature which deal with halide ion-alcohol molecule complexes. However, the focus here will be confined to high level *ab initio* results. $\text{F}^-(\text{CH}_3\text{OH})$ has been the subject of several computational studies. The closest result to the PHPMS data from this laboratory is from high level computations at the MP2(full)/[13s8p6d4f,8s6p4d](+) + CCSD(T)/QZ(+)(2d,2p) level of theory by Wladkowski *et al.* ($\Delta\text{H}^\circ_{298} = -30.0 \text{ kcal mol}^{-1}$).¹⁰⁹ Other high level computations on $\text{F}^-(\text{CH}_3\text{OH})$ include G2,⁷⁹ and MP4(SDTQ)(fc)/6-31++G(d,p)//MP2(full)/6-311++G(d,p) (fc = frozen core),¹⁰⁴ but, surprisingly, these very high level computations do not give results that are more accurate than, for instance, the MP2/**a**//B3LYP/**b** results. It is possible that G2(MP2)(+) (plus ECP for Br^- and I^- containing complexes) would be more accurate than G2.^{144,156,162} Recently, DeTuri *et al.* published results on $\text{F}^-(\text{ROH})$ complexes.⁸¹ At the MP2(fc)/6-311+G(2d,p)//MP2(fc)/6-31G(d) + (ZPE + $\Delta\text{C}_p(298 \text{ K})$) at the HF/6-31G(d) level of theory, and using a scaling factor of 0.8953 they found $\Delta\text{H}^\circ_{298}$ values of $-31.8, -25.5, -33.7,$ and $-33.2 \text{ kcal mol}^{-1}$ for CH_3OH to $(\text{CH}_3)_3\text{COH}$, respectively. With the exception of the unusual $\text{F}^-(\text{CH}_3\text{CH}_2\text{OH})$ result, the general trend is quite reasonable. These computations could be improved by using HF/6-311++G(d,p) for ZPE + $\Delta\text{C}_p(298 \text{ K})$, and MP2(full)/6-31+G(d,p) for the geometry optimizations, but, on the other hand, this would make the computations more time-consuming.

For the $\text{Cl}^-(\text{ROH})$ complexes, only data for $\text{Cl}^-(\text{CH}_3\text{OH})$ and $\text{Cl}^-((\text{CH}_3)_2\text{CHOH})$ are available. Berthier *et al.* used MP2(fc) in combination with extended Gaussian basis sets enlarged with both standard valence polarization orbitals and semi-diffuse Coulomb polarization orbitals.¹¹⁰ For $\text{Cl}^-(\text{CH}_3\text{OH})$ and $\text{Cl}^-((\text{CH}_3)_2\text{CHOH})$, ΔH°_{298} values of -16.9 and -18.5 kcal mol⁻¹, respectively, were calculated. These results are in excellent agreement with the MP2/a//B3LYP/b data. After a BSSE correction, final values of -14.3 and -13.9 kcal mol⁻¹, respectively, were obtained. This shows that for the computations in this chapter, BSSE may still be important, even though it has been neglected as indicated earlier.

For $\text{Br}^-(\text{CH}_3\text{OH})$ Tanabe *et al.* used a very extensive computation at the MP4(SDTQ)/[7s6p4d+ECP/D95+G(p)]//MP2(full)/[7s6p4d+ECP/D95+G(p)] level of theory and found a ΔH°_{335} values of -13.9 kcal mol⁻¹, in good agreement with their FT-ICR result.⁹⁷

Nielsen *et al.* carried out computations on $\Gamma(\text{CH}_3\text{OH})$ and $\Gamma((\text{CH}_3)_2\text{CHOH})$ at the B3LYP/ LanL2DZ+ level of theory, but unfortunately no thermochemical data were reported.⁶⁴

Thus the various computations at high levels still give rise to results that may differ from experimental data. No HF results have been mentioned, however that does not mean that they are necessarily unreliable. HF results on halide ion-alcohol complexes have been reported that showed good agreement with experiments and higher level computations, although these results were very system dependent.⁹²

4.4.5 Structures

The structures of the $\text{X}^-(\text{ROH})$ complexes provide interesting features that give more insight into the observed thermochemistry of the $\text{X}^-(\text{ROH})$ complex formation. Structures of the $\text{X}^-(\text{CH}_3\text{OH})$ complexes have been published in the past, which show minimal basis set effects.^{63,64,79,81,92,97,104,109,110} In Figures 4.13 to 4.16 the MP2/a ([a/e] for $\text{X} = \text{I}$) structures of $\text{X}^-(\text{CH}_3\text{OH})$ ($\text{X} = \text{F}, \text{Cl}, \text{Br}, \text{I}$) are shown, and these structures show some interesting features. Going from $\text{X} = \text{F}$ to Br , the $\text{X}^- \cdots \text{HOCH}_3$ distances

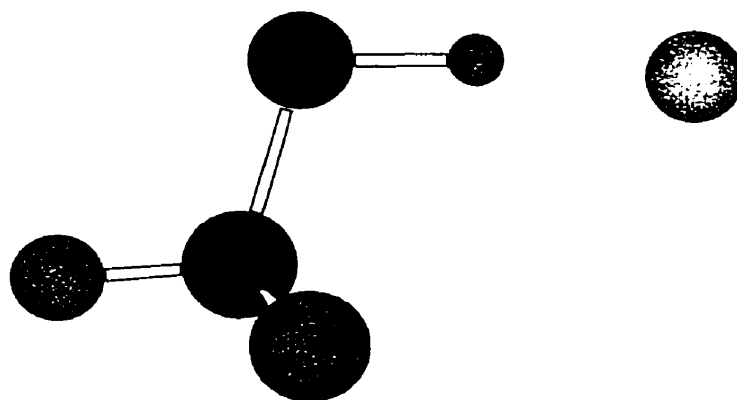


Figure 4.13 Optimized MP2(full)/a structure of F⁻(CH₃OH).

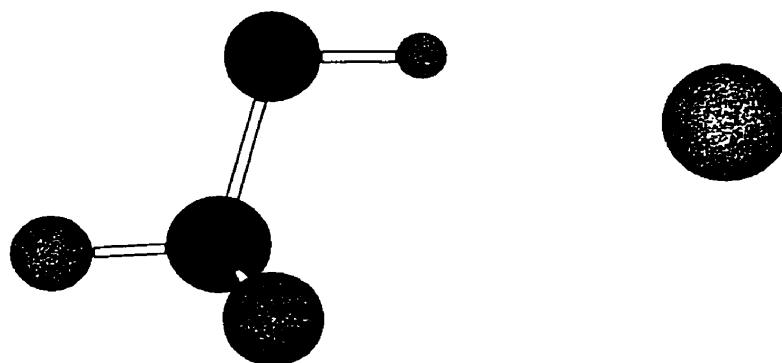


Figure 4.14 Optimized MP2(full)/a structure of Cl⁻(CH₃OH).

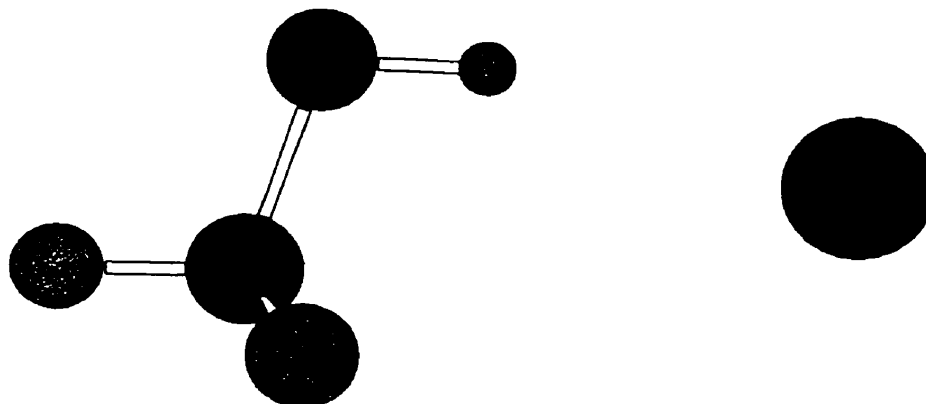


Figure 4.15 Optimized MP2(full)/a structure of Br⁻(CH₃OH).

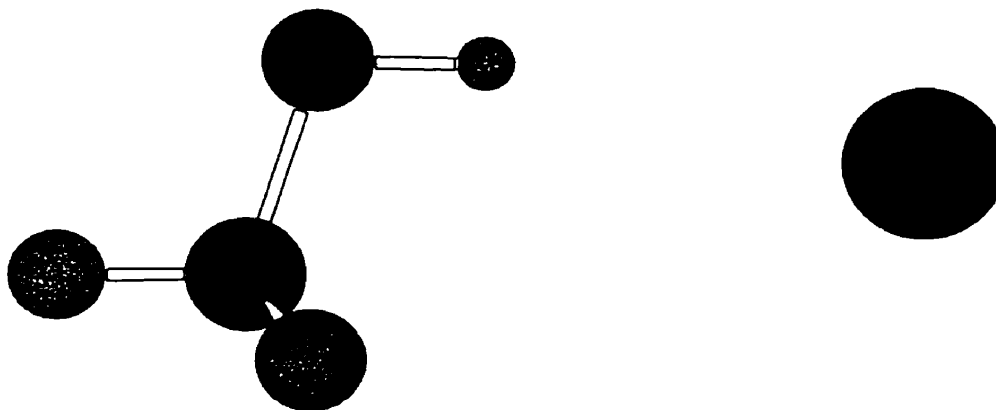


Figure 4.16 Optimized MP2(full)/[a/e] structure of $\Gamma(\text{CH}_3\text{OH})$.

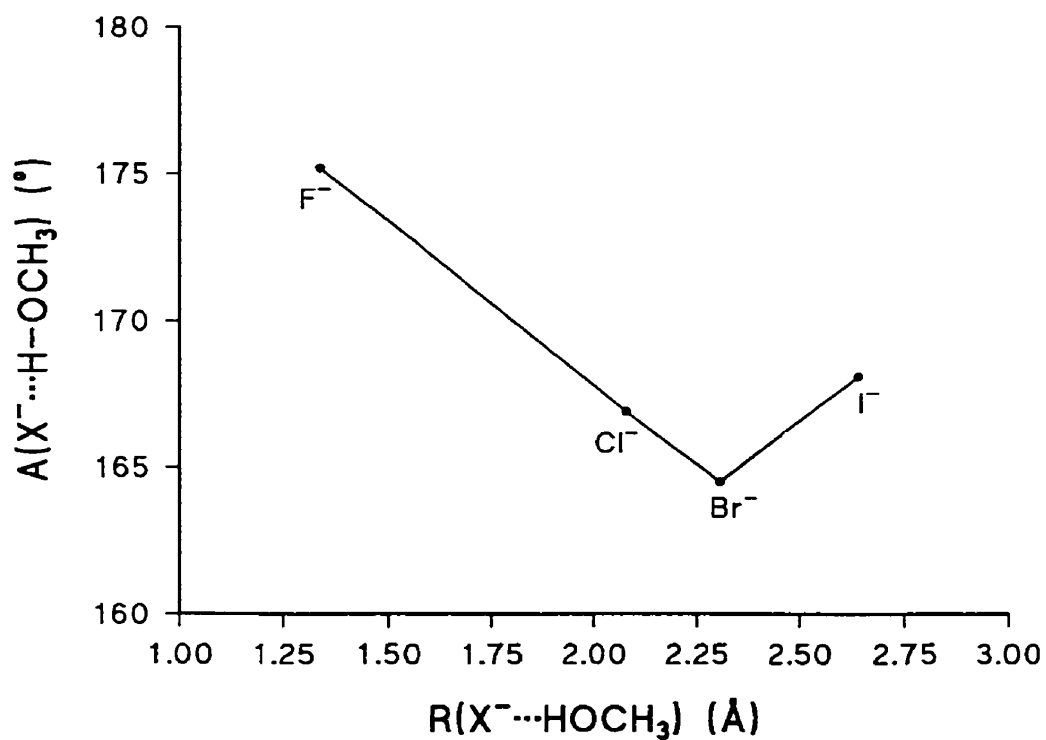


Figure 4.17 Plot of the MP2(full)/a ([a/e] for X = I) calculated $\text{X}^- \cdots \text{H}-\text{OCH}_3$ angle, $A(\text{X}^- \cdots \text{H}-\text{OCH}_3)$, versus the $\text{X}^- \cdots \text{HOCH}_3$ distance, $R(\text{X}^- \cdots \text{HOCH}_3)$, (X = F, Cl, Br, I).

increase, while at the same time the $X^- \cdots H-OCH_3$ angles decrease as shown in Figure 4.17. Both these changes are mainly due to the increase in size of X^- , which will allow more interaction with the permanent dipole moment of CH_3OH as a result of the decrease in importance of a nearly linear hydrogen bonding interaction with the OH group. Going from $X = Br$ to I , one would expect an increase in the $X^- \cdots HOCH_3$ bond distance and this indeed occurs, but instead of a further decrease of the $X^- \cdots H-OCH_3$ bond angle an increase is observed, causing a break in the plot. The most likely explanation may be that Γ is so large that repulsion with the methyl group hydrogen atoms increases with Γ being pushed back. Changes with respect to the RO-H bond length going from ROH to $X^-(ROH)$ ($\Delta R(RO-H)$) for $X = F, Cl, Br, I$ and $R = CH_3, CH_3CH_2, (CH_3)_2CH,$ and $(CH_3)_3C$ can be observed that are directly related to ΔH°_{298} and frequency shifts in the RO-H normal mode vibrational frequencies ($\Delta \nu(RO-H)$). For the $\Gamma(CH_3OH)$ complexes small differences can be found and these may be attributed to iodide ion basis set effects. Comparing the MP2 and B3LYP structural results for $CH_3OH, CH_3CH_2OH, X^-(CH_3OH),$ and $F^-(CH_3CH_2OH),$ only small differences are noticeable. They occur mainly in the $X^- \cdots HOR$ bond distance, with B3LYP results in general being a fraction larger (+0.013 Å, +0.051 Å, +0.028 Å, and +0.019/0.026 Å for $X = F, Cl, Br,$ and I ($[a/d]/[a/e]$), respectively). These differences are small enough to justify the use of B3LYP/b structures for MP2/a//B3LYP/b single point energy computations. As for the MP2 computations on $\Gamma(CH_3OH),$ the B3LYP structures also show some variation depending on the basis set for the iodide ion. These small structural differences cannot explain the large differences in ΔH°_{298} . The B3LYP/b structures for $X^-(ROH)$ ($X = F, Cl; R = (CH_3)_2CH, (CH_3)_3C$) show very similar bonding characteristics for the same halide ion. Going from $X^-(CH_3OH)$ to $X^-((CH_3)_3COH)$ a slight increase in the $X^- \cdots HOR$ bond distance occurs. The main difference between the $F^-(ROH)$ and $Cl^-(ROH)$ complexes is that for $X = F$ the $X^- \cdots HO-R$ bond angle decreases from $R = CH_3$ to $(CH_3)_3C,$ while for $X = Cl$ it increases slightly, as can be seen in Figures 4.18 and 4.19. In the $X^-(ROH)$ complexes ($X = F, Cl; R = (CH_3)_2CH, (CH_3)_3C$) the distance between the halide ion and the methyl group hydrogen atoms is much smaller than in $X^-(CH_3OH).$

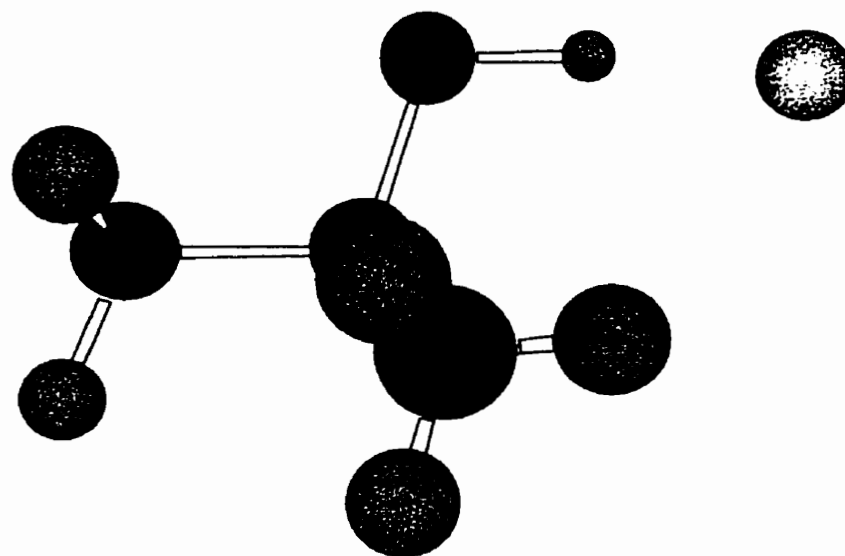


Figure 4.18 Optimized B3LYP/b structure of F⁻((CH₃)₃COH).

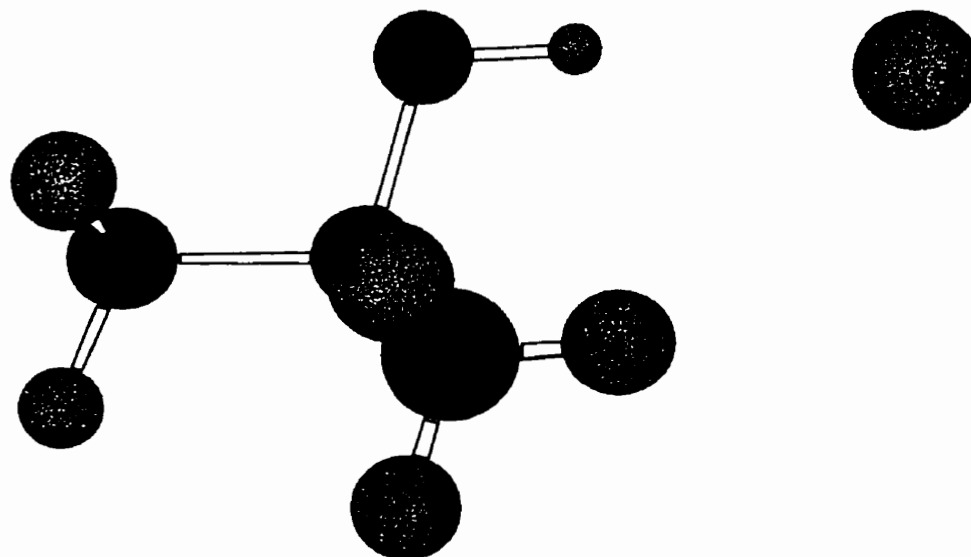


Figure 4.19 Optimized B3LYP/b structure of Cl⁻((CH₃)₃COH).

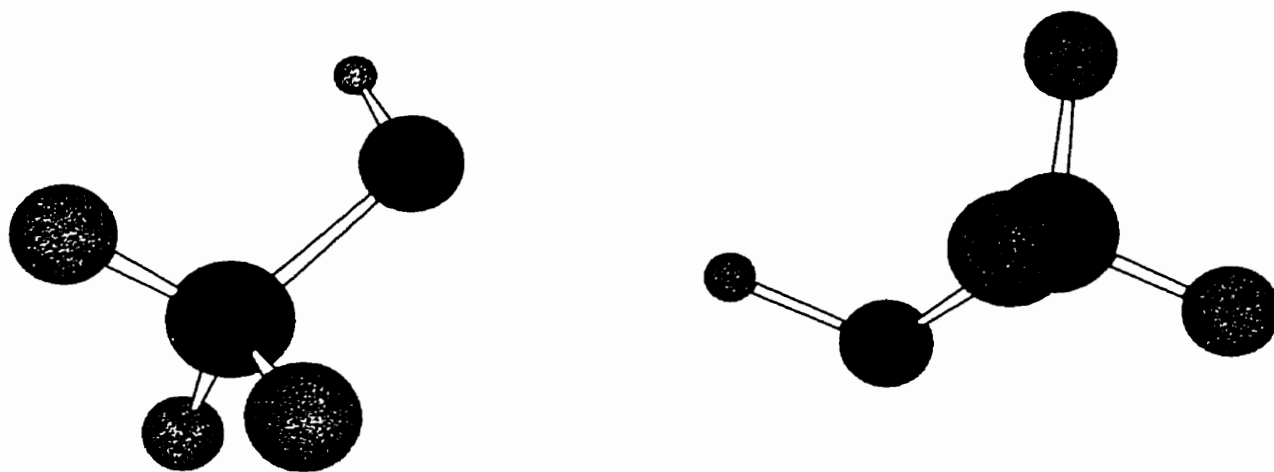


Figure 4.20 Optimized B3LYP/b structure of $(\text{CH}_3\text{OH})(\text{CH}_3\text{OH})$.

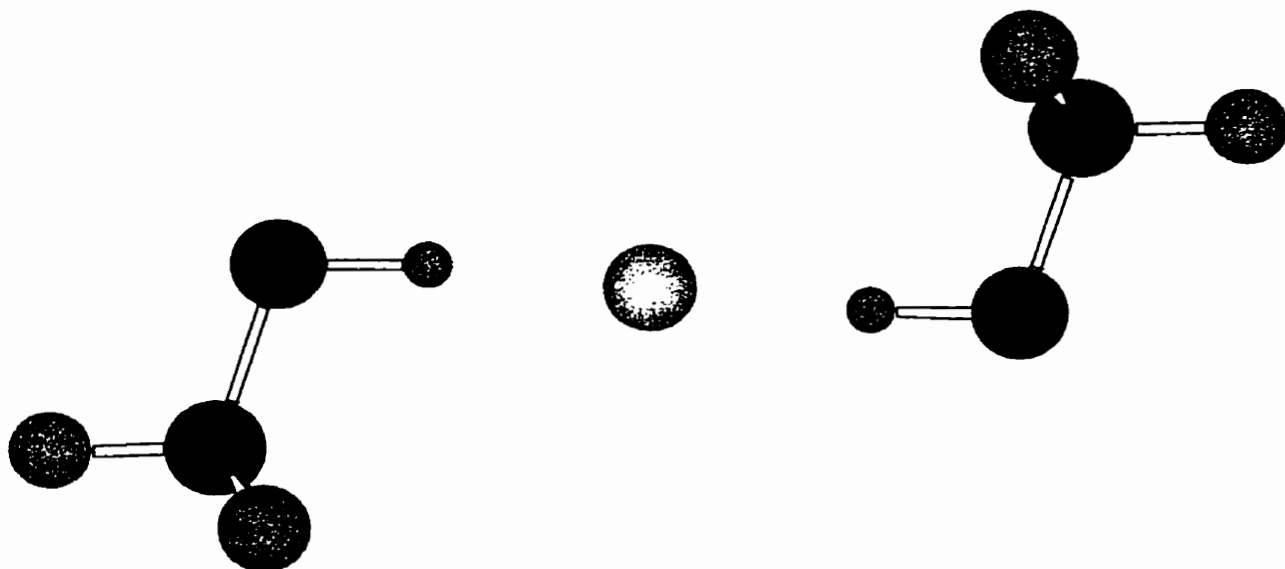


Figure 4.21 Optimized B3LYP/b structure of $(\text{CH}_3\text{OH})\text{F}^-(\text{CH}_3\text{OH})$.

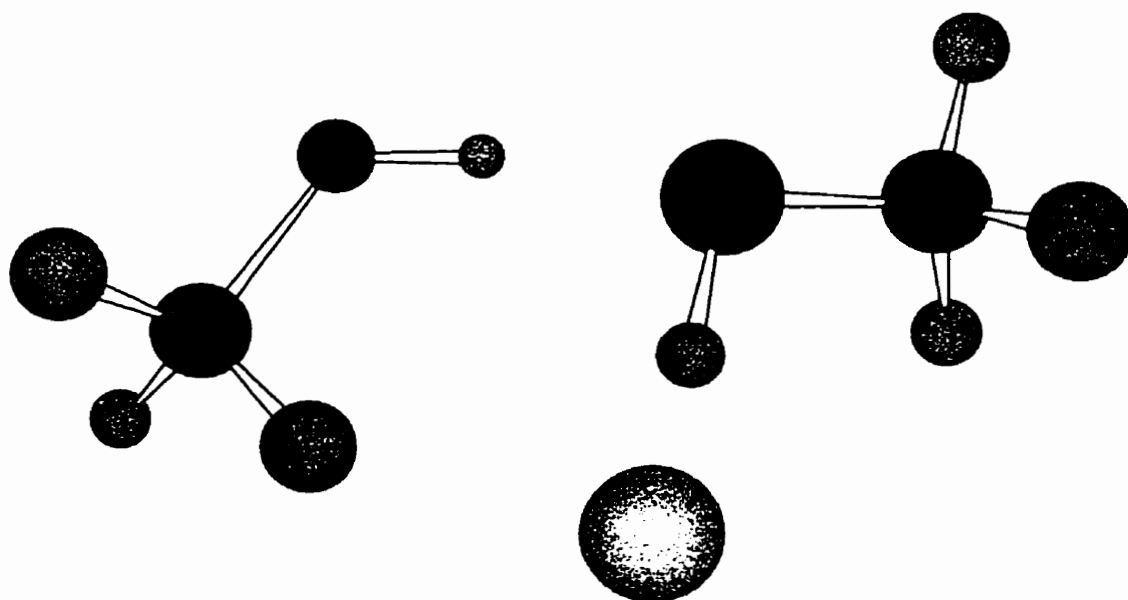


Figure 4.22 Optimized B3LYP/b structure of $\text{F}^-(\text{CH}_3\text{OH})(\text{CH}_3\text{OH})$.

For the fluoride and chloride ion-methanol dimer complexes two stable isomers were found. In Figure 4.20 the B3LYP/6-311+G(d,p) level of theory structure of the methanol dimer is shown. The bond length of the donor OH group is somewhat longer than that of the acceptor OH group (0.970 Å and 0.962 Å, respectively), but no dramatic change is observed relative to methanol monomer. The O–H...OH distance is 1.904 Å, which is fairly short for a non-covalent dipole-dipole interaction. In Figure 4.21 the more stable (CH₃OH)F⁻(CH₃OH) isomer is shown. Relative to F⁻(CH₃OH) there is a fair increase in the F⁻...HOCH₃ bond distance from 1.352 Å to 1.511 Å, mainly due to the dipole-dipole repulsion between the two OH groups. The O–H bond length has been reduced from 1.070 Å to 1.013 Å. The H...F...H bond angle is 180.0°. The F⁻(CH₃OH)(CH₃OH) isomer in Figure 4.22 shows some very interesting structural features. Relative to F⁻(CH₃OH) there is a substantial decrease in the F⁻...HOCH₃ bond distance from 1.352 Å to 1.241 Å, while the O–H bond length increased from 1.070 Å to 1.125 Å. The O–H...OH distance is decreased from 1.904 Å to 1.701 Å, while the donating O–H group bond length increased to 0.993 Å. In Figure 4.23 the (CH₃OH)Cl⁻(CH₃OH) isomer is shown and it is quite obvious that the two methanol molecules are interacting with the chloride ion very differently than in the fluoride ion analogue. The H...Cl⁻...H bond angle is 114.9° confirming the asymmetric nature of this cluster ion. Relative to Cl⁻(CH₃OH) there is a small increase in the Cl⁻...HOCH₃ bond distance from 2.130 Å to 2.167 and 2.178 Å, while the O–H bond lengths have been reduced from 0.991 Å to 0.985 Å. The orientation of the two methanol molecules is such that the chloride ion no longer interacts equivalently with the two methyl group hydrogen atoms as in Cl⁻(CH₃OH). The Cl⁻(CH₃OH)(CH₃OH) isomer in Figure 4.24 shows features similar to the fluoride ion analogue. The Cl⁻...HOCH₃ and O–H...OH distances are 2.026 Å and 1.800 Å, which are still shorter than in Cl⁻(CH₃OH) and (CH₃OH)(CH₃OH). There is also a substantial reduction in the bond length of the OH group interacting with the chloride ion relative to the fluoride ion from 1.125 Å to 1.001 Å.

The G3(MP2) method calculates structures at the MP2(full)/6-31G(d) level of theory. For HF_2^- , H–F bond distances of 1.149 Å were found. Upon complex formation with CH_3OH the symmetric F–H–F structure is lost. Instead a complex that resembles $(\text{CH}_3\text{OH})\text{F}^-(\text{HF})$ is formed. The $\text{F}^- \cdots \text{HF}$ bond distance is 1.271 Å, while the H–F bond length is 1.056 Å. As can be seen in Figure 4.25, F^- interacts with the OH group at a distance of 1.547 Å, while one of the methyl group hydrogen atoms interacts with the fluorine atom from HF at a distance of 2.266 Å. Adding the second methanol molecule to HF_2^- restores the symmetric F–H–F unit, with H–F bond distances of 1.148 Å. There is a slight increase in the $\text{HF}_2^- \cdots \text{HOCH}_3$ bond distances to 1.662 Å, while the $\text{HF}_2^- \cdots \text{H}-\text{CH}_2\text{OH}$ bond distance slightly decreases to 2.260 Å (Figure 4.26).

4.4.6 Natural Population Analysis Charges versus Thermochemistry

As noted in Section 4.4.1, the halide ion-alcohol complexes are bound mainly through ion-dipole and ion-induced dipole interaction, as giving by Equation 4.17. NPA charges calculated at the MP2/a ([a/d] for X = I) level of theory for $\text{X}^-(\text{CH}_3\text{OH})$ (X = F, Cl, Br, I), and MP2/a//B3LYP/b and B3LYP/b for $\text{F}^-(\text{ROH})$ (R = CH_3 , CH_3CH_2 , $(\text{CH}_3)_2\text{CH}$, $(\text{CH}_3)_3\text{C}$) show some interesting correlations between the NPA charges on the halide ions, $q(\text{NPA})(\text{X}^-)$ and $\Delta\text{H}^\circ_{298}$ for the $\text{X}^-(\text{ROH})$ formation. In Figure 4.27 a plot of $-\Delta\text{H}^\circ_{298}$ versus $-q(\text{NPA})(\text{X}^-)$ at the MP2/a ([a/d] for X = I) level of theory for $\text{X}^-(\text{CH}_3\text{OH})$ (X = F, Cl, Br, I) is shown. This linear correlation is expected from an examination of Equation 4.17. It should be noted however, that for the $\text{X}^-(\text{CH}_3\text{OH})$ complexes this is not the only linear relationship that can be obtained from the computations. For the four $\text{X}^-(\text{CH}_3\text{OH})$ complexes, the differences between the standard deprotonation enthalpy of CH_3OH , $\Delta_{\text{acid}}\text{H}^\circ_{298}(\text{CH}_3\text{OH})$, and the standard deprotonation enthalpies of the corresponding acids of the four halide ions, $\Delta_{\text{acid}}\text{H}^\circ_{298}(\text{HX})$, is greater than zero. This means that the proton-transfer reaction (Reaction 4.22)



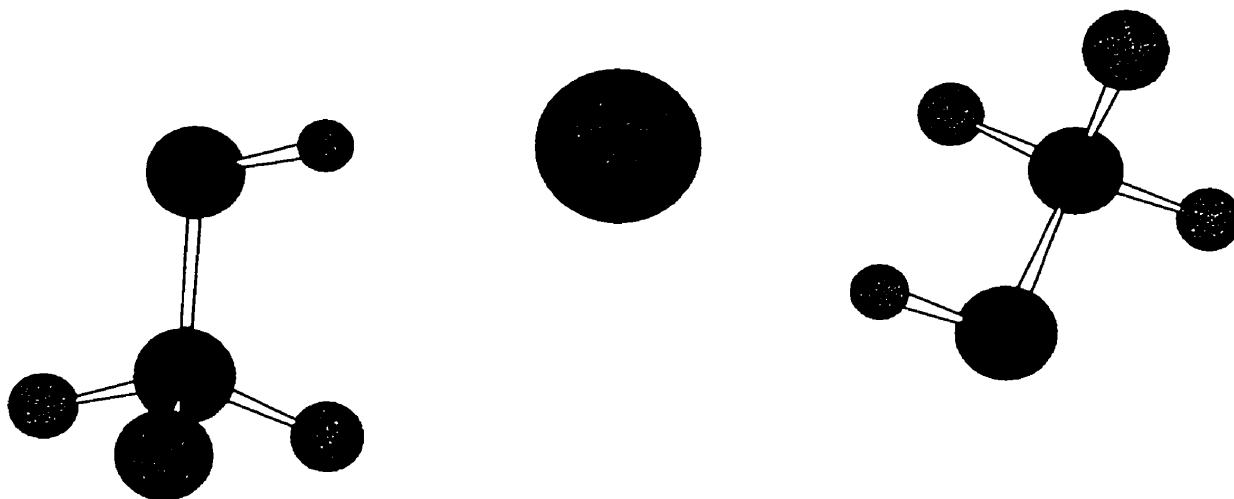


Figure 4.23 Optimized B3LYP/b structure of $(\text{CH}_3\text{OH})\text{Cl}^-(\text{CH}_3\text{OH})$.

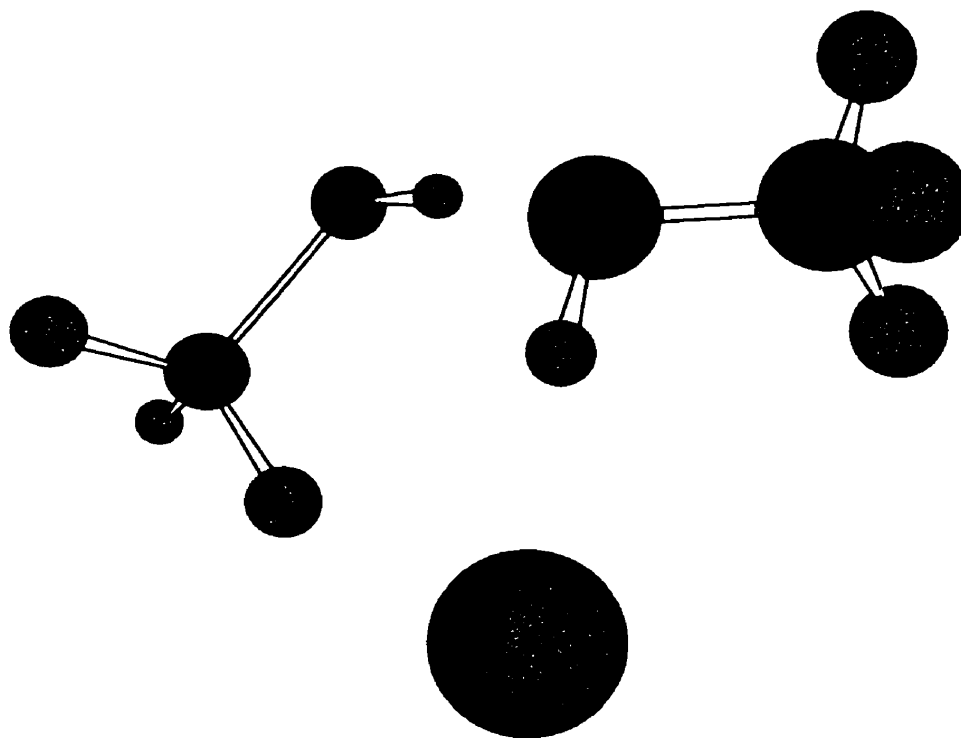


Figure 4.24 Optimized B3LYP/b structure of $\text{Cl}^-(\text{CH}_3\text{OH})(\text{CH}_3\text{OH})$.

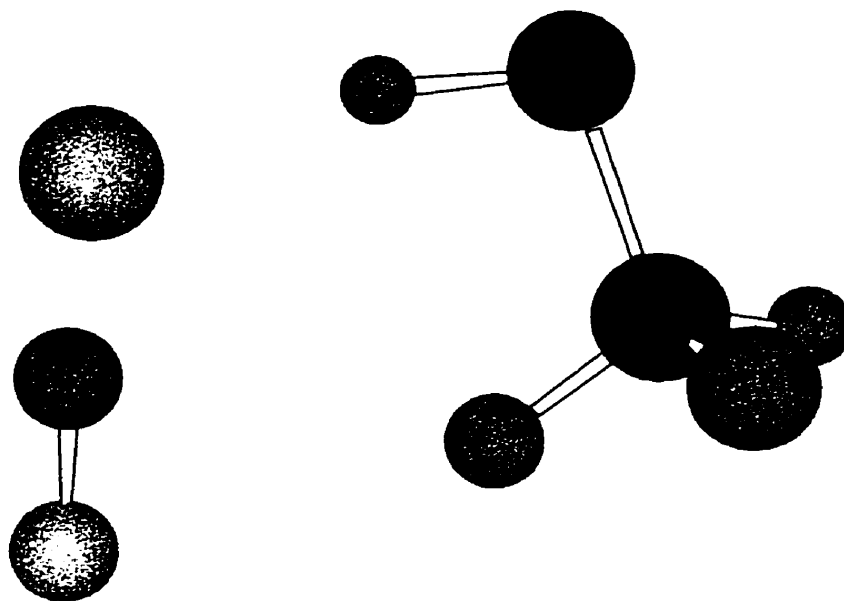


Figure 4.25 Optimized MP2(full)/6-31G(d) structure of HF₂⁻(CH₃OH).

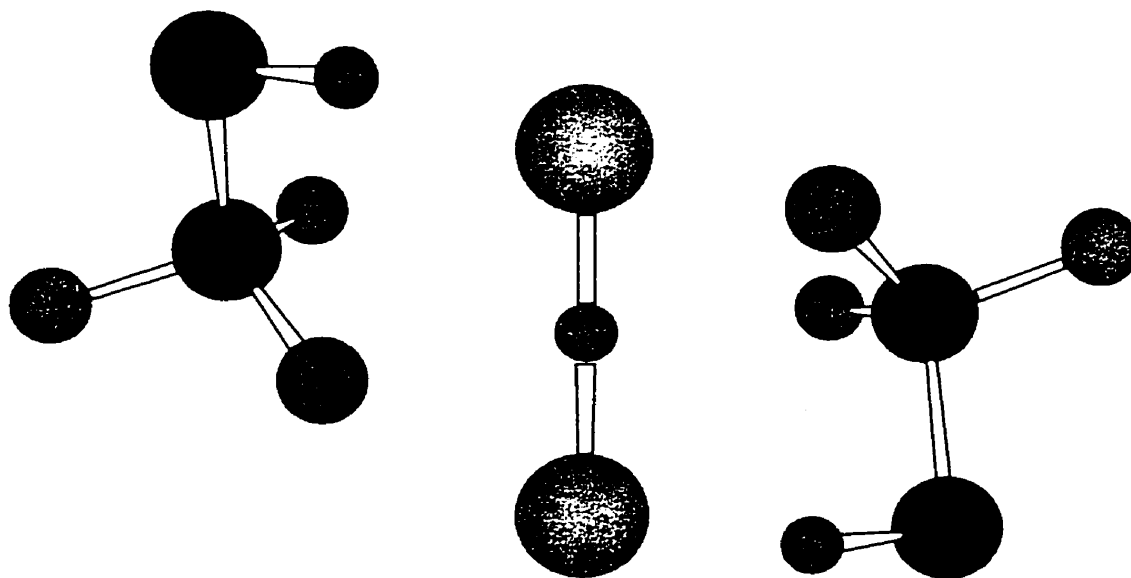


Figure 4.26 Optimized MP2(full)/6-31G(d) structure of (CH₃OH)HF₂⁻(CH₃OH).

does not take place at an appreciable rate. From the data it is clear that, even though there is no proton transfer taking place, the binding of a halide ion to an alcohol molecule leads to some charge transfer from the halide ion to the alcohol molecule. This results in an elongation of the CH₃O–H bonds within the X[−](CH₃OH) complexes compared to “free” CH₃OH. This elongation cannot, except perhaps for F[−](ROH) complexes, be considered as a partial proton transfer. One would expect that in order to achieve efficient proton transfer, a linear X[−]...H–O bond would be most favorable. Based on this, except for F[−](CH₃OH), the other three X[−](CH₃OH) complexes show weaker hydrogen bonding. This is due to the fact that for X = Cl, Br, and I the binding is dominated by the interaction of the charge center with the permanent dipole moment of methanol that is aligned between the C–O and O–H bonds, and not along the O–H bond. As mentioned earlier, for the F[−](ROH) complexes partial proton transfer seems possible. In Section 4.4.1 it was already mentioned that there is a linear relationship between $\Delta_{\text{acid}}H^{\circ}(\text{ROH}) - \Delta_{\text{acid}}H^{\circ}(\text{HF})$ ($\Delta\Delta_{\text{acid}}H^{\circ}$) and ΔH° for F[−](ROH) formation. Using $\Delta_{\text{acid}}H^{\circ}_{298}$ of ROH obtained by DeTuri *et al.* from TCID⁸⁰ and $\Delta_{\text{acid}}H^{\circ}_{298}$ of HF (or better $D_0(\text{H}^+ - \text{F}^-)$ by Martin *et al.* from threshold ion-pair production spectroscopy (TIPPS) experiments¹⁴⁸), and the MP2/a//B3LYP/b ΔH°_{298} values, a similar relationship can be obtained. None of these systems qualifies for proton transfer, but one would expect that if the $\Delta\Delta_{\text{acid}}H^{\circ}$ decreases, the amount of charge transfer would increase as discussed above.

In general, the two methods to calculate NPA charges show the same trends. For the MP2/a//B3LYP/b computations, the NPA charge on F[−] is approximately 0.029e more negative than B3LYP/b, while for H and O they are 0.041e and 0.059e more positive and negative, respectively. By inspecting the ΔH°_{298} and q(NPA)(F[−]) results, both at the MP2/a//B3LYP/b level of theory, it is immediately evident that the above mentioned relationship only holds for F[−](CH₃OH) and F[−](CH₃CH₂OH). For the fluoride ion-*iso*-propyl alcohol and *tert*-butyl alcohol the expected relationship breaks down. This is due to the weaker, less linear, hydrogen bond interactions, as evidenced by a slight increase in the F[−]...HOR distance. This is being compensated for by a stronger ion-dipole interaction and stronger polarization interactions, due to the slight

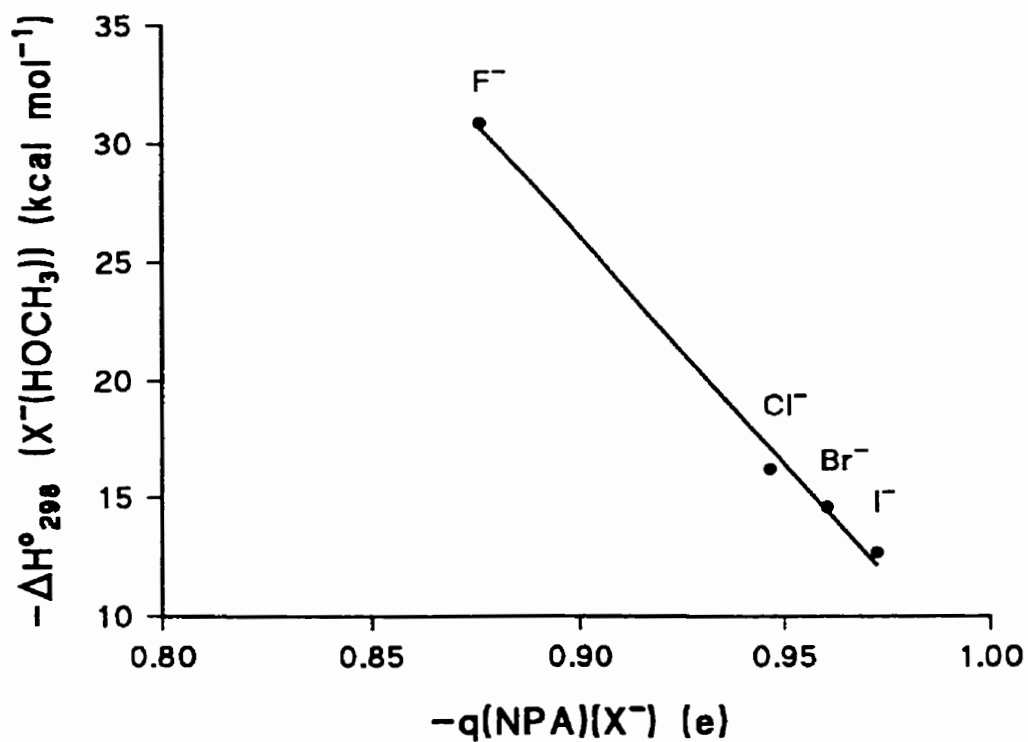
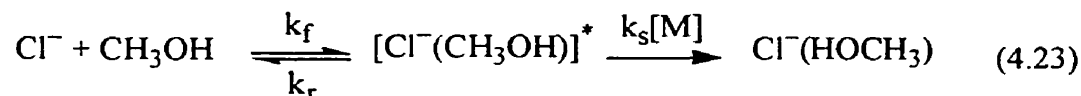


Figure 4.27 Plot of the MP2(full)/a ([a/e] for X = I) negative standard ambient enthalpy change for the $X^- + \text{CH}_3\text{OH} = X^-(\text{CH}_3\text{OH})$ clustering equilibria, $-\Delta H_{298}^\circ (X^-(\text{CH}_3\text{OH}))$ versus the negative NPA charges on the halide ion, $-q(\text{NPA})(X^-)$ (X = F, Cl, Br, I).

decrease in the $F^- \cdots H-OR$ angle, and a large decrease in the $F^- \cdots HC$ distance, respectively.

4.4.7 Kinetics of Complex Formation

The complex formation of the chloride ion methanol cluster is thought to proceed by the reaction mechanism shown in Scheme 4.23.



A similar mechanism has been suggested for the formation of $CH_3O^-(CH_3OH)$.⁹⁸ It can be shown that formation of $Cl^-(HOCH_3)$ does not proceed directly by clustering of Cl^- and CH_3OH , but instead it goes through another ion-neutral complex, indicated here as $[Cl^-(CH_3OH)]^*$. Writing a steady-state expression for Scheme 4.23 gives Equation 4.24,¹⁶³ which can be re-written as Equation 4.25.

$$k_{app} = \frac{k_f k_s [M]}{k_r + k_s [M]} \quad (4.24)$$

$$\frac{1}{k_{app}} = \frac{k_r}{k_f k_s [M]} + \frac{1}{k_f} \quad (4.25)$$

By plotting $1/k_{app}$ versus $1/[M]$, with $M = CH_4$, one can obtain k_f from the intercept. The latter assumption can be made because $[CH_4] \gg [CH_3OH]$. In Figure 4.28 a typical mass spectrum is shown for a $CH_4/CH_3OH/CCl_4$ mixture. As can be seen the Cl^- and $Cl^-(CH_3OH)_n$ ($n = 1-3$) ions are present, as well as some chloride ion-water complexes. In order to obtain kinetic data on the complex formation of $Cl^-(CH_3OH)$, one has to take into account that it is formed by the reactions in Scheme 4.23, but that it is consumed by formation of the chloride ion-methanol dimer (Reaction 4.26)



In Figure 4.29 typical raw data mass-selected time-intensity profiles for the three ions of interest are shown. The large dynamic range of the PHPMS technique is very nicely illustrated. In Figure 4.30 the normalized time-intensity profiles are shown. From the slope of the $^{35}\text{Cl}^-$ normalized time-intensity profile k_{app} can be determined. By performing this kind of experiment at different ion source temperatures and pressures, Figure 4.31 can be constructed. From the intercepts, where $1/[\text{CH}_4]$ is zero or $[\text{CH}_4]$ is infinite, k_f can be determined. At 297 K, 303 K, and 308 K values of $5.00 \times 10^{-11} \text{ cm}^3 \text{ s}^{-1}$, $3.70 \times 10^{-11} \text{ cm}^3 \text{ s}^{-1}$, and $2.62 \times 10^{-11} \text{ cm}^3 \text{ s}^{-1}$, respectively, have been determined. The relative error for these values is around 50%. From transition state theory (TST) Equation 4.27 can be derived.¹⁶³

$$\ln\left(\frac{k_f}{T^2}\right) = \left(\ln\left(\frac{V_m}{N_A T_{\text{STP}}}\right) + \frac{\Delta S^\ddagger}{R} \right) - \frac{\Delta H^\ddagger}{RT} \quad (4.27)$$

In Figure 4.32 Equation 4.27 is plotted for the k_f values determined, and from this plot ΔH^\ddagger and ΔS^\ddagger values of $-9.7 \text{ kcal mol}^{-1}$ and $-2.2 \text{ cal mol}^{-1} \text{ K}^{-1}$, respectively, can be determined. These values do not seem unreasonable, although it may be expected that associated large errors can be associated with them ($\pm 2.0 \text{ kcal mol}^{-1}$ and $\pm 4.0 \text{ cal mol}^{-1} \text{ K}^{-1}$, respectively). The fact that a ΔH^\ddagger value has been determined that is less negative than the ΔH^0 value for the ion-molecule complex in the well, $\text{Cl}^-(\text{CH}_3\text{OH})$, indicates that the PES is indeed more complex than shown in Figure 4.12. This will be discussed further in section 4.4.10.

4.4.8 Vibrational Frequencies

Scaling factors were introduced to the MP2/a and B3LYP/b harmonic normal mode vibrational frequencies of CH_3OH in order to match the experimental values.¹⁶⁴ These scaling factors were used for all subsequent ROH and $\text{X}^-(\text{ROH})_n$ computations and, in

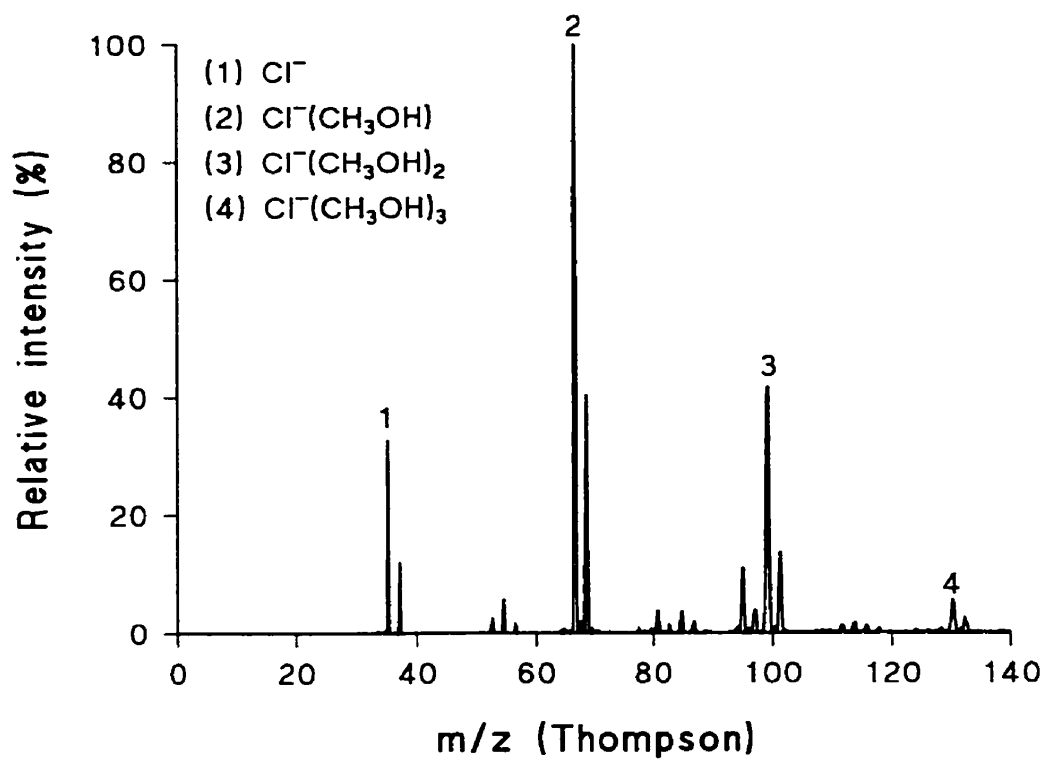


Figure 4.28 High pressure ion source mass spectrum at the following experimental conditions: $P_{\text{ion source}} = 4.0$ Torr, $T_{\text{ion source}} = 298$ K, $P_{\text{reservoir}}(\text{CH}_4) = 765$ Torr, $P_{\text{reservoir}}(\text{CH}_3\text{OH}) = 0.25$ Torr, $P_{\text{reservoir}}(\text{CCl}_4) < 0.01$ Torr.

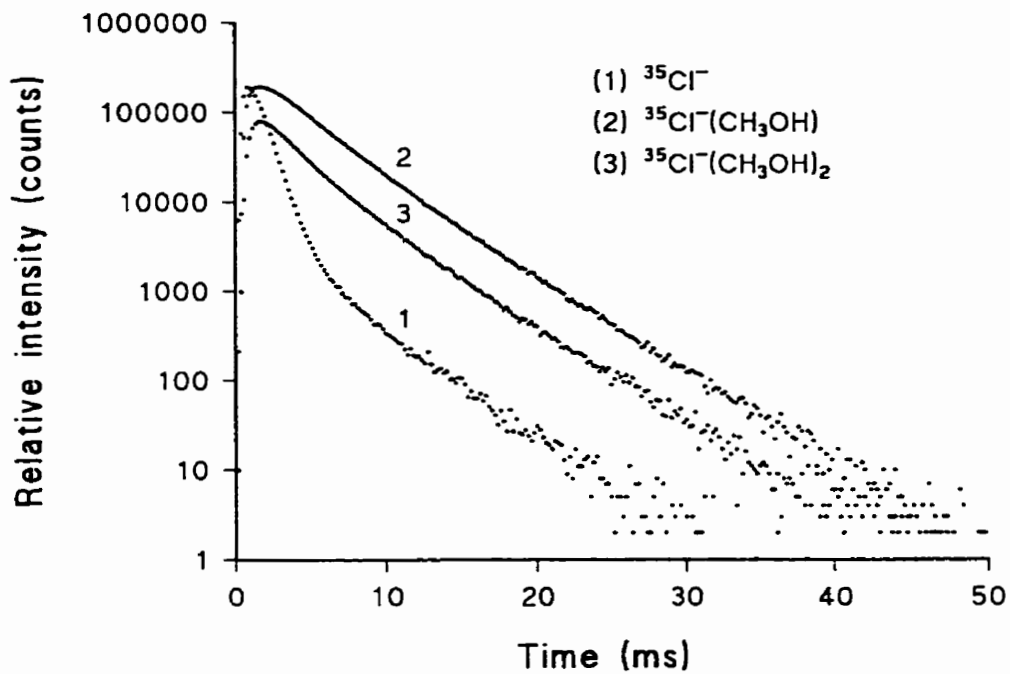


Figure 4.29 Time-intensity profiles for the $^{35}\text{Cl}^-$, $^{35}\text{Cl}^-(\text{CH}_3\text{OH})$, and $^{35}\text{Cl}^-(\text{CH}_3\text{OH})_2$ ions at the ion source conditions of Figure 4.28.

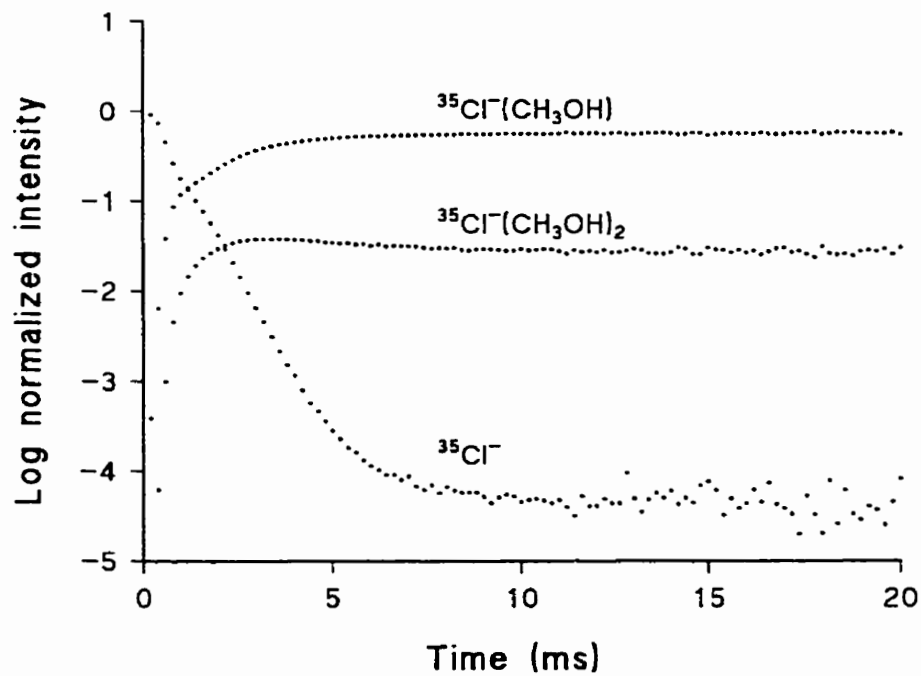


Figure 4.30 Normalized time-intensity profiles of Figure 4.29.

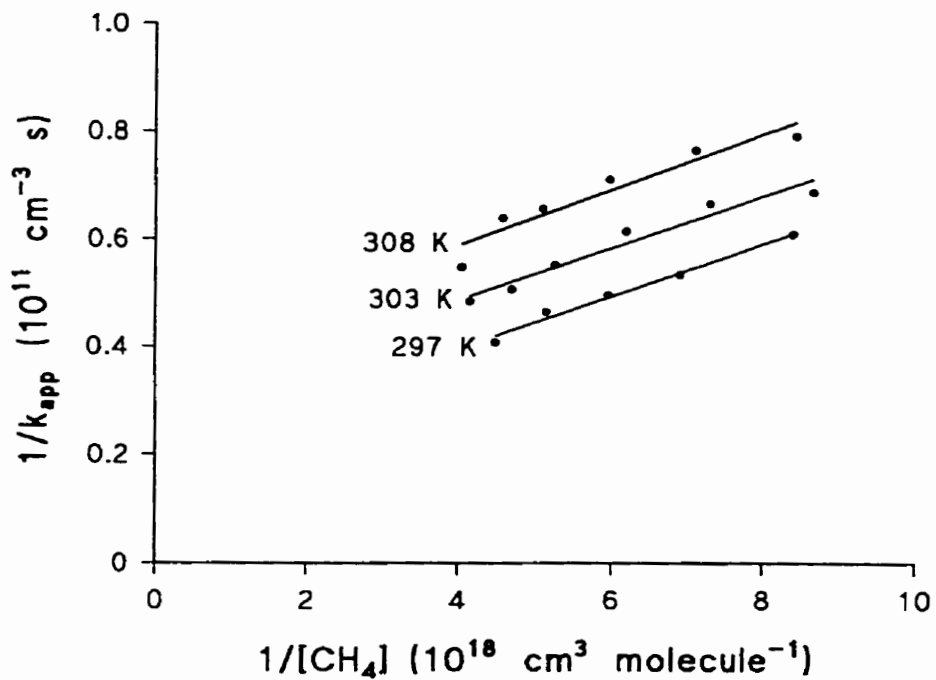


Figure 4.31 Plot of $1/k_{app}$ versus $1/[CH_4]$.

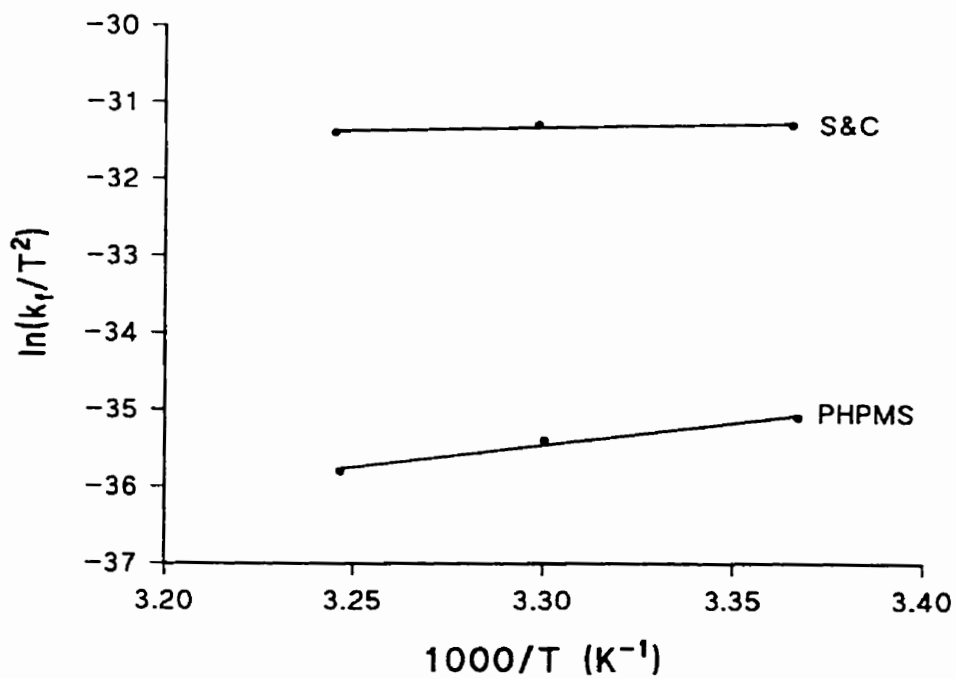


Figure 4.32 Plot of $\ln(k_f/T^2)$ versus $1/T$ (S&C = Su and Chesnavich).

general, good agreement was found between the results from this work and results from a scaled quantum mechanical (SQM) force field method,¹⁰⁹ and HF/6-31G(d) scaled by 0.8953.⁸¹ For CH₃CH₂OH, (CH₃)₂CHOH, and (CH₃)₃COH in general there is good agreement between the scaled MP2/a, B3LYP/b, and HF/6-31G(d) results. For the normal mode vibrational frequencies of the F⁻(CH₃OH) complex, various results have been published in the literature, and most data show some spread in individual frequencies caused by basis set effects. None of the methods used produced extreme deviations however.^{81,104,109} Based on matching thermochemical data such as ΔH⁰₂₉₈, it would be hard to assess the quality of the vibrational frequencies. It would be better of course to have experimental vibrational data on F⁻(CH₃OH) and other F⁻(ROH) complexes. Unfortunately these are not available, and the nature of these systems, mainly due to the very strong bond involved, causes the F⁻(ROH)₂ and F⁻(ROH)₃ complexes to be formed at room temperature. For the F⁻(ROH) complexes (R = CH₃CH₂, (CH₃)₂CH, (CH₃)₃C) only the MP2/a (R = CH₃CH₂ only) and B3LYP/b data from this work, and the HF/6-31G(d) data from DeTuri *et al.* are available.⁸¹ Once again the agreement is in general good, except for the lowest vibrational frequencies of F⁻(CH₃OH) and F⁻((CH₃)₃COH). The *Gaussian* 94 and 98 suites of programs treat the hindered methyl group rotations as harmonic vibrations, while the HF/6-31G(d) results by DeTuri *et al.* were corrected for free methyl group rotations, which is more accurate at temperatures normally used for PHPMS experiments on these kinds of systems.

For the Cl⁻(CH₃OH) and Cl⁻(CH₃OH)₂ clusters, experimental VPDS data are available,⁶³ and this is an excellent opportunity to test the different theoretical models. For the intermolecular Cl⁻...HOCH₃ stretch, Carbacos *et al.* found, indirectly, a value of 232 cm⁻¹, while for the CH₃O-H stretch a value of 3162 cm⁻¹ was obtained. Both the MP2/a (190 cm⁻¹) and B3LYP/b (190 cm⁻¹) results for the Cl⁻...HOCH₃ stretch are closer to the experimental VPDS results than the LMP2/cc-pVDZ result of 307 cm⁻¹ obtained by the same authors. For the CH₃O-H stretch the B3LYP/b result is in very good agreement (3186 cm⁻¹) as is the LMP2/cc-pVDZ result (3198 cm⁻¹), while the MP2/a result is somewhat off (3223 cm⁻¹). For the Cl⁻(CH₃OH)₂ cluster an

experimental $\text{CH}_3\text{O-H}$ stretch value of 3241 cm^{-1} was found. Introduction of the second methanol molecule leads to a shift in the OH stretch of $+79\text{ cm}^{-1}$. In principal two isomers exist, $(\text{CH}_3\text{OH})\text{Cl}^-(\text{CH}_3\text{OH})$ and $\text{Cl}^-(\text{CH}_3\text{OH})(\text{CH}_3\text{OH})$. In Section 4.4.4 it was shown already that $(\text{CH}_3\text{OH})\text{Cl}^-(\text{CH}_3\text{OH})$ is the more abundant isomer. As may be expected, both clusters have distinct IR spectra (Figures 4.33 and 4.34). The y-axis represents absorption and the unit is km mol^{-1} . In $(\text{CH}_3\text{OH})\text{Cl}^-(\text{CH}_3\text{OH})$, both OH groups can be involved in symmetric (3310 cm^{-1}) and asymmetric stretches (3277 cm^{-1}). The asymmetric OH stretch is in good agreement with the VPDS results. In the experimental VPDS spectra a small peak around 3300 cm^{-1} is also visible, but there is significant overlap due to the broad peak width of the symmetric OH stretch around 3241 cm^{-1} . At the LMP2/cc-pVDZ level of theory, scaled values of 3337 cm^{-1} and 3372 cm^{-1} , respectively, are calculated. For the second isomer the B3LYP/**b** normal mode OH stretches are at 3003 cm^{-1} ($\text{Cl}^-(\text{CH}_3\text{O-H})(\text{CH}_3\text{OH})$) and 3360 cm^{-1} ($\text{Cl}^-(\text{CH}_3\text{OH})(\text{CH}_3\text{O-H})$). Compared to the $(\text{CH}_3\text{OH})(\text{CH}_3\text{OH})$ dimer, the first OH (acceptor) group is shifted -402 cm^{-1} , while the second (donor) one is shifted by -196 cm^{-1} (Figure 4.35). In the neutral methanol dimer the two O-H stretches are 3705 cm^{-1} (acceptor) and 3556 cm^{-1} (donor), respectively. This is in excellent agreement with data from molecular beam depletion spectroscopy experiments, which give results of 3684 cm^{-1} and 3574 cm^{-1} , respectively.¹⁶⁵ Compared to free neutral methanol, the acceptor OH group is shifted by only -1 cm^{-1} (3705 cm^{-1} versus 3706 cm^{-1}), while the donor OH group is shifted by -150 cm^{-1} (3556 cm^{-1}). The experimental OH stretch for methanol is 3162 cm^{-1} . Unfortunately for the other $\text{Cl}^-(\text{ROH})$ complexes, and both $\text{Br}^-(\text{ROH})$ complexes, no VPDS data are available. Comparison of the MP2/**a** and B3LYP/**b** harmonic vibrational frequencies with results from MP2(full)/[7s6p4d+ECP/D95+(p)] computations⁹⁷ shows varying agreement. For $\Gamma^-(\text{ROH})$ ($\text{R} = \text{CH}_3, \text{CH}_3\text{CH}_2, (\text{CH}_3)_2\text{CH}$) recent VPDS data have been published. Scaled B3LYP/LanL2DZ+ frequencies, based on matching the $\text{CH}_3\text{O-H}$ stretch in the gas phase, gave excellent agreement for both the $\Gamma^-\cdots\text{HOCH}_3$ stretch (166 cm^{-1} versus 157 cm^{-1}) and the $\text{CH}_3\text{O-H}$ stretch (3331 cm^{-1} versus 3365 cm^{-1}).⁶⁴ It is difficult to determine why the MP2/[**a/e**] and B3LYP/[**b/e**] results are somewhat different, since it

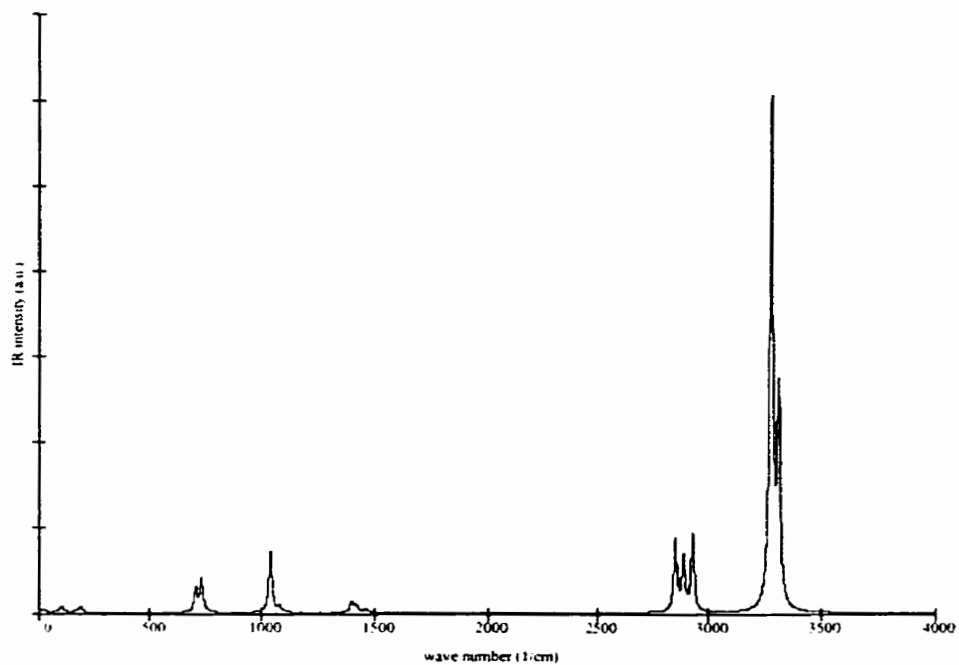


Figure 4.33 Simulated IR spectrum of $(\text{CH}_3\text{OH})\text{Cl}^-(\text{CH}_3\text{OH})$ calculated at the B3LYP/b level of theory and scaled by 0.9640.

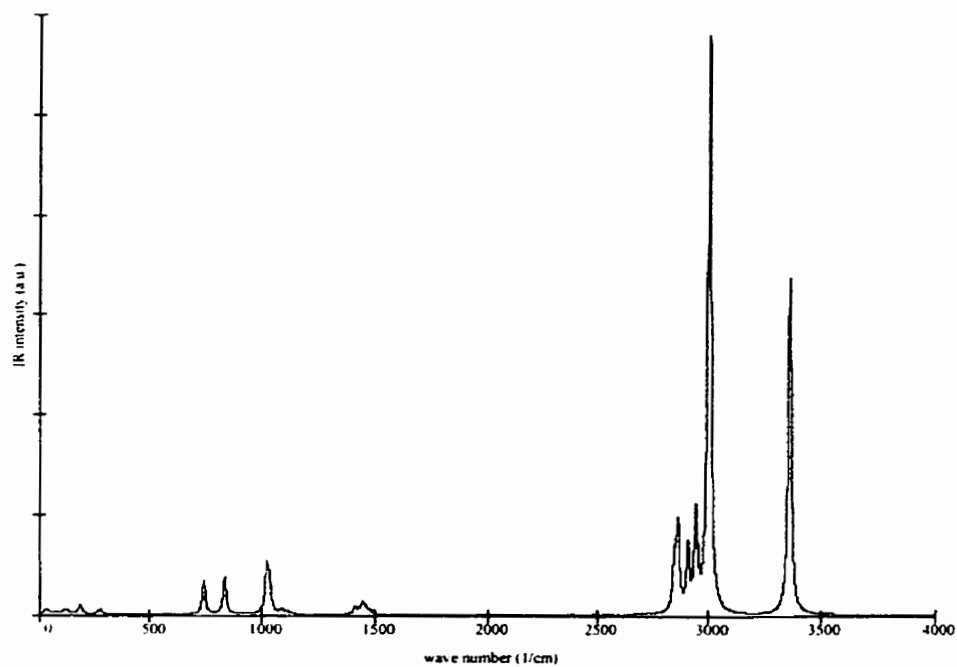


Figure 4.34 Simulated IR spectrum of $\text{Cl}^-(\text{CH}_3\text{OH})(\text{CH}_3\text{OH})$ calculated at the B3LYP/b level of theory and scaled by 0.9640.

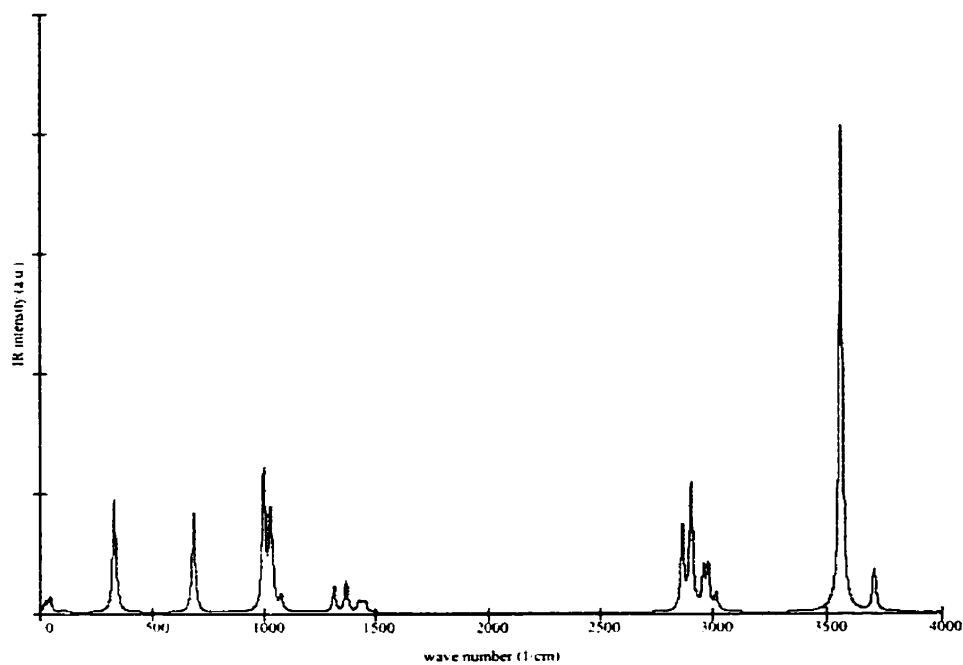


Figure 4.35 Simulated IR spectrum of (CH₃OH)₂ calculated at the B3LYP/b level of theory and scaled by 0.9640.

seems they fit the observed trends well. A different basis set for the iodide ion, and introduction of a correction for anharmonic low frequency vibrational modes, may improve this situation somewhat.

As mentioned before, upon complex formation with the halide ion, the RO–H stretch vibrational frequency is shifted to lower wavenumber relative to “free” ROH. In all calculated ROH IR spectra, the IR intensities of the RO–H stretch vibrations are relatively small. In the $X^-(ROH)$ they have become by far the strongest peaks in the IR spectra for all halide ions. By plotting $-\Delta\nu(RO-H)$ versus $\Delta I(RO-H)$ for going from ROH to $X^-(ROH)$ linear correlations for both the MP2/a and B3LYP/b data are obtained for all alcohol molecules. Because of this, the $X^-(ROH)$ complexes will absorb more IR radiation in the $X^-(H-OR)$ stretches than in the RO–H stretches. Unfortunately, the $X^-(H-OR)$ stretches do not lie in a region of the IR spectrum where there is a large photon density in the Boltzmann distribution of blackbody radiation, which can cause cluster ions to dissociate (Reaction 4.28).



In Appendix C the simulated IR spectra of the some of the other systems studied are shown.

4.4.9 Vibrational Frequencies versus Thermochemistry

In Table 4.11 an overview is given of the ΔH_{298}° values for the different halide ion-alcohol clustering thermochemistry, and the $X^-\cdots HOR$ and RO–H stretch vibrations of the different $X^-(ROH)$ complexes. In Figures 4.36 these data are plotted for the MP2/a ([a/e] for $X = I$) and MP2/a/B3LYP/b results. As can be seen for the MP2/a results for the $X^-(CH_3OH)$ complexes, excellent correlations between $-\Delta H_{298}^{\circ}$ and the $X^-\cdots HOCH_3$ and CH_3O-H stretch vibrations have been obtained. This is in agreement with similar experimental results by Ayotte *et al.* for $X^-(H_2O)$ complexes ($X = Cl, Br, I$).²⁹ By using experimental VPDS data for $Cl^-(CH_3OH)$ ⁶³ and $I^-(CH_3OH)$,⁶⁴ and ΔH°

Table 4.11 Overview of ΔH_{298}° for the $X^{-} + ROH \rightleftharpoons X^{-}(ROH)$ clustering equilibria, and $\nu(X^{-}\cdots HOR)$ and $\nu(RO-H)$ harmonic normal mode vibrational frequencies of the $X^{-}(ROH)$ complexes ($X = F, Cl, Br, I$; $R = CH_3, CH_3CH_2, (CH_3)_2CH, (CH_3)_3C$; **a** = 6-311++G(d,p), **b** = 6-311+G(d,p), **e** = Stuttgart RLC ECP).

X	ROH	method	ΔH_{298}° ^a	$\nu(X^{-}\cdots HOR)$ ^b	$\nu(RO-H)$ ^b
F	CH ₃ OH	MP2/a	-30.9	380	1988
F	CH ₃ OH	MP2/a/B3LYP/b	-31.0	374 ^c	1968 ^c
F	CH ₃ CH ₂ OH	MP2/a	-32.1	337	1761
F	CH ₃ CH ₂ OH	MP2/a/B3LYP/b	-32.0	319 ^c	1824 ^c
F	(CH ₃) ₂ CHOH	MP2/a/B3LYP/b	-33.2	339 ^c	2044 ^c
F	(CH ₃) ₃ COH	MP2/a/B3LYP/b	-34.1	356 ^c	2067 ^c
Cl	CH ₃ OH	MP2/a	-16.6	199	3223
Cl	CH ₃ OH	MP2/a/B3LYP/b	-16.6	190 ^c	3186 ^c
Cl	CH ₃ CH ₂ OH	MP2/a/B3LYP/b	-17.2	160 ^c	3168 ^c
Cl	(CH ₃) ₂ CHOH	MP2/a/B3LYP/b	-18.7	155 ^c	3220 ^c
Cl	(CH ₃) ₃ COH	MP2/a/B3LYP/b	-19.5	139 ^c	3211 ^c
Br	CH ₃ OH	MP2/a	-14.5	165	3347
Br	CH ₃ OH	MP2/a/B3LYP/b	-14.4	176 ^c	3288 ^c
Br	CH ₃ CH ₂ OH	MP2/a/B3LYP/b	-14.7	137 ^c	3268 ^c
I	CH ₃ OH	MP2/[a/e]	-12.7	135	3463
I	CH ₃ OH	B3LYP/[b/e]	-10.1	139	3402

^a kcal mol⁻¹ ^b cm⁻¹ ^c B3LYP/a frequencies

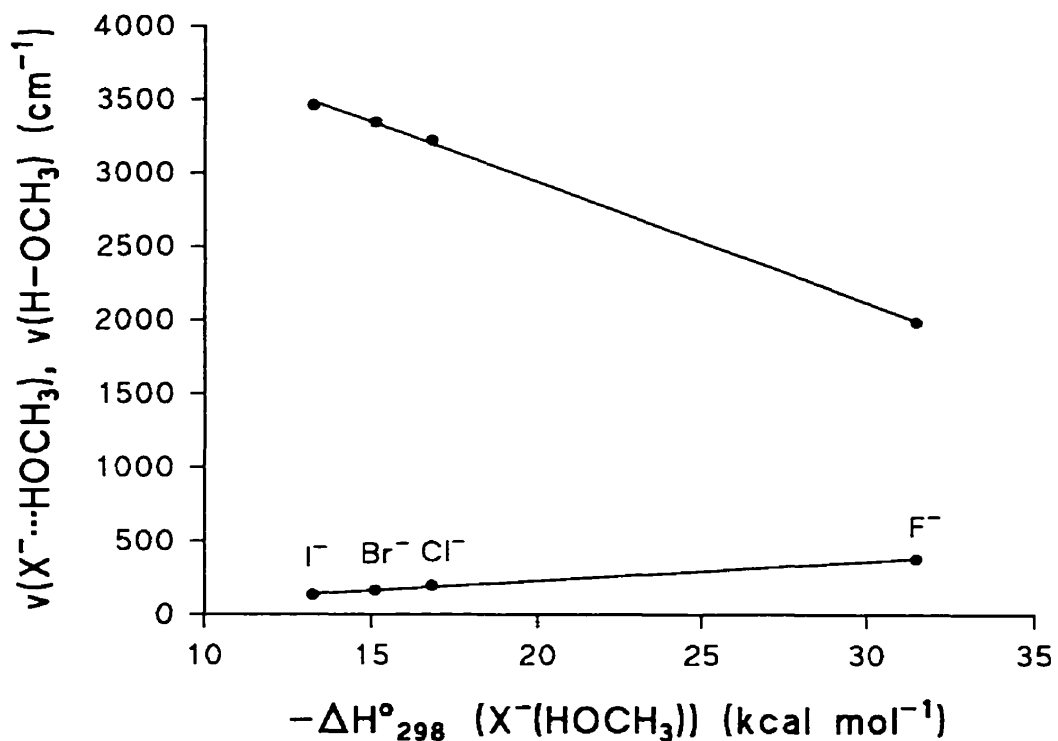


Figure 4.36 Plot of the MP2(full)/a ([a/e] for X = I) calculated $X^{-}\cdots\text{HOCH}_3$ and $\text{CH}_3\text{O}-\text{H}$ normal mode vibrational frequencies, $\nu(X^{-}\cdots\text{HOCH}_3)$ and $\nu(\text{CH}_3\text{O}-\text{H})$, respectively, versus the negative standard ambient enthalpy change to form $X^{-}(\text{CH}_3\text{OH})$, $-\Delta H_{298}^{\circ} (X^{-}(\text{CH}_3\text{OH}))$ (X = F, Cl, Br, I).

values obtained by PHPMS,⁷⁹ one would expect the $X^- \cdots \text{HOCH}_3$ and $\text{CH}_3\text{O}-\text{H}$ stretch vibrations for $X = \text{F}$ and Br to be 385 cm^{-1} and 2769 cm^{-1} , and 197 cm^{-1} and 3252 cm^{-1} , respectively. For $\text{F}^- \cdots \text{HOCH}_3$, and $\text{CH}_3\text{O}-\text{H}$, in the $\text{Br}^- \cdots \text{HOCH}_3$ complex, these predictions, based on experimental data and assuming similar linear correlations with values obtained by computations, would be in excellent agreement with the MP2/a data (380 cm^{-1} and 3247 cm^{-1} , respectively).

The $X^- \cdots \text{HOCH}_3$ stretch cannot be observed experimentally, but can be deduced from the VPDS experiments since they appear in a combination band with the $\text{CH}_3\text{O}-\text{H}$ stretch.^{63,64} This means that for $\text{F}^-(\text{CH}_3\text{OH})$ and $\text{Br}^-(\text{CH}_3\text{OH})$ bands at 3154 cm^{-1} and 3449 cm^{-1} would be observed, respectively. In Figure 4.37 it can be seen that a similar linear correlation exists for the $X^- \cdots \text{HOR}$ and $\text{RO}-\text{H}$ stretch vibrations and $-\Delta H_{298}^\circ$, using $-\Delta H_{298}^\circ$ from the MP2/a//B3LYP/b level computations and B3LYP/b frequencies. For $X^-(\text{ROH})$ ($X = \text{F}, \text{Cl}, \text{Br}, \text{I}$; $\text{R} = (\text{CH}_3)_2\text{CH}, (\text{CH}_3)_3\text{C}$) the $\text{RO}-\text{H}$ stretch vibrations do not lie on the line for the other complexes ($\text{R} = \text{CH}_3, \text{CH}_3\text{CH}_2$). This is caused by the fact that for $\text{R} = (\text{CH}_3)_2\text{CH}$ and $(\text{CH}_3)_3\text{C}$, the $X^- \cdots \text{HOR}$ stretch is no longer a simple motion. There is also a displacement “toward” the CH_3 groups giving a smaller than expected shift to lower wavenumber, based on $-\Delta H_{298}^\circ$.

Unfortunately, no VPDS results are available to test these predictions. The origin of the shift in the $\text{RO}-\text{H}$ stretch in $X^-(\text{ROH})$ compared to “free” ROH is mainly the result of the increase of the $\text{RO}-\text{H}$ bond in $X^-(\text{ROH})$ relative to “free” ROH . This increase in bond length is of course connected to ΔH_{298}° , which is related, as shown previously, to the amount of charge transfer, and the size of the halide ion. This relationship applies to all MP2/a ([a/d] for $X = \text{I}$) computations for the $X^-(\text{ROH})$ complexes ($X = \text{F}, \text{Cl}, \text{Br}, \text{I}$; $\text{R} = \text{CH}_3, \text{CH}_3\text{CH}_2$ ($X = \text{F}$ only)), and all B3LYP/b computations for the $X^-(\text{ROH})$ ($X = \text{F}, \text{Cl}$; $\text{R} = \text{CH}_3, \text{CH}_3\text{CH}_2, (\text{CH}_3)_2\text{CH}, (\text{CH}_3)_3\text{C}$). By plotting $-\Delta H_{298}^\circ$ versus $\nu(\text{RO}-\text{H})$ in $X^-(\text{ROH})$, the data for $\text{R} = (\text{CH}_3)_2\text{CH}, (\text{CH}_3)_3\text{C}$ would deviate from $\text{R} = \text{CH}_3, \text{CH}_3\text{CH}_2$, but by plotting $\Delta R(\text{RO}-\text{H})$ versus $\Delta \nu(\text{RO}-\text{H})$ this deviation disappears for all alkyl groups. The magnitude of the $X^- \cdots \text{HOR}$ bond distance is directly related to ΔH_{298}° , which is further related to the

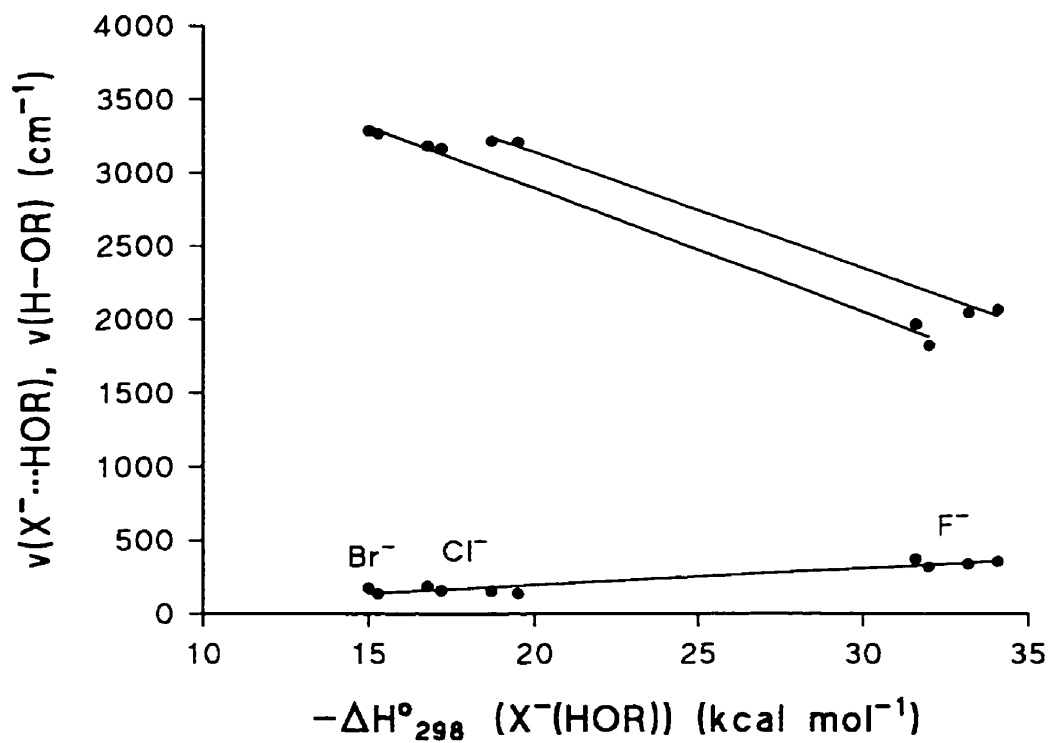


Figure 4.37 Plot of the calculated B3LYP/b $X^{\cdot\cdot\cdot}HOR$ and RO–H normal mode vibrational frequencies, $\nu(X^{\cdot\cdot\cdot}HOR)$ and $\nu(RO-H)$, respectively, versus the MP2(full)/a//B3LYP/b negative standard ambient enthalpy change to form $X^-(ROH)$, $-\Delta H^\circ_{298} (X^-(ROH))$ ($X = F, Cl, Br$; $R = CH_3, CH_3CH_2, (CH_3)_2CH, (CH_3)_3C$).

size of the halide ion. One main conclusion in this respect may be that by simply changing the halide ion no other property in the halide ion-alcohol complexes changes. Thus different parameters are related and they cooperate in such a manner that the net result may look like one linear correlation.

4.4.10 Potential Energy Surfaces

In Figure 4.38 the two parameters that are used to obtain the four MP2/a ([a/e] for X = I) potential energy surfaces for $X^-(\text{CH}_3\text{OH})$, shown in Figures 4.39 to 4.42, are defined. The contour lines represent the energies in kcal mol^{-1} , relative to the minimum energy position. It is very clear that the curve for X = F shows the most symmetric potential energy surface features. This is what one would expect from a hydrogen bonded system, with a linear or near linear $X^-\cdots\text{H}-\text{OCH}_3$ alignment. For X = Cl, Br, and I the potential energy surfaces are less steep, due to the smaller ΔH_{298}° value compared to X = F, and there are more asymmetric features visible. Converting the intramolecular $X^-\cdots\text{H}-\text{OCH}_3$ stretch vibration from cm^{-1} into kcal mol^{-1} ($E = 1.08, 0.57, 0.47,$ and $0.39 \text{ kcal mol}^{-1}$ for X = F, Cl, Br, and I, respectively), shows that if this motion is in its ground state, the halide ion can move freely across a fairly large distance and angle. It had been hoped that from these potential energy surfaces some clear and distinct features would be observable that would indicate how the halide ion gets captured by methanol. Only for the $\text{F}^-(\text{CH}_3\text{OH})$ formation does this appear evident. The more asymmetric nature of the potential energy surfaces for the other three halide ions makes such a simplistic approach impossible.

The relaxed scan potential energy surface computations for the four $X^-(\text{CH}_3\text{OH})$ complexes at the MP2(fc)/6-31+G(d,p) (X = F, Cl) level of theory (MP2(fc)/[6-31+G(d,p)/LanL2DZ(sp)] for X = Br, I) and $\text{Cl}^-(\text{CF}_3\text{OH})$ actually show a more realistic picture of the capture of the halide ions by the methanol molecule. In Figures 4.43 to 4.46 the potential energy surfaces along the $X^-\cdots\text{HOCY}_3$ coordinate are shown. What are very interesting are the transition state and the second, higher energy, saddle point. These are not artifacts, but true intermediates on the potential energy

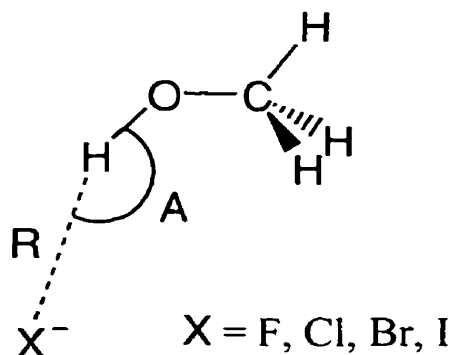


Figure 4.38 Definition of the $X^- \cdots HOCH_3$ distance, $R(X^- \cdots HOCH_3)$, and the $X^- \cdots H-OCH_3$ angle, $A(X^- \cdots H-OCH_3)$, parameters used for the normal potential energy surface scan at the MP2(full)/a ([a/e] for $X = I$) level of theory ($X = F, Cl, Br, I$).

surface. Inspecting structures along the potential energy surface indicates that methanol captures halide ions along the H₃C–OH bond, similar to formation of an S_N2-like complex in Cl[−](CH₃Cl). This was somewhat surprising, because based on the minimum energy structures of the X[−](CH₃OH) complexes it seemed reasonable that the halide ion would align with the OH group. The transition state now corresponds to a rotation of the methanol molecule going from Cl[−](CH₃OH) to Cl[−](HOCH₃). This raises the question of what factor is responsible for the long range capture. One suggestion would be the polarizability of the CH₃ group. The rotation may be driven by alignment with the dipole moment of methanol. As can be seen the small transition state barrier for rotation of the methanol molecule decreases going from X = F to Br, while for the iodide ion there appears to be no barrier at all. Based on the principle of microscopic reversibility the dissociation of Cl[−](CH₃OH) by blackbody radiation in a FT-ICR for instance, would proceed by the reverse trajectory of complex formation.

In the Cl[−](CH₃OH) complex the OH stretch is the strongest absorbing mode of IR radiation, even though it is in a region where the photon density is almost zero at 300 K. Other modes will also absorb the IR radiation, and the energy will be distributed randomly among all degrees of freedom. Coupling among all degrees of freedom will then deposit energy in the OH bond.

In Figure 4.47 the energy profile for the Cl[−] + CF₃OH → CF₃O[−] + HCl proton transfer reaction is shown. Formation of Cl[−](HO CF₃) proceeds along the CF₃O–H bond. Approach of CF₃OH analogous to that for CH₃OH becomes impossible because of the electronic repulsion by the three fluorine atoms. At the G3(MP2) level of theory the ΔH^o₂₉₈ for this reaction is −4.4 kcal mol^{−1} (see Section 7.4.5), while the experimental value is −3.6 kcal mol^{−1}.^{166,167} Cl[−](HO CF₃) is the global minimum. No minimum structure for CF₃O[−](HCl) can be found, instead it is an inflection point along the reaction coordinate. Surprisingly, there is a region along the reaction coordinate that is flat. It corresponds to an isomer of CF₃O[−](HCl), (ClH)CF₃O[−], formed by rotation of HCl to the other side of CF₃O[−]. Dissociation to CF₃O[−] and HCl takes place from this complex. It would be of interest to investigate the unimolecular

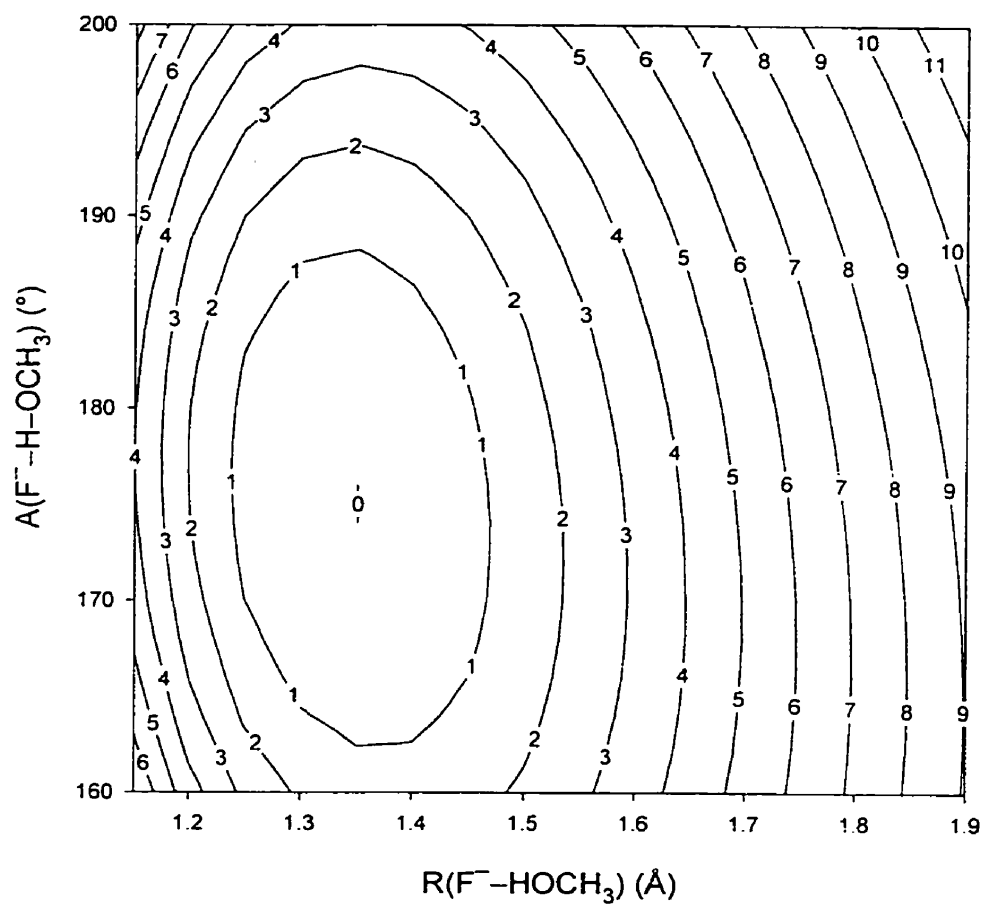


Figure 4.39 Plot of the MP2(full)/a F^- (CH_3OH) potential energy surface (contour lines in kcal mol^{-1}).

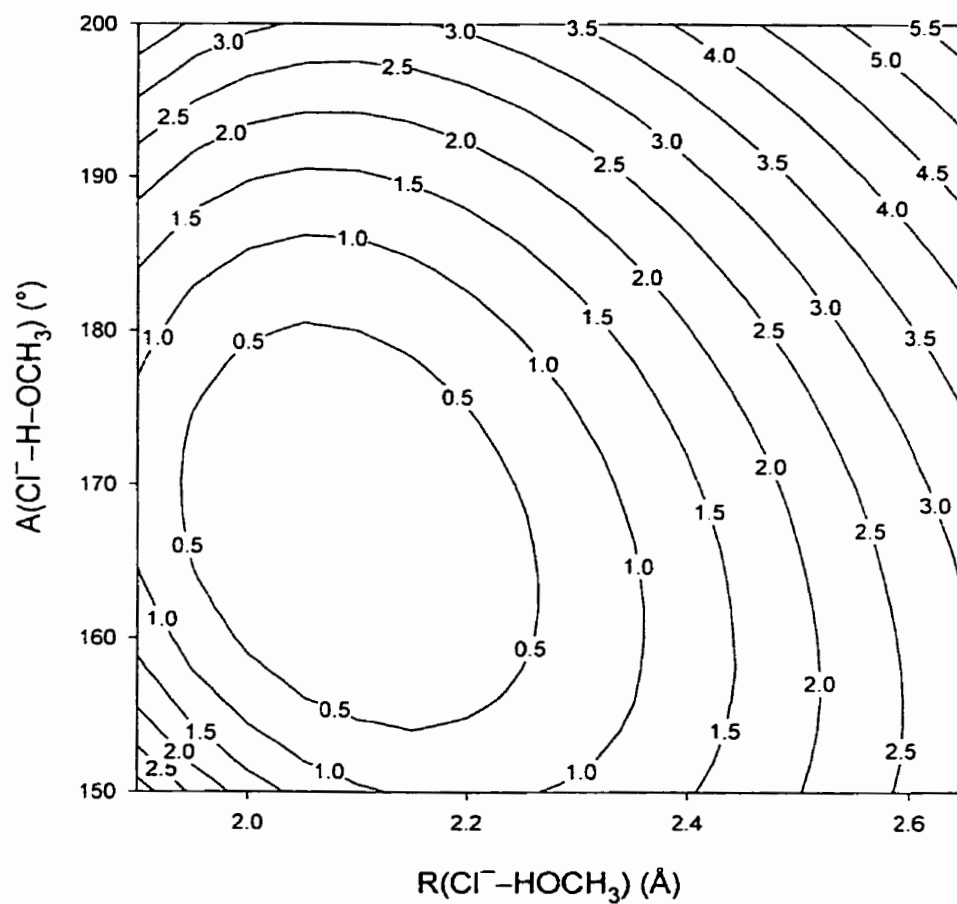


Figure 4.40 Plot of the MP2(full)/a Cl^- (CH_3OH) potential energy surface (contour lines in kcal mol^{-1}).

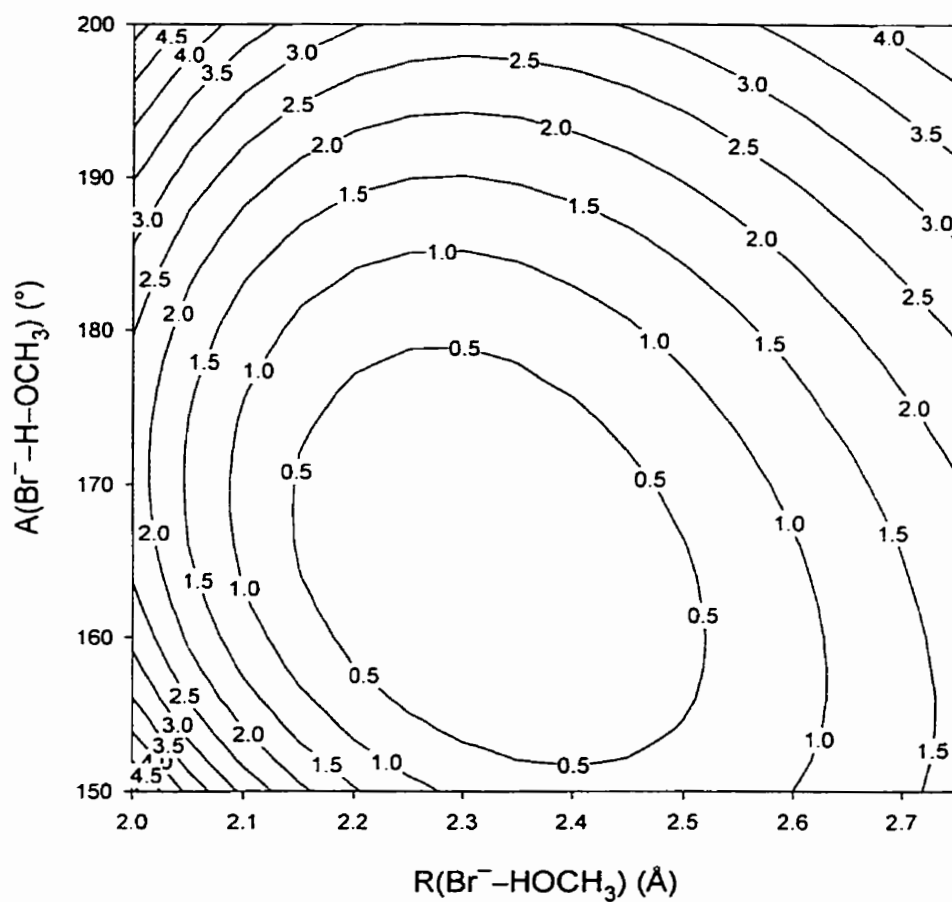


Figure 4.41 Plot of the MP2(full)/a Br^- (CH_3OH) potential energy surface (contour lines in kcal mol^{-1}).

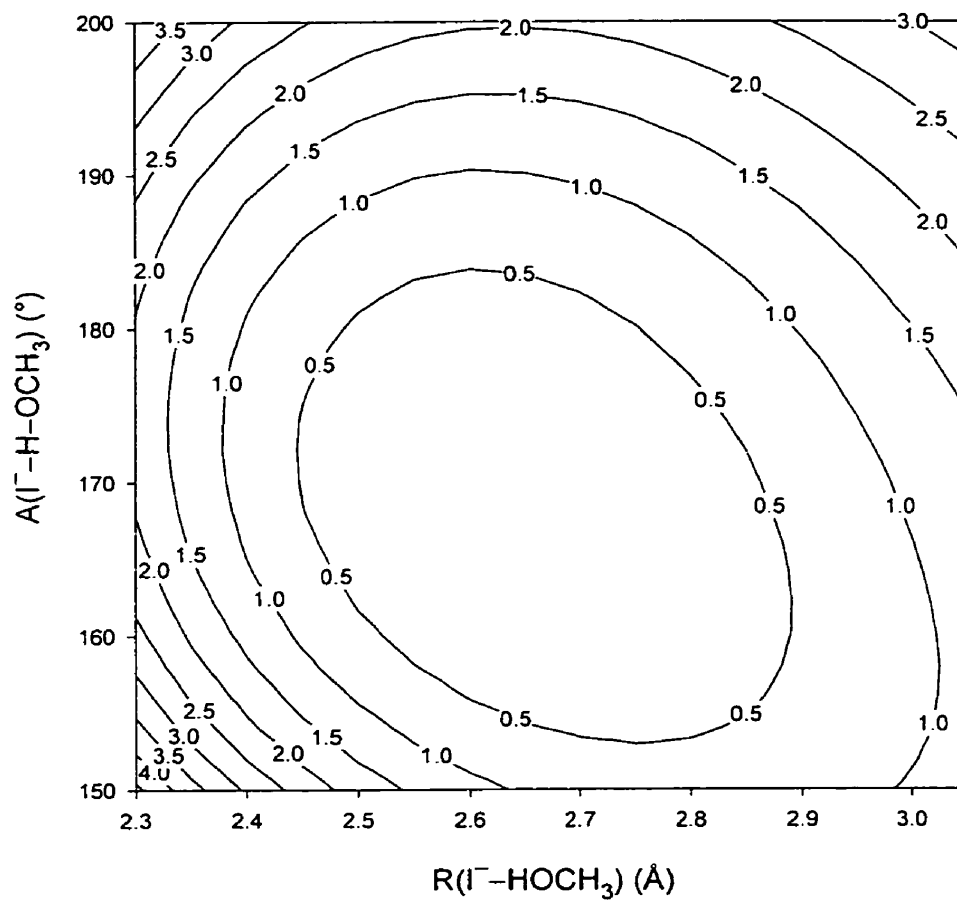


Figure 4.42 Plot of the MP2(full)/[a/e] $\Gamma(\text{CH}_3\text{OH})$ potential energy surface (contour lines in kcal mol^{-1}).

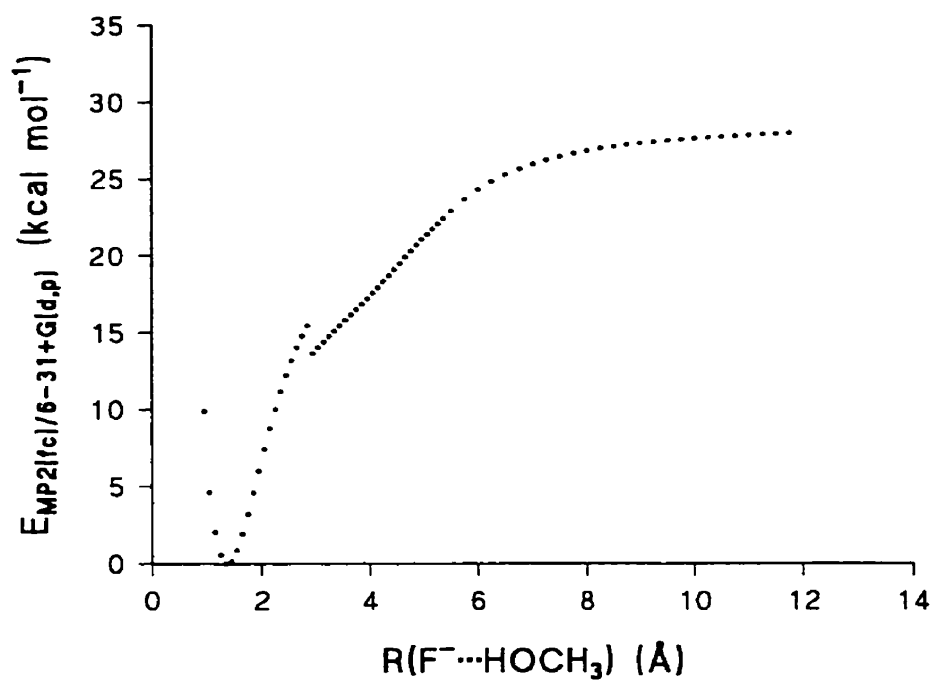


Figure 4.43 Plot of the MP2(fc)/g energy, $E_{\text{MP2}(\text{fc})/6-31+\text{G}(\text{d,p})}$, versus the $\text{F}^- \cdots \text{HOCH}_3$ distance, $R(\text{F}^- \cdots \text{HOCH}_3)$, from a relaxed scan computation.

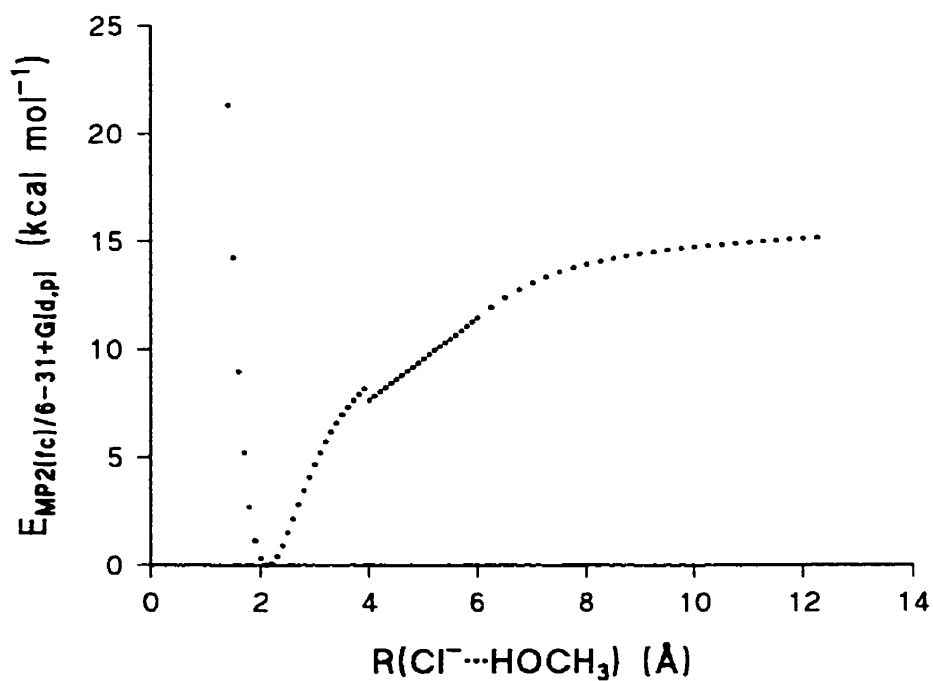


Figure 4.44 Plot of the MP2(fc)/g energy, $E_{\text{MP2}(\text{fc})/6-31+\text{G}(\text{d,p})}$, versus the $\text{Cl}^- \cdots \text{HOCH}_3$ distance, $R(\text{Cl}^- \cdots \text{HOCH}_3)$, from a relaxed scan computation.

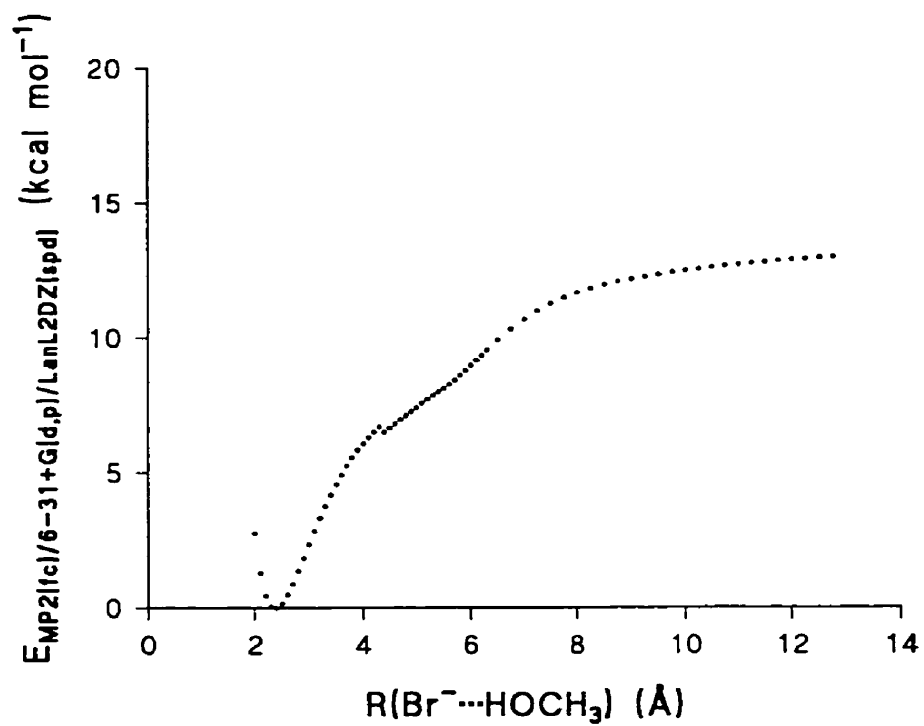


Figure 4.45 Plot of the MP2(fc)/[g/h] energy, $E_{\text{MP2(fc)/[6-31+G(d,p)/LanL2DZ(sp)]}}$, versus the $\text{Br}^- \cdots \text{HOCH}_3$ distance, $R(\text{Br}^- \cdots \text{HOCH}_3)$, from a relaxed scan computation.

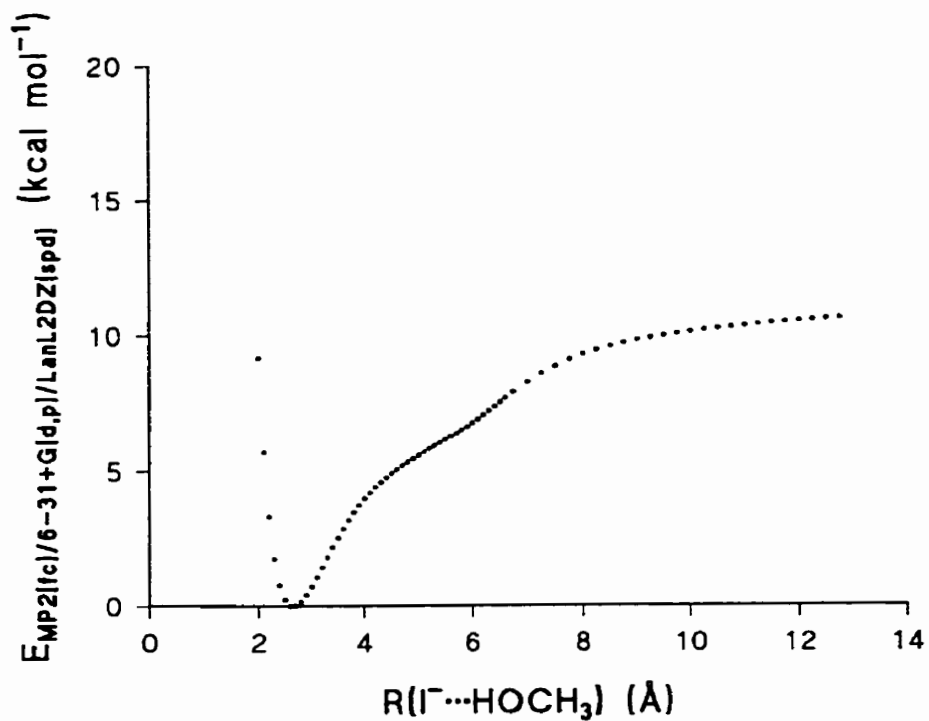
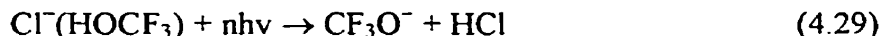


Figure 4.46 Plot of the MP2(fc)/[g/h] energy, $E_{\text{MP2}(\text{fc})/[6-31+\text{G}(\text{d},\text{p})/\text{LanL2DZ}(\text{spd})]}$, versus the $\Gamma \cdots \text{HOCH}_3$ distance, $R(\Gamma \cdots \text{HOCH}_3)$, from a relaxed scan computation.

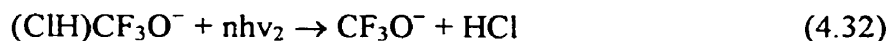
dissociation kinetics of $\text{Cl}^-(\text{HO CF}_3)$ by, for instance, ZTRID experiments in a FT-ICR instrument (Reaction 4.29).



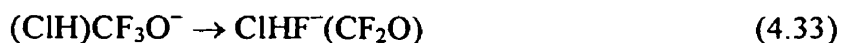
CF_3OH is a stable compound, but it can only be generated *in situ*, so direct clustering of chloride ion onto it in a PHPMS ion source is not possible. Instead, $\text{Cl}^-(\text{HO CF}_3)$ can be formed by a Riveros reaction of Cl^- and $\text{CF}_3\text{OC(O)H}$ (Reaction 4.30).⁴⁶



Recently, Good *et al.* synthesized $\text{CF}_3\text{OC(O)H}$ and characterized it by FT-IR.¹⁶⁸ It is a very stable compound and no isomerization to $\text{CF}_3\text{C(O)OH}$ was observed.¹⁶⁹ This ZTRID experiment would be interesting because the overall observed kinetics would most likely be composed of a two step process (Reactions 4.31 and 4.32).



Another possibility would be that $(\text{ClH})\text{CF}_3\text{O}^-$ could be converted into $\text{ClHF}^-(\text{CF}_2\text{O})$, and finally into $\text{Cl}^-(\text{HF})$ and CF_2O (Reactions 4.33 and 4.34). The latter process is actually energetically more favorable than dissociation to CF_3O^- and HCl , and was observed experimentally by Huey *et al.*¹⁶⁶



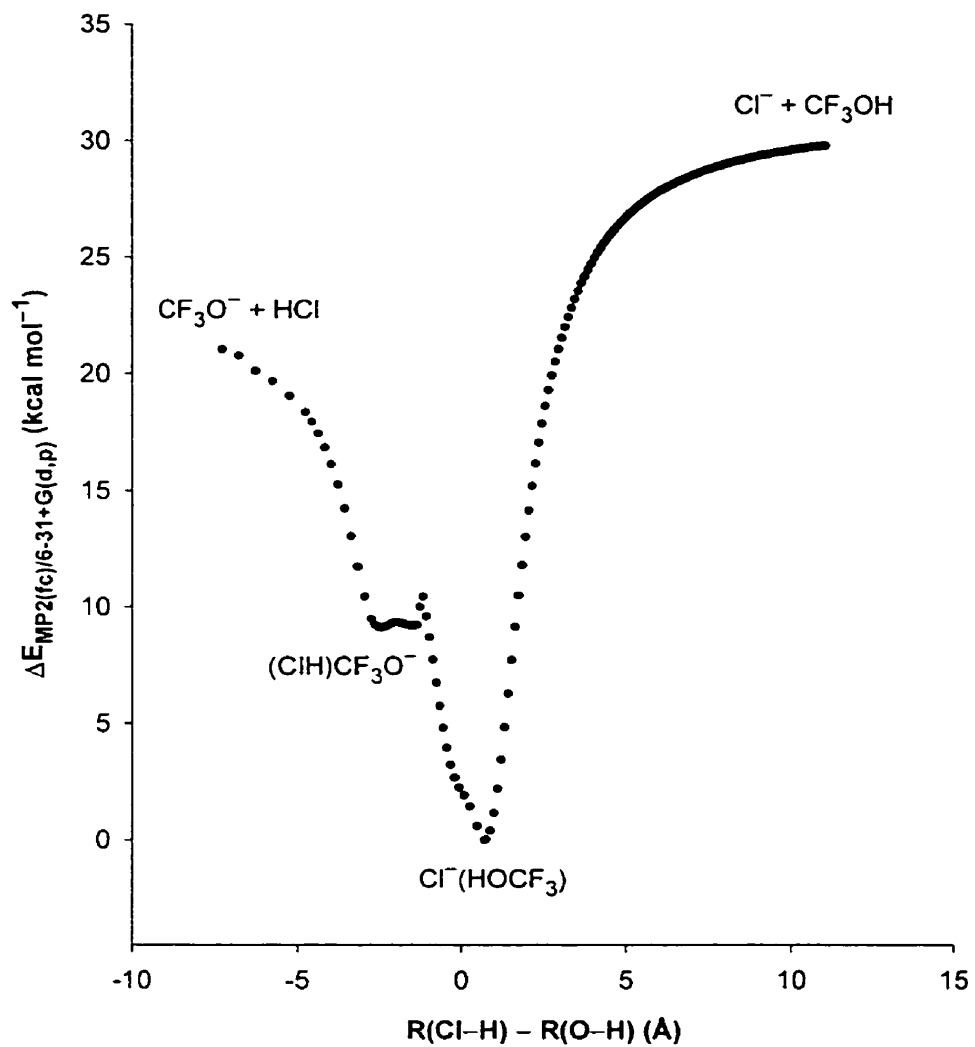


Figure 4.47 MP2(fc)/g energy profile for the $\text{Cl}^- + \text{CF}_3\text{OH} \rightarrow \text{CF}_3\text{O}^- + \text{HCl}$ gas phase proton transfer reaction.

4.5 Conclusions

The different sections in this chapter have discussed a variety of aspects of halide ion-alcohol clusters in the gas phase studied by PHPMS and computational *ab initio* and DFT methods.

The $X^-(\text{CH}_3\text{OH})$ clusters ($X = \text{F}, \text{Cl}, \text{Br}, \text{I}$) show an increase in the $X^-\cdots\text{HOCH}_3$ distance going from $X = \text{F}$ to I , and a decrease in the $X^-\cdots\text{H}-\text{OCH}_3$ angle going from $X = \text{F}$ to Br and a small increase from $X = \text{Br}$ to I . For all alcohol molecules investigated, there is an increase in the $\text{RO}-\text{H}$ bond length (R) going from “free” ROH to $X^-(\text{ROH})$, and this increase is related to the enthalpy of binding of the halide ion to the alcohol. At the B3LYP/b level of theory, two isomers for the fluoride and chloride ion-methanol dimer clusters were found, $(\text{CH}_3\text{OH})X^-(\text{CH}_3\text{OH})$ and $X^-(\text{CH}_3\text{OH})(\text{CH}_3\text{OH})$ ($X = \text{F}, \text{Cl}$). The two $(\text{CH}_3\text{OH})X^-(\text{CH}_3\text{OH})$ clusters show very different relative orientations of the two methanol molecules. In the $X^-(\text{ROH})$ complexes ($X = \text{F}, \text{Cl}; (\text{CH}_3)_2\text{CH}, (\text{CH}_3)_3\text{C}$) there is a stronger interaction between the halide ion and the methyl group hydrogen atoms, accompanied by a shorter $X^-\cdots\text{H}-\text{CH}_2$ distance. Computations at the MP2(full)/6-31G(d) level of theory for the two $\text{HF}_2^-(\text{CH}_3\text{OH})_n$ ($n = 1, 2$) clusters indicate that for $n = 1$ the cluster can be described as $(\text{FH})\text{F}^-(\text{HOCH}_3)$, while for $n = 2$ this is $(\text{CH}_3\text{OH})\text{HF}_2^-(\text{HOCH}_3)$.

For the various $X^-(\text{ROH})_n + \text{ROH} = X^-(\text{ROH})_{n+1}$ clustering equilibria measured, good agreement was obtained for the ΔH° values with existing data, and the new data followed expected trends. Trends can be explained based on the radii of the halide ions, and the polarizability and gas phase acidity of the alcohol molecules. In the higher order clusters, dipole-dipole interactions become more important. Trends in the ΔS° values are less clear and no statements can be made to use these to assign structures.

The MP2/a and MP2/a//B3LYP/b computations provide ΔH°_{298} and ΔS°_{298} values that agree very well with most PHPMS results and other computational results using higher levels of theory. For the $X^-(\text{CH}_3\text{OH})$ complexes the barrier height for methyl group rotation increases going from $X = \text{F}$ to I , as calculated at the MP2/a ([a/e] for $X = \text{I}$) level

of theory. NPA charges indicate that in the $X^-(CH_3OH)$ complexes some charge transfer takes place, even though there is no proton transfer.

Pressure and temperature dependent kinetics measurements for the formation of the $Cl^-(CH_3OH)$ complex indicate that its formation involves a more complex potential energy surface including a transition state that was determined to be around $-9.0 \text{ kcal mol}^{-1}$ below the reactants.

The scaled MP2/a and B3LYP/b normal mode vibrational frequencies for the alcohol molecules ROH agree well with experimental IR and results from other computations. Similar observations can be made for the halide ion-alcohol clusters compared to available experimental VPDS data and results from other computations. Some of the computational results can be used to interpret future VPDS data.

Large shifts in OH stretch frequencies and IR intensities can be observed upon halide ion- alcohol complex formation relative to the “free” alcohol molecule. There is a clear correlation between the ΔH_{298}° for $X^-(ROH)$ formation and the $X^{\cdots}HOR$ and $RO-H$ normal mode vibrational frequencies.

Finally, one- and two-dimensional potential energy surfaces have been calculated for the $X^-(CH_3OH)$ complexes at the MP2 level of theory. From the relaxed scan it has been shown that the halide ion is captured by methanol on the backside by interaction with the three methyl group hydrogen atoms. The transition state corresponds to rotation of the methanol molecule, thereby allowing the halide ion to interact with the dipole moment of methanol and the OH group. The normal scan results reveal the mobility of the halide ion in the complex.

Chloride ion approaches CF_3OH along the O-H, because backside approach as found for methanol is impossible. $Cl^-(HO CF_3)$ is the minimum structure along the potential energy surface. After proton transfer the $CF_3O^-(HCl)$ structure, which is only an inflection point, will undergo isomerization to $(ClH)CF_3O^-$. Conversion to $(FH)Cl^-(CF_2O)$, followed by dissociation into $Cl^-(HF)$ and CF_2O will be energetically more favorable than into CF_3O^- and HCl .

4.6 References and Notes

- 1 Scaiano, J. C. *Acc. Chem. Res.* **1982**, *15*, 252.
- 2 Eriksen, J.; Foote, C. S. *J. Am. Chem. Soc.* **1980**, *102*, 6083.
- 3 Wagner, P. J.; May, M. J.; Haug, A. Graber, D. R. *J. Am. Chem. Soc.* **1970**, *92*, 5269.
- 4 Bernasconi, C. F. *Acc. Chem. Res.* **1978**, *11*, 147.
- 5 Landini, D.; Maia, A.; Montanari, F.; Rolla, F. *J. Org. Chem.* **1983**, *48*, 3774.
- 6 *Ion and Ion Pair in Organic Reactions*; Szwarc, M., Ed.; Wiley: New York, **1972** and **1974**; Vol. 1 and Vol. 2.
- 7 *Mechanisms and Theory in Organic Chemistry*, 3rd ed.; Lowry, T. H.; Schueller-Richardson, K., Ed.; Harper & Row: New York, 1987; Chapter 3.
- 8 Ladwig, C. C.; Lui, R. S. H. *J. Am. Chem. Soc.* **1974**, *96*, 6210 and references therein.
- 9 Grunwald, E.; Winstein, S. *J. Am. Chem. Soc.* **1948**, *70*, 1948.
- 10 Schleyer, P. v. R.; Raber, D. J.; Harris, J. M. *J. Am. Chem. Soc.* **1971**, *93*, 4829 and references cited therein.
- 11 Bentley, T. W.; Carter, G. E. *J. Am. Chem. Soc.* **1982**, *104*, 7541.
- 12 Parker, A. J.; Mayer, U.; Schmidt, R.; Gutmann, V. *J. Org. Chem.* **1978**, *43*, 1843.
- 13 Shaik, S. S. *J. Am. Chem. Soc.* **1984**, *106*, 1227.
- 14 Cooper, K. A.; Hughes, E. D.; Ingold, C. K. *J. Chem. Soc.* **1973**, 1280.
- 15 Seib, R. C.; Shiner, V. J.; Sendijarević, V.; Humski, J. *J. Am. Chem. Soc.* **1978**, *100*, 8133 and references cited therein.
- 16 Richard, J. P.; Jencks, W.P. *J. Am. Chem. Soc.* **1984**, *106*, 1383.
- 17 Cohen, T.; Daniewski, A. R. *J. Am. Chem. Soc.* **1969**, *91*, 533.
- 18 Skell, P. S.; Hall, W. L. *J. Am. Chem. Soc.* **1963**, *85*, 2851.
- 19 Bunnett, J. F. *Angew. Chem. Int. Ed. Engl.* **1962**, *1*, 225.
- 20 Baciocchi, E.; Perruci, P.; Rol, C. *J. Chem. Soc. Perkin Trans. 2* **1975**, *2*, 329.
- 21 Beltrame, P.; Biale, G.; Lloyd, D. J.; Parker, A. J.; Ruane, M; Winstein, S. *J. Am. Chem. Soc.* **1972**, *94*, 2240.

- 22 Ford, W. T.; Pietsek, D. J. *J. Am. Chem. Soc.* **1975**, *97*, 2194 and references cited therein.
- 23 Jensen, J. H.; Gordon, M. S. *J. Am. Chem. Soc.* **1995**, *117*, 8159.
- 24 Jensen, F. *J. Am. Chem. Soc.* **1992**, *114*, 9533.
- 25 Marcus, Y. *Pure Appl. Chem.* **1983**, *55*, 977.
- 26 Marcus, Y. *Pure Appl. Chem.* **1985**, *57*, 1103.
- 27 Takashima, K.; Riveros, J. M. *Mass Spectrom. Rev.* **1998**, *17*, 409 and references cited therein.
- 28 Bailey, C. G.; Kim, J.; Dessent, C. E. H.; Johnson, M. A. *Chem. Phys. Lett.* **1997**, *269*, 122.
- 29 Ayotte, P.; Bailey, C. G.; Weddle, G. H.; Johnson, M. A. *J. Phys. Chem. A* **1998**, *102*, 3067.
- 30 Choi, J.-H.; Kuwata, K. T.; Cao, Y.-B.; Okumura, M. *J. Phys. Chem. A* **1998**, *102*, 503.
- 31 Ayotte, P.; Weddle, G. H.; Kim, J.; Johnson, M. A. *Chem. Phys.* **1998**, *239*, 485.
- 32 Ayotte, P.; Weddle, G. H.; Kim, J.; Johnson, M. A. *J. Am. Chem. Soc.* **1998**, *120*, 12361.
- 33 Ayotte, P.; Weddle, G. H.; Kim, J.; Kelly, J.; Johnson, M. A. *J. Phys. Chem. A* **1999**, *103*, 443.
- 34 Cabarcos, O. M.; Weinheimer, C. J.; Lisy, J. M.; Xantheas, S. S. *J. Chem. Phys.* **1999**, *110*, 5.
- 35 Weis, P.; Kemper, P. R.; Bowers, M. T.; Xantheas, S. S. *J. Am. Chem. Soc.* **1999**, *121*, 3571.
- 36 Dorsett, H. E.; Watts, R. O.; Xantheas, S. S. *J. Phys. Chem. A* **1999**, *103*, 3351.
- 37 Bryce, R. A.; Vincent, M. A.; Hillier, I. A. *J. Phys. Chem. A* **1999**, *103*, 4094.
- 38 Ayotte, P.; Weddle, G. H.; Johnson, M. A. *J. Chem. Phys.* **1999**, *110*, 7129.
- 39 Stuart, S. J.; Berne, B. J. *J. Phys. Chem. A* **1999**, *103*, 10300 and reference cited therein.
- 40 Ayotte, P.; Nielsen, S. B.; Weddle, G. H.; Johnson, M. A.; Xantheas, S. S. *J. Phys. Chem. A* **1999**, *103*, 10665.

- 41 Topol, I. A.; Tawa, G. J.; Burt, S. K.; Rashin, A. A. *J. Chem. Phys.* **1999**, *111*, 10998.
- 42 Majumdar, D.; Kim, J.; Kim, K. S. *J. Chem. Phys.* **2000**, *112*, 101.
- 43 Thompson, W. H.; Hynes, J. T. *J. Am. Chem. Soc.* **2000**, *122*, 6278.
- 44 Chen, H.-Y.; Sheu, W.-S. *J. Am. Chem. Soc.* **2000**, *122*, 7534.
- 45 Roeselová, M.; Kaldor, U.; Jungwirth, P. *J. Phys. Chem. A* **2000**, *104*, 6523.
- 46 Blair, L. K.; Isolani, P. C.; Riveros, J. M. *J. Am. Chem. Soc.* **1973**, *95*, 1057.
- 47 Ridge, D. P.; Beauchamp, J. L. *J. Am. Chem. Soc.* **1974**, *96*, 3595.
- 48 Larson, J. W.; McMahon, T. B. *J. Am. Chem. Soc.* **1983**, *105*, 2944.
- 49 Larson, J. W.; McMahon, T. B. *Can. J. Chem.* **1984**, *62*, 675.
- 50 Riveros, J. M.; Ingemann, S.; Nibbering, N. M. M. *J. Am. Chem. Soc.* **1991**, *113*, 1053.
- 51 Haberland, H.; Schindler, H. G.; Worsnop, D. R. *Ber. Bunsenges. Phys. Chem.* **1984**, *88*, 270.
- 52 Coe, J. C.; Snodgrass, H. G.; Freidhoff, C. B.; McHugh, K. M.; Bowen, K. H. *J. Chem. Phys.* **1987**, *87*, 4302.
- 53 Viggiano, A. A.; Arnold, S. A.; Morris, R. A. *Int. Rev. Phys. Chem.* **1998**, *17*, 147 and references cited therein.
- 54 Combariza, J. E.; Kestner, N. R.; Jortner, J. *J. Chem. Phys. Lett.* **1993**, *203*, 423.
- 55 Combariza, J. E.; Kestner, N. R.; Jortner, J. *J. Chem. Phys.* **1994**, *100*, 2851.
- 56 Xantheas, S. S.; Dunning, T. H., Jr. *J. Phys. Chem.* **1994**, *98*, 13489.
- 57 Xantheas, S. S.; Dang, L. X. *J. Phys. Chem.* **1996**, *100*, 3989.
- 58 Xantheas, S. S. *J. Phys. Chem.* **1996**, *100*, 9703.
- 59 Asada, T.; Nishimoto, K.; Kitaura, K. *J. Phys. Chem.* **1993**, *97*, 7724.
- 60 Sremaniak, L. S.; Perera, L.; Berkowitz, M. L. *Chem. Phys. Lett.* **1994**, *218*, 377.
- 61 Tuñón, I.; Martins-Costa, M. T. C.; Millot, C.; Ruiz-López, M. F. *Chem. Phys. Lett.* **1995**, *241*, 450.
- 62 Johnson, M. S.; Kuwata, K. T.; Wong, C.-K.; Okumura, M. *Chem. Phys. Lett.* **1996**, *260*, 551.
- 63 Carbacos, O. M.; Weinheimer, C. J.; Martinez, T. J.; Lisy, J. M. *J. Chem. Phys.* **1999**, *110*, 9516.

- 64 Nielsen, S. B.; Ayotte, P.; Kelley, J. A.; Johnson, M. A. *J. Chem. Phys.* **1999**, *111*, 9593.
- 65 Castleman, A. W., Jr. *Int. J. Mass Spectrom. Ion. Proc.* **1992**, *118/119*, 167.
- 66 Castleman, A. W., Jr.; Wei, S. *Ann. Rev. Phys. Chem.* **1994**, *45*, 685
- 67 Castleman, A. W., Jr.; Bowen, K. H. *J. Phys. Chem.* **1996**, *100*, 12911.
- 68 Jung, M. E.; Xia, H. *Tetrahedron Lett.* **1988**, *29*, 297.
- 69 Brodbelt, J.; Maleknia, S.; Liou, C.-C.; Lagow, R. *J. Am. Chem. Soc.* **1991**, *113*, 5913.
- 70 Brodbelt, J.; Maleknia, S.; Lagow, R.; Lin, T. Y. *J. Chem. Soc. Chem. Commun.* **1991**, 1705.
- 71 Scheerder, J.; Fochi, M.; Engbersen, J. F. J.; Reinhoudt, D. N. *J. Org. Chem.* **1994**, *59*, 7815.
- 72 Savage, P. B.; Holmgren, S. K.; Gellman, S. H. *J. Am. Chem. Soc.* **1994**, *116*, 4069.
- 73 Worm, K.; Schmidtchen, F. P. *Angew. Chem. Int. Ed. Engl.* **1995**, *34*, 65.
- 74 Scheerder, J.; Engbersen, J. F. J.; Casnati, A.; Ungaro, R.; Reinhoudt, D. N. *J. Org. Chem.* **1995**, *60*, 6448.
- 75 Scheerder, J.; Engbersen, J. F. J.; Reinhoudt, D. N. *Recl. Trav. Chim. Pays-Bays* **1996**, *115*, 307.
- 76 Tamao, K.; Hayashi, T.; Ito, Y. *J. Organometal. Chem.* **1996**, *506*, 85.
- 77 Antonisse, M. M. G.; Snellink-Ruël, B. H. M.; Yigit, I.; Engbersen, J. F. J.; Reinhoudt, D. N. *J. Org. Chem.* **1997**, *62*, 9034.
- 78 Schmidtchen, F. P.; Berger, M. *Chem. Rev.* **1997**, *97*, 1609.
- 79 Bogdanov, B.; Peschke, M.; Tonner, D. S.; Szulejko, J. E.; McMahon, T. B. *Int. J. Mass Spectrom.* **1999**, *185/186/187*, 707 and references cited therein.
- 80 DeTuri, V. F.; Su, M. A.; Ervin, K. M. *J. Phys. Chem. A* **1999**, *103*, 1468 and references cited therein.
- 81 DeTuri, V. F.; Ervin, K. M. *J. Phys. Chem. A* **1999** *103*, 6911.
- 82 Arshadi, M.; Yamdagni, R.; Kebarle, P. *J. Phys. Chem.* **1970**, *74*, 1475.
- 83 Yamdagni, R.; Kebarle, P. *J. Am. Chem. Soc.* **1971**, *93*, 7139
- 84 Yamdagni, R.; Payzant, J. D.; Kebarle, P. *Can. J. Chem.* **1973**, *51*, 2507.
- 85 Keesee, R. G.; Castleman, A. W., Jr. *Chem Phys. Lett.* **1980**, *74*, 139.

- 86 Kebarle, P. *Ann. Rev. Phys. Chem.* **1977**, *28*.
- 87 Caldwell, G.; Kebarle, P. *J. Am. Chem. Soc.* **1984**, *106*, 967.
- 88 Sieck, L. W. *J. Phys. Chem.* **1985**, *89*, 5552.
- 89 Hiraoka, K.; Misuze, S. *Chem. Phys.* **1987**, *118*, 457.
- 90 Hiraoka, K.; Misuze, S. Yamabe, S. *J. Phys. Chem.* **1988**, *92*, 3943.
- 91 Szulejko, J. E.; Wilkinson, F. E.; McMahon, T. B. *Proceedings of the 37th ASMS Conference on Mass Spectrometry and Allied Topics*, May 21-26, 1989, Miami Beach, FL, p. 333.
- 92 Hiraoka, K.; Yamabe, S. *Int. J. Mass Spectrom. Ion. Proc.* **1991**, *109*, 133.
- 93 Evans, D. H.; Keesee, R. G.; Castleman, A. W., Jr. *J. Phys. Chem.* **1991**, *95*, 3358.
- 94 Faigle, J. F. G.; Isolani, P. C.; Riveros, J. M. *J. Am. Chem. Soc.* **1976**, *98*, 2049.
- 95 Larson, J. W.; McMahon, T. B. *J. Am. Chem. Soc.* **1984**, *106*, 517.
- 96 Wilkinson, F. E.; Szulejko, J. E.; Allison, C. E.; McMahon, T. B. *Int. J. Mass Spectrom. Ion Proc.* **1992**, *117*, 487.
- 97 Tanabe, F. K. J.; Morgan, N. H.; Riveros, J. M. *J. Phys. Chem.* **1996**, *100*, 2862.
- 98 Wilkinson, F. E.; Peschke, M.; Szulejko, J. E.; McMahon, T. B. *Int. J. Mass Spectrom. Ion Proc.* **1998**, *175*, 225.
- 99 Wilkinson, F. E.; McMahon, T. B. *Int. J. Mass Spectrom.* **2000**, *199*, 127.
- 100 Moylan, C. R.; Dodd, J. A.; Brauman, J. I. *Chem. Phys. Lett.* **1985**, *118*, 38.
- 101 Moylan, C. R.; Dodd, J. A.; Han, C. C.; Brauman, J. I. *J. Chem. Phys.* **1987**, *86*, 5350.
- 102 Mihalick, J. E.; Gatev, G. G.; Brauman, J. I. *J. Am. Chem. Soc.* **1996**, *118*, 12424.
- 103 Yang, Y.; Linnert, H. V.; Riveros, J. M.; Williams, K. R.; Eyler, J. R. *J. Phys. Chem. A* **1997**, *101*, 2371.
- 104 Bradforth, S. E.; Arnold, D. W.; Metz, R. B.; Weaver, A.; Neumark, D. M. *J. Phys. Chem.* **1991**, *95*, 8066.
- 105 Markovich, G.; Pollack, S.; Giniger, R.; Cheshnovsky, O. *J. Chem. Phys.* **1994**, *101*, 9344.
- 106 Bässmann, C.; Boesl, U.; Yang, D.; Drechsler, G.; Schlag, E. W. *Int. J. Mass Spectrom. Ion Proc.* **1996**, *159*, 153.
- 107 Rosenfeld, R. N.; Jasinski, J. M.; Brauman, J. I. *Chem. Phys. Lett.* **1980**, *71*, 400.

- 108 Peiris, D. M.; Riveros, J. M.; Eyley, J. R. *Int. J. Mass Spectrom. Ion Proc.* **1996**, *159*, 169.
- 109 Wladkowski, B. D.; East, A. L. L.; Mihalick, J. E.; Allen, W. D.; Brauman, J. I. *J. Chem. Phys.* **1994**, *100*, 2058.
- 110 Berthier, G.; Savinelli, R.; Pullman, A. *Int. J. Quantum Chem.* **1997**, *63*, 567.
- 111 Møller, C.; Plesset, M. S. *Phys. Rev.* **1934**, *46*, 618.
- 112 Lee, C.; Yang, W.; Parr, R. G. *Phys. Rev. B* **1988**, *37*, 785.
- 113 Becke, A. D. *J. Chem. Phys.* **1993**, *98*, 1372
- 114 Becke, A. D. *J. Chem. Phys.* **1993**, *98*, 5648.
- 115 Szulejko, J. E.; Fisher, J. J.; McMahon, T. B.; Wronka, J. *Int. J. Mass Spectrom. Ion Proc.* **1988**, *83*, 147.
- 116 Szulejko, J. E.; McMahon, T. B. *Int. J. Mass Spectrom. Ion Proc.* **1991**, *109*, 279.
- 117 Miller, T. M.; Friedman, J. F.; Stevens-Miller, A. E.; Paulson, J. F. *Int. J. Mass Spectrom. Ion Processes* **1995**, *149/150*, 111.
- 118 Oster, T.; Kühn, A.; Illenberger, E. *Int. J. Mass Spectrom. Ion Proc.* **1989**, *89*, 1.
- 119 Fehsenfeld, F. C. *J. Chem. Phys.* **1970**, *53*, 2000.
- 120 Mothes, K. G.; Schindler, R. N. *Ber.Bunsenges. Phys. Chem.* **1971**, *75*, 938.
- 121 Christophorou, L. G.; Mathis, R. A.; James, D. R.; McCorkle, D. L. *J. Phys. D* **1981**, *14*, 1889.
- 122 *TRCVP, Vapor Pressure Database, Version 2.2P*, Thermodynamics Research Center, Texas A&M University, College Station, TX.
- 123 Frisch, M. J.; Trucks, G. W.; Schlegel, H. B.; Gill, P. M. W.; Johnson, B. G.; Robb, M. A.; Cheeseman, J. R.; Keith, T.; Petersson, G. A.; Montgomery, J. A.; Raghavachari, K.; Al-Laham, M. A.; Zakrzewski, V. G.; Ortiz, J. V.; Foresman, J. B.; Peng, C. Y.; Ayala, P. Y.; Chen, W.; Wong, M. W.; Andres, J. L.; Replogle, E. S.; Gomperts, R.; Martin, R. L.; Fox, D. J.; Binkley, J. S.; Defrees, D. J.; Baker, J.; Stewart, J. P.; Head-Gordon, M.; Gonzales, C.; Pople, J. A. *Gaussian 94*, Revision B3, Gaussian Inc., Pittsburgh PA, **1995**.
- 124 Frisch, M. J.; Trucks, G. W.; Schlegel, H. B.; Scuseria, G. E.; Robb, M. A.; Cheeseman, J. R.; Zakrzewski, V. G.; Montgomery, Jr., J. A.; Stratmann, R. E.; Burant, J. C.; Dapprich, S.; Millam, J. M.; Daniels, A. D.; Kudin, K. N.; Strain, M.

- C.; Farkas, O.; Tomasi, J.; Barone, V.; Cossi, M.; Cammi, R.; Mennucci, B.; Pomelli, C.; Adamo, C.; Clifford, S.; Ochterski, J.; Petersson, G. A.; Ayala, P. Y.; Cui, Q.; Morokuma, K.; Malick, D. K.; Rabuck, A. D.; Raghavachari, K.; Foresman, J. B.; Cioslowski, J.; Ortiz, J. V.; Baboul, A. G.; Stefanov, B. B.; Liu, G.; Liashenko, A.; Piskorz, P.; Komaromi, I.; Gomperts, R.; Martin, R. L.; Fox, D. J.; Keith, T.; Al-Laham, M. A.; Peng, C. Y.; Nanayakkara, A.; Gonzalez, C.; Challacombe, M.; Gill, M. W.; Johnson, B.; Chen, W.; Wong, M. W.; Andres, J. L.; Gonzalez, C.; Head-Gordon, M.; Replogle, E. S.; Pople, J. A. *Gaussian 98*, Revision A.7 Gaussian, Inc., Pittsburgh PA, 1998.
- 125 Head-Gordon, M.; Pople, J. A.; Frisch, M. J. *Chem. Phys. Lett.* **1988**, *153*, 503.
- 126 Frisch, M. J.; Head-Gordon, M.; Pople, J. A. *Chem. Phys. Lett.* **1990**, *166*, 275.
- 127 Frisch, M. J.; Head-Gordon, M.; Pople, J. A. *Chem. Phys. Lett.* **1990**, *166*, 280.
- 128 Scott, A. P.; Radom, L. *J. Phys. Chem.* **1996**, *100*, 16503. A value of 0.9489 was obtained by subtracting the scaling factor difference of MP2(fc)/6-31G(d) and MP2(full)/6-31G(d) (0.9434 and 0.9427, respectively) from the scaling factor of MP2(fc)/6-311G(d,p) (0.9496).
- 129 From a least-squares fit of unscaled MP2(full)/6-311++G(d,p) normal mode vibrational frequencies of CH₃OH versus experimental frequencies, a scaling factor of 0.9454 was obtained ($\Delta\nu = 26 \pm 15 \text{ cm}^{-1}$ (0.9454) versus $\Delta\nu = 27 \pm 16 \text{ cm}^{-1}$ (0.9489)).
- 130 Krishnan, R.; Binkley, J. S.; Seeger, R. Pople, J. A. *J. Chem. Phys.* **1980**, *72*, 650.
- 131 Clark, T.; Chandrasekhar, J.; Schleyer, P. von R. *J. Comput. Chem.* **1983**, *4*, 294.
- 132 Gill, P. M. W.; Johnson, B. G.; Pople, J. A.; Frisch, M. J. *Chem. Phys. Lett.* **1992**, *197*, 499.
- 133 Frisch, M. J.; Pople, J. A.; Binkley, J. S. *J. Chem. Phys.* **1984**, *80*, 3265.
- 134 From a least-squares fit of unscaled B3LYP/6-311+G(d,p) normal mode vibrational frequencies of CH₃OH versus experimental frequencies, a scaling factor of 0.9640 was obtained ($\Delta\nu = 28 \pm 12 \text{ cm}^{-1}$ (0.9640) versus $\Delta\nu = 50 \pm 59 \text{ cm}^{-1}$ (1.0000)).
- 135 Hay, P. J.; Wadt, W. R. *J. Chem. Phys.* **1985**, *82*, 284.
- 136 Bergner, A.; Dolg, M.; Kuechle, W.; Stoll, H.; Preuss, H. *Mol. Phys.* **1983**, *80*, 1431.

- 137 LaJohn, L. A.; Christiansen, P. A.; Ross, R. B.; Atashroo, T.; Ermler, W. C. *J. Chem. Phys.* **1987**, *87*, 2812.
- 138 Basis sets were obtained from the Extensible Computational Chemistry Environment Basis Set Database, Version 1.0, as developed and distributed by the Molecular Science Computing Facility, Environmental and Molecular Sciences Laboratory, which is part of the Pacific Northwest Laboratory, P.O. Box 999, Richland, Washington 99352, USA, and funded by the U.S. Department of Energy. The Pacific Northwest Laboratory is a multi-program laboratory operated by Battelle Memorial Institute for the U.S. Department of Energy under contract DE-AC06-76RLO 1830.
- 139 Reed, A. E.; Weinstock, R. B.; Weinhold, F. *J. Chem. Phys.* **1985**, *83*, 735.
- 140 Reed, A. E.; Curtiss, L. A.; Weinhold, F. *Chem. Rev.* **1988**, *88*, 899.
- 141 Curtiss, L. A.; Raghavachari, K.; Redfern, P. C.; Rassolov, V.; Pople, J. A. *J. Chem. Phys.* **1998**, *109*, 7764.
- 142 Hariharan, P. C.; Pople, J. A. *Theoretica Chim. Acta* **1973**, *28*, 213.
- 143 Francl, M. M.; Pietro, W. J.; Hehre, W. J.; Binkley, M. S.; Gordon, M. S.; DeFrees, D. J.; Pople, J. A. *J. Chem. Phys.* **1982**, *77*, 3654.
- 144 Glukhovtsev, M. N.; Pross, A.; McGrath, M. P.; Radom, L. *J. Chem. Phys.* **1995**, *103*, 1878.
- 145 Su, T.; Bowers, M. T. *Int. J. Mass Spectrom. Ion Phys.* **1973**, *12*, 347.
- 146 Grabowski, J. J.; Bierbaum, V. M.; DePuy, C. H. *J. Am. Chem. Soc.* **1983**, *105*, 2565.
- 147 *CRC Handbook of Chemistry and Physics, Ref. Data*, 76th ed., Lide, D. R., Ed.; CRC, Boca Raton, FL, **1995**, 9-42/50, 10-196, 10-202/204, 12-14.
- 148 Martin, J. D. D. *Ph.D. Dissertation*, University of Waterloo, 1998.
- 149 Gong, S. L.; Jervis, R. E. *J. Chem. Phys.* **1995**, *103*, 7081.
- 150 Zhang, W.; Beglinger, Ch.; Stone, J. A. *J. Phys. Chem.* **1995**, *99*, 11673.
- 151 Norrman, K.; McMahon, T. B. *J. Am. Chem. Soc.* **1997**, *118*, 2449.
- 152 Dunbar, R. C.; McMahon, T. B.; Thölmann, D.; Tonner, D. S.; Salahub, D. R.; Wei, D. *J. Am. Chem. Soc.* **1995**, *117*, 12819.
- 153 Thölmann, D.; Tonner, D. S.; McMahon, T. B. *J. Phys. Chem.* **1994**, *98*, 2002.

- 154 Sena, M.; Riveros, J. M. *Rapid Commun. Mass Spectrom.* **1994**, *8*, 1031.
- 155 Dunbar, R. C. *J. Phys. Chem.* **1994**, *98*, 8705.
- 156 Glukhovtsev, M. N.; Pross, A.; Radom, L. *J. Am. Chem. Soc.* **1995**, *117*, 2024.
- 157 v. Szeentpaly, L.; Fuentealba, P.; Preuss, H.; Stoll, H. *Chem. Phys. Lett.* **1982**, *93*, 555.
- 158 Leiniger, T.; Nicklass, A.; Stoll, H.; Dolg, M. Schwerdtfelger, P. *J. Chem. Phys.* **1996**, *105*, 1052.
- 159 Hu, W. P.; Truhlar, D. G. *J. Phys. Chem.* **1994**, *98*, 1049.
- 160 Chao, J.; Hall, K. R.; Marsh, K. N.; Wilhoit, J. *Chem. Ref. Data* **1986**, *15*, 1369.
- 161 East, A. L. L.; Radom, L. *J. Chem. Phys.* **1997**, *106*, 6655.
- 162 Glukhovtsev, M. N.; Pross, A.; Radom, L. *J. Am. Chem. Soc.* **1996**, *118*, 6273.
- 163 Li, C.; Ross, P.; Szulejko, J. E.; McMahon, T. B. *J. Am. Chem. Soc.* **1996**, *118*, 9360.
- 164 Shimanouchi, T. *Tables of Molecular Vibrational Frequencies Consolidated Volume I*; National Bureau of Standards: Washington, DC, **1972**; p. 1.
- 165 Huisken, F.; Kulcke, A.; Laush, C. Lisy, J. M. *J. Chem. Phys.* **1991**, *95*, 3924.
- 166 Huey, L.G.; Dunlea, E.J.; Howard, C.J. *J. Phys. Chem.*, **1996**, *100*, 6504.
- 167 <http://webbook.nist.gov/chemistry/>
- 168 Good, D. A.; Kamboures, M.; Santiano, R.; Francisco, J. S. *J. Phys. Chem. A* **1999**, *103*, 9230.
- 169 Francisco, J. S. Personal communication, **2000**.

Chapter 5

Thermochemistry and structures of solvated S_N2 complexes and transition states in the gas phase

5.1 Introduction

Bimolecular nucleophilic displacement (S_N2) reactions in the condensed phase are among the most important reactions in chemistry (Reaction 5.1), and have been studied from the 1930's onward.¹⁻¹⁰



The acronym S_N2 comes from the fact that the rate of the reactions were found to be first order in both the nucleophile and substrate concentrations, [X⁻] and [RY], respectively (Equation 5.2), making the overall reaction second order.

$$\text{rate} = k[X^-][RY] \quad (5.2)$$

In Figures 5.1-5.4 schematic potential energy profiles of hypothetical condensed phase and gas phase S_N2 reactions are shown. For all four profiles the transition state corresponds to a penta-coordinate complex, [XRY]⁻. The increase in the barrier height going from the gas phase to the condensed phase is mainly due to the differential solvation of the reactants and the transition state. This is caused by the delocalization of the charge in the transition state in contrast to the localized charge in the nucleophile. A large variety of barrier heights have been determined, and these are very much solvent dependent.^{1-6,9} Unfortunately, the solvation order of the nucleophile and transition state for various solvents may be different and, in addition, the solvation of the substrate must also be considered,^{5,6} as well as the effects of counter ions and competitive reactions. In

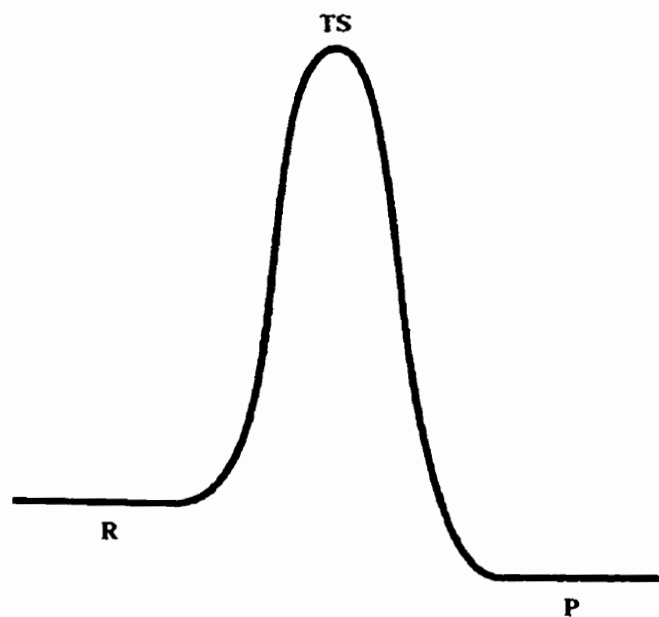


Figure 5.1 Condensed phase unimodal reaction energy profile (R = reactants, TS = transition state, P = products).

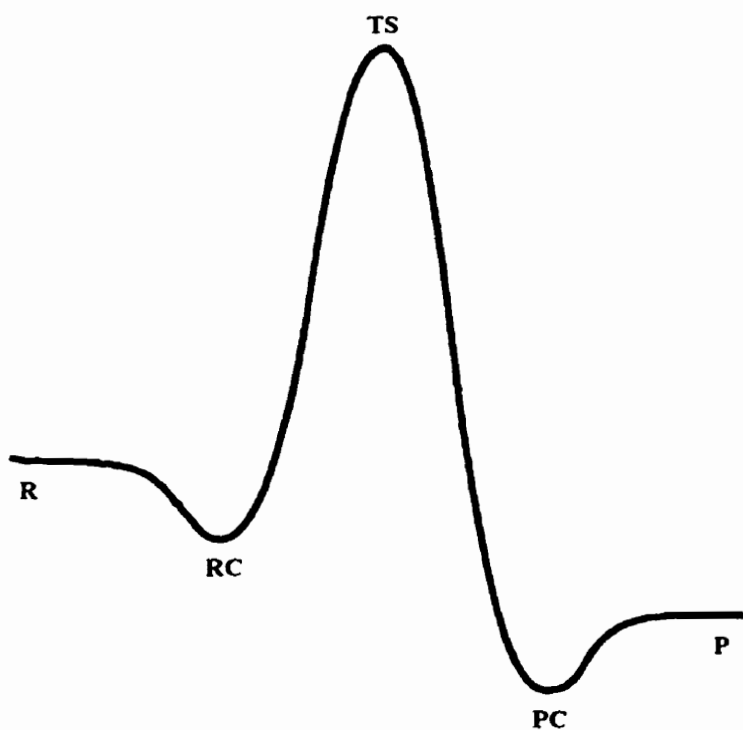


Figure 5.2 Condensed phase double-well reaction energy profile for weak solvation (RC = reactants complex, PC = products complex).

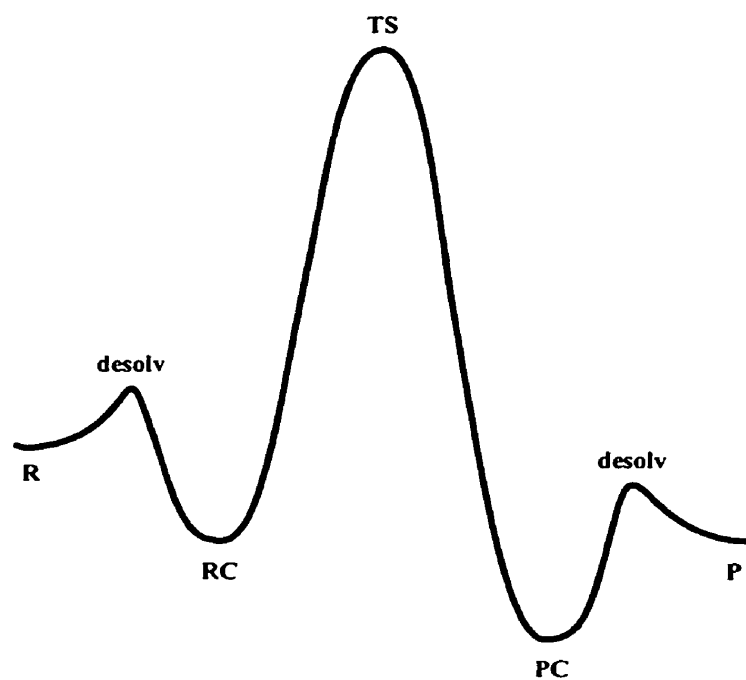


Figure 5.3 Condensed phase double-well reaction energy profile for strong and asynchronous desolvation and ion-molecule complexation (desolv = desolvation).

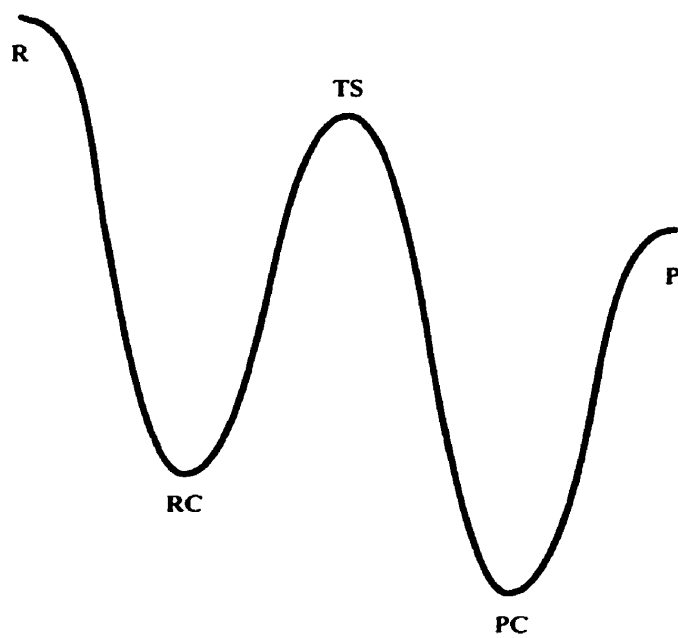
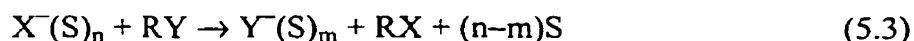


Figure 5.4 Gas phase double-well reaction energy profile.

the condensed phase S_N1 and E2 reactions may compete with S_N2 reactions, and the extent to which this occurs is very sensitive to the nature of the alkyl group R.

In order to bridge the gap between the gas and condensed phases, micro-solvated S_N2 reactions have been performed in the gas phase (Reaction 5.3) using a variety of experimental techniques.¹¹⁻²⁶ By performing these kinds of experiments one hopes to get more insights into the intrinsic contribution of the solvent molecules.



In Table 5.1 an overview is given of the systems investigated to date. As can be seen, the main focus has been on obtaining kinetic data, although isotope effects, cross sections, and product ion distributions were also studied and reported. The main conclusion of this research is that dramatic effects in the reactivity change can be observed with the addition of only one solvent molecule, and that most reactions become too slow to measure with the addition of two or more solvent molecules. With respect to the product ion distributions, some interesting results have been reported. For most mono-solvated reactions only a small fraction of the leaving groups are solvated (Reaction 5.4),^{11-16,19-22,24,25} even though this reaction pathway is more exothermic than formation of the unsolvated leaving group (Reaction 5.5).



For higher order solvated nucleophiles ($n \geq 2$), complex formation (Reaction 5.6) and ligand-switching (Reaction 5.7) become more important.^{24,25}

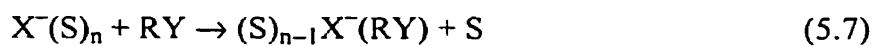
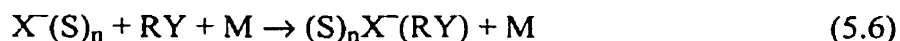


Table 5.1 Overview of published work on solvated S_N2 reactions in the gas phase.

X ⁻ (S) _n	n	RY	method	quantity	reference
OH ⁻ (H ₂ O) _n	0-3	CH ₃ Br	FA	k _{300 K}	11
OH ⁻ (H ₂ O) _n	1	CH ₃ Br	SIFT	k _{300 K}	12
OH ⁻ (H ₂ O) _n	0-2	CH ₃ Cl	Bq	σ(E _T)	13
RO ⁻ (ROH) _n	0-3	CH ₃ Cl	FA	k _{295 K}	14
RO ⁻ (ROH) _n	0-3	CH ₃ Br	FA	k _{295 K}	14
F ⁻ (ROH) _n	0-3	CH ₃ Cl	FA	k _{295 K}	15
F ⁻ (ROH) _n	0-3	CH ₃ Br	FA	k _{295 K}	15
Cl ⁻ (ROH) _n	0-3	CH ₃ Br	FA	k _{295 K}	15
OD ⁻ (D ₂ O) _n	0-2	CH ₃ Cl	VT-SIFT	k _{200-500 K}	16
OH ⁻ (H ₂ O) _n	1	CH ₃ CN	VT-SIFT	k _{240-363 K}	17
OH ⁻ (H ₂ O) _n	0-2	CH ₃ CN	SIFT	k _{298 K}	17
Cl ⁻ (CHCl ₃) _n	0-2	CH ₃ Br/CH ₃ I	KIMMS	k _{398 K}	19
F ⁻ (H ₂ O/D ₂ O) _n	0,1	CH ₃ X/CD ₃ X	FA-SIFT	k _{302 K} , k _H /k _D	20
OH ⁻ (H ₂ O) _n	0-2	CH ₃ Cl	Bq	σ(E _T)	21
OH ⁻ (H ₂ O) _n	0,1	CH ₃ Br	Bq	σ(E _T)	21
OH ⁻ (H ₂ O) _n	0-4	CH ₃ Br	VT-SIFT	k _T	22
F ⁻ (H ₂ O) _n	0-5	CH ₃ Br	VT-SIFT	k _T	24
Cl ⁻ (H ₂ O) _n	1-3	CH ₃ Br	VT-SIFT	k _T	25

FA (flowing afterglow)

SIFT (selected ion flow tube)

Bq (magnetic sector/quadrupole)

VT (variable temperature)

KIMMS (kinetic ion mobility mass spectrometry)

k (rate constant)

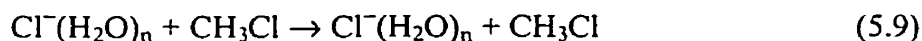
σ (cross section)

E_T (ion kinetic energy)k_H/k_D (deuterium kinetic isotope effect)

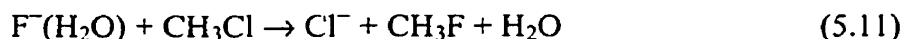
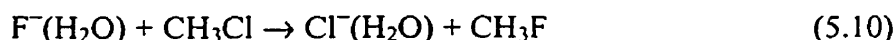
Craig and Brauman showed that introduction of an ω -substituent ($X = \text{CN}, \text{Cl}, \text{OH}$) onto a primary n -alkyl chloride significantly enhanced the rate of a gas phase $\text{S}_{\text{N}}2$ chloride exchange reaction (Reaction 5.8).^{23,26} This was caused by intramolecular micro-solvation of the $\text{S}_{\text{N}}2$ transition state, mainly by through-space ion-dipole interactions.



As can be seen from Table 5.1, most solvated nucleophiles used water or other strongly bound protic solvents, while in the condensed phase it has been known that polar, aprotic solvents cause $\text{S}_{\text{N}}2$ reactions to proceed much faster than in polar, protic solvents.^{5,6} Similar trends can be observed for the growing, but still relatively, small amount of published theoretical work on solvated $\text{S}_{\text{N}}2$ reactions. Morokuma has shown that for Reaction 5.9 ($n = 1, 2$) solvent transfer can take place before, after, and during the Walden inversion of the methyl group.²⁷



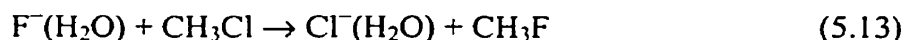
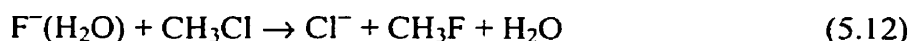
Hu and Truhlar calculated transition state theory rate constants and kinetic isotope effects at the MP2/aug-cc-pVDZ level of theory for Reactions 5.10 and 5.11,²⁸ and found excellent agreement with the experimental data from O'Hair *et al.*²⁰



In addition, the energy of the solvated transition state, $[(\text{H}_2\text{O})\text{FCH}_3\text{Cl}]^-$, was calculated to be $-2.2 \text{ kcal mol}^{-1}$ with respect to the reactants. Bickelhaupt *et al.* investigated the effect of solvation by one to four HF molecules on the E2 and $\text{S}_{\text{N}}2$

reaction of F^- and C_2H_5F .²⁹ The main observation was the increased importance of the S_N2 over the E2 pathway as the number of solvent molecules increased.

Recently, some very interesting articles have been published that reported results on *ab initio* dynamical computations for solvated S_N2 reactions. Tachikawa showed that the reaction between $F^-(H_2O)$ and CH_3Cl can proceed through three pathways (Reactions 5.12-5.14), and that the branching ratios are dependent on the centre-of-mass collision energy.^{30,31}



At a collision energy of $10.0 \text{ kcal mol}^{-1}$, the branching ratios are 0.55:0.04:0.41, while at 17.7 and $25.0 \text{ kcal mol}^{-1}$ they are 0.46:0.18:0.36 and 0.35:0.43:0.22, respectively.³¹ These results show that solvent transfer can be increased. It was also shown that solvent transfer only takes place in a very narrow range of the $HO-H \cdots F^- \cdots CH_3Cl$ angles, thereby explaining why solvent transfer has not been observed often in experiments. Finally, Raugei *et al.* reported data on the energy profiles and stationary points of Reactions 5.15 ($n = 0-2$).³²



Using molecular dynamics (MD) computations they were able to confirm reports by Seeley *et al.* on similar reactions,²⁵ who observed for both $n = 1$ and 2 ligand switching reactions. In addition, for the $n = 1$ reaction, an activation energy of $2.5 \text{ kcal mol}^{-1}$ was measured, while at the B3LYP/6-311+G(d,p) level of theory a value of $-1.9 \text{ kcal mol}^{-1}$ was found. Finally, it is noteworthy that other work on solvated S_N2 reactions has been published, but the main focus was on equilibrium and non-equilibrium solvent effects,

and kinetic solvent isotope effects.³³⁻³⁸ These important topics will not be discussed here however.

As can be seen in Figures 5.2 and 5.3 and from Reaction 5.6, the solvated S_N2 complexes, $(S)_nX^-(RY)$, are intermediates on the potential energy surfaces of S_N2 reactions in the condensed phase and in micro-solvated gas phase reactions. Surprisingly, no experimental thermochemical data on these important cluster ions have been determined to date. As mentioned earlier, most computational data on solvated S_N2 reactions used water as a solvent, while it seems more logical to investigate other practical solvents as well.

In this chapter, a combined PHPMS and computational *ab initio* study will be presented to obtain information on the thermochemistry and structures of solvated S_N2 complexes and transition states. Various solvents were investigated to gain more insight into the intrinsic solvent effects at the microsolvation level. Some of the solvents used in both the experiments and computations do not have any practical use, but it was expected that they could nonetheless provide insight.

5.2 Experimental

All measurements were carried out on a pulsed-ionization high pressure mass spectrometer, configured around a VG 8-80 mass spectrometer.³⁹ The instrument, constructed at the University of Waterloo, has been described in detail in Chapter 2.

Gas mixtures were prepared in a 5 L heated stainless steel reservoir at 350-380 K using CH_4 as a bath gas at pressures of 300-800 Torr. Chloride ion was generated from trace amounts of CCl_4 by DEC of thermalized electrons from 500 μs pulses of a 2 keV electron gun beam. Two methods to generate bromide ion were used. Initially bromide ion was generated from CBr_4 by DEC by injecting 3 μl of a CBr_4/C_6H_6 solution, with $[CBr_4] = 0.287$ M, into the reservoir. The second method to generate bromide ion more efficiently is by a S_N2 reaction between Cl^- and *n*-butyl bromide (Reaction 5.16).



The two alkyl halides ((CH₃)₂CHCl and (CH₃)₂CHBr) and the four solvents (CH₃OH, CH₃CN, (CH₃)₂CO, and CH₃CF₂H) were added in a variety of relative amounts, depending on the ion source temperature and the nature of the experiment involved. The ion source pressure and temperature ranged between 4.0-7.5 Torr and 300-380 K, respectively.

Time-intensity profiles of mass selected ions were monitored using a PC based multi-channel scalar (MCS) data acquisition system, configured at 50-200 μs dwell time per channel over 250 channels. Additive accumulations of ion signals from 1000-2000 electron gun beam pulses were used.

Equilibrium constants (K_{eq}) at different absolute temperatures for the various halide ion-solvent (Reaction 5.17), solvated S_N2 (Reaction 5.18), and S_N2 complex solvation (Reaction 5.19) clustering equilibria are determined from Equations 5.20-5.22, respectively.



$$K_{eq,17} = \frac{\text{Int}(X^-(S))}{\text{Int}(X^-)} \cdot \frac{P^0}{P_{S,source}} \quad (5.20)$$

$$K_{eq,18} = \frac{\text{Int}((S)X^-(RY))}{\text{Int}(X^-(S))} \cdot \frac{P^0}{P_{RY,source}} \quad (5.21)$$

$$K_{eq,19} = \frac{\text{Int}((S)X^-(RY))}{\text{Int}(X^-(RY))} \cdot \frac{P^0}{P_{S,source}} \quad (5.22)$$

In Equations 5.20-5.22 $\text{Int}(X^-(S))/\text{Int}(X^-)$, $\text{Int}((S)X^-(RY))/\text{Int}(X^-(S))$, and $\text{Int}((S)X^-(RY))/\text{Int}(X^-(RY))$ are the ion intensity ratios of the $X^-(S)$ and X^- , $(S)X^-(RY)$ and $X^-(S)$, and $(S)X^-(RY)$ and $X^-(RY)$ ions at equilibrium, respectively, P° is the standard pressure (1 atm), and $P_{S.\text{source}}$ and $P_{RY.\text{source}}$ are the partial pressures (in atm) of the solvent (S) and the S_N2 substrate (RY) in the ion source, respectively.

Equilibrium constants were calculated for various isotope pairs, e.g. $^{35}\text{Cl}^-(S)/(S)^{35}\text{Cl}^-(R^{35}\text{Cl})$ and $^{35}\text{Cl}^-(S)/(S)^{35}\text{Cl}^-(R^{37}\text{Cl})$, and $^{35}\text{Cl}^-(S)/(S)^{35}\text{Cl}^-(R^{79}\text{Br})$ and $^{35}\text{Cl}^-(S)/(S)^{35}\text{Cl}^-(R^{81}\text{Br})$. Only the $^{79}\text{Br}^-(S)/(S)^{79}\text{Br}^-(R^{35}\text{Cl})$ isotope pair was measured. The equilibrium constants for all these isotope pairs need to be corrected for the fact that the partial pressure of RCl and RBr introduced into the reservoir consists of 75% of $R^{35}\text{Cl}$ and 25% $R^{37}\text{Cl}$, and 50% $R^{79}\text{Br}$ and 50% $R^{81}\text{Br}$. In addition, one has to correct for the fact that the peak at the m/z value corresponding to $(S)^{35}\text{Cl}^-(R^{37}\text{Cl})$ also contains the $(S)^{37}\text{Cl}^-(R^{35}\text{Cl})$ (50% of the total ion intensity). The peak at the m/z value corresponding to $(S)^{35}\text{Cl}^-(R^{81}\text{Br})$ also contains $(S)^{37}\text{Cl}^-(R^{79}\text{Br})$ (25% of the total ion intensity). For the above mentioned isotope pairs the corrected equilibrium constants are $K = (4/3)K_{\text{obs}}$, $2K_{\text{obs}}$, $2K_{\text{obs}}$, $(3/2)K_{\text{obs}}$, and $(4/3)K_{\text{obs}}$, respectively. The equilibrium constants for Reaction 5.19 do not need to be corrected.

Carbon tetrabromide, iso-propyl bromide and chloride, n-butyl bromide, and 1,1-difluoroethane were purchased from Aldrich Chemical Company, Inc.. Acetonitrile and benzene were purchased from BDH. Acetone and methanol were purchased from Fisher Scientific. Carbon tetrachloride was purchased from J. T. Baker Chemical Co.. Methane was purchased from Praxair. All chemicals were used as received.

5.3 Computational

All computations were performed using the *Gaussian* 98 and 98W⁴⁰ suites of programs. Geometries were optimized using the HF⁴¹ and MP2(fc)⁴² methods in combination with the 6-31+G(d,p) (a)⁴⁴⁻⁴⁷ basis set. Normal mode vibrational frequencies were calculated at the HF level of theory, scaled by 0.8930,⁴⁸⁻⁵⁰ while for some systems the MP2 level of theory was used, scaled by 0.90.⁴⁸ Single point energy

computations were performed at the MP2(fc) level of theory in combination with the 6-311+G(3df,2p) (b)^{45-47,51} basis set, using the MP2/a geometry. For the systems containing bromine and iodine, similar computations were performed, except that the 6-31+G(d) (c)^{44-47,52} basis set was used for H, C, N, O, and Cl, while for Br and I a modified LanL2DZ ECP basis set, here indicated as LanL2DZ(sp) (d),^{53,54} was used. These normal mode vibrational frequencies were scaled by 0.8970.⁴⁹ For the single point energy computations for bromine and iodine, the LanL2DZ(sp) basis set was used, including an extra f function, indicated as LanL2DZ(sp) (e).^{53,54} For some of the systems investigated, computations were also performed at the G2(MP2) level of theory⁵⁵ to further test the suitability of the above mentioned method on the systems of interest.

Finally, for the $\text{Cl}^- + \text{CH}_3\text{Br}$ and $\text{Cl}^-(\text{H}_2\text{O}) + \text{CH}_3\text{Br}$ reactions, potential energy surface scans⁵⁶ were performed at the MP2/[c/d] level of theory to obtain information on the reorganization of the solvent molecule as the reaction proceeds.

5.4 Results and Discussion

5.4.1 Structures

In Table 5.2 it can be seen that in general the MP2 optimized geometries for the three methyl halides and the five solvent molecules agree well with available experimental data.⁵⁷ The results from the HF geometries also show acceptable agreement. It must be clearly stated that higher levels of theory will most likely give results that are in closer agreement with experimental data, but for the objectives of this study the results obtained seem to be sufficient to provide good qualitative and quantitative results. In Figure 5.5 the MP2 structure of CH_3Cl is shown. Upon chloride ion complex formation, some geometry changes take place in the solvent molecules, but no dramatic changes are observed. These results are summarized in Table 5.3. In Figures 5.6-5.10 the MP2 structures of $\text{Cl}^-(\text{S})$ ($\text{S} = \text{H}_2\text{O}, \text{H}_2\text{S}, \text{NH}_3, \text{PH}_3, \text{SO}_2$) are shown. It is interesting to note that chloride ion interacts with one hydrogen atom of NH_3 , while it actually interacts with two hydrogen atoms of PH_3 . Many results on the geometries of the $\text{S}_\text{N}2$ ion-molecule complexes $\text{X}^-(\text{CH}_3\text{Y})$ have been

Table 5.2 Overview of the computational HF/a, MP2/a and experimental structural data of the solvent and methyl halide molecules studied.

molecule	length ^a / angle ^b	HF	MP2	experiment ^d
CH ₃ Cl	C-H	1.078	1.085	1.11 ± 0.01
	C-Cl	1.786	1.778	1.784 ± 0.003
	H-C-H	110.6	110.0	110 ± 2
CH ₃ Br ^c	C-H	1.076	1.088	1.086
	C-Br	1.954	1.952	1.933
	H-C-H	111.1	110.9	111.2
CH ₃ I ^c	C-H	1.077	1.088	1.084
	C-I	2.148	2.146	2.132
	H-C-H	111.2	111.0	111.2
H ₂ O	O-H	0.943	0.963	0.958
	H-O-H	107.1	105.4	104.45
H ₂ S	S-H	1.327	1.331	1.3455
	H-S-H	94.4	92.9	93.3
NH ₃	N-H	1.000	1.012	1.008 ± 0.004
	H-N-H	108.9	108.1	107.3 ± 0.2
PH ₃	P-H	1.405	1.406	1.415 ± 0.003
	H-P-H	95.7	94.7	93.3 ± 0.2
SO ₂	S-O	1.415	1.482	1.4321
	O-S-O	118.6	119.3	119.536

^a Å

^b °

^c [c/d]

^d from Reference 57

Table 5.3 Overview of the computational MP2/a structural data of the halide ion-solvent molecule complexes.

complex	length ^a /angle ^b	MP2
Cl ⁻ (H ₂ O)	Cl ⁻ ...H	2.191
	O-H	0.986/0.963
	H-O-H	101.5
Cl ⁻ (H ₂ S)	Cl ⁻ ...H	2.169
	S-H	1.368/1.330
	H-S-H	93.1
Cl ⁻ (NH ₃)	Cl ⁻ ...H	2.246
	N-H	1.025/1.014
	H-N-H	105.2/106.1
Cl ⁻ (PH ₃)	Cl ⁻ ...H	3.109/3.210
	P-H	1.398/1.418
	H-P-H	95.8
Cl ⁻ (SO ₂)	Cl ⁻ ...S	2.667
	S-O	1.492
	O-S-O	115.2
Br ⁻ (H ₂ O) ^c	Br ⁻ ...H	2.456
	O-H	0.989/0.971
	H-O-H	101.5

^a Å

^b °

^c [c/d]

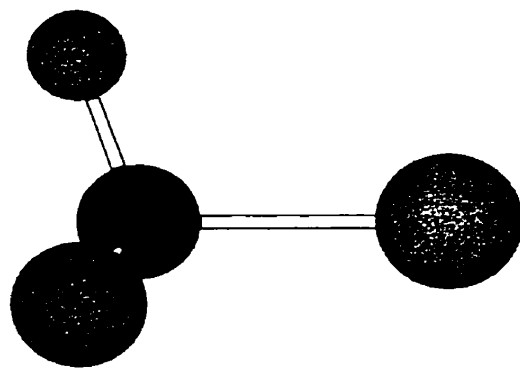


Figure 5.5 Optimized MP2(fc)/a structure of CH₃Cl.



Figure 5.6 Optimized MP2(fc)/a structure of Cl⁻(H₂O).

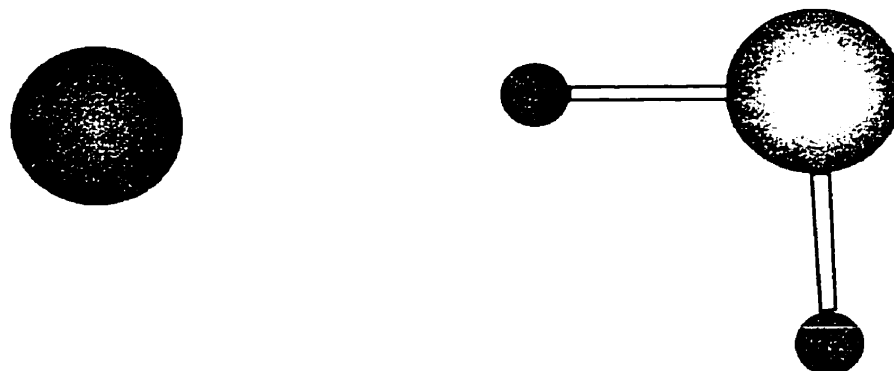


Figure 5.7 Optimized MP2(fc)/a structure of Cl⁻(H₂S).



Figure 5.8 Optimized MP2(fc)/a structure of $\text{Cl}^-(\text{NH}_3)$.

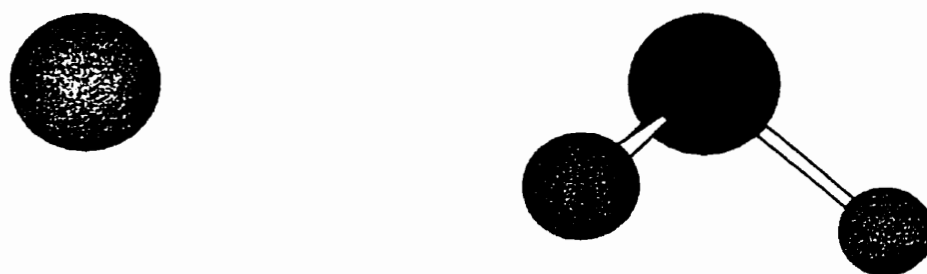


Figure 5.9 Optimized MP2(fc)/a structure of $\text{Cl}^-(\text{PH}_3)$.



Figure 5.10 Optimized MP2(fc)/a structure of $\text{Cl}^-(\text{SO}_2)$.

published already in the literature using a large variety of methods and basis sets.⁵⁸⁻⁶² The present results in Table 5.4 are almost identical to recent results by Glukhovtsev *et al.*^{59,61}

The solvated S_N2 complexes, $(S)X^-(CH_3Y)$ are more interesting from a chemical point of view, and a large variation in structures actually can be observed. In Figures 5.11-5.15 the MP2 structures of the $(S)Cl^-(CH_3Cl)$ complexes ($S = H_2O, H_2S, NH_3, PH_3, SO_2$) are shown. Comparing these with Figures 5.6-5.10 immediately reveals very different bonding characteristics especially relative to the $Cl^-(S)$ complexes, but also to $Cl^-(CH_3Cl)$, and particularly $(SO_2)Cl^-(CH_3Cl)$. For $S = H_2O, H_2S, NH_3$, and PH_3 the $Cl^-(CH_3Cl)$ moiety does not change relative to “free” $Cl^-(CH_3Cl)$. For $(SO_2)Cl^-(CH_3Cl)$ a large increase in the $Cl^- \cdots CH_3Cl$ distance takes place, from 3.256 Å to 3.512 Å. Other interesting features in the $(SO_2)Cl^-(CH_3Cl)$ complex are the interactions of the two oxygen atoms with the two hydrogen atoms ($R(O \cdots H) = 2.368$ Å), and the interactions of the chloride ion with the third hydrogen atom ($R(Cl^- \cdots H) = 3.046$ Å). H_2O and H_2S bind almost identically to $Cl^-(CH_3Cl)$, although the MP2 structures are quite different from the HF structures, with the latter ones being more symmetric. Except for $S = H_2O$, the other three hydrogen bonded solvents show an expected increase in the $Cl^- \cdots H$ distance. Unlike $Cl^-(PH_3)$, in $(PH_3)Cl^-(CH_3Cl)$ the PH_3 molecule is bonded to chloride ion by only one hydrogen atom. Surprisingly, for the $(H_2O)Cl^-(CH_3Br)$ complex a more symmetric structure was obtained (Figure 5.16). It must be stated clearly that the potential energy surface for the solvent molecule motion is fairly flat, and consequently it will be fairly mobile, giving rise to various shallow minima. Similar to the chloride ion complex, the $(H_2O)Br^-(CH_3Cl)$ complex (Figure 5.17) has a symmetric structure with the $Cl^-(CH_3Br)$ and $Br^-(H_2O)$ parts in this complex being almost identical to the “free” complexes.

For the transition states, $[XCH_3Y]^-$, similar comments can be made to those for the ion-molecule complexes earlier. The solvated S_N2 transition states $[(S)ClCH_3Cl]^-$ are shown in Figures 5.18-5.22 and some interesting features can be observed (Table 5.5). For $S = H_2O$ and H_2S , symmetric structures have been obtained. In $[(H_2S)ClCH_3Cl]^-$ the hydrogen atom is not only interacting with the chloride atom on

Table 5.4 Overview of the computational MP2/a structural data of the (un)solvated S_N2 complexes.

X ⁻ (CH ₃ Y)	length ^a	MP2	(S)X ⁻ (CH ₃ Y)	length ^a	MP2	(S)X ⁻ (CH ₃ Y)	length ^a	MP2
Cl ⁻ (CH ₃ Cl)	Cl...C	3.256	(H ₂ O)Cl ⁻ (CH ₃ Cl)	Cl...C	3.269	(H ₂ O)Cl ⁻ (CH ₃ Br) ^b	Cl...C	3.233
	C-Cl	1.808		C-Cl	1.804		C-Br	1.983
Cl ⁻ (CH ₃ Br) ^b	Cl...C	3.201	(H ₂ S)Cl ⁻ (CH ₃ Cl)	H...Cl	2.198	(H ₂ O)Br ⁻ (CH ₃ Cl) ^b	H...Cl	2.239
	C-Br	1.990		Cl...C	3.265		Br...C	3.455
Br ⁻ (CH ₃ Cl) ^b	Br...C	3.453	(NH ₃)Cl ⁻ (CH ₃ Cl)	C-Cl	1.804	(PH ₃)Cl ⁻ (CH ₃ Cl)	C-Cl	1.804
	C-Cl	1.808		H...Cl	2.195		H...Br	2.482
				Cl...C	3.261			
				C-Cl	1.806			
				H...Cl	2.423			
				Cl...C	3.261			
				C-Cl	1.806			
				H...Cl	2.502			
				Cl...C	3.512			
				C-Cl	1.799			
				S...Cl	2.651			

^a Å ^b [c/d]

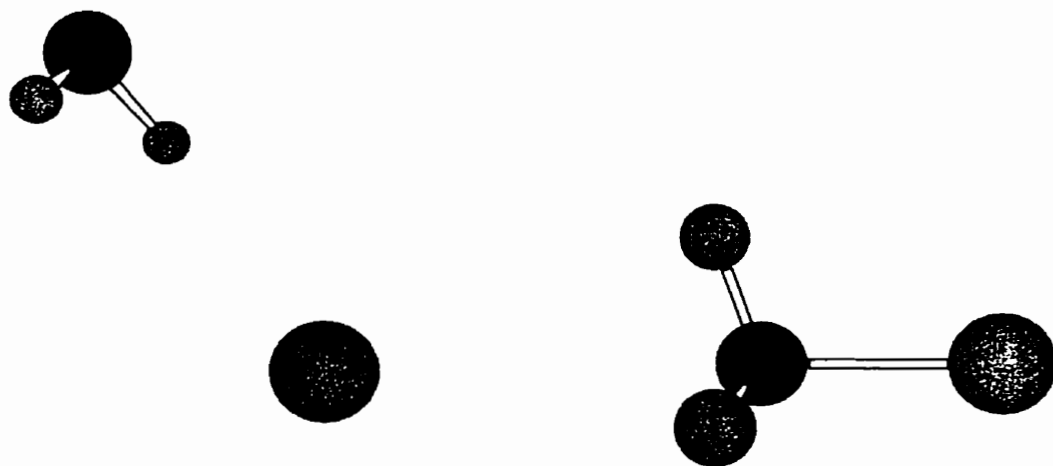


Figure 5.11 Optimized MP2(fc)/a structure of $(\text{H}_2\text{O})\text{Cl}^-(\text{CH}_3\text{Cl})$.

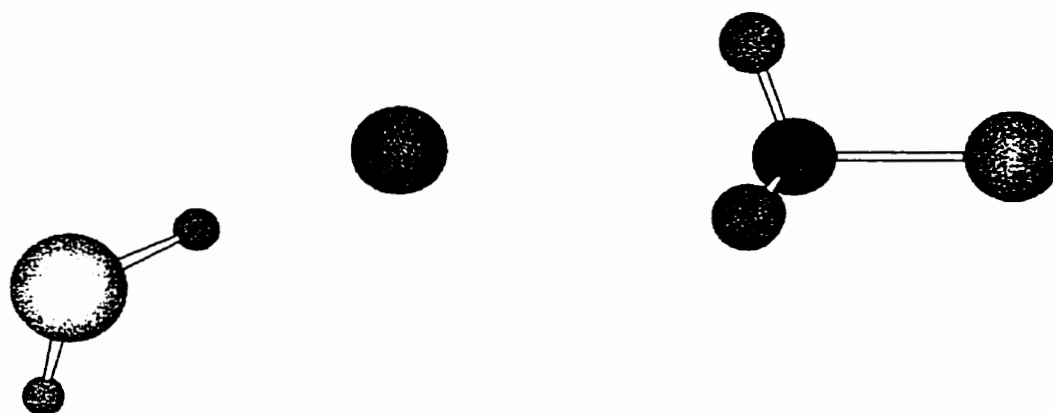


Figure 5.12 Optimized MP2(fc)/a structure of $(\text{H}_2\text{S})\text{Cl}^-(\text{CH}_3\text{Cl})$.

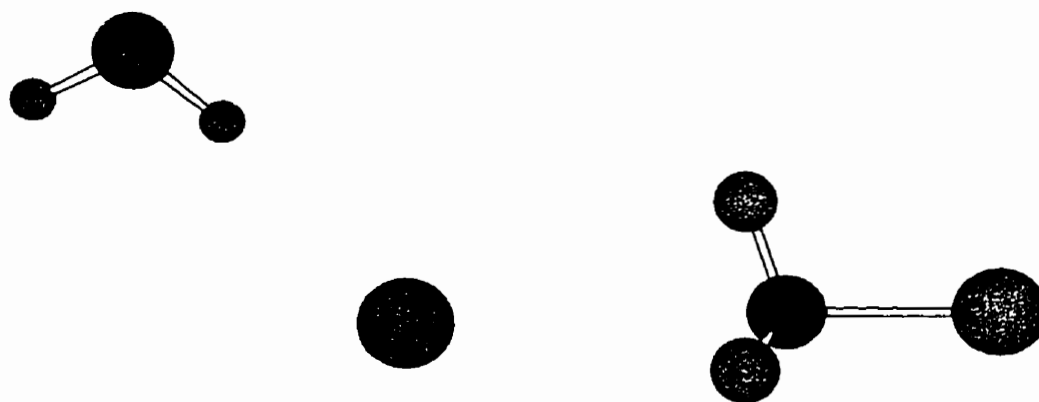


Figure 5.13 Optimized MP2(fc)/a structure of $(\text{NH}_3)\text{Cl}^-(\text{CH}_3\text{Cl})$.

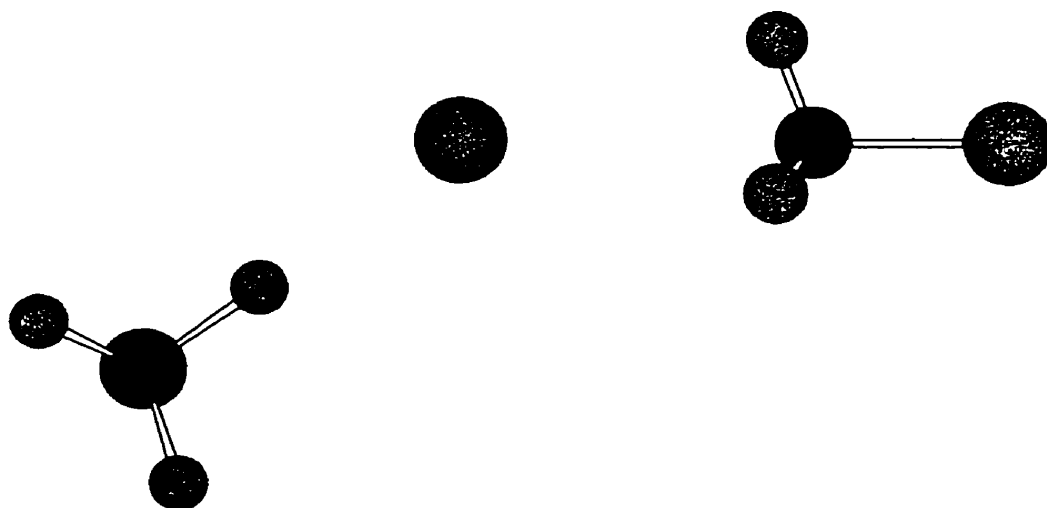


Figure 5.14 Optimized MP2(fc)/a structure of $(\text{PH}_3)\text{Cl}^-(\text{CH}_3\text{Cl})$.

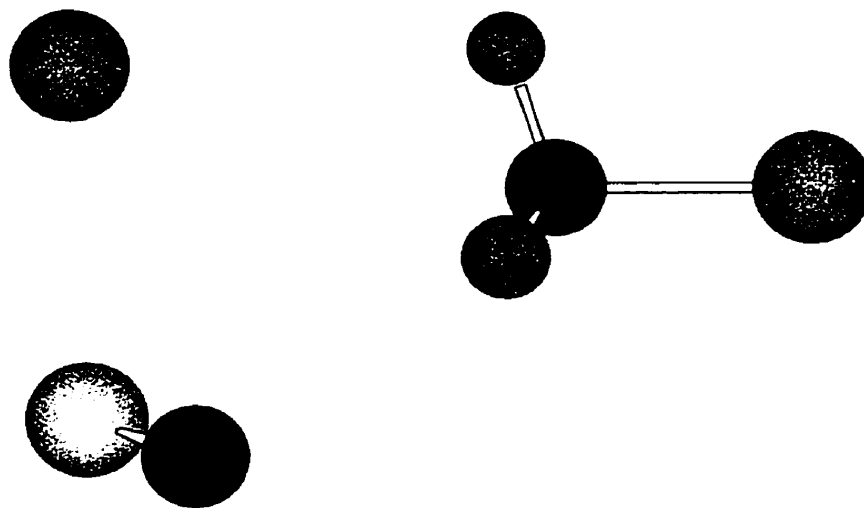


Figure 5.15 Optimized MP2(fc)/a structure of $(\text{SO}_2)\text{Cl}^-(\text{CH}_3\text{Cl})$.

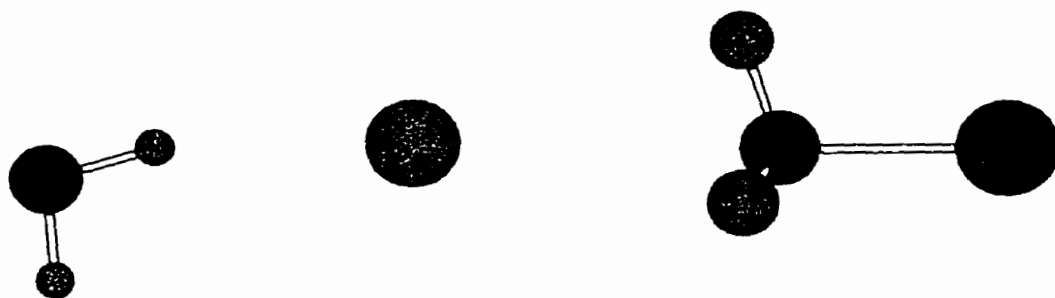


Figure 5.16 Optimized MP2(fc)/[c/d] structure of $(\text{H}_2\text{O})\text{Cl}^-(\text{CH}_3\text{Br})$.

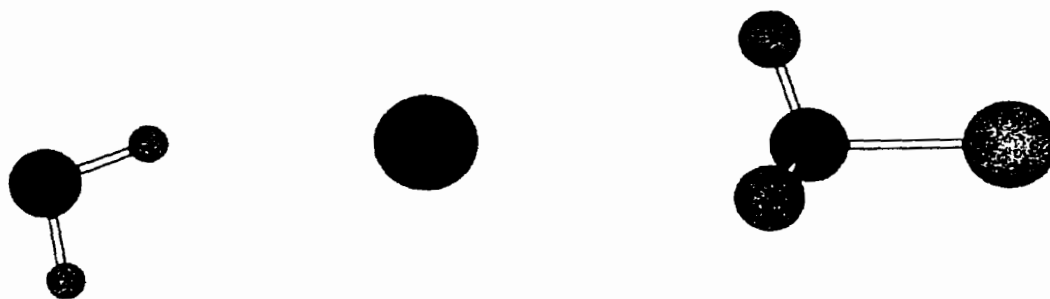


Figure 5.17 Optimized MP2(fc)/[c/d] structure of $(\text{H}_2\text{O})\text{Br}^-(\text{CH}_3\text{Cl})$.

Table 5.5 Overview of the computational MP2/a structural data of the (un)solvated S_N2 transition states.

[XCH ₃ Y] ⁻	length ^a	MP2	[(S)XCH ₃ Y] ⁻	length ^a	MP2	[(S)XCH ₃ Y] ⁻	length ^a	MP2
[ClCH ₃ Cl] ⁻	Cl...C	2.310	[(H ₂ O)ClCH ₃ Cl] ⁻	Cl...C	2.265	[(H ₂ O)ClCH ₃ Br] ^{-b}	Cl...C	2.317
	C...Cl	2.311		C...Cl	2.348		Cl...Br	2.474
[ClCH ₃ Br] ^{-b}	Cl...C	2.371		H...Cl	2.294		H...Cl	2.308
	C...Br	2.430	[(H ₂ S)ClCH ₃ Cl] ⁻	Cl...C	2.277	[(H ₂ O)BrCH ₃ Cl] ^{-b}	Br...C	2.394
[ClCH ₂ CNBr] ^{-b}	Cl...C	2.365		C...Cl	2.333		Cl...Cl	2.398
	C...Br	2.440		H...Cl	2.443		H...Br	2.582
[ClCH ₃ I] ^{-b}	Cl...C	2.414	[(NH ₃)ClCH ₃ Cl] ⁻	Cl...C	2.288	[(H ₂ O)ClCH ₂ CNBr] ^{-b}	Cl...C	2.317
	C...I	2.588		C...Cl	2.329		C...Br	2.476
				H...Cl	2.536		H...Cl	2.453
			[(PH ₃)ClCH ₃ Cl] ⁻	Cl...C	2.288			
				C...Cl	2.332			
				H...Cl	2.650			
			[(SO ₂)ClCH ₃ Cl] ⁻	Cl...C	2.232			
				C...Cl	2.387			
				S...Cl	2.959			

^a Å ^b [c/d]

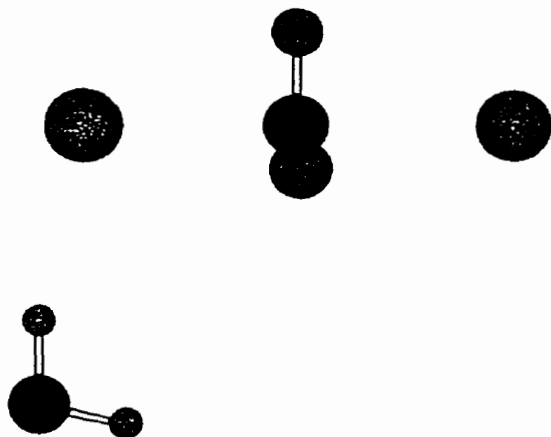


Figure 5.18 Optimized MP2(fc)/a structure of $[(\text{H}_2\text{O})\text{ClCH}_3\text{Cl}]^-$.

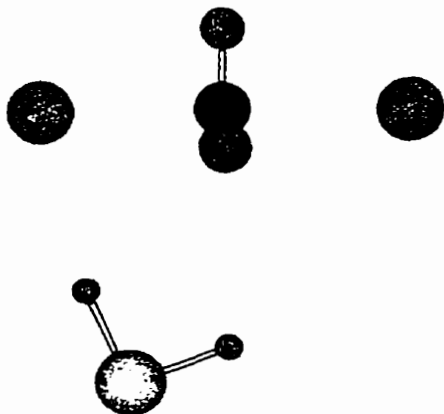


Figure 5.19 Optimized MP2(fc)/a structure of $[(\text{H}_2\text{S})\text{ClCH}_3\text{Cl}]^-$.

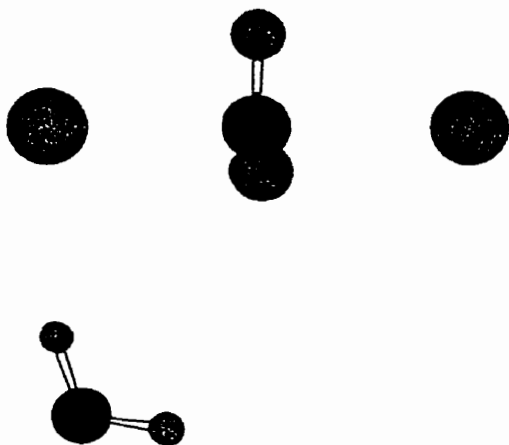


Figure 5.20 Optimized MP2(fc)/a structure of $[(\text{NH}_3)\text{ClCH}_3\text{Cl}]^-$.

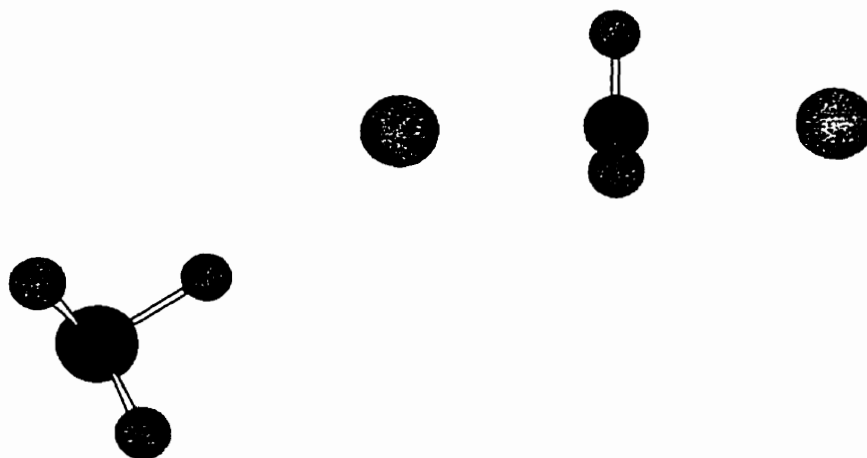


Figure 5.21 Optimized MP2(fc)/a structure of $[(\text{PH}_3)\text{ClCH}_3\text{Cl}]^-$.

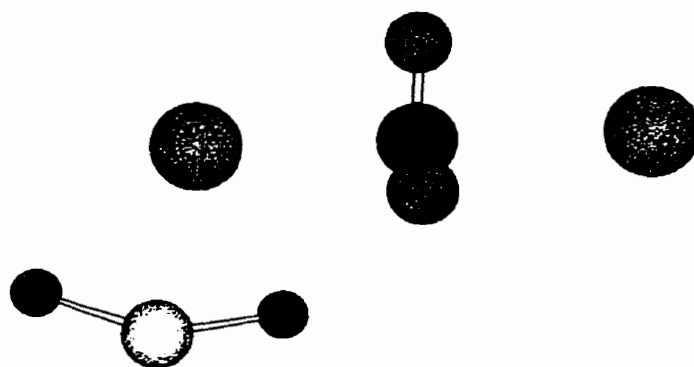


Figure 5.22 Optimized MP2(fc)/a structure of $[(\text{SO}_2)\text{ClCH}_3\text{Cl}]^-$.

the left side, it is also interacting with the chloride atom on the right side. This is not seen for $S = \text{H}_2\text{O}$, although it is by no means suggested that this will facilitate solvent transfer. Morokuma²⁷ and Truhlar and co-workers³³ also found a bridge-like transition state for $S = \text{H}_2\text{O}$, in which the two hydrogen atoms interact with the two chlorine atoms. Attempts to find similar structures failed at the MP2/a level of theory.

The bonding of Cl^- to NH_3 and PH_3 is very different, with NH_3 bonding more like H_2O and H_2S . As in the solvated $\text{S}_{\text{N}}2$ complex, PH_3 only binds to Cl^- by one hydrogen atom in the solvated transition state. The binding of SO_2 in $[(\text{SO}_2)\text{ClCH}_3\text{Cl}]^-$ is very different from that in $(\text{SO}_2)\text{Cl}^-(\text{CH}_3\text{Cl})$. As expected, $R(\text{S}\cdots\text{O})$ has increased from 2.651 Å to 2.959 Å. There is only one oxygen atom interacting with one hydrogen atom at $R(\text{O}\cdots\text{H}) = 2.731$ Å. From all these structures it seems that in going from the solvated $\text{S}_{\text{N}}2$ complex to the transition state, for all solvents a major reorganization in the relative orientation of the solvent molecule must take place. Transition state structures $[(\text{H}_2\text{O})_n\text{ClCH}_3\text{Cl}]^-$ with $n = 1-3$ have been calculated, and various isomers are possible.^{33,37} It seems reasonable to assume that in the condensed phase a much larger number of solvent molecules are involved in solvating the transition state, and that reorganization is much more complex. Still, information on the mono-solvated transition state may already provide some insight into the bulk behavior, and can already reveal differences among solvents. For the water mono-solvated $[\text{ClCH}_3\text{Br}]^-$ transition state, two isomers are possible, $[(\text{H}_2\text{O})\text{ClCH}_3\text{Br}]^-$ and $[(\text{H}_2\text{O})\text{BrCH}_3\text{Cl}]^-$ (Figures 5.23 and 5.24). The halide bonded to the water molecule will have a shorter distance to the carbon atom than in $[\text{ClCH}_3\text{Br}]^-$, while the other halide atom will be further away from the carbon atom.

As expected, $R(\text{H}\cdots\text{X})$ will be shorter for $\text{X} = \text{Cl}$ than for Br , and this will have consequences for the solvation energy (see Section 5.4.3). The $[(\text{H}_2\text{O})\text{ClCH}_2\text{CNBr}]^-$ structure in Figure 5.25 shows that the second hydrogen atom is hydrogen bonded to the cyano group, thereby providing extra stabilization to this transition state relative to $[(\text{H}_2\text{O})\text{ClCH}_3\text{Br}]^-$. In this structure, $R(\text{H}\cdots\text{Cl}) = 2.453$ Å, while $R(\text{H}\cdots\text{N}) = 2.290$ Å.

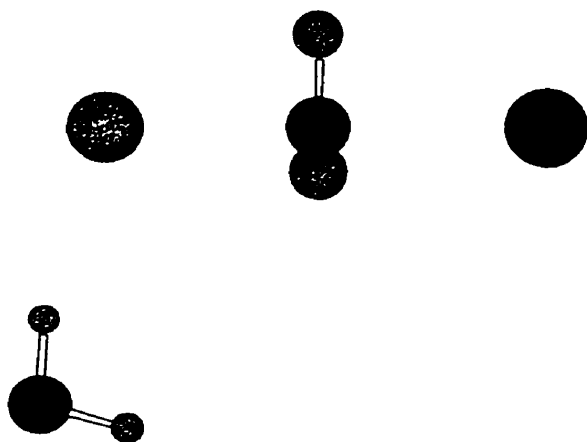


Figure 5.23 Optimized MP2(fc)/[c/d] structure of $[(\text{H}_2\text{O})\text{ClCH}_3\text{Br}]^-$.

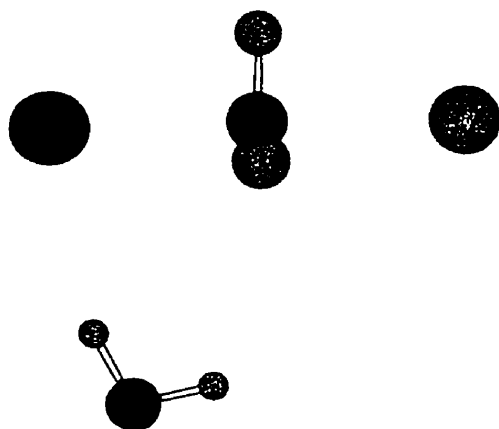


Figure 5.24 Optimized MP2(fc)/[c/d] structure of $[(\text{H}_2\text{O})\text{BrCH}_3\text{Cl}]^-$.

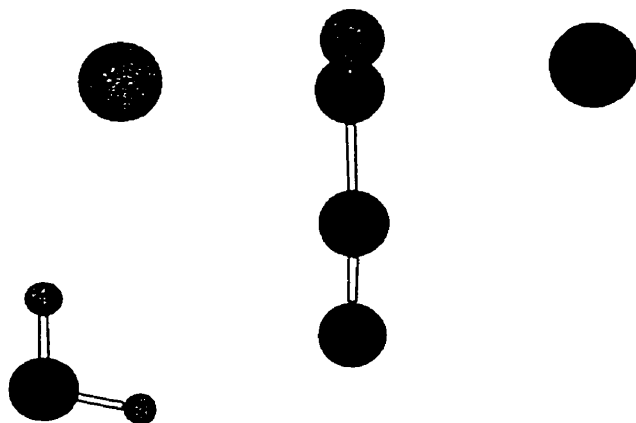


Figure 5.25 Optimized MP2(fc)/[c/d] structure of $[(\text{H}_2\text{O})\text{ClCH}_2\text{CNBr}]^-$.

Finally, it must be mentioned that increasing the number of solvent molecules will provide more and perhaps new insights into the cooperative bonding of the solvents in the ion-molecule complexes and transition states.

5.4.2 Experimental Thermochemistry

In Tables 5.6-5.9 the experimental PHPMS thermochemistry from this work on solvated S_N2 complexes together with available literature values are shown. The corresponding Van't Hoff plots of the systems measured for this study are shown in Figures 5.26-5.35.

Li *et al.* measured the well-depths and some transition state energies for a large number of S_N2 reactions by PHPMS,⁶³ and some of these data are shown in Table 5.6. As already mentioned in Section 5.2, there are two different reactions that can take place that give the solvated S_N2 complex (S)X⁻(RY), Reaction 3 and 4. In Figure 5.36, a thermochemical cycle is shown for the formation of the (S)X⁻(RY) complex from X⁻, RY, and S. The data in Tables 5.6-5.9 in general show good agreement with what might be expected based on the data from Table 5.6. Some systems show some unexpected $-\Delta H^\circ$ and $-\Delta S^\circ$ values, and a reason for this cannot be given. It seems unlikely that this is due to some unusual structural change. The ΔH° values for the bromide ion containing S_N2 complexes, (S)Br⁻((CH₃)₂CHCl), are calculated from measured ΔG°_{300} values and an estimated ΔS° value, $-18.0 \text{ cal mol}^{-1} \text{ K}^{-1}$, based on ΔS° values from Tables 5.7 and 5.8. The general conclusions from these experiments is that Reactions 5.18 and 5.19 indeed have different thermochemistry, and that at the mono-solvated level intrinsic solvent effects are already present and observable.

5.4.3 Computational Thermochemistry

In Table 5.10, the computational thermochemistry for a large variety of halide ion-solvent molecule and S_N2 substrate clustering equilibria, together with available experimental data⁶⁴ are shown. In general, the agreement between ΔH°_{298} values

Table 5.6 Overview of the experimental PHPMS thermochemistry for the $X^- + S \rightleftharpoons X^-(S)$ ($X = \text{Cl}, \text{Br}; S = \text{CH}_3\text{OH}, \text{CH}_3\text{CN}, (\text{CH}_3)_2\text{CO}, \text{CH}_3\text{CF}_2\text{H}$) and $X^- + \text{RY} \rightleftharpoons X^-(\text{RY})$ ($X, Y = \text{Cl}, \text{Br}; R = (\text{CH}_3)_2\text{CH}$) clustering equilibria.

system #	clustering equilibrium	$\Delta H^\circ{}^a$	$\Delta S^\circ{}^b$	reference
	$\text{Cl}^- + (\text{CH}_3)_2\text{CHCl} \rightleftharpoons \text{Cl}^-((\text{CH}_3)_2\text{CHCl})$	-14.7	-23.3	63
	$\text{Cl}^- + (\text{CH}_3)_2\text{CHBr} \rightleftharpoons \text{Cl}^-((\text{CH}_3)_2\text{CHBr})$	-15.2	-24.0	63
	$\text{Cl}^- + \text{CH}_3\text{OH} \rightleftharpoons \text{Cl}^-(\text{CH}_3\text{OH})$	-17.5	-24.0	67
	$\text{Cl}^- + \text{CH}_3\text{CN} \rightleftharpoons \text{Cl}^-(\text{CH}_3\text{CN})$	-15.8	-18.7	63
1	$\text{Cl}^- + (\text{CH}_3)_2\text{CO} \rightleftharpoons \text{Cl}^-((\text{CH}_3)_2\text{CO})$	-14.1	-20.2	this work
2	$\text{Cl}^- + \text{CH}_3\text{CF}_2\text{H} \rightleftharpoons \text{Cl}^-(\text{CH}_3\text{CF}_2\text{H})$	-12.8	-18.4	this work
	$\text{Br}^- + (\text{CH}_3)_2\text{CHCl} \rightleftharpoons \text{Br}^-((\text{CH}_3)_2\text{CHCl})$	-12.4	-20.6	63
	$\text{Br}^- + \text{CH}_3\text{OH} \rightleftharpoons \text{Br}^-(\text{CH}_3\text{OH})$	-14.5	-21.9	67
	$\text{Br}^- + \text{CH}_3\text{CN} \rightleftharpoons \text{Br}^-(\text{CH}_3\text{CN})$	-14.3	-18.7	63
3	$\text{Br}^- + (\text{CH}_3)_2\text{CO} \rightleftharpoons \text{Br}^-((\text{CH}_3)_2\text{CO})$	-11.2	-15.9	this work
4	$\text{Br}^- + \text{CH}_3\text{CF}_2\text{H} \rightleftharpoons \text{Br}^-(\text{CH}_3\text{CF}_2\text{H})$	-10.6	-15.7	this work

^a kcal mol⁻¹, relative errors ± 0.2 kcal mol⁻¹, absolute errors ± 0.4 kcal mol⁻¹

^b cal mol⁻¹ K⁻¹, relative errors ± 1.0 cal mol⁻¹ K⁻¹, absolute errors ± 2.0 cal mol⁻¹ K⁻¹

Table 5.7 Overview of the experimental PHPMS thermochemistry for the $\text{Cl}^-(\text{S}) + \text{RCl} \rightleftharpoons (\text{S})\text{Cl}^-(\text{RCl})$ and $\text{Cl}^-(\text{RCl}) + \text{S} \rightleftharpoons (\text{S})\text{Cl}^-(\text{RCl})$ ($\text{S} = \text{CH}_3\text{OH}, \text{CH}_3\text{CN}, (\text{CH}_3)_2\text{CO}, \text{CH}_3\text{CF}_2\text{H}; \text{R} = (\text{CH}_3)_2\text{CH}$) clustering equilibria.

system #	clustering equilibrium	$\Delta H^{\circ a}$	$\Delta S^{\circ b}$
5	$\text{Cl}^-(\text{CH}_3\text{OH}) + (\text{CH}_3)_2\text{CHCl} \rightleftharpoons (\text{CH}_3\text{OH})\text{Cl}^-((\text{CH}_3)_2\text{CHCl})$	-11.0	-18.1
6	$\text{Cl}^-((\text{CH}_3)_2\text{CHCl}) + \text{CH}_3\text{OH} \rightleftharpoons (\text{CH}_3\text{OH})\text{Cl}^-((\text{CH}_3)_2\text{CHCl})$	-14.6	-20.3
7	$\text{Cl}^-(\text{CH}_3\text{CN}) + (\text{CH}_3)_2\text{CHCl} \rightleftharpoons (\text{CH}_3\text{CN})\text{Cl}^-((\text{CH}_3)_2\text{CHCl})$	-11.0	-18.5
8	$\text{Cl}^-((\text{CH}_3)_2\text{CHCl}) + \text{CH}_3\text{CN} \rightleftharpoons (\text{CH}_3\text{CN})\text{Cl}^-((\text{CH}_3)_2\text{CHCl})$	-11.7	-13.8
9	$\text{Cl}^-((\text{CH}_3)_2\text{CO}) + (\text{CH}_3)_2\text{CHCl} \rightleftharpoons ((\text{CH}_3)_2\text{CO})\text{Cl}^-((\text{CH}_3)_2\text{CHCl})$	-11.7	-19.7
10	$\text{Cl}^-((\text{CH}_3)_2\text{CHCl}) + (\text{CH}_3)_2\text{CO} \rightleftharpoons ((\text{CH}_3)_2\text{CO})\text{Cl}^-((\text{CH}_3)_2\text{CHCl})$	-10.5	-14.4
11	$\text{Cl}^-(\text{CH}_3\text{CF}_2\text{H}) + (\text{CH}_3)_2\text{CHCl} \rightleftharpoons (\text{CH}_3\text{CF}_2\text{H})\text{Cl}^-((\text{CH}_3)_2\text{CHCl})$	-11.3	-18.4
12	$\text{Cl}^-((\text{CH}_3)_2\text{CHCl}) + \text{CH}_3\text{CF}_2\text{H} \rightleftharpoons (\text{CH}_3\text{CF}_2\text{H})\text{Cl}^-((\text{CH}_3)_2\text{CHCl})$	-10.9	-17.5

^a kcal mol⁻¹, relative errors ± 0.2 kcal mol⁻¹, absolute errors ± 0.4 kcal mol⁻¹

^b cal mol⁻¹ K⁻¹, relative errors ± 1.0 cal mol⁻¹ K⁻¹, absolute errors ± 2.0 cal mol⁻¹ K⁻¹

Table 5.8 Overview of the experimental PHPMS thermochemistry for the $\text{Cl}^-(\text{S}) + \text{RBr} \rightleftharpoons (\text{S})\text{Cl}^-(\text{RBr})$ and $\text{Cl}^-(\text{RBr}) + \text{S} \rightleftharpoons (\text{S})\text{Cl}^-(\text{RBr})$ ($\text{S} = \text{CH}_3\text{OH}, \text{CH}_3\text{CN}, (\text{CH}_3)_2\text{CO}, \text{CH}_3\text{CF}_2\text{H}; \text{R} = (\text{CH}_3)_2\text{CH}$) clustering equilibria.

system #	clustering equilibrium	$\Delta H^{\circ a}$	$\Delta S^{\circ b}$
13	$\text{Cl}^-(\text{CH}_3\text{OH}) + (\text{CH}_3)_2\text{CHBr} \rightleftharpoons (\text{CH}_3\text{OH})\text{Cl}^-((\text{CH}_3)_2\text{CHBr})$	-11.8	-21.0
14	$\text{Cl}^-((\text{CH}_3)_2\text{CHBr}) + \text{CH}_3\text{OH} \rightleftharpoons (\text{CH}_3\text{OH})\text{Cl}^-((\text{CH}_3)_2\text{CHBr})$	-14.8	-22.9
15	$\text{Cl}^-(\text{CH}_3\text{CN}) + (\text{CH}_3)_2\text{CHBr} \rightleftharpoons (\text{CH}_3\text{CN})\text{Cl}^-((\text{CH}_3)_2\text{CHBr})$	-12.3	-21.1
16	$\text{Cl}^-((\text{CH}_3)_2\text{CHBr}) + \text{CH}_3\text{CN} \rightleftharpoons (\text{CH}_3\text{CN})\text{Cl}^-((\text{CH}_3)_2\text{CHBr})$	-13.9	-21.5
17	$\text{Cl}^-((\text{CH}_3)_2\text{CO}) + (\text{CH}_3)_2\text{CHBr} \rightleftharpoons ((\text{CH}_3)_2\text{CO})\text{Cl}^-((\text{CH}_3)_2\text{CHBr})$	-11.9	-19.4
18	$\text{Cl}^-((\text{CH}_3)_2\text{CHBr}) + (\text{CH}_3)_2\text{CO} \rightleftharpoons ((\text{CH}_3)_2\text{CO})\text{Cl}^-((\text{CH}_3)_2\text{CHBr})$	-11.9	-20.0
19	$\text{Cl}^-(\text{CH}_3\text{CF}_2\text{H}) + (\text{CH}_3)_2\text{CHBr} \rightleftharpoons (\text{CH}_3\text{CF}_2\text{H})\text{Cl}^-((\text{CH}_3)_2\text{CHBr})$	-11.9	-18.8
20	$\text{Cl}^-((\text{CH}_3)_2\text{CHBr}) + \text{CH}_3\text{CF}_2\text{H} \rightleftharpoons (\text{CH}_3\text{CF}_2\text{H})\text{Cl}^-((\text{CH}_3)_2\text{CHBr})$	-12.4	-23.4

^a kcal mol⁻¹, relative errors ± 0.2 kcal mol⁻¹, absolute errors ± 0.4 kcal mol⁻¹

^b cal mol⁻¹ K⁻¹, relative errors ± 1.0 cal mol⁻¹ K⁻¹, absolute errors ± 2.0 cal mol⁻¹ K⁻¹

Table 5.9 Overview experimental PHPMS thermochemistry for the $\text{Br}^-(\text{S}) + \text{RCl} \rightleftharpoons (\text{S})\text{Br}^-(\text{RCl})$ and $\text{Br}^-(\text{RCl}) + \text{S} \rightleftharpoons (\text{S})\text{Br}^-(\text{RCl})$ ($\text{S} = \text{CH}_3\text{OH}, \text{CH}_3\text{CN}, (\text{CH}_3)_2\text{CO}, \text{CH}_3\text{CF}_2\text{H}$; $\text{R} = (\text{CH}_3)_2\text{CH}$) clustering equilibria.

clustering equilibrium	ΔG°_{300} ^{a,b}	ΔH° ^{a,c}
$\text{Br}^-(\text{CH}_3\text{OH}) + (\text{CH}_3)_2\text{CHCl} \rightleftharpoons (\text{CH}_3\text{OH})\text{Br}^-((\text{CH}_3)_2\text{CHCl})$	-4.9	-10.6
$\text{Br}^-((\text{CH}_3)_2\text{CHCl}) + \text{CH}_3\text{OH} \rightleftharpoons (\text{CH}_3\text{OH})\text{Br}^-((\text{CH}_3)_2\text{CHCl})$	-7.0	-12.4
$\text{Br}^-(\text{CH}_3\text{CN}) + (\text{CH}_3)_2\text{CHCl} \rightleftharpoons (\text{CH}_3\text{CN})\text{Br}^-((\text{CH}_3)_2\text{CHCl})$	-4.5	-9.9
$\text{Br}^-((\text{CH}_3)_2\text{CHCl}) + \text{CH}_3\text{CN} \rightleftharpoons (\text{CH}_3\text{CN})\text{Br}^-((\text{CH}_3)_2\text{CHCl})$	-6.4	-12.0
$\text{Br}^-((\text{CH}_3)_2\text{CO}) + (\text{CH}_3)_2\text{CHCl} \rightleftharpoons ((\text{CH}_3)_2\text{CO})\text{Br}^-((\text{CH}_3)_2\text{CHCl})$	-5.0	-10.4
$\text{Br}^-((\text{CH}_3)_2\text{CHCl}) + (\text{CH}_3)_2\text{CO} \rightleftharpoons ((\text{CH}_3)_2\text{CO})\text{Br}^-((\text{CH}_3)_2\text{CHCl})$	-5.3	-10.7
$\text{Br}^-(\text{CH}_3\text{CF}_2\text{H}) + (\text{CH}_3)_2\text{CHCl} \rightleftharpoons (\text{CH}_3\text{CF}_2\text{H})\text{Br}^-((\text{CH}_3)_2\text{CHCl})$	-5.0	-10.4
$\text{Br}^-((\text{CH}_3)_2\text{CHCl}) + \text{CH}_3\text{CF}_2\text{H} \rightleftharpoons (\text{CH}_3\text{CF}_2\text{H})\text{Br}^-((\text{CH}_3)_2\text{CHCl})$	-4.8	-10.2

^a kcal mol⁻¹

^b relative errors ± 0.2 kcal mol⁻¹, absolute errors ± 0.4 kcal mol⁻¹

^c relative errors ± 0.5 kcal mol⁻¹, absolute errors ± 1.0 kcal mol⁻¹

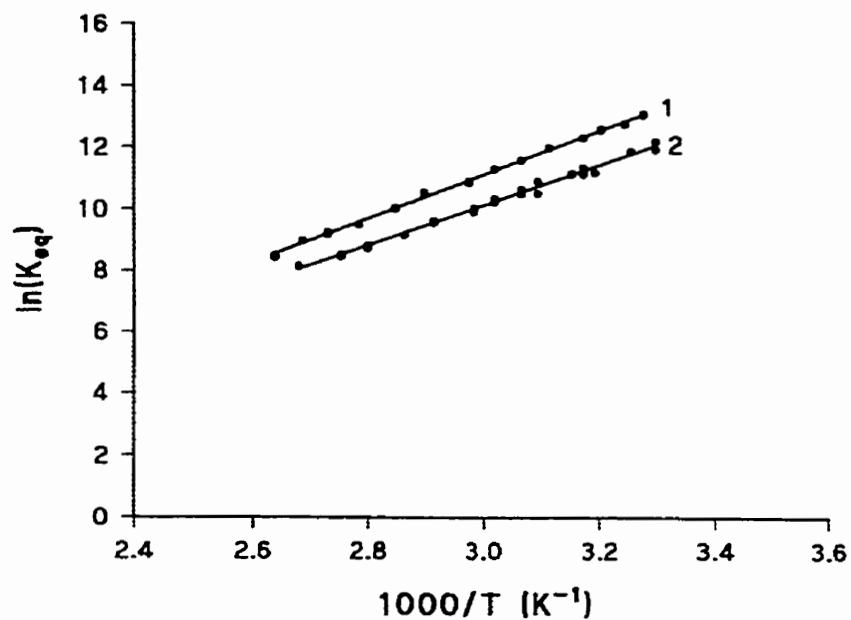


Figure 5.26 Van't Hoff plots for the $Cl^- + S \rightleftharpoons Cl^-(S)$ ($S = (CH_3)_2CO, CH_3CF_2H$) clustering equilibria.

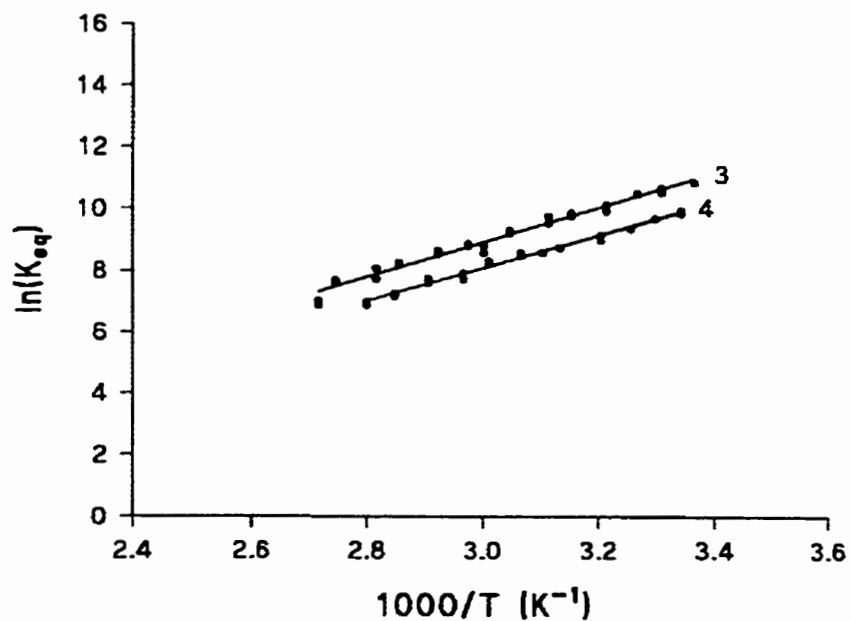


Figure 5.27 Van't Hoff plots for the $Br^- + S \rightleftharpoons Br^-(S)$ ($S = (CH_3)_2CO, CH_3CF_2H$) clustering equilibria.

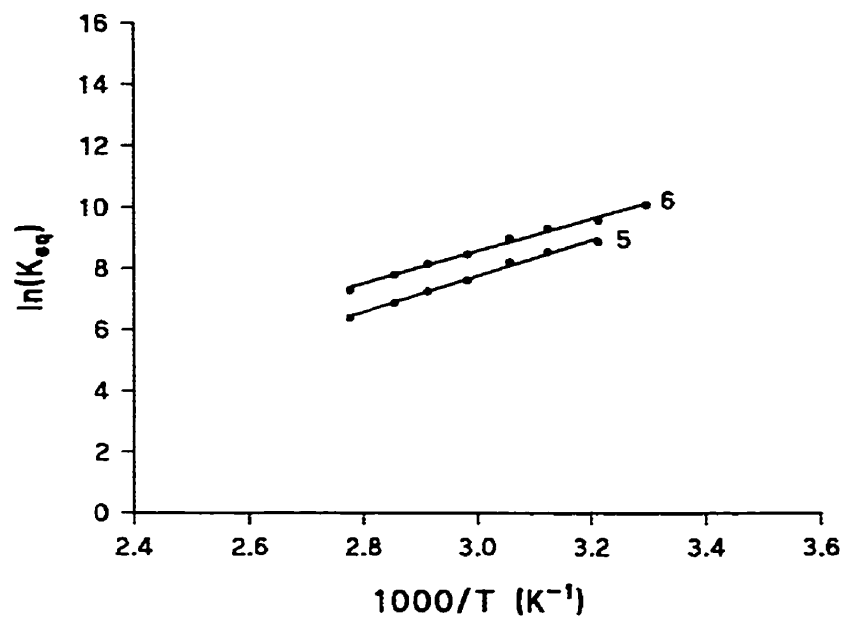


Figure 5.28 Van't Hoff plots for the $Cl^{-}(S) + RCl \rightleftharpoons (S)Cl^{-}(RCl)$ and $Cl^{-}(RCl) + S \rightleftharpoons (S)Cl^{-}(RCl)$ ($S = CH_3OH$; $R = (CH_3)_2CH$) clustering equilibria.

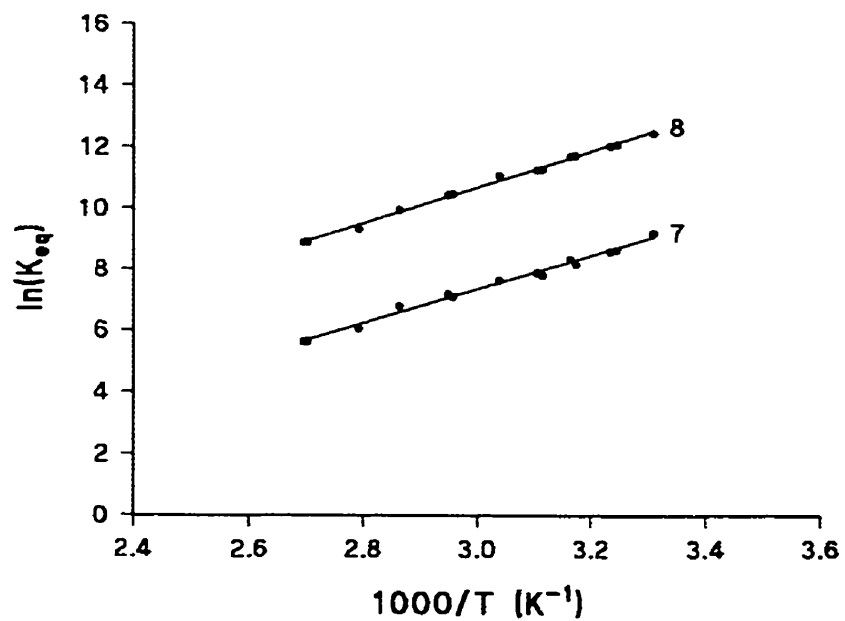


Figure 5.29 Van't Hoff plots for the $Cl^{-}(S) + RCl \rightleftharpoons (S)Cl^{-}(RCl)$ and $Cl^{-}(RCl) + S \rightleftharpoons (S)Cl^{-}(RCl)$ ($S = CH_3CN$; $R = (CH_3)_2CH$) clustering equilibria.

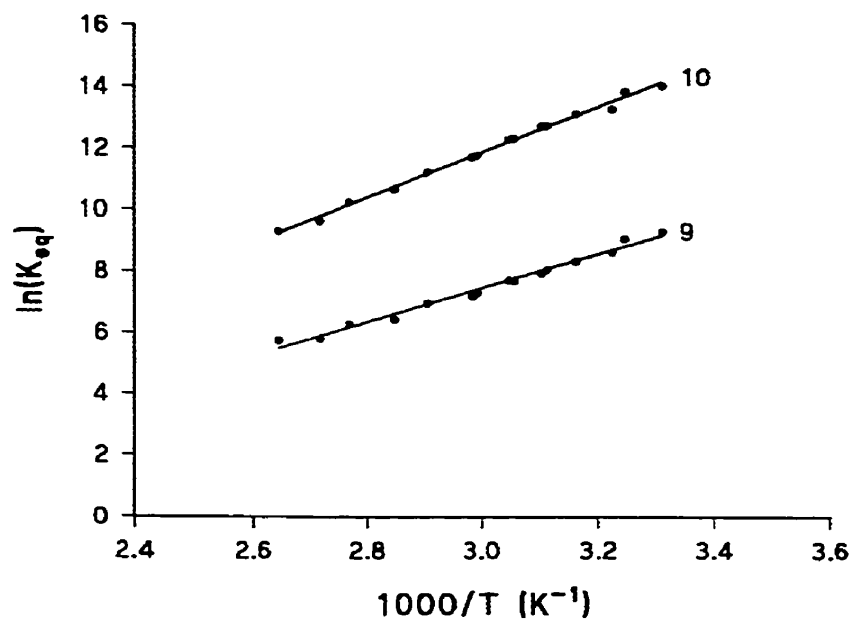


Figure 5.30 Van't Hoff plots for the $Cl^{-}(S) + RCl \rightleftharpoons (S)Cl^{-}(RCl)$ and $Cl^{-}(RCl) + S \rightleftharpoons (S)Cl^{-}(RCl)$ ($S = (CH_3)_2CO$; $R = (CH_3)_2CH$) clustering equilibria.

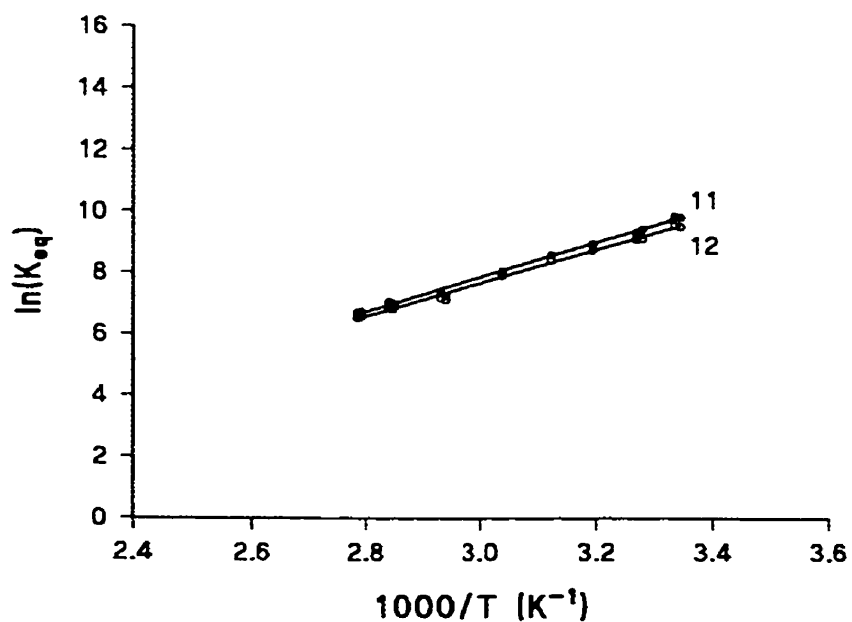


Figure 5.31 Van't Hoff plots for the $Cl^{-}(S) + RCl \rightleftharpoons (S)Cl^{-}(RCl)$ and $Cl^{-}(RCl) + S \rightleftharpoons (S)Cl^{-}(RCl)$ ($S = CH_3CF_2H$; $R = (CH_3)_2CH$) clustering equilibria.

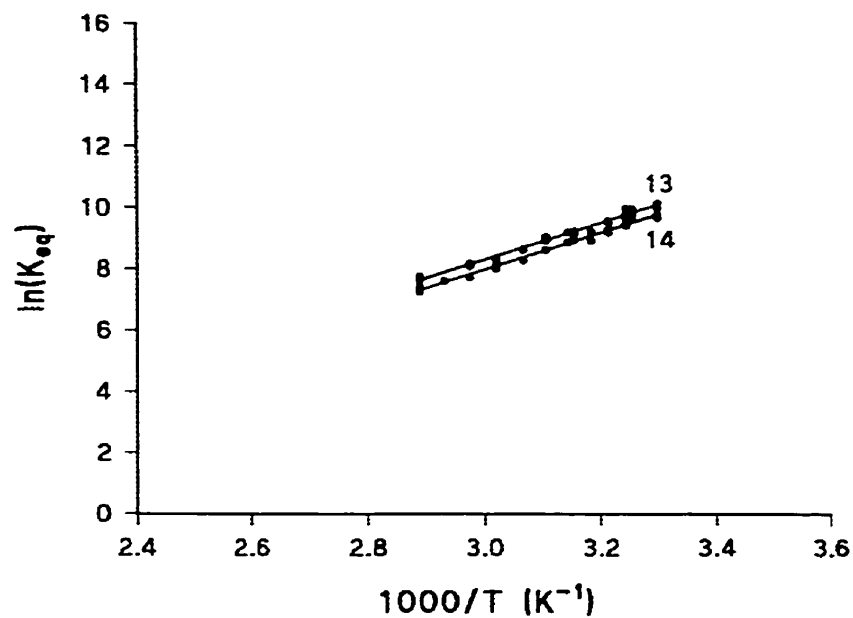


Figure 5.32 Van't Hoff plots for the $Cl^{-}(S) + RBr \rightleftharpoons (S)Cl^{-}(RBr)$ and $Cl^{-}(RBr) + S \rightleftharpoons (S)Cl^{-}(RBr)$ ($S = CH_3OH$; $R = (CH_3)_2CH$) clustering equilibria.

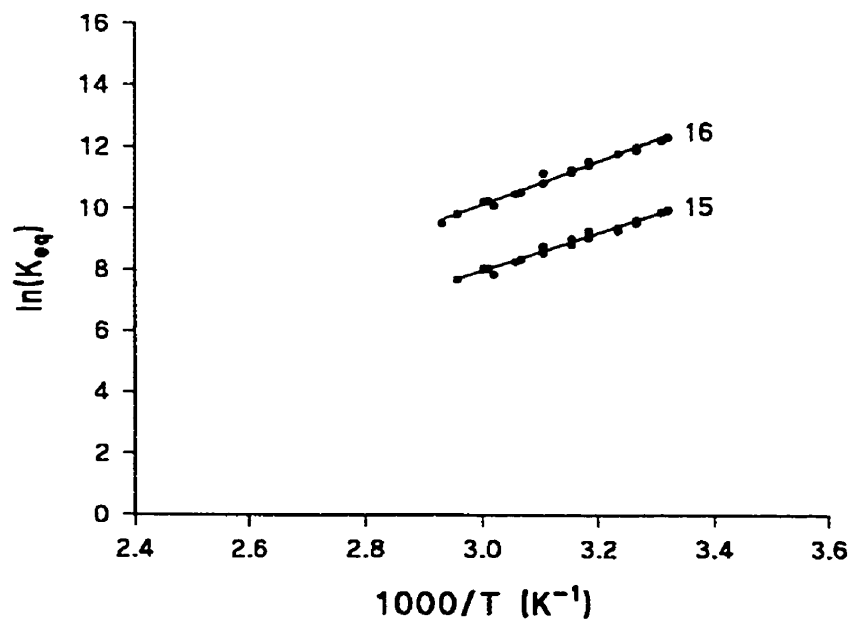


Figure 5.33 Van't Hoff plots for the $Cl^{-}(S) + RBr \rightleftharpoons (S)Cl^{-}(RBr)$ and $Cl^{-}(RBr) + S \rightleftharpoons (S)Cl^{-}(RBr)$ ($S = CH_3CN$; $R = (CH_3)_2CH$) clustering equilibria.

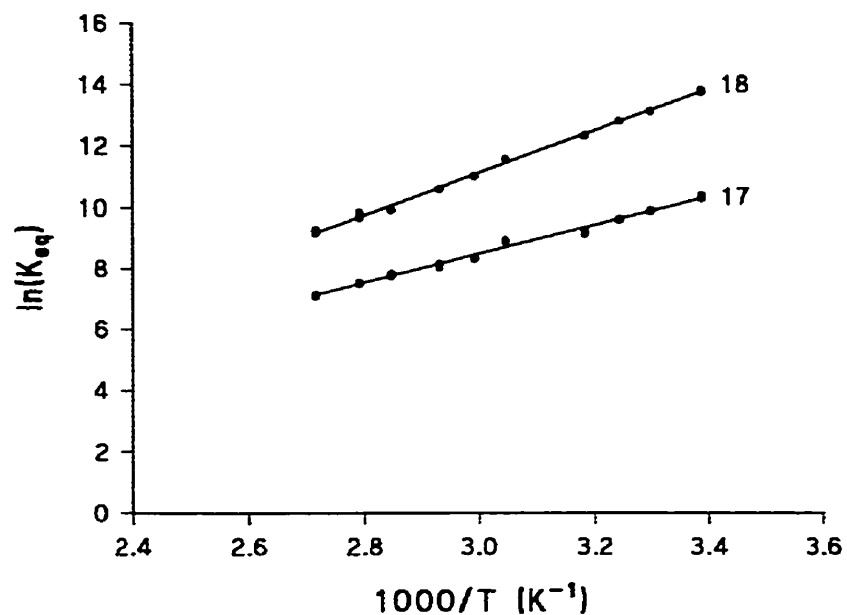


Figure 5.34 Van't Hoff plots for the $Cl^{-}(S) + RBr \rightleftharpoons (S)Cl^{-}(RBr)$ and $Cl^{-}(RBr) + S \rightleftharpoons (S)Cl^{-}(RBr)$ ($S = (CH_3)_2CO$; $R = (CH_3)_2CH$) clustering equilibria.

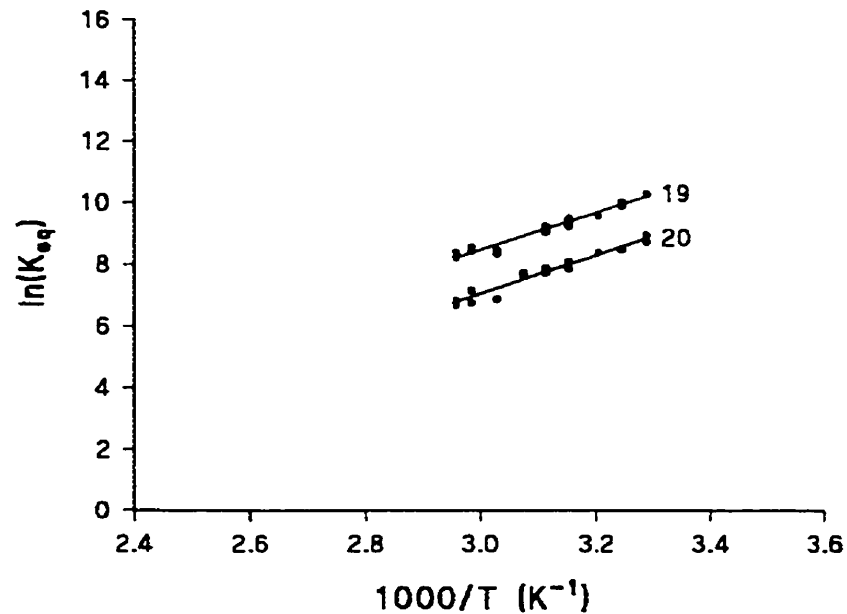
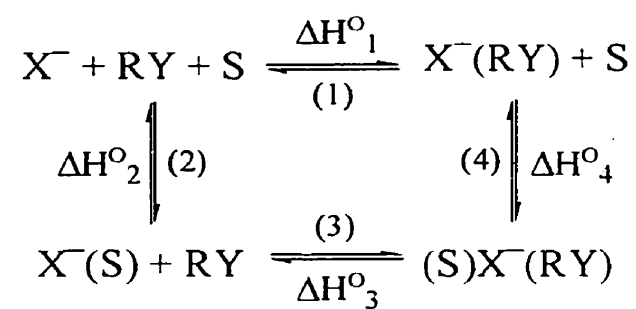


Figure 5.35 Van't Hoff plots for the $Cl^{-}(S) + RBr \rightleftharpoons (S)Cl^{-}(RBr)$ and $Cl^{-}(RBr) + S \rightleftharpoons (S)Cl^{-}(RBr)$ ($S = CH_3CF_2H$; $R = (CH_3)_2CH$) clustering equilibria.

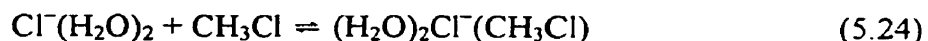


$$\Delta H^{\circ}_1 + \Delta H^{\circ}_4 = \Delta H^{\circ}_2 + \Delta H^{\circ}_3$$

Figure 5.36 Thermochemical cycle for the formation of solvated S_N2 complexes.

from the MP2/b//MP2/a and G2(MP2) computations and ΔH° values from PHPMS experiments are good to excellent. This gave confidence that the results from the MP2/b//MP2/a for the solvated S_N2 systems should give reliable results and trends. For the ΔS°_{298} values from HF/a computations and ΔH° values from PHPMS experiments the agreement is very much system dependent. Systems containing bromine and iodine atoms gave varying results. For most systems studied, the agreement with other available computational data was good.

In Table 5.11 the ΔH°_{298} values for the formation of solvated S_N2 complexes from the MP2/b//MP2/a computations are shown. For these weakly bound systems the calculated ΔS°_{298} values show large inconsistencies with the experimental PHPMS data. The low frequency intermolecular vibrational modes, and their anharmonic character are likely causing the discrepancies, and consequently the ΔS°_{298} values have been omitted. As expected, all values confirm the thermochemical cycle in Figure 5.36. As already mentioned in Section 5.4.1, some structural changes can take place in the $X^-(RY)$ complexes after attachment by a solvent molecule, and this may give rise to unexpected ΔH° and ΔS° values. Tucker and Truhlar found for Reaction 5.23 at the MP2/6-31G(d,p) level of theory a ΔH°_{298} value of $-10.1 \text{ kcal mol}^{-1}$, while for Reaction 5.24 a ΔH°_{298} value of $-9.3 \text{ kcal mol}^{-1}$ was obtained.³³



No other computations with solvents other than water are available for the $X^-(S) + RY$ reactions.

In Table 5.12 the results of the ΔH^\ddagger_{298} values for the progress from the reactants to the transition states for some (un)solvated S_N2 reactions (Reactions 5.25 and 5.26) are presented.

Table 5.10 Overview of the computational and experimental literature thermochemical data for the $X^- + S \rightleftharpoons X^-(S)$ and $X^- + CH_3Y \rightleftharpoons X^-(CH_3Y)$ ($X = Cl, Br$; $S = H_2O, H_2S, NH_3, PH_3, SO_2, CH_3OCH_3$; $Y = Cl, Br, I$) clustering equilibria.

clustering equilibrium	ΔH°_{298} ^a		ΔH° ^a	ΔS°_{298} ^b		ΔS° ^b
	MP2/MP2	G2(MP2)		PHPMS	HF	
$Cl^- + H_2O \rightleftharpoons Cl^-(H_2O)$	-14.5	-14.2	-14.7 ^d	-17.5		-19.7 ^d
$Cl^- + H_2S \rightleftharpoons Cl^-(H_2S)$	-12.8	-12.5		-17.5		
$Cl^- + NH_3 \rightleftharpoons Cl^-(NH_3)$	-8.1	-8.0	-8.2 ^e	-14.9		-15.4 ^e
$Cl^- + PH_3 \rightleftharpoons Cl^-(PH_3)$	-5.3	-6.0		-14.0		
$Cl^- + SO_2 \rightleftharpoons Cl^-(SO_2)$	-21.3	-21.8	-22.2 ^e	-21.4		-21.6 ^e
$Cl^- + CH_3OCH_3 \rightleftharpoons Cl^-(CH_3OCH_3)$	-7.6		-7.5 ^f	-19.0 ^c		-15.3 ^f
$Cl^- + CH_3Cl \rightleftharpoons Cl^-(CH_3Cl)$	-10.4	-10.7	-10.4 ^g	-14.6		-15.3 ^g

^a kcal mol⁻¹ ^b cal mol⁻¹ K⁻¹ ^c MP2/a ^d from reference 68

^e from reference 69 ^f from reference 70 ^g from reference 63

^h from references 71 and 72

Table 5.10 (continued)

clustering equilibrium	ΔH^0_{298} ^a		ΔH^0 ^a	ΔS^0_{298} ^b	
	MP2//MP2	G2(MP2)	PHPMS	HF	PHPMS
$\text{Cl}^- + \text{CH}_3\text{Br} \rightleftharpoons \text{Cl}^-(\text{CH}_3\text{Br})$	-10.4		-12.5 ^g	-14.9	
$\text{Cl}^- + \text{CH}_3\text{I} \rightleftharpoons \text{Cl}^-(\text{CH}_3\text{I})$	-7.6		-9.8 ^h	-14.9 ^c	
$\text{Br}^- + \text{H}_2\text{O} \rightleftharpoons \text{Br}^-(\text{H}_2\text{O})$	-13.2		-11.7 ^d	-16.4	-14.7 ^d
$\text{Br}^- + \text{CH}_3\text{Cl} \rightleftharpoons \text{Br}^-(\text{CH}_3\text{Cl})$	-10.7		-10.9 ^g	-13.6	-20.3 ^g

170

^a kcal mol⁻¹ ^b cal mol⁻¹ K⁻¹ ^c MP2/a ^d from reference 68

^e from reference 69 ^f from reference 70 ^g from reference 63

^h from references 71 and 72

Table 5.11 Overview of the computational MP2//MP2 ΔH_{298}° values for the $X^{-}(S) + CH_3Y = (S)X^{-}(CH_3Y)$ and $X^{-}(CH_3Y) + S = (S)X^{-}(CH_3Y)$ ($X = Cl, Br$; $S = H_2O, H_2S, NH_3, PH_3, SO_2, CH_3OCH_3$; $Y = Cl, Br, I$) clustering equilibria.

clustering equilibrium	ΔH_{298}° ^a
	MP2//MP2
$Cl^{-}(H_2O) + CH_3Cl = (H_2O)Cl^{-}(CH_3Cl)$	-8.5
$Cl^{-}(CH_3Cl) + H_2O = (H_2O)Cl^{-}(CH_3Cl)$	-12.6
$Cl^{-}(H_2S) + CH_3Cl = (H_2S)Cl^{-}(CH_3Cl)$	-8.3
$Cl^{-}(CH_3Cl) + H_2S = (H_2S)Cl^{-}(CH_3Cl)$	-10.7
$Cl^{-}(NH_3) + CH_3Cl = (NH_3)Cl^{-}(CH_3Cl)$	-8.9
$Cl^{-}(CH_3Cl) + NH_3 = (NH_3)Cl^{-}(CH_3Cl)$	-6.6
$Cl^{-}(PH_3) + CH_3Cl = (PH_3)Cl^{-}(CH_3Cl)$	-9.6
$Cl^{-}(CH_3Cl) + PH_3 = (PH_3)Cl^{-}(CH_3Cl)$	-4.5
$Cl^{-}(SO_2) + CH_3Cl = (SO_2)Cl^{-}(CH_3Cl)$	-9.1
$Cl^{-}(CH_3Cl) + SO_2 = (SO_2)Cl^{-}(CH_3Cl)$	-20.0
$Cl^{-}(H_2O) + CH_3Br = (H_2O)Cl^{-}(CH_3Br)$	-8.3
$Cl^{-}(CH_3Br) + H_2O = (H_2O)Cl^{-}(CH_3Br)$	-12.4
$Cl^{-}(CH_3OCH_3) + CH_3I = (CH_3OCH_3)Cl^{-}(CH_3I)$	-9.8
$Cl^{-}(CH_3I) + CH_3OCH_3 = (CH_3OCH_3)Cl^{-}(CH_3I)$	-7.1
$Br^{-}(H_2O) + CH_3Cl = (H_2O)Br^{-}(CH_3Cl)$	-8.4
$Br^{-}(CH_3Cl) + H_2O = (H_2O)Br^{-}(CH_3Cl)$	-10.9

^a kcal mol⁻¹

Table 5.12 Overview of the computational MP2//MP2 ΔH^\ddagger_{298} and experimental ΔH^\ddagger values for the $X^- + CH_2YZ \rightarrow [XCH_2ZY]^-$ and $X^-(S) + CH_2YZ \rightarrow [(S)XCH_2ZY]^-$ ($X = Cl, Br$; $Y = Cl, Br$; $I; Z = H, CN$; $S = H_2O, H_2S, NH_3, PH_3, SO_2, CH_3OCH_3$) reactions.

reaction	ΔH^\ddagger_{298} ^a	
	MP2//MP2	experiment
$Cl^- + CH_3Cl \rightarrow [ClCH_3Cl]^-$	+4.5	+1.0 ± 1.0 ^b , +3.1 ^c , +2.5 ^d , 2.9 ± 1.0 ^e
$Cl^- + CH_3Br \rightarrow [ClCH_3Br]^-$	+2.9	-1.8 ^f , -1.8 ^g , -1.7 ^e , -1.5 ^h , -1.1 ^d , -4.7 ⁱ
$Cl^- + CH_3I \rightarrow [ClCH_3I]^-$	-0.1	-4.6 ± 0.5 ^e , -2.7 ^j
$Cl^- + CH_2CNBr \rightarrow [ClCH_2CNBr]^-$	-5.6	-9.8, -6.1 ^d
$Br^- + CH_3Cl \rightarrow [ClCH_3Br]^-$	+3.1	+5.7 ^g
$Br^- + CH_2CNCl \rightarrow [ClCH_2CNBr]^-$	-6.5	
$Cl^-(H_2O) + CH_3Cl \rightarrow [(H_2O)ClCH_3Cl]^-$	+9.0	
$Cl^-(H_2S) + CH_3Cl \rightarrow [(H_2S)ClCH_3Cl]^-$	+9.3	
$Cl^-(NH_3) + CH_3Cl \rightarrow [(NH_3)ClCH_3Cl]^-$	+7.2	
$Cl^-(PH_3) + CH_3Cl \rightarrow [(PH_3)ClCH_3Cl]^-$	+7.3	

^a kcal mol⁻¹

Table 5.12 (continued)

reaction	$\Delta H^\ddagger_{298}{}^a$	
	MP2//MP2	experiment
$\text{Cl}^-(\text{SO}_2) + \text{CH}_3\text{Cl} \rightarrow [(\text{SO}_2)\text{ClCH}_3\text{Cl}]^-$	+15.5	
$\text{Cl}^-(\text{H}_2\text{O}) + \text{CH}_3\text{Br} \rightarrow [(\text{H}_2\text{O})\text{ClCH}_3\text{Br}]^-$	+7.0	
$\text{Cl}^-(\text{H}_2\text{O}) + \text{CH}_2\text{CNBr} \rightarrow [(\text{H}_2\text{O})\text{ClCH}_2\text{CNBr}]^-$	-1.3	
$\text{Br}^-(\text{H}_2\text{O}) + \text{CH}_3\text{Cl} \rightarrow [\text{ClCH}_3\text{Br}(\text{H}_2\text{O})]^-$	+6.1	

^a kcal mol⁻¹

^b from reference 73

^c from reference 74

^d from reference 75

^e from reference 76

^f from reference 77

^g from reference 63

^h from reference 78

ⁱ from reference 25

^j from reference 79



The values listed for Reactions 5.25 show reasonable to good agreement between available experimental and computational data. It can be seen that the ΔH^\ddagger_{298} values for $S = H_2O$ and H_2S are almost identical, and the same is true for $S = NH_3$ and PH_3 .

Tucker and Truhlar found a ΔH^\ddagger_{298} value of +5.4 kcal mol⁻¹ for Reaction 5.27 at the MP2/6-31G(d,p) level of theory, while for Reaction 5.28 a value of +10.7 kcal mol⁻¹ was obtained.³³



Introducing more solvent molecules will give rise to more solvated transition states as shown by Morokuma.²⁷ For instance, for Reaction 5.28 the isomeric $[(H_2O)ClCH_3Cl(H_2O)]^-$ transition state would also be a valid alternative. A different picture emerges if instead of ΔH^\ddagger_{298} for Reaction 5.26 one takes ΔH^0_{298} for Reaction 5.29.



For $S = H_2O, H_2S, NH_3, PH_3,$ and SO_2 , ΔH^0_{298} values of -9.9, -8.0, -5.3, -2.4, and -11.2 kcal mol⁻¹, respectively, can be found. By plotting the $-\Delta H^0_{298}$ values for Reaction 5.30 versus the $-\Delta H^0_{298}$ values of Reactions 5.29 and 5.31, Figure 5.37 is obtained.



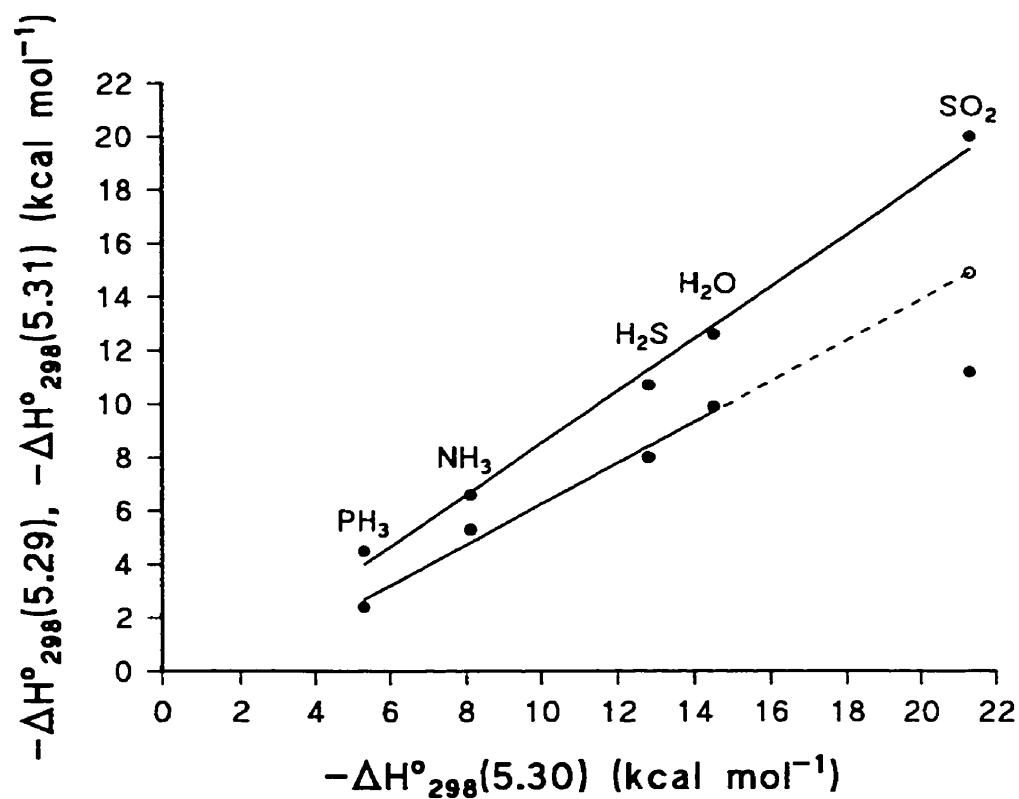
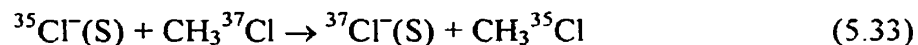


Figure 5.37 Plot of $-\Delta H^\circ_{298}$ for the formation of $\text{Cl}^-(\text{S})$ versus $-\Delta H^\circ_{298}$ for the formation of $(\text{S})\text{Cl}^-(\text{CH}_3\text{Cl})$ and $[(\text{S})\text{ClCH}_3\text{Cl}]^-$ ($\text{S} = \text{H}_2\text{O}, \text{H}_2\text{S}, \text{NH}_3, \text{PH}_3, \text{SO}_2$) (the open circle and dotted line represent the expected value and trend line for $\text{S} = \text{SO}_2$ based on the other four solvent molecules).



Interestingly, both plots appear to show a linear correlation, except for the transition state solvation by SO_2 . From the slopes of the two lines it is confirmed that the solvation of the transition state is less exothermic than the solvation of the $\text{S}_{\text{N}}2$ ion-molecule complex, which is less exothermic than the solvation of the solvent molecule. In Figure 5.38 all data for Reactions 5.14-5.16 from Tables 5.10-5.12 are shown together as schematic potential energy profiles. For all hydrogen bonded solvents, except PH_3 , and SO_2 the transition states $[(\text{S})\text{ClCH}_3\text{Cl}]^-$ are lower in $\Delta\text{H}^\circ_{298}$ than $\text{Cl}^- + \text{CH}_3\text{Cl} + \text{S}$. This means that it would be possible to kinetically excite $^{35}\text{Cl}^-(\text{S})$ for instance and watch for the formation of $^{37}\text{Cl}^-$ or $^{37}\text{Cl}^-(\text{S})$ from CH_3Cl (Reactions 5.32 and 5.33).



Unfortunately, at lower centre-of-mass ion kinetic energies for $^{35}\text{Cl}^-(\text{S})$, chloride ion transfer to CH_3Cl will occur (Reaction 5.34). Furthermore, this is not a direct method to obtain $\Delta\text{H}^\ddagger_{298}$, since it requires *ab initio* input parameters to fit the cross-sections as a function of the centre-of-mass kinetic energies in order to obtain the threshold energy. In addition, because of the competition of Reaction 5.34 with Reactions 5.32 and 5.33, the cross-sections of the latter two reaction will be very small.



For the water mono-solvated transition state of $[\text{ClCH}_3\text{Br}]^-$, two isomers are possible, $[(\text{H}_2\text{O})\text{ClCH}_3\text{Br}]^-$ and $[(\text{H}_2\text{O})\text{BrCH}_3\text{Cl}]^-$. At the MP2/[b/e]/MP2/[c/d] level

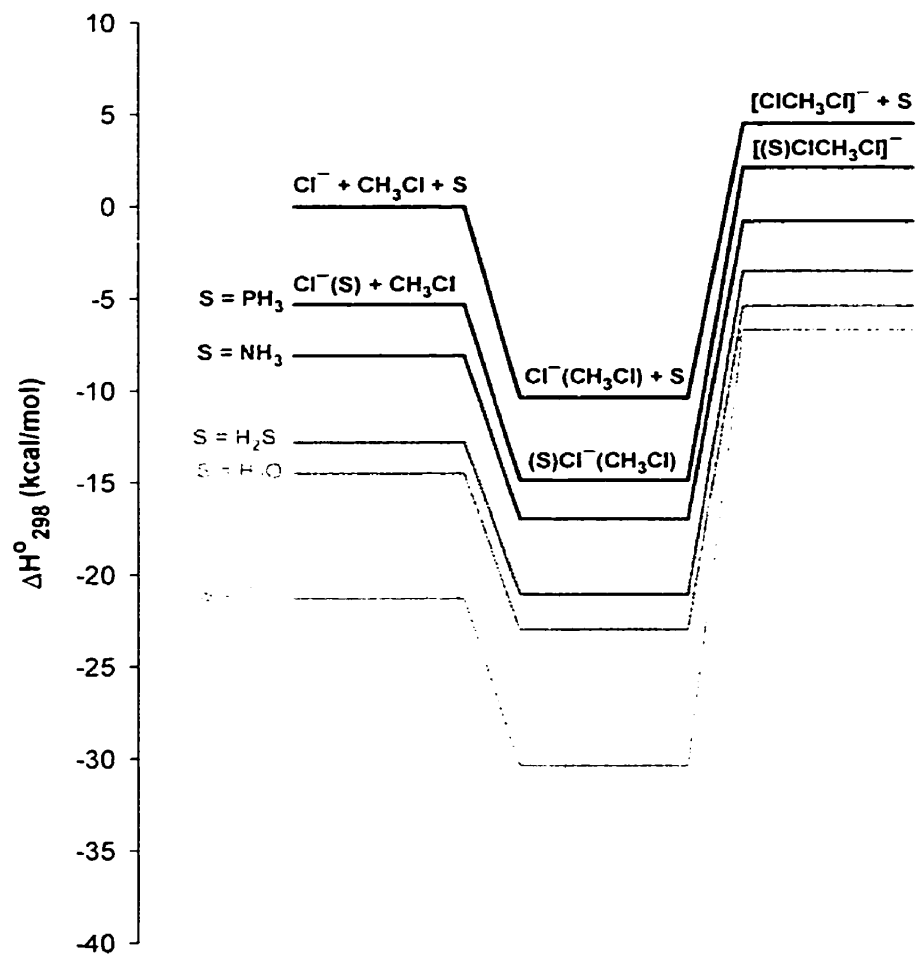


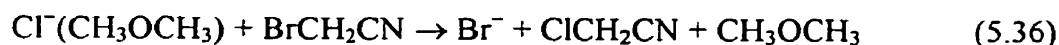
Figure 5.38 Schematic MP2/b//MP2/a potential energy profiles for the $\text{Cl}^- + \text{CH}_3\text{Cl}$ and $\text{Cl}^-(\text{S}) + \text{CH}_3\text{Cl}$ reactions ($\text{S} = \text{H}_2\text{O}, \text{H}_2\text{S}, \text{NH}_3, \text{PH}_3, \text{SO}_2$).

of theory, including zero-point energies and thermal corrections at the MP2/[c/d] level of theory, the first one is only 0.4 kcal mol⁻¹ more favorable. Still the barrier, if present, for the water transfer reaction will be expected to be considerably higher in ΔG°_{298} , mainly due to the unfavorable entropy associated with the bridged transition state for water transfer. Seeley *et al.* found an activation energy for Reaction 5.35 of +2.7 kcal mol⁻¹.²⁵



By correcting the calculated activation energy (+2.9 kcal mol⁻¹) for the non-solvated S_N2 reaction to match the experimental value of -1.8 kcal mol⁻¹, and applying this correction to the calculated activation energy for Reaction 5.35 a value of +2.5 kcal mol⁻¹ is obtained. Even though the agreement is close, the values cannot be compared since they represent different processes. From the potential energy surface in Section 5.4.4 it can be seen that ligand switching is indeed energetically more favorable than the solvated S_N2 reaction.

The main question is, are there, besides the already observed solvated S_N2 mentioned in Section 5.1, other systems possible for which true solvated S_N2 reactions can be observed? Good candidates might be Reactions 5.36 and 5.37.



Both reactions have, in their unsolvated counterparts, negative ΔH^\ddagger values. From Table 5.12 it can be seen that Reaction 5.35 with water as a solvent has a ΔH^\ddagger_{298} value, calculated at the MP2/[b/e]/MP2/[a/d] level of theory, of -0.1 kcal mol⁻¹. Any monosolvated S_N2 reaction will proceed through the (S)X⁻(RY) ion-molecule complex, but unless the solvent molecule donates X⁻ to RY, no S_N2 reaction will take place. In other words, RY should have a larger X⁻ affinity than S. In addition, the

transition state $[(S)XRY]^\ddagger$ should be below the reactants $X^-(S)$ and RY , and the overall energetics of the reaction should be fairly exothermic. This means that overall solvent transfer from X^- to Y^- will favor the reaction, but the reaction may still proceed if this does not take place. In the case of the most commonly used solvent, water, X^- binds more strongly to it than most S_N2 substrates. Consequently, the probability of passing through the ion-molecule complex and transition state will be low. For solvated S_N2 reactions with barriers slightly above the reactants, it should still be possible to observe them by performing these reactions at elevated temperatures. Problems may arise if the solvated nucleophile dissociates by ZTRID, and one would actually observe the non-solvated S_N2 reaction (Reactions 5.38 and 5.39).



This problem can be solved by continuously ejecting X^- from the FT-ICR cell, thus preventing Reaction 5.39 from taking place. Dimethyl ether and diethyl ether bind less strongly to chloride ion than do methyl iodide and bromoacetonitrile, and so they would be ideal candidates. By performing the reactions at different temperatures and measuring the rate constants, the activation energy, E_a , and frequency factor, A , can be obtained from the Arrhenius equation (Equation 5.40), and from these, the ΔH^\ddagger and ΔS^\ddagger (Equations 5.41 and 5.42) can be calculated.

$$\ln(k) = \ln(A) - \frac{E_a}{RT} \quad (5.40)$$

$$E_a = \Delta H^\ddagger + RT \sum n_R^\ddagger \quad (5.41)$$

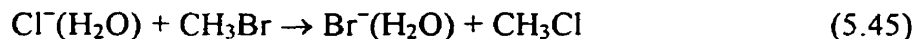
$$A = \frac{kT}{h} \cdot \exp\left(\frac{-\Delta S^\ddagger}{R}\right) \quad (5.42)$$

It does not seem unreasonable to assume that monosolvated S_N2 reactions in the gas phase, even if possible to perform, are the closest one can get to the condensed phase counterparts. Obtaining reliable experimental data is the only possibility to test computational methods, which are very method and/or system dependent and already approach the limit of what is computationally possible. The reactivity of most larger clusters investigated to date shows that no S_N2 processes are taking place.

Producing less strongly bound clusters that will still show some reactivity seems unlikely, especially if one wishes to investigate mechanistic features. Still, this kind of research will be useful and may contribute to renewed interest and research.

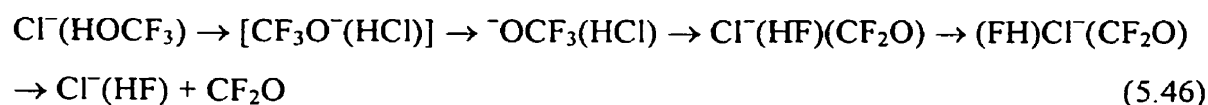
5.4.4 Potential Energy Surfaces

In Figure 5.39 the results for the potential energy surface scans for Reactions 5.43-5.45 are shown.



For the reaction coordinate the difference in the C–Br and C–Cl distances was taken. For Reaction 5.43 the expected profile has been obtained, even though the barrier height relative to the reactants does not seem to agree with experimental data, and with various computational results that support the experimental data. Tureček and co-workers found that accurate PA's can be determined by taking the average PA of two MP2 and B3LYP computations.^{65,66} The reason for this was the fact that, in general, MP2 overestimates the PA, while B3LYP underestimates the PA. A similar

observation has been made for S_N2 transition state energies. For the $[\text{ClCH}_3\text{Br}]^-$ transition state, using the average of MP2/[b/e]//MP2/[c/d] and B3LYP/[b/e]//B3LYP/[c/d] computations, a ΔH_{298}^\ddagger value of $-1.5 \text{ kcal mol}^{-1}$ can be found, in excellent agreement with the experimental value of $-1.8 \text{ kcal mol}^{-1}$.⁶³ Similarly, for the $[\text{ClCH}_3\text{I}]^-$ transition state a value of $-3.9 \text{ kcal mol}^{-1}$ has been found. On the other hand, the main focus here was to obtain more qualitative insight. For Reactions 5.44 and 5.45, two different potential energy surfaces have been obtained, but the difference only appears on the product side. For Reaction 5.45 the same reaction coordinate can be used like for Reaction 5.43. For Reaction 5.44, on the other hand, going from $\text{Br}^-(\text{CH}_3\text{Cl})(\text{H}_2\text{O})$ to $(\text{H}_2\text{O})\text{Br}^-(\text{CH}_3\text{Cl})$ some reaction coordinate for the water transfer should be taken into account. This transfer can be viewed as a rotation of the $\text{Br}^-(\text{CH}_3\text{Cl})$ moiety of the complex. This seems to be an accessible alternative to the symmetric bridge-like transition state that connects the $[(\text{H}_2\text{O})\text{ClCH}_3\text{Br}]^-$ and $[\text{ClCH}_3\text{Br}(\text{H}_2\text{O})]^-$ transition states. The expected increase in the transition state for the solvated S_N2 reaction is clearly observable. The occurrence of rotations in ion-molecule clusters to facilitate isomerization is not uncommon. In Chapter 4 the unimolecular dissociation of the $\text{Cl}^-(\text{HOCF}_3)$ complex into $\text{Cl}^-(\text{HF})$ and CF_2O was mentioned. Close examination shows that this reaction takes place through a series of steps that include internal rotations in some of the intermediates (Scheme 5.46).



It does not seem unlikely, if the lifetime of the $\text{Y}^-(\text{RX})(\text{S})$ complex is long enough and excess internal energy can be redistributed efficiently, that isomerization to the more stable $(\text{S})\text{Y}^-(\text{RX})$ complex may become more feasible, and consequently the relative amount of observable solvated product ions, $\text{Y}^-(\text{S})$, may increase.

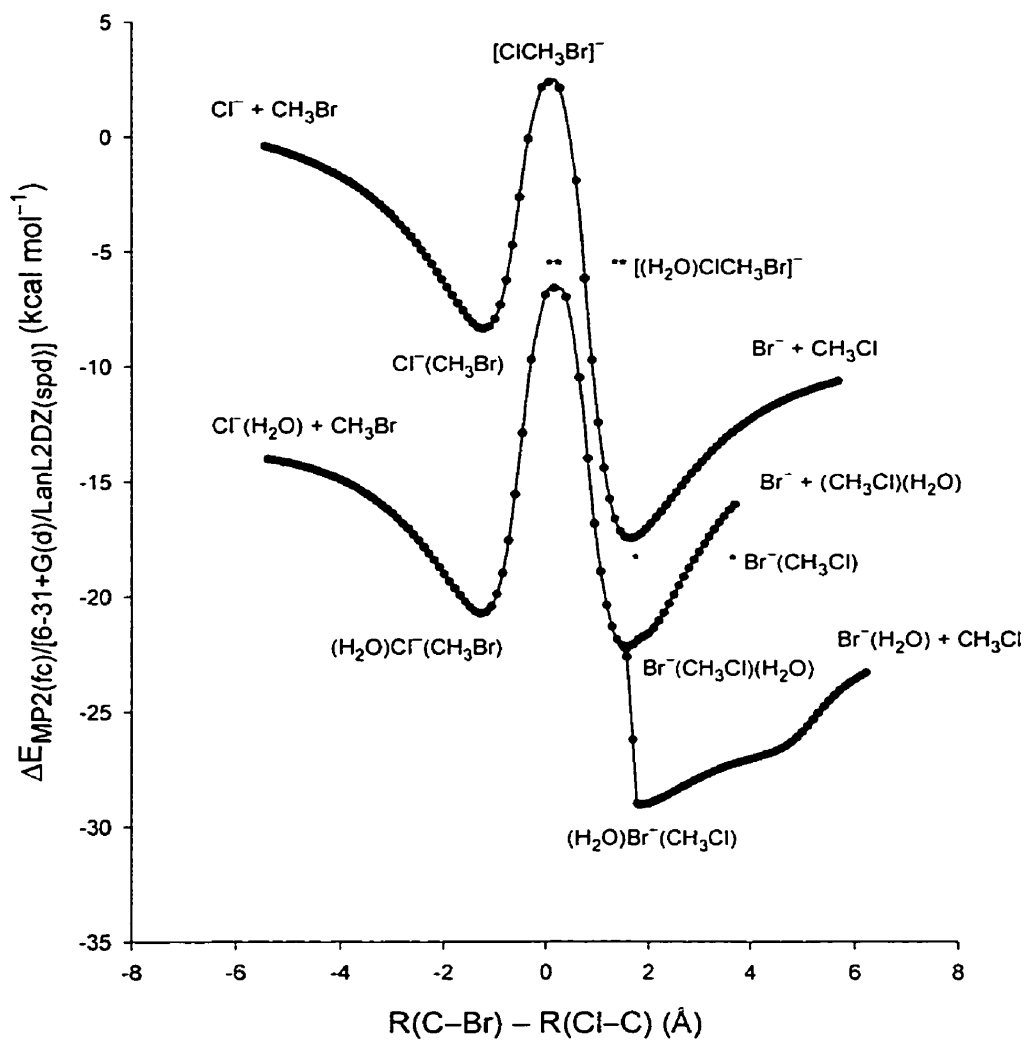


Figure 5.39 MP2[c/d] potential energy profiles for the $Cl^- + CH_3Br \rightarrow Br^- + CH_3Cl$ and $Cl^-(H_2O) + CH_3Br \rightarrow Br^- + (CH_3Cl)(H_2O)$ and $Br^-(H_2O) + CH_3Cl$ reactions.

5.5 Conclusions

In this chapter various aspects of the structures and thermochemistry of solvated S_N2 complexes and transition states have been investigated using PHPMS and *ab initio* computational methods.

The structures of solvated S_N2 complexes, $(S)X^-(CH_3Y)$, and transition states, $[(S)XCH_3Y]^-$, can show very different bonding characteristics than the halide ion-solvent, $X^-(S)$, and S_N2 complexes, $X^-(CH_3Y)$, depending on the solvent. In the $[(H_2O)ClCH_2CNBr]^-$ transition state, the water molecule interacts with the nitrogen atom of the cyano substituent.

The experimental thermochemistry shows solvent effects. The two different equilibria, solvation of S_N2 complexes and solvated S_N2 reactions, have different thermochemistry, and can be understood in terms of a thermochemical cycle. Most data presented are completely new, and may provide a basis to test theoretical models on these systems.

The MP2/b//MP2/a and G2(MP2) computations provide close agreement with experimental thermochemical data for the formation of $X^-(S)$ complexes. The ΔH_{298}° values for the formation of the $(S)X^-(CH_3Cl)$ complexes investigated seem to be reasonable, as opposed to the ΔS_{298}° values. For both the non-solvated and solvated S_N2 transition states investigated, $[XCH_3Y]^-$ and $[(S)XCH_3Y]^-$, respectively, the MP2/b//MP2/a computations seem to overestimate the enthalpies of activation. Two test computations show that an average of B3LYP/b//B3LYP/a and MP2/b//MP2/a computations can provide reliable enthalpies of activation. Linear correlations between enthalpy changes for the formation of $Cl^-(S)$ ($S = H_2O, H_2S, NH_3, PH_3, SO_2$), and enthalpy changes and enthalpies of activation for the formation of $(S)Cl^-(CH_3Cl)$ and $[(S)ClCH_3Cl]^-$, respectively have been found, except for the enthalpy of activation with $S = SO_2$.

To date only a few systems have shown real solvated S_N2 reactivity, notably the $F^-(ROH) + CH_3X$ reactions ($R = H, \text{alkyl}; X = Br, I$). It is believed that reactions between $Cl^-(CH_3OCH_3)$ and CH_2CNBr and CH_3I may also show S_N2 reactivity.

The potential energy profiles for the solvated S_N2 reaction between $Cl^-(H_2O)$ and CH_3Br , calculated at the MP2/[c/d] level of theory, show that formation of Br^- and $Br^-(H_2O)$ proceed through two different profiles. Isomerization from $Br^-(CH_3Cl)(H_2O)$ to $(H_2O)Br^-(CH_3Cl)$ can be accomplished by a rotation of the $Br^-(CH_3Cl)$ moiety. This process is energetically favorable and may lead to a net solvent transfer.

5.6 References and Notes

- 1 Ingold, C. K. *Structure and Reactivity in Organic Chemistry*, 2nd ed., Cornell University Press, Ithaca, NY, 1969 and references cited therein.
- 2 Aziz, F.; Moelwyn-Hughes, E. A. *J. Chem. Soc.* **1959**, 2635.
- 3 Marshall, B. W.; Moelwyn-Hughes, E. A. *J. Chem. Soc.* **1959**, 2640.
- 4 Bathgate, R. H.; Moelwyn-Hughes, E. A. *J. Chem. Soc.* **1959**, 2642.
- 5 Alexander, R.; Ko, E. C. F.; Parker, A. J.; Broxton, T. J. *J. Am. Chem. Soc.* **1968**, *90*, 5049 and references cited therein.
- 6 Parker, A. J. *Chem. Rev.* **1969**, *69*, 1 and references cited therein.
- 7 Hartshorn, S. R. *Aliphatic Nucleophilic Substitution*, Cambridge University Press, London, 1973.
- 8 Streitweiser, Jr., A. *Solvolytic Displacement Reactions*, McGraw-Hill, New York, NY, 1973.
- 9 Alberty, W. J.; Kreevoy, M. M. *Adv. Phys. Org. Chem.* **1978**, *16*, 87 and references cited therein.
- 10 Shaik, S. S.; Schlegel, H. B.; Wolfe, S. *Theoretical Aspects of Physical Organic Chemistry. The S_N2 Mechanism*, Wiley, New York, NY, 1992 and references cited therein.
- 11 Bohme, D. K.; Mackay, G. I. *J. Am. Chem. Soc.* **1981**, *103*, 978.
- 12 Henschman, M.; Paulson, J. F.; Hierl, P. M. *J. Am. Chem. Soc.* **1983**, *105*, 5509.
- 13 Henschman, M.; Hierl, P. M.; Paulson, J. F. *J. Am. Chem. Soc.* **1985**, *107*, 2812.
- 14 Bohme, D. K.; Raksit, A. B. *J. Am. Chem. Soc.* **1984**, *106*, 3447.
- 15 Bohme, D. K.; Raksit, A. B. *Can. J. Chem.* **1985**, *63*, 3007.

- 16 Hierl, P. M.; Ahrens, A. F.; Henschman, M.; Viggiano, A. A.; Paulson, J. F.; Clary, D. C. *J. Am. Chem. Soc.* **1986**, *108*, 3142.
- 17 Hierl, P. M.; Ahrens, A. F.; Henschman, M.; Viggiano, A. A.; Paulson, J. F. *Int. J. Mass Spectrom. Ion Processes* **1987**, *81*, 101.
- 18 Hierl, P. M.; Ahrens, A. F.; Henschman, M. J.; Viggiano, A. A.; Paulson, J. F. *Faraday Discuss. Chem. Soc.* **1988**, *85*, 37.
- 19 Giles, K.; Grimsrud, E. P. *J. Phys. Chem.* **1993**, *97*, 1318.
- 20 O'Hair, R. A. J.; Davico, G. E.; Hacaloglu, J.; Dang, T. T.; DePuy, C. H.; Bierbaum, V. M. *J. Am. Chem. Soc.* **1994**, *116*, 3609.
- 21 Hierl, P. M.; Paulson, J. F.; Henschman, M. J. *J. Phys. Chem.* **1995**, *99*, 15655.
- 22 Viggiano, A. A.; Arnold, S. T.; Morris, R. A.; Ahrens, A. F.; Hierl, P. M. *J. Phys. Chem.* **1996**, *100*, 14397.
- 23 Craig, S. L.; Brauman, J. I. *J. Am. Chem. Soc.* **1996**, *118*, 6786.
- 24 Seeley, J. V.; Morris, R. A.; Viggiano, A. A. *J. Phys. Chem. A* **1997**, *101*, 4598.
- 25 Seeley, J. V.; Morris, R. A.; Viggiano, A. A.; Wang, H.; Hase, W. L. *J. Am. Chem. Soc.* **1997**, *119*, 577.
- 26 Craig, S. L.; Brauman, J. I. *J. Am. Chem. Soc.* **1999**, *121*, 6690.
- 27 Morokuma, K. *J. Am. Chem. Soc.* **1982**, *104*, 3732.
- 28 Hu, W.-P.; Truhlar, D. G. *J. Am. Chem. Soc.* **1994**, *116*, 7797.
- 29 Bickelhaupt, F. M.; Baerends, E. J.; Nibbering, N. M. M. *Chem. Eur. J.* **1996**, *2*, 196.
- 30 Tachikawa, H. *J. Phys. Chem. A* **2000**, *104*, 497.
- 31 Tachikawa, H. *J. Phys. Chem. A* **2001**, *105*, 1260.
- 32 Raugei, S.; Cardini, G.; Schettino, V. *J. Chem. Phys.* **2001**, *114*, 4089.
- 33 Tucker, S. C.; Truhlar, D. G. *J. Am. Chem. Soc.* **1990**, *112*, 3347.
- 34 Zhao, X. G.; Tucker, S. C.; Truhlar, D. G. *J. Am. Chem. Soc.* **1991**, *113*, 826.
- 35 Zhao, X. G.; Lu, D.-H.; Liu, Y.-P.; Lynch, G. C.; Truhlar, D. G. *J. Chem. Phys.* **1992**, *97*, 6369.
- 36 Re, M.; Laria, D. *J. Chem. Phys.* **1996**, *105*, 4584.
- 37 Okuno, Y. *J. Chem. Phys.* **1996**, *105*, 5817.
- 38 Okuno, Y. *J. Am. Chem. Soc.* **2000**, *122*, 2925.

- 39 Szulejko, J. E.; Fisher, J. J.; McMahon, T. B.; Wronka, J. *Int. J. Mass Spectrom. Ion Processes* **1988**, *83*, 147.
- 40 Frisch, M. J.; Trucks, G. W.; Schlegel, H. B.; Scuseria, G. E.; Robb, M. A.; Cheeseman, J. R.; Zakrzewski, V. G.; Montgomery, Jr., J. A.; Stratmann, R. E.; Burant, J. C.; Dapprich, S.; Millam, J. M.; Daniels, A. D.; Kudin, K. N.; Strain, M. C.; Farkas, O.; Tomasi, J.; Barone, V.; Cossi, M.; Cammi, R.; Mennucci, B.; Pomelli, C.; Adamo, C.; Clifford, S.; Ochterski, J.; Petersson, G. A.; Ayala, P. Y.; Cui, Q.; Morokuma, K.; Malick, D. K.; Rabuck, A. D.; Raghavachari, K.; Foresman, J. B.; Cioslowski, J.; Ortiz, J. V.; Baboul, A. G.; Stefanov, B. B.; Liu, G.; Liashenko, A.; Piskorz, P.; Komaromi, I.; Gomperts, R.; Martin, R. L.; Fox, D. J.; Keith, T.; Al-Laham, M. A.; Peng, C. Y.; Nanayakkara, A.; Gonzalez, C.; Challacombe, M.; Gill, M. W.; Johnson, B.; Chen, W.; Wong, M. W.; Andres, J. L.; Gonzalez, C.; Head-Gordon, M.; Replogle, E. S.; Pople, J. A. *Gaussian 98*, Revision A.7 Gaussian, Inc., Pittsburgh PA, **1998**.
- 41 Roothan, C. C. *J. Rev. Mod. Phys.* **1951**, *23*, 69.
- 42 Møller, C.; Plesset, M. S. *Phys. Rev.* **1934**, *46*, 618.
- 43 Hehre, W. J.; Ditchfield, R.; Pople, J. A. *J. Chem. Phys.* **1972**, *56*, 2257.
- 44 Francl, M. M.; Pietro, W. J.; Hehre, W. J.; Binkley, J. S.; Gordon, M. S.; DeFrees, D. J.; Pople, J. A. *J. Chem. Phys.* **1982**, *77*, 3654.
- 45 Clark, T.; Chandrasekhar, J.; Schleyer, P. v. R. *J. Comp. Chem.* **1983**, *4*, 294.
- 46 Krishnam, R.; Binkley, J. S.; Seeger, R.; Pople, J. A. *J. Chem. Phys.* **1980**, *72*, 650.
- 47 Gill, P. M. W.; Johnson, B. G.; Pople, J. A.; Frisch, M. J. *Chem. Phys. Lett.* **1992**, *97*, 499.
- 48 Scott, A. P.; Radom, L. *J. Phys. Chem.* **1996**, *100*, 16502.
- 49 From a least-squares fit of unscaled HF/6-31+G(d,p) normal mode vibrational frequencies of CH₃Cl, H₂O, H₂S, NH₃, PH₃, and SO₂ versus experimental frequencies from reference 50.
- 50 Shimanouchi, T. *Tables of Molecular Vibrational Frequencies Consolidated Volume I*; National Bureau of Standards: Washington, DC, **1972**; p. 1.
- 51 Frisch, M. J.; Pople, J. A.; Binkley, J. S. *J. Chem. Phys.* **1984**, *80*, 3265.
- 52 Hariharan, P. C.; Pople, J. A. *Theoretica Chim. Acta* **1973**, *28*, 213.

- 53 Hay, P. J.; Wadt, W. R. *J. Chem. Phys.* **1985**, *82*, 284.
- 54 Glukhovtsev, M. N.; Pross, A.; McGrath, M. P.; Radom, L. *J. Chem. Phys.* **1995**, *103*, 1878.
- 55 Curtiss, L. A.; Raghavachari, K.; Pople, J. A. *J. Chem. Phys.* **1993**, *94*, 7221.
- 56 *Gaussian 98 User's Reference*, Second Edition, Gaussian Inc., **1999**.
- 57 *CRC Handbook of Chemistry and Physics, Ref. Data*, 76th ed., Lide, D. R., Ed.; CRC, Boca Raton, FL, **1995**.
- 58 Deng, L.; Branchadell, V.; Ziegler, T. *J. Am. Chem. Soc.* **1994**, *116*, 10645 and references cited therein.
- 59 Glukhovtsev, M. N.; Pross, A.; Radom, L. *J. Am. Chem. Soc.* **1995**, *117*, 2024 and references cited therein.
- 60 Glukhovtsev, M. N.; Bach, R. D.; Pross, A.; Radom, L. *Chem. Phys. Lett.* **1996**, *260*, 558.
- 61 Glukhovtsev, M. N.; Pross, A.; Radom, L. *J. Am. Chem. Soc.* **1996**, *118*, 6273 and references cited therein.
- 62 Parthiban, S.; de Oliveira, G.; Martin, J. M. L. *J. Phys. Chem. A* **2001**, *105*, 895 and references cited therein.
- 63 Li, C.; Ross, P.; Szulejko, J. E.; McMahon, T. B. *J. Am. Chem. Soc.* **1996**, *118*, 9360.
- 64 <http://webbook.nist.gov/chemistry/>
- 65 Tureček, F. *J. Phys. Chem. A* **1998**, *102*, 4703.
- 66 Polášek, M.; Tureček, F. *J. Am. Soc. Mass Spectrom.* **2000**, *11*, 380.
- 67 Bogdanov, B.; Peschke, M.; Tonner, D. S.; Szulejko, J. E.; McMahon, T. B. *Int. J. Mass Spectrom.* **1999**, *185/186/187*, 707.
- 68 Hiraoka, K.; Mizuse, S.; Yamabe, S. *J. Phys. Chem.* **1988**, *92*, 3943.
- 69 Evans, D. H.; Keese, R. G.; Castleman, Jr., A. W. *J. Chem. Phys.* **1987**, *86*, 2927.
- 70 Bogdanov, B.; Lee, H. J. S.; McMahon, T. B. Accepted in *Int. J. Mass Spectrom.*
- 71 Dougherty, R. C.; Dalton, J.; Roberts, J. D. *Org. Mass Spectrom.* **1974**, *8*, 77.
- 72 Dougherty, R. C.; Roberts, J. D. *Org. Mass Spectrom.* **1974**, *8*, 81.
- 73 Barlow, S. E.; Van Doren, J. M.; Bierbaum, V. M. *J. Am. Chem. Soc.* **1988**, *110*, 7240.

- 74 Tucker, S. C.; Truhlar, D. G. *J. Am. Chem. Soc.* **1990**, *112*, 3338.
- 75 Wladkowski, B. D.; Brauman, J. I. *J. Phys. Chem.* **1993**, *97*, 13158.
- 76 Graul, S. T.; Bowers, M. T. *J. Am. Chem. Soc.* **1994**, *116*, 3875.
- 77 Caldwell, G.; Magnera, T. F.; Kebarle, P. *J. Am. Chem. Soc.* **1984**, *106*, 959.
- 78 Knighton, W. B.; Bogner, J. A.; O'Connor, P. M.; Grimsrud, E. P. *J. Am. Chem. Soc.* **1993**, *115*, 22079.
- 79 Hu, W.-P.; Truhlar, D. G. *J. Am. Chem. Soc.* **1995**, *117*, 10726.

Chapter 6

Gas phase S_N2 reactions of halide ions and trifluoromethyl halides: front- and backside attack versus complex formation

6.1 Introduction

Bimolecular nucleophilic displacement (S_N2) reactions in the gas phase between halide ions and halomethanes (Reaction 6.1) have been studied extensively for over three decades, both experimentally¹⁻²⁵ and theoretically, by both electronic structure²⁶⁻⁴⁷ and trajectory⁴⁸⁻⁶⁹ computations. In the condensed phase this type of reaction had already received substantial attention from the 1930's on.⁷⁰⁻⁷³



In Figure 6.1 a typical schematic potential energy profile is shown for a condensed phase S_N2 reaction. Due to the high central barrier of 15-30 kcal mol⁻¹, most reactions proceed very slowly. This is mainly caused by strong solvation effects, which are masking the intrinsic reactivity of the species involved. By performing S_N2 reactions in the gas phase, information on energetics, dynamics, and kinetics can be obtained, thereby exposing the role of the solvent in condensed phase reactions. Many experiments and computations have shown that in the gas phase S_N2 reactions proceed through a double-well potential,⁶ as shown in Figure 6.2. A large variety of rates and reaction efficiencies have been observed and these are mainly due to variations in the central barrier height relative to the reactants.

Reaction 6.1 proceeds by three consecutive, elementary processes: (1) formation of an entrance channel ion-molecule complex from the reactants (Reaction 6.2);



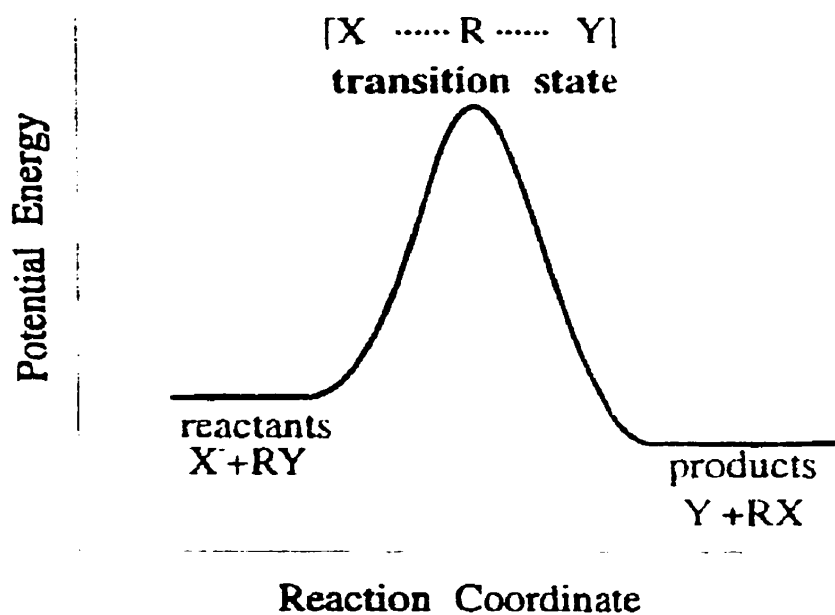


Figure 6.1 Hypothetical potential energy profile for a condensed phase S_N2 reaction.

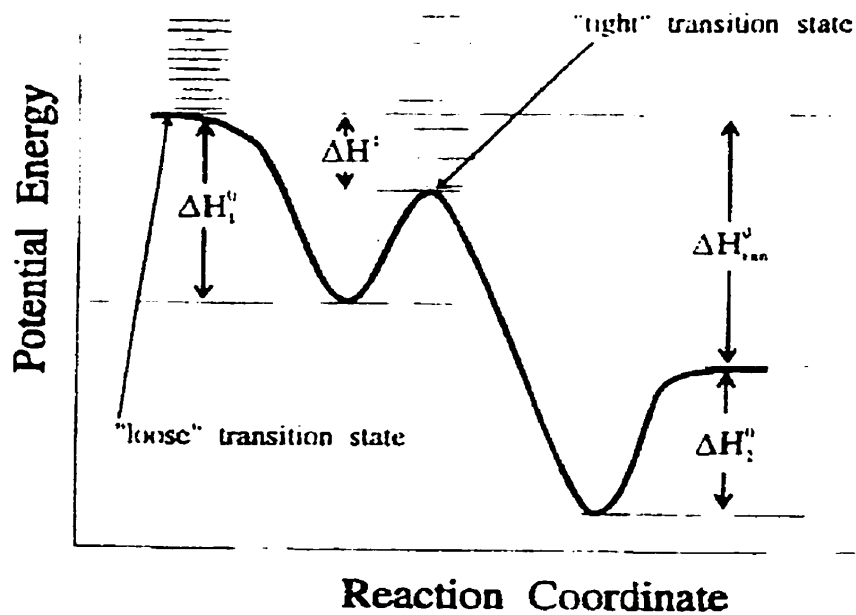


Figure 6.2 Hypothetical potential energy profile for a gas phase S_N2 reaction.

(2) conversion of the entrance channel ion-molecule complex to the exit channel ion-molecule complex through a transition state (Reaction 6.3);



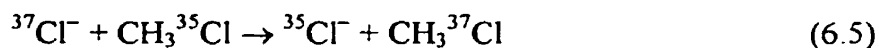
(3) dissociation of the exit channel ion-molecule complex into the products (Reaction 6.4).



The transition state is represented by $[XCH_3Y]^-$, indicating synchronous formation and breaking of the X-C and C-Y bonds, respectively. Under thermal and low-pressure conditions S_N2 reactions proceed through the so-called back-side attack mechanism as indicated by Reaction 6.2.

From many experiments and trajectory computations it has been shown that the energy redistribution in the entrance channel ion-molecule complex may be non-statistical.^{13,15,16,49,52-54, 56,60,63,74-78} This is mainly due to the short life-time, and the poor energy transfer between the intermolecular and intramolecular vibrational modes in certain cases. As a consequence of this the neutral CH_3X product is often in vibrationally excited states.^{13,77}

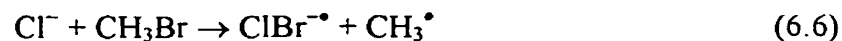
Barlow *et al.* studied the rate coefficients of Reaction 6.5 as a function of the kinetic energy of $^{37}Cl^-$ using a flowing afterglow-selected ion flow tube (FA-SIFT) instrument, and observed an exponential increase going from 0.4 to 2.0 eV.⁷⁹



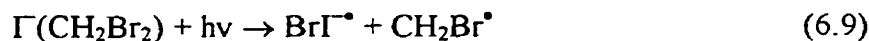
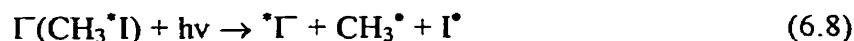
This was explained by assuming a higher energy mechanism with a $[CH_3^{35}Cl^{37}Cl]^-$ transition state, in which the two chlorine atoms are equivalent. The possibility of this so-called front-side attack mechanism has been also confirmed experimentally by Johnson

and co-workers,^{11,80-83} and by Ervin and co-workers,¹⁵ and theoretically by Radom and co-workers,³⁹ and by Ziegler and co-workers.³⁶

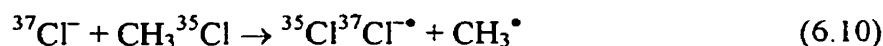
Cyr *et al.* observed, besides displacement reaction products, formation of $\text{ClBr}^{\bullet-}$ and $\text{I}_2^{\bullet-}$ (Reactions 6.6 and 6.7) at elevated centre-of-mass ion kinetic energies (E_{cm}) of the nucleophiles.⁸⁰



Johnson and co-workers observed a higher energy identity reaction channel for $\Gamma(\text{CH}_3^{\bullet}\text{I})$ and formation of $\text{Br}\Gamma^{\bullet}$ from $\Gamma(\text{CH}_2\text{Br}_2)$ upon photo-excitation (Reactions 6.8 and 6.9).^{11,81-83}



Ervin and co-workers also investigated Reaction 6.5 using GIB-tandem mass spectrometry (MS/MS) techniques, and observed a process that closely resembled the data from Barlow *et al.*, but rigorous statistical modeling indicated that the observed reaction proceeded by back-side attack.¹⁵ In addition, formation of $\text{Cl}_2^{\bullet-}$ was observed at $E_{\text{cm}} = (4.3 \pm 0.4) \text{ eV}$ (Reaction 6.10).



In another study on the reaction between fluoride ion and methyl chloride, proton abstraction and formation of $\text{FCl}^{\bullet-}$ was observed at higher centre-of-mass kinetic energies of F^- , besides the $\text{S}_{\text{N}}2$ reaction (Reactions 6.11-13).²⁵



Radom and co-workers showed that at the G2(+) level of theory the back-side $[\text{ClCH}_3\text{Cl}]^-$ transition state is 2.7 kcal mol⁻¹ higher in energy than the reactants,³⁷ which is in good agreement with experimental results, while the front-side $[\text{CH}_3\text{Cl}_2]^-$ transition state is 46.3 kcal mol⁻¹ higher in energy.³⁹ Interestingly, $[\text{CH}_3\text{Cl}_2]^-$ was formed from $\text{Cl}^-(\text{CH}_3\text{Cl})$, and not from $\text{Cl}^-(\text{ClCH}_3)$, which was not located as a stable minimum. On the other hand, stable minima were located for $\text{Br}^-(\text{BrCH}_3)$ and $\Gamma(\text{ICH}_3)$ at the G2(+)(ECP) level of theory.³⁹ The binding energies for these two complexes are much lower than for $\text{Br}^-(\text{CH}_3\text{Br})$ and $\Gamma(\text{CH}_3\text{I})$ (1.7 kcal mol⁻¹ vs. 9.8 kcal mol⁻¹, and 4.6 kcal mol⁻¹ vs. 8.6 kcal mol⁻¹, respectively).

Halide ion-halide interactions are not uncommon in chemistry, although the trihalide anions, X_3^- (X = F, Cl, Br, I), are hypervalent species and actually covalently bound.⁸⁴ Recently the bond dissociation energies were determined for these four species. Values of (23.5 ± 2.5) kcal mol⁻¹ (F_3^-),⁸⁴ (23.6 ± 1.2) kcal mol⁻¹ (Cl_3^-),⁸⁵ (30.3 ± 1.7) kcal mol⁻¹ (Br_3^-),⁸⁵ and (30.1 ± 1.4) kcal mol⁻¹ (I_3^-)⁸⁶ were obtained. Recent photodissociation (PD) experiments and DFT computations on BrICl^- and BrIBr^- show interesting dynamics and chemistry for these novel species.⁸⁷

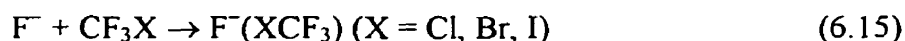
It seems reasonable to assume that by replacing the CH_3 by a CF_3 group it may be possible to make front side attack the main mechanism for the $\text{S}_{\text{N}}2$ reaction. The electronic repulsion between the nucleophile and the fluorine atoms may prevent back-side attack from taking place. In the literature a relatively small number of articles have been published concerning ion-molecule reactions between halide ions and some other anion and trifluoromethyl halide. A short summary will be given here.

Hop and McMahon studied the endothermic $\text{S}_{\text{N}}2$ reaction between bromide ion and dichlorodifluoromethane by FT-ICR (Reaction 6.14).⁸⁸



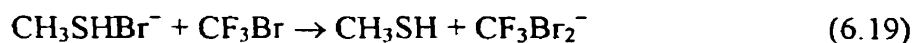
By following the abundance of the chloride ion as a function of the centre-of-mass kinetic energy of the bromide ion, the threshold energy could be obtained after analyzing the data using an empirical model by Armentrout and co-workers.⁸⁹ A threshold value of (21.0 ± 1.2) kcal mol⁻¹ was found. The authors speculated that the reaction proceeded through a front-side attack mechanism, involving a penta-coordinate transition state $[\text{CF}_2\text{Cl}_2\text{Br}]^-$. Finally it was mentioned that “the rapid and linear increase in cross-section at energies slightly above the threshold suggests non-statistical behavior and a collision complex which is either not bound or very weakly bound”.⁸⁸

Morris studied the reactions of oxide ($\text{O}^{\bullet-}$) and superoxide ($\text{O}_2^{\bullet-}$) anions, and halide ions (X^-) with various trifluoromethyl halides (CF_3X) using a variable-temperature-selected ion flow tube (VT-SIFT) instrument.⁹⁰ Large varieties of products, rate constants, and reaction efficiencies were observed. For the reactions between halide ions and trifluoromethyl halides, formation of adduct ions was observed (Reaction 6.15 and 6.16), as well as formation of Br^- and I^- (Reaction 6.17).



In general, the kinetics and efficiencies for these reactions were both low, except for Reaction 6.17 with $\text{X} = \text{Br}$ and I . In a follow-up study, Morris and Viggiano further investigated the latter two reactions as a function of temperature, kinetic energy, internal temperature, and pressure using a VT-SIFT instrument.⁹¹ Under all conditions the association reaction was the major reaction channel. It was concluded that Reactions 6.4 and 6.6 proceed by two different, non-competing complexes, and that the displacement reaction proceeds statistically by the classical Walden inversion mechanism.

Staneke *et al.* performed FT-ICR experiments between various negative ions and chlorofluoro and bromofluoro methanes.⁹² For the reactions between OH⁻ and CF₃Cl and CF₃Br no formation of Cl⁻ and Br⁻ was observed. Formation of Br⁻(BrCF₃) was observed from secondary reactions (Reaction 6.18 and 6.19).



In another study using SIFT, Morris *et al.* investigated the reactions between a large variety of anions (A⁻) and the four trifluoromethyl halides (CF₃X) at 300 K.⁹³ Non-reactivity and complex formation were observed, as well as reactions initiated by electron transfer, which in most cases were fast and efficient.

Surprisingly, to date no thermochemical data for formation of the F⁻(XCF₃) and X⁻(XCF₃) complexes (X= Cl, Br, I), either experimentally or computationally, are available. In addition, no data are available on the thermochemistry of the transition states for both back and front side attack. Even though replacing the CH₃ group by a CF₃ group appears to favor formation of a front side attack complex, it cannot be ruled out *a priori* that back side attack is not possible, or even still more favorable for an S_N2 reaction, as suggested by Morris and Viggiano.⁹¹

In this work the thermochemistry for the equilibrium clustering of chloride and bromide ion onto trifluoromethyl bromide and iodide (Reactions 6.20-6.22) was studied by PHPMS.



In addition, high level DFT and *ab initio* computations were performed to get more insight into the structures of the ion-molecule complexes and the transition states, and to construct potential energy profiles for the front- and back-side attack mechanisms, as well as other possible mechanisms. The quality of the calculated thermochemistry was also evaluated by the agreement with the limited experimental data available to date.

6.2 Experimental

All measurements were carried out on a pulsed-ionization high pressure mass spectrometry (PHPMS) instrument, configured around a VG 8-80 mass spectrometer.⁹⁴ The instrument, constructed at the University of Waterloo, has been described in detail in Chapter 2.

Gas mixtures were prepared in a 5 L heated stainless steel reservoir at 370 K, by using CH₄ as a bath gas at pressures of 700-800 Torr. Chloride ion was generated from trace amounts of CCl₄ by dissociative electron capture of thermalized electrons from 500 μs pulses of a 2 keV electron gun beam. Bromide ion was efficiently generated by an S_N2 reaction between Cl⁻ and *n*-butyl bromide (Equation 6.23).



The two trifluoromethyl halides (CF₃Br and CF₃I) were added to give relative amounts between 0.1% and 1.6%, depending on the ion source temperature and the nature of the experiment involved. The ion source pressure and temperature ranged between 4.0-5.0 Torr and 300-445 K, respectively.

Time intensity profiles of mass selected ions were monitored by using a PC based multichannel scalar (MCS) data acquisition system, configured at 100 μs dwell time per channel over 250 channels. Additive accumulations of ion signals from 2000 electron gun beam pulses were used.

Equilibrium constants (K_{eq}) at different absolute temperatures for the various halide ion-trifluoromethyl halide clustering equilibria (Reactions 6.20-6.22) are determined from Equation 6.24.

$$K_{\text{eq}} = \frac{\text{Int}(X^-(YCF_3))}{\text{Int}(X^-)} \cdot \frac{P^{\circ}}{P_{CF_3Y,\text{source}}} \quad (6.24)$$

In Equation 6.24, $\text{Int}(X^-(YCF_3))/\text{Int}(X^-)$ is the ion intensity ratio of the $X^-(YCF_3)$ and X^- ions at equilibrium, P° is the standard pressure (1 atm), and $P_{CF_3Y,\text{source}}$ is the partial pressure (in atm) of the trifluoromethyl halide in the ion source.

Equilibrium constants were calculated for various isotope pairs, *e.g.* $^{35}\text{Cl}^-/^{35}\text{Cl}^-(^{79}\text{BrCF}_3)$ and $^{35}\text{Cl}^-/^{35}\text{Cl}^-(^{81}\text{BrCF}_3)$, and $^{79}\text{Br}^-/^{79}\text{Br}^-(^{79}\text{BrCF}_3)$ and $^{79}\text{Br}^-/^{79}\text{Br}^-(^{81}\text{BrCF}_3)$. The observed equilibrium constants obtained for these isotope pairs need to be corrected for the fact that the partial pressure of CF_3Br introduced into the reservoir consists for 50% of $\text{CF}_3^{79}\text{Br}$ and 50% of $\text{CF}_3^{81}\text{Br}$. In addition, one has to correct for the fact that the peak at the m/z value corresponding to $^{35}\text{Cl}^-(^{81}\text{BrCF}_3)$ also contains the $^{37}\text{Cl}^-(^{79}\text{BrCF}_3)$ isotope pair (25% of the total ion intensity). For the $^{35}\text{Cl}^-/^{35}\text{Cl}^-(^{79}\text{BrCF}_3)$ isotope pair $K = 2K_{\text{obs}}$, while for $^{35}\text{Cl}^-/^{35}\text{Cl}^-(^{81}\text{BrCF}_3)$ $K = 1.5K_{\text{obs}}$. Similarly for $^{79}\text{Br}^-/^{79}\text{Br}^-(^{79}\text{BrCF}_3)$ and $^{79}\text{Br}^-/^{79}\text{Br}^-(^{81}\text{BrCF}_3)$ K 's of $2K_{\text{obs}}$ and K_{obs} , respectively, can be derived. The equilibrium constants obtained showed very close agreement, indicating that this correction is valid. The equilibrium constants used to calculate the ΔH° and ΔS° values were the averages of six different equilibrium constants from the two isotope pairs.

Trifluoromethyl bromide and iodide were purchased from SCM Specialty Chemical. Methane was purchased from Praxair. Carbon tetrachloride was purchased from J. T. Baker Chemical Co. *n*-Butyl bromide was purchased from Aldrich. All chemicals were used as received.

6.3 Computational

All computations were performed using the *Gaussian 94*⁹⁵ and *98*⁹⁶ suites of programs. Geometries were optimized using the B3LYP method^{97,98} in combination with the 6-311+G(d) (a) basis set for C, F, Cl, and Br,^{99,100} and the LanL2DZ (b) basis set for I

¹⁰¹. Normal mode vibrational frequencies and NPA ¹⁰² charges were calculated at the same level of theory. Single point energy computations were performed on the B3LYP level of theory in combination with the 6-311+G(3df) (c) basis set ¹⁰³⁻¹⁰⁶ on the B3LYP/a geometries. For some of the smaller systems investigated computations were performed using the MP2(full) method ¹⁰⁷ in combination with basis set a for C, F, Cl, and Br, and a modified LanL2DZ basis set for I, ¹⁰⁸ indicated here as LanL2DZ(sp) (d), or using the G3 and G3(MP2) methods.¹⁰⁹

For the formation of F⁻(BrCF₃), Cl⁻(BrCF₃), and Cl⁻(CF₃Br) relaxed potential energy surface scans were performed at the B3LYP/a level of theory with the F⁻...Br, Cl⁻...Br, and Cl⁻...C distances, respectively, as adjustable parameters, and optimizing all other bond distances, bond angles, and dihedral angles. An additional relaxed potential energy surface scan from Cl⁻ + CF₃Cl through Cl⁻(CF₃Cl) to [ClCF₃Cl]⁻ was performed as well. Finally, for the Cl⁻ + CF₃Cl reaction a relaxed potential energy surface scan was performed at the HF/6-31G(d) level of theory, with the Cl⁻...C distance (2.0-7.0 Å) and Cl⁻...C-Cl angle (90-180°) as adjustable parameters and allowing full optimization of all other degrees of freedom.

6.4 Results and Discussion

6.4.1 Structures

In Figures 6.3 to 6.5 the structures of CF₃Cl, CF₃Br, and CF₃I are shown, as calculated at the B3LYP/a (CF₃Cl and CF₃Br) and B3LYP/[a/b] levels of theory. As can be seen in Table 6.1, the agreement between theory and experiment ¹¹⁰⁻¹¹² is good to excellent. Roszak *et al.* performed computations on the same molecules using the MP2 in combination with larger basis sets, and the agreement between reported experimental data and their computational results were in general better than computations from this work.¹¹³ The only noticeable difference for the three molecules is the elongation of the C-X bond length going from X = Cl to I. This is mainly due to the increasing atomic size of the halide. At this level of theory there is excellent agreement for all three molecules with experimental dipole moments and normal mode

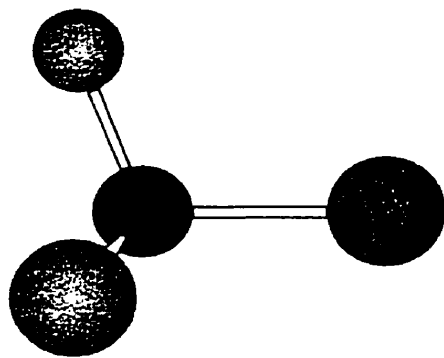


Figure 6.3 Optimized B3LYP/6-311+G(d) structure of CF₃Cl.

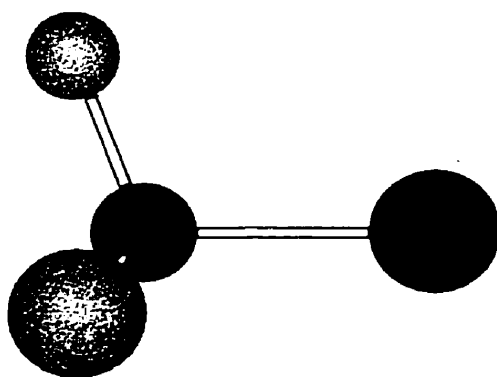


Figure 6.4 Optimized B3LYP/6-311+G(d) structure of CF₃Br.

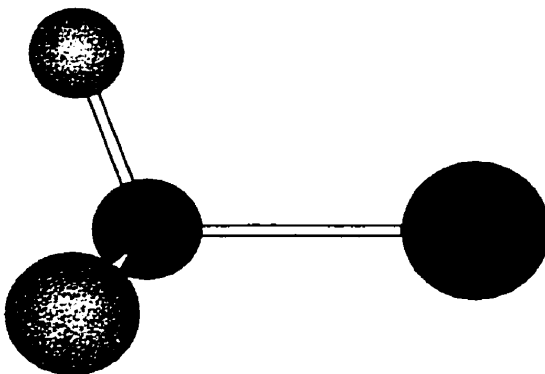


Figure 6.5 Optimized B3LYP/[6-311+G(d)/LanL2DZ] structure of CF₃I.

Table 6.1 Overview of the computational B3LYP/a ([a/b] for X = I) and experimental structural data of CF₃X and CF₃X[•] (X = Cl, Br, I).

structure	R(C-X) ^a		R(C-F) ^a		A(X-C-F) ^b	
	B3LYP/a	experiment	B3LYP/a	experiment	B3LYP/a	experiment
CF ₃ Cl	1.773	1.751 ± 0.005 ^d	1.333	1.328 ± 0.002 ^d	110.4	108.6 ± 0.4 ^d
CF ₃ Cl [•]	2.640		1.362		112.5	
CF ₃ Br	1.949	1.91 ± 0.03 ^e	1.333	1.34 ± 0.02 ^e	110.3	109.5 ± 2.0 ^e
CF ₃ Br [•]	2.762		1.363		112.3	
CF ₃ I ^c	2.162	2.135 ± 0.030 ^f	1.336	1.340 ± 0.021 ^f	110.6	108.4 ± 1.9 ^f

^a Å

^b °

^c B3LYP/[a/b]

^d from Reference 110

^e from Reference 111

^f from Reference 112

vibrational frequencies (see Section 6.4.4). For CF₃Cl, CF₃Br, and CF₃I dipole moments of 0.52 D, 0.66 D, and 1.08 D, respectively, were calculated, while experimentally values of 0.50 D, 0.65 D, and 1.05 D, respectively, have been determined.¹¹⁴ Attachment of an electron to the lowest unoccupied molecular orbital (LUMO) of the trifluoromethyl halides to form the corresponding radical anions causes some large structural changes. Elongation of the C–X bond by approximately 50% is the most noticeable feature, raising the question whether or not X[−](CF₃•) is a better description for CF₃X^{•−} (X = Cl, Br, I). In Figure 6.6 the B3LYP/a structure of CF₃Cl^{•−} is shown. Elongation can be explained by the fact that the LUMO is an anti-bonding σ-type orbital of a₁ symmetry almost entirely localized on the C–X bond. The extra electron is mostly localized on the halide.¹¹³ Small increases of the C–F bonds and the X–C–F angle of around 0.03 Å and 2.0°, respectively, can be observed.

Unfortunately, no experimental data for the three CF₃X^{•−} species are available. Compared to the results by Roszak *et al.* for CF₃X^{•−} (X = Cl, Br) the C–X bonds are slightly longer.¹¹³

Complex formation of X[−] and CF₃Y gives rise to two possible ion-molecule complexes (Reactions 6.25 and 6.26).



Formation of X[−](YCF₃) and X[−](CF₃Y) can be associated with front- and back-side attack mechanisms, respectively. In Figures 6.7-6.10 the structures of F[−](BrCF₃), F[−](CF₃Br), Cl[−](ClCF₃), and Cl[−](CF₃Cl) are shown. In X[−](YCF₃), X[−] interacts with the positive end of the dipole moment in CF₃Y. In X[−](CF₃Y) on the other hand, X[−] experiences repulsion from the three fluorine atoms in CF₃Y. Results in Table 6.2 show that structural features in both the X[−](YCF₃) and X[−](CF₃Y) complexes are

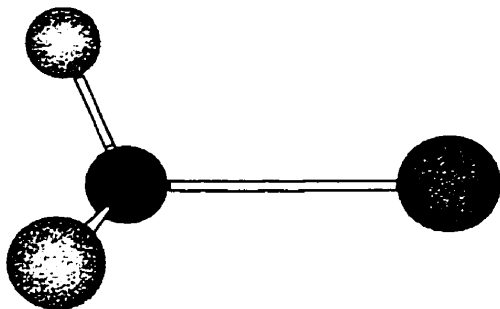


Figure 6.6 Optimized B3LYP/6-311+G(d) structure of CF_3Cl^- .

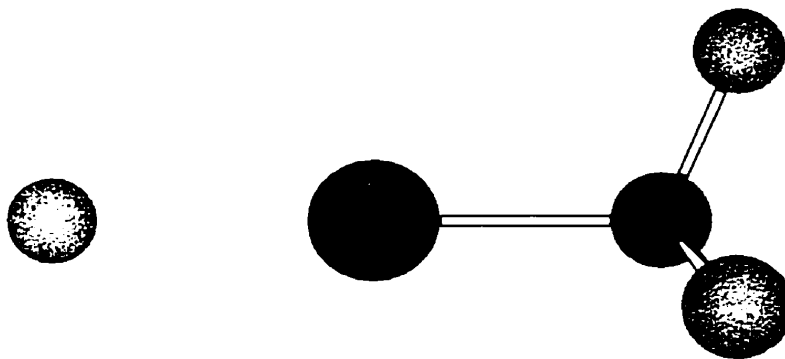


Figure 6.7 Optimized B3LYP/6-311+G(d) structure of $\text{F}^-(\text{BrCF}_3)$.

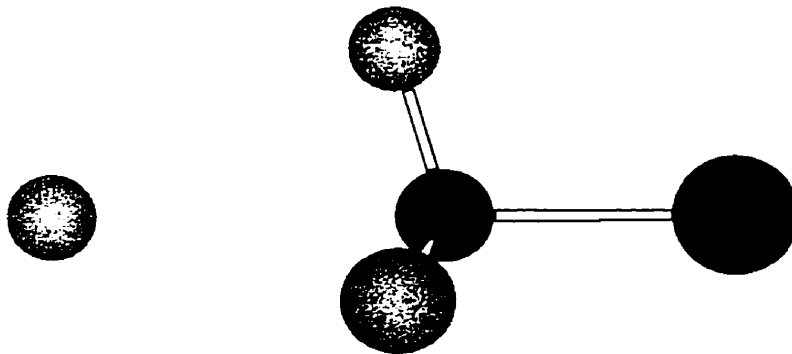


Figure 6.8 Optimized B3LYP/6-311+G(d) structure of $\text{F}^-(\text{CF}_3\text{Br})$.

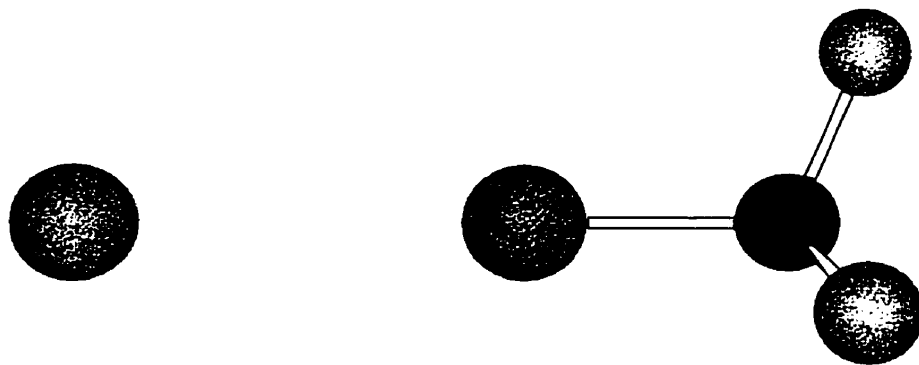


Figure 6.9 Optimized B3LYP/6-311+G(d) structure of $\text{Cl}^-(\text{ClCF}_3)$.

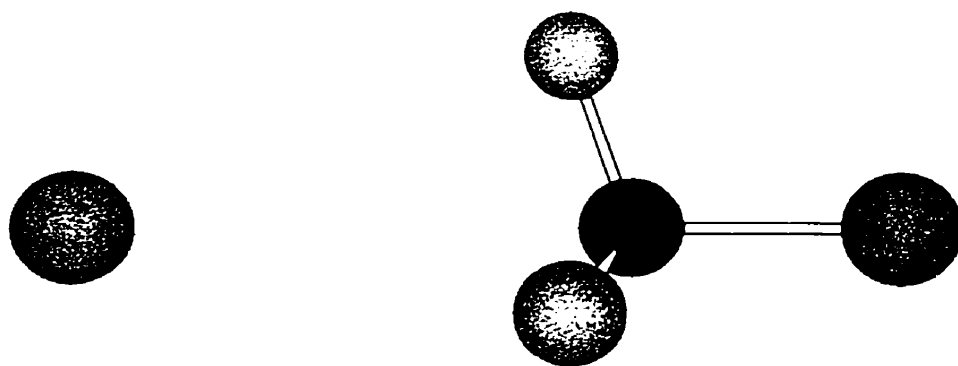


Figure 6.10 Optimized B3LYP/6-311+G(d) structure of $\text{Cl}^-(\text{CF}_3\text{Cl})$.

Table 6.2 Overview of the computational B3LYP/a structural data of the $X^-(YCF_3)$ and $X^-(CF_3X)$ complexes ($X = F, Cl, Br$; $Y = Cl, Br, I$).

structure	$R(C-Y)^a$	$R(C-F)^a$	$R(X \cdots Y)^a$	$R(X \cdots C)^a$	$A(Y-C-F)^b$
$F^-(BrCF_3)$	1.997	1.366	2.210		113.3
$F^-(CF_3Br)$	2.073	1.308		2.768	105.6
$Cl^-(ClCF_3)$	1.761	1.352	3.004		112.2
$Cl^-(CF_3Cl)$	1.829	1.319		3.770	108.2
$Cl^-(BrCF_3)$	1.974	1.356	2.875		112.5
$Cl^-(CF_3Br)$	2.013	1.317		3.724	108.0
$Cl^-(ICF_3)^c$	2.238	1.361	2.967		112.9
$Cl^-(CF_3I)^c$	2.258	1.317		3.714	108.1
$Br^-(ClCF_3)$	1.761	1.350	3.198		112.0
$Br^-(CF_3Cl)$	1.820	1.321		4.103	108.6
$Br^-(BrCF_3)$	1.976	1.354	3.047		112.4
$Br^-(CF_3Br)$	2.004	1.319		4.030	108.3
$Br^-(ICF_3)^c$	2.243	1.359	3.122		112.8
$Br^-(CF_3I)^c$	2.248	1.319		4.000	108.4

^a Å ^b ° ^c B3LYP/[a/b]

different relative to each other and “free” CF_3Y . In general, the C–Y bond in both the $\text{X}^-(\text{YCF}_3)$ and $\text{X}^-(\text{CF}_3\text{Y})$ complexes is longer than in CF_3Y , with the first one shorter than the second one. $\text{Cl}^-(\text{ClCF}_3)$ is the only exception for all systems investigated. For the C–F bonds in $\text{X}^-(\text{YCF}_3)$ a small increase is observed relative to CF_3Y , while for $\text{X}^-(\text{CF}_3\text{Y})$ a small decrease takes place. The $\text{X}^-\cdots\text{YCF}_3$ distances in the $\text{X}^-(\text{YCF}_3)$ complexes show expected and unexpected trends. For $\text{X} = \text{Cl}$ and Br , and constant Y , $\text{R}(\text{X}^-\cdots\text{Y})$ increases from $\text{X} = \text{Cl}$ to Br for all Y 's, as expected due to the larger ion radius and more diffuse nature of the latter. For $\text{X} = \text{Cl}$ or Br , and $\text{Y} = \text{Cl}$, Br , and I , $\text{R}(\text{X}^-\cdots\text{Y})$ decreases going from $\text{Y} = \text{Cl}$ to Br , while it increases going from $\text{Y} = \text{Br}$ to I . For the $\text{X}^-(\text{CF}_3\text{Y})$ complexes different and more logical trends are observed. Going from $\text{Y} = \text{Cl}$ to I in $\text{X}^-(\text{CF}_3\text{Y})$, $\text{R}(\text{X}^-\cdots\text{C})$ decreases. Finally, in the $\text{X}^-(\text{YCF}_3)$ complexes the Y–C–F angles are larger than in CF_3Y , while in the $\text{X}^-(\text{CF}_3\text{Y})$ complexes they are somewhat smaller. Similar observations have been made for CH_3X , $\text{X}^-(\text{CH}_3\text{X})$, and $\text{X}^-(\text{XCH}_3)$ ($\text{X} = \text{Br}$, I) at the MP2(fc)/[6-31+G(d)/LanL2DZ(sp)] level of theory.^{37,39} For both $\text{X}^-(\text{CH}_3\text{X})$ and $\text{X}^-(\text{XCH}_3)$ small increases in $\text{R}(\text{C}–\text{X})$ relative to CH_3X take place. For $\text{R}(\text{C}–\text{H})$ a small decrease relative to CH_3X takes place in $\text{X}^-(\text{CH}_3\text{X})$, while a small increase takes place in $\text{X}^-(\text{XCH}_3)$. Finally, in $\text{X}^-(\text{CH}_3\text{X})$ a small decrease in X–C–H angles takes place, while in $\text{X}^-(\text{XCH}_3)$ these do not change relative to CH_3X .

For the back- and front-side attack mechanisms separate transition states are possible, indicated by $[\text{XCF}_3\text{Y}]^-$ and $[\text{CF}_3\text{XY}]^-$, respectively. In Table 6.3 the results for the four $[\text{XCF}_3\text{Y}]^-$ transition states are summarized, while in Figures 6.11 and 6.12 the structures of $[\text{FCF}_3\text{Br}]^-$ and $[\text{ClCF}_3\text{Cl}]^-$ are shown. It is interesting, but not unexpected, that the $\text{C}\cdots\text{Br}$ distances in $[\text{FCF}_3\text{Br}]^-$ and $[\text{ClCF}_3\text{Br}]^-$ are shorter than in $[\text{BrCF}_3\text{Br}]^-$. Similarly, the $\text{C}\cdots\text{Cl}$ distance in $[\text{ClCF}_3\text{Cl}]^-$ is shorter than in $[\text{ClCF}_3\text{Br}]^-$. The C–F distances are a little bit shorter than in the $\text{X}^-(\text{CF}_3\text{Y})$ complexes. Compared to the $\text{Cl}\cdots\text{C}$ distance in $[\text{ClCH}_3\text{Cl}]^-$, as calculated at the B3LYP/6-311+G(d,p) level of theory, of 2.371 Å, the substitution of hydrogen atoms by fluorine atoms increases this distance by 0.117 Å.⁴⁰ The $[\text{CF}_3\text{XY}]^-$ front-side attack transition states calculated for this work show features similar to results for $[\text{CH}_3\text{X}_2]^-$ by Glukhovtsev *et*

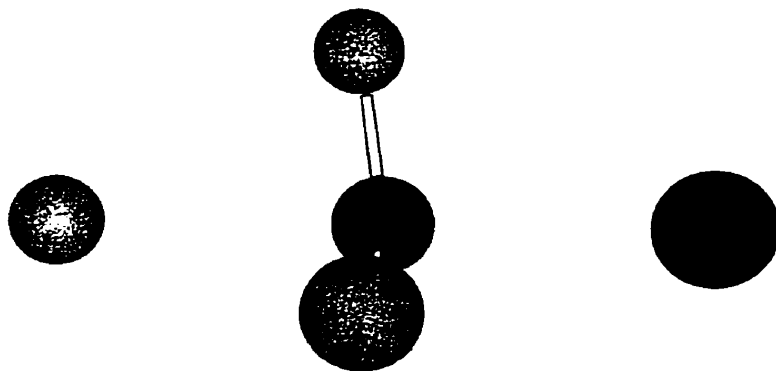


Figure 6.11 Optimized B3LYP/6-311+G(d) structure of $[\text{FCF}_3\text{Br}]^-$.

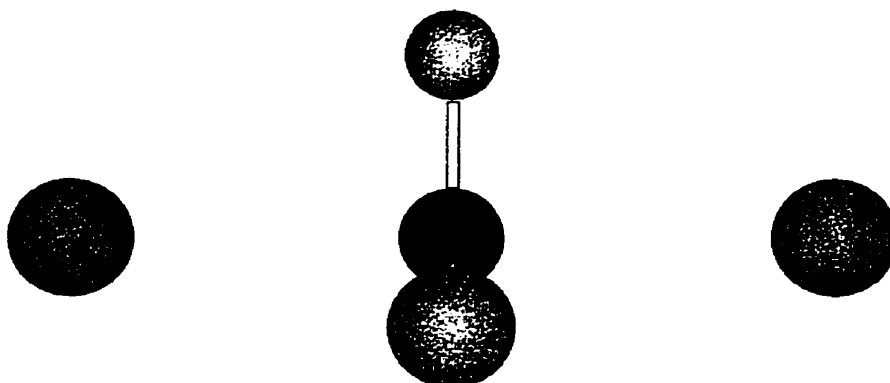


Figure 6.12 Optimized B3LYP/6-311+G(d) structure of $[\text{ClCF}_3\text{Cl}]^-$.

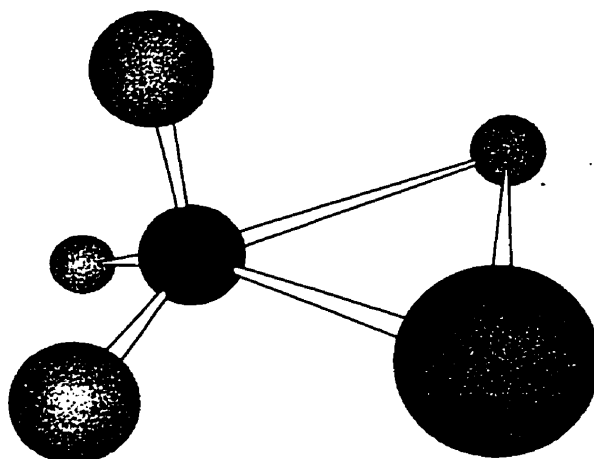


Figure 6.13 Optimized B3LYP/6-311+G(d) structure of $[\text{CF}_3\text{Cl}_2]^-$.

Table 6.3 Overview of the computational B3LYP/a structural data of the $[\text{XCF}_3\text{Y}]^-$ transition states (X, Y = F, Cl, Br).

structure	$\text{R}(\text{X}\cdots\text{C})^a$	$\text{R}(\text{C}\cdots\text{Y})^a$	$\text{R}(\text{C}-\text{F})^a$	$\text{A}(\text{X}\cdots\text{C}-\text{F})^b$	$\text{A}(\text{F}-\text{C}-\text{F})^b$
$[\text{FCF}_3\text{Br}]^-$	2.244	2.293	1.298	81.8	120.0
$[\text{ClCF}_3\text{Cl}]^-$	2.488	2.488	1.284	90.0	120.0
$[\text{ClCF}_3\text{Br}]^-$	2.536	2.630	1.283	89.1	120.0
$[\text{BrCF}_3\text{Br}]^-$	2.667	2.667	1.283	90.0	120.0

^a Å ^b °

Table 6.4 Overview of the computational B3LYP/a structural data of the $[\text{CF}_3\text{XY}]^-$ transition states (X, Y = Cl, Br).

	structure		
	$[\text{CF}_3\text{Cl}_2]^-$	$[\text{CF}_3\text{ClBr}]^-$	$[\text{CF}_3\text{Br}_2]^-$
$\text{R}(\text{C}\cdots\text{X})^a$	2.410	2.437	2.638
$\text{R}(\text{C}\cdots\text{Y})^a$	2.410	2.618	2.646
$\text{R}(\text{X}\cdots\text{Y})^a$	3.151	3.317	3.487
$\text{R}(\text{C}-\text{F}_\text{A})^a$	1.325	1.325	1.326
$\text{R}(\text{C}-\text{F}_\text{BX})^a$	1.360	1.325	1.353
$\text{R}(\text{C}-\text{F}_\text{BY})^a$	1.360	1.360	1.353
$\text{A}(\text{X}\cdots\text{C}\cdots\text{Y})^b$	81.6	81.9	82.6
$\text{A}(\text{X}\cdots\text{C}-\text{F}_\text{A})^b$	97.6	95.3	97.3
$\text{A}(\text{Y}\cdots\text{C}-\text{F}_\text{A})^b$	97.6	100.2	97.6
$\text{A}(\text{X}\cdots\text{C}-\text{F}_\text{BX})^b$	82.7	83.1	81.7
$\text{A}(\text{Y}\cdots\text{C}-\text{F}_\text{BY})^b$	82.7	81.1	81.2

^a Å ^b °

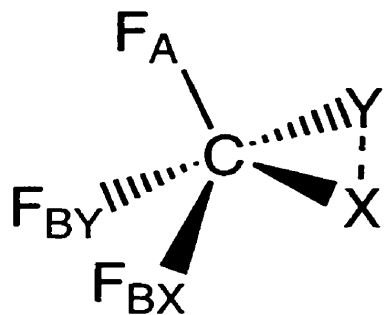


Figure 6.14 Atom labeling in the $[CF_3XY]^-$ transition states.

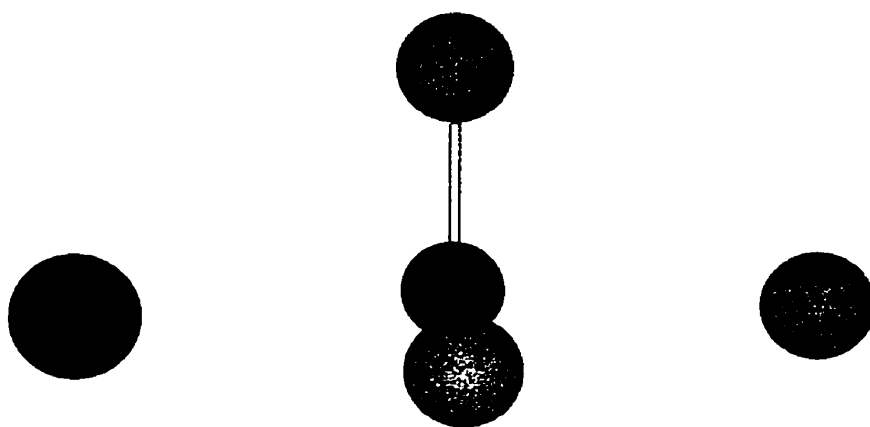


Figure 6.15 Optimized B3LYP/6-311+G(d) structure of $[BrCF_2Cl_2]^-$.

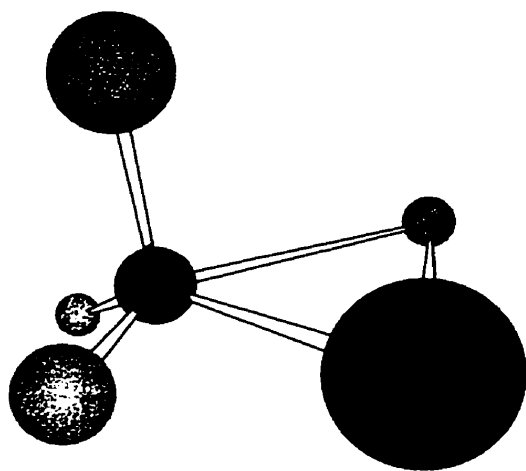


Figure 6.16 Optimized B3LYP/6-311+G(d) structure of $[CF_2Cl_2Br]^-$.

*al.*³⁹ The results for $[\text{CF}_3\text{Cl}_2]^-$, $[\text{CF}_3\text{ClBr}]^-$, and $[\text{CF}_3\text{Br}_2]^-$ are shown in Table 6.4, while the structure of $[\text{CF}_3\text{Cl}_2]^-$ is shown in Figure 6.13. In Figure 6.14 the labeling of the $[\text{CF}_3\text{XY}]^-$ transition states as used in Table 6.4 is shown. For $[\text{CF}_3\text{Cl}_2]^-$ the difference in the C...Cl distances is 0.078 Å shorter than in $[\text{ClCF}_3\text{Cl}]^-$, while in $[\text{CF}_3\text{Br}_2]^-$ it is only around 0.025 Å shorter relative to $[\text{BrCF}_3\text{Br}]^-$. The X...Y distance increases as expected from $[\text{CF}_3\text{Cl}_2]^-$ to $[\text{CF}_3\text{Br}_2]^-$, but in all three structures it is approximately 0.40-0.50 Å longer than in the XY^\bullet . The C-F distances are a little bit longer than in the $[\text{XCF}_3\text{Y}]^-$ transition states, with the C-F_A bond length shorter than the C-F_B bond length. There are some small variations in the various interatomic angles, but these are too minor to be relevant to the discussion here. Equations 6.14 and 6.17 are the only reactions performed experimentally to date, and Equation 6.14 is the only one for which a threshold energy has been determined. Replacing one of the fluorine atoms for a chlorine atom has some effect on the $[\text{BrCF}_2\text{Cl}_2]^-$ and $[\text{CF}_2\text{Cl}_2\text{Br}]^-$ transition states relative to $[\text{ClCF}_3\text{Br}]^-$ and $[\text{CF}_3\text{ClBr}]^-$, respectively (Figures 6.15 and 6.16). In both structures small increases in the C...X, C...Y, X...Y, and C-F bond lengths can be observed. In $[\text{CF}_2\text{Cl}_2\text{Br}]^-$ the C-Cl bond length is longer than in $[\text{BrCF}_2\text{Cl}_2]^-$ (1.777 Å and 1.705 Å, respectively). Compared to structures of $[\text{CH}_3\text{Cl}_2]^-$ and $[\text{CH}_3\text{Br}_2]^-$ at the MP2/6-31+G(d) and MP2/[6-31+G(d)/ECP] level of theory,³⁹ respectively, the X...X distances are actually longer than in $[\text{CF}_3\text{Cl}_2]^-$ and $[\text{CF}_3\text{Br}_2]^-$ from this work.

Finally, in Table 6.5 a summary is given for the B3LYP/a and MP2(full)/a (d for X, Y = I) results of the XY and XY^\bullet systems (X, Y = Cl, Br, I). As expected there is an increase in the X-Y distance going from XY to XY^\bullet . In general the agreement between the MP2 results and experiment¹¹⁵ is closer than with the B3LYP data, but the B3LYP may still be considered adequate to be used.

6.4.2 Experimental and Computational Thermochemistry

For the complex formation equilibria of the halide ion-trifluoromethyl halides (Reaction 6.26 and 6.27) no experimental thermochemistry is available in the

literature. In Figure 6.17 the experimental Van't Hoff plots for the formation of $\text{Cl}^-(\text{BrCF}_3)$ and $\text{Br}^-(\text{BrCF}_3)$ are shown. In Table 6.6 a summary of the available experimental and computational thermochemistry is given for the formation of the various $\text{X}^-(\text{YCF}_3)$ and $\text{X}^-(\text{CF}_3\text{Y})$ complexes. It can be seen that the agreement between the experiment and computations is good to excellent. Except for the formation of $\text{F}^-(\text{BrCF}_3)$, $\text{Br}^-(\text{ICF}_3)$, and maybe $\text{Cl}^-(\text{ClCF}_3)$ all other systems cannot be measured by our technique. For all back-side attack complexes, $\text{X}^-(\text{CF}_3\text{Y})$, the ΔG° value is larger than zero, so these complexes exist only at very low temperatures. Measuring the experimental thermochemistry for the formation of $\text{F}^-(\text{BrCF}_3)$ is only possible at temperatures higher than 500 K. At those temperatures there will be significant competition from the displacement reaction. The ΔH° value for Reaction 6.23 was determined from ΔG° values at 432 K and 446 K and the ΔS°_{298} value from the DFT computations. By increasing the ion source temperature, the total ion intensity dropped quickly and had completely disappeared at 460 K, most probably due to electrostatic plugging of the ion exit aperture by HI, or perhaps I_2 , formed by electron radiolysis of CF_3I . The close agreement between experiment and theory gives confidence that the chosen level of theory is suitable for these kinds of systems.

Besides nucleophilic displacement and complex formation, formation of XY and XY^\bullet by Y^+ and Y^\bullet abstraction, respectively, are also possible processes that need to be considered while exploring the potential energy diagram (Reactions 6.27 and 6.28) of the reaction between X^- and CF_3Y .



In Table 6.7 the computational ΔH°_{298} values for the various possible reaction channels are summarized, as well as the experimental data if available. The latter come from Table 6.8, where a summary is given of the available experimental $\Delta_f H^\circ$ values of the species used.¹¹⁶

Table 6.5 Overview of the computational B3LYP/c//B3LYP/a and MP2(full)/a and experimental structural data of XY and XY^{-•} (X, Y = Cl, Br, I).

structure	R(X-Y) ^a		
	B3LYP/c//B3LYP/a	MP2(full)/a	experiment
Cl ₂	2.053	2.024	1.988 ^c
Cl ₂ ^{-•}	2.755	2.650	
ClBr	2.191	2.164	
ClBr ^{-•}	2.865	2.747	
Br ₂	2.330	2.303	2.283 ^c
Br ₂ ^{-•}	2.990	2.869	
I ₂ ^b	2.710	2.692	2.666 ^c
I ₂ ^{-•b}	3.381	3.282	

^a Å

^b LanL2DZ(sp)

^c from Reference 115

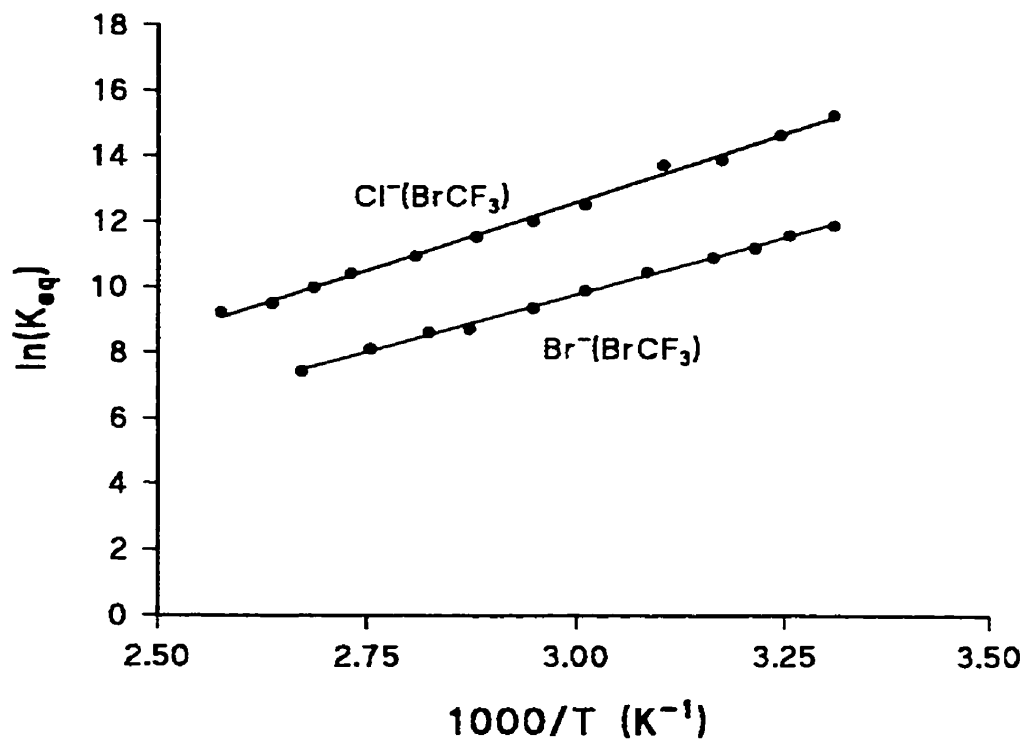


Figure 6.17 Van't Hoff plots for the halide ion-trifluoro methyl halide clustering equilibria $X^- + CF_3Y = X^-(CF_3Y)$ ($X = Cl, Br; Y = Br$).

Table 6.6 Overview of the experimental PHPMS and computational B3LYP/c//B3LYP/a thermochemistry for the formation of $X^-(YCF_3)$ and $X^-(CF_3Y)$ complexes ($X = F, Cl, Br, Y = Cl, Br, I$).

clustering equilibrium	ΔH^0_{298} ^a		ΔH^0 ^a		ΔS^0_{298} ^b		ΔS^0 ^b	
	B3LYP/c//B3LYP/a	PHPMS	B3LYP/a	PHPMS	B3LYP/a	PHPMS	B3LYP/a	PHPMS
$F^- + CF_3Br \rightleftharpoons F^-(BrCF_3)$	-30.9		-24.8					
$F^- + CF_3Br \rightleftharpoons F^-(CF_3Br)$	-8.2		-22.1					
$Cl^- + CF_3Cl \rightleftharpoons Cl^-(ClCF_3)$	-9.8		-21.2					
$Cl^- + CF_3Cl \rightleftharpoons Cl^-(CF_3Cl)$	-2.3		-17.3					
$Cl^- + CF_3Br \rightleftharpoons Cl^-(BrCF_3)$	-14.9		-22.3	-16.5				-24.5
$Cl^- + CF_3Br \rightleftharpoons Cl^-(CF_3Br)$	-2.4		-17.8					
$Cl^- + CF_3I \rightleftharpoons Cl^-(ICF_3)$ ^c	-21.5		-22.3	-23.6				
$Cl^- + CF_3I \rightleftharpoons Cl^-(CF_3I)$ ^c	-2.6		-17.2					
$Br^- + CF_3Cl \rightleftharpoons Br^-(ClCF_3)$	-8.0		-20.5					
$Br^- + CF_3Cl \rightleftharpoons Br^-(CF_3Cl)$	-1.4		-15.5					

^a kcal mol⁻¹

^b cal mol⁻¹ K⁻¹

^c B3LYP/[b/c]//B3LYP/[a/b]

Table 6.6 (continued)

clustering equilibrium	ΔH°_{298} ^a		ΔS°_{298} ^b	
	B3LYP/c//B3LYP/a	PHPMS	B3LYP/a	PHPMS
$\text{Br}^- + \text{CF}_3\text{Br} \rightleftharpoons \text{Br}^-(\text{BrCF}_3)$	-12.5	-13.9	-21.8	-22.2
$\text{Br}^- + \text{CF}_3\text{Br} \rightleftharpoons \text{Br}^-(\text{CF}_3\text{Br})$	-1.2		-15.7	
$\text{Br}^- + \text{CF}_3\text{I} \rightleftharpoons \text{Br}^-(\text{ICF}_3)$ ^c	-18.7		-21.9	
$\text{Br}^- + \text{CF}_3\text{I} \rightleftharpoons \text{Br}^-(\text{CF}_3\text{I})$ ^c	-1.7		-15.7	

^a kcal mol⁻¹

^b cal mol⁻¹ K⁻¹

^c B3LYP/[b/c]//B3LYP/[a/b]

Table 6.7 Overview of the computational B3LYP/c//B3LYP/a and experimental thermochemistry of the $X^- + CF_3Y \rightarrow Y^- + CF_3X$, $XY^{\bullet} + CF_3^{\bullet}$, $CF_3Y^{\bullet} + X^{\bullet}$, and $CF_3^- + XY$ reactions ($X = F, Cl, Br$; $Y = Cl, Br$).

reaction	ΔH°_{298} ^a	
	B3LYP/c//B3LYP/a	experiment ^b
$F^- + CF_3Br \rightarrow Br^- + CF_4$	-59.6	-59.4
$Cl^- + CF_3Cl \rightarrow Cl^- + CF_3Cl$	0.0	0.0
$Cl^- + CF_3Cl \rightarrow Cl_2^{\bullet} + CF_3^{\bullet}$	+45.2	+57.4
$Cl^- + CF_3Cl \rightarrow CF_3Cl^{\bullet} + Cl^{\bullet}$	+67.6	NA
$Cl^- + CF_3Cl \rightarrow CF_3^- + Cl_2$	+69.6	+70.2
$Cl^- + CF_3Br \rightarrow Br^- + CF_3Cl$	-10.8	-10.5
$Cl^- + CF_3Br \rightarrow ClBr^{\bullet} + CF_3^{\bullet}$	+33.7	NA
$Cl^- + CF_3Br \rightarrow CF_3Br^{\bullet} + Cl^{\bullet}$	+57.8	+63.2
$Cl^- + CF_3Br \rightarrow CF_3^- + ClBr$	+58.1	+59.6
$Br^- + CF_3Cl \rightarrow Cl^- + CF_3Br$	+10.8	+10.5
$Br^- + CF_3Cl \rightarrow ClBr^{\bullet} + CF_3^{\bullet}$	+44.4	NA
$Br^- + CF_3Cl \rightarrow CF_3Cl^{\bullet} + Br^{\bullet}$	+64.8	NA
$Br^- + CF_3Cl \rightarrow CF_3^- + ClBr$	+68.9	+70.1
$Br^- + CF_3Br \rightarrow Br^- + CF_3Br$	0.0	0.0
$Br^- + CF_3Br \rightarrow Br_2^{\bullet} + CF_3^{\bullet}$	+33.6	+43.3
$Br^- + CF_3Br \rightarrow CF_3Br^{\bullet} + Br^{\bullet}$	+54.9	+57.4
$Br^- + CF_3Br \rightarrow CF_3^- + Br_2$	+58.5	+59.9

^a kcal mol⁻¹

^b from Reference 116

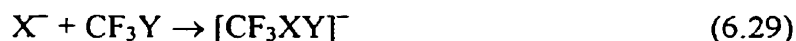
Table 6.8 Overview of the experimental standard heats of formation ($\Delta_f H^\circ$) of various neutrals and (radical) anions.

structure	$\Delta_f H^\circ$ ^a	structure	$\Delta_f H^\circ$ ^a
F [•]	+19.0	F ⁻	-59.4
Cl [•]	+29.0	Cl ⁻	-54.4
Br [•]	+26.7	Br ⁻	-50.9 ± 0.2
I [•]	+25.5	I ⁻	-45.1
CF ₃ [•]	-112.4	CF ₃ ⁻	-154.7 ± 4.4
Cl ₂	0.0	Cl ₂ ^{-•}	-55.3 ± 4.6
ClBr	+3.5	ClBr ^{-•}	NA
Br ₂	+7.4	Br ₂ ^{-•}	-50.3
I ₂	+14.9	I ₂ ^{-•}	-43.3 ± 0.1
CF ₄	-223.0	CF ₄ ^{-•}	NA
CF ₃ Cl	-169.2	CF ₃ Cl ^{-•}	NA
CF ₃ Br	-155.1	CF ₃ Br ^{-•}	-176.3 ± 4.6

^a kcal mol⁻¹ ^b from Reference 116.

Except for the reactions involving radicals and radical anions as products, in general the agreement is very good to excellent. It is surprising that the EA of ClBr has never been determined. In Table 6.9 the calculated EA's (in eV) and BDE's (in kcal mol⁻¹) of the various species involved in the different reactions have been summarized. Results from B3LYP, MP2, G3, G3(MP2), and experiments are shown.

For the few systems investigated, G3 and G3(MP2) perform very well to excellently. Except for the EA of CF₃[•] and the BDE of ClBr, the chosen B3LYP/c//B3LYP/a method performs less accurately than the MP2(full)/a computations. Use of different basis sets or use of composite methods like G2, G3, and so on may be more accurate, but also more time consuming and consequently more expensive. In Table 6.10 the calculated activation enthalpies, ΔH[‡]₂₉₈, for the front- and back-side attack mechanisms (Reactions 6.29 and 6.30) relative to the reactants are summarized, including the only experimental results available.⁸⁸



Morris' and Viggiano's suggestion that Reaction 6.17 proceeds through the classical Walden inversion or a back-side attack mechanism already seemed to be a very reasonable conclusion based on all their observations.⁹¹ On the other hand, arguments that the three fluorine atoms might shield attack on the carbon also seem reasonable *a priori*. This assumption is confirmed by the fact that Staneke *et al.* failed to observe formation of Br⁻ from the reaction between OH⁻ and CF₃Br.⁹² Results from the present work confirm that Morris and Viggiano were indeed correct, since ΔH[‡]₂₉₈ for [FCF₃Br]⁻ is -6.3 kcal mol⁻¹. Hop and McMahon suggested that Reaction 6.14 would proceed through the front-side attack transition state [CF₃Cl₂Br]⁻.⁸⁸ Comparison of the front- (+47.2 kcal mol⁻¹) and back-side (+24.6 kcal mol⁻¹) attack mechanisms versus the experimental threshold energy of (+21.0 ± 1.2) kcal mol⁻¹, shows clearly that Reaction 6.15 also proceeds through a back-side attack mechanism.

Table 6.9 Overview of the computational B3LYP/c//B3LYP/a, MP2(full)/a, G3, and G3(MP2), and experimental electron affinities (EA) and bond dissociation energies (BDE) of various (radical) neutrals and radical anion.

reaction	ΔH_{298}° ^{a,b}	ΔH_{298}° ^{a,b}	ΔH_{298}° ^{a,b}	ΔH_{298}° ^{a,b}	ΔH° ^{a,b}
	B3LYP/c//B3LYP/a	MP2(full)/a	G3	G3(MP2)	experiment ^d
$\text{Cl}^{\bullet} + \text{e}^{-} \rightarrow \text{Cl}^{-}$	-3.68	-3.16	-3.61	-3.67	-3.61
$\text{Cl}_2 + \text{e}^{-} \rightarrow \text{Cl}_2^{-\bullet}$	-2.84	-2.47	-2.45	-2.47	-2.40
$\text{ClBr} + \text{e}^{-} \rightarrow \text{ClBr}^{-\bullet}$	-2.85	-2.46			NA
$\text{Br}^{\bullet} + \text{e}^{-} \rightarrow \text{Br}^{-}$	-3.56	-3.13			-3.36
$\text{Br}_2 + \text{e}^{-} \rightarrow \text{Br}_2^{-\bullet}$	-2.87	-2.56			-2.55
$\text{I}_2 + \text{e}^{-} \rightarrow \text{I}_2^{-\bullet c}$	-2.97	-2.53			-2.52
$\text{CF}_3^{\bullet} + \text{e}^{-} \rightarrow \text{CF}_3^{-}$	-1.79	-1.52			-1.83 ^e
$\text{CF}_3\text{Cl} + \text{e}^{-} \rightarrow \text{CF}_3\text{Cl}^{-\bullet}$	-0.75			-0.86	NA
$\text{CF}_3\text{Br} + \text{e}^{-} \rightarrow \text{CF}_3\text{Br}^{-\bullet}$	-1.18				-0.92
$\text{Cl}_2 \rightarrow 2\text{Cl}^{\bullet}$	+54.8	+42.1	+56.8	+57.5	+58.0
$\text{ClBr} \rightarrow \text{Cl}^{\bullet} + \text{Br}^{\bullet}$	+52.6	+42.3			+52.2
$\text{Br}_2 \rightarrow 2\text{Br}^{\bullet}$	+49.4	+41.3			+46.0

^a eV

^b kcal mol⁻¹

^c LanL2DZ(sp) basis set for I

^d from reference 116

^e from Reference 132

Table 6.9 (continued)

reaction	$\Delta H^0_{298}{}^{a,b}$	$\Delta H^0_{298}{}^{a,b}$	$\Delta H^0_{298}{}^{a,b}$	$\Delta H^0_{298}{}^{a,b}$	$\Delta H^0{}^{a,b}$
	B3LYP/c//B3LYP/a	MP2(full)/a	G3	G3(MP2)	experiment ^d
$\text{Cl}_2^- \rightarrow \text{Cl}^- + \text{Cl}^\bullet$	+35.4	+26.0	+30.3	+29.7	+29.9
$\text{ClBr}^- \rightarrow \text{Cl}^- + \text{Br}^\bullet$	+33.4	+26.1			NA
$\text{ClBr}^- \rightarrow \text{Br}^- + \text{Cl}^\bullet$	+36.2	+26.8			NA
$\text{Br}_2^- \rightarrow \text{Br}^- + \text{Br}^\bullet$	+33.5	+26.6			+26.1

^a eV^b kcal mol⁻¹^c LanL2DZ(sp) basis set for I^d from reference 116^e from Reference 132

Table 6.10 Overview of the computational B3LYP/c//B3LYP/a thermochemistry of the $X^- + CF_3Y \rightarrow [XCF_3Y]^-$ and $[CF_3XY]^-$ reactions ($X = F, Cl, Br$; $Y = Cl, Br$).

reaction	ΔH_{298}^\ddagger ^a	
	B3LYP/c//B3LYP/a	experiment
$F^- + CF_3Br \rightarrow [FCF_3Br]^-$	-6.3	
$Cl^- + CF_3Cl \rightarrow [ClCF_3Cl]^-$	+20.7	
$Cl^- + CF_3Cl \rightarrow [CF_3Cl_2]^-$	+43.9	
$Cl^- + CF_3Br \rightarrow [ClCF_3Br]^-$	+15.5	
$Cl^- + CF_3Br \rightarrow [CF_3ClBr]^-$	+36.3	
$Br^- + CF_3Cl \rightarrow [BrCF_3Cl]^-$	+26.2	
$Br^- + CF_3Cl \rightarrow [CF_3ClBr]^-$	+47.1	
$Br^- + CF_3Br \rightarrow [BrCF_3Br]^-$	+20.8	
$Br^- + CF_3Br \rightarrow [CF_3Br_2]^-$	+39.9	
$Br^- + CF_2Cl_2 \rightarrow [BrCF_2Cl_2]^-$	+24.6	+21.0 ± 1.2 ^b
$Br^- + CF_2Cl_2 \rightarrow [CF_2Cl_2Br]^-$	+47.2	

^a kcal mol⁻¹ ^b from Reference 88.

Since ΔG° for the $X^-(CF_3Y)$ complex is larger than zero at room temperature, it is clear that Reaction 6.14 proceeds through a so-called direct mechanism, *i.e.* there is no formation of an entrance channel ion-molecule complex. This then actually resembles a condensed phase S_N2 reaction (Reaction 6.31).



In Table 6.10 all transition states for back-side attack are lower in energy than for the front-side attack mechanism. Unfortunately it was not possible to test the computations by performing similar experiments to those of Hop and McMahon on a FT-ICR. GIB experiments like Ervin and co-workers performed on Reaction 6.5 would probably be a better alternative,¹⁵ since this technique provides much more sensitive measurements of cross sections and threshold energies.

The higher energy transition state $[CF_3XY]^-$ may also be determined experimentally. Close inspection of the NPA charges (see Section 6.4.4 for more details) indicates that it closely resembles a $[CF_3^\bullet XY^\bullet]$ complex. Monitoring the cross section of XY^\bullet as a function of the centre-of-mass energy of X^- may give information of the energy of $[CF_3XY]^-$ relative to the reactants X^- and CF_3Y . In Table 6.11 the ΔH^\ddagger_{298} values for the various transition states investigated have been summarized in terms of centre-of-mass (E_{cm}) and laboratory-frame (E_{lab}) ion kinetic energy of the nucleophiles. E_{cm} and E_{lab} are related by Equation 6.32, where M_{CF_3Y} is the mass of the CF_3Y neutral, and M_{X^-} is the mass of the halide ion. These values may be used as starting points for future threshold CID experiments.

$$E_{cm} = \frac{M_{CF_3Y}}{M_{X^-} + M_{CF_3Y}} \cdot E_{lab} \quad (6.32)$$

Table 6.11 Overview of the E_{cm} and E_{lab} values from computational B3LYP/c//B3LYP/a

$\Delta H_{298}^{\ddagger}$ values for the various $X^{-} + \text{CF}_3\text{Y} \rightarrow [\text{XCF}_3\text{Y}]^{-}$ and $[\text{CF}_3\text{XY}]^{-}$ reactions ($X, Y = \text{Cl}, \text{Br}$).

X^{-}	CF_3Y	TS	M_{ion}^a	M_{target}^a	$\Delta H_{298}^{\ddagger b}$	E_{cm}^c	E_{lab}^c
$^{35}\text{Cl}^{-}$	$\text{CF}_3^{35}\text{Cl}$	$[\text{}^{35}\text{ClCF}_3^{35}\text{Cl}]^{-}$	35	104	20.7	0.90	1.20
$^{35}\text{Cl}^{-}$	$\text{CF}_3^{35}\text{Cl}$	$[\text{CF}_3^{35}\text{Cl}_2]^{-}$	35	104	43.9	1.90	2.55
$^{35}\text{Cl}^{-}$	$\text{CF}_3^{79}\text{Br}$	$[\text{}^{35}\text{ClCF}_3^{79}\text{Br}]^{-}$	35	148	15.5	0.67	0.83
$^{35}\text{Cl}^{-}$	$\text{CF}_3^{79}\text{Br}$	$[\text{CF}_3^{35}\text{Cl}^{79}\text{Br}]^{-}$	35	148	36.3	1.58	1.95
$^{79}\text{Br}^{-}$	$\text{CF}_3^{35}\text{Cl}$	$[\text{}^{79}\text{BrCF}_3^{35}\text{Cl}]^{-}$	79	104	26.2	1.14	2.00
$^{79}\text{Br}^{-}$	$\text{CF}_3^{35}\text{Cl}$	$[\text{CF}_3^{79}\text{Br}^{35}\text{Cl}]^{-}$	79	104	47.1	2.04	3.60
$^{79}\text{Br}^{-}$	$\text{CF}_3^{79}\text{Br}$	$[\text{}^{79}\text{BrCF}_3^{79}\text{Br}]^{-}$	79	148	20.8	0.90	1.38
$^{79}\text{Br}^{-}$	$\text{CF}_3^{79}\text{Br}$	$[\text{CF}_3^{79}\text{Br}_2]^{-}$	79	148	39.9	1.73	2.66

^a amu

^b kcal mol⁻¹

^c eV

In Figures 6.18-6.20, all computational B3LYP/c//B3LYP/a ΔH_{298}° and $\Delta H_{298}^{\ddagger}$ values for the various reactions are summarized in schematic potential energy diagrams.

Even though the substitution of fluorine atoms for hydrogen atoms cannot reverse the order of back- and front-side attack mechanisms in gas phase S_N2 reactions, the difference between the two transition states has been reduced considerably. This is mainly due to the large increase in the $\Delta H_{298}^{\ddagger}$ values for back-side attack, and a small decrease in the $\Delta H_{298}^{\ddagger}$ values for front-side attack.

The relationship between kinetics and thermodynamics plays an important role in chemistry. Marcus derived an expression, the Marcus equation, that relates the activation energy to the thermodynamics of electron-transfer reactions in solution (Equation 6.33).¹¹⁶

$$\Delta E^{\ddagger} = \Delta E_0^{\ddagger} + \frac{\Delta E}{2} + \frac{(\Delta E)^2}{16\Delta E_0^{\ddagger}} \quad (6.33)$$

In Figure 6.21 a typical gas phase S_N2 double well potential energy diagram is shown together with the definitions of ΔE^{\ddagger} and ΔE shown in Equation 6.33. ΔE_0^{\ddagger} can be determined from the Marcus additivity postulate (Equation 6.34).¹¹⁶

$$\Delta E_0^{\ddagger} = \frac{1}{2}(\Delta E_{XX}^{\ddagger} + \Delta E_{YY}^{\ddagger}) \quad (6.34)$$

In Equation 6.34 ΔE_{XX}^{\ddagger} and ΔE_{YY}^{\ddagger} are the intrinsic kinetic contributions to the activation energy for the metathetical gas phase S_N2 Reactions 6.35 and 6.36.



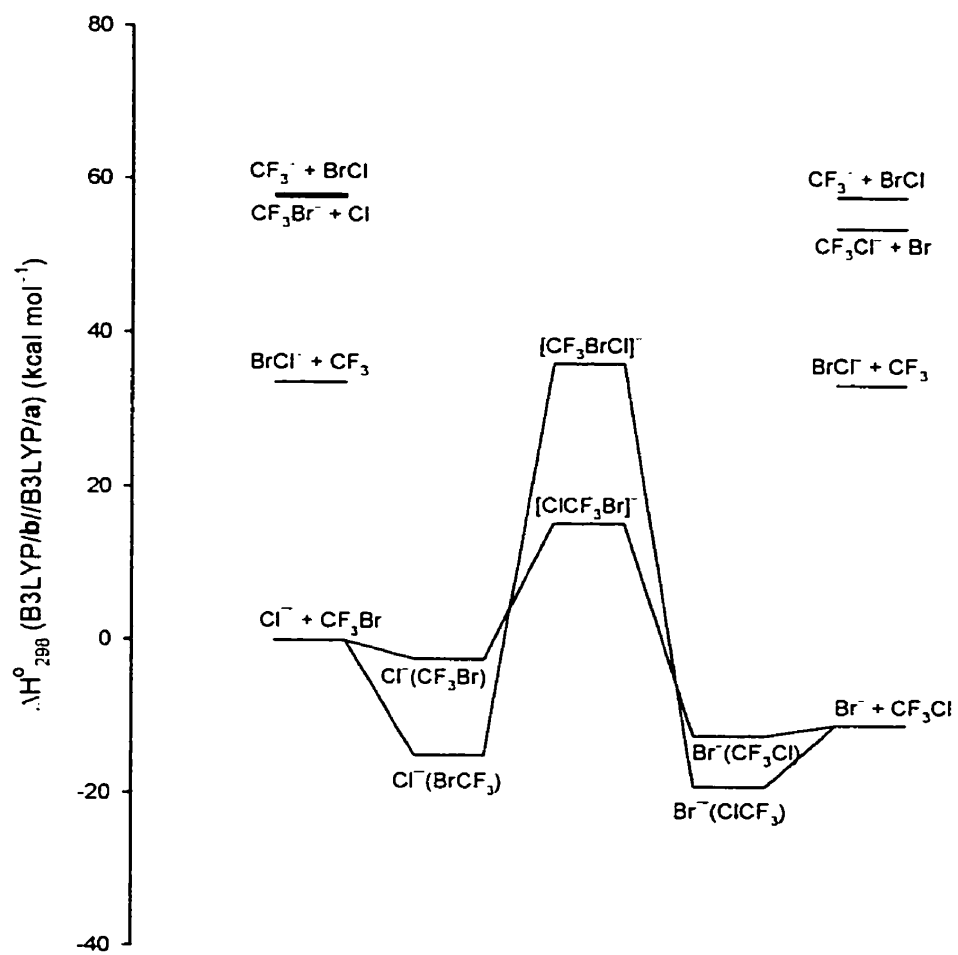


Figure 6.19 Schematic B3LYP/c//B3LYP/a potential energy profile for the various $\text{Cl}^- + \text{CF}_3\text{Br}$ reactions.

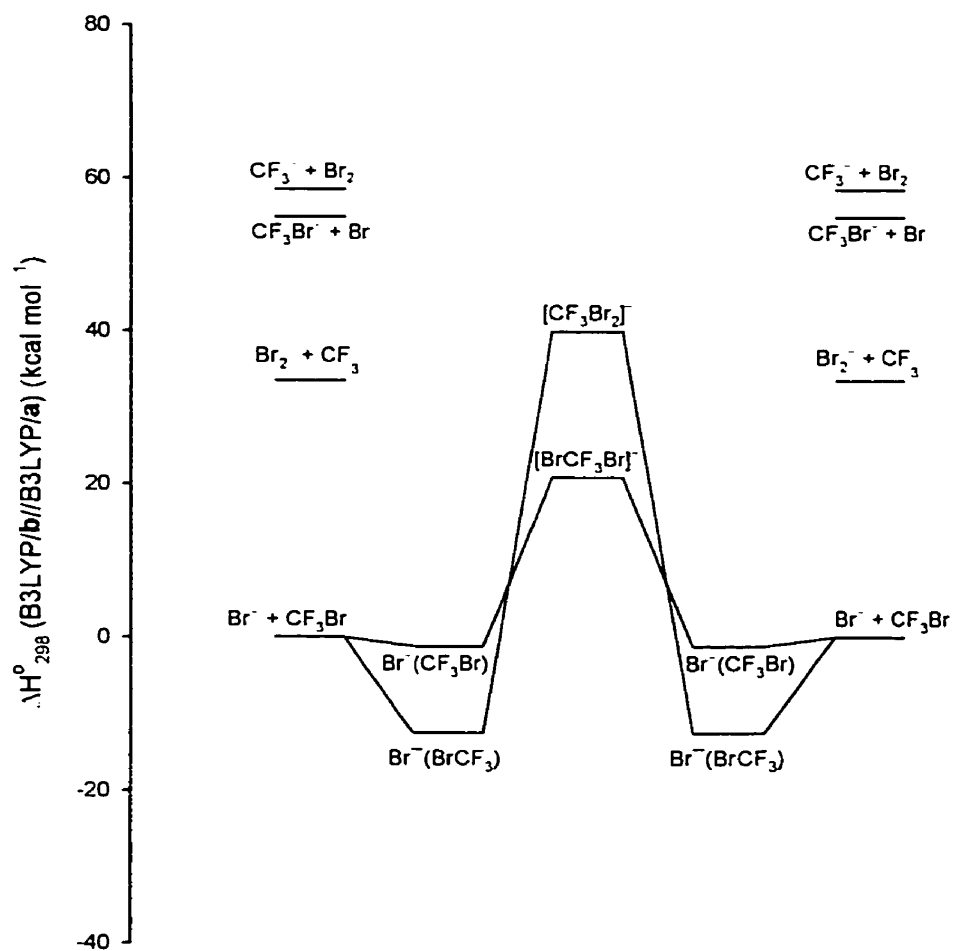


Figure 6.20 Schematic B3LYP/c//B3LYP/a potential energy profile for the various $\text{Br}^- + \text{CF}_3\text{Br}$ reactions.

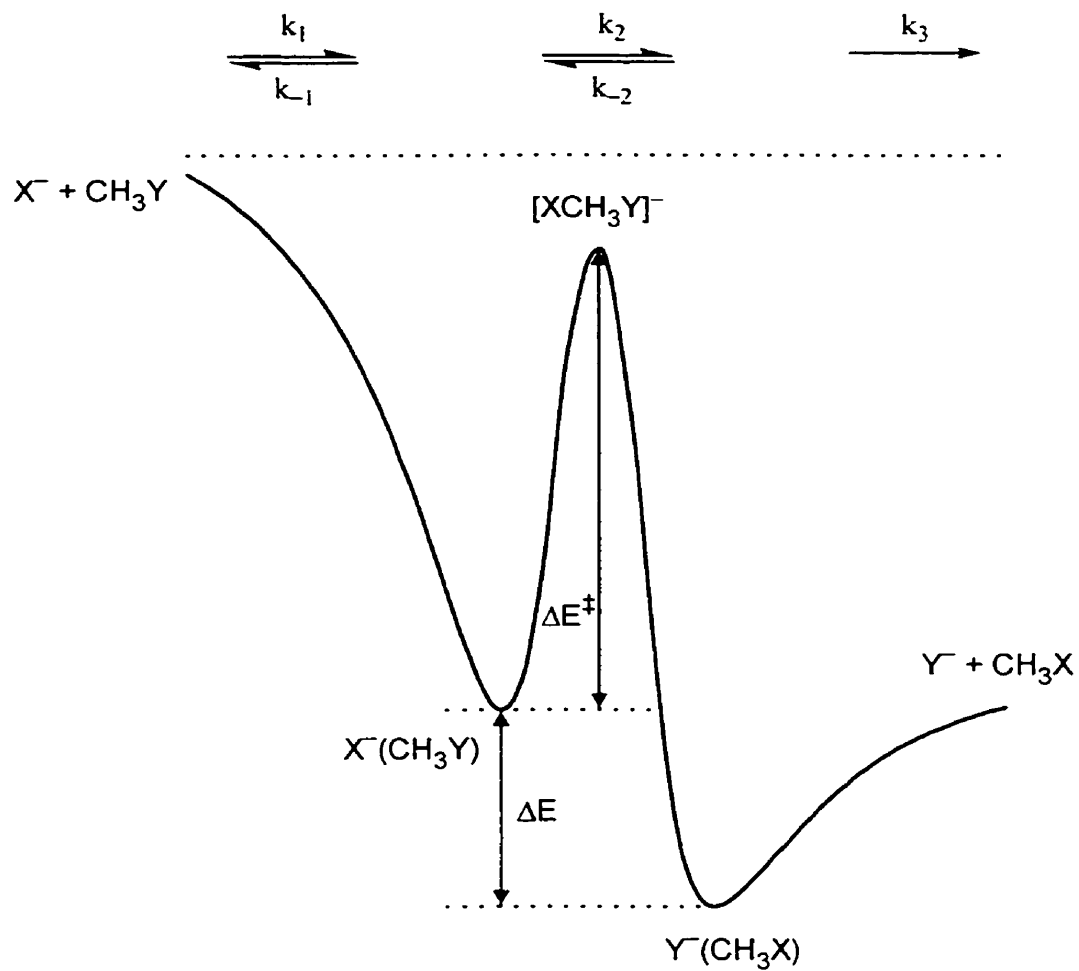


Figure 6.21 Gas phase double well potential energy diagram with the definitions of ΔE^\ddagger and ΔE for the Marcus expression applied to S_N2 reactions.

Brauman and co-worker showed experimentally and by using RRKM modeling that Equation 6.33 applies to a large variety of non-identity gas phase S_N2 reactions.^{9.117-120} This was confirmed theoretically by Wolfe *et al.* from *ab initio* computations.^{121,122} In Figure 6.22 it can be seen that the origin of the barrier comes from the avoided crossing from two potential energy surfaces related to Reactions 6.37 and 6.38.



This model assumes that the S_N2 reactions will be initiated by electron transfer reactions. Despite the limited amount of data available, it will be interesting to investigate if the high kinetic energy S_N2 reactions described in this chapter also follow Equation 6.33. From the B3LYP/c//B3LYP/a computations it can be determined that ΔE_{ClCl}^\ddagger and ΔE_{BrBr}^\ddagger are +23.0 and +22.0 kcal mol⁻¹, respectively. This gives a ΔE_0^\ddagger value of +22.5 kcal mol⁻¹. ΔE_{ClBr} has a value of -9.8 kcal mol⁻¹, which results in a ΔE^\ddagger value of +17.9 kcal mol⁻¹ from Equation 6.33. By using the B3LYP/c//B3LYP/a results an identical value can be obtained. This gives rise to a B value of 10.0 kcal mol⁻¹, which is close to proposed B values for halide ion-methyl halide S_N2 reactions by Shaik and Pross of approximately 14 kcal mol⁻¹.¹²³ Considering the condensed-phase-like appearance of the potential energy surfaces of the halide ion-trifluoromethyl halide reactions, the result here may be clear proof that condensed phase S_N2 reactions are indeed initiated by electron transfer reactions.

Finally, it has to be briefly mentioned that at the G3(MP2) level of theory the $\Delta_f H_{298}^\circ$ values of CF₃Cl and CF₃Cl[•] have been calculated to be -173.1 kcal mol⁻¹ and -193.0 kcal mol⁻¹, respectively. The first value is in good agreement with the experimental result of -169.2 kcal mol⁻¹.¹²⁴

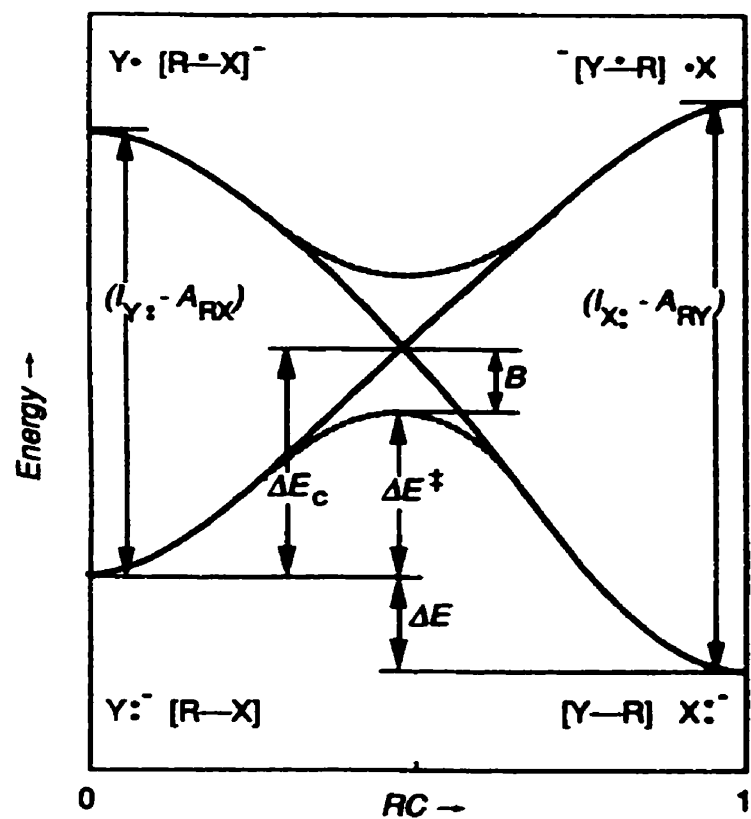


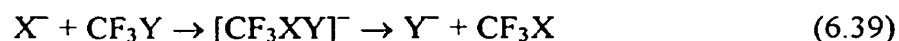
Figure 6.22 State correlation diagram for the non-identity S_N2 reaction $Y^- + RX \rightarrow X^- + RY$.

6.4.3 Normal Mode Vibrational Frequencies

In Section 6.4.1 it was shown that the B3LYP/a level of theory ([a/b] for CF₃I) is able to generate structures and dipole moments of the CF₃X molecules that are in good to excellent agreement with experimental data. This agreement was the main reason to use this level of theory for the subsequent computations on the ion-molecule complexes and transition states.

Unlike in Chapter 4 there will no extended discussion on the trends in normal mode vibrational frequencies and the agreement with experimental data, if available, for the various X⁻(YCF₃) and X⁻(CF₃Y) complexes, or the different XY molecules and their corresponding radical anions, XY^{-•}. In Table 6.12 an overview is given of the calculated and experimental normal mode vibrational frequencies of CF₃Cl, CF₃Br, and CF₃I.¹²⁵ The excellent agreement confirms once again that the B3LYP/a level of theory seems to be an acceptable choice.

As mentioned in Section 6.4.2, the [CF₃XY]⁻ transition state seems to closely resemble a [CF₃[•] XY^{-•}] complex, and it may be not only the transition state for a high kinetic energy S_N2 reaction (Reaction 6.39), but it may also be the transition state for XY^{-•} formation (Reaction 6.40).



In the [CF₃XY]⁻ transition state, the imaginary frequency corresponds to a combined C←X and C→Y motion. In addition, there is a X↔Y motion, and the corresponding frequency is very close to the frequency in “free” XY^{-•}. In [CF₃Cl₂]⁻, [CF₃ClBr]⁻, and [CF₃Br₂]⁻ the values are 179 cm⁻¹, 140 cm⁻¹, and 100 cm⁻¹, respectively, while in Cl₂^{-•}, ClBr^{-•}, and Br₂^{-•} the values are 198 cm⁻¹, 163 cm⁻¹, and 118 cm⁻¹, respectively. This is not a strong evidence, for formation of XY^{-•} can

Table 6.12 Overview of the computational B3LYP/a ([a/b] for X = I) and experimental normal mode vibrational frequencies for CF₃X (X = Cl, Br, I).

normal mode	v(CF ₃ Cl) ^a		v(CF ₃ Br) ^a		v(CF ₃ I) ^a	
	B3LYP/a	experiment ^b	B3LYP/a	experiment ^b	B3LYP/[a/b]	experiment ^b
CX bend	344	350	300	306	266	260
CX bend	344	350	300	306	266	260
CF ₃ s-deform	462	476	339	349	276	286
CF ₃ d-deform	553	563	541	547	531	537
CF ₃ d-deform	553	563	541	547	531	537
CX str	772	781	750	760	735	742
CF ₃ s-str	1074	1105	1057	1089	1048	1080
CF ₃ d-str	1180	1212	1174	1210	1154	1187
CF ₃ d-str	1180	1212	1174	1210	1154	1187

^a cm⁻¹

^b from Reference 117

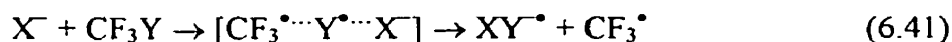
s (symmetric)

d (double)

deform (deformation)

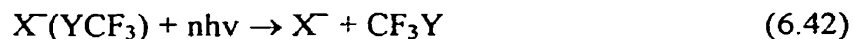
str (stretch)

proceed through another transition state (Reaction 6.41), as to where Y^\bullet transfer takes place.



The imaginary frequency in the $[XCF_3Y]^-$ transition state is larger than in the isomeric $[CF_3XY]^-$ transition state. For all three systems investigated it is consistently around $510i$, while for the front-side attack transition state it decreases from $210i$ to $185i$ to $163i$. Examination of the motion of the imaginary frequency in the $[XCF_3Y]^-$ transition state shows that it is an umbrella-like inversion of the CF_3 group as in NH_3 . This may be indicative of a direct mechanism, and it may explain the constant value for the three systems investigated. This may also explain the increased barrier height, relative to CH_3 . Substitution of one of the fluorine atoms by a chlorine atom decreases the imaginary frequencies in $[ClCF_2ClBr]^-$ and $[CF_2Cl_2Br]^-$ to $428i$ and $176i$, respectively.

Finally, it should be possible to obtain thermochemical and kinetics data on the $X^-(YCF_3)$ clusters by ZTRID. This is possible due to the strong absorption of black-body IR radiation by the C–F normal mode vibrations, causing the cluster to dissociate on a relatively fast time scale despite the medium to strong bonding (Reaction 6.42)



6.4.4 Natural Population Analysis Charges

When going from CF_3Cl to CF_3I the NPA charge on the halide atom increases from $0.00 e$ to $+0.15 e$. As expected, all fluorine atoms bear considerable negative charge, around $-0.33 e$, while the carbon atom is positively charged, ranging from $+0.88 e$ in CF_3I to $+1.00 e$ in CF_3Cl . This explains why X^- prefers to interact with Y in CF_3Y , but that back-side attack on carbon is possible. Upon formation of the $X^-(YCF_3)$ complex some charge redistribution takes place. First of all, charge transfer from X^- to the

CF₃Y part takes place, ranging from +0.08 *e* in Cl⁻(ClCF₃) to +0.22 *e* in Br⁻(ICF₃). The NPA charge on Y becomes more positive, while on carbon it becomes less positive to around +0.90 *e*. All fluorine atoms become more negatively charged to around -0.39 *e*. Formation of the X⁻(CF₃Y) complexes show a very different picture. First of all no charge transfer from X⁻ to CF₃Y takes place. In addition, the charges on the fluorine atoms become a little bit less negative, around -0.31 *e*, while the NPA charge on Y becomes negative. The charge on carbon becomes slightly more positive.

More interesting are the charges in the back- and front-side attack transition states. The wave function for the transition state [XCF₃Y]⁻ has partly a valence bond (VB) triple ion configuration X⁻CF₃⁺Y⁻. The transition state is basically nothing more than a CF₃⁺ transfer from X⁻ to Y⁻. In all [XCF₃Y]⁻ transition states investigated, the B3LYP/a NPA charge on X and Y is -0.70 *e*, while on the CF₃ part it is +0.40 *e* (q(C) around +1.25 *e* and q(F) around -0.27 *e*). Unlike for [XCH₃Y]⁻ transition states, where a decrease in |q(CH₃)|^{1/2} was observed going from [ClCH₃Cl]⁻ to [BrCH₃Br]⁻ ³⁷ here no decrease is observed in |q(CF₃)|^{1/2}. In the [CF₃XY]⁻ transition states a very different picture emerges. Both X and Y have NPA charges around -0.48 *e*, thereby making the CF₃ part neutral, with q(C) = +1.05 *e* and q(F) = -0.37 *e*. This confirms the [CF₃[•]XY^{•-}] nature of the [CF₃XY]⁻ transition state.

Finally, in [BrCF₂Cl₂]⁻ and [CF₂Cl₂Br]⁻ the only changes in the various NPA charges from substituting a fluorine atom for a chlorine atom is in the carbon atom. In the first transition state it is +0.80 *e*, while in the second it is +0.66 *e*. The new chlorine atom has NPA charges of +0.14 *e* and 0.00 *e* in both structures, respectively.

6.4.5 Potential Energy Surfaces

In Figure 6.23 the B3LYP/a potential energy surfaces for Reactions 6.43 and 6.44 are shown.





Morris and Viggiano observed both reaction channels in relative ratios that were strongly temperature and pressure dependent.⁹¹ For the reaction coordinate $R(\text{C}-\text{Br}) - R(\text{C}-\text{F})$ (ΔR) was chosen. As expected, the ion-dipole interaction for the formation of $\text{F}^-(\text{BrCF}_3)$ becomes important at longer ΔR values. The very high exothermicity of Reaction 6.43 may have pulled the transition state energy below that of the reactants. This reaction was the first clear example to show that a CF_3 group will not necessarily prevent back-side attack by a nucleophile in a gas phase $\text{S}_{\text{N}}2$ reaction. Formation of the $\text{F}^-(\text{CF}_3\text{Br})$ complex starts taking place at shorter ΔR values. As expected, the well-depth for the $\text{Br}^-(\text{CF}_4)$ complex is very shallow.

In Figure 6.24 results for relaxed scan computations on the $\text{Cl}^-(\text{BrCF}_3)$ and $\text{Cl}^-(\text{CF}_3\text{Br})$ complexes are shown, confirming that also for less exothermic well-depths complex formation proceeds along a Morse-like potential.

More interesting is the three-dimensional HF/6-31G(d) potential energy surface for the $\text{Cl}^- + \text{CF}_3\text{Cl}$ system shown in Figures 6.25 and 6.26. It can be seen clearly that only a linear approach of CF_3Cl by Cl^- will lead to crossing the barrier at threshold. Any approach other than that will lead to non-reactive backward scattering of Cl^- . At kinetic energies higher than the threshold energy, it appears to be possible to initiate reactive collisions that do not necessarily require a co-linear approach. Consequently a larger cone of Cl^- back-side approach becomes available, and an additional increase in the cross section may be expected. It is beyond the scope of this thesis to go into a detailed discussion like that done by Ervin on the Reaction 6.5.⁶⁸ In Figure 6.27 the same reaction is shown along the reaction coordinate $\Delta R(\text{C}-\text{Cl})$ as calculated at the B3LYP/a level of theory. If the reaction only proceeds by linear approach of CF_3Cl by Cl^- , and crossing of the barrier would proceed by the hard-sphere line-of-centre model, for which the cross sections are given by Equations 6.45 and 6.46,⁶⁸ Figure 6.28 can be drawn.

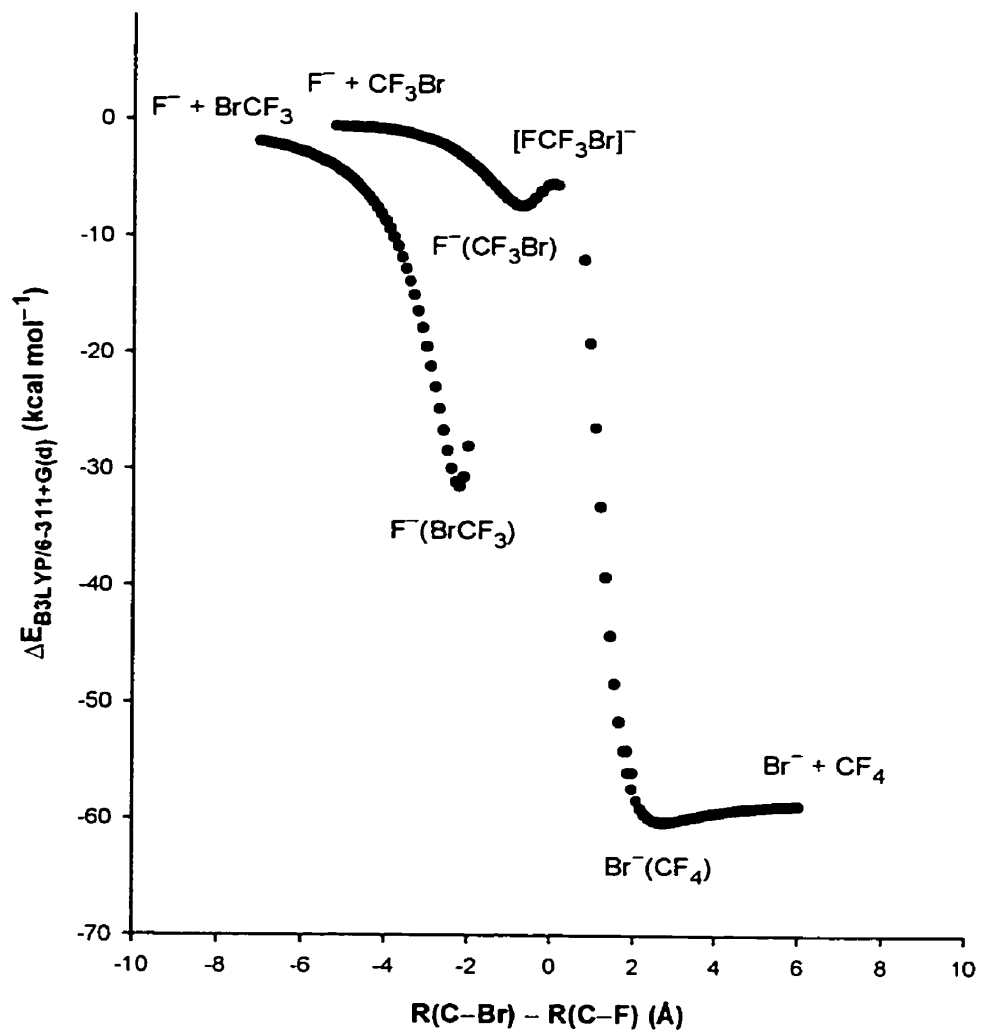


Figure 6.23 B3LYP/a potential energy surfaces for the $F^- + CF_3Br \rightarrow Br^- + CF_4$ and $F^- + CF_3Br \rightleftharpoons F^-(BrCF_3)$ reactions.

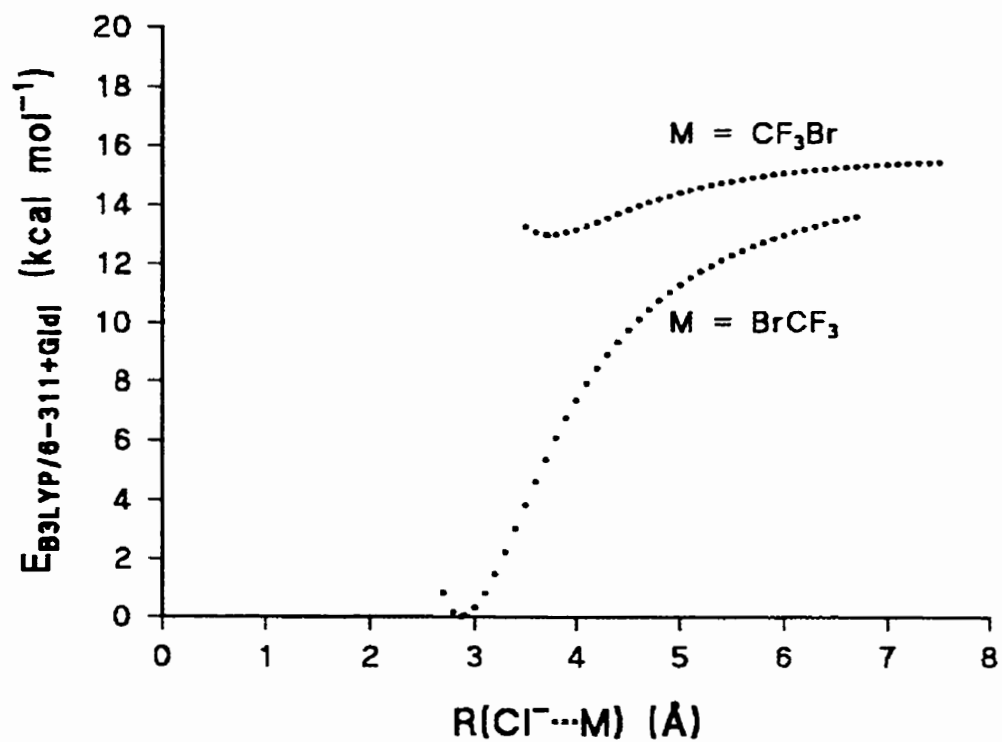


Figure 6.24 B3LYP/a potential energy scans for the $\text{Cl}^- + \text{CF}_3\text{Br} \rightleftharpoons \text{Cl}^-(\text{BrCF}_3)$ and $\text{Cl}^- + \text{CF}_3\text{Br} \rightleftharpoons \text{Cl}^-(\text{BrCF}_3)$ clustering equilibria.

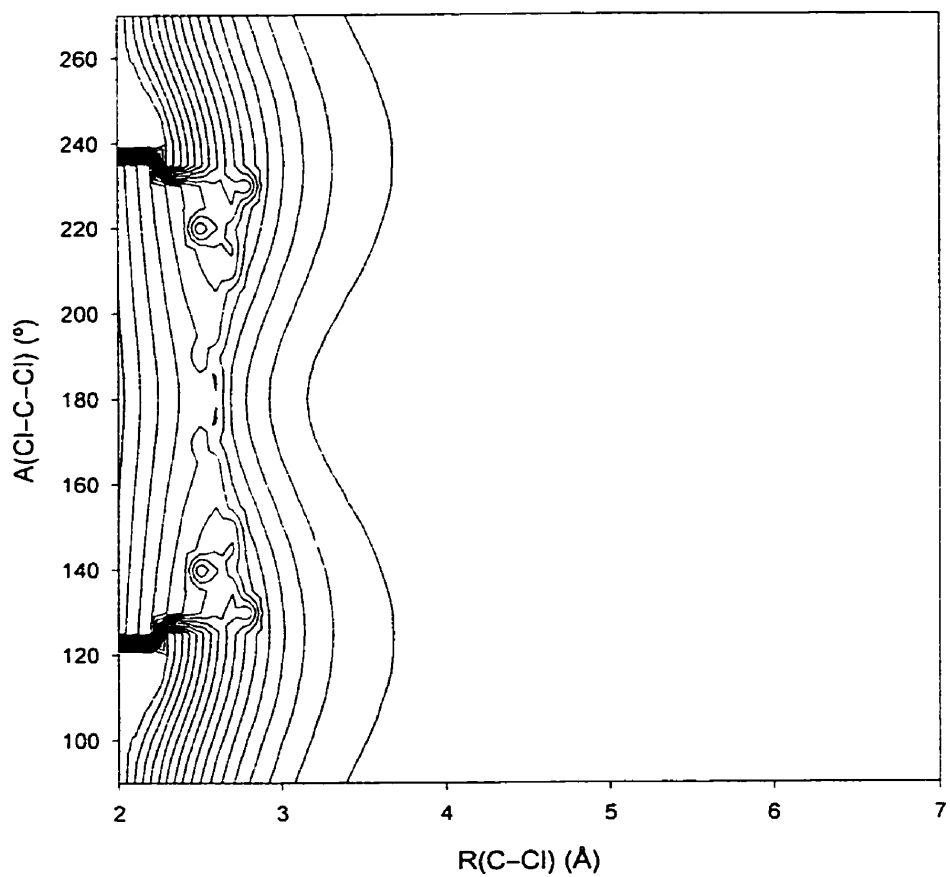


Figure 6.25 HF/6-31G(d) potential energy surface for the $\text{Cl}^- + \text{CF}_3\text{Cl}$ back-side attack $\text{S}_{\text{N}}2$ reaction ($0 \leq E_{\text{HF/6-31G(d)}} \leq 80 \text{ kcal mol}^{-1}$, contour lines in 5 kcal mol^{-1} increments).

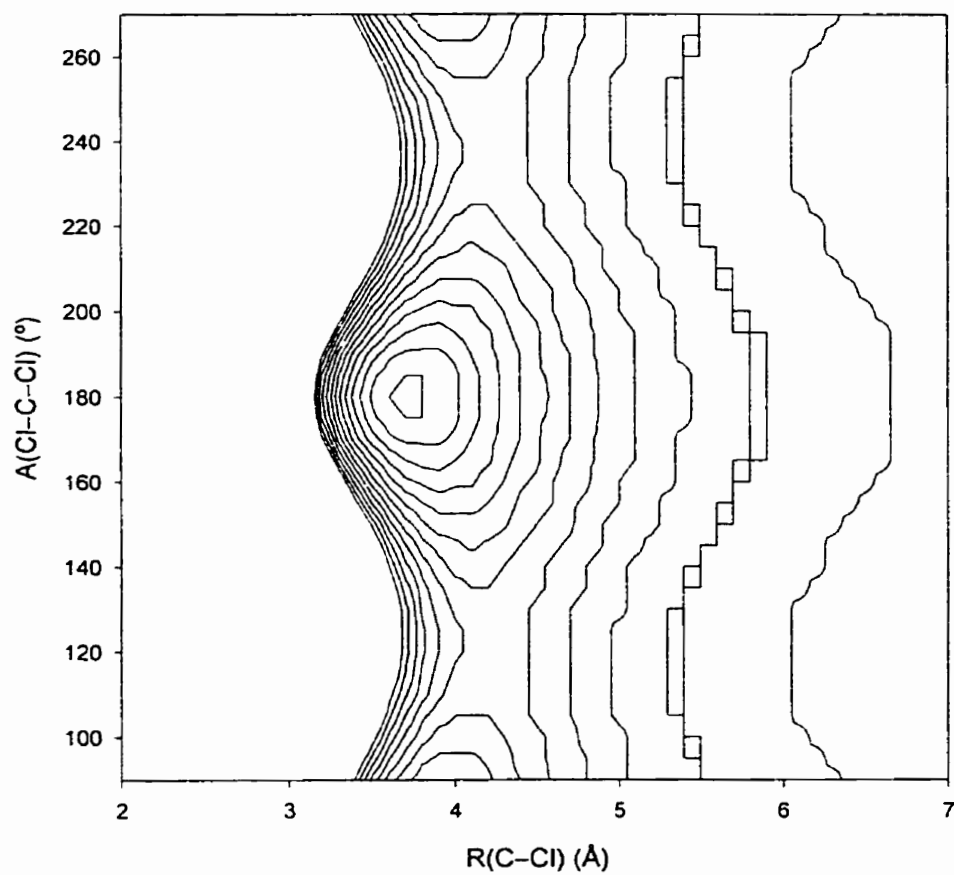


Figure 6.26 HF/6-31G(d) potential energy surface for the $\text{Cl}^- + \text{CF}_3\text{Cl}$ back-side attack $\text{S}_{\text{N}}2$ reaction ($-5 \leq E_{\text{HF/6-31G(d)}} \leq 0 \text{ kcal mol}^{-1}$, contour lines in $0.25 \text{ kcal mol}^{-1}$ increments).

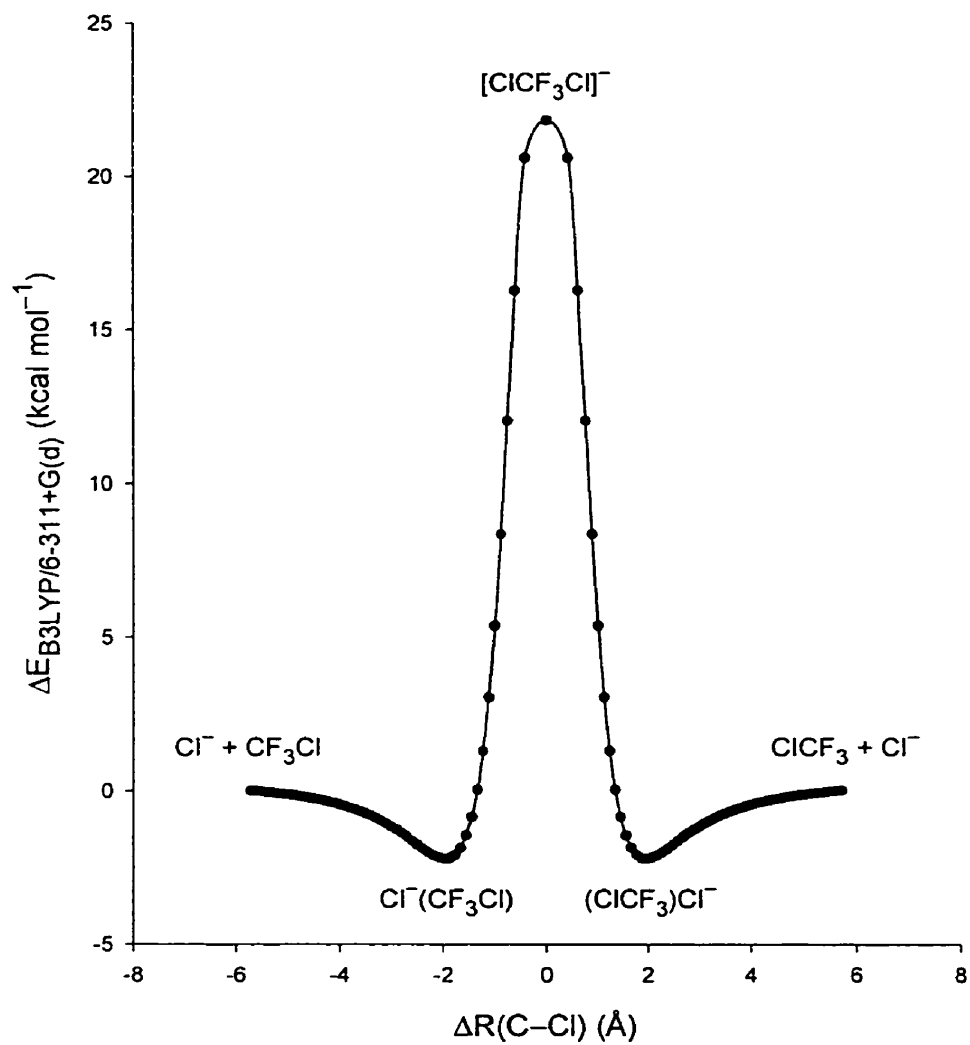


Figure 6.27 B3LYP/a threshold energy pathway for the $\text{Cl}^- + \text{CF}_3\text{Cl} \rightarrow [\text{ClCF}_3\text{Cl}]^- \rightarrow \text{ClCF}_3 + \text{Cl}^-$ back-side attack S_N2 reaction.

$$\sigma(E_T) = 0 \text{ if } E_T \leq \epsilon_0 \quad (6.45)$$

$$\sigma(E_T) = \pi d^2 \left(\frac{E_T - \epsilon_0}{E_T} \right) \text{ if } E_T > \epsilon_0 \quad (6.46)$$

In Equation 6.46, d is the hard-sphere diameter (sum of the radii of the two reactants), E_T is the relative translational energy, and ϵ_0 is the threshold energy of the reaction. In Figure 6.28 a value of $24.9 \text{ kcal mol}^{-1}$ for ϵ_0 from the HF computations was used, while for d a value of $4.36 \times 10^{-8} \text{ cm}$ was used. This value is the sum of the radius of Cl^- (1.81 \AA)¹²⁶ and the radius of CF_3Cl (2.55 \AA).¹²⁷⁻¹³¹ In the gas phase the CF_3Cl molecule can rotate freely and randomly, and the chance that Cl^- encounters a perfectly linearly aligned CF_3Cl molecule is 1 in $(360)^2$. The πd^2 term has to be divided by this number. In addition, it has to be considered that even if the $[\text{ClCF}_3\text{Cl}]^-$ transition state at threshold is formed, there is a 50% chance that it will dissociate back to the original reactants (Reaction 6.47).



In Figure 6.29 the results from Hop and McMahon are shown for Reaction 6.14.⁸⁸ It can be seen that their data do not flatten off as predicted in Figure 6.28. This has been explained by Ervin for Reaction 6.5.⁶⁸ As the kinetic energy of Cl^- is increased above the threshold energy, crossing of the barrier become feasible for a larger range of Cl-C-Cl angles. This means that reactive collisions can take place, that do not necessarily go through the $[\text{ClCF}_3\text{Cl}]^-$ transition state. In Figure 6.30, the barrier height as a function of the Cl-C-Cl angle is shown. The dots come from the HF/6-31G(d) computations, and the line is an empirical fit. By converting the barrier heights to E_{cm} values, and calculating angle corrected cross sections as done before for the linear $\text{Cl}^- + \text{CF}_3\text{Cl}$ reactive collision at threshold energy, one can obtain Figure 6.31. It is clear that now the data from Hop and McMahon in Figure 6.29 can be

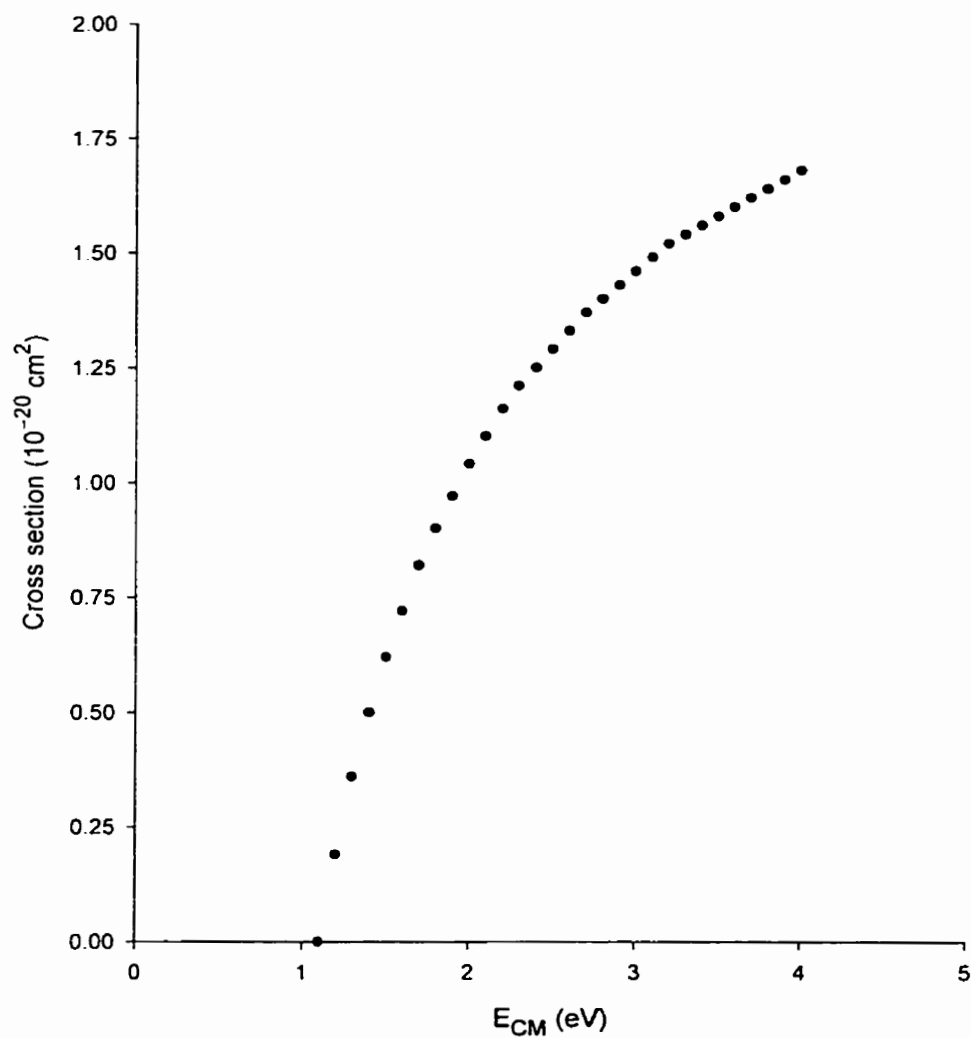


Figure 6.28 HF/6-31G(d) threshold energy pathway hard-sphere line-of-centre cross section for the $\text{Cl}^- + \text{CF}_3\text{Cl} \rightarrow [\text{ClCF}_3\text{Cl}]^- \rightarrow \text{ClCF}_3 + \text{Cl}^-$ back-side attack $\text{S}_{\text{N}}2$ reaction as a function of Cl^- centre-of-mass kinetic energy.

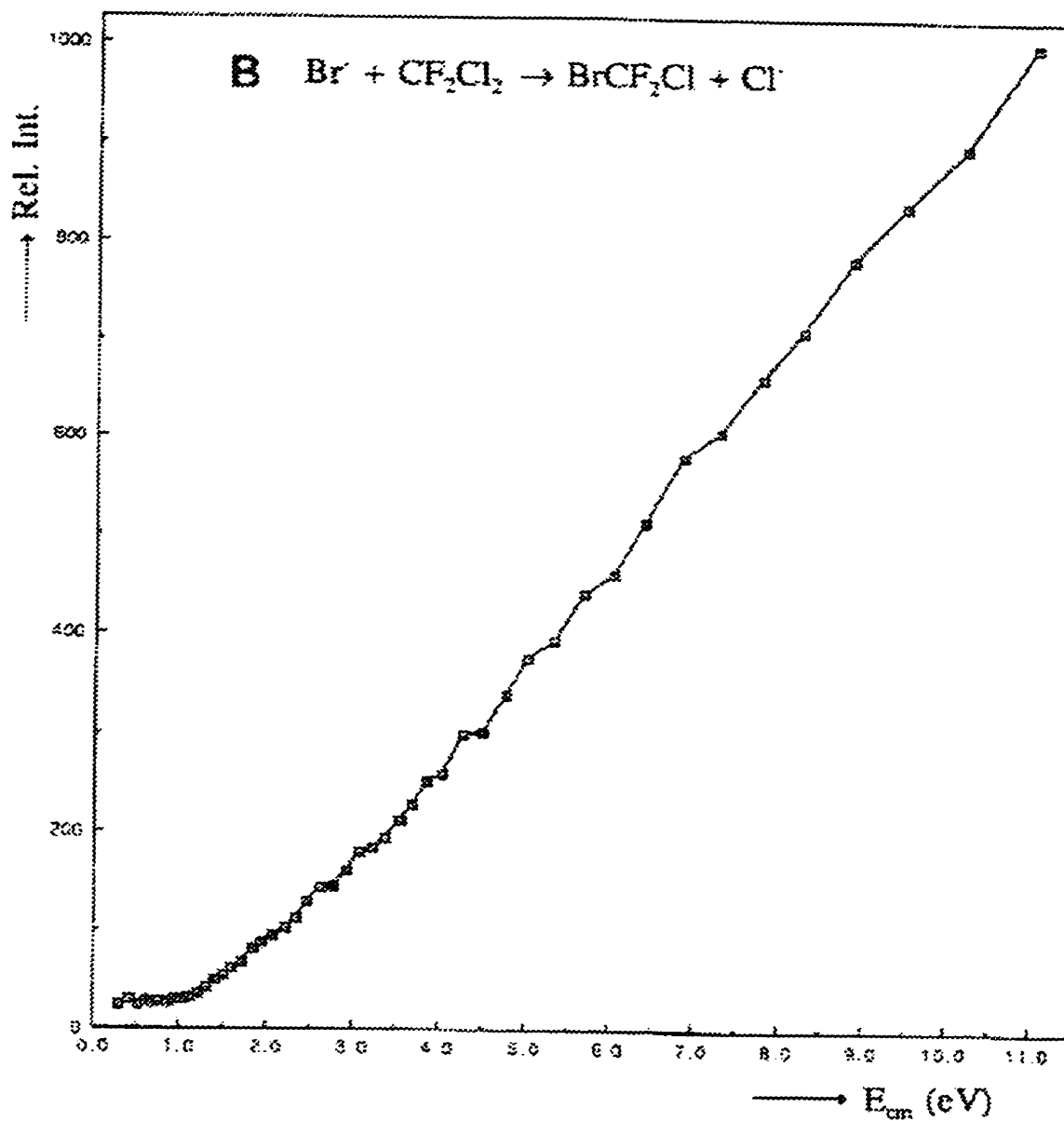


Figure 6.29 Experimental relative Cl^- intensity as a function of the Br^- centre-of-mass kinetic energy of the $\text{Br}^- + \text{CF}_2\text{Cl}_2 \rightarrow \text{Cl}^- + \text{CF}_2\text{ClBr}$ $\text{S}_{\text{N}}2$ reaction (from Reference 88).

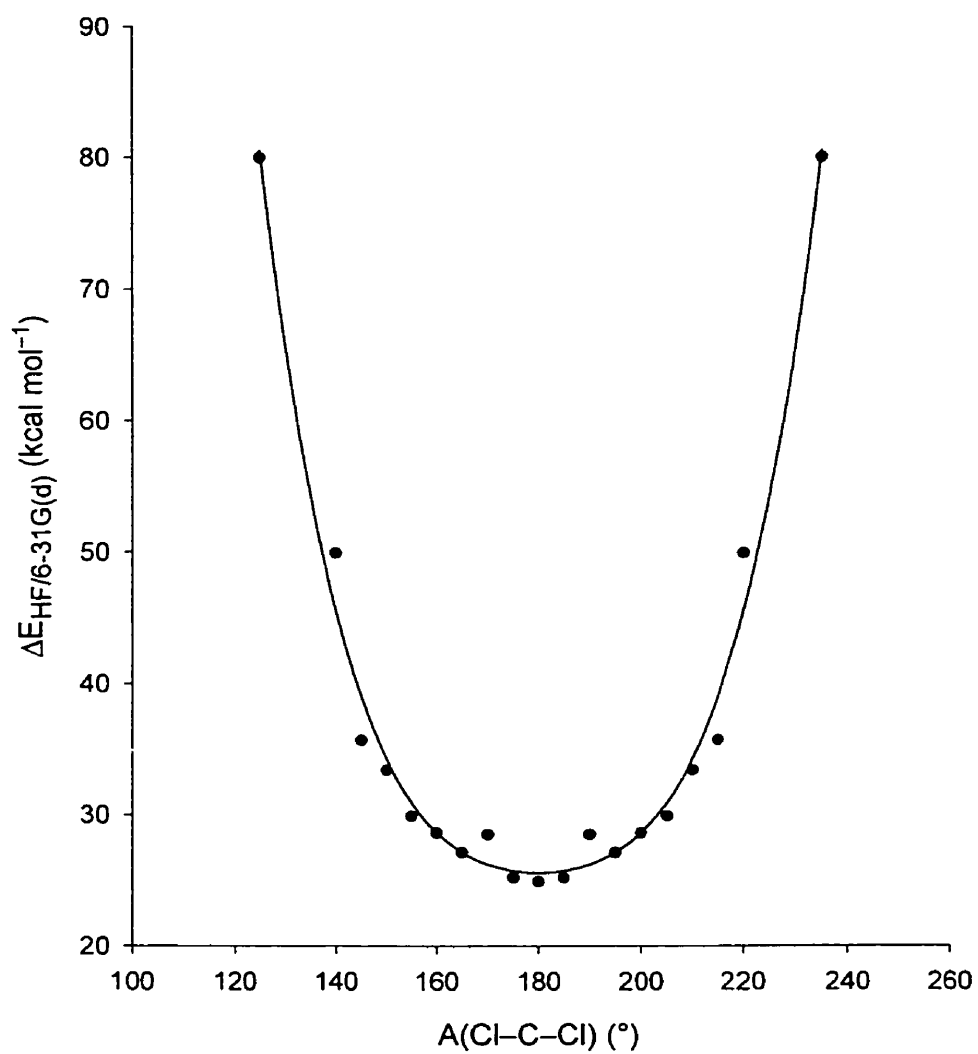


Figure 6.30 HF/6-31G(d) barrier height as a function of the Cl–C–Cl angle from the $\text{Cl}^- + \text{CF}_3\text{Cl}$ potential energy surface in Figure 6.24.

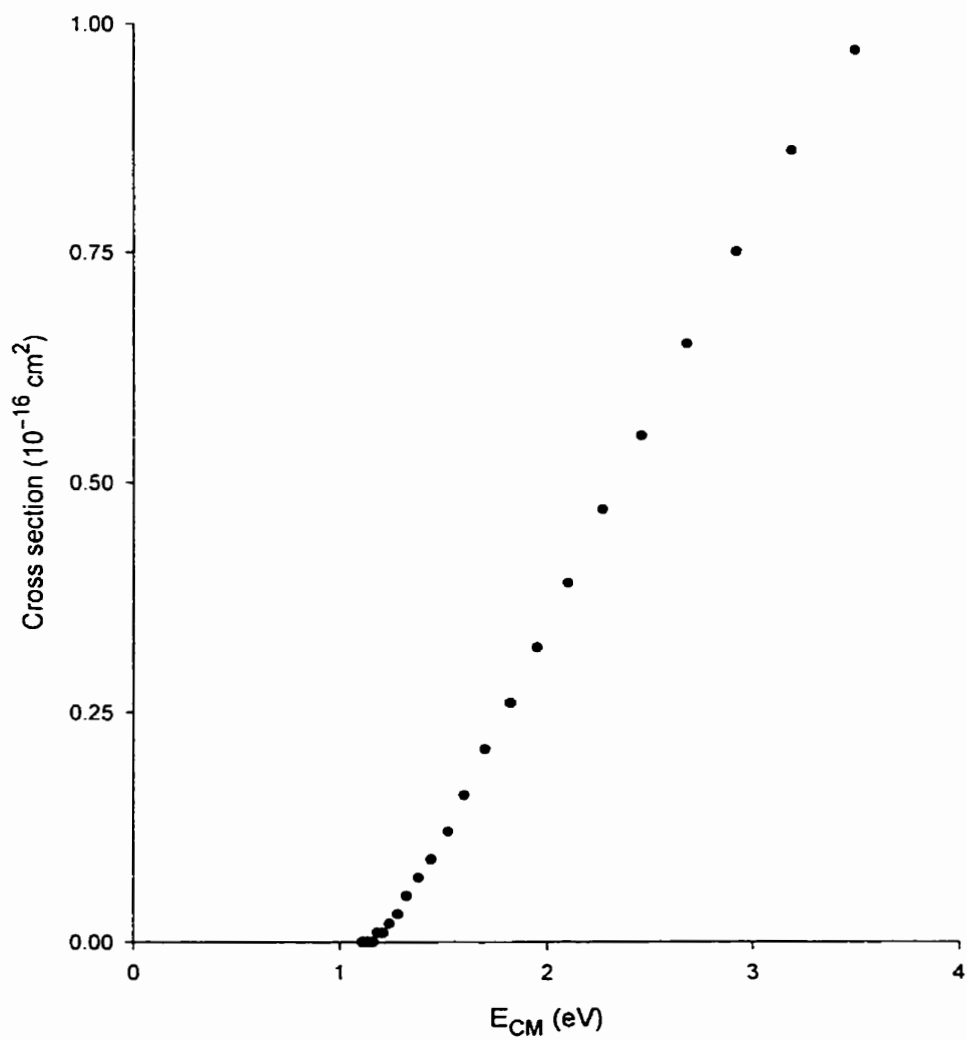


Figure 6.31 HF/6-31G(d) angle-corrected hard-sphere line-of-centre cross section for the $\text{Cl}^- + \text{CF}_3\text{Cl} \rightarrow [\text{ClCF}_3\text{Cl}]^- \rightarrow \text{ClCF}_3 + \text{Cl}^-$ back-side attack $\text{S}_{\text{N}}2$ reaction as a function of Cl^- centre-of-mass kinetic energy.

reproduced qualitatively, and that the values are in the correct range as measured by DeTuri *et al.*¹⁵ It would be interesting to see these experiments done and to treat the data as Ervin had, and to use the potential energy data to perform trajectory calculation to get more insight into kinetics and dynamics of this direct mechanism reaction. Finally it would be interesting to perform a crossed-beam experiment of a kinetic energy resolved Cl^- beam and a perpendicular CF_3^*Cl beam. Angle resolved detection of the $^*\text{Cl}^-$ product ions from the $\text{S}_{\text{N}}2$ reaction may be expected to show a wider distribution as the kinetic energy of Cl^- is increased.

6.5 Conclusions

The B3LYP/a level of theory is able to calculate structures, dipole moments, and normal mode vibrational frequencies of CF_3X ($\text{X} = \text{F}, \text{Cl}, \text{Br}, \text{I}$) that are in good agreement with experimental data. Two isomeric cluster ions of the halide ions with the trifluoromethyl halides were found, $\text{X}^-(\text{YCF}_3)$ and $\text{X}^-(\text{CF}_3\text{Y})$. These correspond to front- and back-side attack mechanism complexes, respectively. Associated with these two different mechanisms are two transition state structures, $[\text{XCF}_3\text{Y}]^-$ and $[\text{CF}_3\text{XY}]^-$.

From PHPMS experiments, ΔH° and ΔS° values for the formation of the $\text{Cl}^-(\text{BrCF}_3)$, $\text{Cl}^-(\text{ICF}_3)$ (ΔH° only), and $\text{Br}^-(\text{BrCF}_3)$ complexes were determined. There was good agreement with $\Delta\text{H}^\circ_{298}$ values from B3LYP/c//B3LYP/a computations, and $\Delta\text{S}^\circ_{298}$ values from the B3LYP/a computations. In addition to the thermochemistry of the $\text{S}_{\text{N}}2$ reactions, the thermochemistry of other, higher energy pathways was determined. The agreement of the B3LYP/c//B3LYP/a computations when the reaction includes radicals and radical anions is poorer than in case of closed shell species. It was shown that the $\text{S}_{\text{N}}2$ reaction between a halide ion and a trifluoromethyl halide proceeds through a back-side attack transition state. The $\text{Cl}^- + \text{CF}_3\text{Br} \rightarrow \text{Br}^- + \text{CF}_3\text{Cl}$ reaction was shown to follow the Marcus theory, which means that even at high kinetic energies the back-side $\text{S}_{\text{N}}2$ reaction may be initiated by electron transfer. From normal mode vibrational analysis and NPA charges it was shown that the $[\text{CF}_3\text{XY}]^-$ transition state closely resembles a $[\text{CF}_3^* \text{XY}^{\bullet-}]$ complex. The back-side attack $\text{S}_{\text{N}}2$ reaction through the $[\text{XCF}_3\text{Y}]^-$ transition state

appears to be a direct mechanism, since the imaginary frequency is independent of the identity of X and Y.

Finally, potential energy surfaces have been determined for a few reactions and clustering equilibria. The suggestion by Morris and Viggiano that the formation of Br^- from the reaction between F^- and CF_3Br comes from back-side nucleophilic displacement is indeed correct, showing that the CF_3 group does not have to hinder attack on the carbon atom despite the presence of three electronegative fluorine atoms. At threshold, the back-side $\text{S}_{\text{N}}2$ reaction between kinetically excited Cl^- and CF_3Cl proceeds through a $[\text{ClCF}_3\text{Cl}]^-$ transition state. Above the threshold, co-linear approach of CF_3Cl by Cl^- is no longer necessary to initiate the reaction. Barrier crossing can occur at a wider range of Cl-C-Cl angles, hereby increasing the cross section. Correcting the hard-sphere line-of-centre cross section reproduces experimental data by Hop and McMahon, and the data are in the proper range of published GIB cross section data.

6.6 References

- 1 Bohme, D. K.; Young, L. B. *J. Am. Chem. Soc.* **1970**, *92*, 7354.
- 2 Young, L. B.; Lee-Ruff, E.; Bohme, D. K. *Chem. Commun.* **1973**, 35.
- 3 Bohme, D. K.; Mackay, G. I.; Payzant, J. D. *J. Am. Chem. Soc.* **1974**, *96*, 4027.
- 4 Tanaka, K.; Mackay, G. I.; Payzant, J. D.; Bohme, D. K. *Can. J. Chem.* **1976**, *54*, 1643.
- 5 Brauman, J. I.; Olmstead, W. M.; Lieder, C. A. *J. Am. Chem. Soc.* **1974**, *96*, 4030.
- 6 Olmstead, W. N.; Brauman, J. I. *J. Am. Chem. Soc.* **1977**, *99*, 4219 and references cited therein.
- 7 Caldwell, G.; Magnera, T. F.; Kebarle, P. *J. Am. Chem. Soc.* **1984**, *106*, 959.
- 8 De Puy, C. H.; Gronert, S.; Mullin, A.; Bierbaum, V. M. *J. Am. Chem. Soc.* **1990**, *112*, 8650.
- 9 Wladkowski, B. D.; Brauman, J. I. *J. Phys. Chem.* **1993**, *97*, 13158 and references cited therein.
- 10 Knighton, W. B.; Bogнар, J. A.; O'Connor, P. M.; Grimsrud, E. P. *J. Am. Chem. Soc.* **1993**, *115*, 12079 and references cited therein.

- 11 Cyr, D. M.; Scarton, M. G.; Johnson, M. A. *J. Chem. Phys.* **1993**, *99*, 4869.
- 12 Viggiano, A. A.; Morris, R. A.; Su, T. *J. Am. Chem. Soc.* **1994**, *116*, 2213.
- 13 Graul, S. T.; Bowers, M. T. *J. Am. Chem. Soc.* **1994**, *116*, 3875 and references cited therein.
- 14 Li, C.; Ross, P.; Szulejko, J. E.; McMahon, T. B. *J. Am. Chem. Soc.* **1996**, *118*, 9360 and references cited therein
- 15 DeTuri, V. F.; Hintz, P. A.; Ervin, K. E. *J. Phys. Chem. A* **1997**, *101*, 5969 and references cited therein.
- 16 Craig, S. L.; Brauman, J. I. *Science* **1997**, *276*, 1536 and references cited therein.
- 17 Dessent, C. E. H.; Johnson, M. A. *J. Am. Chem. Soc.* **1997**, *119*, 5067.
- 18 Lehman, L.; Matejcek, S.; Illenberger, E. *Ber. Bunsenges. Phys. Chem.* **1997**, *101*, 287.
- 19 Ayotte, P.; Kim, J.; Kelley, J. A.; Nielsen, S. B.; Johnson, M. A. *J. Am. Chem. Soc.* **1999**, *121*, 6950 and references cited therein.
- 20 Kuznetsov, A. M. *J. Phys. Chem. A* **1999**, *103*, 1239.
- 21 Flores, A. E.; Gronert, S. *J. Am. Chem. Soc.* **1999**, *121*, 2627.
- 22 Lehman, L.; Illenberger, E. *Int. J. Mass Spectrom.* **1999**, *185/186/187*, 463.
- 23 Bierbaum, V. M.; Davico, G. E. *J. Am. Chem. Soc.* **2000**, *122*, 1740.
- 24 Langer, J.; Matejcek, S.; Illenberger, E. *Phys. Chem. Chem. Phys.* **2000**, *2*, 1001.
- 25 Angel, L. A.; Ervin, K. M. *Proceedings of the 48th ASMS Conference on Mass Spectrometry and Allied Topics*, June 11-15, 2000, Long Beach, CA, WPB 060.
- 26 Shi, Z.; Boyd, R. J. *J. Am. Chem. Soc.* **1989**, *111*, 1575 and references cited therein.
- 27 Tucker, S. C.; Truhlar, D. G. *J. Phys. Chem.* **1989**, *93*, 8138 and references cited therein.
- 28 Zulicke, L.; Vetter, R. *J. Am. Chem. Soc.* **1990**, *112*, 5136.
- 29 Shi, Z.; Boyd, R. J. *J. Am. Chem. Soc.* **1990**, *112*, 6789 .
- 30 Shi, Z.; Boyd, R. J. *J. Am. Chem. Soc.* **1991**, *113*, 1072.
- 31 Shi, Z.; Boyd, R. J. *J. Am. Chem. Soc.* **1991**, *113*, 2434.
- 32 Gronert, S. *J. Am. Chem. Soc.* **1991**, *113*, 6041.
- 33 Jensen, F. *Chem. Phys. Lett.* **1992**, *196*, 368.
- 34 Lee, I.; Kim, C. K.; Lee, B.-S. *J. Org. Chem.* **1994**, *59*, 4490.

- 35 Wladkowski, B. D.; Allen, W. D.; Brauman, J. I. *J. Phys. Chem.* **1994**, *98*, 13532 and references cited therein.
- 36 Deng, L.; Branchadell, V.; Ziegler, T. *J. Am. Chem. Soc.* **1994**, *116*, 10645 and references cited therein.
- 37 Glukhotsev, M. N.; Pross, A.; Radom, L. *J. Am. Chem. Soc.* **1995**, *117*, 2024 and references cited therein.
- 38 Glukhotsev, M. N.; Pross, A.; Radom, L. *J. Am. Chem. Soc.* **1995**, *118*, 6273 and references cited therein.
- 39 Glukhotsev, M. N.; Pross, A.; Schlegel, H. B.; Bach, R. B.; Radom, L. *J. Am. Chem. Soc.* **1996**, *118*, 11258 and references cited therein.
- 40 Glukhotsev, M. N.; Bach, R. D.; Pross, A.; Radom, L. *Chem. Phys. Lett.* **1996**, *260*, 558.
- 41 McKee, M. L. *J. Org. Chem.* **1997**, *62*, 7942.
- 42 Uggerud, E. *J. Chem. Soc. Perkin Trans.* **1999**, 1459.
- 43 Hoz, S.; Basch, H.; Wolk, J. L.; Hoz, T.; Rozentel, E. *J. Am. Chem. Soc.* **1999**, *121*, 7724.
- 44 Gronert, S.; Fong, L.-M. *Int. J. Mass Spectrom.* **1999**, *192*, 185.
- 45 Moliner, V.; Williams, I. H. *J. Am. Chem. Soc.* **2000**, *122*, 10895.
- 46 Safi, B.; Choho, K.; Geerlings, P. *J. Phys. Chem. A* **2001**, *105*, 591.
- 47 Parthiban, S.; de Oliveira, G.; Martin, J. M. L. *J. Phys. Chem. A* **2001**, *105*, 895 and references cited therein.
- 48 Vande Linde, S. R.; Hase, W. L. *J. Phys. Chem.* **1990**, *94*, 2778 and references cited therein.
- 49 Vande Linde, S. R.; Hase, W. L. *J. Phys. Chem.* **1990**, *94*, 6148.
- 50 Tucker, S. C.; Truhlar, D. G. *J. Am. Chem. Soc.* **1990**, *112*, 3338.
- 51 Hase, W. L.; Cho, Y. J. *J. Chem. Phys.* **1993**, *98*, 8626.
- 52 Wang, H.; Peslherbe, G. H.; Hase, W. L. *J. Am. Chem. Soc.* **1994**, *116*, 9644.
- 53 Wang, H.; Zhu, L.; Hase, W. L. *J. Phys. Chem.* **1994**, *98*, 1608.
- 54 Hase, W. L. *Science* **1994**, *266*, 998.
- 55 Peslherbe, G. H.; Wang, H.; Hase, W. L. *J. Chem. Phys.* **1995**, *102*, 5626.

- 56 Wang, H.; Hase, W. L. *J. Am. Chem. Soc.* **1995**, *117*, 9347 and references cited therein.
- 57 Hu, W.-P.; Truhlar, D. G. *J. Am. Chem. Soc.* **1995**, *117*, 10726.
- 58 Wang, H.; Hase, W. L. *Chem. Phys.* **1996**, *212*, 247.
- 59 Peslherbe, G. H.; Wang, H.; Hase, W. L. *J. Am. Chem. Soc.* **1996**, *118*, 2257.
- 60 Wang, H.; Goldfield, E. M.; Hase, W. L. *J. Chem. Soc. Faraday Trans.* **1997**, 737 and references cited therein.
- 61 Wang, H.; Hase, W. L. *J. Am. Chem. Soc.* **1997**, *119*, 3093 and references cited therein.
- 62 Mann, D. J.; Hase, W. L. *J. Phys. Chem. A* **1998**, *102*, 6208.
- 63 Su, T.; Wang, H.; Hase, W. L. *J. Phys. Chem. A* **1998**, *102*, 9819 and references cited therein.
- 64 Igarashi, M.; Tachikawa, H. *Int. J. Mass Spectrom. Ion. Processes* **1998**, *181*, 151.
- 65 Li, G.; Hase, W. L. *J. Am. Chem. Soc.* **1999**, *121*, 7124 and references cited therein.
- 66 Raugai, S.; Cardini, G.; Schettino, V. *J. Chem. Phys.* **1999**, *111*, 10887 and references cited therein.
- 67 Hernández, M. I.; Campos-Martínez, J.; Villarreal, P.; Schmatz, S.; Clary, D. C. *Phys. Chem. Chem. Phys.* **1999**, *1*, 1197.
- 68 Ervin, K. M. *Int. J. Mass Spectrom.* **1999**, *185/186/187*, 343.
- 69 Schmatz, S. *Chem. Phys. Lett.* **2000**, *330*, 188.
- 70 Gleave, J. L.; Hughes, E. D.; Ingold, C. K. *J. Chem. Soc.* **1935**, 236.
- 71 Ingold, C. K. "Structure and Reactivity in Organic Chemistry", 2nd ed., Cornell University Press, Ithaca, NY, **1969**.
- 72 Hartshorn, S. R. "Aliphatic Nucleophilic Substitution", Cambridge University Press, London, **1973**.
- 73 Streitweiser, Jr., A. "Solvolytic Displacement Reactions", McGraw-Hill, New York, NY, **1973**.
- 74 Viggiano, A. A.; Morris, R. A.; Paschkewitz, J. S.; Paulson, J. *J. Am. Chem. Soc.* **1992**, *114*, 10477.
- 75 Seeley, J.; Morris, R. A.; Viggiano, A. A.; Wang, H.; Hase, W. L. *J. Am. Chem. Soc.* **1997**, *119*, 571.

- 76 Craig, S. L.; Zhong, M.; Brauman, J. I. *J. Am. Chem. Soc.* **1998**, *120*, 12125.
- 77 Ren, J.; Brauman, J. I. *Proceedings of the 48th ASMS Conference on Mass Spectrometry and Allied Topics*, June 11-15, **2000**, Long Beach, CA, ThPB 265.
- 78 Tonner, D. S.; McMahon, T. B. *J. Am. Chem. Soc.* **2000**, *122*, 8783.
- 79 Barlow, S. E.; Van Doren, J. M.; Bierbaum, V. M. *J. Am. Chem. Soc.* **1988**, *110*, 7240.
- 80 Cyr, D. M.; Scarton, M. G.; Wiberg, K. B.; Johnson, M. A.; Nonose, S.; Hirokawa, J.; Tanaka, H.; Kondow, T.; Morris, R. A.; Viggiano, A. A. *J. Am. Chem. Soc.* **1995**, *117*, 1828.
- 81 Cyr, D. M.; Posey, L. A.; Bishea, G. A.; Han, C.-C.; Johnson, M. A. *J. Am. Chem. Soc.* **1991**, *113*, 9697.
- 82 Cyr, D. M.; Bishea, G. A.; Scarton, M. G.; Johnson, M. A. *J. Chem. Phys.* **1992**, *97*, 5991.
- 83 Cyr, D. M.; Bishea, G. A.; Han, C.-C.; Posey, L. A.; Johnson, M. A. *Soc. Photo-Opt. Instrum. Eng. (SPIE) Proc.* **1992**, *1638*, 74.
- 84 Artau, A.; Nizzi, K. A.; Hill, B. T.; Sunderlin, L. S.; Wenthold, P. G. *J. Am. Chem. Soc.* **2000**, *122*, 10667 and references cited therein.
- 85 Nizzi, K. E.; Pommerening, C. A.; Sunderlin, L. S. *J. Phys. Chem. A* **1998**, *102*, 7674.
- 86 Nizzi, K. E.; Pommerening, C. A.; Sunderlin, L. S. Do, K.; Klein, T. P.; Pommerening, C. A.; Sunderlin, L. S. *J. Am. Soc. Mass Spectrom.* **1997**, *8*, 688.
- 87 Sanov, A.; Sanford, T.; Butler, L. J.; Vala, J.; Kosloff, R.; Lineberger, W. C. *J. Phys. Chem. A* **1999**, *103*, 10244.
- 88 Hop, C. E. C. A.; McMahon, T. B. *J. Phys. Chem.* **1991**, *95*, 10582.
- 89 Sunderlin, L. S.; Aristov, N.; Armentrout, P. B. *J. Am. Chem. Soc.* **1987**, *109*, 78 and references cited therein.
- 90 Morris, R. A. *J. Chem. Phys.* **1992**, *97*, 2372.
- 91 Morris, R. A.; Viggiano, A. A. *J. Phys. Chem.* **1994**, *98*, 3740.
- 92 Staneke, P. O.; Groothuis, G.; Ingemann, S.; Nibbering, N. M. M. *Int. J. Mass Spectrom. Ion Processes* **1995**, *149-150*, 99.

- 93 Morris, R. A.; Viggiano, A. A.; Miller, T. M.; Seeley, J. V.; Arnold, S. T.; Paulson, J. F.; Van Doren, J. M. *J. Phys. Chem.* **1996**, *100*, 10641.
- 94 Szulejko, J. E.; Fisher, J. J.; McMahon, T. B.; Wronka, J. *Int. J. Mass Spectrom. Ion Processes* **1988**, *83*, 147.
- 95 Frisch, M. J.; Trucks, G. W.; Schlegel, H. B.; Gill, P. M. W.; Johnson, B. G.; Robb, M. A.; Cheeseman, J. R.; Keith, T.; Petersson, G. A.; Montgomery, J. A.; Raghavachari, K.; Al-Laham, M. A.; Zakrzewski, V. G.; Ortiz, J. V.; Foresman, J. B.; Peng, C. Y.; Ayala, P. Y.; Chen, W.; Wong, M. W.; Andres, J. L.; Replogle, E. S.; Gomperts, R.; Martin, R. L.; Fox, D. J.; Binkley, J. S.; Defrees, D. J.; Baker, J.; Stewart, J. P.; Head-Gordon, M.; Gonzales, C.; Pople, J. A. *Gaussian 94*, Revision B3, Gaussian Inc., Pittsburgh PA, 1995.
- 96 Frisch, M. J.; Trucks, G. W.; Schlegel, H. B.; Scuseria, G. E.; Robb, M. A.; Cheeseman, J. R.; Zakrzewski, V. G.; Montgomery, Jr., J. A.; Stratmann, R. E.; Burant, J. C.; Dapprich, S.; Millam, J. M.; Daniels, A. D.; Kudin, K. N.; Strain, M. C.; Farkas, O.; Tomasi, J.; Barone, V.; Cossi, M.; Cammi, R.; Mennucci, B.; Pomelli, C.; Adamo, C.; Clifford, S.; Ochterski, J.; Petersson, G. A.; Ayala, P. Y.; Cui, Q.; Morokuma, K.; Malick, D. K.; Rabuck, A. D.; Raghavachari, K.; Foresman, J. B.; Cioslowski, J.; Ortiz, J. V.; Baboul, A. G.; Stefanov, B. B.; Liu, G.; Liashenko, A.; Piskorz, P.; Komaromi, I.; Gomperts, R.; Martin, R. L.; Fox, D. J.; Keith, T.; Al-Laham, M. A.; Peng, C. Y.; Nanayakkara, A.; Gonzalez, C.; Challacombe, M.; Gill, M. W.; Johnson, B.; Chen, W.; Wong, M. W.; Andres, J. L.; Gonzalez, C.; Head-Gordon, M.; Replogle, E. S.; Pople, J. A. *Gaussian 98*, Revision A.7 Gaussian, Inc., Pittsburgh PA, 1998.
- 97 Lee, C.; Yang, W.; Parr, R. G. *Phys. Rev. B* **1988**, *37*, 785.
- 98 Becke, A. D. *J. Chem. Phys.* **1993**, *98*, 1372, 5648.
- 99 Krishnan, R.; Binkley, J. S.; Seeger, R.; Pople, J. A. *J. Chem. Phys.* **1980**, *72*, 650.
- 100 Clark, T.; J. Chandrasekhar, J.; Schleyer, P.v.R. *J. Comp. Chem.* **1983**, *4*, 294.
- 101 Hay P. J.; Wadt, W. R. *J. Chem. Phys.* **1985**, *82*, 284.
- 102 Reed, A. E.; Curtiss, L. A.; Weinhold, F. *Chem. Rev.* **1988**, *88*, 899 and references cited therein.
- 103 Krishnan, R.; Binkley, J.S.; Seeger, R.; Pople, J.A. *J. Chem. Phys.* **1980**, *72*, 650.

- 104 Clark, T.; Chandrasekhar, J.; Spitznagel, G.W.; Schleyer, P. von R. *J. Comp. Chem.* **1983**, *4*, 294.
- 105 Gill, P.M.W.; Johnson, B.G.; Pople, J.A.; Frisch, M.J. *Chem. Phys. Lett.* **1992**, *197*, 499.
- 106 Frisch, M.J.; Pople, J.A.; Binkley, J.S. *J. Chem. Phys.* **1984**, *80*, 3265.
- 107 Møller, C.; Plesset, M. S. *Phys. Rev.* **1934**, *46*, 618.
- 108 Glukhovtsev, M. N.; Pross, A.; McGrath, M. P. Radom, L. *J. Chem. Phys.* **1995**, *103*, 1878.
- 109 Curtiss, L. A.; Raghavachari, K.; Redfern, P. C.; Rassolov, V.; Pople, J. A. *J. Chem. Phys.* **1998**, *109*, 7764.
- 110 Bartell, L. S.; Brockway, L. O. *J. Chem. Phys.* **1955**, *23*, 1860.
- 111 Bowen, H. J. M. *Trans. Faraday Soc.* **1954**, *50*, 444.
- 112 Wong, C.; Schomaker, V. *J. Chem. Phys.* **1958**, *28*, 1010.
- 113 Roszak, S.; Koski, W. S.; Kaufman, J. J.; Balasubramanian, K. *J. Chem. Phys.* **1997**, *106*, 7709.
- 114 CRC *Handbook of Chemistry and Physics*, Ref. Data, 76th ed., Lide, D. L. (Ed), CRC, Boca Raton, FL, **1995**.
- 115 Herzberg, G. "*Molecular Spectra and Molecular Structure, I. Spectra of Diatomic Molecules*", 2nd ed., Van Nostrand Reinhold Company, New York, NY, **1950**.
- 116 Marcus, R. A. *Annu. Rev. Phys. Chem.* **1964**, *15*, 155.
- 117 Pellerite, M. J.; Brauman, J. I. *J. Am. Chem. Soc.* **1980**, *102*, 5993.
- 118 Pellerite, M. J.; Brauman, J. I. *J. Am. Chem. Soc.* **1983**, *105*, 2672.
- 119 Dodd, J. A.; Brauman, J. I. *J. Am. Chem. Soc.* **1984**, *106*, 5356.
- 120 Dodd, J. A.; Brauman, J. I. *J. Phys. Chem.* **1986**, *90*, 3559.
- 121 Wolfe, S.; Mitchell, D. J.; Schlegel, H. B. *J. Am. Chem. Soc.* **1981**, *103*, 7692.
- 122 Wolfe, S.; Mitchell, D. J.; Schlegel, H. B. *J. Am. Chem. Soc.* **1981**, *103*, 7694.
- 123 Shaik, S. S.; Pross, A. *J. Am. Chem. Soc.* **1982**, *104*, 2708.
- 124 <http://webbook.nist.gov/chemistry/>
- 125 Shimanouchi, T. *Tables of Molecular Vibrational Frequencies Consolidated Volume I*; National Bureau of Standards: Washington, DC, **1972**, 1.
- 126 Batana, A.; Bruno, J.; Munn, R. W. *Mol. Phys.* **1997**, *92*, 1029.

- 127 Hirschfelder, J. O.; Curtiss, C. F.; Bird, R. B. *"Molecular Theory of Gasses and Liquids"* John Wiley & Sons, Inc, 1954. The cross section of CF₃Cl was estimated from the experimental cross sections of CCl₄ (reference 128), CCl₃F (reference 129), CCl₂F₂ (reference 130), and CF₄ (reference 131).
- 128 Landolt-Börnstein, *Physikalisch-Chemische Tabellen*, Springer in Reference 127.
- 129 *Thermodynamic Properties of Trichloromonofluoromethane*, Kinetic Chemical, Inc. 1938 in Reference 127.
- 130 *Thermodynamic Properties of Dichlorodifluoromethane*, Circular 12, Am. Soc. Refrig. Eng. 1931 in Reference 127.
- 131 MacCormack, K. E.; Schneider, W. G. *J. Chem. Phys.* 1951, 19, 849 in Reference 127.
- 132 Deyerl, H.-J.; Alconcel, L. S.; Continetti, R. E. *J. Phys. Chem. A* 2001, 105, 552.

Chapter 7

Thermochemistry, structures, dynamics, and infrared spectroscopy of chloride ion-fluorinated ether and acetone complexes and neutrals in the gas phase

7.1 Introduction

The study of structures and thermochemistry of solvated gas phase ions continues to be an active field of research, providing insight into solvation processes, and the difference in intrinsic reactivity between the gas and condensed phases.¹⁻⁵ Especially interesting are systems where multiple bonding interactions are possible. In both the gas and condensed phases,⁶⁻¹¹ metal ion-crown ether complexes have been studied extensively, both experimentally and theoretically.¹² Less attention has been paid to weakly bound anion-containing complexes, where multiple bonding interactions may be present. Various articles¹³⁻²² and reviews^{23,24} have described condensed phase systems in which anions are interacting with the host molecule mainly by multiple hydrogen bonding or by ion-dipole interactions. Similar gas phase systems are fairly rare, and are mainly limited to perfluorinated crown ethers²⁵ and cryptands²⁶ binding to F^- and O_2^- . Larson and McMahon speculated on the possibility of multiple site interactions in $Cl^-((CF_2H)_2O)$ complexes based on ΔG°_{298} values from exchange equilibria relative to $Cl^-(CF_3OCF_2H)$, studied by ICR.²⁷ No information on standard entropy changes (ΔS°) could be obtained, thus preventing a more definitive proof for the occurrence of chelation. In addition, Larson and McMahon also measured by ICR the ΔG°_{298} values for three $Cl^- + \text{acetone-}F_n \rightleftharpoons Cl^-(\text{acetone-}F_n)$ equilibria ($\text{acetone-}F_n = CF_2HC(O)CF_2H$, $CF_3C(O)CF_2H$, $CF_3C(O)CF_3$). Zhang *et al.* used PHPMS to deduce that in chloride ion-diol complexes bidentate interactions take place.²⁸ This was shown experimentally by the standard entropy change accompanying the clustering reactions. PHPMS is one of the few experimental techniques able to provide ΔS° values for gas phase clustering

reactions, and an excellent example that illustrate the use of ΔS° is the work by Norman and McMahon.^{29,30} From different ΔS° values, obtained by deconvoluting the relevant Van't Hoff plots, they showed the existence of low and high temperature isomers for the gas phase clustering of $t\text{-C}_4\text{H}_9^+$ onto various small organic molecules,²⁹ and the folding of $\text{CH}_3(\text{CH}_2)_8\text{CO}_2^-$ to give intramolecular solvation.³⁰

In this work, the clustering of chloride ion onto various (fluorinated) ethers and acetones has been investigated by PHPMS and high level *ab initio* and DFT computational methods. By varying the number and positions of the electronegative fluorine atoms, and the functionality of the molecules, one would expect, *a priori*, changes in the structures of the cluster ions, accompanied by changes in the thermochemistry. The computations were performed to obtain more insight into the structures, especially where various rotamers and isomers are possible, to find a method to model the thermochemistry of these systems accurately compared to experiment, to obtain more insight into the change in normal mode vibrational frequencies and IR intensities upon complex formation, to test the suitability of the G3(MP2) composite method to obtain $\Delta_{\text{acid}}\text{H}^\circ_{298}$ values of the various fluorinated acetones, and to get more insight into the dynamics of the complex formation by performing relaxed potential energy surface scans.

Recently there has been a fair amount of interest in fluorinated ethers.³¹⁻⁴¹ This class of compounds has been developed to replace chlorofluorocarbons (CFC). Unfortunately these compounds may also contribute to global warming by their long atmospheric lifetimes, and their strong absorption of thermal radiation between 800 and 1400 cm^{-1} . The occurrence of chloride ion-fluorinated ether complexes in the atmosphere, and especially in the ionosphere, seems very unlikely, mainly due to the low concentrations of both chloride ions and the fluorinated ethers at those altitudes.

Finally, the Fourier-transform IR (FT-IR) spectra of $\text{CH}_3\text{C}(\text{O})\text{CH}_2\text{F}$, $\text{CF}_3\text{C}(\text{O})\text{CH}_3$, $\text{CF}_3\text{C}(\text{O})\text{CF}_2\text{H}$, and $\text{CF}_3\text{C}(\text{O})\text{CF}_3$ were recorded. This was done to test the quality of the computations, and because no IR spectra of the first and third compounds are available in the National Institute of Science and Technology (NIST) EPA Gas-Phase Infrared Database.⁴²

7.2 Experimental

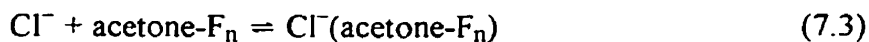
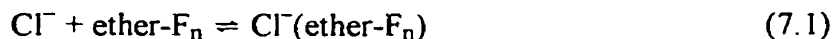
All measurements were carried out on a PHPMS instrument, configured around a VG 8-80 mass spectrometer. The instrument, constructed at the University of Waterloo, has been described in detail in Chapter 2.⁴³

Gas mixtures were prepared in a 5 L heated stainless steel reservoir at 370 K, by using CH₄ as a bath gas at pressures of 40-900 Torr. Chloride ion was generated from trace amounts of CCl₄ by DEC of thermalized electrons from 500 μs pulses of a 2 keV electron gun beam.

The five ethers ((CH₃)₂O, (CH₃CH₂)₂O, CH₃OCF₃, (CF₂H)₂O, and CF₃OCF₂H) and five acetones (CH₃C(O)CH₃, CH₃C(O)CH₂F, CF₃C(O)CH₃, CF₃C(O)CF₂H, and CF₃C(O)CF₃) were added to give relative amounts between 0.06% and 75%, and 0.05% and 5.5% (partial pressure), respectively, depending on the ion source temperature and the nature of the experiment involved. The ion source pressure and temperature ranged between 4.0-8.0 Torr and 300-600 K, respectively.

Time intensity profiles of mass selected ions were monitored by using a PC based multi-channel scalar (MCS) data acquisition system, configured between 50 and 200 μs dwell time per channel over 250 channels. Additive accumulations of ion signals resulting from 500-2000 electron gun beam pulses were typically used. Figures 7.1 and 7.2 illustrate typical data obtained from the equilibrium experiments.

Equilibrium constants (K_{eq}) at different absolute temperatures for the various chloride ion-ether (Reactions 7.1 and 7.2) and acetone (Reaction 7.3) clustering equilibria



can be determined from Equation 7.4 and 7.5:

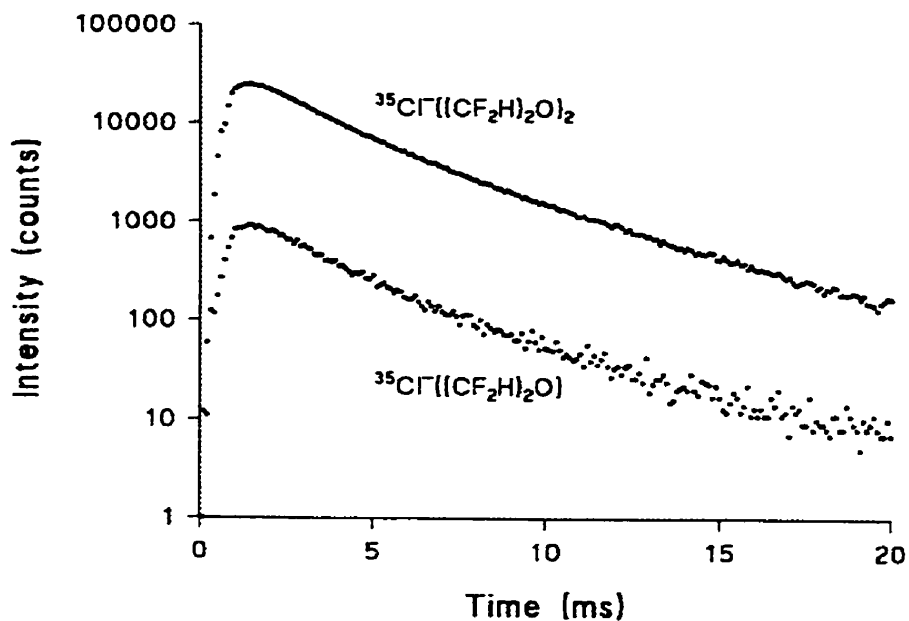


Figure 7.1 Time-intensity profile for the $\text{Cl}^-((\text{CF}_2\text{H})_2\text{O}) + (\text{CF}_2\text{H})_2\text{O} = \text{Cl}^-((\text{CF}_2\text{H})_2\text{O})_2$ clustering equilibrium at the following experimental conditions: $P_{\text{ion source}} = 4.00 \text{ Torr}$, $T_{\text{ion source}} = 352 \text{ K}$, $P(\text{CH}_4) = 3.97 \text{ Torr}$, $P((\text{CF}_2\text{H})_2\text{O}) = 0.03 \text{ Torr}$, $P(\text{CCl}_4) \ll 0.01 \text{ Torr}$.

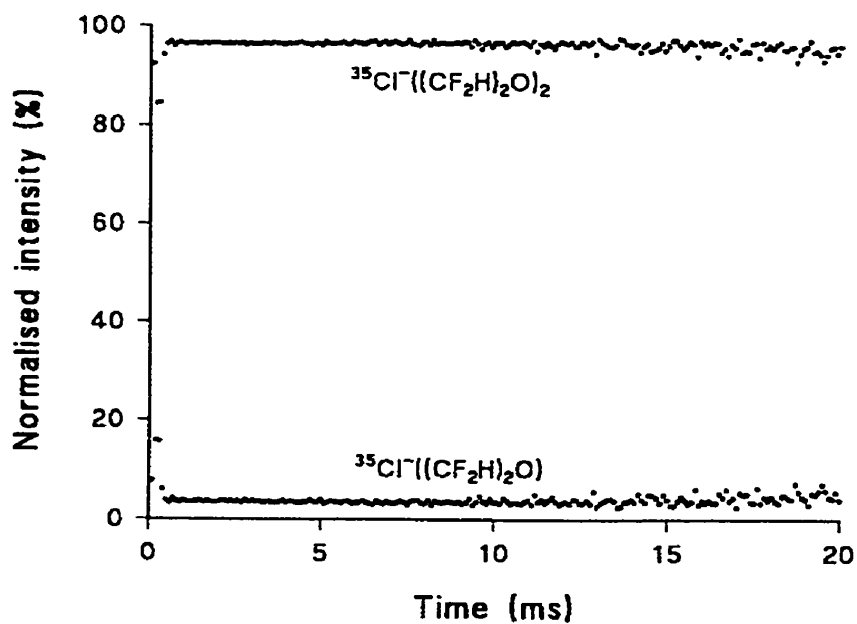


Figure 7.2 Normalized time-intensity profile of Figure 7.1.

$$K_{\text{eq}} = \frac{\text{Int}(\text{Cl}^-(\text{M}))}{\text{Int}(\text{Cl}^-)} \cdot \frac{P^\circ}{P_{\text{M.source}}} \quad (7.4)$$

$$K_{\text{eq}} = \frac{\text{Int}(\text{Cl}^-(\text{ether} - \text{F}_n)_2)}{\text{Int}(\text{Cl}^-(\text{ether} - \text{F}_n))} \cdot \frac{P^\circ}{P_{\text{ether-F}_n.\text{source}}} \quad (7.5)$$

In Equation 7.4, $\text{Int}(\text{Cl}^-(\text{M}))/\text{Int}(\text{Cl}^-)$ is the ion intensity ratio of the $\text{Cl}^-(\text{M})$ ($\text{M} = \text{ether-F}_n$ or acetone-F_n) and Cl^- ions at equilibrium, P° is the standard pressure (1 atm), and $P_{\text{M.source}}$ is the partial pressure (in atm) of the (fluorinated) ethers or acetones in the ion source. All equilibrium constants were essentially independent of the partial pressure of the various (fluorinated) ethers and acetones, and the ion source pressure.

All IR spectra were recorded on a Bruker IFS-55 FT-IR spectrometer. The fluorinated acetones were introduced in a stainless steel gas cell at room temperature with a path length of 22 cm and at pressures between 5 and 20 Torr. Absorption spectra were recorded from 500-5000 cm^{-1} by adding 30 scans at 1 cm^{-1} resolution using AgCl windows.

Dimethyl ether was purchased from Matheson of Canada Ltd.. Diethyl ether and acetone were purchased from BDH Inc. 1,1,1-Trifluorodimethyl ether and 1,1,1,3,3-Pentafluorodimethyl ether were purchased from Syn Quest Labs Inc. 1,1,3,3-Tetrafluorodimethyl ether was purchased from PCR Research Chemicals Inc.. Fluoroacetone was purchased from Sigma Aldrich Canada, 1,1,1-Trifluoroacetone was purchased from SCM Specialty Chemicals. 1,1,1,3,3-Pentafluoroacetone was purchased from Columbia Organic Chemicals Co. Hexafluoroacetone was purchased from Chemicals Procurement Laboratories Inc. Methane was purchased from Praxair. Carbon tetrachloride was purchased from J. T. Baker Chemical Co. All chemicals were used as received.

7.3 Computational

All computations were performed using the *Gaussian* 98 and 98W⁴⁴ suites of programs. Geometries were optimized at the HF⁴⁵ and MP2(fc)⁴⁶ levels of theory using

the 6-31G(d) (a)⁴⁷⁻⁴⁸ basis set for C, H, O, and F, and the 6-31+G(d) (b)⁴⁷⁻⁵¹ basis set for Cl. Normal mode vibrational frequencies were calculated at the HF level of theory and scaled by 0.8953,⁵² using the same basis sets as for the HF geometry optimization. Single point and NPA⁵³ computations were performed at the MP2 level of theory using the 6-311+G(2df,p) (c)^{49,51,54,55} basis set for C, H, O, and F, and the 6-311++G(3df,3pd) (d)^{49,51,54,55} basis set for Cl.

The motivation to use the 6-31G(d) basis set for C, H, O, and F in HF geometry optimizations and frequency computations, and MP2 geometry optimizations, and the use of the 6-311+G(2df,p) basis set for MP2 single point computations is mainly based on the work by East and Radom.⁵⁶ For a fairly large number of molecules they determined that experimental methyl group rotational barriers could be accurately reproduced by using the MP2/6-311+G(2df,p)//MP2/6-31G(d) level of theory. Since there was some interest *a priori* to look also at the effect of complex formation on methyl group rotational barrier heights, it seemed a logical choice to use a similar method. For CH₃C(O)CH₃, (CF₂H)₂O, CF₃C(O)CF₃, Cl⁻(CH₃C(O)CH₃), Cl⁻((CF₂H)₂O), and Cl⁻(CF₃C(O)CF₃) entropies were also calculated using the hindered rotor approximation.⁵⁷

The choice of 6-311++G(3df,3pd) as the Cl basis set for the MP2 single point computations is due to the smallest difference in EA(Cl[•]) between theory and experiment (3.54 eV versus 3.6127 eV).⁵⁸ For the HF geometry optimizations and frequency computations, and the MP2 geometry optimizations the use of 6-31+G(d) as the Cl basis set was mainly determined by cost considerations. Use of, for instance, 6-31++G(d) or 6-311++G(d,p) does not improve the value of the calculated EA(Cl[•])'s, which show large discrepancies with the experimental EA (2.48 eV for HF and 3.16 eV for MP2).

For CH₃C(O)CH₃, CH₃C(O)CH₂F, CF₃C(O)CH₃, CF₃C(O)CF₂H, and CF₃C(O)CF₃ geometry optimizations and frequency computations were performed using the B3LYP method⁵⁹⁻⁶¹ in combination with the 6-311++G(3d,3p) basis set.^{49,51,54,55}

For Cl⁻(CF₃C(O)CF₃) additional computations were performed using the B3LYP method in combination with the 6-311++G(3df,3pd) (Cl) and 6-311++G(3d,3p) (C, F, O) basis sets.

For some systems thermochemistry was calculated using the hindered rotor approximation by specifying the Freq=HindRot keyword in the *Gaussian 98* command line.⁶²

G3(MP2) enthalpies,⁶³ H_{298}° (G3(MP2)), were calculated for Cl^- , CH_3OCF_3 , CF_3O^- , CH_3Cl , $\text{Cl}^-(\text{CH}_3\text{OCF}_3)$, $\text{CF}_3\text{O}^-(\text{CH}_3\text{Cl})$, and $[\text{ClCH}_3\text{OCF}_3]^-$ to construct a schematic energy profile for the $\text{Cl}^- + \text{CH}_3\text{OCF}_3 \rightarrow \text{CF}_3\text{O}^- + \text{CH}_3\text{Cl}$ gas phase $\text{S}_{\text{N}}2$ reaction.

Standard ambient deprotonation enthalpy changes, $\Delta_{\text{acid}}H_{298}^{\circ}$, were calculated at the G3⁶³ and G3(MP2) levels of theory for a series of small to medium sized organic and inorganic molecules to test the suitability of these composite methods for these systems, as well as on the fluorinated acetones to evaluate experimental $\Delta_{\text{acid}}H^{\circ}$ results.

Finally, relaxed potential energy surface scans were performed for $\text{Cl}^-(\text{CH}_3\text{C}(\text{O})\text{CH}_3)$ and $\text{Cl}^-(\text{CF}_3\text{C}(\text{O})\text{CF}_3)$ at the MP2/[a/b] level of theory.⁶² For some points along the reaction coordinate, the $\text{Cl}^-\cdots\text{CO}$ distance, the structures were optimized to get more insights into the complex formation and the factors that determine it. For the $\text{Cl}^-(\text{CH}_3\text{C}(\text{O})\text{CH}_3)$ complex this distance was set between 4.0 Å and 14.0 Å, while for the $\text{Cl}^-(\text{CF}_3\text{C}(\text{O})\text{CF}_3)$ complex it was set between 2.2 Å and 12.2 Å.

7.4 Results and Discussion

7.4.1 Structures

The MP2/6-31(d) structures of the various rotamers of $(\text{CH}_3)_2\text{O}$, $(\text{CH}_3\text{CH}_2)_2\text{O}$, CH_3OCF_3 , $(\text{CF}_2\text{H})_2\text{O}$, $\text{CF}_3\text{OCF}_2\text{H}$, and CF_3OCF_3 are shown in Figures 7.3 to 7.12. Recently, results of optimized structures for several of the same molecules, but only the most stable rotamers, calculated at the MP2 and QCISD/6-31G(d), and B3LYP/6-311++G(3df,3pd) levels of theory were published.³⁶⁻³⁸ For a discussion of the structural features of $(\text{CH}_3)_2\text{O}$ calculated at the MP2/6-31G(d) level of theory versus experiment the reader is referred to recent work by Good and Francisco.³⁶ For $(\text{CH}_3\text{CH}_2)_2\text{O}$ no systematic study of the various rotamers was performed. For $(\text{CF}_2\text{H})_2\text{O}$ and $\text{CF}_3\text{OCF}_2\text{H}$, four and two stable rotamers were found, respectively.

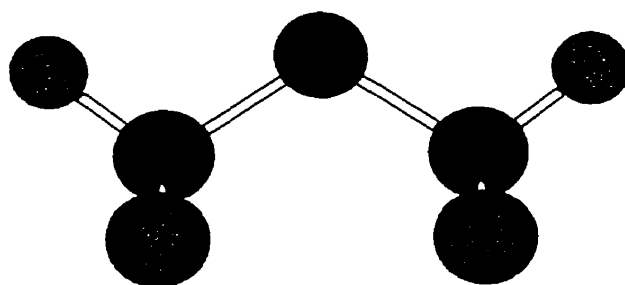


Figure 7.3 Optimized MP2/6-31G(d) structure of $(\text{CH}_3)_2\text{O}$.

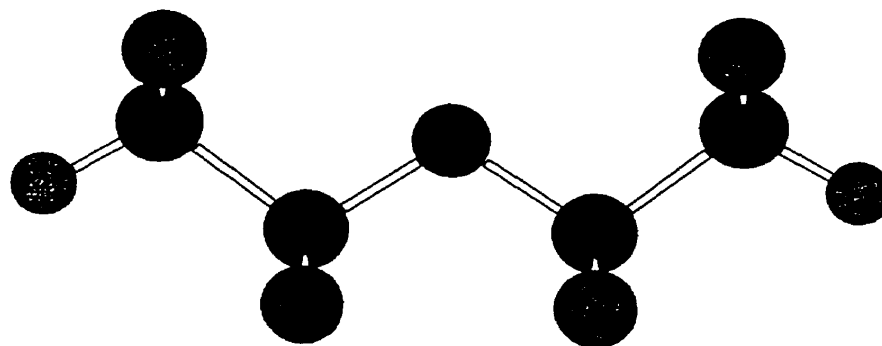


Figure 7.4 Optimized MP2/6-31G(d) structure of $(\text{CH}_3\text{CH}_2)_2\text{O}$ (rotamer 1).

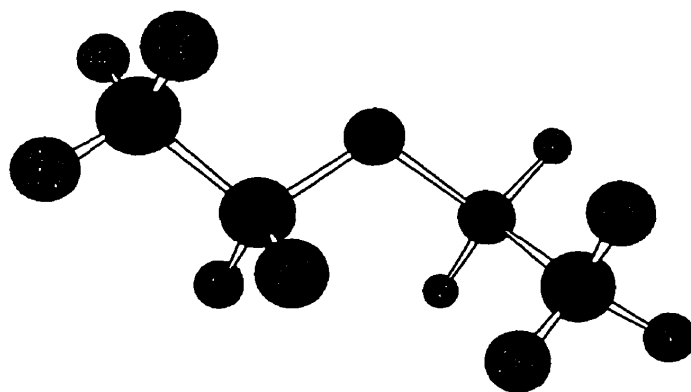


Figure 7.5 Optimized MP2/6-31G(d) structure of $(\text{CH}_3\text{CH}_2)_2\text{O}$ (rotamer 2).

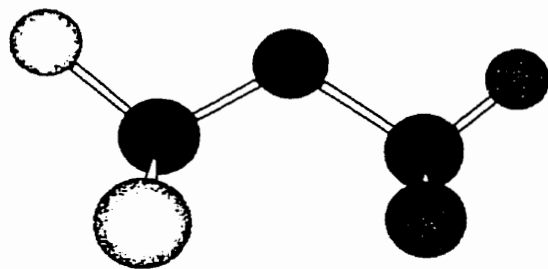


Figure 7.6 Optimized MP2/6-31G(d) structure of CH₃OCF₃.

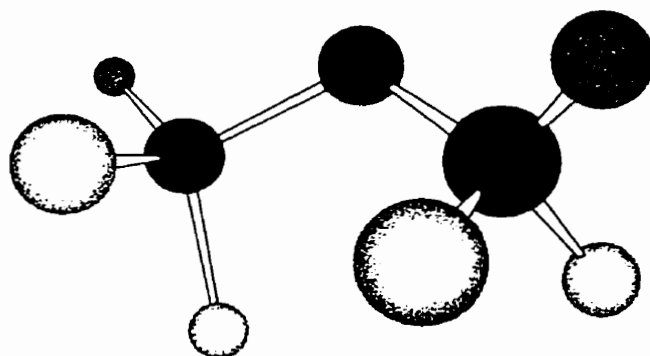


Figure 7.7 Optimized MP2/6-31G(d) structure of (CF₂H)₂O (rotamer 1).

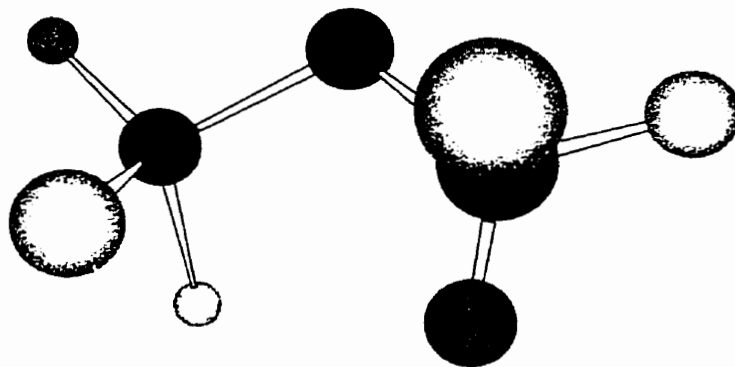


Figure 7.8 Optimized MP2/6-31G(d) structure of (CF₂H)₂O (rotamer 2).

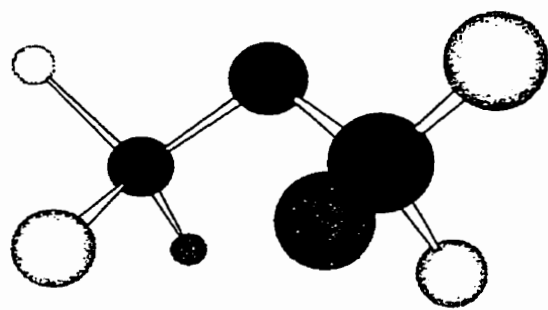


Figure 7.9 Optimized MP2/6-31G(d) structure of $(\text{CF}_2\text{H})_2\text{O}$ (rotamer 3).

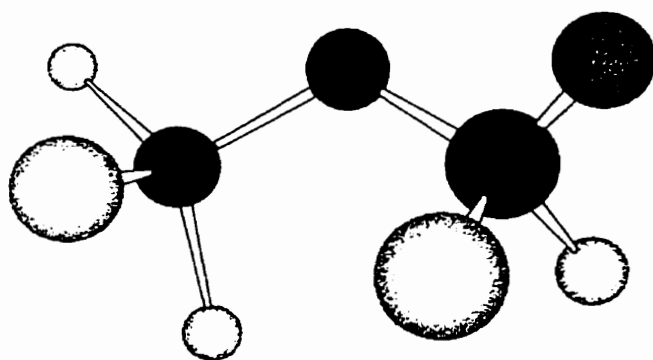


Figure 7.10 Optimized MP2/6-31G(d) structure of $\text{CF}_3\text{OCF}_2\text{H}$ (rotamer 1).

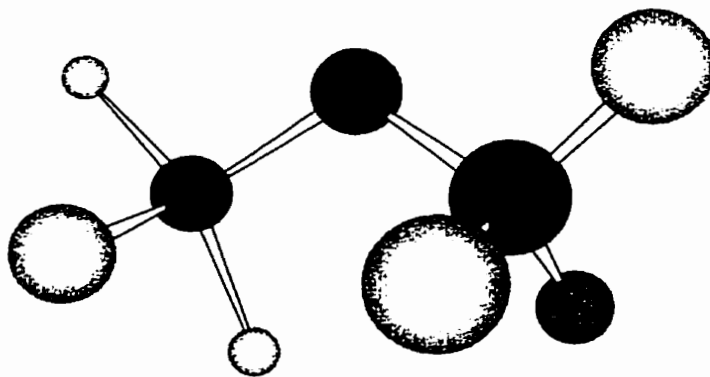


Figure 7.11 Optimized MP2/6-31G(d) structure of $\text{CF}_3\text{OCF}_2\text{H}$ (rotamer 2).

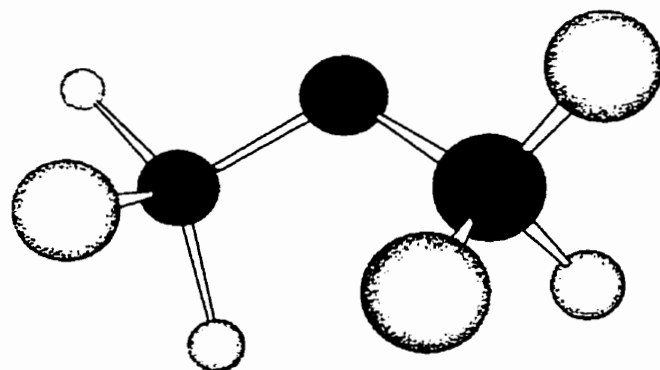


Figure 7.12 Optimized MP2/6-31G(d) structure of $(\text{CF}_3)_2\text{O}$.

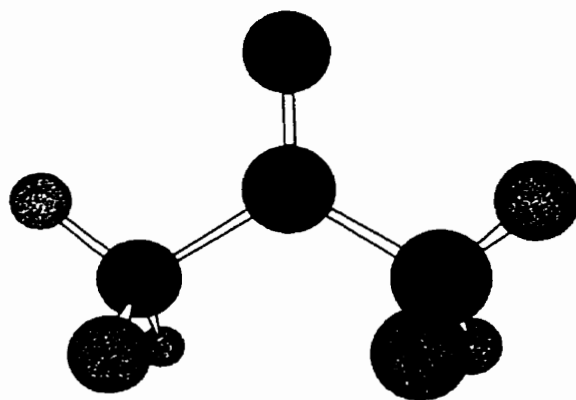


Figure 7.13 Optimized MP2/6-31G(d) structure of $\text{CH}_3\text{C}(\text{O})\text{CH}_3$.

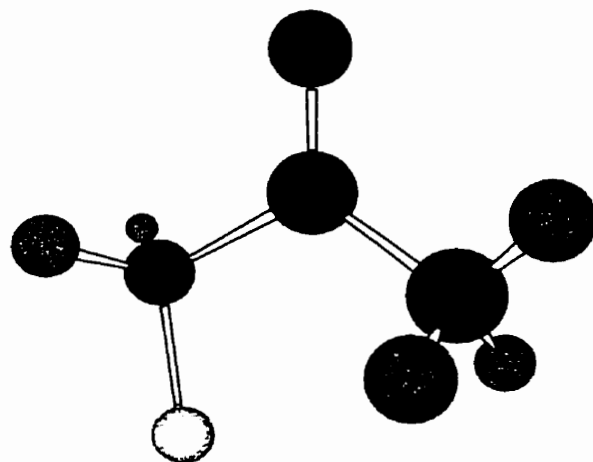


Figure 7.14 Optimized MP2/6-31G(d) structure of $\text{CH}_3\text{C}(\text{O})\text{CH}_2\text{F}$ (rotamer 1).

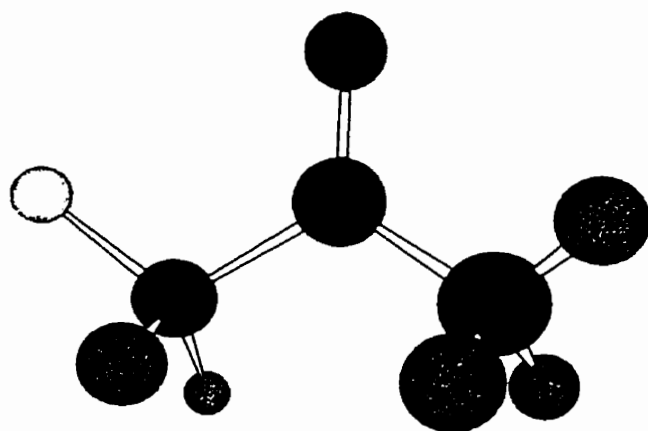


Figure 7.15 Optimized MP2/6-31G(d) structure of $\text{CH}_3\text{C}(\text{O})\text{CH}_2\text{F}$ (rotamer 2).

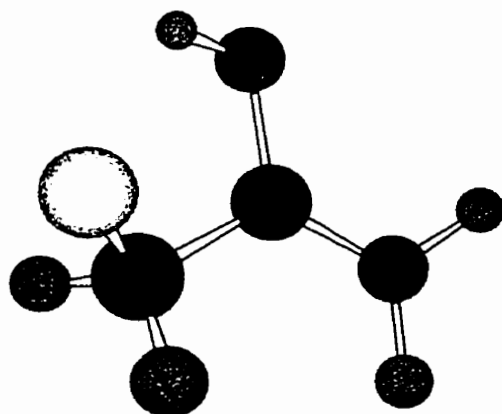


Figure 7.16 Optimized MP2/6-31G(d) structure of $\text{CH}_2\text{C}(\text{OH})\text{CH}_2\text{F}$.

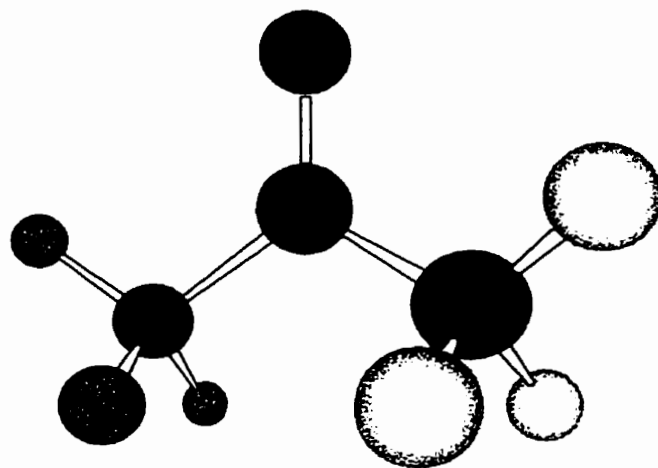


Figure 7.17 Optimized MP2/6-31G(d) structure of $\text{CH}_3\text{C}(\text{O})\text{CF}_3$.

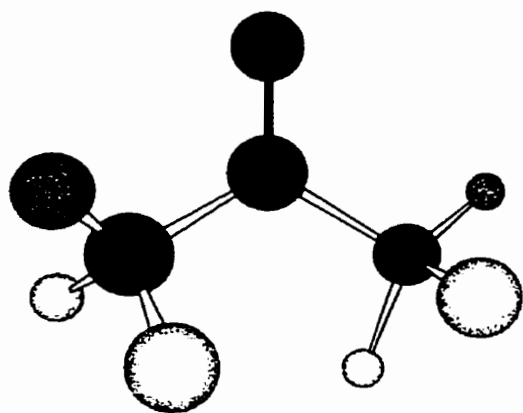


Figure 7.18 Optimized MP2/6-31G(d) structure of CH₂FC(O)CH₂F.

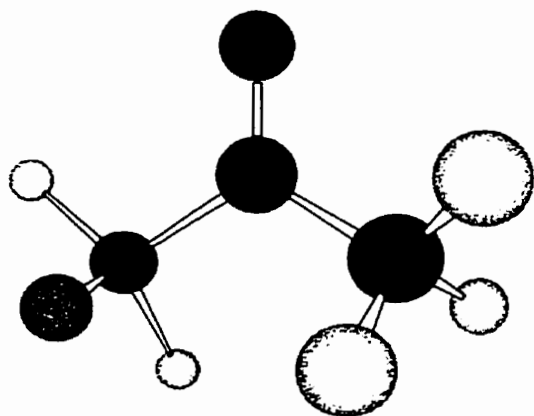


Figure 7.19 Optimized MP2/6-31G(d) structure of CF₃C(O)CF₂H.

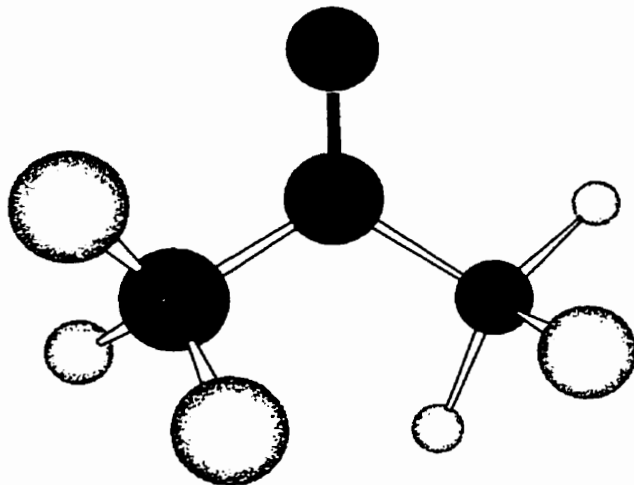


Figure 7.20 Optimized MP2/6-31G(d) structure of CF₃C(O)CF₃.

Unfortunately, no microwave or electron diffraction experiments have been performed on the fluorinated ethers to determine experimentally the most stable structures and the possible existence of the various rotamers. Calculations on $(\text{CF}_3)_2\text{O}$ at the MP2/3-21G and MP2/6-31G(d,p) levels of theory show good agreement with this work.^{37,38} $(\text{CF}_3)_2\text{O}$ shows an eclipsed structure to minimize the repulsion among the fluorine atoms. A dihedral angle, $\angle\text{FCCF}$, of 46.8° between the two upward fluorine atoms and the two carbon atoms was found. In Figures 7.13 to 7.20 the structures of acetone and the four fluorinated acetones are shown. Unlike the situation for the fluorinated ethers, no other stable rotamers have been sought, except for $\text{CH}_3\text{C}(\text{O})\text{CH}_2\text{F}$. Choi and Boyd calculated the structures of the various fluorinated acetones at the HF/STO-3G and 4-31G levels of theory.^{64,65} The structures of the two stable CH_2F group rotamers for this molecule, and one of the possible enol isomers have been calculated. For the acetone molecule at the MP2/6-31G(d) level of theory the agreement with the experimentally determined structure is good to excellent.⁶⁶ The various bond lengths are all within 0.015 \AA , and the bond angles within 1.3° .

Introducing fluorine has no noticeable effect on the CO and CH bond lengths. The CC bond lengths change relative to acetone, and in general they will increase if the methyl group carbon atom is attached to fluorine atoms. In both $\text{CH}_3\text{C}(\text{O})\text{CH}_2\text{F}$ and $\text{CF}_3\text{C}(\text{O})\text{CH}_3$ the $\text{CH}_3\text{-C}$ bond length decreases slightly relative to acetone. Small differences in CF bond lengths are observed, depending mainly on whether or not the fluorine atoms are in upward or downward orientations, relative to the direction of the carbonyl group. There seems to be no clear trend of the effect of fluorine substitution on the CCO bond angles. In general, the relative methyl group orientations are such as to minimize the repulsion among fluorine atoms on opposite groups, and between fluorine atoms and the carbonyl oxygen atom. In $\text{CF}_3\text{C}(\text{O})\text{CF}_3$ the upward fluorine atoms FCCF dihedral angle is -57.5° . In the shown enol isomer of $\text{CH}_3\text{C}(\text{O})\text{CH}_2\text{F}$ there is an intramolecular hydrogen bond, $\text{O-H}\cdots\text{F-C}$. This seems to be the most stable enol isomer, since the gas phase deprotonation enthalpy for $\text{CH}_2\text{-H}$ is smaller than for CFH-H (see Section 7.4.5). Despite the seemingly favorable structure, the enol isomer is $12.7 \text{ kcal mol}^{-1}$ less stable than its keto isomer, calculated at the MP2/c//MP2/a level of theory. The results for the five (fluorinated) acetones

calculated at the B3LYP/6-311++G(3d,3p) level of theory show no real significant deviations from the MP2/6-31G(d) results. For the C=O bond lengths the B3LYP results are in general smaller by 0.017-0.026 Å. For the C(O)-C bond length the results in general are larger. For C(O)-C bond lengths to CH₃ or CH₂F groups the value is 0.001-0.004 Å, while to CF₂H and CF₃ groups it is 0.016-0.022 Å. For both the C-H and C-F bonds the B3LYP results are smaller by 0.002-0.004 Å and 0.001-0.008 Å, respectively. Finally, the B3LYP O-C-C bond angles are equal to or smaller than the MP2 results by 0.1-0.7°.

More interestingly, from the point of view of the work presented here, are the structures of the chloride ion-ether and acetone complexes that are shown in Figures 7.21 to 7.42. Smith *et al.* published a structure for the Cl⁻((CH₃)₂O) complex, calculated at the MP2/[D95+*/D95+**] level of theory.⁶⁷ In the most stable isomer of Cl⁻((CH₃)₂O) found in this work, the chloride ion interacts with only two hydrogen atoms, one from each methyl group. The Cl⁻...H distance is 2.795 Å, which is much smaller than the 3.2 Å found by Smith *et al.*, which appears to be a transition state structure, since the chloride ion interacts with four hydrogen atoms⁶⁶. Upon complex formation with the chloride ion, the C-O-C angle is virtually unchanged. For the chloride ion-diethyl ether complex, at least two isomers are possible. In the first one, the chloride ion interacts with two hydrogen atoms from the two CH₂ units, while in the second isomer the chloride ion interacts with two hydrogen atoms, one from a CH₂ unit and one from a CH₃ unit on different sides of the oxygen atom. The calculated thermochemistry for the latter isomer has closer agreement with the experimental PHPMS data (see Section 7.4.4). The introduction of a CF₃ group changes the chloride ion binding as expected. Cl⁻(CH₃OCF₃) resembles a S_N2 backside attack complex. Relative to CH₃OCF₃, the O-CH₃ distance increases from 1.442 Å to 1.472 Å, while the O-CF₃ distance decreases from 1.345 Å to 1.328 Å. However, the chloride ion does not interact identically with all hydrogen atoms, as occurs, for instance, in the Cl⁻(CH₃Cl) complex.⁶⁸ In Cl⁻(CH₃OCF₃) the Cl⁻CO bond angle is 171.5°, while the COC bond angle is 115.2°, compared to 114.4° in CH₃OCF₃. For the Cl⁻((CF₂H)₂O) cluster, four different rotamers are possible, three of them singly hydrogen bonded,

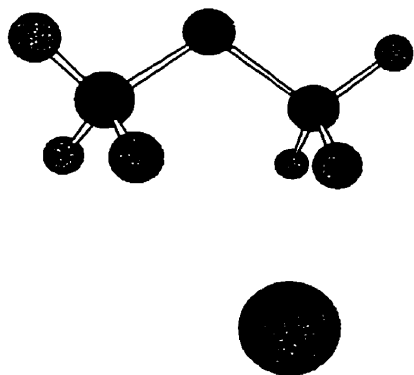


Figure 7.21 Optimized MP2/[6-31+G(d)/6-31G(d)] structure of $\text{Cl}^-((\text{CH}_3)_2\text{O})$.

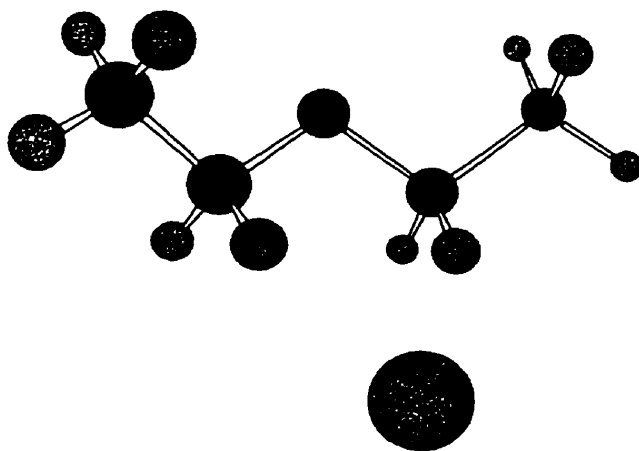


Figure 7.22 Optimized MP2/[6-31+G(d)/6-31G(d)] structure of $\text{Cl}^-((\text{CH}_3\text{CH}_2)_2\text{O})$ (rotamer 1).

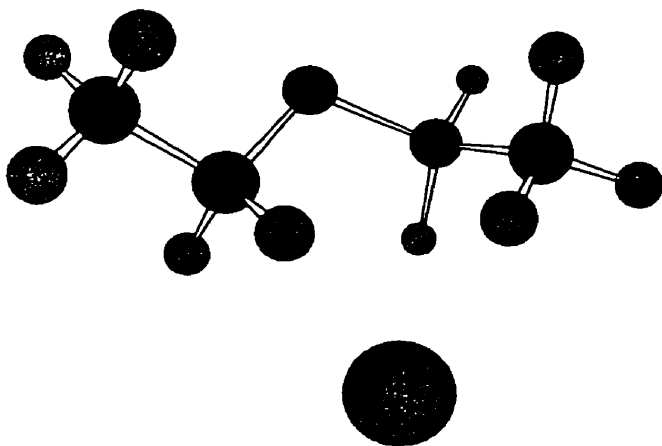


Figure 7.23 Optimized MP2/[6-31+G(d)/6-31G(d)] structure of $\text{Cl}^-((\text{CH}_3\text{CH}_2)_2\text{O})$ (rotamer 2).

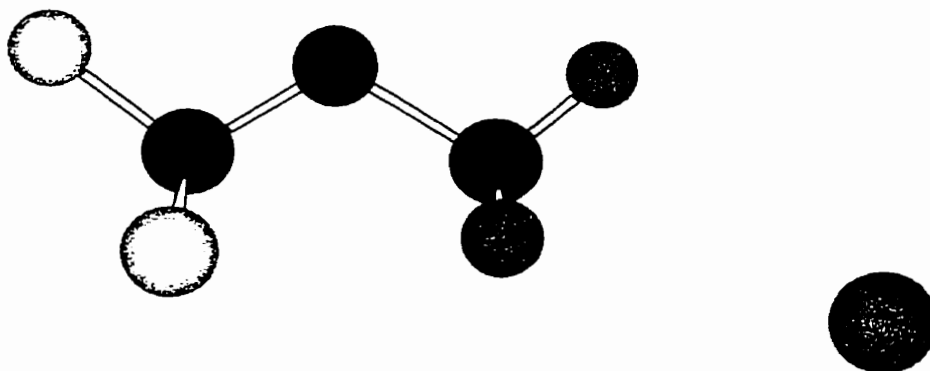


Figure 7.24 Optimized MP2/[6-31+G(d)/6-31G(d)] structure of $\text{Cl}^-(\text{CH}_3\text{OCF}_3)$.

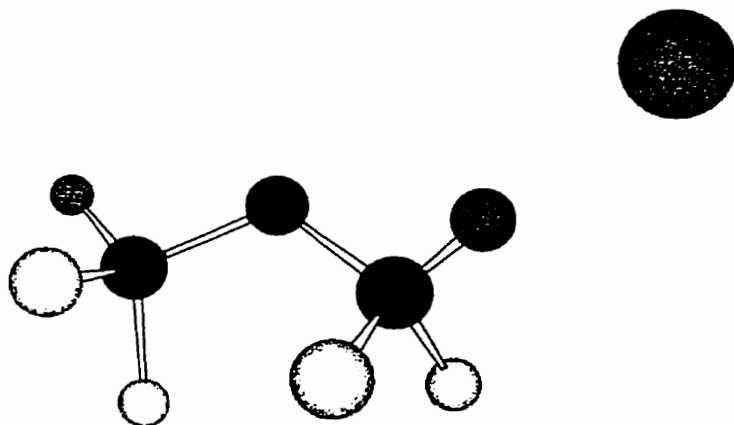


Figure 7.25 Optimized MP2/[6-31+G(d)/6-31G(d)] structure of $\text{Cl}^-((\text{CF}_2\text{H})_2\text{O})$ (rotamer 1).

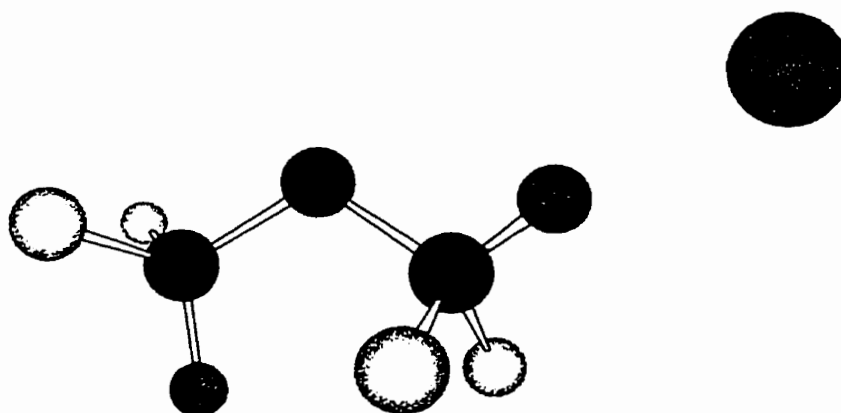


Figure 7.26 Optimized MP2/[6-31+G(d)/6-31G(d)] structure of $\text{Cl}^-((\text{CF}_2\text{H})_2\text{O})$ (rotamer 2, isomer 1).

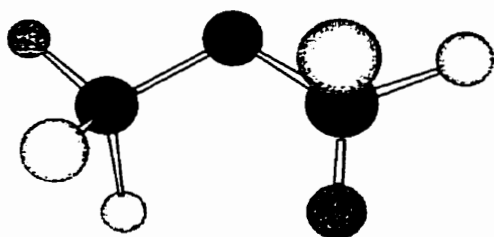


Figure 7.27 Optimized MP2/[6-31+G(d)/6-31G(d)] structure of $\text{Cl}^-((\text{CF}_2\text{H})_2\text{O})$ (rotamer 2, isomer 2).

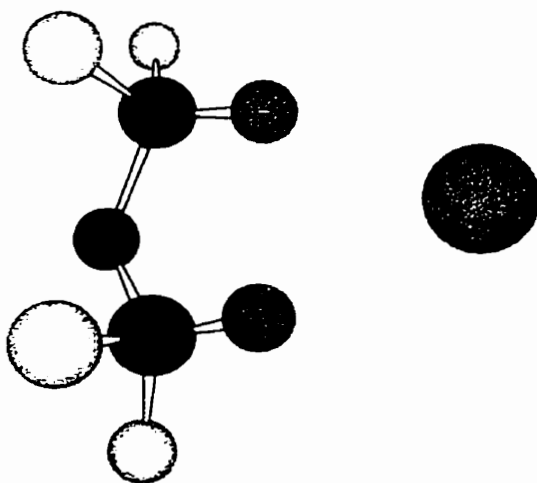


Figure 7.28 Optimized MP2/[6-31+G(d)/6-31G(d)] structure of $\text{Cl}^-((\text{CF}_2\text{H})_2\text{O})$ (rotamer 4).

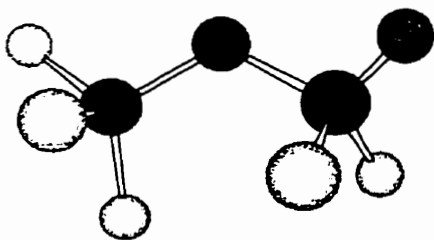


Figure 7.29 Optimized MP2/[6-31+G(d)/6-31G(d)] structure of $\text{Cl}^-(\text{CF}_3\text{OCF}_2\text{H})$ (rotamer 1).

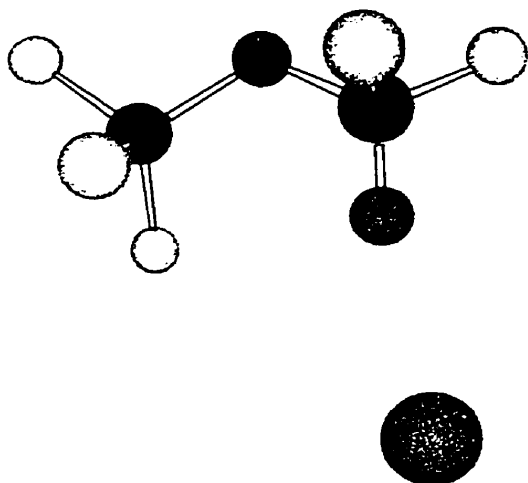


Figure 7.30 Optimized MP2/[6-31+G(d)/6-31G(d)] structure of Cl⁻(CF₃OCF₂H) (rotamer 2).

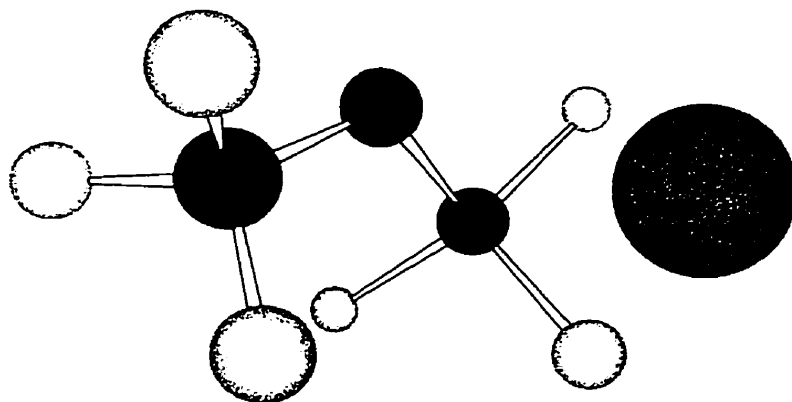


Figure 7.31 Optimized MP2/[6-31+G(d)/6-31G(d)] structure of Cl⁻((CF₃)₂O).

and one doubly hydrogen bonded. Rotamers 1 and 2 each have the chloride ion interacting with one of the two hydrogen atoms. Compared to rotamer 4, both the $\text{Cl}^- \cdots \text{H}$ distances and the $\text{Cl}^- \text{HC}$ bond angles are smaller and closer to being linear, respectively. In rotamer 4, there is not only interaction with two hydrogen atoms, but the chloride ion is also aligned with the dipole moment of $(\text{CF}_2\text{H})_2\text{O}$. For the $\text{Cl}^-(\text{CF}_2\text{HO}(\text{CF}_3))$ complex, two rotamers are possible. In both cases the $\text{Cl}^- \text{HC}$ bond angle is close to being linear. In most clusters investigated, the C–O bond containing the hydrogen atom that interacts with the chloride ion increases in length relative to the neutral, while the C–O bond with no hydrogen atom(s) interacting decreases in length. In $\text{Cl}^-((\text{CF}_3)_2\text{O})$ the FCCF dihedral angle, containing the upward fluorine atoms, has been reduced to 39.7° . More interesting is the fact that the chloride ion interaction with the carbon atom is an almost linear alignment with one of the C–F bonds. This resembles a $\text{S}_{\text{N}}2$ backside attack complex of Cl^- with $(\text{CF}_3)_2\text{O}$, with F^- as a hypothetical leaving group instead of CF_3O^- . The $\text{Cl}^- \cdots \text{C}$ distance is 3.775 \AA , which is notably longer than the $\text{Cl}^- \cdots \text{O}$ distance of 3.322 \AA . The NPA charges in $(\text{CF}_3)_2\text{O}$, calculated at the MP2/c//MP2/a level of theory, confirm that the carbon atom will be the only probable site with which the chloride ion can interact. The two di-solvated chloride ion-fluorinated ether complexes shown in Figures 7.32 and 7.33, $\text{Cl}^-(\text{CH}_3\text{OCF}_3)_2$ and $\text{Cl}^-((\text{CF}_2\text{H})_2\text{O})_2$, show characteristics that are very close to the mono-solvated clusters. It is interesting, but not surprising, to note that the hydrogen bonded arrangement around Cl^- in $\text{Cl}^-((\text{CF}_2\text{H})_2\text{O})_2$ is tetrahedral like. In this way the repulsive interaction between the two $(\text{CF}_2\text{H})_2\text{O}$ molecules is minimized. Compared to $\text{Cl}^-((\text{CF}_2\text{H})_2\text{O})$, the $\text{Cl}^- \cdots \text{H}$ distances have slightly increased, from around 2.436 \AA to 2.470 \AA . Formation of $\text{Cl}^-(\text{CH}_3\text{C}(\text{O})\text{CH}_3)$ causes only minor changes in the acetone moiety relative to “free” acetone. These include a small increase in the CO and upward CH bond lengths, and the CCO bond angle, and a small decrease in the CC and downward CH bond lengths. The $\text{Cl}^- \cdots \text{HC}$ bond lengths of 2.668 \AA are in the order of magnitude that one would expect from the obtained ΔH_{298}° value. This value is 0.127 \AA smaller than the same kind of bonding in $\text{Cl}^-(\text{CH}_3\text{OCH}_3)$, which has a much smaller ΔH_{298}° value ($-13.1 \text{ kcal mol}^{-1}$ versus $-7.3 \text{ kcal mol}^{-1}$). For

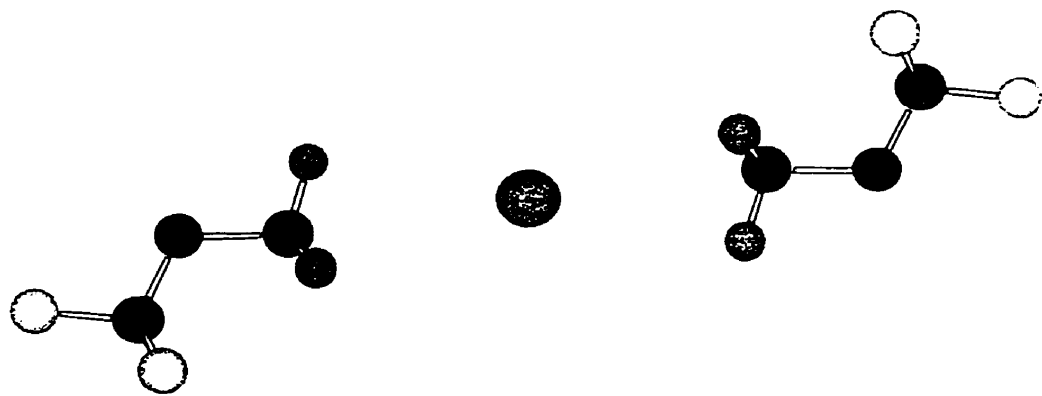


Figure 7.32 Optimized MP2/[6-31+G(d)/6-31G(d)] structure of $\text{Cl}^-(\text{CH}_3\text{OCF}_3)_2$.

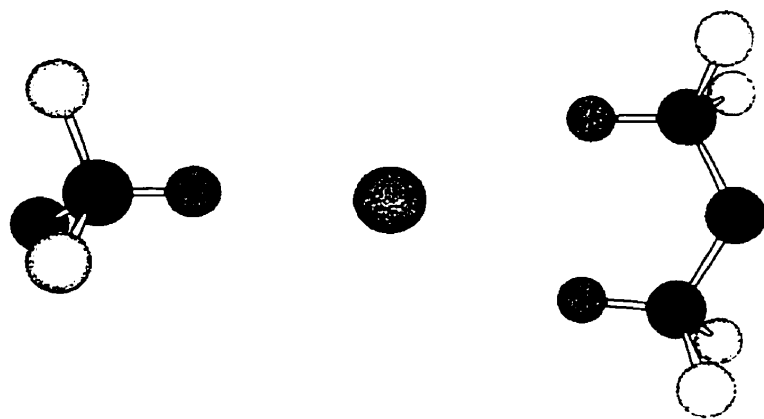


Figure 7.33 Optimized MP2/[6-31+G(d)/6-31G(d)] structure of $\text{Cl}^-((\text{CF}_2\text{H})_2\text{O})_2$.

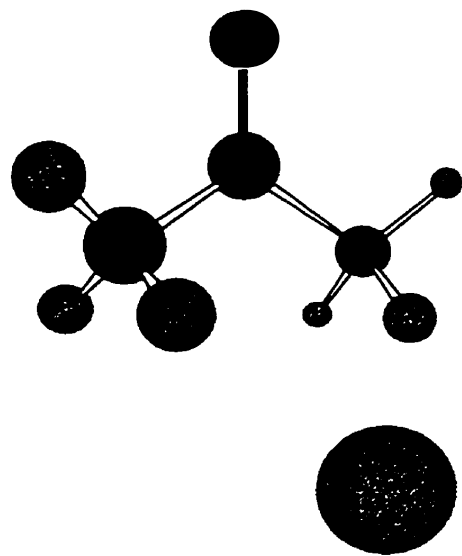


Figure 7.34 Optimized MP2/[6-31+G(d)/6-31G(d)] structure of $\text{Cl}^-(\text{CH}_3\text{C}(\text{O})\text{CH}_3)$.

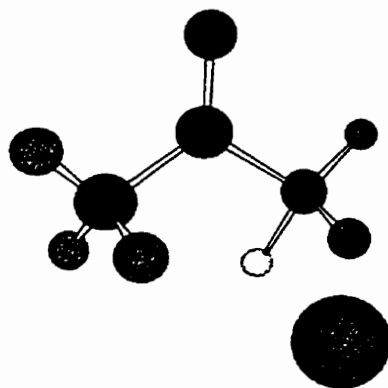


Figure 7.35 Optimized MP2/[6-31+G(d)/6-31G(d)] structure of $\text{Cl}^-(\text{CH}_3\text{C}(\text{O})\text{CH}_2\text{F})$ (rotamer 1).

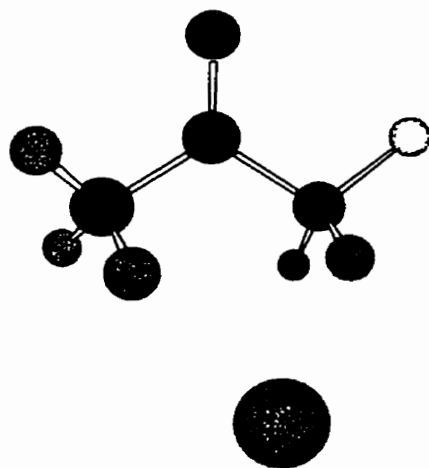


Figure 7.36 Optimized MP2/[6-31+G(d)/6-31G(d)] structure of $\text{Cl}^-(\text{CH}_3\text{C}(\text{O})\text{CH}_2\text{F})$ (rotamer 2).

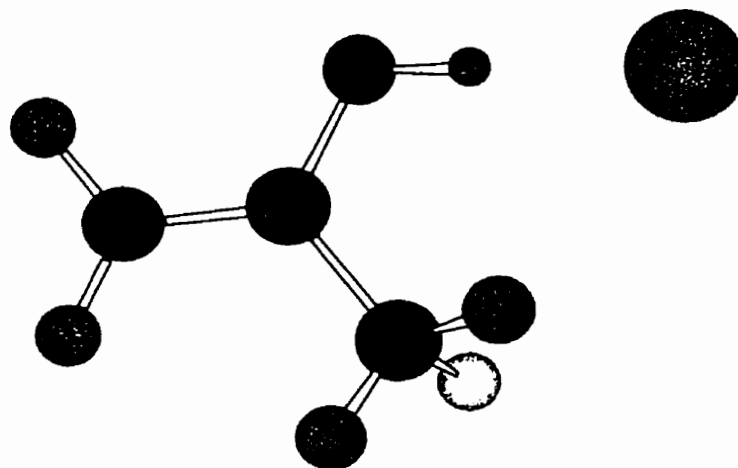


Figure 7.37 Optimized MP2/[6-31+G(d)/6-31G(d)] structure of $\text{Cl}^-(\text{CH}_2\text{C}(\text{OH})\text{CH}_2\text{F})$.

$\text{Cl}^-(\text{CH}_3\text{C}(\text{O})\text{CH}_2\text{F})$ two stable rotamers are possible, which are closely associated with the neutral rotamers. In Figure 7.35 the $\text{Cl}^-\cdots\text{H}-\text{CH}_2$ and $\text{Cl}^-\cdots\text{H}-\text{CHF}$ bond lengths are 2.715 Å and 2.560 Å, respectively, while in Figure 7.36 they are 2.589 Å and 2.642 Å, respectively. These are the two most significant differences between these two structures. The $\text{Cl}^-(\text{CH}_2\text{C}(\text{OH})\text{CH}_2\text{F})$ complex shows some interesting features compared to its neutral counterpart. Firstly, the chloride ion is interacting with both the OH group and one of the hydrogen atoms in the CH_2F group. The latter interaction has replaced the intramolecular hydrogen bond, $\text{O}-\text{H}\cdots\text{F}-\text{C}$, in the neutral enol isomer. The $\text{Cl}^-\cdots\text{HO}$ bond length of 2.088 Å is almost identical to the same bond length in $\text{Cl}^-(\text{HOCH}_3)$ at the MP2(full)/6-311++G(d,p) level of theory. The $\text{Cl}^-\cdots\text{H}-\text{CHF}$ bond length of 2.666 Å is much smaller than the $\text{Cl}^-\cdots\text{H}-\text{CH}_2$ bond length in $\text{Cl}^-(\text{HOCH}_3)$ of 3.413 Å. Upon formation of the chloride ion complex the O–H bond length increases from 0.975 Å to 1.002 Å, while the C–O bond length decreases from 1.372 Å to 1.355 Å. Finally, the $\text{Cl}^-\cdots\text{H}-\text{O}$ bond angle of 173.0° is very close to the $\text{F}^-\cdots\text{H}-\text{O}$ bond angle in $\text{F}^-(\text{HOCH}_3)$. The structure of the $\text{Cl}^-(\text{CH}_3\text{C}(\text{O})\text{CF}_3)$ complex is quite different from the corresponding ether complex $\text{Cl}^-(\text{CH}_3\text{OCF}_3)$. The chloride ion interacts with only one of the CH_3 hydrogen atoms. The $\text{Cl}^-\cdots\text{H}-\text{CH}_2$ bond length of 2.375 Å is much smaller than that in the chloride ion-acetone complex, $\text{Cl}^-(\text{CH}_3\text{C}(\text{O})\text{CH}_3)$, while the $\text{Cl}^-\cdots\text{H}-\text{C}$ bond angle is close to linear. Formation of the chloride ion complex does not change the $\text{CH}_3\text{C}(\text{O})\text{CF}_3$ structure to any significant extent. The bonding in the $\text{Cl}^-(\text{CF}_2\text{HC}(\text{O})\text{CF}_2\text{H})$ complex is fairly similar to $\text{Cl}^-(\text{CF}_2\text{HO CF}_2\text{H})$, although some important differences are present. In the $\text{Cl}^-(\text{CF}_2\text{HO CF}_2\text{H})$ complex the two $\text{Cl}^-\cdots\text{HCF}_2$ bond lengths are 2.436 Å and 2.438 Å, respectively, while in $\text{Cl}^-(\text{CF}_2\text{HC}(\text{O})\text{CF}_2\text{H})$ they are 2.700 Å and 2.726 Å, respectively. The latter two are even somewhat larger than those in $\text{Cl}^-(\text{CH}_3\text{C}(\text{O})\text{CH}_3)$. At first this seems surprising, since going from $\text{Cl}^-(\text{CH}_3\text{OCH}_3)$ to $\text{Cl}^-(\text{CF}_2\text{HO CF}_2\text{H})$ there is a large decrease in the $\text{Cl}^-\cdots\text{H}-\text{CF}_2$ bond lengths. In the $\text{Cl}^-(\text{CF}_2\text{HC}(\text{O})\text{CF}_2\text{H})$ complex the $\text{Cl}^-\cdots\text{CO}$ distance is 2.800 Å, and so it seems that interaction of the chloride ion with the carbonyl group carbon atom is important as well, such as for the hydrogen bonding interactions with the two CF_2H groups. The $\text{Cl}^-\cdots\text{H}-\text{CF}_2$ bond

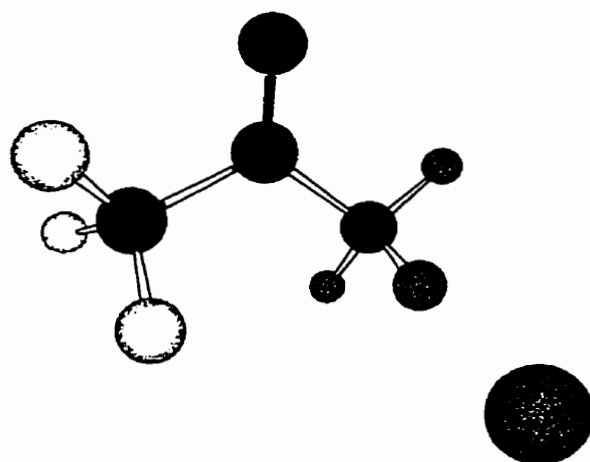


Figure 7.38 Optimized MP2/[6-31+G(d)/6-31G(d)] structure of $\text{Cl}^-(\text{CH}_3\text{C}(\text{O})\text{CF}_3)$.

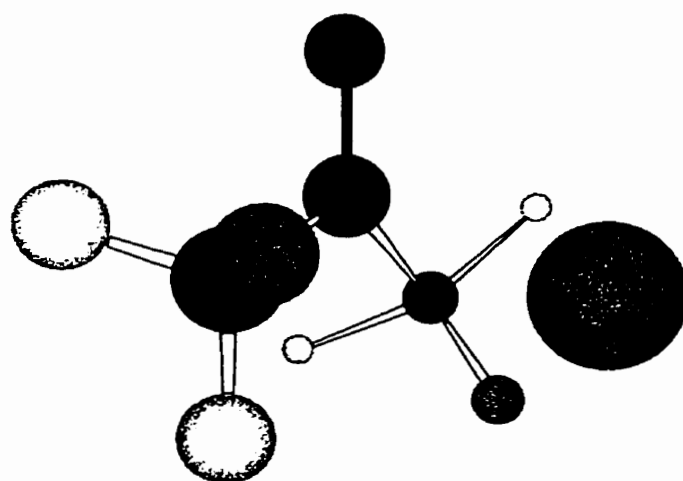


Figure 7.39 Optimized MP2/[6-31+G(d)/6-31G(d)] structure of $\text{Cl}^-(\text{CF}_2\text{HC}(\text{O})\text{CF}_2\text{H})$.

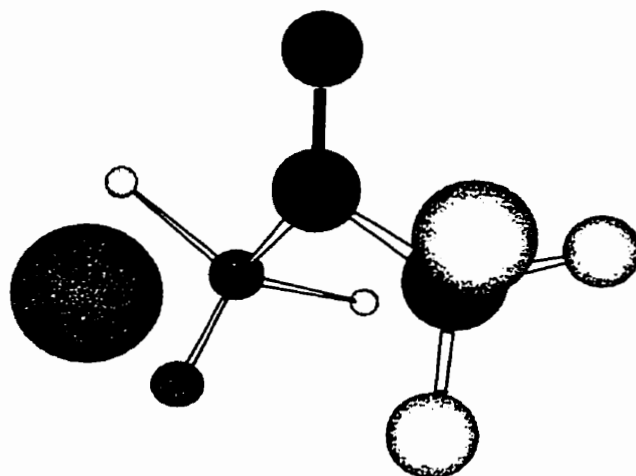


Figure 7.40 Optimized MP2/[6-31+G(d)/6-31G(d)] structure of $\text{Cl}^-(\text{CF}_3\text{C}(\text{O})\text{CF}_2\text{H})$.

angles in $\text{Cl}^-(\text{CF}_2\text{HC}(\text{O})\text{CF}_2\text{H})$ of 97.0° and 102.0° , respectively, are very different from 158.0° and 158.2° , respectively, in $\text{Cl}^-(\text{CF}_2\text{HO}\text{CF}_2\text{H})$. In the $\text{Cl}^-(\text{CF}_2\text{HO}\text{CF}_2\text{H})$ complex the hydrogen bonding is more directed along the C–H bond, which may be expected to be more favorable than as in the $\text{Cl}^-(\text{CF}_2\text{HC}(\text{O})\text{CF}_2\text{H})$ complex. In the $\text{Cl}^-(\text{CF}_3\text{C}(\text{O})\text{CF}_2\text{H})$ complex, the chloride ion seems to prefer to interact with the carbonyl group carbon atom, rather than with the very acidic hydrogen atom. The $\text{Cl}^-\cdots\text{CO}$ distance is 2.524 \AA , while the $\text{Cl}^-\cdots\text{HCF}_2$ distance is 2.928 \AA . This observation was very surprising, because *a priori* it was expected that a complex similar to $\text{Cl}^-(\text{CF}_3\text{OCF}_2\text{H})$ would be obtained. In the latter complex the $\text{Cl}^-\cdots\text{HCF}_2$ distance is 2.282 \AA , and the $\text{Cl}^-\cdots\text{H}-\text{CF}_2$ angle is 175.7° . Replacing the ether functional group by a carbonyl functional group apparently makes a huge difference in the bonding characteristics, and it is very interesting to understand what factor(s) is (are) responsible for this. In the $\text{Cl}^-(\text{CF}_3\text{C}(\text{O})\text{CF}_3)$ complex, the $\text{Cl}^-\cdots\text{CO}$ distance is 2.272 \AA , much shorter than in the $\text{Cl}^-(\text{CF}_3\text{C}(\text{O})\text{CF}_2\text{H})$ complex. Minor or no changes in the C=O, C–F, and C–C bond lengths are observed. The most interesting feature in the $\text{Cl}^-(\text{CF}_3\text{C}(\text{O})\text{CF}_3)$ complex is the relative orientation of the two CF_3 groups. In the neutral $\text{CF}_3\text{C}(\text{O})\text{CF}_3$ molecule, the F–C–C–F dihedral angle is -57.5° , while in the chloride ion complexes it has been increased to 0.0° . The two CF_3 groups are facing away from the chloride ion in such a way as to minimize repulsion among Cl^- and the fluorine atoms, even at the expense of increased repulsion among the fluorine atoms in both CF_3 groups. Larson and McMahon speculated on the possibilities of either a tetrahedral-like, covalently bonded complex, $(\text{CF}_3)_2\text{ClCO}^-$, or an electrostatically bonded complex where the chloride ion interacts with the carbonyl group carbon atom from below the hexafluoroacetone molecule, as shown in Figure 7.42.²⁷ If CN^- is used instead of Cl^- , the formation of a covalently bonded complex, $(\text{CF}_3)_2\text{CNCO}^-$, will be more likely, especially at relative low temperatures. In that case, relative large $-\Delta H^\circ$ and $-\Delta S^\circ$ values should be obtained. Computations at the HF/6-31G(d) level of theory indicate that $(\text{CF}_3)_2\text{CNCO}^-$ may exist. At higher temperatures, an electrostatically bonded complex, $\text{CN}^-(\text{CF}_3\text{C}(\text{O})\text{CF}_3)$, may dominate, which should give rise to ΔH°

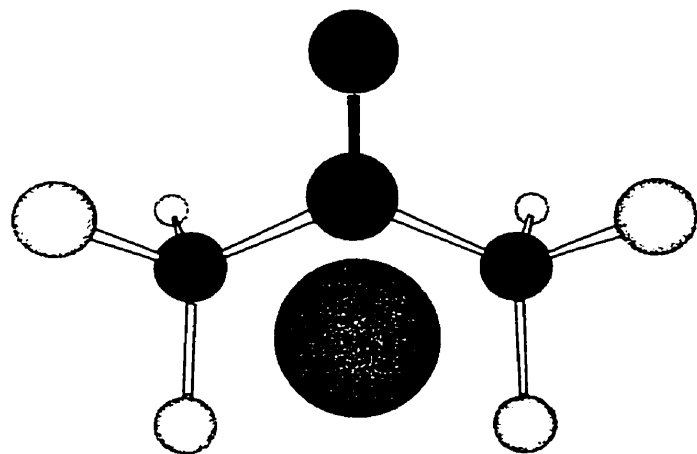


Figure 7.41 Optimized MP2/[6-31+G(d)/6-31G(d)] structure of $\text{Cl}^-(\text{CF}_3\text{C}(\text{O})\text{CF}_3)$.

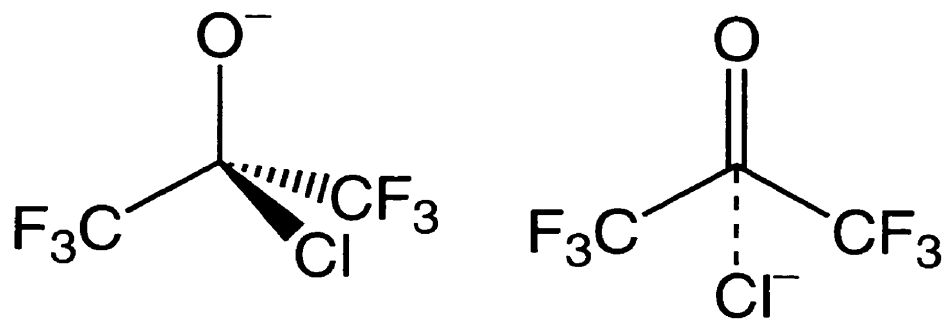


Figure 7.42 Proposed covalent and electrostatic chloride ion-hexafluoroacetone complexes.

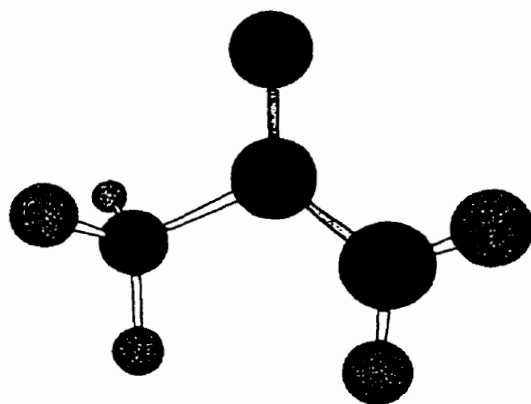


Figure 7.43 Optimized MP2(full)/6-31G(d) structure of $\text{CH}_3\text{C}(\text{O})\text{CH}_2^-$.

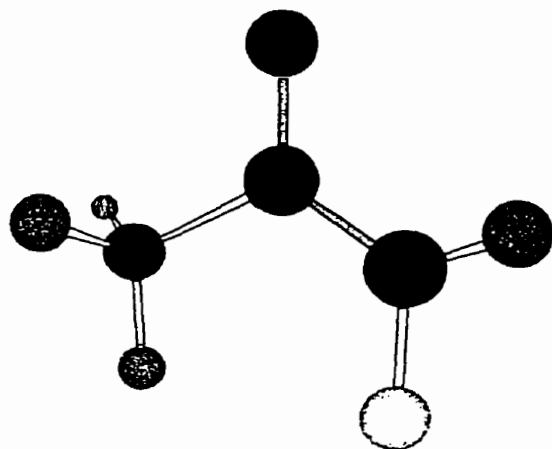


Figure 7.44 Optimized MP2(full)/6-31G(d) structure of $\text{CH}_3\text{C}(\text{O})\text{CHF}^-$.

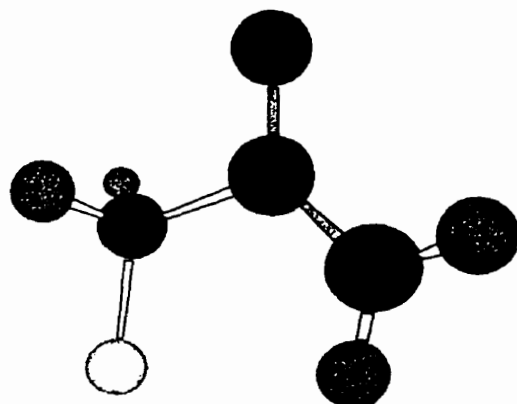


Figure 7.45 Optimized MP2(full)/6-31G(d) structure of $\text{CH}_2\text{C}(\text{O})\text{CH}_2\text{F}^-$.

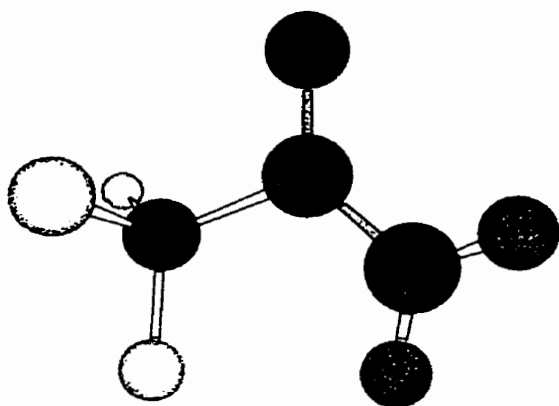


Figure 7.46 Optimized MP2(full)/6-31G(d) structure of $\text{CF}_3\text{C}(\text{O})\text{CH}_2^-$.

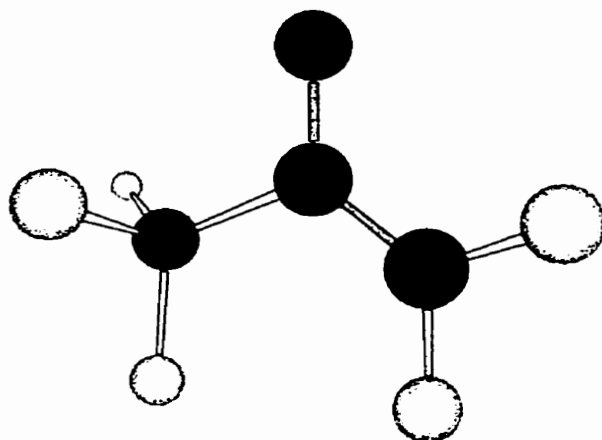


Figure 7.47 Optimized MP2(full)/6-31G(d) structure of $\text{CF}_3\text{C}(\text{O})\text{CF}_2^-$.

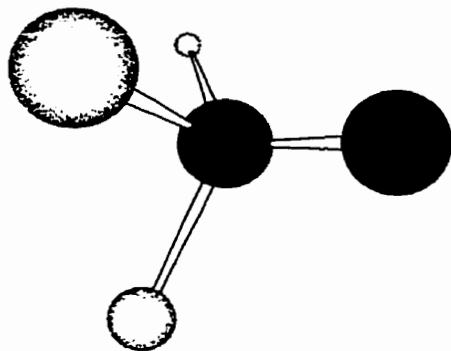


Figure 7.48 Optimized MP2(full)/6-31G(d) structure of CF_3O^- .

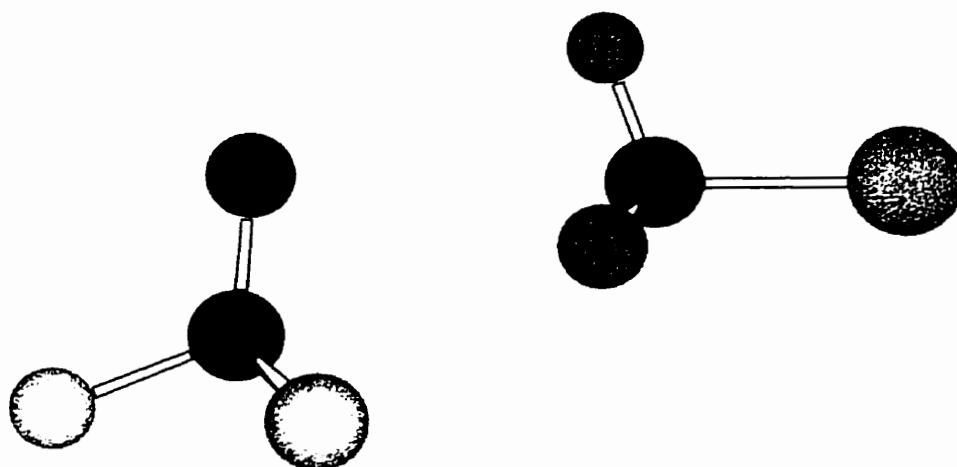


Figure 7.49 Optimized MP2(full)/6-31G(d) structure of $\text{CF}_3\text{O}^-(\text{CH}_3\text{Cl})$.

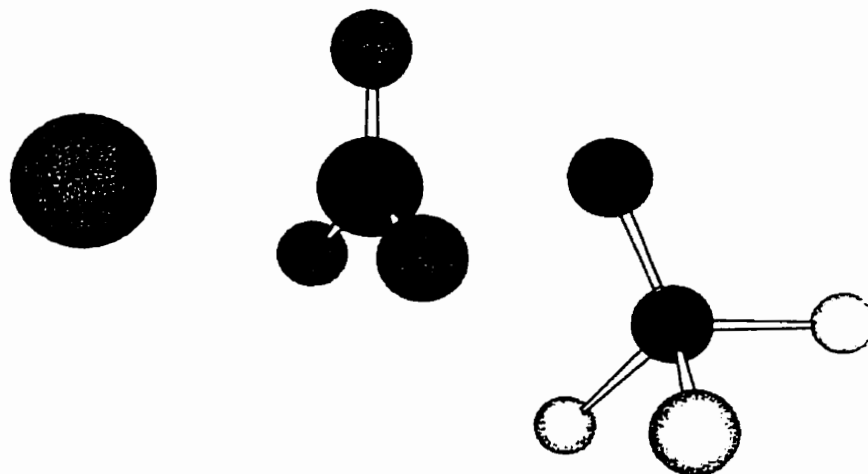


Figure 7.50 Optimized MP2(full)/6-31G(d) structure of $[\text{ClCH}_3\text{OCF}_3]^-$.

and ΔS° values closer to $\text{Cl}^-(\text{CF}_3\text{C}(\text{O})\text{CF}_3)$. For the B3LYP/[6-311++G(3df,3pd)/6-311++G(3d,3p)] structure of $\text{Cl}^-(\text{CF}_3\text{C}(\text{O})\text{CF}_3)$, no big changes are observed relative to the MP2 structure. The $\text{Cl}^-\cdots\text{CO}$ distance is 2.291 Å, and there is a small increase in the C=O bond length from 1.188 Å in $\text{CF}_3\text{C}(\text{O})\text{CF}_3$ to 1.220 Å in $\text{Cl}^-(\text{CF}_3\text{C}(\text{O})\text{CF}_3)$.

In Figures 7.43 to 7.47 the MP2(full)/6-31G(d) structures of deprotonated acetone, fluoroacetone (2 isomers), 1,1,1-trifluoroacetone, and pentafluoroacetone are shown. The structures of the corresponding neutral conjugated acids are essentially identical to the same structures calculated at the MP2(fc)/6-31G(d) level of theory. Upon deprotonation the C–C bond length will decrease, while the C–O bond length will increase. Delocalization of the negative charge will give both the C–C and C–O bonds a bond order of 1.5, as predicted from Lewis theory. The O–C–C bond angle containing the carbon atom from which the proton was abstracted will increase to around $(129 \pm 3)^\circ$, while the other O–C–C bond angle will decrease to around $(113 \pm 3)^\circ$. No dramatic changes in the C–H, C–F, or C–C bond lengths, other than the ones mentioned before, have been observed.

The MP2(full)/6-31G(d) structure of CF_3O^- in Figure 7.48 is closest to B3LYP/DZP++ results from Morris *et al.* who used various other methods as well.⁶⁹ The $\text{CF}_3\text{O}^-(\text{CH}_3\text{Cl})$ complex in Figure 7.49 has an almost linear $\text{CF}_3\text{O}^-\cdots\text{C}-\text{Cl}$ alignment. In addition, there may be some interaction between two hydrogen atoms and two fluorine atoms, which are separated by only 2.447 Å, shorter than the $\text{CF}_3\text{O}^-\cdots\text{C}$ and $\text{CF}_3\text{O}^-\cdots\text{H}$ distances of 2.883 Å and 2.738 Å, respectively. The $[\text{ClCH}_3\text{OCF}_3]^-$ transition state in Figure 7.50 shows no unexpected features. The $\text{Cl}\cdots\text{CH}_3$ and $\text{CH}_3\cdots\text{OCF}_3$ distances are 2.301 Å and 1.928 Å, respectively. The $\text{Cl}\cdots\text{CH}_3\cdots\text{OCF}_3$ angle is 176.7° . In the CF_3O^- moiety the C–O bond length has increased, while the C–F bond lengths have decreased relative to CF_3O^- .

7.4.2 Experimental Thermochemistry

In Tables 7.1 and 7.2, overviews are given of the experimental thermochemical data obtained for the chloride ion-(fluorinated) ether and acetone complex clustering

equilibria. As can be seen from these two Tables, the ΔH° and ΔS° values depend very much on the number of fluorine atoms and the substitution pattern. In Figures 7.51 to 7.53, the Van't Hoff plots from which the ΔH° and ΔS° values are determined are shown. As seen in Figures 7.21 to 7.42, very different bonding characteristics can be observed in the various chloride ion- (fluorinated) ether and acetone complexes, which should be reflected in characteristic ΔH° and ΔS° values. PHPMS is one of the few experimental techniques to obtain ΔS° values directly, and these can be a very useful tool to assign structural features of gas phase ions. The ΔH° and ΔS° values for chloride ion binding to dimethyl and diethyl ether can be compared to data obtained recently in our laboratory on chloride ion binding to cyclic and linear alkanes (Reaction 7.6).⁷⁰



For $\text{R} = c\text{-C}_5\text{H}_{10}$ and $n\text{-C}_5\text{H}_{12}$, ΔH° and ΔS° values of -7.4 and -7.9 kcal mol⁻¹, and -16.4 and -18.1 cal mol⁻¹ K⁻¹, respectively, were determined. These values seem reasonable for the weak, mainly ion-induced dipole, interactions in these types of clusters. The difference between $(\text{CH}_3)_2\text{O}$ and $(\text{CH}_3\text{CH}_2)_2\text{O}$ is mainly due to a larger polarizability of the latter ($\alpha = 5.8$ Å³ versus 10.2 Å³).⁶⁶ As can be seen in Figures 7.22 and 7.23 there are at least two rotamers and isomers of $\text{Cl}^-((\text{CH}_3\text{CH}_2)_2\text{O})$, each with their own distinct thermochemistry. In Section 7.4.3 the computational results will be discussed in more detail. It cannot be excluded, in fact it seems reasonable to assume, that the $\text{Cl}^-((\text{CH}_3\text{CH}_2)_2\text{O})$ complexes in the high pressure ion source consist of a statistical distribution of the various isomers and rotamers. Close resemblance of experimental and theoretical data for a specific rotamer/isomer, by no means proves that it would be the main structure in the high pressure ion source. The example of the $\text{Cl}^-((\text{CH}_3\text{CH}_2)_2\text{O})$ complex shows that these weakly bound systems can be stabilized by multiple, non-classical hydrogen bonds. It may be expected that this effect will become even more pronounced if the alkyl chain length in, for instance CH_3OR ($\text{R} =$

Table 7.1 Overview of the experimental and computational thermochemical data for the chloride ion-ether clustering equilibria

$\text{Cl}^-(\text{ether-F}_n)_m + \text{ether-F}_n \rightleftharpoons \text{Cl}^-(\text{ether-F}_n)_{m+1}$ (ether = $(\text{CH}_3)_2\text{O}$, $(\text{CH}_3\text{CH}_2)_2\text{O}$, CH_3OCF_3 , $(\text{CF}_2\text{H})_2\text{O}$, $\text{CF}_3\text{OCF}_2\text{H}$, $(\text{CF}_3)_2\text{O}$; $m = 0, 1$).

clustering equilibrium	$\Delta H^{\circ a}$		$\Delta S^{\circ b}$		$\Delta S^{\circ}_{298} b$
	PHPMS	MP2//MP2	PHPMS	PHPMS	
$\text{Cl}^- + (\text{CH}_3)_2\text{O} \rightleftharpoons \text{Cl}^-((\text{CH}_3)_2\text{O})$ (rotamer 1)	-7.5	-7.3	-15.3	-15.3	-15.8
$\text{Cl}^- + (\text{CH}_3\text{CH}_2)_2\text{O} \rightleftharpoons \text{Cl}^-((\text{CH}_3\text{CH}_2)_2\text{O})$ (rotamer 1)	-9.0	-7.8	-19.1	-19.1	-15.7
$\text{Cl}^- + (\text{CH}_3\text{CH}_2)_2\text{O} \rightleftharpoons \text{Cl}^-((\text{CH}_3\text{CH}_2)_2\text{O})$ (rotamer 2)		-8.9			-17.6
$\text{Cl}^- + \text{CH}_3\text{OCF}_3 \rightleftharpoons \text{Cl}^-((\text{CH}_3\text{OCF}_3))$ (rotamer 1)	-13.6	-12.5	-19.8	-19.8	-17.2
$\text{Cl}^-((\text{CH}_3\text{OCF}_3)) + \text{CH}_3\text{OCF}_3 \rightleftharpoons \text{Cl}^-((\text{CH}_3\text{OCF}_3)_2)$ (rotamer 1)	-12.7	-10.6	-23.7	-23.7	-12.4
$\text{Cl}^- + (\text{CF}_2\text{H})_2\text{O} \rightleftharpoons \text{Cl}^-((\text{CF}_2\text{H})_2\text{O})$ (rotamer 1)	-28.2	-14.4	-31.3	-31.3	-18.8
$\text{Cl}^- + (\text{CF}_2\text{H})_2\text{O} \rightleftharpoons \text{Cl}^-((\text{CF}_2\text{H})_2\text{O})$ (rotamer 2, isomer 1)		-12.4			-17.7
$\text{Cl}^- + (\text{CF}_2\text{H})_2\text{O} \rightleftharpoons \text{Cl}^-((\text{CF}_2\text{H})_2\text{O})$ (rotamer 2, isomer 2)		-16.1			-19.0
$\text{Cl}^- + (\text{CF}_2\text{H})_2\text{O} \rightleftharpoons \text{Cl}^-((\text{CF}_2\text{H})_2\text{O})$ (rotamer 4)		-24.5			-20.2

^a kcal mol⁻¹, relative errors ± 0.2 kcal mol⁻¹, absolute errors ± 0.4 kcal mol⁻¹

^b cal mol⁻¹ K⁻¹, relative errors ± 1.0 cal mol⁻¹ K⁻¹, absolute errors ± 2.0 cal mol⁻¹ K⁻¹

Table 7.1 (continued)

clustering equilibrium	ΔH^0_a		$\Delta H^0_{298}_a$		ΔS^0_b	
	PHPMS	MP2//MP2	PHPMS	MP2//MP2	PHPMS	HF
$\text{Cl}^-((\text{CF}_2\text{H})_2\text{O}) + (\text{CF}_2\text{H})_2\text{O} \rightleftharpoons \text{Cl}^-((\text{CF}_2\text{H})_2\text{O})_2$ (rotamer 4)	-21.4	-18.7	-33.7	-17.7		
$\text{Cl}^- + \text{CF}_3\text{OCF}_2\text{H} \rightleftharpoons \text{Cl}^-(\text{CF}_3\text{OCF}_2\text{H})$ (rotamer 1)	-17.5	-17.3	-20.8	-19.5		
$\text{Cl}^- + \text{CF}_3\text{OCF}_2\text{H} \rightleftharpoons \text{Cl}^-(\text{CF}_3\text{OCF}_2\text{H})$ (rotamer 2)		-17.6		-19.8		
$\text{Cl}^- + (\text{CF}_3)_2\text{O} \rightleftharpoons \text{Cl}^-((\text{CF}_3)_2\text{O})$ (rotamer 1)		-4.9		-16.0		

^a kcal mol⁻¹, relative errors ± 0.2 kcal mol⁻¹, absolute errors ± 0.4 kcal mol⁻¹

^b cal mol⁻¹ K⁻¹, relative errors ± 1.0 cal mol⁻¹ K⁻¹, absolute errors ± 2.0 cal mol⁻¹ K⁻¹

Table 7.2 Overview of the experimental and computational thermochemical data for the chloride ion-acetone clustering equilibria $\text{Cl}^- + \text{acetone-F}_n = \text{Cl}^-(\text{acetone-F}_n)$ (acetone-F_n = CH₃C(O)CH₃, CH₃C(O)CH₂F, CH₃C(O)CF₃, CF₃C(O)CF₂H, CF₃C(O)CF₃).

clustering equilibrium	$\Delta H^0{}^a$	$\Delta H_{298}^0{}^a$	$\Delta S^0{}^b$	$\Delta S_{298}^0{}^b$
	PHPMS	MP2//MP2	PHPMS	HF
$\text{Cl}^- + \text{CH}_3\text{C}(\text{O})\text{CH}_3 = \text{Cl}^-(\text{CH}_3\text{C}(\text{O})\text{CH}_3)$	-14.1	-13.1	-20.2	-20.8
$\text{Cl}^- + \text{CH}_3\text{C}(\text{O})\text{CH}_2\text{F} = \text{Cl}^-(\text{CH}_3\text{C}(\text{O})\text{CH}_2\text{F})$ (rotamer 1)	-18.4	-13.8	-24.5	-20.3
$\text{Cl}^- + \text{CH}_3\text{C}(\text{O})\text{CH}_2\text{F} = \text{Cl}^-(\text{CH}_3\text{C}(\text{O})\text{CH}_2\text{F})$ (rotamer 2)		-17.8		-22.8
$\text{Cl}^- + \text{CH}_3\text{C}(\text{OH})\text{CHF} = \text{Cl}^-(\text{CH}_3\text{C}(\text{OH})\text{CHF})$		-22.3		-20.7
$\text{Cl}^- + \text{CH}_3\text{C}(\text{O})\text{CF}_3 = \text{Cl}^-(\text{CH}_3\text{C}(\text{O})\text{CF}_3)$	-13.7	-13.0	-18.4	-18.7
$\text{Cl}^- + \text{CF}_2\text{HC}(\text{O})\text{CF}_2\text{H} = \text{Cl}^-(\text{CF}_2\text{HC}(\text{O})\text{CF}_2\text{H})$		-26.4		-21.3
$\text{Cl}^- + \text{CF}_3\text{C}(\text{O})\text{CF}_2\text{H} = \text{Cl}^-(\text{CF}_3\text{C}(\text{O})\text{CF}_2\text{H})$	-26.1	-26.8	-29.9	-22.2
$\text{Cl}^- + \text{CF}_3\text{C}(\text{O})\text{CF}_3 = \text{Cl}^-(\text{CF}_3\text{C}(\text{O})\text{CF}_3)$	-28.8	-27.8	-37.6	-25.2

^a kcal mol⁻¹, relative errors ±0.2 kcal mol⁻¹, absolute errors ±0.4 kcal mol⁻¹^b cal mol⁻¹ K⁻¹, relative errors ±1.0 cal mol⁻¹ K⁻¹, absolute errors ±2.0 cal mol⁻¹ K⁻¹

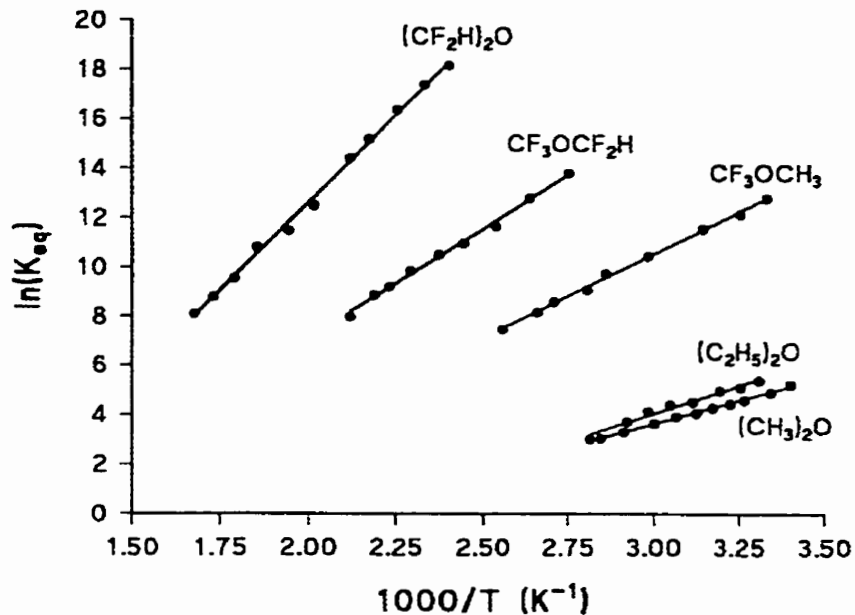


Figure 7.51 Van't Hoff plots for the chloride ion-ether clustering equilibria
 $\text{Cl}^- + \text{ether-F}_n \rightleftharpoons \text{Cl}^-(\text{ether-F}_n)$ (ether-F_n = (CH₃)₂O, (CH₃CH₂)₂O, CH₃OCF₃,
 (CF₂H)₂O, CF₃OCF₂H).

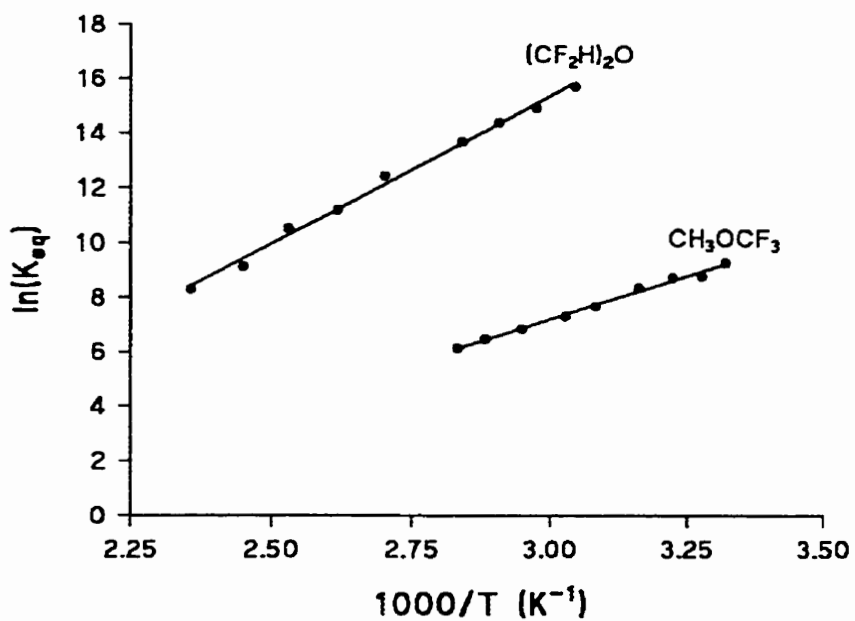


Figure 7.52 Van't Hoff plots for the chloride ion-ether clustering equilibria
 $\text{Cl}^-(\text{ether-F}_n) + \text{ether-F}_n \rightleftharpoons \text{Cl}^-(\text{ether-F}_n)_2$ (ether-F_n = CH₃OCF₃, (CF₂H)₂O).

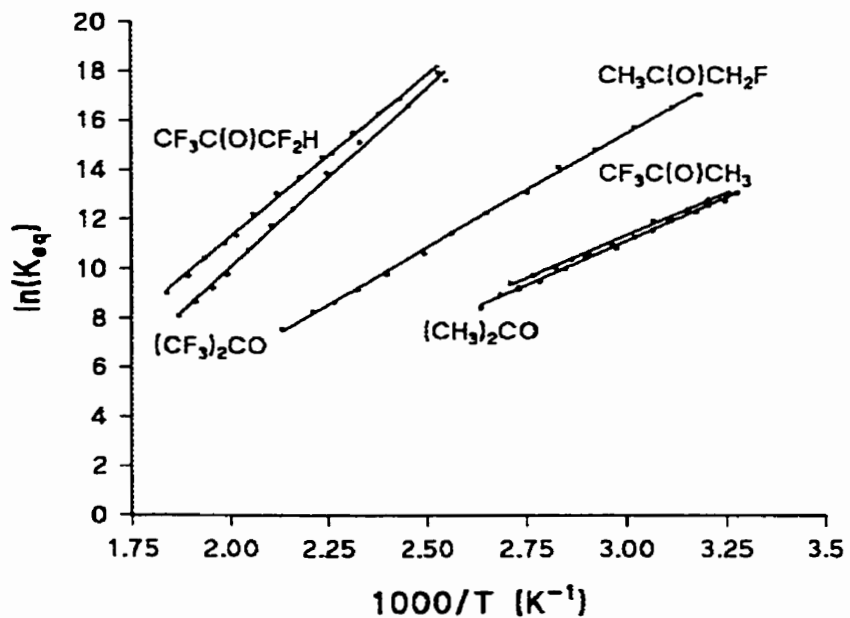


Figure 7.53 Van't Hoff plots for the chloride ion-acetone clustering equilibria $Cl^- + \text{acetone-F}_n = Cl^-(\text{acetone-F}_n)$ (acetone-F_n = CH₃C(O)CH₃, CH₃C(O)CH₂F, CH₃C(O)CF₃, CF₃C(O)CF₂H, CF₃C(O)CF₃).

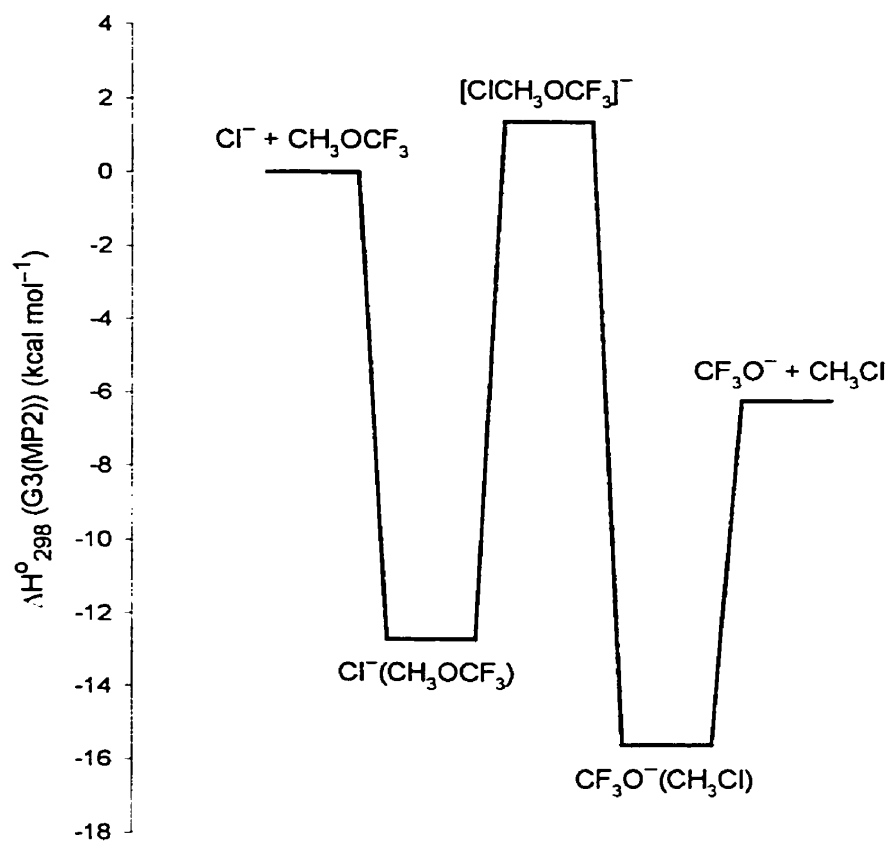
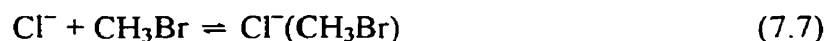


Figure 7.54 Schematic G3(MP2) energy profile for the $\text{Cl}^- + \text{CH}_3\text{OCF}_3 \rightarrow \text{CF}_3\text{O}^- + \text{CH}_3\text{Cl}$ gas phase $\text{S}_{\text{N}}2$ reaction.

alkyl), increases. There are some problems associated with obtaining more qualitative data on this. First of all it may be that the folding of the alkyl group around the chloride ion will be slow on the scale of the PHPMS experiments, thus preventing attainment of an equilibrium population. Second of all, there will be many conformers possible for both the neutral and chloride ion complex, and it seems almost impossible to abstract the distinct thermochemistry from the overall data. As already mentioned, the $\text{Cl}^-(\text{CH}_3\text{OCF}_3)$ complex resembles a $\text{S}_{\text{N}}2$ backside attack complex, even though the binding is not completely symmetric. For a similar, true $\text{S}_{\text{N}}2$ system, Reaction 7.7, values for ΔH° and ΔS° of $-12.5 \text{ kcal mol}^{-1}$ ⁷¹ and $-19.0 \text{ cal mol}^{-1} \text{ K}^{-1}$,⁷² respectively, were determined, with the latter obtained from *ab initio* computations.



CF_3O^- was present in the ion source, and from a schematic energy profile calculated at the G3(MP2) level of theory, shown in Figure 7.54, it seems reasonable to assume that it has been formed by a $\text{S}_{\text{N}}2$ type reaction. (Reaction 7.8).

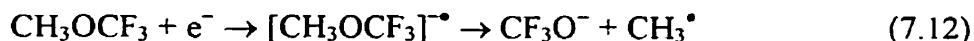


In the literature other reactions have been described to generate CF_3O^- , and these are shown in Reactions 7.9 to 7.11.⁶⁹



Each of these reactions involve ions that are relatively more difficult to generate than Cl^- , or they involve chemicals that are more unpleasant than CH_3OCF_3 . The

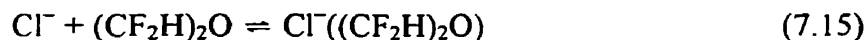
energy profile of Reaction 7.8 and its accompanying thermochemistry will be discussed in more detail in Section 7.4.3. The CF_3O^- formed can also cluster with CH_3OCF_3 , forming $\text{CF}_3\text{O}^-(\text{CH}_3\text{OCF}_3)$. The latter ion is present in very small intensity, but nonetheless equilibrium was observed. It seems unlikely that CF_3O^- may also be generated through dissociative electron capture by CH_3OCF_3 (Reaction 7.12).



Electron radiolysis of CH_3OCF_3 into CF_3O^* and CH_3^* , followed by electron capture by CF_3O^* also seems a very unlikely process (Reactions 7.13 and 7.14). The first process is $95.7 \text{ kcal mol}^{-1}$ endothermic, while the second process is $101.2 \text{ kcal mol}^{-1}$ exothermic, making the overall process $5.5 \text{ kcal mol}^{-1}$ exothermic.⁴² The probability of the two step process is low, despite the favorable overall energetics, mainly due to the low concentrations of the species involved.



Larson and McMahon measured ΔG_{298}° for the clustering of chloride ion onto 1,1,3,3-tetrafluorodimethyl ether (Reaction 5.15) and pentafluorodimethyl ether (Reaction 7.16) by ICR, from exchange equilibria with various chloride ion clusters.²⁷



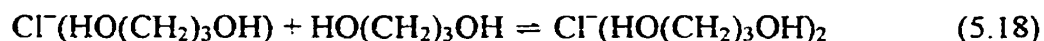
Values of $-17.0 \text{ kcal mol}^{-1}$ and $-12.1 \text{ kcal mol}^{-1}$, respectively were obtained. From the present PHPMS data, ΔG_{298}° values of $(-18.8 \pm 1.0) \text{ kcal mol}^{-1}$ and (-11.3 ± 1.0)

kcal mol⁻¹, respectively, can be determined, in reasonable to good agreement with the ICR values. The relatively large negative values for ΔH° and ΔS° for Reaction 7.18 seem very reasonable. Zhang *et al.* measured the thermochemistry by PHPMS for the equilibrium clustering reaction of chloride ion onto 1,3-propanediol (Reaction 7.17), and found ΔH° and ΔS° values of (-28.3 ± 1.7) kcal mol⁻¹ and (-34.0 ± 0.7) cal mol⁻¹ K⁻¹, respectively.²⁸



The ΔH° value for Reaction 7.16 of -17.5 kcal mol⁻¹ is equal to the ΔH° value for chloride ion bonding to methanol.⁷³ The difference in ΔS° values for both equilibria is mainly due to the fact that in the $\text{Cl}^-(\text{CH}_3\text{OH})$ complex, chloride ion has some interaction with two methyl group hydrogen atoms, thereby hindering the methyl group rotation to a certain degree.

In general, it is expected that multiple hydrogen bonding interactions will be thermodynamically more favorable than single hydrogen bonding. If one compares the ΔH° and ΔS° values for Reactions 7.15 and 7.16, which give rise to double and single hydrogen bonding, respectively, one can make an estimate of the changes in ΔH° and ΔS° for going from a single to a double hydrogen bond. From the PHPMS data, $\Delta\Delta H^\circ$ and $\Delta\Delta S^\circ$ values of -10.7 kcal mol⁻¹ and -10.5 cal mol⁻¹ K⁻¹, respectively, can be determined. Converting these values to $\Delta\Delta G_{298}^\circ$ (-7.4 kcal mol⁻¹) gives excellent agreement with the $\Delta\Delta G_{298}^\circ$ value of -7.4 kcal mol⁻¹ by Larson and McMahon from their ICR experiments.²⁷ The ΔH° and ΔS° values for the two desolvation equilibria, Reaction 7.2, with ether = CH_3OCF_3 and $\text{CF}_3\text{OCF}_2\text{H}$, also seem reasonable compared to similar systems reported in the literature. Zhang *et al.* also determined the thermochemistry for the equilibrium clustering reaction between chloride ion and two molecules of 1,3-propanediol (Reaction 7.18), and found ΔH° and ΔS° values of (-20.8 ± 0.7) kcal mol⁻¹ and (-36.2 ± 0.3) cal mol⁻¹ K⁻¹, respectively.²⁸



The data for formation of $\text{Cl}^-(\text{CF}_2\text{H})_2\text{O}$ shows a similar trend as Reaction 7.18, *e.g.* a decrease in $-\Delta H^\circ$ of approximately 8 kcal mol⁻¹, and a small increase in $-\Delta S^\circ$ of approximately 2 cal mol⁻¹ K⁻¹. Additional hindrance of two more CF₂H rotations is the main factor for this more negative ΔS° value.

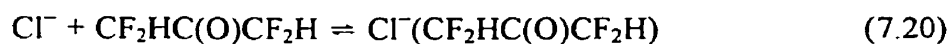
In the $\text{Cl}^-(\text{CF}_2\text{H})_2\text{O}$ cluster the bonding to the chloride ion seems so favorable, that it is reasonable to assume that a third (CF₂H)₂O molecule may not directly interact with the chloride ion. Instead, this third solvent molecule may start making up the so-called second solvation shell. If this is actually true, it will bind to one or both (CF₂H)₂O solvent molecule(s), most likely by hydrogen bonding. The two types of hydrogen bonds that are most likely to occur have one, or maybe both, hydrogen atom(s) interacting with either a fluorine atom, CF₂HO CF₂-H...F-CFHOCF₂H, or the oxygen atom, CF₂HO CF₂-H...O(CF₂H)₂. It may then be expected that the ΔH° and ΔS° values for the tri-solvation of chloride ion by 1,1,3,3-tetrafluorodimethyl ether (Reaction 7.19) will both be substantially less negative than the corresponding desolvation.



From Tables 7.1 and 7.2 it can be seen that changing the functional group from alkoxy to carbonyl has an important influence on the effect of fluorine substitution to the chloride ion affinities and the types of binding in the corresponding clusters. As mentioned already in Section 7.4.1, the chloride affinity for acetone is much larger than for dimethyl ether. This is mainly due to the larger polarizability (6.4 Å³ versus 5.5 Å³),⁶⁶ but more importantly, the larger dipole moment of acetone (2.88 D versus 1.69 D).⁶⁶ The ΔH° and ΔS° values from this work are in excellent agreement with earlier data from our laboratory (-14.2 kcal mol⁻¹ and -21.9 cal mol⁻¹ K⁻¹,

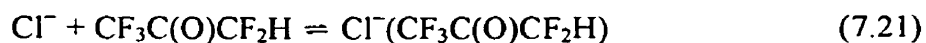
respectively),⁷⁴ and data from Kebarle and co-workers ($-13.7 \text{ kcal mol}^{-1}$ and $19.6 \text{ cal mol}^{-1} \text{ K}^{-1}$).⁷⁵

The substitution of only one hydrogen atom for fluorine has a significant impact on the observed thermochemistry. A more detailed discussion of this system will be given in Section 7.4.3. Going from CH_3OCH_3 to CH_3OCF_3 , a large change in ΔH° and ΔS° values was observed. Furthermore there is a large change in the type of chloride interaction. This larger change is not observed when going from $\text{CH}_3\text{C}(\text{O})\text{CH}_3$ to $\text{CH}_3\text{C}(\text{O})\text{CF}_3$. Instead, both ΔH° and ΔS° become less negative. As can be seen in Figure 7.38, the chloride ion only interacts with one of the hydrogen atoms in $\text{Cl}^-(\text{CH}_3\text{C}(\text{O})\text{CF}_3)$ as compared to two in $\text{Cl}^-(\text{CH}_3\text{C}(\text{O})\text{CH}_3)$. For Reaction 7.20 only a ΔG°_{298} result from ICR experiments by Larson and McMahon is available for comparison.²⁷



A ΔG°_{298} value of $-18.1 \text{ kcal mol}^{-1}$ was found, but unfortunately no ΔS° value is available. In Figure 7.39 it could already be seen that in the $\text{Cl}^-(\text{CF}_2\text{HC}(\text{O})\text{CF}_2\text{H})$ complex the bonding is different from the corresponding ether complex $\text{Cl}^-(\text{CF}_2\text{HO}(\text{O})\text{CF}_2\text{H})$. Based on these two structures it seems reasonable to assume that for Reactions 7.15 and 7.20 the ΔS° values will be fairly close.

For reactions 7.21 and 7.22 Larson and McMahon obtained ΔG°_{298} values by ICR for both of $-16.3 \text{ kcal mol}^{-1}$.²⁷



From Figures 7.40 and 7.41 it can be seen that the binding characteristics in both complexes are very similar. The ΔH° values of $-26.1 \text{ kcal mol}^{-1}$ and $-28.8 \text{ kcal mol}^{-1}$,

respectively, show the very strong binding in these complexes. The large ΔS° values of $-29.9 \text{ cal mol}^{-1} \text{ K}^{-1}$ and $-37.6 \text{ cal mol}^{-1} \text{ K}^{-1}$, respectively, indicate that upon complex formation the CF_2H and/or CF_3 group rotations become hindered. Using the ΔH° and ΔS° values from PHPMS, ΔG°_{298} values for Reactions 24 and 25 of $(-17.6 \pm 1.0) \text{ kcal mol}^{-1}$ and $(-17.2 \pm 1.0) \text{ kcal mol}^{-1}$, respectively, can be found. These are in good agreement with the ICR results by Larson and McMahon.

In Section 7.4.5 there will be a discussion of the influence of the fluorine substitution on $\Delta_{\text{acid}}H^\circ$ and it will be shown that for the fluorinated acetones there is no correlation between this quantity and ΔH° . The electric dipole moment seems to be a logical first choice. In $\text{Cl}^-(\text{CH}_3\text{C}(\text{O})\text{CH}_3)$ the chloride ion is not aligned along the $\text{C}=\text{O}$ bond, the direction of the electric dipole moment in acetone. Similar to one isomer of $\text{Cl}^-(\text{CH}_3\text{OCH}_3)$, that particular structure would represent a transition state. An identical argument can be made for other chloride ion-acetone complexes. In addition to the orientation of the electric dipole moment, the magnitude of the electric dipole moment for the various acetones studied does not seem to correlate with the observed ΔH° values, under the assumption of only ion-dipole interactions taking place. The introduction of fluorine atoms in general increases the polarizability, as can be seen going from CH_4 to CF_4 ($\alpha(\text{CH}_4) = 2.59 \text{ \AA}^3$, $\alpha(\text{CH}_3\text{F}) = 2.97 \text{ \AA}^3$, $\alpha(\text{CF}_3\text{H}) = 3.57 \text{ \AA}^3$, and $\alpha(\text{CF}_4) = 3.84 \text{ \AA}^3$).⁶⁶ This increase works out to be approximately 0.31 \AA^3 per fluorine atom. It seems reasonable to assume that this kind of behavior applies to the fluorinated acetones as well, relative to acetone itself. Surprisingly, going from ethane to 1,1,1-trifluoroethane gives rise to a small decrease in the polarizability, from 4.47 \AA^3 to 4.40 \AA^3 . Going further to hexafluoroethane increases the polarizability to 6.82 \AA^3 . This corresponds to an increase of 0.39 \AA^3 per fluorine atom. From ethane to acetone the polarizability increases to 6.39 \AA^3 . These trends may indicate that the ion-induced dipole moment interactions may be mainly responsible for the observed trends in the ΔH° values. Unfortunately, no reliable values for the polarizabilities from the HF/6-31G(d) may be expected, but computations at, for instance, the QCISD(T)/aug-cc-pVTZ level of theory are not feasible. The influence of an ion-quadrupole interaction, especially in $\text{Cl}^-(\text{CF}_3\text{C}(\text{O})\text{CF}_3)$, may not be excluded, but the exact

direction and magnitude of the quadrupole moment of $\text{CF}_3\text{C}(\text{O})\text{CF}_3$ has not been determined. The importance of ion-quadrupole interactions in gas phase cluster ions has recently been shown for $\text{Na}^+(\text{C}_6\text{H}_6)$ ⁷⁶ and $\text{Cl}^-(\text{C}_6\text{F}_6)$.⁷⁷ Sodium and chloride ions seem to interact with the π -cloud above the benzene ring, which is the z-axis direction of the quadrupole moment of both C_6H_6 and C_6F_6 . Calculations on a variety of other chloride ion-fluorohydrocarbon clusters show that these systems can indeed bind very strongly.⁷⁷

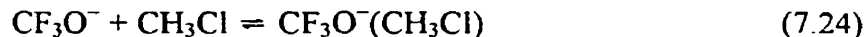
7.4.3 Computational Thermochemistry

As can be seen in Tables 7.1 and 7.2, for almost all systems investigated there is excellent agreement between thermochemical data from PHPMS experiments and from *ab initio* computations at the MP2/[c/d]/MP2[a/b] level of theory. This is especially true for ΔH° versus ΔH°_{298} values, but also for many ΔS° versus ΔS°_{298} values. It can be seen that for the various isomers and rotamers intrinsic thermochemical data have been determined. Smith *et al.* calculated the complexation energy of chloride ion onto dimethyl ether and found a value of $-6.90 \text{ kcal mol}^{-1}$, at the MP2/[cc-pVTZ+3s2p2d/cc-pVTZ+sp]/MP2/[D95+*/D95+**] level of theory, after correcting for the BSSE.⁶⁷ As already mentioned in Section 7.4.2, it cannot be excluded that in the PHPMS ion source various rotamers and/or isomers co-exist, and the computational results seem to confirm that. The example of $\text{Cl}^-((\text{CH}_3\text{CH}_2)_2\text{O})$ illustrates this nicely.

There is excellent agreement between the MP2/[c/d]/MP2/[c/d] and G3(MP2) results for the ΔH°_{298} values of Reaction 7.23 ($-12.5 \text{ kcal mol}^{-1}$ and $-12.7 \text{ kcal mol}^{-1}$, respectively).

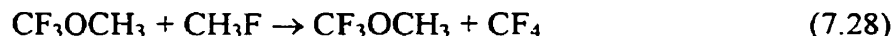
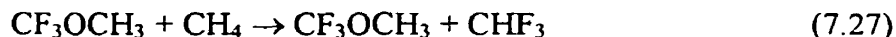


For the clustering of CF_3O^- onto CH_3Cl , Reaction 7.24, a ΔH°_{298} value at the G3(MP2) level of $-9.4 \text{ kcal mol}^{-1}$ was calculated.



Additional computations at the G3(MP2) level of theory indicate that the $[\text{ClCH}_3\text{OCF}_3]^-$ transition state is $1.4 \text{ kcal mol}^{-1}$ above the reactants Cl^- and CH_3OCF_3 , thus proving that Reaction 7.11 can proceed in the PHPMS ion source at elevated temperatures.

Good and Francisco determined $\Delta_f\text{H}^\circ_{298}$ of CH_3OCF_3 at the G2(MP2) level of theory and found a value of $-212.7 \text{ kcal mol}^{-1}$, using an isodesmic reaction scheme (Reaction 7.25 to 7.28).³⁵



In Table 7.3 an overview is given of the G3(MP2) standard ambient enthalpies and heats of formation, H°_{298} (G3(MP2)) and $\Delta_f\text{H}^\circ_{298}$ (G3(MP2)), respectively, and G3 and experimental standard ambient heats of formation, $\Delta_f\text{H}^\circ_{298}$ (G3) and $\Delta_f\text{H}^\circ_{298}$ (exp), respectively, for a variety of molecules needed to determine $\Delta_f\text{H}^\circ_{298}$ (CF_3OCH_3). As can be seen the agreement between the G3 and experimental data is excellent.⁶³ G3(MP2) performs slightly poorer overall, but the data are still in good to excellent agreement with the available experimental data. The G3(MP2) standard ambient reaction enthalpies, $\Delta_r\text{H}^\circ_{298}$ (G3(MP2)), for reactions 7.28 to 7.31 are $+5.2 \text{ kcal mol}^{-1}$, $-2.8 \text{ kcal mol}^{-1}$, $+20.2 \text{ kcal mol}^{-1}$, and $+2.3 \text{ kcal mol}^{-1}$, respectively. Using these results and $\Delta_f\text{H}^\circ_{298}$ (G3(MP2)) values from Table 7.3, a $\Delta_f\text{H}^\circ_{298}$ (CF_3OCH_3)

Table 7.3 Overview of the standard ambient G3(MP2) enthalpies, H_{298}° (G3(MP2)), and standard ambient G3(MP2), G3, and experimental heats of formation, $\Delta_f H_{298}^{\circ}$ (G3(MP2)), $\Delta_f H_{298}^{\circ}$ (G3), and $\Delta_f H_{298}^{\circ}$ (exp) of a series of molecules used to determine the standard ambient heat of formation of CH_3OCF_3 .

structure	H_{298}° (G3(MP2)) ^a	$\Delta_f H_{298}^{\circ}$ (G3(MP2)) ^b	$\Delta_f H_{298}^{\circ}$ (G3) ^b	$\Delta_f H_{298}^{\circ}$ (exp) ^b
H ₂	-1.166831			0.0
³ C	-37.786978			170.2 ± 0.1 ^d
³ O ₂	-150.161023			0.0
F ₂	-199.335331			0.0
H ₂ O	-76.338628	-57.3	-57.5 ^c	-57.80 ± 0.01 ^d
CH ₄	-40.418281	-16.5	-18.2 ^c	-17.9 ± 0.1 ^d
CH ₃ F	-139.566003	-56.4		-57.4 ± 1.2 ^d
CH ₂ F ₂	-238.734186	-109.0	-108.4 ^c	-107.7 ± 0.4 ^d
CF ₃ H	-337.913810	-168.9	-166.6 ^c	-166.6 ± 0.8 ^d
CF ₄	-437.090064	-226.6	-223.9 ^c	-223.0 ± 0.3 ^d
CH ₃ OH	-115.547922	-47.4		-48.0 ± 0.1 ^d
CF ₃ OH	-413.076586	-220.5		-217.1 ± 4.2 ^d
CH ₃ OCH ₃	-154.766441	-43.2	-44.4 ^c	-44.0 ± 0.1 ^d
CH ₃ OCF ₃	-452.294116	-215.7 ± 0.1		

^a hartree

^b kcal mol⁻¹

^c from reference 63

^d from reference 42

(G3(MP2)) of (-215.7 ± 0.1) kcal mol⁻¹ can be determined. This is in good agreement with the G2(MP2) results by Good and Francisco³⁵. The experimental $\Delta_f H^\circ$ (CF₃OH) has been determined from experimental $\Delta_f H^\circ$ (CF₃O⁻) (-253.0 ± 2.2) kcal mol⁻¹,⁴² $\Delta_f H^\circ$ (H⁺) (-356.7) kcal mol⁻¹,⁴² and $\Delta_{\text{acid}} H^\circ$ (CF₃OH) (-329.8 ± 2.0) kcal mol⁻¹.⁷³ The $\Delta_f H^\circ_{298}$ (CF₃OH) (G3(MP2)) is somewhat more negative than previous computations.⁷³

The only system that showed significant differences between the experimental PHPMS data and computational results is Reaction 7.29.



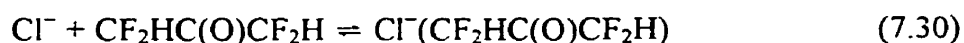
It can be seen in Table 7.2 that the computational thermochemistry of rotamer 2 has the best agreement with the experimental PHPMS data. This system has the interesting feature that the neutral rotamer 1 (Figure 7.14) is lower in energy than rotamer 2 (Figure 7.15), but that the chloride ion complex with rotamer 1 (Figure 7.35) is actually higher in energy than the chloride ion complex with rotamer 2 (Figure 7.36). Unfortunately, no explanation has been found that can account for this feature. Of course it will be impossible to have a 100% population of the neutral rotamer 2. It may be that what has been observed by PHPMS is actually a steady state and not a true equilibrium.

The systems with the largest discrepancies between ΔS° and ΔS°_{298} values are for the formation of the following five cluster ions: Cl⁻((CF₂H)₂O), Cl⁻(CF₃C(O)CF₂H), Cl⁻(CF₃C(O)CF₃), Cl⁻((CF₂H)₂O)₂, and Cl⁻(CH₃OCF₃)₂. In the first three systems it is thought that hindrance of the CF₂H and/or CF₃ group rotations takes place. The *Gaussian 98* suite of programs treats these torsional motions as harmonic vibrations, thus giving rise to large errors in the entropy. By using a method developed by Ayala and Schlegel,⁵⁷ which is implemented in *Gaussian 98*, hindered rotations can be identified by using the Freq=HindRot keyword. If a hindered rotation has been identified, automatically modified thermodynamical functions will be used to calculate the correct entropy, heat capacity, and so on. Of course the level of theory will also

have a large influence. For instance, using the B3LYP/[6-311++G(3df,3pd)/6-311++G(3d,3p)] level of theory, a S_{298}° value for $\text{Cl}^{-}(\text{CF}_3\text{C}(\text{O})\text{CF}_3)$ of $102.415 \text{ cal mol}^{-1} \text{ K}^{-1}$ was calculated using the harmonic oscillator approximation. Using the hindered rotor approximation a value of $102.695 \text{ cal mol}^{-1} \text{ K}^{-1}$ was determined. For the same cluster, but using the HF/[6-31+G(d)/6-31G(d)] level of theory a value of $106.944 \text{ cal mol}^{-1} \text{ K}^{-1}$ was determined using the harmonic oscillator approximation, while a value of $111.788 \text{ cal mol}^{-1} \text{ K}^{-1}$ was obtained using the hindered rotor approximation.

7.4.4 Experiment versus Computations

In general the agreement between the experimental and computational thermochemistry is very good, especially for the ΔH_{298}° values. For the clustering of chloride ion onto 1,1,3,3-tetrafluoroacetone, Reaction 7.30, Larson and McMahon determined ΔG_{298}° to be $-16.3 \text{ kcal mol}^{-1}$.²⁷

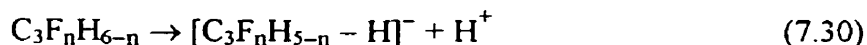


By using ΔH_{298}° from the MP2/[c/d]/MP2/[a/b] computations ($-27.0 \text{ kcal mol}^{-1}$), a ΔS_{298}° value of $-29.9 \text{ cal mol}^{-1} \text{ K}^{-1}$ can be determined. This value is somewhat smaller than the ΔS° value by PHPMS for Reaction 23 of $-31.3 \text{ cal mol}^{-1} \text{ K}^{-1}$. This difference can be understood based on the difference in the structures of $\text{Cl}^{-}(\text{CF}_2\text{HOCF}_2\text{H})$ and $\text{Cl}^{-}(\text{CF}_2\text{HC}(\text{O})\text{CF}_2\text{H})$, as discussed in Section 7.4.1. As already discussed in Section 7.4.3, for some systems the ΔS_{298}° values calculated at the HF/[a/b] level of theory agree well with experimental results. Systems where hindrance of methyl group rotations takes place can be treated successfully within the hindered rotor approximation by applying a higher level of theory. It cannot be expected that computations will always provide almost perfect agreement with

experiment in order to consider them suitable. On the other hand it would have been much more difficult to interpret the experimental results without the computations.

7.4.5 Gas Phase Acidities of Fluorinated Acetones

Farid and McMahon measured the standard ambient gas phase deprotonation enthalpies, $\Delta_{\text{acid}}H^{\circ}_{298}$, for acetone and five fluorinated acetones by bracketing experiments on an ICR instrument.⁷⁹ The results indicated that fluorine substitution provides a net stability effect of planar carbanions, although the increase in stability can be considered irregular. Initially it was assumed that there might be a direct correlation between the standard enthalpy change for the various chloride ion acetone complexation equilibria (Reaction 3), ΔH° , and the deprotonation enthalpy for Reaction 7.30, $\Delta_{\text{acid}}H^{\circ}$.^{73,80}



$\Delta_{\text{acid}}H^{\circ}_{298}$ values for acetone and the four fluorinated acetones were calculated at the G3(MP2) level of theory. In order to verify the suitability of G3(MP2) to calculate accurate $\Delta_{\text{acid}}H^{\circ}_{298}$ values, test computations on a series of small to medium sized (in)organic acids were performed at the G3 and G3(MP2) level of theory and compared to literature data.⁴² In Table 7.4 an overview is given of the calculated G3 and G3(MP2) standard ambient enthalpies, H°_{298} (G3) and H°_{298} (G3(MP2)), for the various acids and their conjugate bases. In order to convert these H°_{298} values to $\Delta_{\text{acid}}H^{\circ}_{298}$ values for Reaction 7.31, Equation 7.32 was used.



$$\Delta_{\text{acid}}H^{\circ}_{298}(\text{HA}) = H^{\circ}_{298}(\text{H}^+) + H^{\circ}_{298}(\text{A}^-) - H^{\circ}_{298}(\text{HA}) \quad (7.32)$$

In Equation 7.35, $H_{298}^{\circ} (H^+)$ is taken as 0.002360 hartree. As can be seen from Table 7.5, there is good to excellent agreement between the G3 and G3(MP2) results, and in most cases between the computational and experimental data. DeTuri and Ervin showed that for H_2O , CH_3OH , C_2H_2 , and HF , MP2 in combination with the 6-311+G(d,p) and 6-311++G(d,p) basis sets, G2 and G2(MP2) gave mean absolute deviations with experimental data of 0.5, 0.5, 0.7, and 0.7 kcal mol⁻¹, respectively.⁸¹ For the $\Delta_{acid}H_{298}^{\circ}$ values of $CH_3C(O)CHF-H$ and $CF_3C(O)CF_2-H$ there seem to be large discrepancies with the ICR data from Farid and McMahon, but for $CF_3C(O)CH_3$ there is perfect agreement.⁷⁹ As already discussed in Section 7.4.1, there is hydrogen bonding taking place in the chloride ion-acetone complexes investigated, but it is less pronounced than expected. Especially the chloride ion-pentafluoroacetone complex, $Cl^-(CF_3C(O)CF_2H)$, seems to conflict with the ICR results of Farid and McMahon.⁷⁹ Under low pressure ICR conditions, the following equilibrium was observed (Reaction 7.33)



Proton transfer in the $Cl^-(CF_3C(O)CF_2H)$ complex, as shown in Figure 7.40, seems to be an unfavorable process. In addition, the difference in G3(MP2) $\Delta_{acid}H_{298}^{\circ}$ values between HCl and $CF_3C(O)CF_2H$ would prevent an exothermic proton transfer. The difference is too large for the reaction to be perhaps entropy driven, *i.e.* $\Delta_{acid}G_{298}^{\circ} < 0$ kcal mol⁻¹. The presence of a higher energy complex, $Cl^-(H-CF_2C(O)CF_3)$, from which the proton transfer occurs might be another possibility. Under low pressure ICR conditions there is no stabilization of the intermediate $Cl^-(CF_3C(O)CF_2H)$ complex, as takes place in the high pressure source.

Finally, it is surprising that in the $Cl^-(CH_3C(O)CH_2F)$ complex the chloride ion prefers to interact with two hydrogens from both methyl groups, even though the G3(MP2) $\Delta_{acid}H_{298}^{\circ}$ value of the CH_3 group is 19.0 kcal mol⁻¹ lower than the CH_2F group. Attempts to locate other stable minima where chloride ion interacts exclusively

Table 7.4 Overview of the standard ambient G3(MP2) and G3 enthalpies, H^0_{298} (G3(MP2)) and H^0_{298} (G3), of a series of small to medium sized (in)organic acids and their conjugated bases.

neutral	H^0_{298} (G3(MP2)) ^a	H^0_{298} (G3) ^a	anion	H^0_{298} (G3(MP2)) ^a	H^0_{298} (G3) ^a
HF	-100.355477	-100.397801	F ⁻	-99.763933	-99.806828
HCl	-460.349212	-460.651359	Cl ⁻	-459.819999	-460.121239
H ₂ O	-76.338628	-76.378265	HO ⁻	-75.717174	-75.756934
CH ₃ OH	-115.547922	-115.624915	CH ₃ O ⁻	-114.939055	-115.015963
CF ₃ OH	-413.076586		CF ₃ O ⁻	-412.554319	
C ₂ H ₂	-77.198153	-77.272275	C ₂ H ⁻	-76.598215	-76.671128
CH ₃ CO ₂ H	-228.777174	-228.934396	CH ₃ CO ₂ ⁻	-228.224276	-228.382205
CF ₃ CO ₂ H	-526.263532		CF ₃ CO ₂ ⁻	-525.748266	
CH ₃ C(O)CH ₃	-192.838667	-192.990774	CH ₃ C(O)CH ₂ ⁻	-192.252102	-192.403867
CH ₃ C(O)CH ₂ F	-291.991094		CH ₃ C(O)CHF ⁻	-291.408062	
			CH ₂ C(O)CH ₂ F ⁻	-291.417117	
CF ₃ C(O)CH ₃	-490.333258		CF ₃ C(O)CH ₂ ⁻	-489.778498	
CF ₃ C(O)CF ₂ H	-688.640700		CF ₃ C(O)CF ₂ ⁻	-688.089959	

^a hartree

Table 7.5 Overview of the standard ambient G3(MP2), G3, and experimental deprotonation enthalpies, $\Delta_{\text{acid}}H^{\circ}_{298}$ (G3(MP2)), $\Delta_{\text{acid}}H^{\circ}_{298}$ (G3), and $\Delta_{\text{acid}}H^{\circ}_{298}$ (exp), of a series of small to medium sized (in)organic acids.

neutral	$\Delta_{\text{acid}}H^{\circ}_{298}$ (G3(MP2)) ^a	$\Delta_{\text{acid}}H^{\circ}_{298}$ (G3) ^a	$\Delta_{\text{acid}}H^{\circ}_{298}$ (exp) ^{a,b}
HF	372.7	372.3	371.6 ± 0.2
HCl	333.6	334.1	333.4 ± 0.002
H ₂ O	391.4	391.4	390.7 ± 0.1
CH ₃ OH	383.6	383.6	381.8 ± 1.0
CF ₃ OH	329.2		329.8 ± 2.0
C ₂ H ₂	377.9	378.7	378.0 ± 0.7
CH ₃ CO ₂ H	348.4	348.0	348.1 ± 2.2
CF ₃ CO ₂ H	324.8		323.8 ± 2.9
CH ₃ C(O)CH ₂ -H	369.6	369.8	369.1 ± 2.1
CH ₃ C(O)CHF-H	380.7		366.1 ± 2.1
H-CH ₂ C(O)CH ₂ F	361.7		357.1 ± 2.1
CF ₃ C(O)CH ₂ -H	349.6		349.5 ± 2.1
CF ₃ C(O)CF ₂ -H	347.1		337.6 ± 4.2

^a kcal mol⁻¹ ^b from reference 42

with hydrogen atoms from the CH₃ group, like in Cl⁻(CH₃OCF₃), either by single or multiple hydrogen bonding, failed.

7.4.6 Vibrational Frequencies of Fluorinated Acetones

Recently Good and Francisco measured the FT-IR spectra of CH₃OCF₃, (CF₂H)₂O, and CF₃OCF₂H and calculated the normal mode vibrational frequencies at various levels of theory.³⁶ The best agreement (rms error of 2.7%) between experiment and theory was obtained using the B3LYP/6-311++G(3df,3pd) level of theory, and these results were used to assign the various modes. The HF/6-31G(d) results scaled by 0.8953 from this work in general agree very well. Surprisingly, no experimental FT-IR spectra of CH₃C(O)CH₂F and CF₃C(O)CF₂H are available in the NIST/EPA Gas-Phase Infrared Database. There are FT-IR spectra available for CH₃C(O)CH₃, CH₃C(O)CF₃, and CF₃C(O)CF₃.⁴² The quality of the calculated normal mode vibrational frequencies relative to experimental results is not so important for calculating thermochemical data. They may become more important for instance when doing Master Equation modeling to interpret the kinetics of ZTRID experiments or RRKM modeling for calculating unimolecular dissociation constants.⁸² In those cases both the frequency and the IR intensities need to be known. Unfortunately the absolute IR intensities have only been determined for a few fluorinated ethers and perfluoro alkanes.^{40,83-87} These results can be used to find a level of theory that gives good agreement with both the frequencies and the IR intensities. De Oliveira and co-workers found that for CH₄, CH₃F, CH₂F₂, CHF₃, and CF₄ B3LYP/6-311++G(3d,3p) computations performed best.⁸³ Applying this level of theory to C₂F₆ gives good agreement with experimental data on C₂F₆ by Ballard and co-workers.⁸⁴ They found values of 714 cm⁻¹ ((37.9 ± 1.2) km mol⁻¹), 1116 cm⁻¹ ((284.8 ± 4.2) km mol⁻¹), and 1250 cm⁻¹ ((1020.1 ± 18.1) km mol⁻¹), while the B3LYP/6-311++G(3d,3p) computation gives values of 703 cm⁻¹ (32 km mol⁻¹), 1099 cm⁻¹ (285 km mol⁻¹), and 1250 cm⁻¹ (1096 km mol⁻¹). Calculations at the MP2/6-31G(d,p) level of theory by Papasavva *et al.* showed very good agreement with experimental IR intensities, but the

normal mode vibrational frequencies deviate more than the B3LYP/6-311++G(3d,3p) results.⁸⁷ No attempts were made to assign the various normal mode vibrational frequencies as done by Good and Francisco.³⁶ In Figures 7.55 to 7.71 the experimental FT-IR and simulated IR HF/6-31G(d) and B3LYP/6-311++G(3d,3p) spectra of $\text{CH}_3\text{C}(\text{O})\text{CH}_3$, $\text{CH}_3\text{C}(\text{O})\text{CH}_2\text{F}$, $\text{CH}_3\text{C}(\text{O})\text{CF}_3$, $\text{CF}_3\text{C}(\text{O})\text{CF}_2\text{H}$, and $\text{CF}_3\text{C}(\text{O})\text{CF}_3$ are shown. The normal mode vibrational frequencies and IR intensities for all these spectra have been summarized in Tables 7.6 to 7.10. The $\text{CH}_3\text{C}(\text{O})\text{CF}_3$ and $\text{CF}_3\text{C}(\text{O})\text{CF}_3$ spectra are identical to the spectra in the NIST/EPA Gas-Phase Infrared Database, thus providing more confidence in the other two spectra. It has to be noted that the FT-IR spectra and the simulated IR spectra from Good and Francisco in general showed the same main features, but that individual peak intensities differed, depending on the compound of interest. A similar comment applies to the spectra discussed in this section. In addition it has to be mentioned that no detailed discussion will be provided on the differences between the two methods relative to each other and relative to the experimental data. Only general trends will be discussed.

Going from $\text{CH}_3\text{C}(\text{O})\text{CH}_3$ to $\text{CF}_3\text{C}(\text{O})\text{CF}_3$ the frequency of the CO stretch increases by approximately 80 cm^{-1} , and both the HF/6-31G(d) and B3LYP/6-311++G(3d,3p) results follow that same trend, even though the absolute values may differ by as much as 80 cm^{-1} . More important is the fact that the relative intensity of the CO stretch decreases in favor of C-C and C-F stretches in the $800\text{-}1500\text{ cm}^{-1}$ range. This makes chloride ion complexes of these fluorinated acetones and some ethers ideal model systems for ZTRID experiments in a FT-ICR instrument. The strong blackbody IR absorption in this region will most likely promote fast dissociation kinetics of even relatively strongly bound complexes. The introduction of more fluorine atoms also causes the absolute IR intensities of the CO stretch of the HF/6-31G(d) and B3LYP/6-311++G(3d,3p) results to come closer together.

The general appearances of all simulated HF/6-31G(d) and B3LYP/6-311++G(3d,3p) IR spectra relative to the FT-IR spectra shows no clear trend, and a similar statement can be made for the individual peaks and their calculated absolute IR intensities. HF/6-31G(d) computations use a lot less CPU time than the B3LYP/6-311++G(3d,3p) computations, but of course quality of the results will be the first

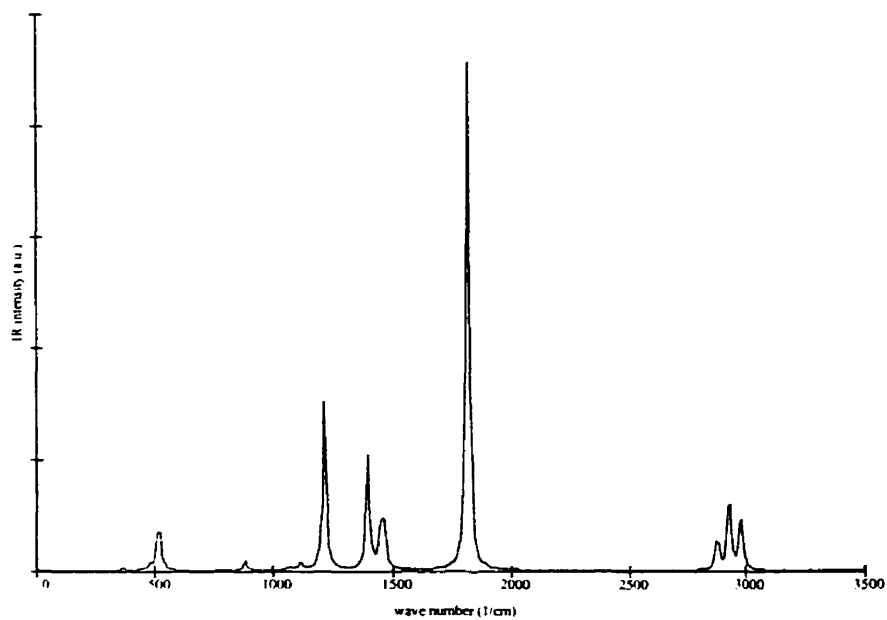


Figure 7.55 Simulated IR spectrum of $\text{CH}_3\text{C}(\text{O})\text{CH}_3$ from HF/6-31G(d) computations.

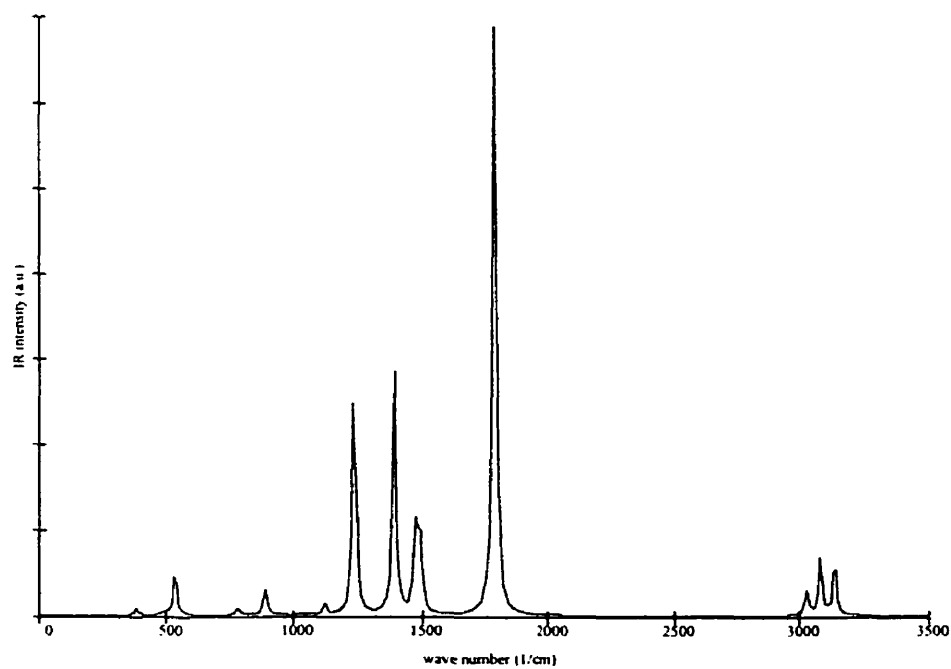


Figure 7.56 Simulated IR spectrum of $\text{CH}_3\text{C}(\text{O})\text{CH}_3$ from B3LYP/6-311++G(3d,3p) computations.

Table 7.6 Overview of the scaled HF/6-31G(d), B3LYP/6-311++G(3d,3p), and experimental normal mode vibrational frequencies and IR intensities of CH₃C(O)CH₃.

mode	HF/6-31G(d) ^a		B3LYP/6-311++G(3d,3p)		experiment	
	ν^b	Int _{abs} ^c	ν^b	Int _{abs} ^b	ν^b	Int _{rel}
1	45	0	35	0	105	
2	128	0	133	0	109	
3	359	1	379	2	385	W
4	476	3	490	1	484	W
5	515	23	534	14	530	M
6	758	0	782	2	777	W
7	878	0	885	0	877	
8	880	4	886	9	891	M
9	1066	1	1083	0	1066	
10	1110	3	1118	3	1091	M
11	1210	76	1233	71	1216	S
12	1384	8	1388	18	1364	M
13	1392	49	1389	55	1364	S
14	1439	0	1464	0	1410	
15	1442	0	1468	2	1426	
16	1445	21	1474	30	1435	M
17	1461	18	1492	19	1454	M
18	1810	229	1783	197	1731	S
19	2868	4	3021	1	2937	W
20	2875	12	3028	7	2937	W
21	2917	0	3074	0	2963	
22	2925	39	3081	17	2972	M
23	2975	15	3135	12	3019	M
24	2976	14	3136	6	3019	W

^a Scaled by 0.8953 ^b cm⁻¹ ^c km mol⁻¹ W (weak) M (medium) S (strong)

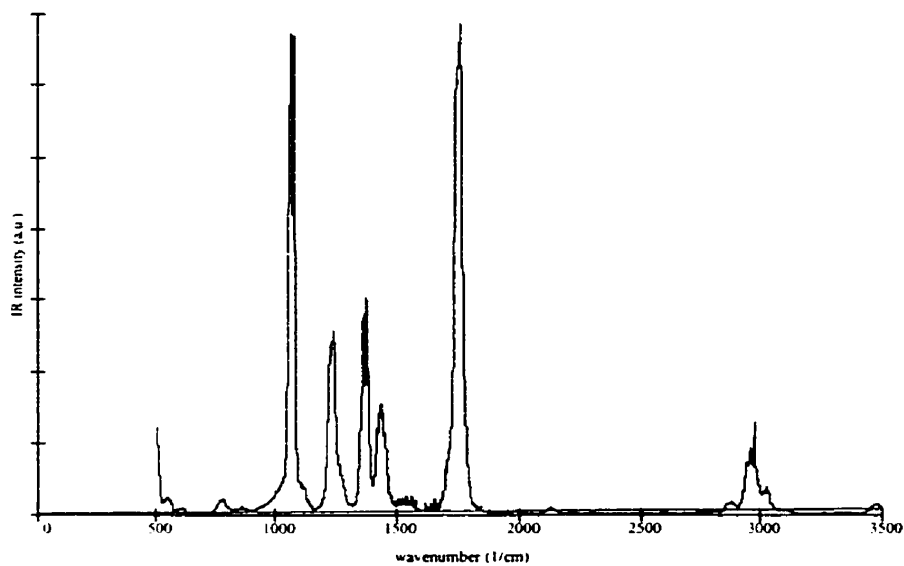


Figure 7.57 Experimental FT-IR spectrum of $\text{CH}_3\text{C}(\text{O})\text{CH}_2\text{F}$.

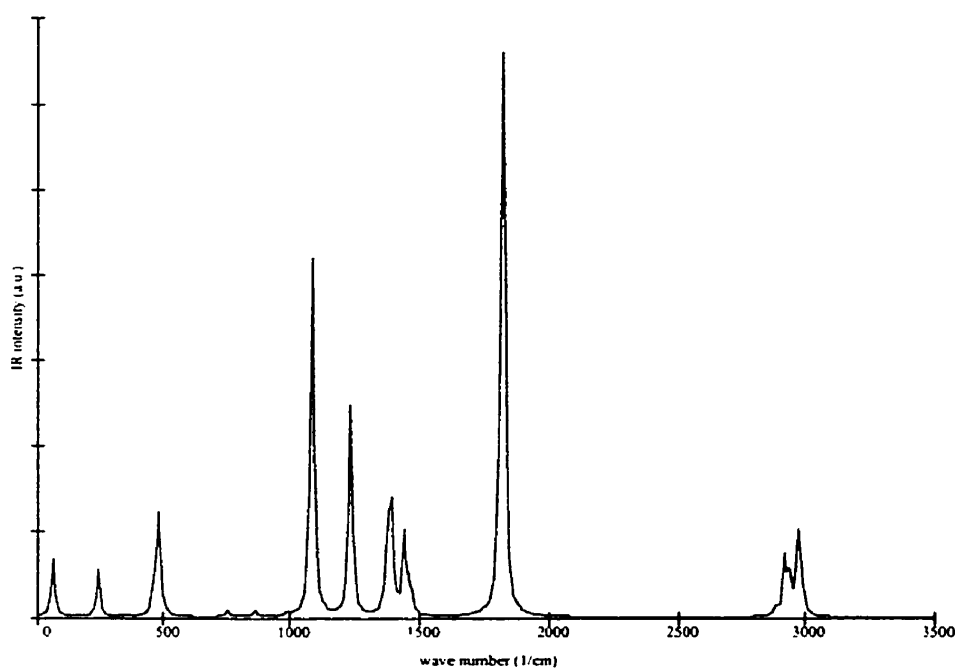


Figure 7.58 Simulated IR spectrum of $\text{CH}_3\text{C}(\text{O})\text{CH}_2\text{F}$ (rotamer 1) of HF/6-31G(d) computations.

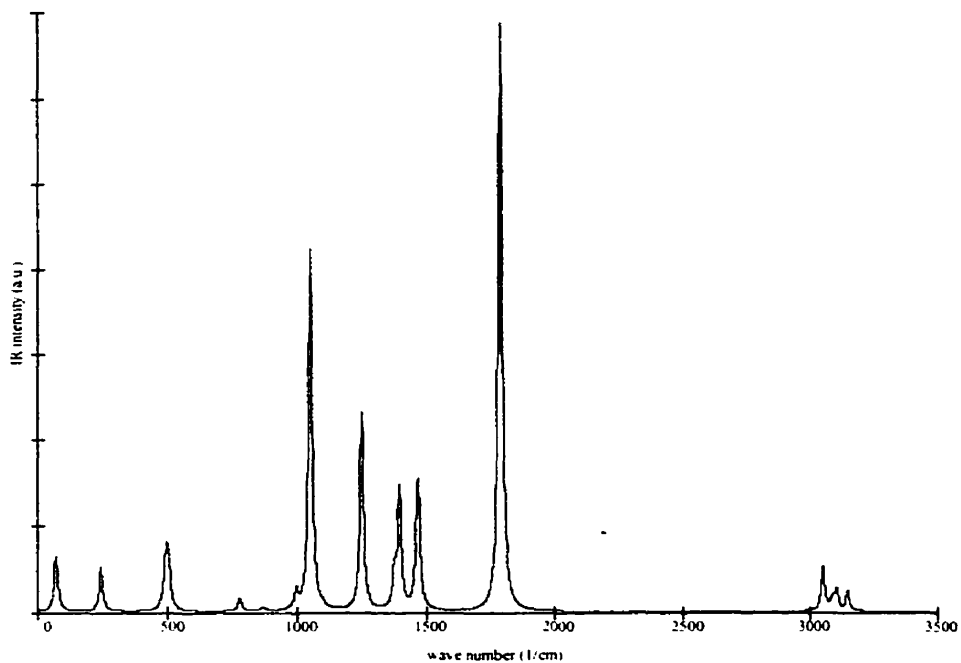


Figure 7.59 Simulated IR spectrum of $\text{CH}_3\text{C}(\text{O})\text{CH}_2\text{F}$ (rotamer 1) of B3LYP/6-311++G(3d,3p) computations.

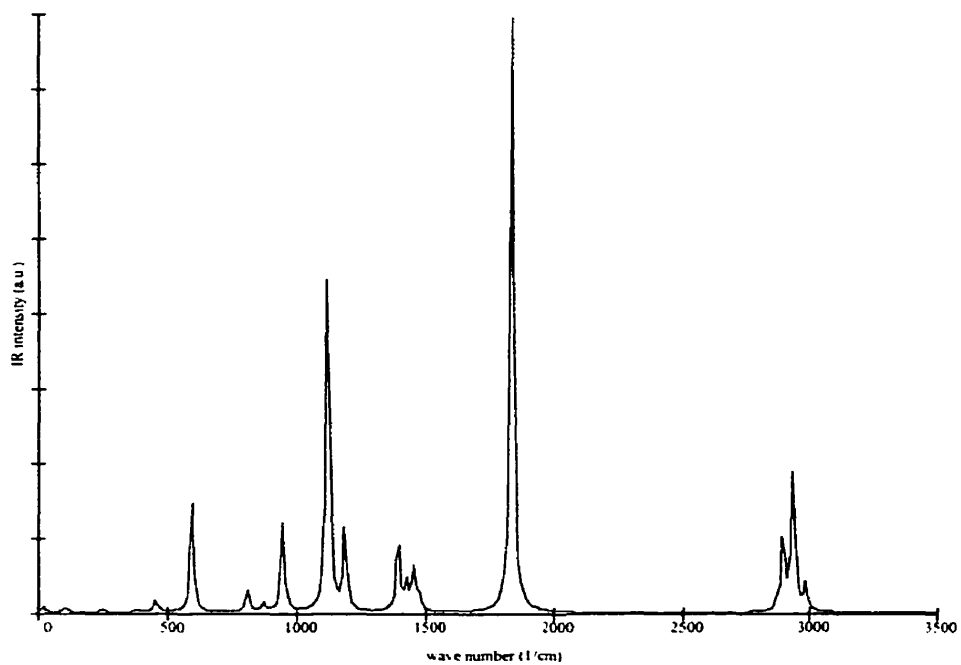


Figure 7.60 Simulated IR spectrum of $\text{CH}_3\text{C}(\text{O})\text{CH}_2\text{F}$ (rotamer 2) of HF/6-31G(d) computations.

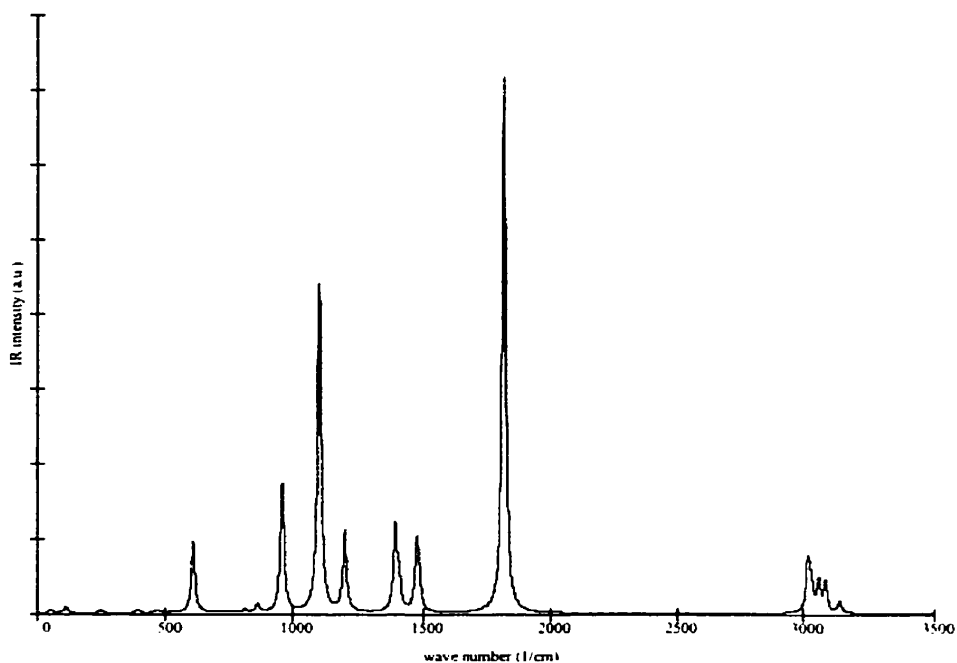


Figure 7.61 Simulated IR spectrum of $\text{CH}_3\text{C}(\text{O})\text{CH}_2\text{F}$ (rotamer 2) of B3LYP/6-311++G(3d,3p) computations.

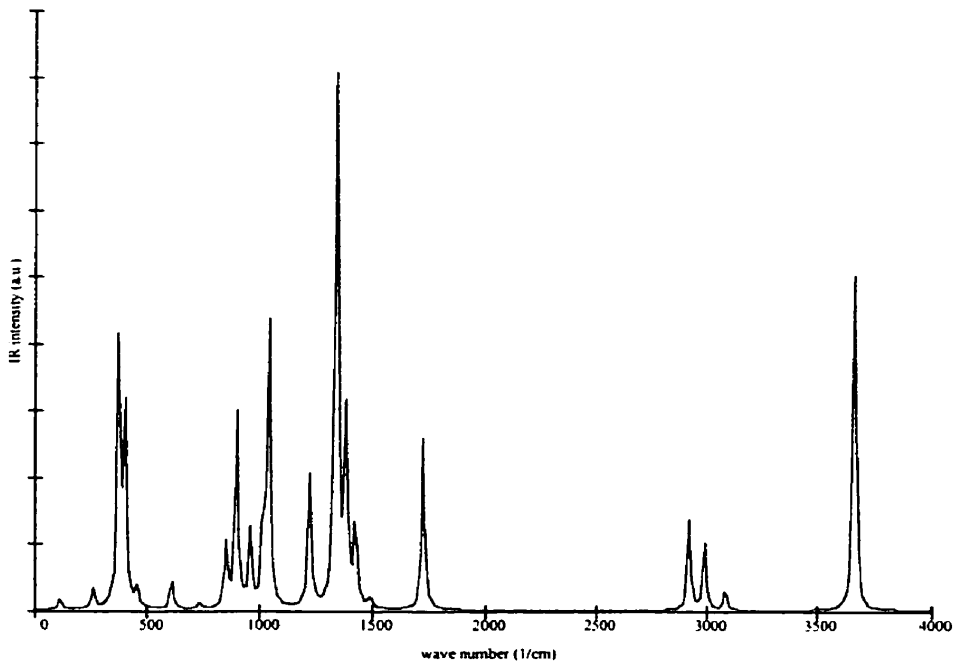


Figure 7.62 Simulated IR spectrum of $\text{CH}_2\text{C}(\text{OH})\text{CH}_2\text{F}$ (enol) of HF/6-31G(d) computations.

Table 7.7 Overview of the scaled HF/6-31G(d), B3LYP/6-311++G(3d,3p), and experimental normal mode vibrational frequencies and IR intensities of CH₃C(O)CH₂F.

mode	HF/6-31G(d) ^a		B3LYP/6-311++G(3d,3p)		experiment	
	ν^b	Int _{abs} ^c	ν^b	Int _{abs} ^c	ν^b	Int _{rel}
1	60 (17)	17 (2)	69 (51)	16 (1)		
2	149 (105)	0 (2)	128 (111)	0 (2)		
3	240 (245)	14 (1)	239 (248)	13 (1)		
4	459 (379)	5 (1)	471 (392)	1 (1)		
5	477 (451)	33 (4)	491 (464)	16 (1)		
6	493 (589)	4 (37)	502 (606)	12 (24)		
7	749 (800)	2 (7)	771 (808)	4 (1)	776	W
8	860 (861)	2 (3)	861 (857)	1 (3)	858	W
9	984 (937)	1 (34)	991 (954)	5 (43)		
10	1081 (1093)	107 (0)	1046 (1094)	106 (7)	1059	S
11	1092 (1113)	0 (127)	1095 (1097)	1 (104)	1070	S
12	1229 (1181)	60 (27)	1247 (1194)	57 (27)	1230	M
13	1232 (1249)	3 (0)	1253 (1272)	2 (0)		
14	1375 (1386)	27 (27)	1372 (1387)	10 (28)	1362	M
15	1390 (1419)	28 (9)	1392 (1402)	35 (10)	1373	M
16	1438 (1443)	20 (6)	1460 (1464)	15 (2)		
17	1447 (1451)	9 (11)	1466 (1471)	20 (21)	1436	M
18	1465 (1472)	6 (4)	1469 (1481)	10 (9)		
19	1814 (1832)	207 (212)	1788 (1812)	173 (180)	1751	S
20	2884 (2871)	3 (2)	3033 (3015)	0 (17)		
21	2921 (2893)	17 (27)	3049 (3028)	12 (8)	2873	W
22	2939 (2920)	10 (2)	3085 (3056)	3 (10)	2943	W
23	2970 (2932)	21 (48)	3100 (3082)	6 (10)	2960	W
24	2982 (2980)	12 (9)	3144 (3137)	6 (4)	2978	W

^a Scaled by 0.8953 ^b cm⁻¹ ^c km mol⁻¹ W (weak) M (medium) S (strong)

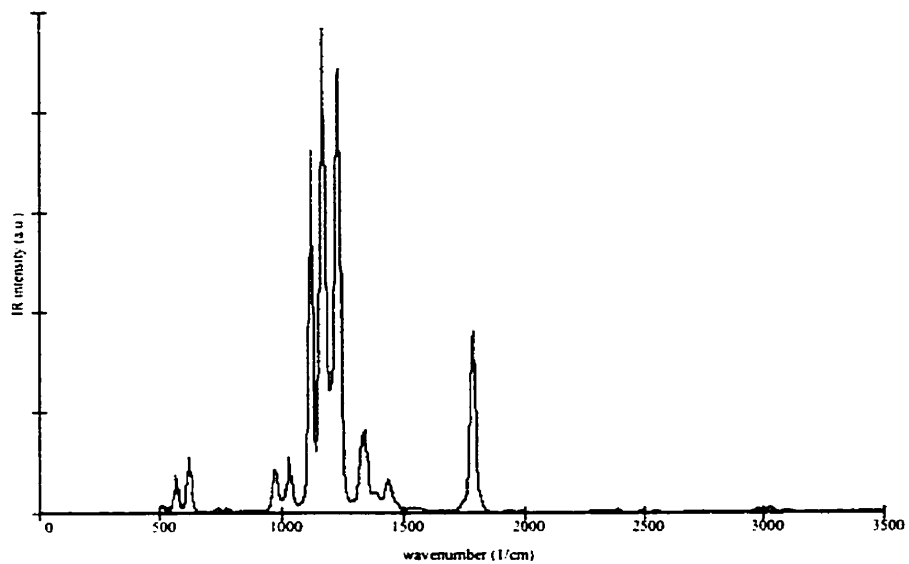


Figure 7.63 Experimental FT-IR spectrum of $\text{CH}_3\text{C}(\text{O})\text{CF}_3$.

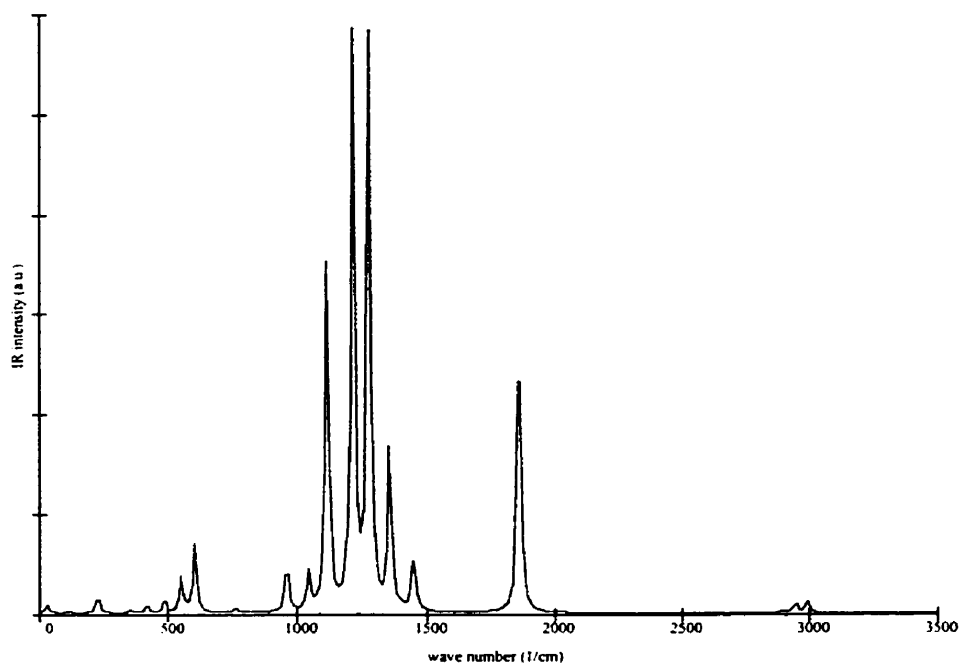


Figure 7.64 Simulated IR spectrum of $\text{CH}_3\text{C}(\text{O})\text{CF}_3$ from HF/6-31G(d) computations.

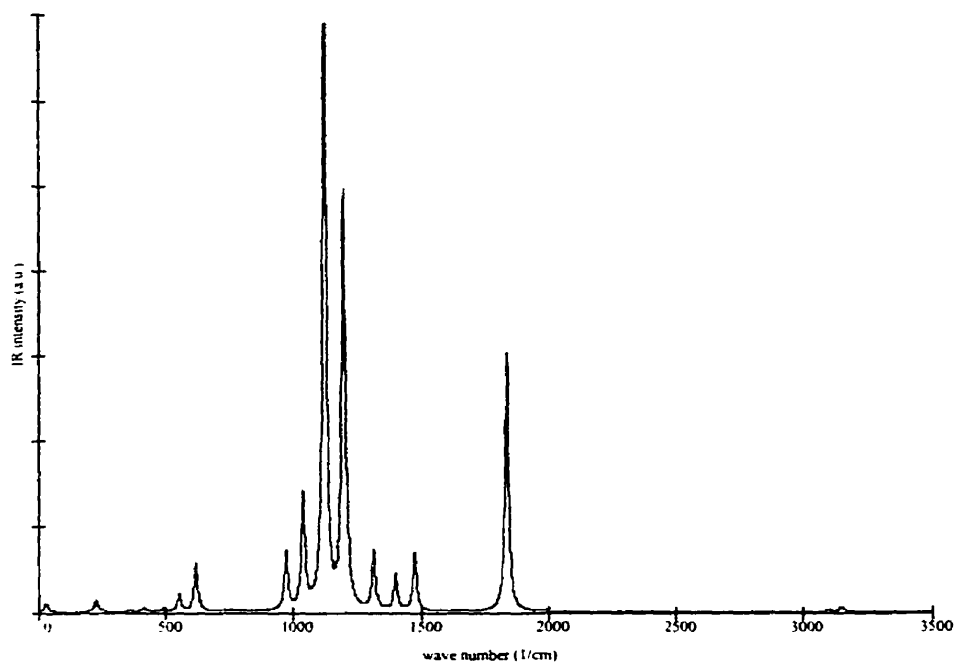


Figure 7.65 Simulated IR spectrum of $\text{CH}_3\text{C}(\text{O})\text{CF}_3$ from B3LYP/6-311++G(3d,3p) computations.

Table 7.8 Overview of the scaled HF/6-31G(d), B3LYP/6-311++G(3d,3p), and experimental normal mode vibrational frequencies and IR intensities of $\text{CH}_3\text{C}(\text{O})\text{CF}_3$.

mode	HF/6-31G(d) ^a		B3LYP/6-311++G(3d,3p)		experiment	
	ν^b	Int _{abs} ^c	ν^b	Int _{abs} ^c	ν^b	Int _{rel}
1	28	5	32	5		
2	107	1	114	0		
3	223	6	227	5		
4	230	3	231	2		
5	353	1	358	1		
6	416	4	414	2		
7	486	7	492	2		
8	550	18	551	10	564	W
9	600	35	616	28	616	W
10	620	1	622	1		
11	755	2	754	1		
12	955	26	966	34	965	W
13	1038	20	1035	67	1024	W
14	1110	174	1116	147	1115	S
15	1211	293	1119	209	1163	S
16	1270	287	1194	245	1227	S
17	1352	85	1311	35	1331	W
18	1399	2	1396	21		
19	1444	23	1470	25	1432	W
20	1446	10	1472	10		
21	1855	162	1833	152	1782	M
22	2888	1	3040	0	2871	W
23	2946	5	3096	1	2976	W
24	2988	6	3149	3	3029	W

^a Scaled by 0.8953 ^b cm^{-1} ^c km mol^{-1} W (weak) M (medium) S (strong)

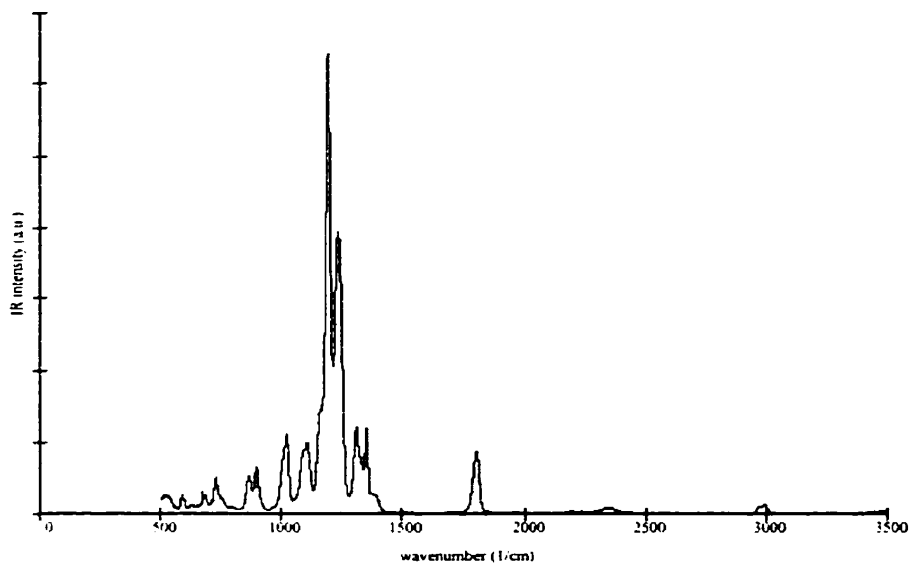


Figure 7.66 Experimental FT-IR spectrum of $\text{CF}_3\text{C}(\text{O})\text{CF}_2\text{H}$.

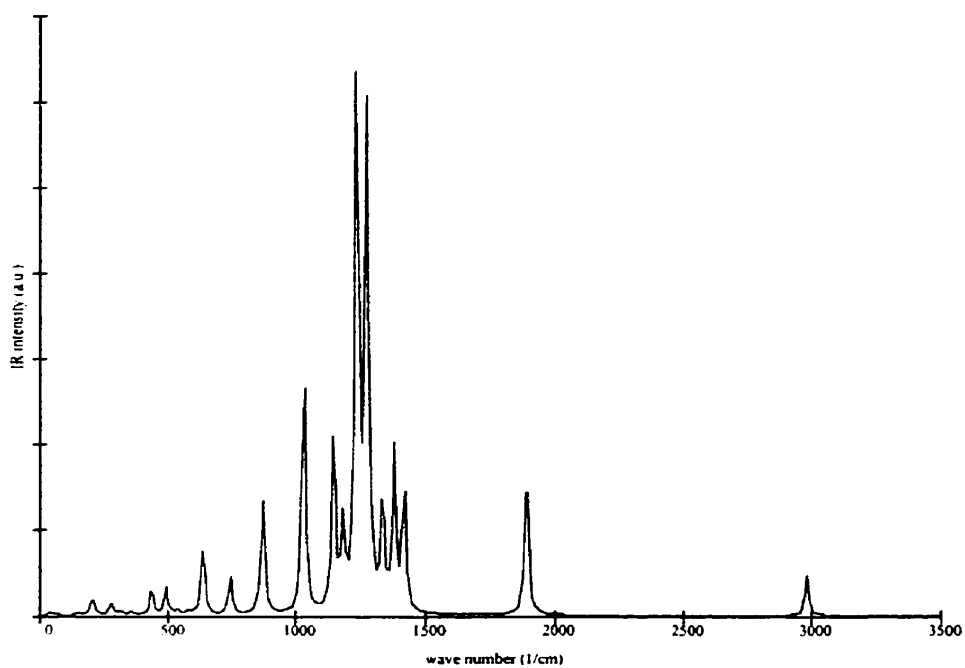


Figure 7.67 Simulated IR spectrum of $\text{CF}_3\text{C}(\text{O})\text{CF}_2\text{H}$ from HF/6-31G(d) computations.

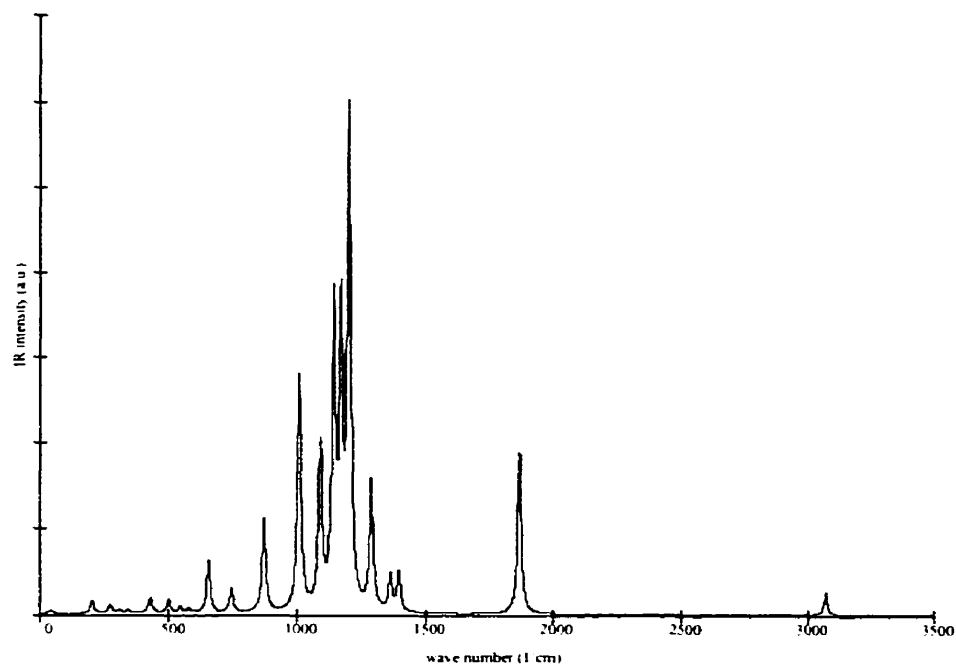


Figure 7.68 Simulated IR spectrum of $\text{CF}_3\text{C}(\text{O})\text{CF}_2\text{H}$ from B3LYP/6-311++G(3d,3p) computations.

Table 7.9 Overview of the scaled HF/6-31G(d), B3LYP/6-311++G(3d,3p), and experimental normal mode vibrational frequencies and IR intensities of CF₃C(O)CF₂H.

mode	HF/6-31G(d) ^a		B3LYP/6-311++G(3d,3p)		experiment	
	ν ^b	Int _{abs} ^c	ν ^b	Int _{abs} ^c	ν ^c	Int _{rel}
1	41	1	41	1		
2	55	1	47	1		
3	149	1	150	0		
4	205	12	206	8		
5	276	8	274	5		
6	310	2	311	2		
7	353	2	345	2		
8	434	17	428	9		
9	490	16	497	8		
10	536	3	541	4		
11	577	2	576	3		
12	633	42	651	31	727	W
13	739	22	740	14	865	W
14	867	76	866	55	895	W
15	1027	150	1002	139	1024	W
16	1143	113	1083	95	1107	W
17	1180	47	1134	175	1163	W
18	1233	348	1163	166	1193	S
19	1272	305	1195	288	1238	M
20	1334	71	1282	76	1311	W
21	1379	95	1356	21	1352	W
22	1417	77	1389	23		
23	1885	100	1866	95	1801	W
24	2978	25	3068	13	2994	W

^a Scaled by 0.8953 ^b cm⁻¹ ^c km mol⁻¹ W (weak) M (medium) S (strong)

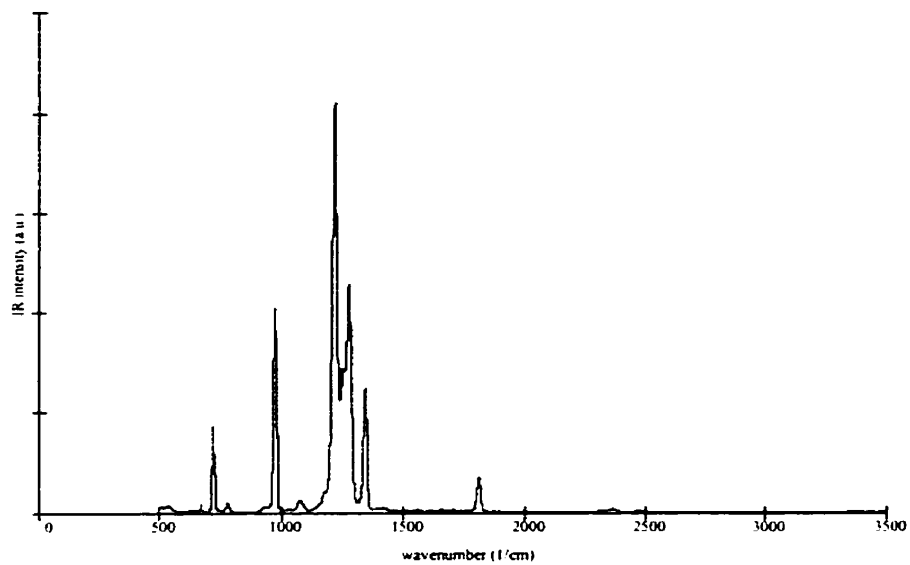


Figure 7.69 Experimental FT-IR spectrum of $\text{CF}_3\text{C}(\text{O})\text{CF}_3$.

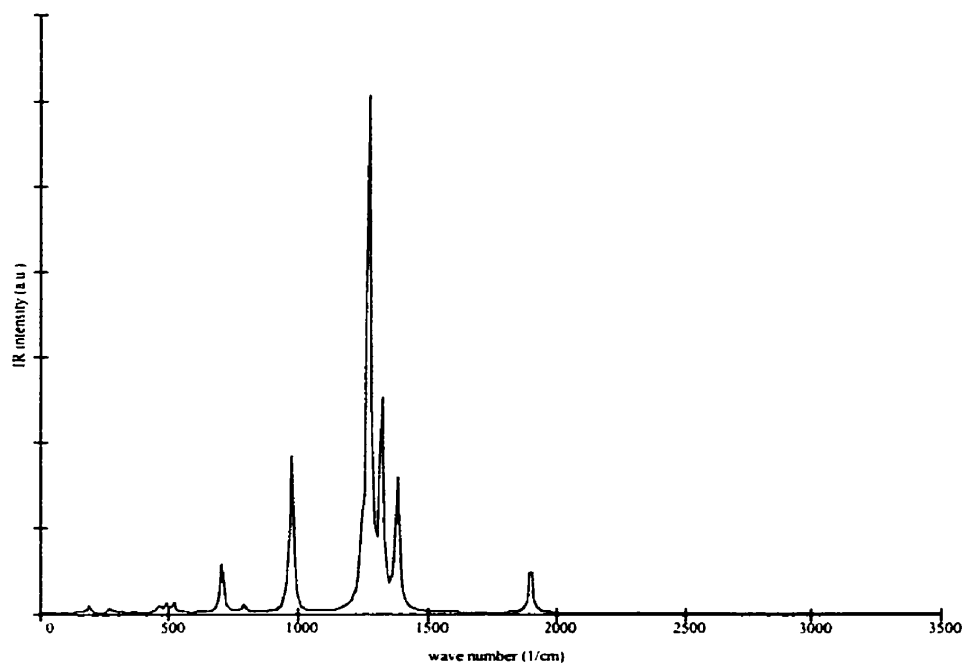


Figure 7.70 Simulated IR spectrum of $\text{CF}_3\text{C}(\text{O})\text{CF}_3$ from HF/6-31G(d) computations.

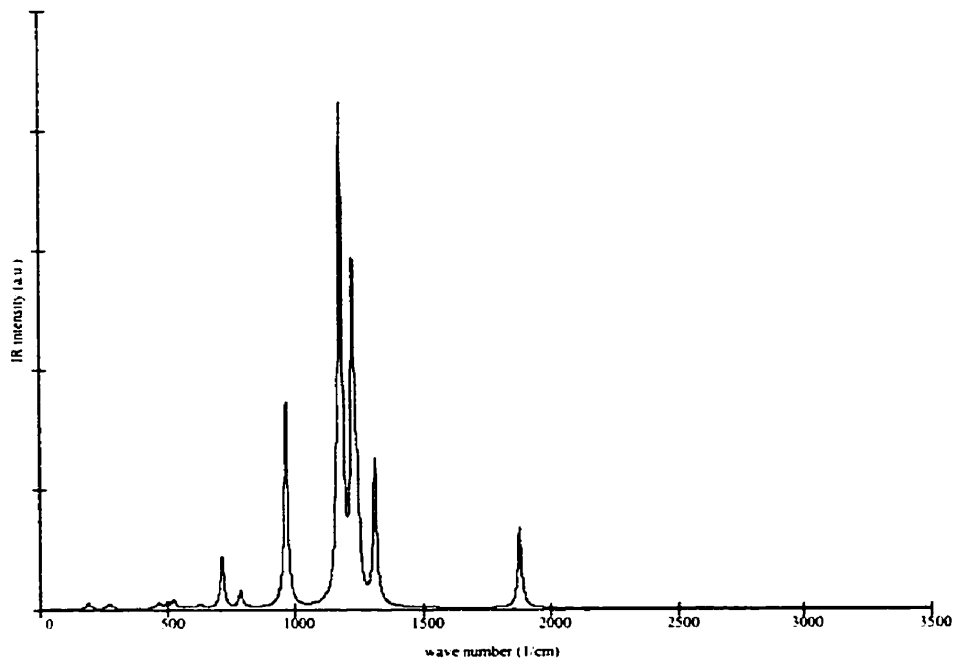


Figure 7.71 Simulated IR spectrum of $\text{CF}_3\text{C}(\text{O})\text{CF}_3$ from B3LYP/6-311++G(3d,3p) computations.

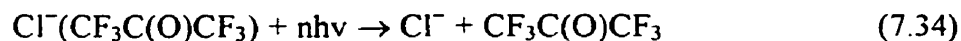
Table 7.10 Overview of the scaled HF/6-31G(d), B3LYP/6-311++G(3d,3p), and experimental normal mode vibrational frequencies and IR intensities of $\text{CF}_3\text{C}(\text{O})\text{CF}_3$.

mode	HF/6-31G(d) ^a		B3LYP/6-311++G(3d,3p)		experiment	
	ν^b	$\text{Int}_{\text{abs}}^c$	ν^b	$\text{Int}_{\text{abs}}^c$	ν^b	Int_{rel}
1	42	0	39	0		
2	45	0	43	0		
3	143	1	145	1		
4	189	11	191	6		
5	258	0	255	0		
6	274	7	271	5		
7	313	1	311	0		
8	365	1	366	0		
9	463	10	462	6		
10	491	13	496	6		
11	518	14	521	9		
12	524	0	530	0		
13	622	1	623	4		
14	702	77	709	53	717	W
15	763	2	761	0		
16	790	12	783	17	779	W
17	968	245	960	214	974	M
18	1213	2	1115	1		
19	1242	70	1160	58	1073	W
20	1265	239	1177	509	1219	S
21	1269	581	1224	333	1259	M
22	1317	335	1242	110	1274	M
23	1377	217	1310	151	1342	M
24	1895	83	1875	85	1807	W

^a Scaled by 0.8953 ^b cm^{-1} ^c km mol^{-1} W (weak) M (medium) S (strong)

priority. As long as there are no experimental absolute IR intensities of these compounds available a thorough test of the two methods will be impossible.

More interesting and not investigated experimentally is the effect of chloride ion complex formation upon the IR spectrum of the neutral. In Figure 7.72 the simulated IR spectra of $\text{CF}_3\text{C}(\text{O})\text{CF}_3$ at the B3LYP/6-311++G(3d,3p) level of theory (solid) and $\text{Cl}^-(\text{CF}_3\text{C}(\text{O})\text{CF}_3)$ at the B3LYP/[6-311++G(3df,3pd)/6-311++G(3d,3p)] level of theory (dotted) are shown. The most obvious change is the large shift in the CO stretch frequency of -215 cm^{-1} , and a large increase in the absolute IR intensity of $+239\text{ km mol}^{-1}$. Most other peaks in the $600\text{-}1400\text{ cm}^{-1}$ range show shifts to smaller wave numbers, while both increases and decreases in the absolute IR intensities take place. These features make the $\text{Cl}^-(\text{CF}_3\text{C}(\text{O})\text{CF}_3)$ an interesting systems on which to perform ZTRID experiments (Equation 7.34).



Obtaining the unimolecular dissociation constants, $k_{\text{uni}}(T)$, at different absolute temperatures and performing Master Equation modeling using the DFT data for input of the normal mode vibrational frequencies and corresponding absolute IR intensities will provide a good test for the quality of the computations. Another test would be when one day it will be possible to record FT-IR spectra of trapped ions in a FT-ICR or ion trap mass spectrometer (ITMS). Upon complex formation with chloride ion three new, intramolecular normal mode vibrations are introduced, and both red and blue shifts are observed for the other vibrations already present in the neutrals. There is no clear correlation between the shift in C–H normal mode vibrations, $\Delta\nu(\text{C-H})$, and ΔH_{298}° , as was observed for $\Delta\nu(\text{RO-H})$ in $\text{X}^-(\text{HOR})$ clusters ($\text{X} = \text{F}, \text{Cl}, \text{Br}, \text{I}$; $\text{R} = \text{CH}_3, \text{CH}_3\text{CH}_2, (\text{CH}_3)_2\text{CH}, (\text{CH}_3)_3\text{C}$).⁸⁸ At this point in time VPDS would be an excellent tool to investigate the C–H stretches in the different $\text{Cl}^-(\text{ether})$ and $\text{Cl}^-(\text{acetone})$ complexes.⁸⁹

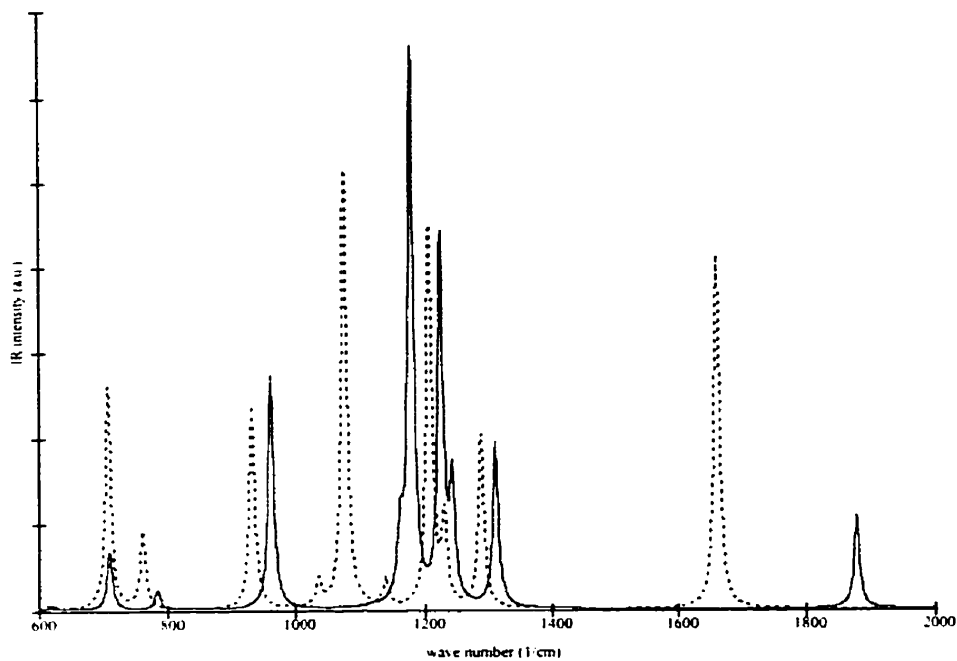


Figure 7.72 Simulated IR spectrum of CF₃C(O)CF₃ (solid line) and Cl⁻(CF₃C(O)CF₃) (dotted line) from B3LYP/[6-311++G(3df,3pd)/6-311++G(3d,3p)] computations.

7.4.7 Rotational Barriers

For CH_3OCF_3 , rotational barriers of $1.20 \text{ kcal mol}^{-1}$ (CH_3) and $3.08 \text{ kcal mol}^{-1}$ (CF_3) were calculated at the MP2/c//MP2/a levels of theory. In the $\text{Cl}^-(\text{CH}_3\text{OCF}_3)$ complex, rotational barriers of $1.02 \text{ kcal mol}^{-1}$ (CH_3) and $2.87 \text{ kcal mol}^{-1}$ (CF_3) were calculated at the MP2/[c/d]//MP2/[a/b] level of theory. Recently, Good and Francisco calculated the rotational barriers for the methyl groups in $(\text{CH}_3)_2\text{O}$, CH_3OCF_3 , $(\text{CF}_2\text{H})_2\text{O}$, and $\text{CF}_3\text{OCF}_2\text{H}$ at the B3LYP/6-311++(3df,3pd) level of theory.³⁶ Values of 2.4, 1.1, 3.6, and 2.9 kcal mol^{-1} , respectively, were obtained. Except for $(\text{CH}_3)_2\text{O}$, no experimental microwave data are available.⁹⁰ In reality, the rotations of the CH_3 , CF_3 , and CF_2H groups in the four molecules will most likely show coupling of both methyl groups present. This will give rise to complicated two-dimensional potential energy surfaces.

Very little theoretical work has been published on the influence of complex formation on barrier heights of methyl group rotations. De Turi and Ervin showed that going from ROH to $\text{F}^-(\text{HOR})$ ($\text{R} = \text{CH}_3, \text{CH}_3\text{CH}_2, (\text{CH}_3)_2\text{CH}, (\text{CH}_3)_3\text{C}$), only for $\text{R} = \text{CH}_3$ does the rotational barrier, calculated at the MP26-311+G(2df,2p)//MP2/6-31G(d) level, decrease (from $1.1 \text{ kcal mol}^{-1}$ to $0.3 \text{ kcal mol}^{-1}$).⁹¹ For the other three alcohol molecules, the rotational barriers increase by $\sim 0.9 \text{ kcal mol}^{-1}$. The main source for the decrease in the rotational barriers of the CH_3 and CF_3 groups are the increases of the C–O and C–F distances, upon complex formation with Cl^- and CH_3OCF_3 . For $\text{Cl}^-((\text{CH}_3)_2\text{O})$, no structure for the so-called staggered-eclipsed conformation was found, thus making determination of the CH_3 barrier in this complex impossible. Of course the binding in $\text{Cl}^-((\text{CH}_3)_2\text{O})$ is completely different from $\text{Cl}^-(\text{CH}_3\text{OCF}_3)$. It does not seem unreasonable to assume that the barrier for CH_3 rotation in $\text{Cl}^-((\text{CH}_3)_2\text{O})$ will be somewhat larger than in $(\text{CH}_3)_2\text{O}$. In $\text{Cl}^-((\text{CF}_2\text{H})_2\text{O})$ a large increase in the rotational barrier compared to $(\text{CF}_2\text{H})_2\text{O}$ can be observed, from $1.0 \text{ kcal mol}^{-1}$ to $7.5 \text{ kcal mol}^{-1}$, thus adding to the suggestion that the CF_2H rotations get locked in the chloride ion complex.

In $\text{CH}_3\text{C}(\text{O})\text{CH}_2\text{F}$ the rotational barrier going from rotamer 1 to 2 is $4.4 \text{ kcal mol}^{-1}$, as calculated at the MP2/c//MP2/a level of theory. Going from rotamer 2 to 1 the barrier is $2.2 \text{ kcal mol}^{-1}$. In the $\text{Cl}^-(\text{CH}_3\text{C}(\text{O})\text{CH}_2\text{F})$ complex the barriers have been changed to $0.5 \text{ kcal mol}^{-1}$ and $2.3 \text{ kcal mol}^{-1}$, as calculated at the MP2/[c/d]//MP2/[a/b] level of theory. This may indicate that upon chloride ion complex formation methyl group rotations do not necessarily become more hindered. It would be very interesting to determine the barriers for the CF_3 groups' rotations in $\text{CF}_3\text{C}(\text{O})\text{CF}_3$ and $\text{Cl}^-(\text{CF}_3\text{C}(\text{O})\text{CF}_3)$, but that would be computationally too expensive.

7.4.8 Natural Population Analysis Charges

NPA charges calculated at the MP2/c//MP2/a level of theory indicated that replacing hydrogen atoms by fluorine atoms hardly changes the NPA charges on the remaining hydrogen atom(s). In fact the NPA charge of the hydrogen atoms in $(\text{CF}_2\text{H})_2\text{O}$ and $\text{CF}_3\text{OCF}_2\text{H}$ are somewhat less positive than in $(\text{CH}_3)_2\text{O}$. For CF_3OCH_3 there is a small increase in the NPA charges on the three hydrogen atoms relative to $(\text{CH}_3)_2\text{O}$. The NPA charges in the chloride ion-(fluorinated) ether complexes were calculated at the MP2/[c/d]//MP2/[a/b] level of theory. In $\text{Cl}^-((\text{CH}_3)_2\text{O})$ no charge transfer from Cl^- to the hydrogen atoms interacting with it is observed. In fact, the hydrogen atoms interacting with Cl^- will have a smaller NPA charge, while the upward hydrogen atoms will have a substantially larger NPA charge (from $0.15e$ to $0.20e$). In the $\text{Cl}^-((\text{CF}_2\text{H})_2\text{O})$ and $\text{Cl}^-(\text{CF}_3\text{OCF}_2\text{H})$ clusters more charge transfer from Cl^- can be observed. More interesting is the fact that a fairly large increase in the NPA of the hydrogen atom(s) interacting with Cl^- is observed. The smallest increase is, as expected, for $\text{Cl}^-(\text{CH}_3\text{OCF}_3)$, followed by $\text{Cl}^-((\text{CF}_2\text{H})_2\text{O})$ (rotamers 1 and 2 more than rotamer 4), and $\text{Cl}^-(\text{CF}_3\text{OCF}_2\text{H})$. Hardly any changes in NPA charges are observed on the carbon, oxygen, and fluorine atoms upon complex formation with chloride ion.

7.4.9 Potential Energy Surfaces

In Figures 7.73 and 7.74 the MP2(fc)/[6-31+G(d)/6-31G(d)] potential energy surfaces for the formation of the $\text{Cl}^-(\text{CH}_3\text{C}(\text{O})\text{CH}_3)$ and $\text{Cl}^-(\text{CF}_3\text{C}(\text{O})\text{CF}_3)$ complexes are shown. For the reaction coordinate the $\text{Cl}^-\cdots\text{CO}$ distance was chosen. It has to be stated clearly that from the level of theory used, no reliable energetics can be determined, but the general trend will be maintained if a higher level single point energy computations would be performed.

In Sections 7.4.2 and 7.4.3 it was already shown that chloride ion binds much more strongly to hexafluoroacetone than to acetone itself. From Figure 7.73 and 7.74 it can be seen that the well for $\text{Cl}^-(\text{CF}_3\text{C}(\text{O})\text{CF}_3)$ progresses more steeply at relatively short distances and then flattens off at around 6 Å from the equilibrium $\text{Cl}^-\cdots\text{CO}$ distance. The well for the $\text{Cl}^-(\text{CH}_3\text{C}(\text{O})\text{CH}_3)$ complex progresses less steeply and flattens off around 8-10 Å from the equilibrium $\text{Cl}^-\cdots\text{CO}$ distance. Inspection of structures along the two reaction coordinates clearly indicates that the chloride ion approaches $\text{CH}_3\text{C}(\text{O})\text{CH}_3$ and $\text{CF}_3\text{C}(\text{O})\text{CF}_3$ very differently. At distances longer than 8.0 Å chloride ion interacts with acetone as if it is aligned with the C=O bond, which is also the direction of the dipole moment of acetone. As the chloride ion gets closer it deviates from the original approach and the interaction with the two hydrogen atoms, as in the equilibrium structure, becomes more important. For the hexafluoroacetone a completely different picture emerges. Even though the dipole moment of $\text{CF}_3\text{C}(\text{O})\text{CF}_3$ is still aligned along the C=O bond, chloride ion will not approach from along this bond, because of repulsion with the electronegative fluorine atoms. Instead, it will approach from the side, thereby perhaps interacting with the quadrupole moment of hexafluoroacetone. As the chloride ion gets closer to the C=O carbon atom, the CF_3 groups start rotating away to minimize the repulsion among chloride ion and the fluorine atoms. This process starts taking place around a $\text{Cl}^-\cdots\text{CO}$ distance of 4.0 Å. These two examples nicely illustrate that the whole process of complex formation can be quite complicated. By simply looking at the equilibrium structure of an ion-molecule complex, one cannot tell how these two entities formed the complex and what factors were mainly responsible. Of course the reverse trajectory will be

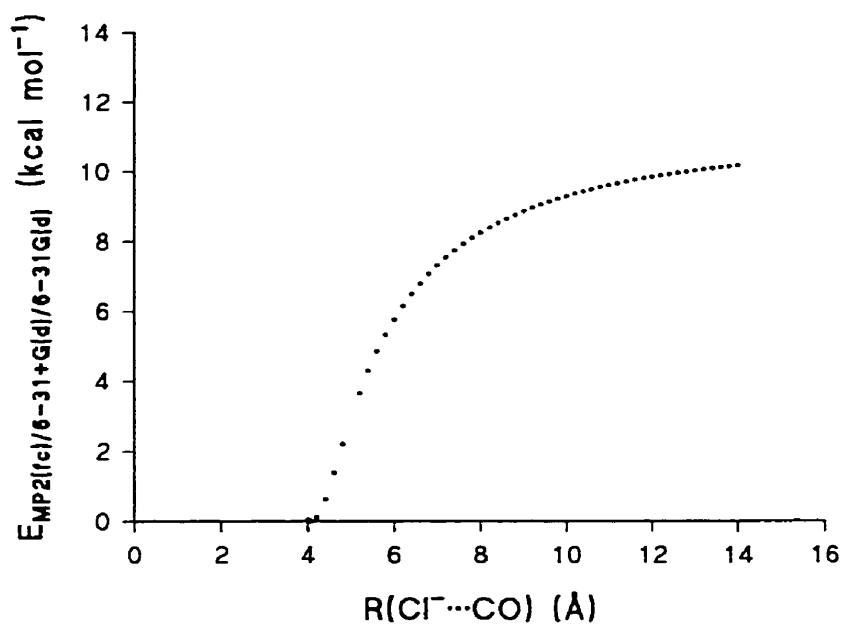


Figure 7.73 Plot of the MP2/[a/b] energy, $E_{\text{MP2}(\text{fc})/6-31+\text{G}(\text{d})/6-31\text{G}(\text{d})}$, versus the $\text{Cl}^- \cdots \text{CO}$ distance in $\text{Cl}^-(\text{CH}_3\text{C}(\text{O})\text{CH}_3)$, $\text{R}(\text{Cl}^- \cdots \text{CO})$, from a relaxed potential energy surface scan.

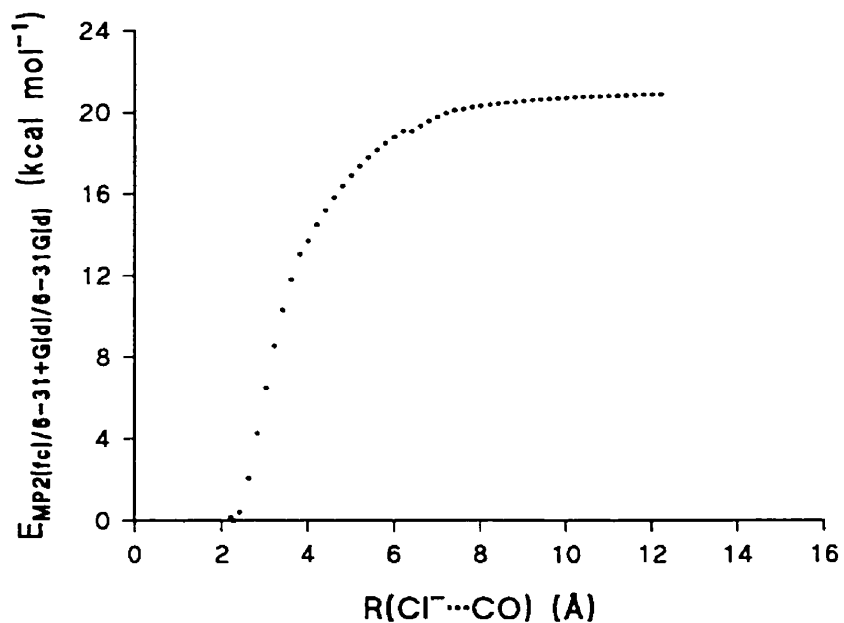


Figure 7.74 Plot of the MP2/[a/b] energy, $E_{\text{MP2}(\text{fc})/6-31+\text{G}(\text{d})/6-31\text{G}(\text{d})}$, versus the $\text{Cl}^- \cdots \text{CO}$ distance in $\text{Cl}^-(\text{CF}_3\text{C}(\text{O})\text{CF}_3)$, $\text{R}(\text{Cl}^- \cdots \text{CO})$, from a relaxed potential energy surface scan.

followed when the two chloride ion complexes dissociate under the influence of collisions or light.

7.5 Conclusions

In this chapter various aspects concerning the structures, thermochemistry, gas phase acidity, spectroscopy, and dynamics of chloride ion-(fluorinated) ether and acetone complexes and their neutrals have been investigated using PHPMS, FT-IR, and computational *ab initio* and DFT methods.

For the various neutral ethers and acetones the MP2/6-31G(d) structures agree well with other computational results in literature. For the ethers various rotamers were considered. For the acetones the MP2/6-31G(d) and B3LYP/6-311++G(3d,3p) results were nearly identical. The different chloride ion-ether and acetone complexes showed some interesting features. For the ethers various rotamers and isomers were found. The $\text{Cl}^-(\text{CH}_3\text{OCF}_3)$ resembles a $\text{S}_{\text{N}}2$ backside attack complex, and formation of CF_3O^- actually takes place in the high pressure ion source.

In the most stable structure of the $\text{Cl}^-((\text{CF}_2\text{H})_2\text{O})$ complex the chloride ion interacts with both hydrogen atoms. As for the neutral $\text{CH}_3\text{C}(\text{O})\text{CH}_2\text{F}$, the corresponding chloride ion complex also has two rotamers, but the relative stabilities have been reversed. In the $\text{Cl}^-(\text{CF}_3\text{C}(\text{O})\text{CF}_2\text{H})$ complex the chloride ion does not interact with the very acidic hydrogen atom. Instead it prefers to interact with the CO carbon atom. In the $\text{Cl}^-(\text{CF}_3\text{C}(\text{O})\text{CF}_3)$ complex the chloride ion also interacts with the CO carbon atom. The two CF_3 groups have rotated away from the chloride ion.

The fluorine atom substitution also introduces a large variety in the experimental and computational thermochemistry. In general there is good to excellent agreement between ΔH° from PHPMS and $\Delta\text{H}^\circ_{298}$ from MP2/[c/d]/MP2/[a/b] computations. For most of the systems studied the HF/[a/b] computations provide $\Delta\text{S}^\circ_{298}$ values that are in good agreement with ΔS° values from PHPMS. For the formation of the $\text{Cl}^-((\text{CF}_2\text{H})_2\text{O})$ and $\text{Cl}^-(\text{CF}_3\text{C}(\text{O})\text{CF}_3)$ complexes there are large discrepancies between ΔS° and $\Delta\text{S}^\circ_{298}$. In these two systems the CF_2H and CF_3 group rotations get hindered upon complex

formation. Attempts were made to correct for this by using the hindered rotor approximation instead of the harmonic oscillator approximation for the torsional motions. In general, there is good to excellent agreement between the ΔG°_{298} values from ICR experiments by Larson and McMahon, and ΔS°_{298} values calculated from the ΔH° and ΔS° from this work. The general trends in ΔH° can be rationalized on the trends in the polarizability.

At the G3(MP2) level of theory, a $\Delta_f H^\circ_{298}$ for CH_3OCF_3 of (-215.7 ± 0.1) kcal mol⁻¹ was determined. The G3 and G3(MP2) methods provide $\Delta_{\text{acid}} H^\circ_{298}$ values that are in excellent agreement with experimental data. For $\text{CF}_3\text{C}(\text{O})\text{CF}_2\text{H}$ a large discrepancy with the $\Delta_{\text{acid}} H^\circ$ value of Farid and McMahon, determined by ICR was found.

FT-IR spectra were recorded for $\text{CH}_3\text{C}(\text{O})\text{CH}_2\text{F}$, $\text{CH}_3\text{C}(\text{O})\text{CF}_3$, $\text{CF}_3\text{C}(\text{O})\text{CF}_2\text{H}$, and $\text{CF}_3\text{C}(\text{O})\text{CF}_3$. For the first and third ketones, no data were previously available, while spectra recorded for the second and fourth ketones were identical to literature spectra. In general, good agreement can be obtained between the experimental and computations at HF/6-31G(d) (scaled by 0.8953) and B3LYP/6-311++G(3d,3p) levels of theory. Formation of the chloride ion complex of $\text{CF}_3\text{C}(\text{O})\text{CF}_3$ causes a large shift in the C=O normal mode vibrational frequency and the IR intensity.

For a few systems it was shown by computations that the barrier height of (fluorinated) methyl group rotations will be lowered upon chloride ion complex formation.

Finally, relaxed potential energy surface scan computations at the MP2/[a/b] level of theory indicate that $\text{Cl}^-(\text{CH}_3\text{C}(\text{O})\text{CH}_3)$ is formed by initial approach of Cl^- along the C=O bond of the acetone molecules, hereby interacting with the dipole moment. The $\text{Cl}^-(\text{CF}_3\text{C}(\text{O})\text{CF}_3)$ complex conversely is being formed by approach of Cl^- from the side of the hexafluoro acetone molecule while perhaps interacting with the quadrupole moment of the neutral.

7.6 References

- 1 Koch, W.; Hase, W. L. (Eds) *Int. J. Mass Spectrom.* **2000**, *201*, 1-336.
- 2 Bouchoux, G.; Hoppilliard, Y.; Tabet, J.-C. (Eds) *Int. J. Mass Spectrom.* **2000**, *199*, 1-286.
- 3 Bowers, M. T.; Graul, S.; Kenttämä, H. I. (Eds) *Int. J. Mass Spectrom.* **2000**, *195-196*, 1-698.
- 4 Schwarz, H. (Ed) *Int. J. Mass Spectrom.* **1999**, *185/186/187*, 1-1002.
- 5 Takashima, K.; Riveros, J. M. *Mass Spectrom. Rev.* **1998**, *17*, 409.
- 6 Blair, S. M.; Brodbelt, J. S.; Marchand, A. P.; Kumar, K. A.; Chong, H.-S. *Anal. Chem.* **2000**, *72*, 2433 and references cited therein.
- 7 More, M.; Ray, D.; Armentrout, P. D. *J. Am. Chem. Soc.* **1999**, *121*, 417 and references cited therein.
- 8 Barlow, S. E.; Tinkle, M. D. *Rapid Comm. Mass Spectrom.* **1999**, *13*, 390 and references cited therein.
- 9 Mele, A.; Pezzetta, D.; Selvaa, A. *Int. J. Mass Spectrom.* **1999**, *193*, L1-L6.
- 10 Reiche, K. B.; Starke, I.; Kleinpeter, E.; Holdt, H.-J. *Rapid Comm. Mass Spectrom.* **1998**, *12*, 1021 and references cited therein.
- 11 Dearden, D. V.; Chu, I.-H. *J. Incls. Phenom. Mol. Recog. Chem.* **1997**, *29*, 269 and references cited therein.
- 12 Hill, S. E.; Feller, D. *Int. J. Mass Spectrom.* **2000**, *201*, 41 and references cited therein.
- 13 Cattani, A.; Schmidtchen, F. P. *J. Prakt. Chem. Chem. Zeit.* **1999**, *341*, 291.
- 14 Antonisse, M. M. G.; Snellink-Ruël, B. M. H.; Yigit, I.; Engbersen, J. F. J.; Reinhoudt, D. N. *J. Org. Chem.* **1997**, *62*, 9034.
- 15 Tamao, K.; Hayashi, T.; Ito, Y. *J. Organomet. Chem.* **1996**, *506*, 85.
- 16 Scheerder, J.; Engbersen, J. F. J.; Casnati, A.; Ungaro, R.; Reinhoudt, D. N. *J. Org. Chem.* **1995**, *60*, 6448.
- 17 Savage, P. B.; Holingren, S. K.; Gellman, S. H. *J. Am. Chem. Soc.* **1994**, *116*, 4069.
- 18 Scheerder, J.; Fochi, M.; Engbersen, J. F. J.; Reinhoudt, D. N. *J. Org. Chem.* **1994**, *59*, 7815.

- 19 Kaufman, D. E.; Otten, A. *Angew. Chem.* **1994**, *33*, 1832.
- 20 Hawthorne, M. F.; Yang, X.; Zheng, Z. *Pure Appl. Chem.* **1994**, *66*, 245.
- 21 Farnham, W. B.; Roe, D. C.; Dixon, D. A.; Calabrese, J. C.; Harlow, R. L. *J. Am. Chem. Soc.* **1990**, *112*, 7707.
- 22 Jung, M. E.; Xia, H. *Tetrahedron Lett.* **1988**, *29*, 297.
- 23 Schmidtchen, F. P.; Berger, M. *Chem. Rev.* **1997**, *97*, 1609.
- 24 Scheerder, J.; Engbersen, J. F. J.; Reinhoudt, D. N. *Recl. Trav. Chim. Pays-Bas* **1996**, *115*, 307.
- 25 Brodbelt, J. S.; Maleknia, S.; Liou, C.-C.; Lagow, R. *J. Am. Chem. Soc.* **1991**, *113*, 5913.
- 26 Brodbelt, J. S.; Maleknia, S.; Lagow, R. Lin, T. Y. *J. Chem. Soc. Chem. Commun.* **1991**, 1705.
- 27 Larson, J. W.; McMahon, T. B. *J. Phys. Chem.* **1984**, *88*, 1083.
- 28 Zhang, W.; Beglinger, Ch.; Stone, J. A. *J. Phys. Chem.* **1995**, *99*, 11673.
- 29 Norrman, K.; McMahon, T. B. *J. Am. Chem. Soc.* **1997**, *118*, 2449.
- 30 Norrman, K.; McMahon, T. B. *J. Phys. Chem A* **1999**, *103*, 7008.
- 31 Good, D. A.; Kamboures, M.; Santiano, R.; Francisco, J. S. *J. Phys. Chem. A* **1999**, *103*, 9230.
- 32 Good, D. A.; Li, Y.; Francisco, J. S. *Chem. Phys. Lett.* **1999**, *313*, 267.
- 33 Good, D. A.; Francisco, J. S. *J. Phys. Chem. A* **1999**, *103*, 5011.
- 34 Christensen, L. K.; Wallington, T. J.; Guschin, A.; Hurley, M. D. *J. Phys. Chem. A* **1999**, *103*, 4202.
- 35 Good, D. A.; Francisco, J. S. *J. Phys. Chem. A* **1998**, *102*, 7143.
- 36 Good, D. A.; Francisco, J. S. *J. Phys. Chem. A* **1998**, *102*, 1854.
- 37 Orgel, V. B.; Ball, D. W.; Zehe, M. J. *J. Mol. Struct. (Theochem)* **1997**, *417*, 195.
- 38 Buono, R. A.; Zauhar, R. J.; Venanzi, C. A. *J. Mol. Struct. (Theochem)* **1996**, *370*, 97.
- 39 Hsu, K.-J.; DeMore, W. B. *J. Phys. Chem.* **1995**, *99*, 11141.
- 40 Suga, A.; Mochizuki, Y.; Nagasaki, N.; Gotoh, Y.; Ito, H.; Yamashita, S. Uchimaru, T.; Sugie, M.; Sekiya, A.; Kondo, S.; Aoyagi, M. *Chem. Lett.* **1994**, 2365.
- 41 Zhang, Z.; Saini, R. D.; Kurylo, M. J.; Huie, R. E. *J. Phys. Chem.* **1992**, *96*, 9301.

- 42 <http://webbook.nist.gov/chemistry/>
- 43 Szulejko, J. E.; Fisher, J. J.; McMahon, T. B.; Wronka, J. *Int. J. Mass Spectrom. Ion Processes* **1988**, *83*, 147.
- 44 Frisch, M. J.; Trucks, G. W.; Schlegel, H. B.; Scuseria, G. E.; Robb, M. A.; Cheeseman, J. R.; Zakrzewski, V. G.; Montgomery, Jr., J. A.; Stratmann, R. E.; Burant, J. C.; Dapprich, S.; Millam, J. M.; Daniels, A. D.; Kudin, K. N.; Strain, M. C.; Farkas, O.; Tomasi, J.; Barone, V.; Cossi, M.; Cammi, R.; Mennucci, B.; Pomelli, C.; Adamo, C.; Clifford, S.; Ochterski, J.; Petersson, G. A.; Ayala, P. Y.; Cui, Q.; Morokuma, K.; Malick, D. K.; Rabuck, A. D.; Raghavachari, K.; Foresman, J. B.; Cioslowski, J.; Ortiz, J. V.; Baboul, A. G.; Stefanov, B. B.; Liu, G.; Liashenko, A.; Piskorz, P.; Komaromi, I.; Gomperts, R.; Martin, R. L.; Fox, D. J.; Keith, T.; Al-Laham, M. A.; Peng, C. Y.; Nanayakkara, A.; Gonzalez, C.; Challacombe, M.; Gill, M. W.; Johnson, B.; Chen, W.; Wong, M. W.; Andres, J. L.; Gonzalez, C.; Head-Gordon, M.; Replogle, E. S.; Pople, J. A. *Gaussian 98*, Revision A.7 Gaussian, Inc., Pittsburgh PA, 1998.
- 45 Roothan, C. C. *J. Rev. Mod. Phys.* **1951**, *23*, 69.
- 46 Møller, C.; Plesset, M. S. *Phys. Rev.* **1934**, *46*, 618.
- 47 Hariharan, P. C.; Pople, J. A. *Theoretica Chim. Acta* **1973**, *28*, 213.
- 48 Francl, M. M.; Petro, W. J.; Hehre, W. J.; Binkley, J. S.; Gordon, M. S.; DeFrees, D. J.; Pople, J. A. *J. Chem. Phys.* **1982**, *77*, 3654.
- 49 Clark, T.; Chandrasekhar, J.; von R. Schleyer, P. *J. Comp. Chem.* **1983**, *4*, 294.
- 50 Krishnam, R.; Binkley, J. S.; Seeger, R.; Pople, J. A. *J. Chem. Phys.* **1980**, *72*, 650.
- 51 Gill, P. M. W.; Johnson, B. G.; Pople, J. A.; Frisch, M. J. *Chem. Phys. Lett.* **1992**, *197*, 499
- 52 Scott, A. P.; Radom, L. *J. Phys. Chem.* **1996**, *100*, 16502.
- 53 Reed, A. E.; Weinstock, R. B.; Weinhold, F. *J. Chem. Phys.* **1985**, *83*, 735.
- 54 Krishnan, R.; Binkley, J. S.; Seeger, R.; Pople, J. A. *J. Chem. Phys.* **1980**, *72*, 650
- 55 Frisch, M. J.; Pople, J. A.; Binkley, J. S. *J. Chem. Phys.* **1984**, *80* 3265.
- 56 East, A. L. L.; Radom, L. *J. Chem. Phys.* **1997**, *106*, 6655.
- 57 Ayala, P. Y.; Schlegel, H. B. *J. Chem. Phys.* **1998**, *108*, 2314 and references cited therein.

- 58 Trainham, R.; Fletcher, G.D.; Larson, D.J. *J. Phys. B*, **1987**, *20*, L777.
- 59 Lee, C.; Yang, W.; Parr, R. G. *Phys. Rev. B*. **1988**, *37*, 785.
- 60 Becke, A. D. *J. Chem. Phys.* **1993**, *98*, 1372.
- 61 Becke, A. D. *J. Chem. Phys.* **1993**, *98*, 5648.
- 62 *Gaussian 98* User's Reference, Second Edition, Gaussian Inc., **1999**.
- 63 Curtiss, L. A.; Raghavachari, K.; Redfern, P. C.; Rasolov, V.; Pople, J. A. *J. Chem. Phys.* **1998**, *109*, 7764.
- 64 Choi, S. C.; Boyd, R. J. *Can. J. Chem.* **1985**, *63*, 836.
- 65 Choi, S. C.; Boyd, R. J. *Can. J. Chem.* **1986**, *64*, 2042.
- 66 *CRC Handbook of Chemistry and Physics*, Ref. Data, 76th ed., Lide, D. L. (Ed), CRC, Boca Raton, FL, **1995**.
- 67 Smith, G. D.; Jaffe, R. L.; Partridge, H. *J. Phys. Chem. A* **1997**, *101*, 1705.
- 68 Glukhovtsev, M. N.; Pross, A.; Radom, L. *J. Am. Chem. Soc.* **1995**, *117*, 2024 and references cited therein.
- 69 Morris, R. A.; Miller, T. M.; Paulson, J. F.; Viggiano, A. A.; Feldmann, M. T.; King, R. A.; Schaefer III, H. F. *J. Chem. Phys.* **1999**, *110*, 8436.
- 70 Gamble, T. N. *M.Sc. Thesis*, University of Waterloo, **2000**.
- 71 Li, C.; Ross, P.; Szulejko, J. E.; McMahon, T. B. *J. Am. Chem. Soc.* **1996**, *118*, 9360.
- 72 Wang, H.; Peslherbe, G. H.; Hase, W. L. *J. Am. Chem. Soc.* **1994**, *116*, 9644.
- 73 Bogdanov, B.; Peschke, M.; Tonner, D. S.; Szulejko, J. E.; McMahon, T. B. *Int. J. Mass Spectrom.* **1999**, *185/186/187*, 707.
- 74 Szulejko, J. E. *Unpublished results*, University of Waterloo, **1995**.
- 75 French, M. A.; Ikuta, S.; Kebarle, P. *Can. J. Chem.* **1982**, *60*, 1907.
- 76 Hoyau, S.; Norrman, K.; Ohanessian, G.; McMahon, T. B. *J. Am. Chem. Soc.* **1999**, *121*, 8864.
- 77 Bogdanov, B. *Unpublished results*, University of Waterloo, **2000**.
- 78 Huey, L.G.; Dunlea, E.J.; Howard, C.J. *J. Phys. Chem.*, **1996**, *100*, 6504 and references cited therein.
- 79 Farid, R.; McMahon, T. B. *Can. J. Chem.* **1980**, *58*, 2307.
- 80 Larson, J. W.; McMahon, T. B. *J. Am. Chem. Soc.* **1983**, *105*, 2944.

- 81 DeTuri, V. F.; Su, M. A.; Ervin, K. M. *J. Phys. Chem. A* **1999**, *103*, 1468.
- 82 Dunbar, R. C.; McMahon, T. B.; Thöllman, D.; Tonner, D. S.; Salahub, D. R.; Wei, D. *J. Am. Chem. Soc.* **1995**, *117*, 12819.
- 83 de Oliveira, A. E.; Haiduke, R. L. A.; Bruns, R. E. *Spectrochimica Acta Part A* **2000**, *56*, 1329.
- 84 Ballard, J.; Knight, R. J.; Newnham, D. A. *J. Quant. Spectrosc. Radiat. Transfer* **2000**, *66*, 199.
- 85 Heathfield, A. E.; Anastasi, C.; Ballard, J.; Newnham, D. A.; McCulloch, A. J. *Quant. Spectrosc. Radiat. Transfer* **1998**, *59*, 91.
- 86 McKean, D. C.; Kindness, A.; Wilkie, N.; Murphy, W. F. *Spectrochimica Acta Part A* **1996**, *52*, 445.
- 87 Papasavva, S.; Illinger, K. H.; Kenny, J. F. *J. Phys. Chem.* **1996**, *100*, 10100.
- 88 Bogdanov, B.; McMahon, T. B. *J. Phys. Chem. A* **2000**, *104*, 7871.
- 89 Kelley, J. A.; Weber, J. M.; Lisle, K. M.; Robertson, W. H.; Ayotte, P.; Johnson, M. *A. Chem. Phys. Lett.* **2000**, *327*, 1.
- 90 Fately, W. G.; Miller, F. A. *Spectrochimica Acta* **1962**, *18*, 977.
- 91 DeTuri, V. F.; Ervin, K. M. *J. Phys. Chem. A* **1999**, *103*, 6911.

Chapter 8

Conclusions

In Chapter 4 the thermochemistry and structures of halide ion-alcohol complexes, $X^-(ROH)_n$, were studied. The main conclusions are that the $HF_2^-(HOCH_3)_n$ clusters for $n = 1$ can be described as $(FH)F^-(HOCH_3)$, and for $n = 2$ as $(CH_3OH)HF_2^-(HOCH_3)$. For the various $X^-(ROH)_n + ROH = X^-(ROH)_{n+1}$ clustering equilibria measured, good agreement was obtained for the ΔH° values with existing data, and the new data followed expected trends. Results from computations at the MP2(full)/6-311++G(d,p) and MP2(full)/6-311++G(d,p)/B3LYP/6-311+G(d,p) levels of theory provided ΔH°_{298} and ΔS°_{298} values that agree very well with most PHPMS results. Pressure and temperature dependent kinetics measurements for the formation of the $Cl^-(CH_3OH)$ indicate that a more complex potential energy surface than initially expected is involved. Scaled MP2(full)/6-311++G(d,p) and B3LYP/6-311+G(d,p) normal mode vibrational frequencies agree well with available IR and VPDS results for neutral alcohol and halide ion-methanol complexes, respectively.

In Chapter 5 the thermochemistry and structures of solvated S_N2 complexes, $(S)X^-(RY)$, and transition states, $[(S)XRY]^-$, were studied. It was found that the structures of $(S)X^-(CH_3Y)$ and $[(S)XCH_3Y]^-$ can be very different from the halide ion-solvent, $X^-(S)$, and S_N2 complexes, $X^-(CH_3Y)$, depending on the solvent. The experimental PHPMS thermochemistry shows solvent effects, and the solvation of a S_N2 complexes and a solvated S_N2 reaction have different ΔH° and ΔS° values. The MP2(fc)/6-311+G(3df,2p)//MP2(fc)/6-31+G(d,p) computations provide good ΔH°_{298} values compared to available experimental data for the formation of $Cl^-(S)$ and $(S)Cl^-(CH_3Cl)$ complexes, but the ΔH^\ddagger_{298} values for the $[(S)ClCH_3Cl]^-$ transition states seem to be overestimated. Linear correlations for the ΔH°_{298} values for the formation of $Cl^-(S)$ ($S = H_2O, H_2S, NH_3, PH_3, SO_2$), and ΔH°_{298} and ΔH^\ddagger_{298} for the formation of

(S)Cl⁻(CH₃Cl) and [(S)ClCH₃Cl]⁻ have been found, except for ΔH[#]₂₉₈ with S = SO₂. Finally the potential energy profile for the solvated S_N2 reaction between Cl⁻(H₂O) and CH₃Br has been calculated at the MP2(fc)/[6-31+G(d)/LanL2DZ(sp)] level of theory. Formation of Br⁻ and Br⁻(H₂O) proceeds through two different profiles. Isomerization from Br⁻(CH₃Cl)(H₂O) to (H₂O)Br⁻(CH₃Cl) is energetically favorable, and can be accomplished by rotation of the Br⁻(CH₃Cl) part.

In Chapter 6 the reactions between halide ions and trifluoromethyl halides were studied. For the formation of the Cl⁻(BrCF₃), Cl⁻(ICF₃), and Br⁻(BrCF₃) complexes the thermochemistry was determined by PHPMS. Good agreement with ΔH^o₂₉₈ and ΔS^o₂₉₈ values calculated at the B3LYP/6-311+G(3df)/B3LYP/6-311+G(d) and the B3LYP/6-311+G(d) levels of theory, respectively, was obtained. For the halide ion-trifluoromethyl halide complexes, two isomers have been found, X⁻(YCF₃) and X⁻(CF₃Y). These correspond to front- and backside S_N2 mechanism complexes, respectively. Associated with these two different mechanisms are two transition states, [CF₃XY]⁻ and [XCF₃Y]⁻. The S_N2 reaction between halide ions and trifluoromethyl halides proceeds through a backside attack transition state. The Cl⁻ + CF₃Br → Br⁻ + CF₃Cl reaction was shown to follow the Marcus theory, indicating that at high kinetic energies of X⁻ the backside S_N2 reaction may still be initiated by electron transfer. In addition, it appears to be a direct mechanism. The frontside S_N2 transition state closely resembles a [CF₃[•]XY^{•-}] complex. At threshold, the backside attack S_N2 reaction between kinetically excited Cl⁻ and CF₃Cl proceeds through the [ClCF₃Cl]⁻ transition state. Above the threshold, a co-linear approach is no longer necessary to initiate the reaction, and barrier crossing can occur at a wider range of Cl-C-Cl angles, thereby increasing the cross section.

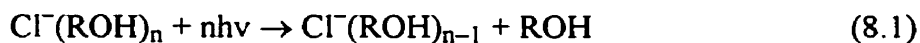
In Chapter 7 the structures, thermochemistry, gas phase acidity, and IR spectroscopy of chloride ion-(fluorinated) ether and acetone complexes and the corresponding neutrals have been studied. The Cl⁻(CH₃OCF₃) complex resembles a S_N2 complex, and formation of CF₃O⁻ was observed in the PHPMS source. In the most stable Cl⁻(CF₂H)₂O complex the chloride ion interacts with both hydrogen atoms, thereby hindering the CF₂H group rotations. In the Cl⁻(CF₃C(O)CF₂H) complex, the chloride ion does not interact with the

very acidic hydrogen atom. Instead it interacts with the carbonyl group carbon atom. In the $\text{Cl}^-(\text{CF}_3\text{C}(\text{O})\text{CF}_3)$ complex a similar kind of binding is observed, and the two CF_3 groups have rotated away from the chloride ion. The agreement between the ΔH° and ΔS° values from PHPMS, and the ΔH_{298}° values from MP2(fc)/[6-311++G(3df,3pd)/6-311+G(2df,p)]//MP2(fc)/[6-31+G(d)/6-31G(d)] computations and the ΔH_{298}° values from HF/[6-31+G(d)/6-31G(d)] computations, respectively, is very close except for systems with hindered methyl group rotations. Attempts to correct for this did not improve them to any useful extent. New FT-IR spectra for $\text{CH}_3\text{C}(\text{O})\text{CH}_2\text{F}$ and $\text{CF}_3\text{C}(\text{O})\text{CF}_2\text{H}$ were recorded, and literature spectra for $\text{CF}_3\text{C}(\text{O})\text{CH}_3$ and $\text{CF}_3\text{C}(\text{O})\text{CF}_3$ could be reproduced. Good agreement between the experiments and scaled HF/6-31G(d) and unscaled B3LYP/6-311++G(3d,3p) computations was obtained.

The PHPMS experiments performed for this thesis have provided new and additional insights into the structures of a variety of negative gas phase cluster ions, and in combination with computational quantum chemistry methods characteristics of various potential energy surfaces have been elucidated.

After summarizing what has been learned from the research performed for this thesis, it seems more than appropriate to provide some outlook on what kind of future research may be possible. I would have loved to perform these experiments myself, but that would have added at least another 200 pages to this thesis. In addition, I would have been a graduate student for another one to two years.

The study of the kinetics of the unimolecular dissociation by ZTRID of chloride ion-alcohol complexes in a FT-ICR (Reaction 8.1) will be a good test case to further investigate the influence of the number of IR absorbing vibrations on the rate of dissociation for a series of systems with fairly identical binding energies.



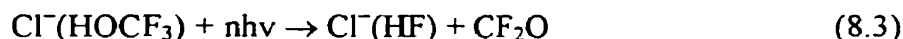
Modeling the kinetics by a program like VARIFLEX will require input parameters like normal mode vibrational frequencies, IR intensities, and so on from computations like

performed in Chapter 4. The same input parameters will be required to model the internal energy distributions of the chloride ion-alcohol complexes.

It would be very interesting if VPDS spectra of the various halide ion-alcohol complexes will be measured in the future, not only to test the computations published in this thesis, but also to get more insights into the anharmonic character, and the coupling of various vibrations.

Measuring the standard enthalpy (ΔH°) and entropy (ΔS°) changes for the clustering of the HF_2^- ion onto H_2O and CH_3OH will test the G3(MP2) computations in Chapter 4. It seems that drift cell experiments, as can be performed by Bowers and co-workers, are more appropriate than PHPMS experiments, mainly due to the small intensities of the HF_2^- ions in the high pressure ion source using a NF_3/CH_4 mixture.

The ion-molecule reaction between chloride ion and $\text{CF}_3\text{OC}(\text{O})\text{H}$ (Reaction 8.2), and the subsequent unimolecular dissociation of the $\text{Cl}^-(\text{HO}\text{CF}_3)$ cluster ion (Reaction 8.3) seem worthwhile to perform, even though they will most likely not provide new insights into existing knowledge on ion-molecule reactions or unimolecular dissociation (just for the fun of them).



Performing solvated $\text{S}_{\text{N}}2$ reactions in a FT-ICR between solvated chloride ions and bromoacetonitrile (Reaction 8.4), in combination with MP2 and B3LYP level of theory computations, will provide additional insights into the influence of solvation and the type of solvent on the kinetics and thermochemistry of gas phase and condensed phase reactions.



In addition, these reactions would provide a real opportunity to test various computations.

It would please me if, in the near future, Professor Kent Ervin and his co-workers will use their guided ion beam instrument to study the S_N2 reactions between halide ions and trifluoromethyl halide molecules (Reaction 8.5).



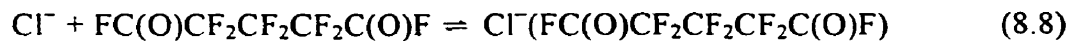
Not only will these experiments provide data to test the computations performed for Chapter 6, but I believe that these systems have the potential to show some unexpected chemistry. From a fundamental point of view, they are important enough to be investigated in more detail, and I know they will be sooner than later.

The research described in Chapter 7 has also provided ideas for future research. First of all it would be interesting to perform ZTRID experiments on the following cluster ions: Cl⁻(CF₂HO CF₂H), Cl⁻(CH₃C(O)CH₃), Cl⁻(CH₃C(O)CF₃), and Cl⁻(CF₃C(O)CF₃). Especially the first and fourth clusters have very strong bonding between chloride ion and the neutral. The C–F vibrations strongly absorb IR radiation, and consequently relatively fast unimolecular dissociation may be expected. The second and third cluster ions have identical binding enthalpies, but the presence of the three C–F bond may have the third one dissociate faster. Preliminary calculations where the blackbody radiation distribution at room temperature was deconvoluted with the calculated B3LYP level of theory IR spectra of the Cl⁻(CH₃C(O)CH₃) and Cl⁻(CH₃C(O)CF₃) cluster ions showed that the second one will absorb approximately four times more photons, and consequently a faster unimolecular dissociation rate will be expected.

Experimental determination of the central barrier height for the S_N2 reaction between chloride ion and CH₃OCF₃ (Reaction 8.6) by ion kinetic energy resolved experiments in for instance a guided ion beam instrument will test the accuracy of the G3(MP2) result for the new S_N2 reaction.



Finally, it would be interesting to measure the thermochemistry of the clustering of chloride ion onto FC(O)CF₂CF₂CF₃ and FC(O)CF₂CF₂CF₂C(O)F (Reaction 8.7 and 8.8).



High level *ab initio* computations, like used in Chapter 7, have shown that that the cyclic, bidentate isomer of the $\text{Cl}^-(\text{FC(O)CF}_2\text{CF}_2\text{CF}_2\text{C(O)F})$ cluster ion is approximately $7.5 \text{ kcal mol}^{-1}$ more stable than the isomer in which chloride ion interacts with only one carbonyl group carbon atom. The differences in the ΔH° and ΔS° values, obtained by PHPMS, for Reactions 8.7 and 8.8 will provide the ΔH° and ΔS° values to form the cyclic isomer.

These are all the ideas I could think of, but I have no doubt that a more experienced eye will see much more than mine in all of this.

Appendix A

Electronic energies

Table A1 Overview of the results from B3LYP/6-311+G(d,p), MP2(full)/6-311++G(d,p)//B3LYP/6-311+G(d,p), and B3LYP/6-311++G(3df,3pd)//B3LYP/6-311+G(d,p) computations for the halide ions and alcohols (**d** = LanL2DZ, **e** = CRENBL ECP, **f** = Stuttgart RLC ECP).

structure	E(B3LYP) ^a	ZPE + $\Delta C_p(298) + RT$ ^a	S ₂₉₈ ⁰ ^b	E(MP2//B3LYP) ^a	E(B3LYP//B3LYP) ^a
F ⁻	-99.888693	0.002360	34.768	-99.697594	-99.888693
Cl ⁻	-460.303727	0.002360	36.586	-459.752769	-460.303708
Br ⁻	-2574.237796	0.002360	39.013	-2572.962975	-2574.237618
I ⁻ (d)	-11.472110	0.002360	40.428	-11.247856	-11.472110
I ⁻ (e)	-111.540456	0.002360	40.428		
I ⁻ (f)	-11.521080	0.002360	40.428	-11.284480	-11.521080
CH ₃ OH	-115.764943	0.055336	57.005	-115.482991	-115.774315
CH ₃ CH ₂ OH	-155.095063	0.084857	64.681	-154.702352	-155.106871
(CH ₃) ₂ CHOH	-194.424250	0.113894	71.242	-193.922969	-194.438780
(CH ₃) ₃ COH	-233.752389	0.142542	77.481	-233.145339	-233.769570

^a hartree

^b cal mol⁻¹ K⁻¹

Table A2 Overview of the results from B3LYP/6-311+G(d,p), MP2(full)/6-311++G(d,p)//B3LYP/6-311+G(d,p), and B3LYP/6-311++G(3df,3pd)//B3LYP/6-311+G(d,p) computations for the halide ion-alcohol complexes (**d** = LanL2DZ, **e** = CRENL ECP, **f** = Stuttgart RLC ECP).

structure	E(B3LYP) ^a	ZPE + $\Delta C_p(298) + RT$ ^a	S^0_{298} ^b	E(MP2//B3LYP) ^a	E(B3LYP//B3LYP) ^a
F ⁻ (CH ₃ OH)	-215.702020	0.055764	69.144	-215.227991	-215.713088
F ⁻ (CH ₃ CH ₂ OH)	-255.033061	0.084926	77.250	-254.448728	-255.046777
F ⁻ ((CH ₃) ₂ CHOH)	-294.363096	0.114575	81.406	-293.671804	-294.379514
F ⁻ ((CH ₃) ₃ COH)	-333.692743	0.143345	86.706	-322.895757	-333.711618
Cl ⁻ (CH ₃ OH)	-576.092547	0.057794	74.394	-575.262571	-576.102522
Cl ⁻ (CH ₃ CH ₂ OH)	-615.422599	0.087243	81.725	-614.482494	-615.435246
Cl ⁻ ((CH ₃) ₂ CHOH)	-654.751747	0.116445	84.662	-653.705668	-654.767053
Cl ⁻ ((CH ₃) ₃ COH)	-694.080672	0.145102	90.365	-692.929321	-694.098563
Br ⁻ (CH ₃ OH)	-2690.022970	0.057909	76.568	-2688.469163	-2690.031979
Br ⁻ (CH ₃ CH ₂ OH)	-2729.352918	0.087351	83.755	-2727.688925	-2729.364492
I ⁻ (CH ₃ OH) (d)	-127.260198	0.057926	79.786		-127.270910
I ⁻ (CH ₃ OH) (e)	-227.331016	0.056959	74.153		-227.342767
I ⁻ (CH ₃ OH) (f)	-127.305385	0.058025	79.177		-127.314609

^a hartree

^b cal mol⁻¹ K⁻¹

Table A3 Overview of the results from B3LYP/6-311+G(d,p) and MP2(full)/6-311++G(d,p)//B3LYP/6-311+G(d,p) computations for the alcohol dimers and halide ion-alcohol dimers.

structure	E(B3LYP) ^a	ZPE + $\Delta C_p(298) + RT$ ^a	S ₂₉₈ ^o ^b	E(MP2//B3LYP) ^a
(CH ₃ OH) ₂	-231.539163	0.109648	91.445	-230.976788
((CH ₃) ₂ CHOH) ₂	-388.857063	0.222923	116.855	-387.858091
(CH ₃ OH)F ⁻ (CH ₃ OH)	-331.501818	0.110604	103.390	-330.745451
F ⁻ (CH ₃ OH) ₂	-331.494487	0.108644	97.233	-330.741110
((CH ₃) ₂ CHOH)F ⁻ ((CH ₃) ₂ CHOH)	-488.821762	0.224210	129.176	-487.630775
F ⁻ ((CH ₃) ₂ CHOH) ₂	-488.813993	0.222045	122.976	-487.627129
(CH ₃ OH)Cl ⁻ (CH ₃ OH)	-691.878268	0.111450	110.150	-690.770084
Cl ⁻ (CH ₃ OH) ₂	-691.877775	0.111765	102.595	-690.769522

^a hartree

^b cal mol⁻¹ K⁻¹

Table A4 Overview of the results from MP2(full)/6-311++G(d,p) computations for the halide ions, alcohols, and halide ion-alcohol complexes (**d** = LanL2DZ, **f** = Stuttgart RLC ECP).

structure	E(MP2) ^a	ZPE + $\Delta C_p(298) + RT$ ^a	S ⁰ ₂₉₈ ^b
F ⁻	-99.697594	0.002360	34.768
Cl ⁻	-459.752769	0.002360	36.586
Br ⁻	-2572.962975	0.002360	39.013
I ⁻ (d)	-11.247856	0.002360	40.428
I ⁻ (f)	-11.284480	0.002360	40.428
CH ₃ OH	-115.483074	0.053885	57.025
CH ₃ CH ₂ OH	-154.702463	0.082377	65.753
F ⁻ (CH ₃ OH)	-215.228221	0.054583	68.935
F ⁻ (CH ₃ CH ₂ OH)	-254.449117	0.082678	76.478
Cl ⁻ (CH ₃ OH)	-575.262891	0.056469	73.468
Br ⁻ (CH ₃ OH)	-2688.469472	0.056564	76.528
I ⁻ (CH ₃ OH) (d)	-126.759658	0.056779	77.464
I ⁻ (CH ₃ OH) (f)	-126.788352	0.056776	77.815

^a hartree

^b cal mol⁻¹ K⁻¹

Table A5 Overview of the results from G3(MP2) computations for the $F^-(HF)_n(CH_3OH)_m$ systems ($n = 0, 1$; $m = 0, 1, 2$).

structure	$H^0_{298}(G3(MP2))^a$
F^-	-99.763933
HF_2^-	-200.191177
HF	-100.355477
CH_3OH	-115.547922
$F^-(CH_3OH)$	-215.358830
$HF_2^-(CH_3OH)$	-315.794870
$(CH_3OH)HF_2^-(CH_3OH)$	-431.334655

^a hartree

Table A6 Overview of the results from HF/6-31+G(d,p), MP2(fc)/6-31+G(d,p), MP2(fc)/6-311+G(3df,2p)//MP2(fc)/6-31+G(d,p), and G2(MP2) computations for the chloride ion-solvent complexes.

structure	E(HF) ^a	ZPE + $\Delta C_{p,298}$ + RT ^a	S ₂₉₈ ^o ^b	E(MP2) ^a	E(MP2//MP2) ^a	H ₂₉₈ ^o (G2(MP2)) ^a
Cl ⁻	-459.539661	0.002360	36.586	-459.671145	-459.765463	-459.797359
CH ₃ Cl	-499.098847	0.039996	55.987	-499.380955	-499.507865	-499.540480
H ₂ O	-76.031230	0.024427	44.953	-76.233108	-76.318219	-76.326232
H ₂ S	-398.675916	0.018323	49.070	-398.811961	-398.893227	-398.920281
NH ₃	-56.200911	0.036625	45.918	-56.392046	-56.450578	-56.453369
PH ₃	-342.455042	0.026956	50.158	-342.580242	-342.646790	-342.670367
SO ₂	-547.175704	0.011109	59.195	-547.698388	-547.950458	-548.003068
Cl ⁻ (CH ₃ Cl)	-958.652787	0.042776	78.005	-959.067324	-959.290336	-959.354819
Cl ⁻ (H ₂ O)	-535.590615	0.027689	64.043	-535.928436	-536.107718	-536.146295
Cl ⁻ (H ₂ S)	-858.230254	0.021087	67.770	-858.502207	-858.679422	-858.737609
Cl ⁻ (NH ₃)	-515.750910	0.039712	67.604	-516.076755	-516.229649	-516.263526
Cl ⁻ (PH ₃)	-802.000805	0.029746	72.708	-802.259507	-802.421120	-802.477324
Cl ⁻ (SO ₂)	-1006.741732	0.013863	74.358	-1007.399956	-1007.750268	-1007.835118

^a hartree

^b cal mol⁻¹ K⁻¹

Table A7 Overview of the results from HF/6-31+G(d,p), MP2(fc)/6-31+G(d,p), MP2(fc)/6-31+G(3df,2p)//MP2(fc)/6-31+G(d,p), and G2(MP2) computations for the solvated S_N2 complexes and transition states.

structure	E(HF) ^a	ZPE + ΔC _p (298) + RT ^a	S ⁰ ₂₉₈ ^b	E(MP2) ^a	E(MP2//MP2) ^a	H ⁰ ₂₉₈ (G2(MP2)) ^a
(H ₂ O)Cl ⁻ (CH ₃ Cl)	-1034.702656	0.069539	112.877	-1035.323511	-1035.630941	
(H ₂ S)Cl ⁻ (CH ₃ Cl)	-1357.342353	0.062985	117.142	-1357.897495	-1358.202437	
(NH ₃)Cl ⁻ (CH ₃ Cl)	-1014.863440	0.081563	115.508	-1015.472361	-1015.753553	
(PH ₃)Cl ⁻ (CH ₃ Cl)	-1301.113446	0.071611	118.926	-1301.655808	-1301.946204	
(SO ₂)Cl ⁻ (CH ₃ Cl)	-1505.853548	0.055812	110.449	-1506.796822	-1507.274514	
[ClCH ₂ Cl] ⁻	-958.628254	0.041241	71.424	-959.039843	-959.265087	-959.334555
[(H ₂ O)ClCH ₂ Cl] ⁻	-1034.672545	0.066041	59.857	-1035.289599	-1035.599531	
[(H ₂ S)ClCH ₂ Cl] ⁻	-1357.313053	0.060591	106.144	-1357.864385	-1358.172025	
[(NH ₃)ClCH ₂ Cl] ⁻	-1014.835915	0.079044	100.919	-1015.441549	-1015.725353	
[(PH ₃)ClCH ₂ Cl] ⁻	-1301.086784	0.070122	114.973	-1301.625411	-1301.917673	
[(SO ₂)ClCH ₂ Cl] ⁻		0.052342	107.247	-1506.754517	-1507.233368	

^a hartree

^b cal mol⁻¹ K⁻¹

Table A8 Overview of the results from HF/6-31+G(d), HF/[6-31+G(d)/LanL2DZ(sp)], MP2(fc)/6-31+G(d), MP2(fc)/[6-31+G(d)/LanL2DZ(sp)], MP2(fc)/6-311+G(3df,2p)//MP2(fc)/6-31+G(d), and MP2(fc)/[6-311+G(3df,2p)/LanL2DZ(spdf)]//MP2(fc)/[6-31+G(d)/LanL2DZ(sp)] computations for bromine and iodine containing S_N2 substrates and solvent molecules.

structure	E(HF) ^a	ZPE + $\Delta C_p(298)$ + RT ^a	S ⁰ ₂₉₈ ^b	E(MP2) ^v	E(MP2//MP2) ^u
Cl ⁻	-459.539661	0.002360	36.586	-459.671145	-459.765463
Br ⁻	-13.014047	0.002360	39.013	-13.134602	-13.163111
H ₂ O	-76.017743	0.024330	44.985	-76.209777	-76.317961
CH ₃ OCH ₃		0.079043	65.206	-154.514629	-154.717446
CH ₃ Cl	-499.094158	0.040440	55.966	-499.357468	-499.507808
CH ₃ Br	-52.552013	0.039861	58.786	-52.803051	-52.904611
CH ₃ I		0.038040	60.812	-51.011475	-51.114039
CH ₂ CNCl	-590.818152	0.041311	68.295	-591.362630	-591.581528
CH ₂ CNBr	-144.275713	0.040799	71.089	-144.803712	-144.979917

^a hartree

^b cal mol⁻¹ K⁻¹

Table A9 Overview of the results from HF/6-31+G(d), HF/[6-31+G(d)/LanL2DZ(sp)], MP2(fc)/6-31+G(d), MP2(fc)/[6-31+G(d)/LanL2DZ(sp)], MP2(fc)/6-311+G(3df,2p)//MP2(fc)/6-31+G(d), and MP2(fc)/[6-311+G(3df,2p)/LanL2DZ(sp)]//MP2(fc)/[6-31+G(d)/LanL2DZ(sp)] computations for bromine and iodine containing (un)solvated S_N2 complexes and transition states.

structure	E(HF) ^a	ZPE + ΔC _p (298) + RT ^a	S ^o ₂₉₈ ^b	E(MP2) ^a	E(MP2//MP2) ^a
Cl ⁻ (H ₂ O)	-535.577464	0.027617	64.059	-535.905483	-536.107407
Cl ⁻ (CH ₃ OCH ₃)		0.081938	82.768	-614.198025	-614.495543
Cl ⁻ (CH ₃ Br)	-512.105246	0.042665	80.442	-512.487557	-512.687048
Cl ⁻ (CH ₃ I)		0.040768	82.475	-510.695661	-510.896252
Br ⁻ (H ₂ O)	-89.047902	0.027503	67.556	-89.362895	-89.502868
Br ⁻ (CH ₃ Cl)	-512.118834	0.043230	81.348	-512.502054	-512.688353
(H ₂ O)Cl ⁻ (CH ₃ Br)	-588.140750	0.069289	113.639	-588.717150	-589.027114
(CH ₃ OCH ₃)Cl ⁻ (CH ₃ I)		0.119924	111.523	-665.215884	-665.625159
(H ₂ O)Br ⁻ (CH ₃ Cl)	-588.151758	0.069770	117.930	-588.728870	-589.025947
[ClCH ₃ Br] ⁻	-512.089202	0.041515	74.132	-512.470467	-512.664758
[ClCH ₃ I] ⁻		0.039772	75.843	-510.683474	-510.879039
[ClCH ₂ CNBr] ⁻	-603.813303	0.042345	83.127	-604.483218	-604.753736
[(H ₂ O)ClCH ₃ Br] ⁻		0.065201	101.476	-588.694536	-588.998621
[(H ₂ O)BrCH ₃ Cl] ⁻		0.065074	97.742	-588.691985	-588.998133
[(H ₂ O)ClCH ₂ CNBr] ⁻	-679.844982	0.069111	103.639	-680.710012	-681.090121

^a hartree

^b cal mol⁻¹ K⁻¹

Table A10 Overview of the results from B3LYP/[6-31+G(d)/LanL2DZ(sp,d)] and B3LYP/[6-311+G(3df,2p)/LanL2DZ(sp,df)]/B3LYP/[6-31+G(d)/LanL2DZ(sp,d)] computations for the CH₃Y and [ClCH₃Y]⁻ systems (Y = Br, I).

structure	E(B3LYP) ^a	ZPE + ΔC _p (298) + RT ^a	S ^o ₂₉₈ ^b	E(B3LYP//B3LYP) ^a
Cl ⁻		0.002360	36.586	-460.303727
CH ₃ Br	-53.087334	0.040081	61.041	-53.104969
CH ₃ I	-51.302833	0.039658	62.953	-51.321417
[ClCH ₃ Br] ⁻	-513.367131	0.041473	73.904	-513.416940
[ClCH ₃ I] ⁻	-511.586282	0.041213	76.065	-511.636563

^a hartree

^b cal mol⁻¹ K⁻¹

Table A11 Overview of the results from B3LYP/6-311+G(d) and B3LYP/6-311+G(3df)/B3LYP/6-311+G(d) computations for halide ions and radicals, and some fluorinated hydrocarbons.

structure	E(B3LYP) ^a	ZPE + $\Delta C_p(298) + RT$ ^a	S ^o ₂₉₈ ^b	E(B3LYP//B3LYP) ^a
F ⁻	-99.888693	0.002360	34.768	-99.886333
Cl ⁻	-460.303727	0.002360	36.586	-460.303727
Br ⁻	-2574.238739	0.002360	39.013	-2574.238308
CF ₃ ⁻	-337.740204	0.013572	65.306	-337.755859
Cl [•]	-460.166882	0.002360	37.964	-460.168403
Br [•]	-2574.105734	0.002360	40.390	-2574.107570
CF ₃ [•]	-337.670663	0.016250	65.482	-337.692899
CF ₄	-437.626380	0.021550	67.570	-437.655648
C ₂ F ₆	-675.483439	0.036458	83.192	-675.528398
CF ₂ Cl ₂	-1158.302211	0.018539	73.429	-1158.328074

^a hartree

^b cal mol⁻¹ K⁻¹

Table A12 Overview of the results from B3LYP/6-311+G(d) and B3LYP/6-311+G(3df)//B3LYP/6-311+G(d) computations for dihalides, trifluoromethyl halides, and their corresponding radical anions (**d** = LanL2DZ(sp) and LanL2DZ(spdf)//LanL2DZ(sp), **f** = LanL2DZ).

structure	E(B3LYP) ^a	ZPE + ΔC _P (298) + RT ^a	S ^o ₂₉₈ ^b	E(B3LYP//B3LYP) ^a
Cl ₂	-920.409625	0.004694	53.410	-920.424073
ClBr	-3034.339451	0.004560	57.403	-3034.359715
Br ₂	-5148.276018	0.004423	58.683	-5148.293512
I ₂ (d)	-22.790944	0.004326	62.372	-22.799226
CF ₃ Cl	-797.963902	0.020017	70.518	-797.991266
CF ₃ Br	-2911.882199	0.019618	73.486	-2911.908297
CF ₃ I (e)	-349.114217	0.019333	75.827	-349.137795
Cl ₂ ^{•-}	-920.526203	0.004320	57.492	-920.528211
ClBr ^{•-}	-3034.461578	0.004297	61.492	-3034.464041
Br ₂ ^{•-}	-5148.396366	0.004274	62.845	-5148.398752
I ₂ ^{•-} (d)	-22.900041	0.004262	66.301	-22.901167
CF ₃ Cl ^{•-}	-797.996534	0.017984	80.869	-798.016771
CF ₃ Br ^{•-}	-2911.929498	0.017939	83.049	-2911.949905

^a hartree

^b cal mol⁻¹ K⁻¹

Table A13 Overview of the results from B3LYP/6-311+G(d) and B3LYP/6-311+G(3df)//B3LYP/6-311+G(d) computations for halide ion-trifluoromethyl halide complexes.

structure	E(B3LYP) ^a	ZPE + $\Delta C_p(298)$ + RT ^a	S ^o ₂₉₈ ^b	E(B3LYP//B3LYP) ^a
F ⁻ (BrCF ₃)	-3011.821132	0.021849	83.493	-3011.846162
F ⁻ (CF ₃ Br)	-3011.782658	0.022549	86.178	-3011.810601
Cl ⁻ (ClCF ₃)	-1258.282677	0.022451	85.937	-1258.310746
Cl ⁻ (CF ₃ Cl)	-1258.271133	0.022920	89.841	-1258.299154
Cl ⁻ (BrCF ₃)	-3372.210507	0.021921	87.769	-3372.235779
Cl ⁻ (CF ₃ Br)	-3372.189795	0.022571	92.253	-3372.216453
Cl ⁻ (ICF ₃)	-809.451333	0.021586	90.076	-809.475677
Cl ⁻ (CF ₃ I)	-809.421420	0.022329	95.178	-809.446226
Br ⁻ (ClCF ₃)	-3372.214228	0.022464	89.069	-3372.242460
Br ⁻ (CF ₃ Cl)	-3372.204030	0.022910	94.078	-3372.232318
Br ⁻ (BrCF ₃)	-5486.141103	0.021915	90.734	-5486.166450
Br ⁻ (CF ₃ Br)	-5486.122607	0.022552	96.801	-5486.149127
Br ⁻ (ICF ₃)	-2923.381617	0.021570	92.912	-2923.405834
Br ⁻ (CF ₃ I)	-2923.354281	0.022308	99.120	-2923.379392

^a hartree

^b cal mol⁻¹ K⁻¹

Table A14 Overview of the results from B3LYP/6-311+G(d) and B3LYP/6-311+G(3df)//B3LYP/6-311+G(d) computations for halide ion-trifluoromethyl halide transition states.

structure	E(B3LYP) ^a	ZPE + $\Delta C_p(298)$ + RT ^a	S ⁰ ₂₉₈ ^b	E(B3LYP//B3LYP) ^a
[FCF ₃ Br] ⁻	-3011.779573	0.021362	81.797	-3011.806367
[ClCF ₃ Cl] ⁻	-1258.232855	0.021440	82.679	-1258.261052
[CF ₃ Cl ₂] ⁻	-1258.157068	0.020597	82.001	-1258.223280
[ClCF ₃ Br] ⁻	-3372.158809	0.021314	85.745	-3372.186699
[CF ₃ ClBr] ⁻	-3372.127769	0.020520	85.168	-3372.152720
[BrCF ₃ Br] ⁻	-5486.085081	0.021196	88.849	-5486.112718
[CF ₃ Br ₂] ⁻	-5486.057163	0.020430	88.128	-5486.081507
[BrCF ₂ Cl ₂] ⁻	-3732.499265	0.019229	89.100	-3732.525456
[CF ₂ Cl ₂ Br] ⁻	-3732.467146	0.019963	88.041	-3732.490170

^a hartree

^b cal mol⁻¹ K⁻¹

Table A15 Overview of the results from MP2(full)/6-311+G(d), G3, and G3(MP2) computations for halide ions and radicals, bihalide neutrals and radical anions, and trifluoromethyl halides and radical anions.

structure	E(MP2) ^a	E(PMP2) ^a	ZPE + $\Delta C_p(298)$ + RT	S ₂₉₈ ⁰ ^a	H ₂₉₈ ⁰ (G3) ^a	H ₂₉₈ ⁰ (G3(MP2)) ^a
Cl ⁻	-459.752769		0.002360	36.586	-460.121239	-459.819999
Cl [•]		-459.636512	0.002360	37.964	-459.988598	-459.684882
Br ⁻	-2572.962976		0.002360	39.013		
Br [•]		-2572.847837	0.002360	40.390		
Cl ₂	-919.340198		0.004742	53.287	-920.067768	-919.461443
Cl ₂ ^{••}		-919.430390	0.004350	57.003	-920.158048	-919.552288
ClBr	-3032.551663		0.004587	57.291		
ClBr ^{••}		-3032.641843	0.004324	60.906		
Br ₂	-5145.761186		0.004742	58.546		
Br ₂ ^{••}		-5145.852758	0.004292	62.164		
I ₂ (d)	-22.544091		0.004335	62.247		
I ₂ ^{••} (d)		-22.637572	0.004269	65.784		
CF ₃ ⁻	-337.087686		0.014058	64.935		
CF ₃ [•]		-337.034592	0.016654	65.338		
CF ₃ Cl						-797.067885
CF ₃ Cl ^{••}						-797.079514

^a hartree

^b cal mol⁻¹ K⁻¹

Table A16 Overview of the results from HF/6-31G(d), MP2(fc)/6-31G(d), and MP2(fc)/6-311+G(2df,p)//MP2(fc)/6-31G(d) computations of (fluorinated) ethers.

structure	E(HF) ^a	ZPE + $\Delta C_p(298)$ + RT ^a	S ^o ₂₉₈ ^b	E(MP2) ^a	E(MP2//MP2) ^a
(CH ₃) ₂ O (rotamer 1)	-154.064745	0.082467	64.812	-154.503455	-154.700252
(CH ₃) ₂ O (rotamer 2)	-154.060636	0.081475	62.871	-154.498840	-154.696013
(CH ₃ CH ₂) ₂ O (rotamer 1)	-323.144885	0.139430	80.462	-232.845644	-233.138386
(CH ₃ CH ₂) ₂ O (rotamer 2)	-232.142233	0.139484	81.317	-232.843495	-233.136090
CF ₃ OCH ₃ (rotamer 1)	-450.675551	0.062997	77.665	-451.613857	-452.128217
CF ₃ OCH ₃ (rotamer 2)	-450.673726	0.062051	74.251	-451.612331	-452.126307
CF ₃ OCH ₃ (rotamer 3)	-450.671367	0.061997	73.402	-451.609375	-452.123310
(CF ₂ H) ₂ O (rotamer 1)	-549.524865	0.058016	81.629	-550.630361	-551.253074
(CF ₂ H) ₂ O (rotamer 2)	-549.526302	0.058085	83.364	-550.631448	-551.256325
(CF ₂ H) ₂ O (rotamer 3)	-549.521840	0.057036	77.772	-550.626798	-551.252583
(CF ₂ H) ₂ O (rotamer 4)	-549.525109	0.058094	82.463	-550.629912	-551.254764
(CF ₂ H) ₂ O (rotamer 5)	-549.526181	0.057151	77.650	-550.631403	-551.256315
(CF ₂ H) ₂ O (rotamer 6)	-549.521537	0.057069	78.709	-550.626798	-551.252587

^a hartree

^b cal mol⁻¹ K⁻¹

Table A16 (continued)

structure	E(HF) ^a	ZPE + $\Delta C_p(298)$ + RT ^a	S ₂₉₈ ⁰ ^b	E(MP2) ^a	E(MP2//MP2) ^a
CF ₃ OCF ₂ H (rotamer 1)	-648.396173	0.050440	85.107	-649.668538	-650.395458
CF ₃ OCF ₂ H (rotamer 2)	-648.396188	0.050497	86.897	-649.668117	-650.396113
CF ₃ OCF ₂ H (rotamer 3)	-648.395820	0.049570	81.167	-649.667895	-650.396933
CF ₃ OCF ₂ H (rotamer 4)	-648.394789	0.049452	79.886	-649.666944	-650.393933
(CF ₃) ₂ O (rotamer 1)	-747.265516	0.042845	88.470	-748.705081	-749.536351

^a hartree^b cal mol⁻¹ K⁻¹

Table A17 Overview of the results from HF/[6-31+G(d)/6-31G(d)], MP2(fc)/[6-31+G(d)/6-31G(d)], and MP2(fc)/[6-311++G(3df,3pd)//6-311+G(2df,p)]//MP2(fc)/[6-31+G(d)/6-31G(d)] computations of chloride ion-(fluorinated) ether complexes.

structure	E(HF) ^a	ZPE + $\Delta C_p(298)$ + RT ^a	S ⁰ ₂₉₈ ^b	E(MP2) ^a	E(MP2//MP2) ^a
Cl ⁻	-459.539661	0.002360	36.586	-459.671145	-459.765463
Cl ⁻ ((CH ₃) ₂ O) (rotamer 1, isomer 1)	-613.609468	0.085358	85.629	-614.175879	-614.477893
Cl ⁻ ((CH ₃) ₂ O) (rotamer 1, isomer 1)	-613.608917	0.084409	82.865	-614.175879	-614.477893
Cl ⁻ ((CH ₃ CH ₂) ₂ O) (rotamer 1)	-691.689037	0.142281	101.369	-692.515550	-692.916819
Cl ⁻ ((CH ₃ CH ₂) ₂ O) (rotamer 2)	-691.687515	0.142305	100.303	-692.515263	-692.916123
Cl ⁻ (CH ₃ OCF ₃) (rotamer 1)	-910.226124	0.065644	97.097	-911.286254	-911.913868
Cl ⁻ (CH ₃ OCF ₃) (rotamer 2)	-910.219777	0.064699	93.471	-911.285012	-911.912240
Cl ⁻ (CH ₃ OCF ₃) (rotamer 3)	-910.217368	0.064609	92.467	-911.282023	-911.909299
Cl ⁻ (CH ₃ OCF ₃) ₂ (rotamer 1)	-1360.913008	0.130388	162.365	-1362.903363	-1364.060752
Cl ⁻ ((CF ₂ H) ₂ O) (rotamer 1)	-1009.075870	0.060715	99.393	-1010.303422	-1011.041836
Cl ⁻ ((CF ₂ H) ₂ O) (rotamer 2, isomer 1)	-1009.079249	0.060770	102.201	-1010.306910	-1011.041836
Cl ⁻ ((CF ₂ H) ₂ O) (rotamer 2, isomer 2)	-1009.074070	0.060758	100.932	-1010.301691	-1011.047683
Cl ⁻ ((CF ₂ H) ₂ O) (rotamer 4)	-1009.088027	0.060871	98.895	-1010.315937	-1011.059633
Cl ⁻ ((CF ₂ H) ₂ O) (rotamer 5)	-1009.079241	0.059830	94.961	-1010.306911	-1011.047682

^a hartree

^b cal mol⁻¹ K⁻¹

Table A17 (continued)

structure	E(HF) ^a	ZPE + ΔC _p (298) + RT ^a	S ⁰ ₂₉₈ ^b	E(MP2) ^a	E(MP2//MP2) ^a
Cl((CF ₂ H) ₂ O) ₂ (rotamer 3)	-1558.633256	0.120916	163.583	-1560.958841	-1562.346196
Cl(CF ₃ OCF ₂ H) (rotamer 1)	-1107.950808	0.053052	102.180	-1109.343683	-1110.188743
Cl(CF ₃ OCF ₂ H) (rotamer 2)	-1107.950218	0.053126	103.678	-1109.322986	-1110.189819
Cl(CF ₃ OCF ₂ H) (rotamer 3)	-1107.949943	0.052185	97.715	-1107.943048	-1110.189823
Cl(CF ₃ OCF ₂ H) (rotamer 4)	-1107.949149	0.052052	97.192	-1109.341866	-1110.187014
Cl-((CF ₃) ₂ O) (rotamer 1)	-1206.802009	0.045631	109.012	-1208.358432	-1209.310048

^a hartree

^b cal mol⁻¹ K⁻¹

Table A18 Overview of the results from HF/6-31G(d), MP2(fc)/6-31G(d), and MP2(fc)/6-311+G(2df,p)//MP2(fc)/6-31G(d) computations of (fluorinated) acetones, and HF/[6-31+G(d)/6-31G(d)], MP2(fc)/[6-31+G(d)/6-31G(d)], and MP2(fc)/[6-311++G(3df,3pd)//6-311+G(2df,p)]//MP2(fc)/[6-31+G(d)/6-31G(d)] computations of chloride ion-(fluorinated) acetone complexes.

structure	E(HF) ^a	ZPE + $\Delta C_p(298)$ + RT ^a	S ₂₉₈ ^o ^b	E(MP2) ^a	E(MP2//MP2) ^a
CH ₃ C(O)CH ₃	-191.962236	0.086928	73.485	-192.523905	-192.749444
CH ₃ C(O)CH ₂ F (rotamer 1)	-290.806707	0.081340	76.358	-291.533605	-291.868284
CH ₃ C(O)CH ₂ F (rotamer 2)	-290.801496	0.081274	79.608	-291.528985	-291.864683
CH ₃ C(OH)CHF	-290.770867	0.081170	74.972	-291.500899	-291.844400
CH ₃ C(O)CF ₃	-488.534634	0.067901	85.185	-489.598368	-490.143962
CF ₃ HC(O)CF ₂ H	-587.359736	0.063259	89.032	-588.588264	-589.243381
CF ₃ C(O)CF ₂ H	-686.226744	0.055912	92.151	-687.624719	-688.384307
CF ₃ C(O)CF ₃	-785.094843	0.048674	95.557	-786.661909	-787.525883
Cl ⁻	-459.539661	0.002360	35.586	-459.671145	-459.765463
Cl ⁻ (CH ₃ C(O)CH ₃)	-651.514823	0.089822	89.260	-652.202721	-652.536240
Cl ⁻ (CH ₃ C(O)CH ₂ F) (rotamer 1)	-750.358933	0.084396	92.644	-751.210819	-751.656553
Cl ⁻ (CH ₃ C(O)CH ₂ F) (rotamer 2)	-750.360396	0.084171	93.419	-751.212268	-751.659123

^a hartree

^b cal mol⁻¹ K⁻¹

Table A18 (continued)

structure	E(HF) ^a	ZPE + $\Delta C_p(298) + RT$ ^a	S ⁰ ₂₉₈ ^b	E(MP2) ^a	E(MP2//MP2) ^a
Cl ⁻ (CH ₃ C(OH)CHF)	-750.335746	0.084040	90.823	-751.194293	-751.650116
Cl ⁻ (CH ₃ C(O)CF ₃)	-948.084236	0.070577	103.098	-949.269976	-949.930480
Cl ⁻ (CF ₃ HC(O)CF ₂ H)	-1046.923401	0.066095	104.335	-1048.273085	-1049.051400
Cl ⁻ (CF ₃ C(O)CF ₂ H)	-1145.786170	0.058720	106.554	-1147.306697	-1148.192931
Cl ⁻ (CF ₃ C(O)CF ₃)	-1244.644499	0.051243	106.970	-1246.341653	-1247.335911

^a hartree

^b cal mol⁻¹ K⁻¹

Table A19 Overview of the results from HF and MP2(fc) computations for chloride ion and radical using various basis sets.

basis set	Cl [•]		Cl ⁻		EA(Cl [•]) ^b	
	E(HF) ^a	E(PMP2) ^a	E(HF) ^a	E(MP2) ^a	HF	MP2
6-31G(d)	-459.447964	-459.553533	-459.525997	-459.652104	2.12	2.68
6-31+G(d)	-459.448712	-459.555218	-459.539660	-459.671145	2.48	3.16
6-311G(d)	-459.473065	-459.586248	-459.564046	-459.700264	2.48	3.10
6-311+G(2df)	-459.477073	-459.632186	-459.565425	-459.759138	2.41	3.46
6-311+G(3df)	-459.477192	-459.635319	-459.565423	-459.765463	2.40	3.54

^a hartree

^b eV

Appendix B

Gaussian input files

Appendix B1

Example Frequency Calculation

%chk=CH2CNClHF631+Gd.chk

rhf/6-31+g(d) Opt=(MaxCycle=100) Freq=(ReadIso,NoRaman) NoSym

CH2CNCl HF/6-31+G(d)

0 1

C

H 1 B1

H 1 B2 2 A1

Cl 1 B3 2 A2 3 D1

C 1 B4 2 A3 3 D2

N 5 B5 2 A4 1 D3

B1 1.070000

B2 1.070000

B3 1.760000

B4 1.540000

B5 1.160000

A1 109.471203

A2 109.471231

A3 109.471203

A4 151.992219

D1 119.999993

D2 -120.000015

D3 -180.000000

298.15 1.0 0.8970

12

1

1

35

12

14

Appendix B2

Example Transition State Calculation

%chk=FCF3BrTSB3LYP6311+Gd.chk

#P rb3lyp/6-311+g(d) Opt=(Z-Matrix,TS,NoEigenTest,NRScale) Freq SCF=Direct
NoSym

[FCF3Br]- B3LYP/6-311+G(d)

-1 1

C

F	1	B1				
F	1	B2	2	A1		
F	1	B3	2	A2	3	D1
F	1	B4	2	A3	3	D2
Br	1	B5	3	A4	2	D3

B1	2.100000
B2	1.350000
B3	1.350000
B4	1.350000
B5	2.500000
A1	90.000000
A2	90.000000
A3	90.000000
A4	90.000000
D1	120.000000
D2	-120.000000
D3	180.000000

Appendix B3

Example ECP Calculation

```
%chk=CH3BrMP2631+GdLanL2DZspd.chk  
# rmp2/gen Pseudo=Read Opt=(MaxCycle=100) NoSym
```

```
CH3Br MP2(fc)/[6-31+G(d)/LanL2DZ(sp)]
```

```
0 1
```

```
C
```

```
H      1      B1
```

```
H      1      B2  2      A1
```

```
H      1      B3  2      A2  3      D1
```

```
Br     1      B4  2      A3  4      D2
```

```
B1      1.070000
```

```
B2      1.070000
```

```
B3      1.070000
```

```
B4      1.910000
```

```
A1     109.471251
```

```
A2     109.471218
```

```
A3     109.471203
```

```
D1     -120.000014
```

```
D2     -120.000001
```

```
C H 0
```

```
6-31+g(d)
```

```
****
```

```
Br 0
```

```
S 2 1.00
```

```
  1.15900000   -3.03787690
```

```
  0.71070000   3.37037350
```

```
S 1 1.00
```

```
  0.19050000   1.00000000
```

```
P 2 1.00
```

```
  2.69100000  -0.11898000
```

```
  0.44460000   1.04244710
```

```
P 1 1.00
```

```
  0.13770000   1.00000000
```

```
S 1 1.00
```

```
  0.06400000   1.00000000
```

```
P 1 1.00
```

```
  0.04020000   1.00000000
```

```
D 1 1.00
```

```
  0.39100000   1.00000000
```

Br 0

Br-ECP 3 28

F POTENTIAL

4

1	213.61439690	-28.00000000
2	41.05853800	-134.92688520
2	8.70865300	-41.92719130
2	2.60746610	-5.93364200

S-F POTENTIAL

4

0	54.19806820	3.00000000
1	32.90535580	27.34306420
2	13.67448900	118.80288470
2	3.03411520	43.43548760

P-F POTENTIAL

5

0	54.25633400	5.00000000
1	26.00955930	25.05042520
2	28.20129950	92.61574630
2	9.43410610	95.82490160
2	2.53217640	26.26849830

D-F POTENTIAL

5

0	87.63287210	3.00000000
1	61.73733770	22.55335570
2	32.43851040	178.12419880
2	8.75371990	76.99241620
2	1.66331890	9.48182700

Appendix B4

Example Scan Calculation

%chk=FCF3BrB3LYP6311+GdScan1.chk

rb3lyp/6-311+g(d) Opt=(ModRedundant,MaxCycle=100) NoSym

[FCF3Br]- B3LYP/6-311+G(d) scan C-F

-1 1

C

F 1 2.243888

F 1 1.297756 2 81.896315

F 1 1.297603 2 81.834384 3 120.002270

F 1 1.297603 2 81.834384 4 119.995459

Br 1 2.292500 4 98.144756 5 -103.783264

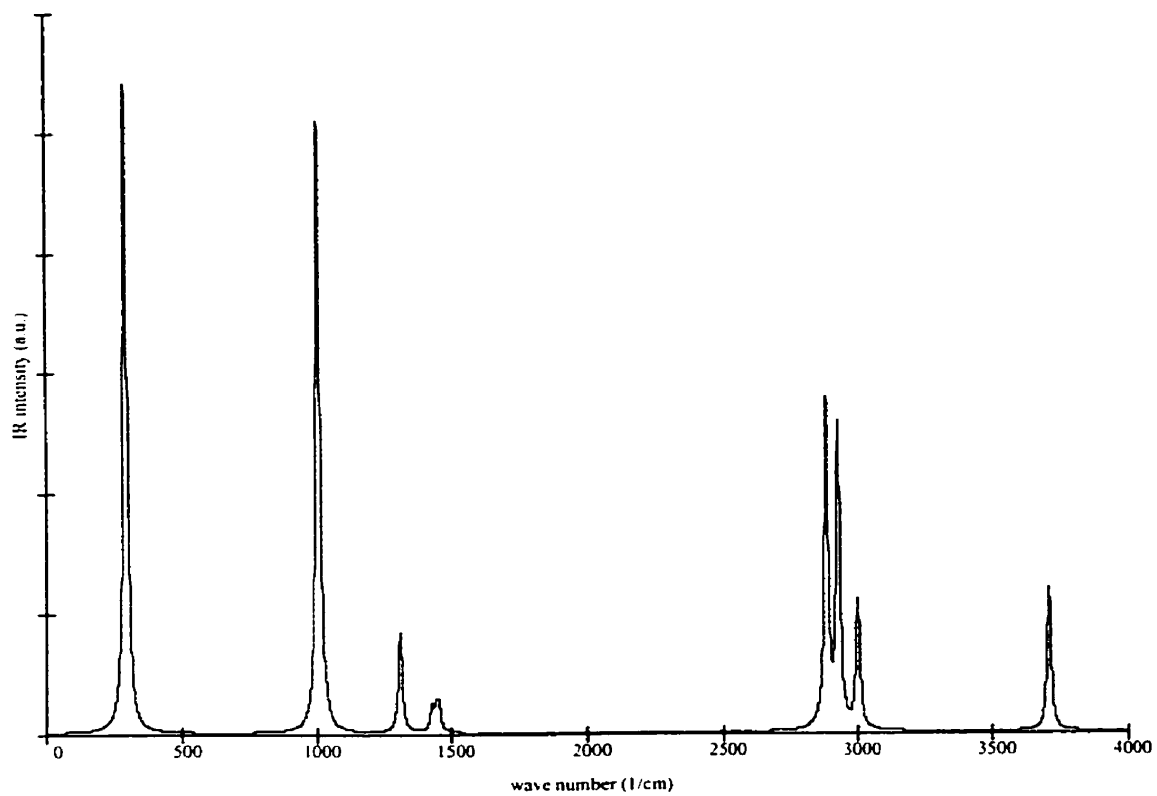
1 2 2.20 S 50 0.10

Appendix C

Simulated IR spectra

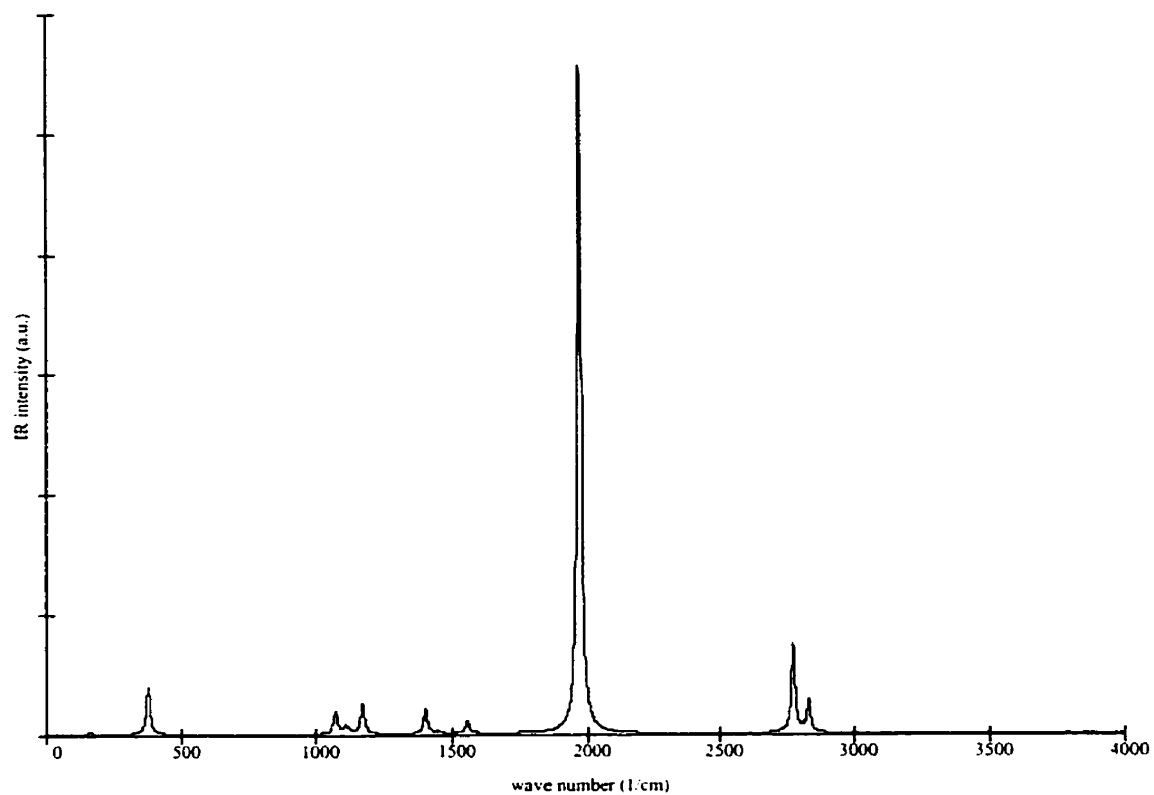
Appendix C1

Simulated scaled B3LYP/6-311+G(d,p) IR spectrum of CH₃OH.



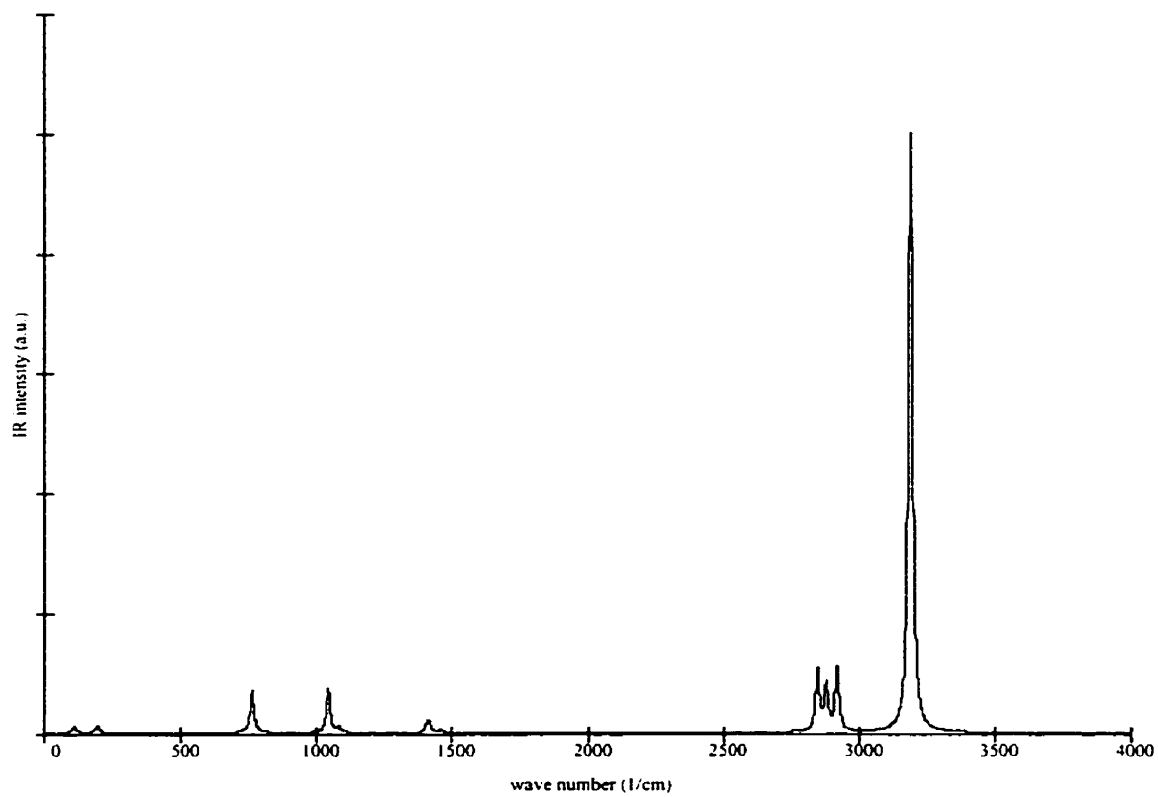
Appendix C2

Simulated scaled B3LYP/6-311+G(d,p) IR spectrum of $F^-(CH_3OH)$.



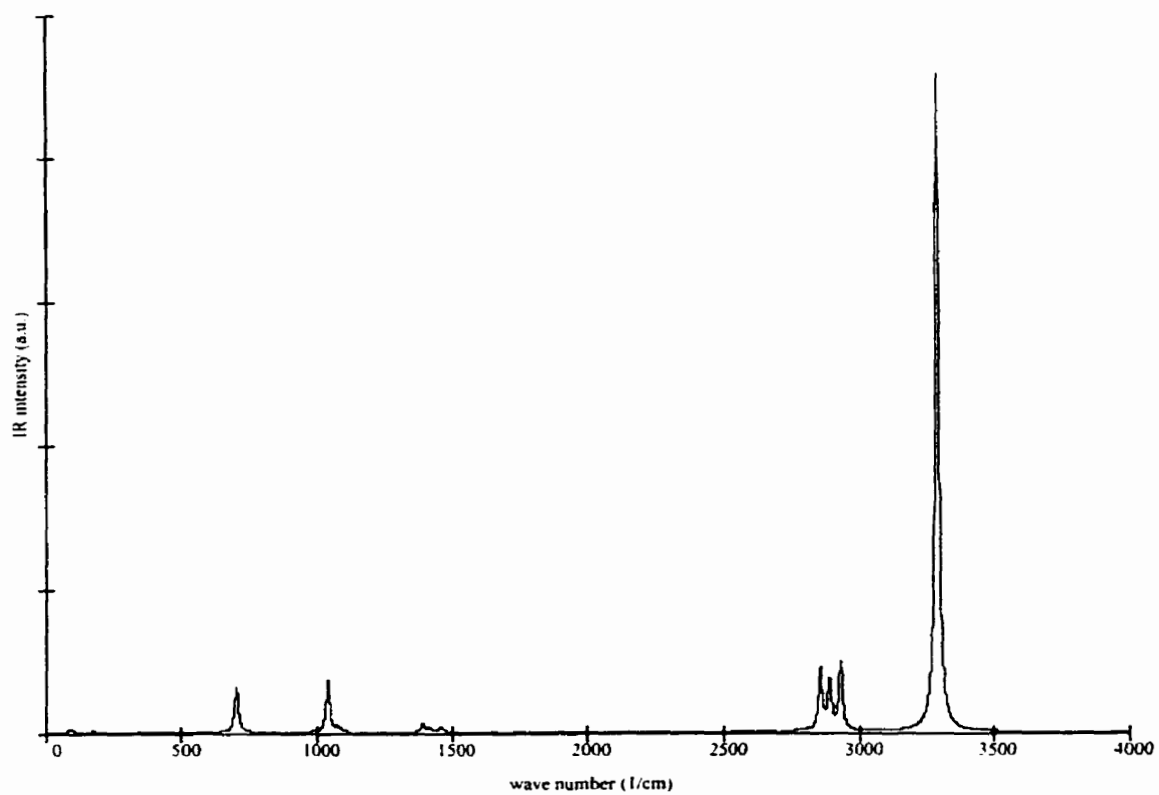
Appendix C3

Simulated scaled B3LYP/6-311+G(d,p) IR spectrum of $\text{Cl}^-(\text{CH}_3\text{OH})$.



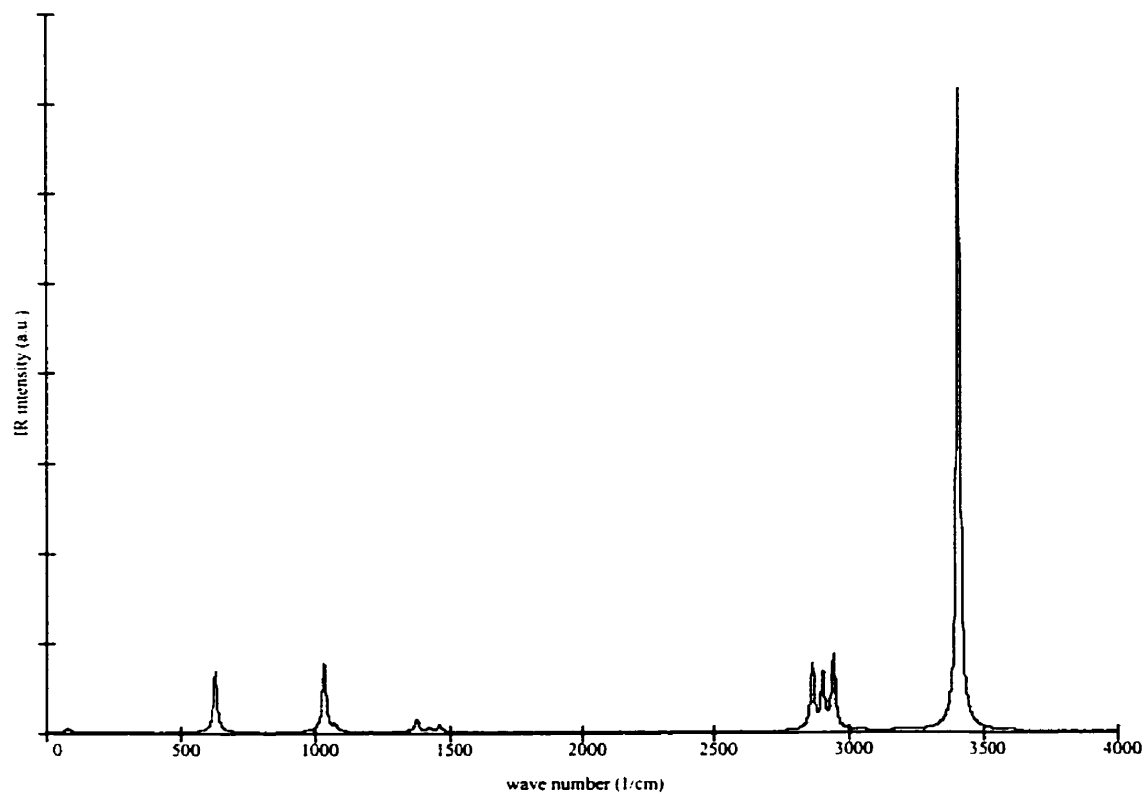
Appendix C4

Simulated scaled B3LYP/6-311+G(d,p) IR spectrum of $\text{Br}^-(\text{CH}_3\text{OH})$.



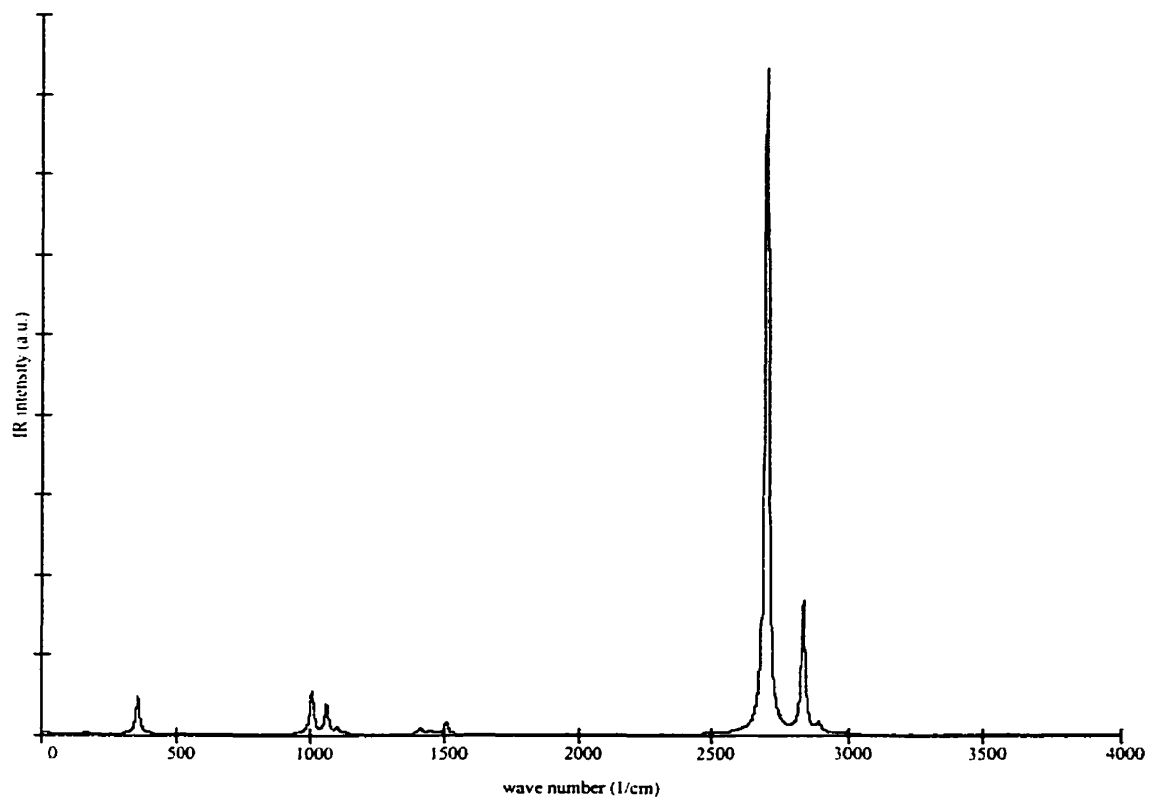
Appendix C5

Simulated scaled B3LYP/[Stuttgart RLC ECP/6-311+G(d,p) IR spectrum of $\Gamma^-(\text{CH}_3\text{OH})$.



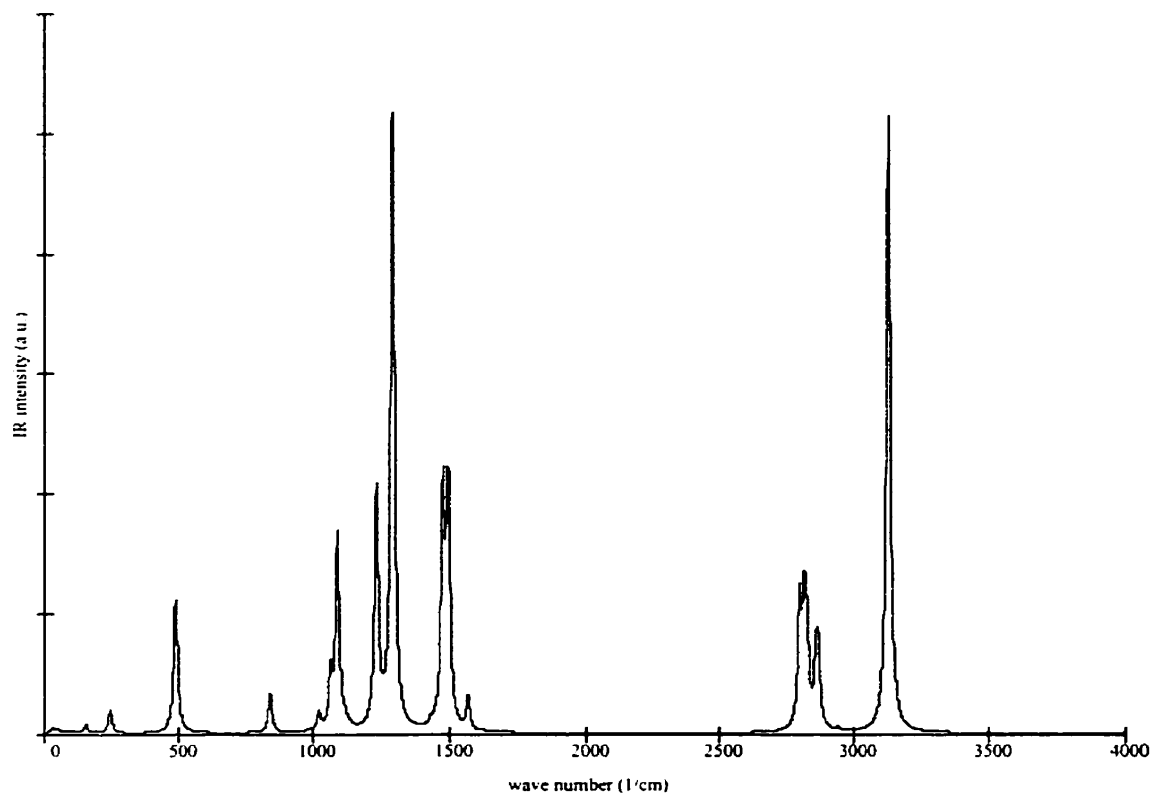
Appendix C6

Simulated scaled B3LYP/6-311+G(d,p) IR spectrum of $(\text{CH}_3\text{OH})\text{F}^-(\text{CH}_3\text{OH})$.



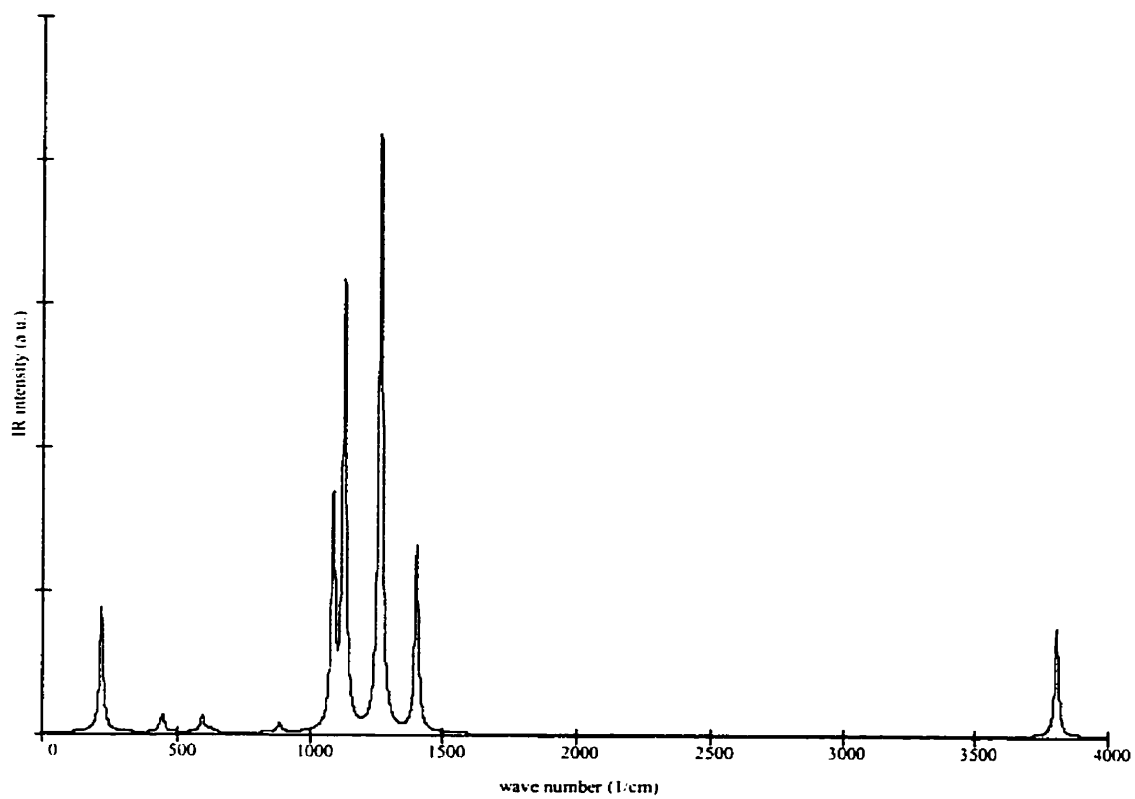
Appendix C7

Simulated scaled B3LYP/6-311+G(d,p) IR spectrum of $F^-(CH_3OH)(CH_3OH)$.



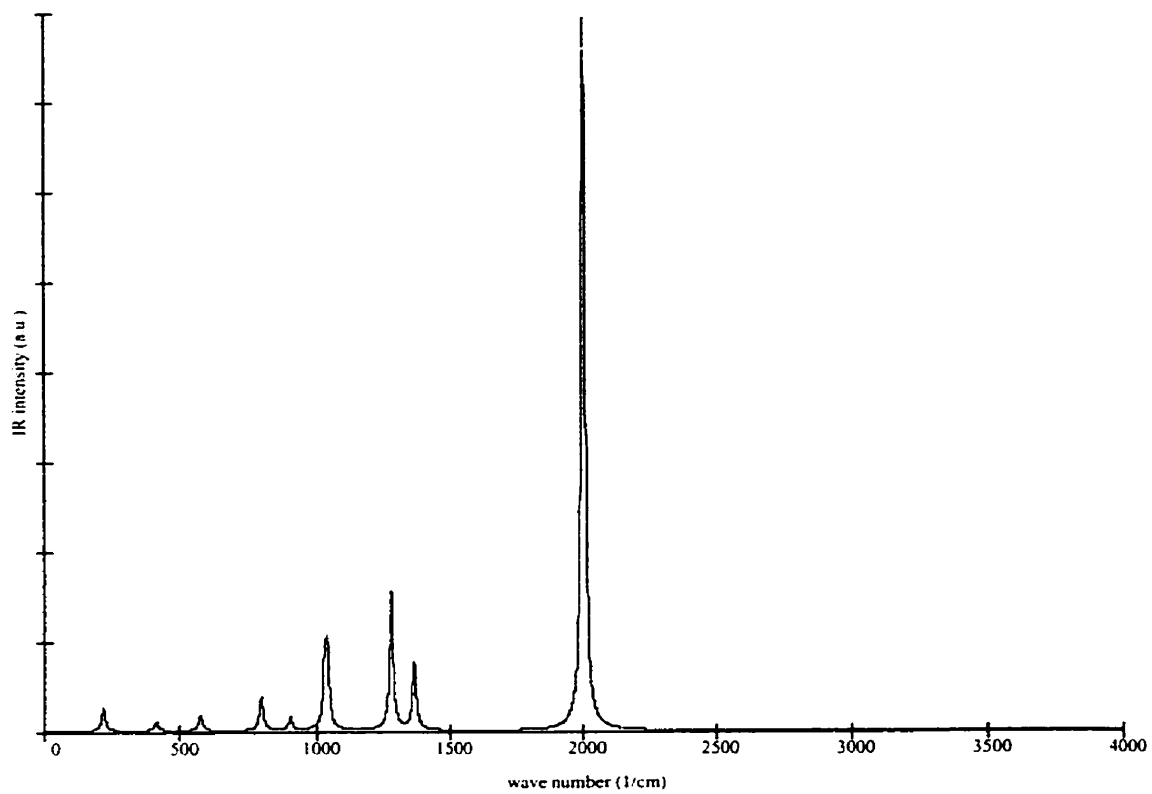
Appendix C8

Simulated unscaled B3LYP/6-311++G(3d,3p) IR spectrum of CF₃OH.



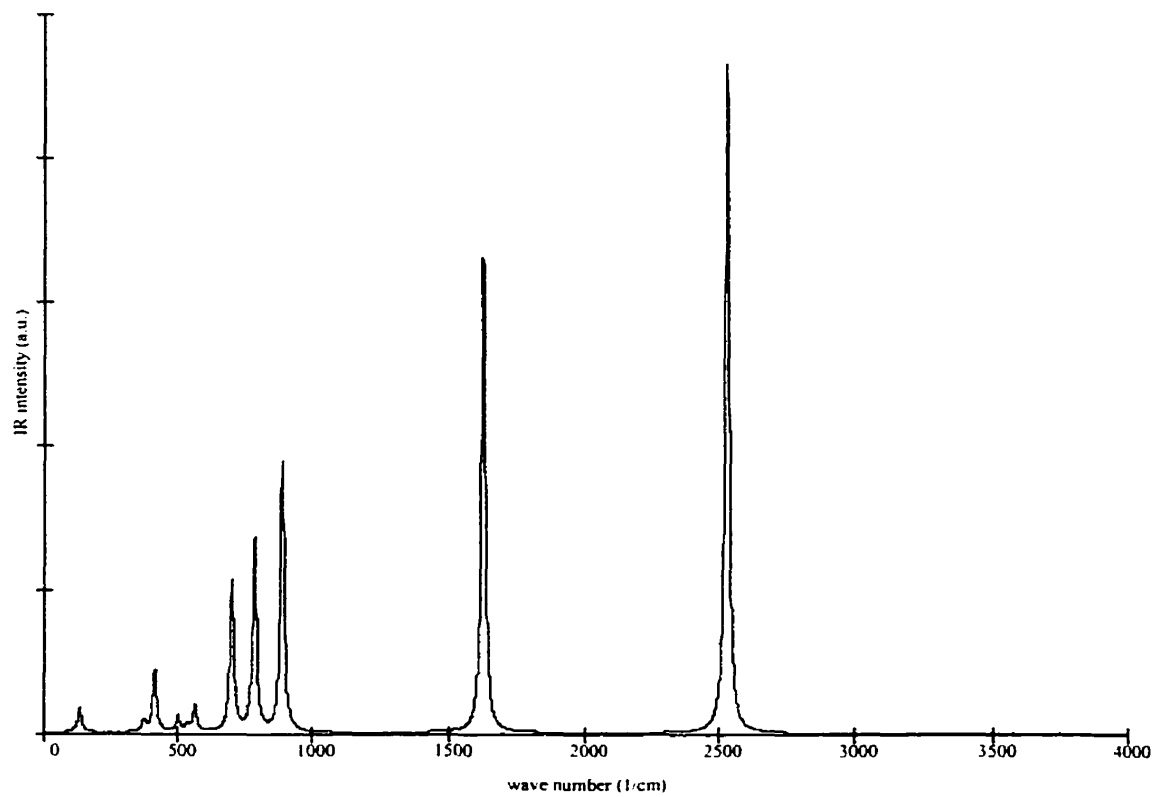
Appendix C9

Simulated scaled MP2(fc)/6-31+G(d,p) IR spectrum of $\text{Cl}^-(\text{CF}_3\text{OH})$.



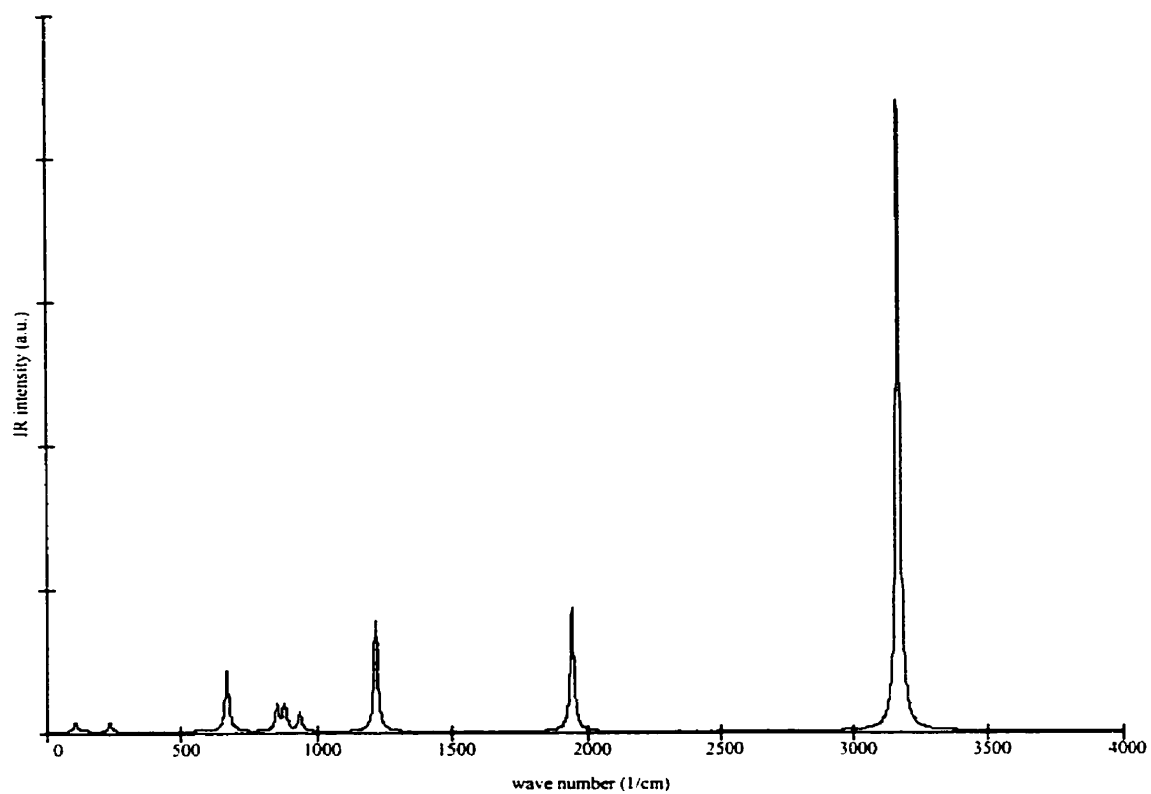
Appendix C10

Simulated scaled MP2(fc)/6-31+G(d,p) IR spectrum of $(\text{ClH})\text{CF}_3\text{O}^-$.



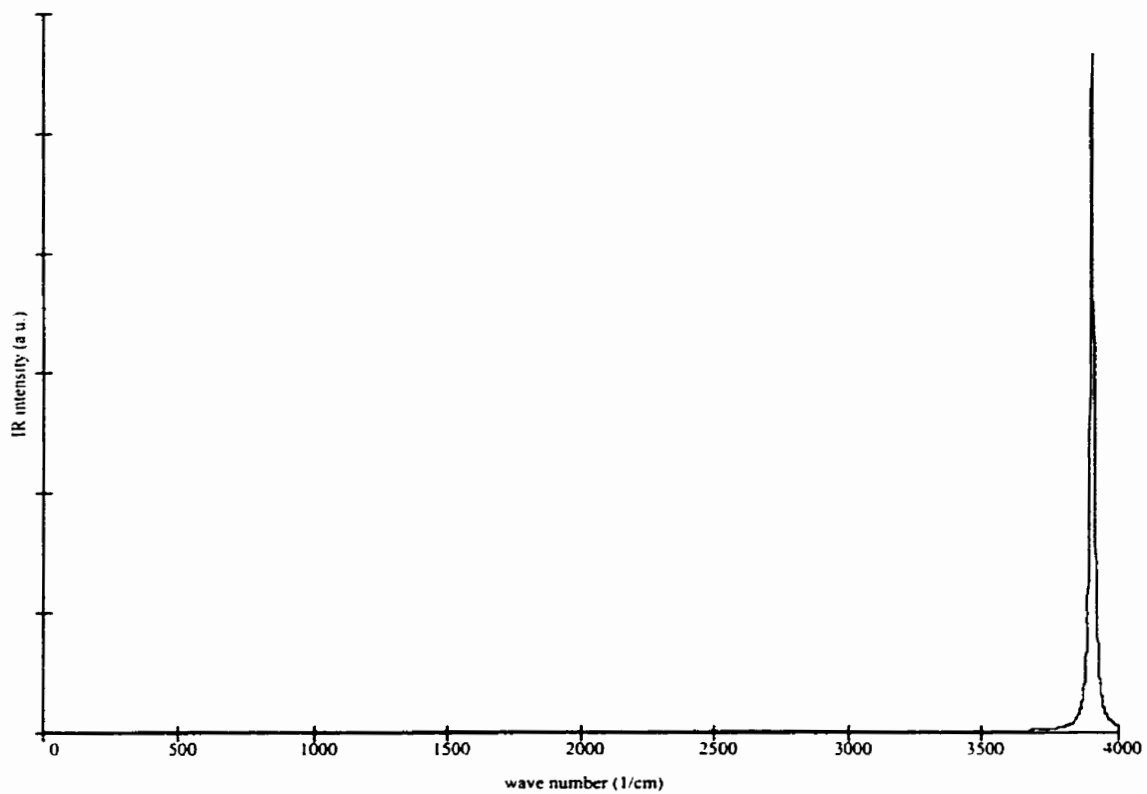
Appendix C11

Simulated scaled MP2(fc)/6-31+G(d,p) IR spectrum of (FH)Cl⁻(CF₂O).



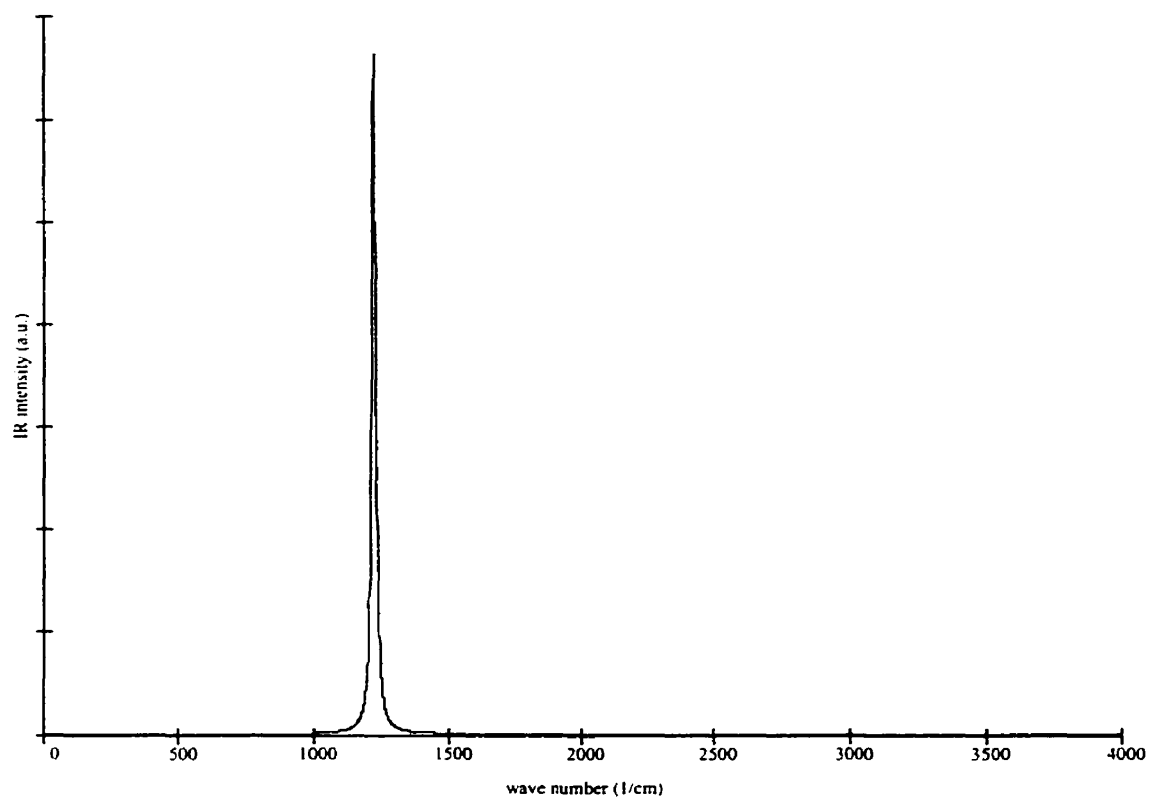
Appendix C12

Simulated scaled HF/6-31G(d) IR spectrum of HF.



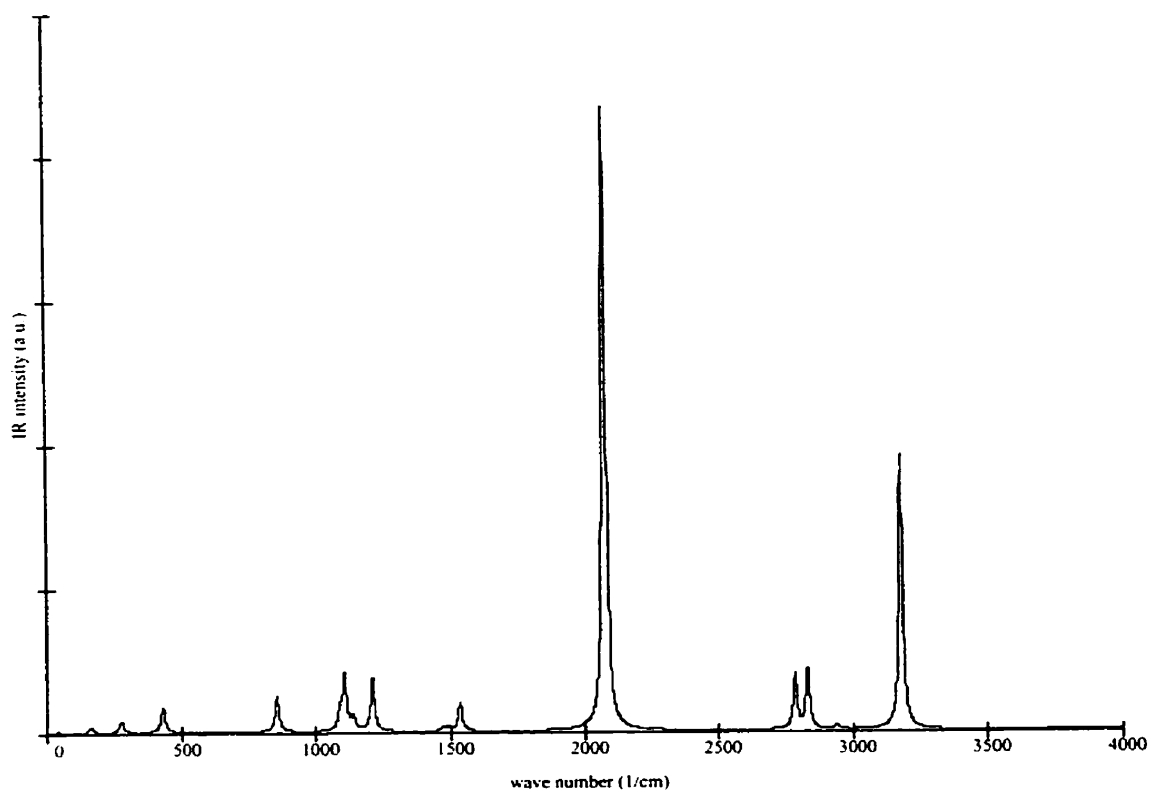
Appendix C13

Simulated scaled HF/6-31G(d) IR spectrum of HF_2^- .



Appendix C14

Simulated scaled HF/6-31G(d) IR spectrum of $\text{HF}_2^-(\text{CH}_3\text{OH})$.



Appendix C15

Simulated scaled HF/6-31G(d) IR spectrum of $(\text{CH}_3\text{OH})\text{HF}_2^-(\text{CH}_3\text{OH})$.

